MONTAN UNIVERSITÄT
WWW.UNILEOBEN.AC.AT

DISSERTATION

Genesis of orogenic gold in the Latimojong district, South Sulawesi, Indonesia

Andy Yahya Al Hakim
(M.Sc. der Institute of Technology Bandung)

Montanuniversität Leoben
Department Angewandte Geowissenschaften und Geophysik
Lehrstuhl für Geologie und Lagerstättenlehre

Supervisor: Univ.-Prof.Dr.mont. Frank Melcher

Leoben, October 2017

Affidavit:

I declare in lieu of oath, that I wrote this thesis and performed the associated research myself, using only literature cited in this volume

Leoben, 15 October 2017

Andy Yahya Al Hakim

Al Inshirah
[94:5] so surely along the hardship there is ease.
[94:6] surely with that hardship comes more ease.

ABSTRACT

The Awak Mas and Salu Bullo gold deposits are situated in the Latimojong Metamorphic Complex, Sulawesi, Indonesia. These deposits are hosted in pumpellyite- to greenschist-facies metasedimentary and metavolcanic rocks. Total gold contents equals to 50 tonnes Au at 1.4 ppm. The present study focusses on the petrographical, mineralogical, and geochemical study of metasedimentay and metavolcanic rocks, as well as the characteristics of ore-forming fluids, concluding with a genetic model of mineralisation and a metamorphic *P-T* path of the ore hosting formations.

Based on the mineral compositions of chromian spinel, clinopyroxene and whole-rock data, it is inferred that the metavolcanic rocks at Latimojong formed in a suprasubduction zone (SSZ) environment. Chromian spinel spans a wide compositional range (Al- and Cr-rich) and may have crystallized from IAB-type melts at different stages of fractional crystallization. Growing clinopyroxene phenocrysts in the melt trapped floating chromite crystals on their way upward.

Metabasites and meta-andesites have low REE concentrations and flat chondrite-normalized patterns. Metasedimentary rocks show negative Eu anomaly, high LREE/HREE ratios, consistent with derivation from continental crust. The results of this study do not support the existence of ophiolite rocks body within the mineralized area in the Latimojong Metamorphic Complex.

All microscopically visible gold occurs as inclusions within sulphide (mainly pyrite) or as crack filling, less commonly free grains occur in quartz. Grain sizes of gold ($Au_{85-88}Ag_{12-15}$) range from submicroscopic (<2 µm) to 50 µm. Mineralized veins contain chalcopyrite, fahlore, often associated with covellite, galena and sphalerite. Albite, dolomite-ankerite, chlorite, and white mica are the alteration minerals.

The results of in situ laser ablation-inductively coupled mass spectrometry and electron microprobe analyses in different types of pyrite provide evidence for trace element enrichment of Co, Ni, As and low Cu, Zn, Se, Bi, Au, Ag. Spot analyses of plagioclase feldspar show an increasing Ce-anomaly and decreasing Eu-anomaly with increasing distance from the vein. Positive Eu-anomaly in albite

may indicate reducing hydrothermal fluids and implying significant plagioclase fractionation.

The chlorite geothermometer applied to metamorphic host rocks indicates temperatures ranging from 227-346°C. Formation temperature calculations using carbonaceous materials suggest that the metamorphic conditions vary between 316-395°C. Oxygen and carbon isotopes of carbonates indicate that the isotopic composition of altered host rock shifted towards lighter values during interaction with hydrothermal fluids, resulting in distinctive isotopic ratios between hydrothermally altered and unaltered host rock.

Fluid inclusions in quartz and carbonate veins are dominated by H_2O-bearing fluids. Minor aqueous-carbonic phases ($CO_2 \pm N_2$) were detected with a mole fraction <0.15. The gold bearing fluids were mainly homogenously trapped at approximately 180-250°C and 0.8-1.3 kbar, corresponding to a depth <5 km. The salinity of mineralized quartz veins is between 1.4 and 7.3 eq mass% NaCl. Trapping conditions of fluids in the dolomite and barren quartz are at 165-387°C and <1.15 kbar. The bisulphide complex is considered as the main ligand for gold deposition. Iron-rich and carbonaceous rocks prove to be the important geochemical traps for the release of gold from hydrothermal solution.

It is suggested that there is no contribution of intrusive rocks to the gold mineralization in Awak Mas and Salu Bullo, as the halogen data do not fit to magmatic sources. The fluids circulating in the Latimojong are comparable to deep-seated fluids with some contribution of shallow water, probably meteoric water. Metamorphic reactions in the metasedimentary rocks during the retrogression stage are considered as the main source of ascending fluids to form the Au-mineralization at Latimojong.

ZUSAMMENFASSUNG

Die Awak Mas und Salu Bullo Goldlagerstätten befinden sich im Latimojong-Komplex, in Sulawesi, Indonesien. Die Lagerstätten werden durch Pumpellyit- bis grünschieferfazielle Metasedimente und Metavulkanite aufgebaut. Der Gesamtresourcen der Lagerstätte werden auf 50 t Gold geschätzt. Der Durchschnittsgehalt beträgt 1,4 ppm Au.

Der Fokus dieser Arbeit liegt auf der petrographischen, mineralogischen und geochemischen Untersuchung der Metasedimente und Metavulkanite. Des Weiteren werden die Eigenschaften der mit der Vererzung in Verbindung gebrachten Fluide, die Genese im Allgemeinen und die *P-T*-Bedinungen der Gesteine untersucht.

Die Mineralzusammensetzung der Chrom-Spinelle und der Klinopyroxene, sowie die Gesamtgeochemie der Gesteine, legen eine Bildung der Metavulkanite in einer Suprasubduktionszone nahe. Die in ihrer Zusammensetzung stark varierenden Chrom-Spinelle können durch mehrere Phasen einer fraktionierten Kristallisation aus einer Magmenkammer entstanden sein. Einige Chrom-Spinelle wurden während der Kristallisation von Klinopyroxen-Phänokristallen aus einer Schmelze vom Inselbogenbasalttyp eingefangen.

Die Metabasite und Metaandesite weisen geringe REE-Konzentration auf und weichen nur geringfügig von der Geochemie von Chondriten ab. Die Metasedimente sind geprägt durch eine negative-Eu-Anomalie, mit hohen LREE/HREE-Verhältnissen, analog zur kontinentalen Kruste. Die Ergebnisse dieser Arbeit widerlegen die Existenz eines Ophiolitkörpers innerhalb der untersuchten, mineralisierten Gesteine des Latimojong-Komplexes.

Das im Mikroskop erkennbare Gold liegt als Einschluss im Sulfid, hauptsächlich Pyrit, oder in Rissen vor, selten als freies Gold in Quarzgängen. Die Korngröße des Goldes (Au85-88Ag12-15) reicht von < 2 µm bis 50 µm. Mineralisierte Gänge enthalten Chalkopyrit, Fahlerz, oft assoziiert mit Covellin, Galenit und Sphalerit. Als Alterationsminerale treten Albit, Dolomit-Ankerit, Chlorit und Muskovit auf.

Die Ergebnisse der LA-ICP-MS und Mikrosonden-Messungen an Pyriten belegen Anreicherungen von Spurenelementen, wie Co, Ni, As und Abreicherungen an Cu, Zn, Se, Bi, Au, Ag. Punktmessungen der Plagioklase zeigen eine Ce-

Anomalie, die mit zunehmendem Abstand zu mineralisierten Gängen zunimmt. Entgegengesetzt dazu verhält sich die Eu-Anomalie, die mit zunehmenden Abstand abnimmt. Die positive Eu-Anomalie impliziert hydrothermale Fluide, sowie signifikante Plagioklas-Fraktionierung.

Die Chloritphasen dienen als Geothermometer und legen einen Temperaturbereich von 227-346 °C für die Metamorphose nahe. Berechnungen anhand von Ramanspektren der Graphitphasen ergeben einen Temperaturbereich von 315-395°C für den Höhepunkt der Metamorphose. Isotopenverhältnisse von Sauerstoff und Kohlenstoff der Karbonate ermöglichen eine klare Unterscheidung zwischen alterierten und nicht alterierten Gesteinen.

In Quarz und Karbonaten befinden sich wasserhältige Flüssigkeitseinschlüsse, die gelöstes CO_2 ± N_2 im Bereich < 0,15 Mol-% aufweisen. Die goldhaltigen Fluide wurden hauptsächlich bei einer Temperatur von 180-250 °C und 0,8-1,3 kbar, was einer Tiefe von < 5 km entspricht, eingeschlossen. Die Salinität der mineralisierten Quarzgänge liegt zwischen 1,4-7,3 äqu. Massen-% NaCl. Einschlussbedingungen der Fluide im Dolomit und unmineralisierten Quarz liegen im Bereich von 165-387 °C und < 1,15 kbar. Der Bisulfid-Komplex wird als der Hauptligand für das Gold angesehen. Eisenreiche und karbonatische Gesteine sind die wichtigsten Faktoren, die zur Ausfällung des Goldes aus den hydrothermalen Lösungen geführt haben.

Messungen an Halogenen widerlegen einen Bezug von Intrusivgesteinen zur Mineralisierung in Awak Mas und Salu Bullo. Es is anzunehmen, dass die Metamorphose zur tiefliegenden Freisetzung der Fluide führte, die in dem System zirkulierten. Dabei kam es zur Vermischung mit Oberflächenwässern und einer Ausfällung im Gold und Sulfide in Quarzgängen Vererzung.

ACKNOWLEDGEMENTS

First and above all, I would like to thank God the almighty, for protection and abilility to proceed successfully. The following document summarizes three years of effort and achievement. It is a privilege to express due acknoledgement and appreciation to the following people for their invaluable assistance in the completion of this study.

I would like to thank my supervisor, Prof. Dr.mont. Frank Melcher for his invaluable guidance, idea, patience and support. I have learnt a lot from him about science, work, and ethics during my PhD. As a mineralogist, economic geologist and Alps enthusiast, he has been very influential in helping me to become the person that I am today, and for that I am very grateful. “No matter what we are going through, there is always a light at the end of tunnel”, that is what I remember from him when he closed his session at the SGA Meeting 2017 in Québec City. Without his continual support and ceaseless encouragement, I would not have been able to accomplish this work.

Thank you to Prof. Dr.phil. Walter Prochaska for the contributions, ideas and helpful discussions during this research. I appreciate the great help from Prof. Dr.rer.nat. Gerd Rantitsch, Ass.Prof. Dr.mont. Heinrich Mali and Prof. Dr. Ronald Bakker, for the helpful discussion and their interest in this dissertation theme. I appreciate the great support of Dr. Federica Zaccarini for EMPA analyses, Dr. Achim Bechtel for stable isotope analyses, Prof. Dr.mont. Thomas Meisel for whole-rock geochemical analyses and their interpretation, Prof. Sarah-Jane Barnes and Dany Savard (UQAC) for providing the pyrite standard materials for LA-ICP-MS.

I would like to thank Peter Onuk for the assistance in LA-ICP-MS, Sabine Feuchter for her help on thin section preparation, Brigitte Mang for kindness and assistance. Monika Feichter, Birgit Kain-Bückner, Gustav Hanke are acknowledged for their great friendship and support. Maik Zimmermann is thanked for his assistance with the microprobe. I have a wonderful atmosphere during working together during my stay in Leoben.

I would like to thank PT Masmindo Dwi Area (MDA) for providing access to the mine site, accomodation and allowing to collect samples. Heru Widyanarko, Wahyu Diartito, Nita Harsoyo, Hirawan, Yulianus and the staff of the PT MDA are thanked for their assistance.

I would also like to thank ASEA-UNINET-OeAD for providing doctorate scholarship from 2015-2018 and field grant for me and Prof. Melcher in 2016. Lisa Genger and teams are thanked for their kindness.

Thanks to my valuable friends in Leoben: Anda, Mukmin, Imelda, Yani, Ria, Riki, Bethel, Fahim, Anung, Joel, Hamid, Ghadeer, David, Claudia, Heidi, Roland and

Tizi. Max Berger is thanked for translating the abstract into German. Ernowo is acknowledged for the fruitful discussion.

Lecturers and colleagues in the Mining Engineering Department of Institute of Technology Bandung are thanked for their encouragement. All my teachers and friends, who have suppported me and not mentioned here, are gratefully acknowledged.

Much appreciation goes to my family, Abah Eddy and Sukis, Umi Anis, Ibu Zulaikha, Rofi, Padi, Mas Yudi, Mbak Lusy for their pray, support, and love.

Finally, I thank a special to Vidya and Aqila, who have been very tolerant over the years and for the endless support.

Leoben, October 2017

TABLE OF CONTENTS

LIST OF FIGURES

LIST OF TABLES

LIST OF UNITS AND ABBREVIATIONS

a.p.f.u.	atoms per formula unit
ppm	parts per million
ppb	parts per billion
vol	volume
V_m	molar volume
wt%	weight percent
χ	chemical compostition
µm	micrometer
mm	millimeter
°C	degree celcius
g/cm^3	density of fluid inclusions as gram per centimeter cubic
eq. mass% NaCl	salinity of fluid inclusions

n	number/quantity
b.d.l.	Below Detection Limit
EMPA	Electron Microprobe Analysis
IAB	Island-Arc Basalts
i.e.	*id est*; for example
LA-ICP-MS	Laser Ablation Inductively Coupled Plasma Mass Spectrometry
LILE	Large Ion Litophile Elements
MORB	Mid-Ocean Ridge Basalts
OIB	Oceanic Island Basalts
P -T	Pressure Temperature
REE	Rare Earth Elements
LREE	Light Rare Earth Elements
HREE	High Rare Earth Elements
REY	Rare Earth Elements + Yttrium
HFSE	High Field Strength Elements
RSCM	Raman Spectroscopy of Carbonaceous Materials
SEM-EDX	Scanning Electron Microscope Energy Dispersive X-ray Analysis
s.d.	Standard deviation
T_m ; T_h	Final dissolution temperature; homogenization temperature of fluid inclusions
WDS	Wavelength Dispersive Spectroscopy
XRF	X-ray Fluorescence Spectroscopy

1. INTRODUCTION

The Indonesian archipelago, 13,000 islands stretching for a distance of 5,200 km, contains Cenozoic volcano-plutonic arcs. These arcs range approximately 9,000 km in total length with 80% comprising segments containing known mineral deposits (Carlile and Mitchell 1994). The archipelago is situated along a complex convergence zone along the Southeastern margin of the Eurasian plate, and along the Eastern part of Indonesia, which is considered as a part of the Pacific and Australian plates. The motions of these plates are known and their positions provide limits to the zone within which the South East Asian collage of micro plates and sub-plate fragments can be moved in reconstructions (Hamilton 1979; Hall 2002).

The archipelago can be simply divided into two major tectonic settings: the western region, also known as the Sunda shelf or Sundaland, and the eastern region, also called the Sahul Shelf (Katili 1974). The complex magmatism and plate motions resulted in contrasting features between West and East Sulawesi. The tectonic activities in this arc system developed a significant number of metal prospects that vary in each metallogenic province within the islands. Some of the gold mining sites in South Sulawesi are located in a mountainous area in the Luwu Regency. The detailed drilling in the Latimojong Mountains from the early nineties until 2012 resulted in discovery of three main prospects: Awak Mas, Sallu Bullo and Tarra.

There have been numerous models for the origin of the Awak Mas and Salu Bullo gold deposits, including meta-sedimentary hosted disseminated gold or mesothermal gold deposit (Querubin and Walters 2012; Hakim and Melcher 2015; Harjanto et al. 2015; Hakim and Melcher 2016a, 2016b; Harjanto et al. 2016a; Harjanto et al. 2016b; Tuakia et al. 2016; Hakim and Melcher 2017b). Some authors also invoked the role of intrusion and suggested the genetic model of intrusion-related gold deposits (Archibald et al. 1996; van Leeuwen and Pieters 2011). The recent feasibility study also considered a high level, low-sulphidation epithermal system (Cube 2017).

Many questions, however, remain open for the area considered in this thesis. This study presents the combination of different mineralogical and geochemical

tehcniques to understand gold mineralization, mainly in the Awak Mas and Salu Bullo prospects.

1.1. Objectives of this study

The final objectives of this research are to examine the ore deposits of Awak Mas and Salu Bullo based on the geological mapping, drill hole data and existing information, in order to:

a. characterize the geologic setting of Awak Mas and Salu Bullo prospects;
b. describe the ore and gangue mineralogy and quantify the mineral chemistry;
c. determine the alteration mineralogy and mineral paragenesis;
d. determine the characteristics of the mineralising fluids using a fluid inclusion (microthermometry and crush leach) study;
e. characterize the formation temperature using Raman spectroscopy on carbonaceous material;
f. determine the carbon and oxygen isotope data of carbonate samples; and
g. establish a genetic model for the mineralization.

1.2. Organization of the thesis

The thesis is organized into 10 chapters. Chapter 1 outlines the study background, location of the study area and major objectives of the research. Chapter 2 describes the regional geology and metallogeny of Indonesia. The geology, tectonic setting and metallogenic evolution of Sulawesi are discussed in Chapter 3. Local geology and historical exploration in the Awak Mas and Salu Bullo regions are also summarized in Chapter 3. Chapter 4 provides methodology and analytical techniques. The petrographical analyses and the mineral chemistry of the metavolcanic, metasedimentary rocks and veins are documented in Chapter 5. Chapter 5 also provides the whole rock geochemistry results and tectonic settings of metavolcanic and metasedimentary rocks. The ore mineralogy, hydrothermal alteration and mineral chemistry of ore minerals are presented in Chapter 6. Chapter 7 describes fluid inclusion studies using microthermometry, crush leach and Raman spectroscopy techniques. Chapter 7 contains the results of carbon-oxygen isotope and geothermometry of carbonate

based on crush leach analysis.Chapter 8 outlines the Raman spectroscopy on carbonaceous materials in order to determine the formation temperature in the studied area. Chapter 9 includes the data discussion, metallogenic model for gold precipitation and implications for exploration. Chapter 10 contains the conclusions. Unless otherwise indicated, all Figures in this manuscript have been redrawn by the author.

1.3. Location, access and physiography

The Awak Mas and the surrounding exploration area prospects are situated within a 7th Generation CoW area of 14,390 Ha and are owned by PT Masmindo Dwi Area (as per June 2017 becomes a wholly owned subsidiary of Nusantara Resources Limited). The Awak Mas and Salu Bullo deposits are located in a mountainous area of the Latimojong Mountains, in the Luwu Regency, South Sulawesi Province, Indonesia. The nearest major town is the coastal port of Palopo, which is 67 km northeast of the project site (Fig. 1). The project location is accessed by 367 km of concrete and asphalt road from the provincial capital of Ujung Pandang (Makassar) to Belopa, and 45 km on subordinate asphalt and gravel roads to the site (Fig. 2A). The Bua airport is approximately 2.5 to 3 hours from the site.

Topography in the studied area ranges from moderate to extremely rugged in the western half of the CoW. The highest level in close proximity to the area of Awak Mas is the summit of Mount Rantemario (3,478 m above sea level) in the eastern side of the project area. The topography of the Awak Mas district ranges from 800 to 1,400 meter above sea level. Slope gradients are steepest within the southern to western portions grading to moderate towards the northern and eastern sections.

Dense primary forest exists in the northern region of CoW and is generally less accessible in regions of higher elevation (Figs. 2C-D). Major drainage systems are Salu Siwa, Salu Lombok, and Salu Tolobo. The Salu Siwa is the most dominant river in the CoW and forms a north-south trending valley that appears to coincide with the major suture zone. The zone divides the Western Latimojong sequence from the Lamasi Complex.

Fig. 1. Location of the Awak Mas project (Tetra Tech 2013)

Fig. 2. Field photographs of the Awak Mas and Salu Bullo.
(A) Accesibility to the Awak Mas exploration camp. (B) Awak Mas exploration camp. (C) Awak Mas area with the background of Latimojong Mountain. Picture looking West. Coordinates: S3°21'35.8" E120°07'10.6"). (D) Salu Bullo area with the background of Latimojong Mountains. Picture looking North. Coordinates: S3°22'21.9" E120°08'18.1").

2. REGIONAL GEOLOGY OF INDONESIA

2.1. Introduction

Geological investigations of the Indonesian archipelago started at the beginning of the 20th century (van Bemmelen 1949; Katili 1974; Hamilton 1979). The complex history of tectonic events and processes includes subduction and magmatic arcs, migration and rotation of crustal fragments, back-arc spreading, ophiolite emplacement and collision resulting in arc reversal, strike slip faulting and crustal extension (Carlile and Mitchell 1994). The Indonesian archipelago can be divided into two major tectonic units; the western and eastern Indonesian unit, separated by the Makassar Straits. The tectonic reconstruction and plate tectonic evolution of SE Asia and SW Pacific during the Cenozoic is based on Hall (2002) and is illustrated in Figure 3.

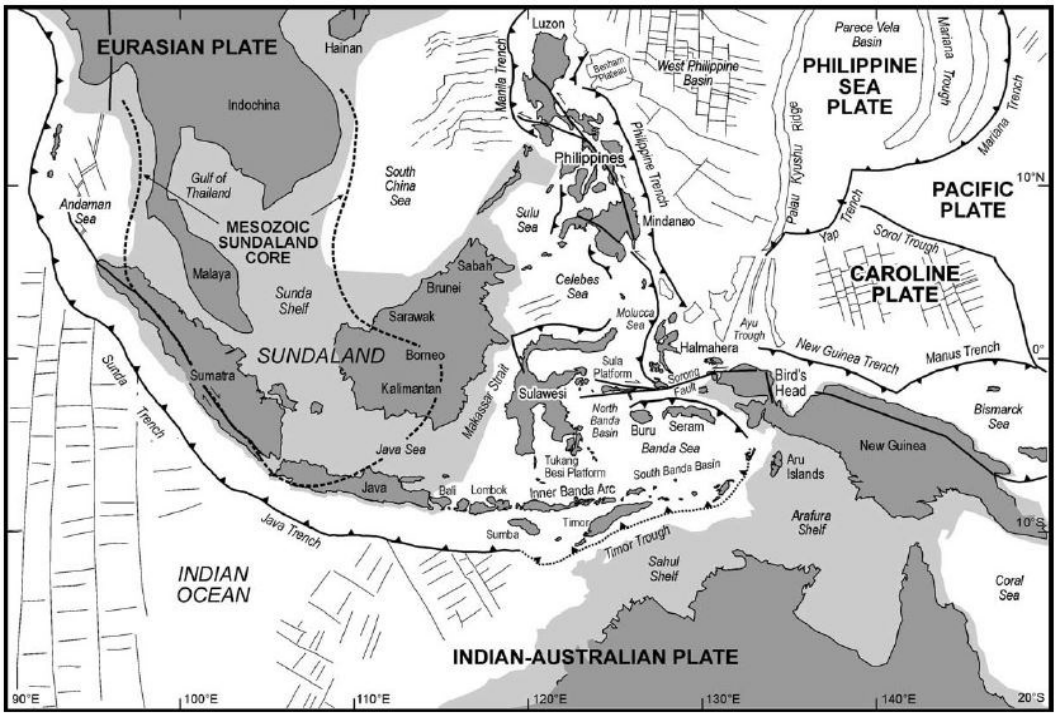

Fig. 3. Tectonic setting of Indonesia and principal geographical features of the region covered in the South East Asia reconstructions.
The light shaded areas are the continental shelves of Eurasia and Australia drawn at the 200 m isobaths (Hall 2002)

West Indonesia is situated in the zone of subduction of the Indian-Australian Plate underneath the Asian Plate. At the surface, this junction is expressed by the formation of an island-arc, namely the Sunda-Banda arc extending from North Sumatera to Banda Island (van Bemmelen 1949). The basement to the arc varies

from Mesozoic to late Paleozoic platform sedimentary rocks deposited on continental crust that are intruded by two mica granites in Sumatera, through Cretaceous to Tertiary melange and ophiolite in central and eastern Java and to oceanic crust in the Banda arc (Hamilton 1979).

The western region of Indonesia, also known as Sunda shelf or the so called Sundaland, occupies the partially submerged southeastern part of the Eurasian continental mass. Sundaland region shows tectonic features of an Early Cretaceous to Late Cretaceous magmatic arc, extending through Sumatera and the Java Sea. It shows both extinct and active subduction during the Tertiary and develops a zone along Sumatera, Java, Bali, Sumbawa, Flores, and Banda islands. Back-arc basin extension due to subduction rollback occurs in Sumatera, Java, North Natuna (formerly the so called South China Sea) and Kalimantan.

East Indonesia is developed as a complex small puzzle of plates moving between the India-Australia and the Pacific Plates. The Philippine arcs, a complex of modern and ancient island-arcs and continental fragments, terminates southwards in the Maluku Sea collision zone where the opposed Halmahera and Sangihe arcs are actively converging. The eastern region, also known as Sahul shelf, extends from Sulawesi through the eastern part of the archipelago including the Indian-Australian continental shelf, extending from Papua through the Arafura Sea and the Southern part of Timor Sea.

Continental blocks are not developed and rocks mostly have an oceanic affinity. However, small microcontinents interacted with volcanic arcs and back-arc basins during the Mesozoic and trapped in older Pacific and Indian Ocean floor rocks. Theses Cretaceous accretionary-collision complexes are tectonically disrupted rocks, and distributed in Java (the Luk Ulo Complex of Central Java), Sulawesi (the Bantimala and Latimojong Complex) and South Kalimantan (the Meratus Complex)(Wakita 2000). In order to illustrate the regional geology of Indonesia, the regional east-west cross section of Indonesian archipelago is shown in Figure 4.

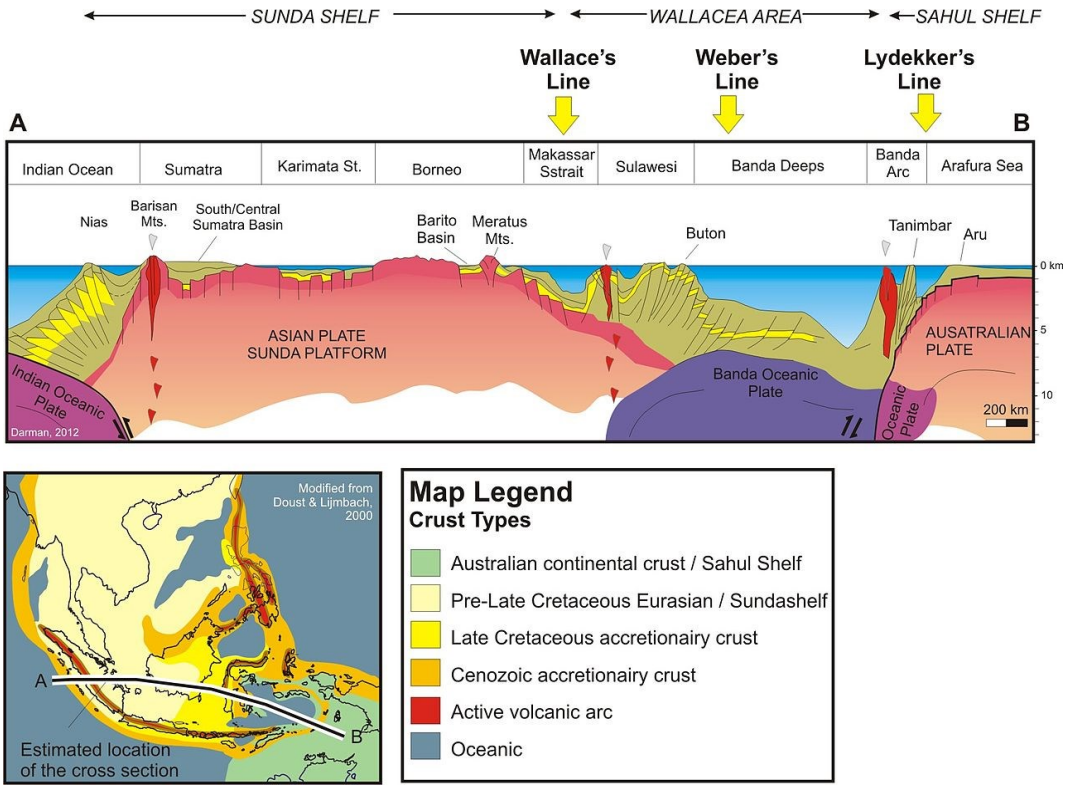

Fig. 4. Regional east-west cross section of Indonesia (Darman and Sidi 2000)

2.2 Plate tectonic model of the Indonesian region in relation to major mineral deposits

Hall (2002) reconstructs the plate movements of SE Asia and SW Pacific and distingishes three big “circums”: (i) Circum Asia, (ii) Circum Asia-Pacific-Australia and (iii) Circum Australia. The first two circums are related to the development of the Indonesian archipelago; meanwhile the last Circum is more related to the plate tectonics in Australia, surrounding New Guinea and Micronesia.

Seven main arcs are related to the Indonesian archipelago (Carlile and Mitchell 1994): (i) Sumatera-Meratus arc, (ii) Sunda-Banda arc; (iii) Aceh arc; (iv) Central Kalimantan arc; (v) Sulawesi-East Mindanao arc; (vi) Halmahera arc; and (vii) Medial Irian Jaya arc. Eight further arcs are relatively small and deeply eroded have not been taken into discussion in this chapter, but also be presented together with the major arcs in Table 5. The main magmatic arcs in the Indonesian archipelago and the major gold and copper deposits are given in the Figure 5. The literature discussion from Katili (1974), Hamilton (1979), Carlile and Mitchell (1994) and Hall (2002) related to the plate tectonics and the contribution

of the magmatic arc to the mineralization is summarized Table 1 and in sub-Chapter 2.2.1 to 2.2.7.

Table 1. Selected features of the major magmatic arcs of Indonesia (summarized from Carlile and Mitchell (1994) and (Hall 2002)

No	Arc	Age	Crustal Type	Upper Basement	Length (km)
1	Sumatera-Meratus	Middle and Late Cretaceous	Continental	Ophiolite and pre-Tertiary schists	2,000
2	Sunda - Banda	Neogene	[1]Continental [2]Island-arc	[1]Sumatera-Meratus arc and its basement [2]Basalts	3,700
3	Aceh	Neogene	Continental	Pre-Tertiary Schists	320
4	Central Kalimantan	Mid Tertiary and Neogene	Continental	Schwanner Arc and its basement	1,150
5	Sulawesi-East Mindanao	Neogene	[1]Continental [2]Island-arc	[1]Schists and ophiolite [2]Basalts	1,200
6	Halmahera	Neogene	[1]Continental [2]Island-arc	[1]Schists [2]Basalts	350
7	Medial Irian Jaya	Neogene	Continental	Sediments	500
8	Schwanner*	Late Early Cretaceous	Continental	Schists and granites	1,450
9	Sunda Shelf*	Late Cretaceous	Continental	Schists	1,600
10	Northwest Borneo*	Neogene	Flysch over continental	Paleocene flysch	530
11	West Sulawesi*	Neogene	Continental	Schist and ophiolie	1,065
12	Moon Utawa*	Neogene	Continental	Schist and ophiolie	330
13	Sumba Timor*	Paleogene and Neogene	Continental	Sediments	400
14	Coastal Irian Jaya*	Inferred Neogene	-	-	-
15	Talaud*	Neogene	Island-arc	Volcanic rock and melange complex in northeast Sulawesi	-

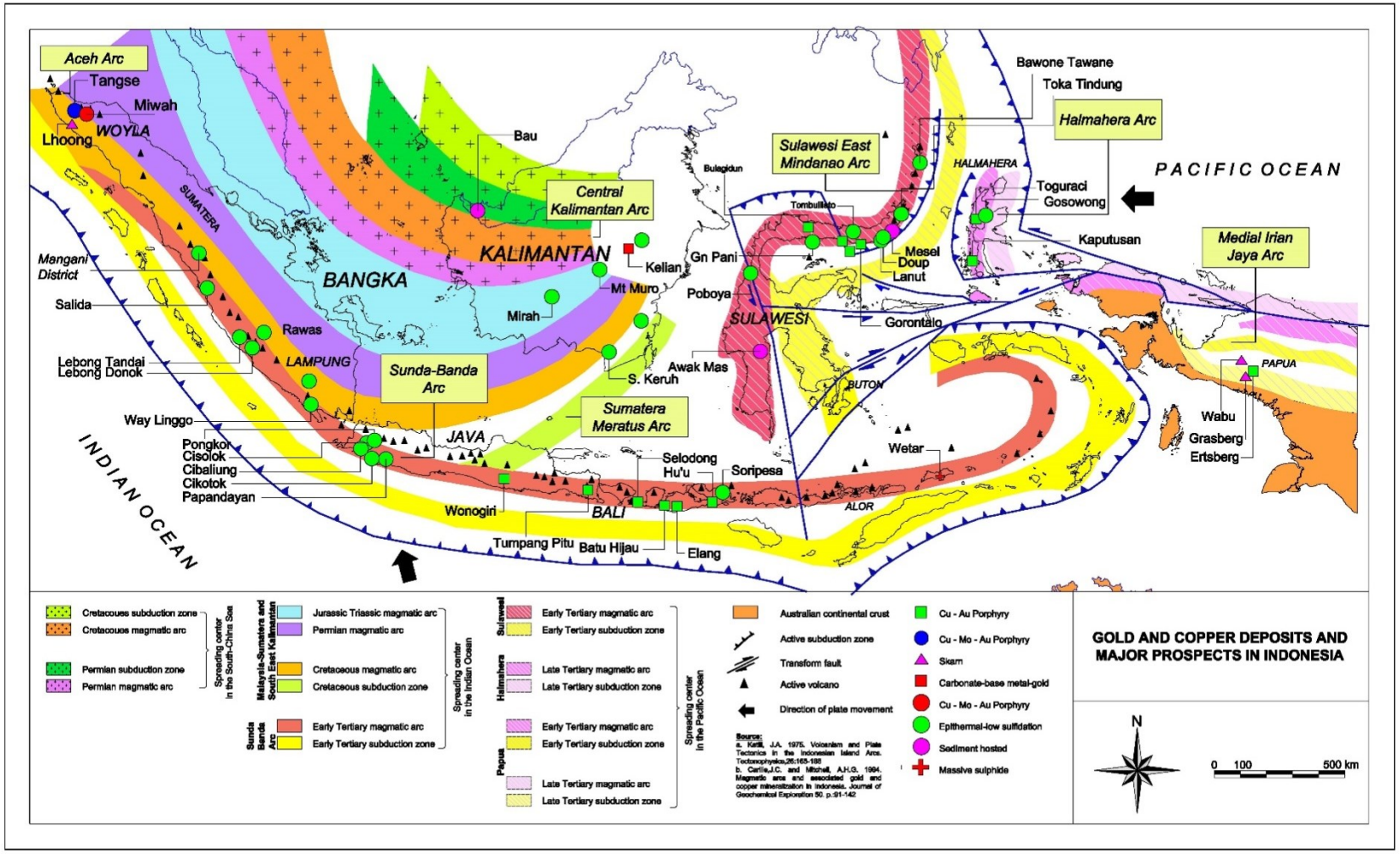

Fig. 5. Regional geology and major gold and copper deposits in Indonesia (modified after Katili 1974, Hamilton 1979; Carlile and Mitchell 1994, Carlile and Mitchell 1994; Garwin et al. 2005).

2.2.1 Sumatera-Meratus Arc

The Sumatera-Meratus arc (Middle and Late Cretaceous), is a continental arc, extending along the inferred southern edge of Sundaland from North Sumatera through the tip of west Java to east Kalimantan (Carlile and Mitchell 1994). During the end of the Triassic or Early Jurassic, Sundaland had become a single continental landmass with Thailand, Myanmar and the Malayan peninsula and collided along sutures extending from offshore of northeast Sumatera into Kalimantan. These collisions resulted in the Triassic Tin belt of South East Asia and possibly the mesothermal gold belt of medial Malaya and Thailand.

During the Middle Jurassic and Late Early Cretaceous, the southern margin of Sundaland was probably a passive continental margin, facing west in Sumatera and south in Kalimantan. Sumatra is underlain by continental crust, dating from Permo-Carboniferous to which were accreted a number of terranes during the Mesozoic. Paleomagnetism in the Sumatra-Meratus arc (or the so called Thay – Malaya Peninsula and Sunda Shelf - Hall 2002) indicates post-Cretaceous clockwise rotations in Thailand and northern Malaysia, followed by counterclockwise rotations of Cretaceous and possibly younger rocks further to the south, including the Celebes Sea and Borneo (Hall 2002). The mineralization in the arc is not well expressed due to the extensive uplift and erosion during the Tertiary.

Mineralization

A lateritic iron deposit is reported from Sebuku islands, located in the Cretaceous granitoid at Pulau Laut, South Kalimantan (Setijadji et al. 2010). The Sungai Keruh gold deposit is hosted by a potassic altered monzonite porphyry intruded into volcanics and sediments, characterized by quartz-carbonate veins, resembling mixed features of both epithermal (intermediate sulphidation) and porphyry style mineralization (van Leeuwen 1994). The Timburu gold deposit is hosted by brecciated ultramafic rocks, phyllic, altered quartz-diorite, and probably related to orogenic deposit type (van Leeuwen 1994; Setijadji et al. 2010)(Table 2).

2.2.2 Sunda-Banda Arc

The Sunda-Banda Arc is a continental and island-arc which interacted during the Neogene. It extends from north Sumatera through Java to east Damar, comprising Sumatera, West Java and possibly parts of central Java. It was constructed on the southern margin of Sundaland (Carlile and Mitchell 1994). The Sumateran volcanic rocks are dominantly sub-aerial and mostly consist of Early Miocene volcanic rocks, and mudstones; Mesozoic and Paleozoic basement including Late Mesozoic ophiolitic rocks in Woyla, Aceh; and plutons of the Late Cretaceous magmatic arc.

In the Bayah dome (West Java), Early Pliocene andesitic dykes intrude mid-Miocene sediments and andesitic tuffs overlying gabbros. Syn-volcanic uplift in the Late Cenozoic is indicated by Early Miocene marine mudstones at an elevation up to 1,100 metres in the Barisan Range, and mid-Miocene marine sedimentary rocks above 900 metres on the Bayah Dome.

In the east of Central Java, no pre-Tertiary rocks are recorded; the area is probably underlain by thinned crust of late Cenozoic extension tectonics. During the Neogene, islands arcs were active in subaerial and in shallow marine environments and do not appear to have been accompanied by a significant syn-volcanic uplift.

Mineralization

The Sunda-Banda arc is well mineralized with abundant epithermal low sulphidation and porphyry systems. This arc shows the contrast between low sulphidation epithermal deposits in the western part of the arc, and porphyry copper deposits in the eastern and southern part. In western Java, the main prospects for epithermal gold-copper are the Pongkor and Cibaliung mines. The new prospect named Arinem epithermal prospect is under development. Old mines terminating operations were Cikidang, Cirotan, Cisungsang and Cineam.

Research related with the epithermal gold deposits in West Java was carried out mainly in Pongkor (Basuki et al. 1994; Marcoux and Milési 1994; Warmada et al. 2003; Syafrizal et al. 2005, 2005; Warmada et al. 2007). Other epithermal deposits studied in West Java are Cikidang (Rosana and Matsueda 2002),

Cibaliung (Angeles et al. 2002; Harijoko et al. 2004), Cisungsang (Yuningsih et al. 2014), Cirotan (Milesi et al. 1994), Cineam (Widi and Matsueda 1998), and South-eastern Java (Hakim and Sulistijo 2013).

Porphyry deposits in the Sunda-Banda arc are Wonogiri (Imai et al. 2007), Batu Hijau (Arif and Baker 2004; Imai and Ohno 2005; Idrus et al. 2007), Tumpang Pitu, Selodong and Elang (Hammarstrom et al. 2013). A summary of the deposits described in the text is given in Table 2.

2.2.3 Aceh Arc

The Aceh arc formed during the Neogene and represents a trench offshore of northern part of Sumatra, which was interacting with volcanics on the mainland (Table 1). It is possible that the arc was active in the earliest Middle Miocene (Carlile and Mitchell 1994). The evidence of the subduction zone is the oceanic Mergui Basin beneath the rifted northern Sumatera basement of the Sunda continent.

Mineralization

The mineralization in the Aceh arc is characterized by porphyry copper-molybdenum in Tangse (Sillitoe 1994), porphyry and iron skarn in Lhoong (Susanto and Suparka 2012; Hakim et al. 2013), high sulphidation epithermal deposit in Miwah (Mulja et al. 2003) and Martabe (Sutopo 2013; Saing et al. 2016), and sedimentary exhalative Pb-Zn in Dairie (Table 2).

Miwah is hosted by andesitic to dacitic volcanic rocks occuring as a product of tensional fractures and intruded by a Pliocene rhyodacite within 25 km of the Sumatera Fault. The Martabe high sulphidation gold-copper deposits, located in Batangtoru, North Sumatera, is hosted by Tertiary volcanic and sedimentary rocks that form part of the Great Sumatran Fault complex (Sutopo 2013). The deposit consists of six ore bodies deposits occur over a 7-km strike length in Batangtoru, the largest of which is Purnama. The ore bodies are characterized by silicified massive ore, quartz veins, banded sulphide veins and cavity filling (Saing et al. 2016). Stratiform sedimentary exhalative lead-zinc deposits were reported in Dairie, Sopokomil, North Sumatera (Herald Resources ltd unpub. data, 1997; (Middleton 2003).

Table 2 Summary of deposits referred to the text

Name	Arc	Age	Host Rock	Type	Tonnage and Grade	Reference
Sebuku	Sumatera-Meratus	Cretaceous	Granite	Iron laterite	41.6% Fe-total	Setijadji et al. (2010)
Sungai Keruh	Sumatera-Meratus	Cretaceous	Potassic porphyry intruded into volcanic and sediments	IS-Epithermal	1.95-2.66 ppm (ore), 1.26-1.41 ppm (oxide ore)	van Leeuwen (1994)
Timburu	Sumatera-Meratus	Cretaceous	Ultramafic rocks around porphyry intrusions	Mesothermal (?)	n.a.	van Leeuwen (1994)
Pongkor	Sunda-Banda	Oligocene-Early Miocene (2.05±0.05 Ma)	Andesitic breccia, tuff, lapilli, andesite intercalated limestone and sandstone, basement shale and sandstone. Host rock overlain by the Miocene sedimentary rock	LS Epithermal	5Mt at 12 ppm Au and 137 ppm Ag, cut off grade 4 ppm Au	Basuki et al. (1994), Greffie et al. (2002), Warmada et al. (2003), Syafrizal et al. (2005), Warmada et al. (2007), Imai and Watanabe (2007)
Cikidang	Sunda-Banda	Early Miocene	Volcanic rock of lapilli tuff and breccia	LS Epithermal	0.4 Mt at 10.2 ppm Au and 43 ppm Ag	Rosana and Matsueda (2002)
Cibaliung	Sunda-Banda	Middle-Late Miocene (11.18-10.65 Ma)	Basaltic andesite volcanics intercalated tuffaceous sediment overlain unconformably by dacitic tuff, younger sediments and basalts flows	LS Epithermal	1.3 Mt at 10.42 ppm Au and 60.7 ppm Ag at cut off grade 3 ppm	Angeles et al. (2002), Harijoko et al. (2004)
Cisungsang	Sunda-Banda	Miocene	Breccia tuff, limestone	Mesothermal	n.a.	Yuningsih et al. (2014)
Cirotan	Sunda-Banda	Miocene (1.7 Ma ±0.1 Ma)	Calc-alkaline rhyolitic-dacitic, quartz microdiorite (Miocene) cutting volcano-sedimentary series	Epithermal overprinted porphyry tin	Average grade 2.0-2.5 ppm	Milesi et al. (1994)
Ciarinem	Sunda-Banda	Oligocene-Middle Miocene (8.8-9.4 Ma)	Andesitic tuff, tuff breccias, lava overlain unconformably by andesitic breccias and tuff	Epithermal	Inferred reserve is 2 Mt at 5.7 ppm Au and 41.5 ppm Ag at cut off grade 4 ppm	Yuningsih et al. (2014)
Cineam	Sunda-Banda	Oligocene-Miocene	Andesite-dacite intruded by diorite, granodiorite, andesite and dacite intrusive	Epithermal	Average grade 6-15 ppm Au	Widi and Matsueda (1998)

Name	Arc	Age	Host Rock	Type	Tonnage and Grade	Reference
Wonogiri	Sunda-Banda	Neogene	Dioritic-andesitic intrusive rock	Epithermal overprinted porphyry	Approximately 9-10 ppm Au	Imai et al. (2007)
Batu Hijau	Sunda-Banda	Late Miocene-Mid Pliocene (intrusion at tonalite 3.7±0.12–3.67±0.10 Ma)	Andesitic tuff, breccia, fine-grained volcaniclastic sandstones and mudstones, and porphyritic andesite	Porphyry copper	968 Mt at 0.41% Cu and 0.29 ppm Au	Arif and Baker (2004),Imai and Ohno (2005), Idrus et al. (2007). Age reference: Garwin (2000)
Tumpang Pitu	Sunda-Banda	Lower to upper Miocene	Strongly altered volcanic breccias, tuff, sandstones and andesite lava with limestone intercalations	HS epithermal and porphyry Cu-Au (Mo)	Porphyry 0.40%Cu, 0.45ppmAu Epithermal 0.55ppm Au, 18ppm Ag	Intrepid Mines ltd Comp. report, 2011
Selodong and Elang	Sunda-Banda	Late Miocene	Andesitic-rhyodacitic volcanic rock	Porphyry Au-Cu and HS Epithermal	Inferred resource 66.75 Mt at 0.43 ppm and 0.27%	Garwin et al. (2005)
Tangse	Aceh	Miocene Mineralization 13 ± 0.25 Ma Alteration 9 Ma	Andesitic-porphyritic	Porphyry Cu-Mo	600 Mt low grade ore (Cu 0.05-0.2%, Mo 50-150 ppm) including 30 Mt with Cu 0.3-0.6% and Mo 100-300 ppm	Sillitoe (1994)
Geunteut, Lhoong	Aceh	Middle Miocene (14.3±0.5 Ma)	Granodiorite and diorite intrusions	Fe-skarn overprinted by porphyry system		Susanto and Suparka (2012), Hakim et al. (2013)
Miwah	Aceh	Plio-Pleistocene	Andesitic to dacitic lavas, tuffs and agglomerate	HS epithermal	103.9Mt at 0.94 ppm Au, 2.68 ppm Ag	Mulja et al. (2003)
Martabe	Aceh	Miocene	Volcanic rock, basalt, andesite, dacite. Phreatomagmatic facies host high-grade when contact with structural complexity	HS epithermal	66.7 Mt at 1.74 ppm Au and 21.5 ppm Ag	Sutopo (2013), Saing et al. (2016) (Saing et al. 2016)

Name	Arc	Age	Host Rock	Type	Tonnage and Grade	Reference
Dairie	Aceh	Permo-Carboniferous	Laminated carbonaceous shale and dolomitic siltstone	Lead-zinc sedimentary exhalative	6.232Mt at 16%Zn and 9.9%Pb	Herald Resources ltd unpub. data, 1997; Middleton, 2003
Kelian	Kalimantan	Lower Miocene	Andesitic-rhyolitic	Hydrothermal breccia and veins (Davies *et al*., 2008)	92.1 Mt at 2.61 ppm Au	van Leeuwen et al. (1990), Abidin (1998), Setiabudi et al. (2007), Davies et al. (2008a), Davies et al. (2008b)
Masupa Ria	Kalimantan	Late Oligocene Intrusion 24.6±0.4 Ma; Alteration 25.2±0.2Ma	Andesite, dacite, pyroclastics, basaltic flows, breccias with epiclastic fragments with intercalated sandstone and limestone	LS Epithermal	308 ton at 12.8 ppm Au	Abidin (1998)
Mt Muro	Kalimantan	Miocene (?)	Andesite porphyry and breccias	LS Epithermal	Proven reource 5.94 Mt at 2.5 ppm and 59 ppm Ag and probable reserves 6.82 Mt at 2.5 ppm Au and 59 ppm Ag	Straits Resources Limited Comp. Report, 2012
Lamandau	Kalimantan	Diorite porphyry: 82.1±1.7 Ma and 78.7±2.3 Ma	Diorite porphyry	IOCG	n.a.	Li et al. (2015)
Gosowong	Halmahera	Miocene, 2.9-2.4 Ma	Shallow marine, intermediate-basic volcanic and volcaniclastic rock	LS Epithermal	0.99 Mt at 27 ppm Au and 38 ppm Ag	(Carlile et al. 1998), Gemmell (2007)
Kencana	Halmahera	Miocene Andesite 3.73±0.22 Ma Mineralization 2.925±0.026 Ma	Andesite volcanic, volcaniclastic rock and diorite intrusion	LS Epithermal	4.4 Mt at 27.9 ppm Au	Clark (2013)
Toguraci	Halmahera	Pliocene	Basalts with diorite intrusives	LS Epithermal overprint porphyry	0.41 Mt at 27 ppm Au	Garwin et al. (2005)
Buru	Halmahera	n.a.	Mica schist	Orogenic	n.a.	Idrus et al. (2014a)

Name	Arc	Age	Host Rock	Type	Tonnage and Grade	Reference
Grasberg	Irian Jaya	Igneous Complex 3.33±0.12 to 3.01±0.06 Ma Porphyry 2.9 Ma	Brecciated igneous rocks; below 3,500 m were diorite or monzodiorite; above 3,500 m mainly andesitic	Porphyry Cu-Au	Open Pit: 77 Mt at 1.1% Cu, 1.37 ppm Au, 2.83 ppm Ag Underground 447 Mt at 1.19% Cu, 0.96 ppm Au, 3.75 ppm Ag	MacDonald and Arnold (1994), Mathur et al. (2000), Pollard et al. (2006), Annual Report Freeport McMoRan, 2014
Deep Ore Zone	Irian Jaya	Tertiary age, 3.25 Ma	Siliclastic carbonate and siltstone formation intruded by I-type intrusions	Ca-Mg Silicate Skarn	47 Mt at 0.56% Cu, 0.68 ppm Au, 2.27% Ag	Coutts et al. (1999), Annual Report Freeport McMoRan, 2014
Big Gossan	Irian Jaya	2.82 Ma±0.04 Ma	Fault at the contact between carbonate rich sedimentary rock and clastic-carbonate sedimentary rock	Cu-Au Skarn	17 Mt at 2.39% Cu, 1.02 ppm Au, 15.15 ppm Ag	Meinert et al. (1997), Prendergast et al. (2006) Annual Report Freeport McMoRan, 2014
Kucing Liar	Irian Jaya	3.01±0.02 Ma*	Limestone and sandstone	Sediment hosted Cu-Au overprinted by Cu-Au porphyry-skarn	152 Mt at 1.31% Cu, 1.11 ppm Au, 7.45 ppm Ag	*Age dating Mathur in Prendergast et al. (2006), Annual Report Freeport McMoRan, 2014 **New (2006)
Deep Level Mine Zone	Irian Jaya	Tertiary age	Siliclastic carbonate and siltstone formation intruded by I-type intrusions	Cu-Au Skarn	65 Mt at 0.92% Cu, 0.74 ppm Au, 4.60 ppm Ag	Annual Report Freeport McMoRan, 2014

*) Major deposits in the Sulawesi arc were excluded from this table and shown separately in Table 3. LS=low sulphidation, IS=intermediate sulphidation, HS=high sulphidation, IOCG: Iron-oxide-copper-gold. n.a.=not available

2.2.4 Kalimantan Arc

The Kalimantan (Borneo) arc is a continental arc, ranging from the Early Cretaceous (in Schwaner Mountain arc), Middle Tertiary (Central Kalimantan arc) to the Middle Miocene (Northeast Kalimantan arc)(Carlile and Mitchell 1994)(Table 5).

The Schwaner Mountain arc, a wide east-trending belt of calc-alkaline rocks, consists of predominantly tonalitic to granodioritic batholiths of Cretaceous age. These rock intruding low-grade regional metamorphic rocks of the Schwaner Mountain. The Central Kalimantan arc is tentatively projected from northeastern Kalimantan southwards through central to west Kalimantan into Serawak. Pre-Cretaceous rocks including Mesozoic sedimentary units above the Late Palaeozoic schists and phyllites were consolidated during an Early Mesozoic orogeny (Carlile and Mitchell 1994). The Northwest Kalimantan arc is inferred from scattered areas of andesitic rock, located in the northwest of Kalimantan and eastern Serawak.

Most of Kalimantan area, with the exception of Sarawak and Sabah, was part of Sundaland region at the beginning of the Cenozoic (Hall 2002). Intrusions of Late Triassic granites represent the continuation of the Early Mesozoic Southeast-Asian tin belt and have been intruded again by Early Cretaceous plutons of the Schwaner Mountains arc. During Late Miocene to Quarternary, a basalt complex developed in Kalimantan, becoming the youngest eruptive rocks. Flysch sediments, a general term of a sedimentary deposit consisting of thin beds of shale or marl alternating with coarser strata such as sandstone or conglomerate, underlie these arcs.

Mineralization

The main gold mineralization in Central Kalimantan is Kelian, a transition between epithermal and porphyry style mineralization. This deposit was classified as sulfide and base metal-rich low sulphidation epithermal deposit, as carbonate-base metal gold deposit, as intermediate sulphidation epithermal deposit and as hydrothermal breccia and vein deposit (Abidin 1998; Setiabudi et al. 2007; Davies et al. 2008b; Davies et al. 2008a). The Kelian gold deposit is associated with a

Lower Miocene magmatic center, and constitutes the largest Tertiary volcanic-related ore deposit, which occur along an east-northeast trending belt in East Kalimantan. Mineralization occurred during the emplacement of andesitic and rhyolitic rocks.

The Masupa Ria deposit in the Barito Basin, Central Kalimantan, is a type of epithermal precious metal bearing veins, associated with residual quartz and quartz-clay alteration. The Masupa Ria volcanics, which are the main host rocks, were intruded by subvolcanic andesites, and are dominated by andesitic flows, fragmental rocks, and high level intrusions of calc-alkaline composition (Abidin 1998).

The Mt. Muro deposit, located in Central Kalimantan, consists of gold-bearing quartz veins that formed in an epithermal environment during the mid-Tertiary calc alkaline volcanism of Central Kalimantan (Carlile and Mitchell 1994) after Simmons and Browne, 1990). The Long Laai deposit shows different characteristics of an epithermal system, where gold occurs with cassiterite greisen and skarn, in vicinity to a granodioritic intrusion ((Carlile and Mitchell 1994) after Hutchison, 1989).

A series of Cenozoic epithermal gold deposits and Fe-Au-Cu-Au deposits are located in the Lamandau region of Kuching belt, southwestern Kalimantan (Li et al. 2015). The Lamandau deposit is hosted by diorite porphyry. Based on in-situ zircon U-Pb dating, diorite porphyry formed between 82.1±1.7 Ma and 78.7±2.3 Ma. The magnetite has a volcanic origin with low REE and high Cu-Au contents. No significant mineralization was reported from the Northwest Kalimantan arc, although the Bau deposit, a sediment-hosted disseminated gold deposit, could be a part of this arc. However, it is located in Sarawak district, Malaysia. In the Schwaner Mountain arc, several skarn occurrences are associated with Lower Cretaceous plutons but contain no significant mineralization.

2.2.5 Sulawesi Arc

Formerly the Sulawesi-East Mindanao arc (Neogene) extended from southwestern Sulawesi through the north arm of Sulawesi to Sangihe island and continued into eastern Mindanao, Philipines during Early and Mid-Miocene (Table

5). During the Late Mio-Pliocene, two distinct arcs developed, *i.e.* a calc-alkaline arc in the northeast (Kavalieris et al. 1992) and a shoshonitic arc to the southwest (Carlile et al. 1990; Priadi et al. 1994).

Other small magmatic arcs present in Sulawesi are the West Sulawesi arc, formed during Late Miocene to Pliocene; and Talaud arc, formed during Neogene. Both magmatic arcs are deeply eroded and contain only small indications of mineralization, rather than Sulawesi-East Mindanao arc. The discussion related with the tectonic evolution and the metallogeny of Sulawesi arc is presented in more detail in Chapter 3.2.

Mineralization

The mineralization in Sulawesi occurs in a variety of deposit types carrying gold, copper, nickel, asphalt and iron. The number of metal deposits in the Sulawesi arc is significant, although the Sunda-Banda arc contributes more. The type of deposits varies between western and eastern arc, related to different metallogenic provinces. The western arc, formed as an arc collision terrane, hosts gold-copper-molybdenum deposits; whereas the mineralization in the eastern arc is related to lateritic deposits as a weathering product of ultramafic rocks.

North Sulawesi contains copper-gold porphyries in the Tombulilato district; high sulphidation mineralization in Motomboto (Kavalieris et al. 1992) and Bakan (Hadjana 2012); sediment-hosted gold deposit at Mesel (Turner et al. 1994); and gold-silver-barite±base metal mineralization in Binabase in Sangihe (Wisanggono et al. 2012). The Binabase deposit has similarities to Wetar, occuring in the Sunda Banda arc.

Low sulphidation deposits in the northern arm of Sulawesi are Doup, Lanut and Ratatotok (Kavalieris et al. 1992; Turner et al. 1994; van Leeuwen and Pieters 2011). A carbonate stockwork deposit was identified in Bolangitang, and disseminated gold mineralization at Gunung Pani (Kavalieris et al. 1990). Minor skarn deposits occur in the western end of the north arm and small volcanogenic base metal sulphide deposits occur in Sangkaropi. Nickel laterite is still actively being mined in Sorowako and Pomalaa, and asphalt was also mined on the Buton

islands. The features of various deposits in Sulawesi are discussed in detail in Chapter 3.3.

2.2.6 Halmahera Arc

Halmahera arc is related with the Philipine arc, and formed as a complex of modern-ancient island-arcs and continental fragments during the Neogene. The movement of the Philipine arc to the south of the Molucca Sea Collision zones resulted in the interaction with the Halmahera and Sangihe arcs from the opposite side. The Halmahera arc extends from Bacan in the south, through the northern arm of Halmahera and through the western of Morotai. Exposed basement in the southern part of the Halmahera arc on Bacan consists of schists, with Palaeogene basaltic and andesitic rocks further north (Carlile and Mitchell 1994) after Sufni Hakim and Hall, 1991). The andesitic arc in Halmahera consists of Neogene intrusions and volcanic rocks, buried locally by Quarternary volcanoes. Ophiolitic rocks, formed in an early Mesozoic intra-oceanic arc, represent the basement of east Halmahera. These ophiolites are overlain by Cretaceous, Eocene and Oligocene arc volcanic rocks and all older rock is unconformably covered by carbonate.

Mineralization

A chain of active volcanoes forms the west of Halmahera and cuts across a few kilometers to the north of the Gosowong districts. The mineralization is confined to the Kaputusan porphyry copper-gold deposits on Bacang (Carlile and Mitchell 1994) after Bering, 1986), Gosowong, Kencana and Toguraci epithermal gold deposits (Carlile et al. 1998; Gemmell 2007; Clark 2013) and several low-grade porphyry style copper-gold deposits at Tobobo and Bora (Carlile et al. 1998). The epithermal deposits on the Buru Islands gave rise to an artisanal gold-rush in 2012. Based on the preliminary study, it probably represents a metamorphic rock-hosted gold mineralization (Idrus et al. 2014b).

2.2.7 Papua Arc

Papua arc (formerly Medial Irian Jaya arc) is located in Eastern Indonesia, with two other minor arcs: Moon-Utawa and Coastal Irian Jaya arc. According to

Hamilton (1979), Papua arc is a type of transition between continental, oceanic and island-arc provinces. The continental province consists of the sediment cover of the Australian craton, the oceanic province developed from ophiolite and island-arc volcanics from the Pacific plate. The transitional province consists of highly deformed and regionally metamorphic rocks as a product of the collision of the Australian and the Pacific plates (Carlile and Mitchell 1994) after Dow et al. 1988).

By the Early Eocene (50 Ma) the northern margins of the Australian continent and New Guinea collided with the Sepik island-arc, causing subduction and emplacement of the Sepik and Papuan ophiolites. After this event, the New Guinea margin remained as a passive margin for most of the Paleogene (Surjono and Wijayanti 2011). By 25 Ma, eastern Indonesia becomes an active margin during due to the subduction of the New Guinea margin underneath the Phillipines-Halmahera margins. Northern Australian fragments also began to interact with the South East Asia margin in Sulawesi along the Sorong Fault, forming the Bird´s Head region.

Mineralization

The magmatic arc in Papua is well endowed with gold and copper, reflected by the past and present resource estimates. 47 percent of gold and 52 percent of copper in Indonesia were produced from the Grasberg porphyry deposit (Garwin et al. 2005)(Fig. 6). The Ertsberg district in the mountainous Central ranges of Papua is well known for its Cu-Au skarn and porphyry-related deposits. In this area, a number of mineralization types occur. These are: (i) the Grasberg Cu-Au porphyry deposits (MacDonald and Arnold 1994; Mathur et al. 2000; Pollard et al. 2006), (ii) Big Gossan skarn Cu-Au, (iii) Wanagon Gold deposits (Prendergast et al. 2006), (iv) Kucing Liar skarn deposits and (v) oxidized gold skarn deposits in Wabu (Prendergast et al. 2006) after Sunyoto (1999).

The eastern extension into Papua New Guinea also contains the world class deposits: Porgera and Ok Tedi (Carlile et al. 1990; Tarkian and Stribrny 1999). Aneka Tambang (gold company) conducted semi-detailed exploration, structural

mapping, drilling and geochemical survey in Oksibil, located in the Moon-Utawa arc with possibly calc-skarn deposits.

Fig. 6. Aerial photograph of Grasberg gold mine (courtesy of PT Freeport Indonesia)

3. REGIONAL GEOLOGY AND METALLOGENY OF SULAWESI

3.1 Regional geology of Sulawesi

Sulawesi is located in the middle of Indonesian archipelago. The three plates (the Eurasia, the Pacific and the Australian plates) converge and interact, resulting in a complex geological situation, consist of metamorphic complexes, ophiolite terrains, volcanic arcs, granitoid belts and sedimentary basins.

Sukamto (1978) divided Sulawesi into four lithotectonic units, which are bounded by large-scale tectonic dislocations and thrust faults. These are from west to east: (i) the West-North Sulawesi volcano-plutonic arc, (ii) the Central Sulawesi metamorphic belt, (iii) the East Sulawesi Ophiolite belt, and (iv) the Continental Fragments of Banggai-Sula, Tukang Besi and Buton. The regional geology and the sketch of Sulawesi orogeny are illustrated in Figure 7 and Figure 8.

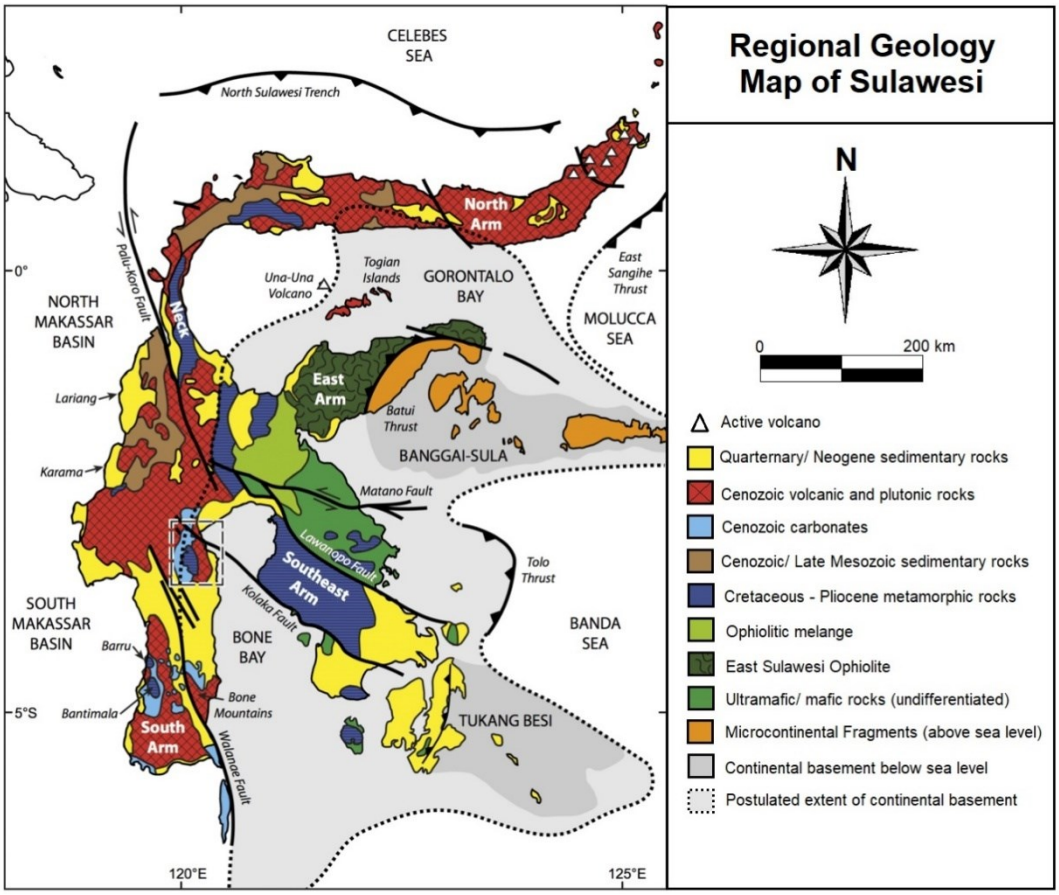

Fig. 7. Regional geology of Sulawesi (modified after White et al. 2017. The location of current study (the Latimojong Metamorphic Complex) is shown by the black dash-box.

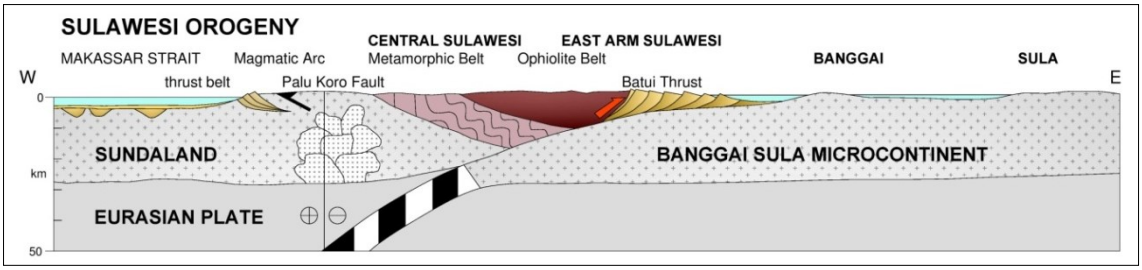

Fig. 8. Sketch of the Sulawesi orogeny (modified from Simandjuntak and Barber 1996).

3.2 Geological and metallogenic evolution of Sulawesi

Regionally, tectonic reconstructions place south Sulawesi against the southeast coast of Kalimantan, prior to the opening of the Makassar Strait during the Eocene. The strait is bound by the Sulawesi Sea on the north and by the East Java Sea on the South. The strait formed by the vertical sinking of a subducting oceanic plate to the east of western Sulawesi during the Miocene, leading to trench roll-back (Guntoro 1999). This vertical sinking was accommodated by extension and rifting of continental crust above the subduction zone at a previous site of collision. Figure 9 shows the development of Sulawesi from the Early Cretaceous to the Middle Late Eocene. The explanation is as follows.

The SW Sulawesi Microcontinent was subducted beneath SE Kalimantan (East Java Sea Microplate), generating an accretionary complex (Fig. 9A). The SW Sulawesi Microcontinent collided with SE Kalimantan, resulting in the uplift of the Meratus Mountains and the emplacement of the basement complexes. The continuing movement of the Pacific Plate was accommodated by the formation of a new subduction zone to the east of SW Sulawesi (Fig. 9B). The whole area of the Meratus Mountains was uplifted, associated with block faulting. Off to the east the Banggai-Sula Microcontinent was approaching (Fig. 9C). The vertical sinking of the subducting plate causing back-arc spreading and the opening of the Makassar Strait with the formation of oceanic crust (Fig. 9D). The collision of the East Sulawesi ophiolite with SW Sulawesi causing the termination of the rifting in the Makassar Strait (Fig. 9E). The collision of the Banggai-Sula Microcontinent with East Sulawesi causing the change of subduction polarity in which the oceanic crust in the eastern part of the Makassar Strait was subducted beneath SW Sulawesi (Fig. 9F). Further on, the collision caused the anticlockwise rotation

of SW Sulawesi and the compression in the North Makassar Basin. This led to the formation of a series of east dipping thrust faults.

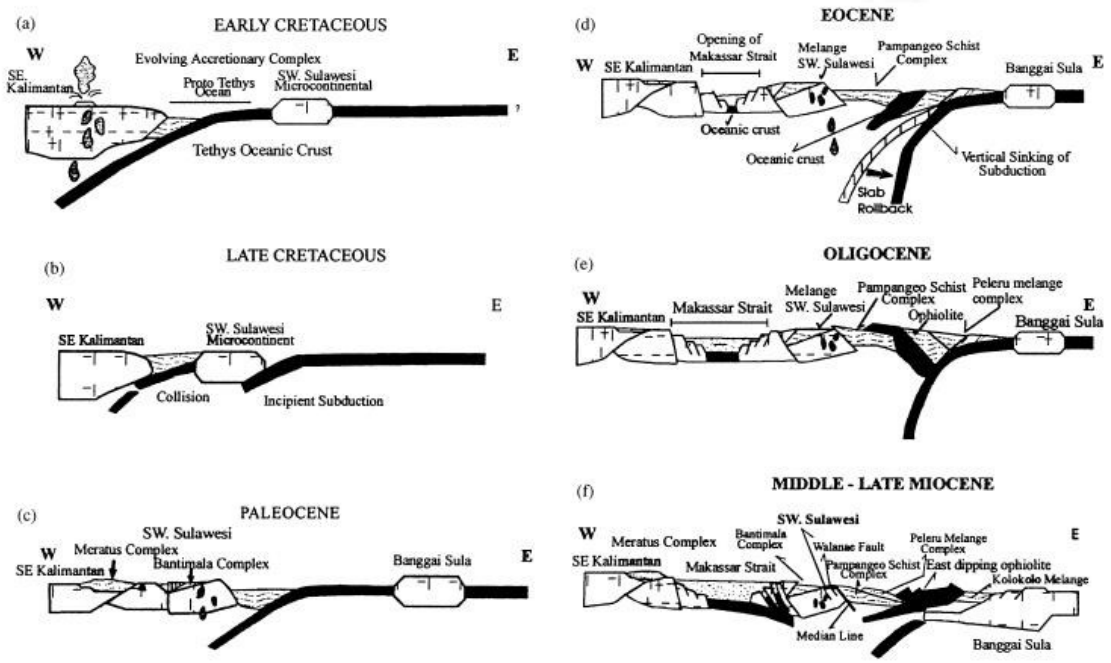

Fig. 9. Development of Sulawesi from the Early Cretaceous to the Middle-Late Miocene (Guntoro 1999).

3.2.1 West and North Sulawesi Volcano-Plutonic Arc

North Sulawesi consists of a mountainous terrain although rarely reaching altitudes higher than 2,000 masl. The landscape of the Northern part of the province is dominated by the presence of (partly eroded) volcanic cones, some of which are still active. The northern part of Sulawesi consists of Neogene island-arcs, built upon a Paleogene volcanic-sedimentary basement and underlain by oceanic crust. Low-K tholeiitic basalt developed during Paleogene magmatism. Post-collisional magmatism in the north of the Sulawesi arc produced felsic to mafic volcanics that are related to rifting of the former arc rather than to subduction.

West Sulawesi can be divided into three parts: Southwest (SW), Central West (CW) and Northwest (NW) Sulawesi (van Leeuwen and Pieters 2011). A depression separating Northwest and Central West Sulawesi is filled with Quarternary sediments. Western Sulawesi contains an almost complete Late Mesozoic to Cenozoic stratigraphic sequence ranging from Late Cretaceous to

Recent. The basement of the west Sulawesi is continental fragments, with Pre-Tertiary accretionary and mélange complexes developed, and overlain by Late Cretaceous flysch deposit.

Pre-Tertiary accretionary and mélange complexes are exposed in the Bantimala and Barru blocks in Southwest Sulawesi and in the Latimojong Complex in Central Sulawesi. They consist of imbricated tectonic slices of both continental and oceanic rocks, which have been metamorphosed to greenschist-amphibolite and blueschist facies conditions (Sukamto 1986; Bergman et al. 1996; Wakita et al. 1996). During the Paleogene, calc-alkaline magmatism was intermittent and localized. The voluminous high-K calc-alkaline (mostly granitoids) and shoshonitic to ultrapotassic rocks developed during Neogene Magmatism. In the Late Paleogene, sedimentation in western Sulawesi was characterized by syn-rift silicilastics. It was overlain by platform and deeper marine carbonates, and by pelitic sediments in the northern area of western Sulawesi. The Neogene marine sediments interlayered with the volcaniclastic rocks developed the Celebes Molasse.

3.2.2 Central Sulawesi Metamorphic Belt

This belt extends from central and eastern arm as a collision zone between fragments of the Eurasian plate during the Late Oligocene or Early Miocene (Maulana 2009). This belt consists of sheared metamorphic rock including Pompangeo schist, mélange complex and Miocene ophiolite. This belt is an accretionary complex, which divides eastern and western Sulawesi. The major structures are fold and thrust belts with a thrust in the eastern part of the Makassar Strait, and the strike-slip Central Sulawesi fault named Palu-Koro fault (direction in NNW) and Montano fault (direction NNW).

3.2.3 East Sulawesi Ophiolite Belt

This belt extends from central Sulawesi across the east and southeast arms, including the Buton and Muna Islands. The east Sulawesi provinces are typical of a suture tectonic setting, with a basement of continental fragments, accretionary rock/ mélange and ophiolite complexes, deposited during Mesozoic

and Paleogene (Simandjuntak and Barber 1996; Parkinson 1998; Kadarusman et al. 2004). The ophiolite series comprises residual mantle peridotite, gabbro, sheeted dolerites and basaltic volcanic rocks. The Neogene magmatism in eastern Sulawesi is minor and localized. Deposition of the Celebes Molasse occured during Neogene sedimentation. The belts are interpreted as a Neogene accretionary complex formed by westward dipping subduction and by partial underthrusting of the Sula and Tukang Besi platforms.

3.2.4 The Banggai-Sula and Tukang Besi continental fragments

The Banggai-Sula and Tukang Besi continental fragments are parts of New Guinea, located in the eastern and southeastern parts of Sulawesi. These continental fragments may have been transported westward from the Australian Plate along a left lateral fault of the Sorong system (Elburg and Foden 1999). This event represents the collision between the Eurasian (Sundaland) and Indo-Australian (New Guinea) plates.

The continental fragments show the typical characteristics of metamorphic and igneous continental rocks with shallow and deep marine sediments of Palaeozoic and Mesozoic ages. The sedimentary rocks were deposited during drifting of the fragments after Mesozoic rifting (Hamilton 1979). The Tukang Besi fragments were submerged and the Upper Neogene and Quarternary reef limestone covers the exposed part of the platform.

3.3 Major metal deposits in Sulawesi

3.3.1 Northern Sulawesi

Northern Sulawesi contains arc-related mineralization including Cu-Au porphyry (Lowder and Dow 1978; Carlile et al. 1990; Perelló 1994), porphyry Mo (Soeria-Atmadja et al. 1999), volcanogenic massive sulphide Cu-Pb-Zn, magnetite skarn Cu-Au (Kavalieris et al. 1992)(Fig. 11).

Carbonate-hosted Au or sediment-hosted disseminated gold (Turner et al. 1994) and metamorphogenic Au are found in metamorphic basement rocks to the west of North Sulawesi arc (Kavalieris et al. 1994). Other styles of mineralization include Volcanic Massive Sulphide, intrusion related base metal-Au, Fe±Au

skarn, alluvial Au, and Fe beach sand (van Leeuwen and Pieters, 2011) are also found in this region.

3.3.2 Western Sulawesi

The porphyry Mo, orogenic or intrusion related Au are the main mineralization types in Western Sulawesi. This arc is less mineralized compared to Northern Sulawesi. Volcanic Massive Sulphide, Fe±Au skarn, and Mn-ironstones were also discovered in Western Sulawesi region (van Leeuwen and Pieters, 2011). The area for this study (Awak Mas and Salu Bullo)(Fig. 12) are located in this metallogenic province.

3.3.3 Eastern Sulawesi

The main mineralization types are nickel and iron laterites, primary and secondary chromian spinel, alluvial Au, and epithermal Au-Sb (van Leeuwen and Pieters, 2011). In 2008, placer gold prospects were discovered in Bombana and Langkowala causing gold rush with more than 60,000 local miners work in this area (Idrus et al. 2011)(Fig. 12).

3.3.4 Banggai-Sula and Tukang Besi

This province does not contain any significant known mineralization. Indications of Sn,W, Zr and Ta were detected in stream sediment samples from Banggai and Labulo Islands in the Banggai-Sula Province (Sukmana, 2006 in van Leeuwen and Pieters 2011). This might lead to the discovery of mineralization types, which have not been reported before from this area.

The main deposits type discussed on the text are illustrated in Figures 10–12 and Tables 3-4.

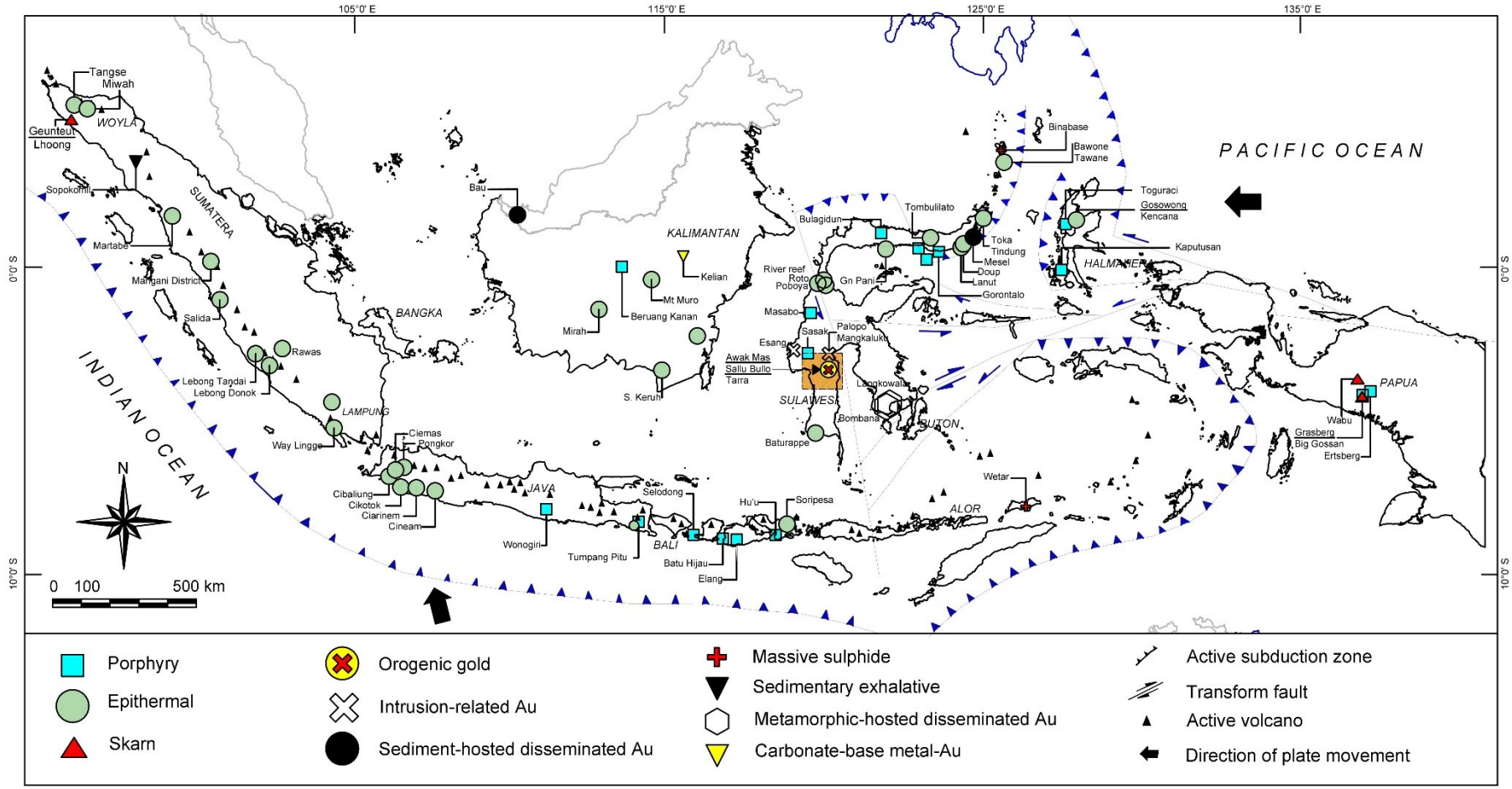

Fig. 10. Major gold-copper deposit in Indonesia (modified after Katili 1974, Hamilton 1979; Carlile and Mitchell 1994, Carlile and Mitchell 1994; Garwin et al. 2005 with an additional new data). Location of the studied area is shown by orange box.

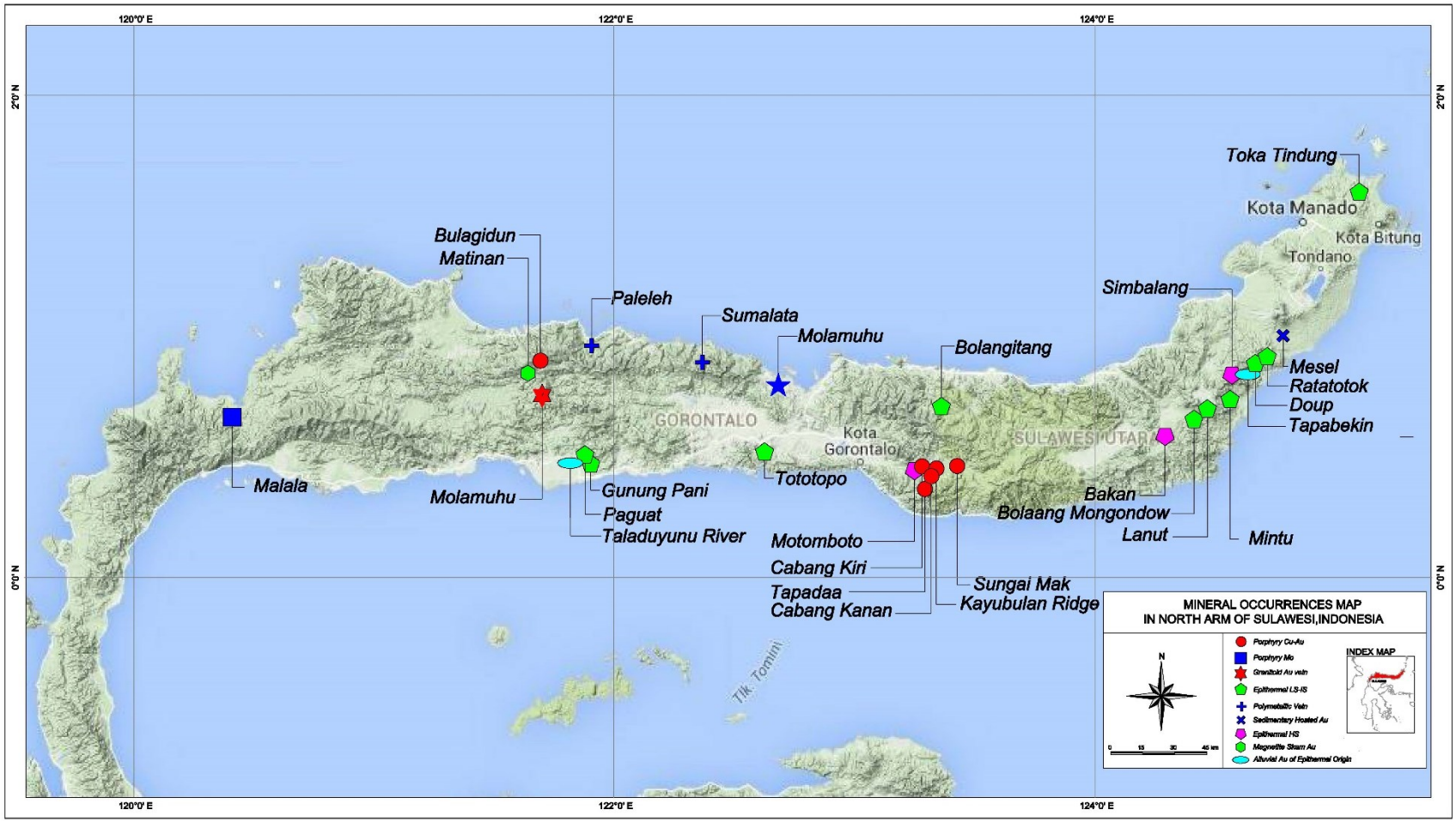

Fig. 11. Mineral occurrences in Northern Arm of Sulawesi (modified after Katili 1974, Hamilton 1979; Carlile and Mitchell 1994, Carlile and Mitchell 1994; Garwin et al. 2005 with an additional new data)

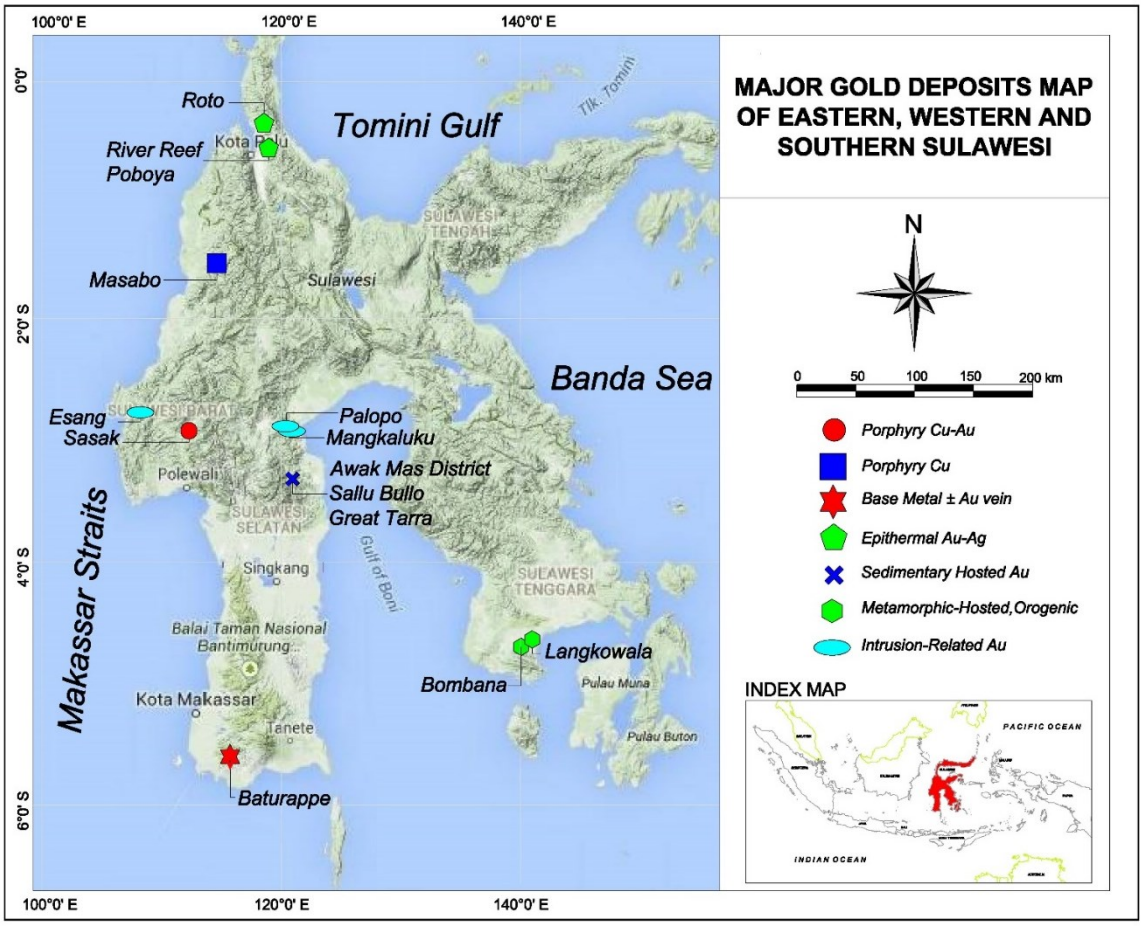

Fig. 12. Major gold deposits in Eastern, Western and Southern Sulawesi Sulawesi (modified after Katili 1974, Hamilton 1979; Carlile and Mitchell 1994, Carlile and Mitchell 1994; Garwin et al. 2005 with an additional new data)

Table 3. Features of various mineral deposits in Northern Sulawesi

Deposit	Age	Host rock	Type	Deposit Style	Tonnage Grade	Au/Ag	Metal Sgnature	Mneralogy	Alteration	References
Bakan	na	diorite & andesite volcanics	HS-epith. Au-Ag	Dissem Au-Ag in Sil core zones	16.87 Mt at 0.96 ppm Au	na		Py-En-Cv	Vug Sil-Al, Kln-Al, ill-Sm	1,2
Binabase	Pliocene (?)	andesitic tuff and tuff breccia	a.HS-epith. Au-Ag* b.supergene enriched related with LS-epith **	Qz-Py-Brt-bx; Ba-En vn	27.3 Mt at 0.95 ppm Au, 13.6 ppm Ag	1:1	Au,Ag,Cu	Py-(Ccp-Cv-En-Sph); Au in Py lattice	Al-Kln-Brt-Py	3* 4**
Bulagidun	Host rock 9.4 Ma Alteration 8.15 Ma	Hydro-thermal collapse; bx asso-ciated with diorite & Qz diorite	Porphyry Cu-Au	sulphide cement fillng bx	37 Mt at 0.6 ppm Au 0.61% Ag	na	na	Ccp-Py-Mgt, Au with Ccp	(upper) Ms-Chl-Or-Qz-ill-Kln; (inner) Bt-Qz-Mgt (outer) Chl-Ep	5, 6
Bolangi-tang	Pliocene	Sub volcanic andesite	a. LS-epith. Au * b.IS-epith. Au-Ag **	Qz-Cbvn-stk	4 Mt at 2.72 ppm Au, 21 ppm Ag	8: 1	Au,Ag,Cu, Pb,Zn	Electrum minor py	Qz-ill-Ad;Chl-Ep-Py	*7, **6
Doup	Middle Miocene	Qz diorite, sed rock	a.LS-epith. Au-Ag* b. IS-epith.Au-Ag **	Qz-Rhodo-Base metal vn	17 Mt at 2.15 ppm Au	2:1	Au,Ag,As, Cu,Pb,Zn	Py-Gn-Sph-(Ccp)	Ser-Ill-Cb-Ad	*8 **6
Dunu	Alteration 12.5 Ma (bt)	diorite porphyry & tourmaline bx	Porphyry Cu-Au±Mo	Stk&Bx	na	na	na	na	(inner) Bt-Qz-Ab (outer) Chl-Act-Ep	6

Deposit	Age	Host rock	Type	Deposit Style	Tonnage Grade	Au/Ag	Metal Sgnature	Mneralogy	Alteration	References
Gunung Pani	Host rock Pliocene ~ 3.2 Ma	rhyodacite volcanics; dome-diatreme complex	a.Dome related gold* b.LS-epith. Au** c.IS-epith. Au-Ag ***	Qz-adu-py encrustation on fissure, bx zones Qzvn,dissem,fractures,bx	9.9 Mt at 1.57 ppm Au	<1	Au,As,Sb	Au as electrum & native form in py	1)Qz-Ad-Ser 2) Chl-Ser	*9 **8 ***6
Lanut	Middle Miocene	Interbedded volcanics &sedimentary rocks	IS-epith. Au-Ag	Qz stwk; fracture dissm,bx	19 Mt @ 1.8 ppm Au	na	Au (Ag, Cu, Pb)	Free Au minor py,Ccp, bo	1)Qz-Ad-Ill 2)Chl-Ill-Py	8 6
Mesel	Middle Miocene	limestone, jasperiod rocks	Sediment hosted	replacement; minor Qz vn	8.8 Mt @ 7.10 ppm Au (pre mining)	<0.5	Au, As, Sb, Hg,Tl	Py, Apy, Mar	na	10, 11,6
Mintu	na	na	LS-epith. Au-Ag	Qz vn	na	na	na	na	na	8
Molamuhu	na	dacitic volcanics	Vein Mo	Qz vn	na	na	Mo	Ccp, Mol	na	8
Motom-boto, Kayubulan, Sungai Mak Cabang Kanan, Kiri	Pliocene 0.84-1.89 (Al)	andesitic volcanic; granodiorite	HS-epith. Au-Ag, Porphyry Cu	Hydroth, bx, Vn ; structure over 5 km long	3.5 Mt @ 1.5% Cu, 4.0 ppm Au	25:1	1) Au,Cu, As Ag, Te,Cu, Pb,Zn, Hg) 2) Au, Ag, Cu, As	Py-En-Luz, Au		6, 8, 12, 13
Paleleh	Late Miocene	Diorite, andesite volcanics ; dioritic dyke	a.Poly-metallic vein *	Qz vn&bx zones	1 Mt @ 6.2 ppm Au, 5 ppm Ag (pre mining)	1:1	Au,Ag,Cu, Pb,Zn	Py-Po-Gn (Ccp Sph)	Qz-Ill-Chl	*8 **6

Deposit	Age	Host rock	Type	Deposit Style	Tonnage Grade	Au/Ag	Metal Sgnature	Mneralogy	Alteration	References
Ratatotok	na	Siliclastic-Cbonate, overlain by andesitic volcanic - volcaniclastic	b.intrusion related BM-Au ** a.LS-epith. Au-Ag b.Sediment-Hosted Au **	Qz vn in paloe-karst bx fill	Closed in 2004, having produced 1.9 Moz	na	Au (As, Sb,Hg,Ti)	Au-Apy-Py-Sti-Jasp	Silty Cb-Carbona-tization, Silicifica-tion, Argilitiza-tion	*8 **10 14 6
Riska	Pliocene	Andesitic pyroclastics	HS-epith. Au-Ag	hydroth bx; fractures, dissem	1 Mt at 1.5 ppm Au (pre mining)	3:1	Au, Ag, Cu	Py-En-Luz	Qz-Al-(Dck-Prl-Diasp)	2, 6
Sangihe Island	7.01±0.89 Ma	andesitic volcanic lapilli tuff,lava,interbedded sediments	HS-epith. Au-Ag. Porphyry-style Cu-Au	auriferous Au vn	na	na	Cu,Pb,Zn, Ag	Ccp-Clc	Clay-Sil-Chl-	6
Sumalata	na	andesitic volcanic	a.Polymetallic vein* b.intrusion related BM-Au	bearing shear zone	na	na	Cu,Pb,Zn, (Au,Ag)	Gn-Sph-Ccp-Qz-Cal		*8 **6
Tanoyan	Pliocene (?)	Andesitic bx/aggl.	a.LS-epith. Au* b.IS-epith. Au-Ag**	Qz-chald vn	2.2 Mt at 1.3 ppm Au	1:1	Au, Ag, (Cu)	Py (Ccp)	Qz-Clay	*8 **
Tapaada District	Alteration 5-2.5 Ma (bt)	Qz diorite; andesite,volcanics	Porphyry Cu-Au	Stk & dissem	43 MT at 0.08 ppm Au,0.54 %Cu	na	na	Py-Ccp-Bo; chalk blanket up	Qz-Chl-Bt-Anh-Ab-Mgt	8 6

Deposit	Age	Host rock	Type	Deposit Style	Tonnage Grade	Au/Ag	Metal Sgnature	Mneralogy	Alteration	References
								to 40m thick		
Toka Tindung	Pliocene HR(1.7 - 2.7 Ma) 1.8-2.2 Ma(ad)	andesitic volcaniclastics	LS-epith. Au-Ag	Qz - Chald – Ad, Stk,Vn	15.5 Mt at 3.4 ppm Au, 8 ppm Ag	2:1	Au, As, Sb, Hg,Mo	Electrum & native form; Ag-Se Sulph, Py	Qz-Ad-Chl-ill	6
Tototopo	Pliocene	Rhyodacite volc; dome diatreme complex	a.LS-epith. Au b.IS-epith. Au-Ag**	Qz-Vn	5.4 Mt at 3 ppm Au	na	Au, As, Sb,(Pb),Ag	Au as electrum & native form; Py-(Apy-Stib-Sph-Gn)	Qz-Ad-Ill-Py	**6;1

Table 4. Features of Various Deposits in Western Sulawesi

Deposit	Age	Host rock	Type	Deposit Styles	Tonnage and Grade	Au-Ag ratio	Metal Signature	Mineralogy	Alteration	References
Awak Mas, Sallu Bullo, Tarra	Late Cretaceous (?)-Pliocene (?)	Metasediments, metavolcanics	a.Sediment Hosted (orogenic Au)* b.Intrusion related-Au **	Qz-Ab-Cb Vn, Bx	20.4 Mt at 0.82 ppm Au (2011)	9:1	Au-Sb- As (Hg)	Py (Ccp-Sph-Ttr-En-Luz - Gn)	Ab-Cb-Sil-Chl-Ep-Pmp-Act	*15 **6 *This study
Esang	na	meta-sediments	intrusion related Au	Qz-Cb-vn	na	na	na	Py, Apy–Po-Ccp	Qz-Ser /ill-Py	6
Malala	Host rock: 4 Ma	quartz monzonite	Porphyry Mo	Qz-Kfs-veins	100 Mt at 0.14% MoS_2	na	Mo-Cu-Pb-Zn	Mo-Mgt-py-sphga-Ccp	1)Qz-Bt-Kfs 2)Cb-Ser/ill-Chl	6
Masabo	Late Miocene	syenite dykes; metabasalt	Porphyry Cu	1) Diss 2) Qz veinlet	na	na	Cu-Mo-Pb-Zn-Bo	py-Ccp-po	1) Act-Ab 2) Bt-mgt	6

Deposit	Age	Host rock	Type	Deposit Styles	Tonnage and Grade	Au-Ag ratio	Metal Signature	Mineralogy	Alteration	References
Mangka-luku	na	meta-sediments, Qz monzonite	intrusion related-Au	Qz-Cb-vn	na	<3	Pliocene	Au as electrum; Py-Apy (Arg-Ccp-Cv)	1) Kfs-Bt-Act-Qz 2) Qz-Chl-Ser/ill 3) Qz-Ch-Ep-Act	6
Palopo	Miocene	volcanic and metasediments	Intrusion related-Au	Super-gene enrichment, Qz-Cb-vn	na	na	Au-Pb-Zn-Cu	Apy-Py (Ccp-cov-Cct), Au as electrum; Arg	1) Bt-Kfs-Act-Qz-Chl 2)Qz-Chl-Ser(Prl) 3)Qz-Chl-Ep-Act-Cb	16,17
Poboya	Pliocene	meta-monzonite, gneiss, schist	Epith. Au-Ag	Qz-Cb-vn; stk	6.7 Mt at 4.33 ppm Au (2013)	<1	Au-Cu-As-Sb-Pb	Py-Sph-Gn-Ccp	Kln-Dck-Qz-al	6,18; 19;
Sasak	Late Miocene	monzonite stocks; & dykes; Bx	Porphyry Cu-Au	1)Diss Py +Ccp 2)Qz-Kfs-Sulph	na	na	Cu-Au-Pb-Zn	Py-Ccp-Bou-Mgt	1) Bt-Mgt 2) Ser-Ill-Chl	6

Abbreviations for Tables 3-4.
Aca=acanthite. Act=actinolite. Ad=adularia. Aggl=agglomerate. Al=alunite. Ab=albite. Anh=anhydrite. And=andalusite. Arg=argentite. Apy=arsenopyrite. Au=gold. Brt=barite. Bou=boulangerite. Bt=Bt. Bx=breccias. Cal=calcite. Cb= carbonate. Chald=chalcedony. Cct=chalcocite. Chl=Chlorite. Cin=cinnabar. Ccp=chalcopyrite. Cv=covellite. Dias=diaspore. Dck=dickite. Dissem=disseminated. Dol=dolomite. En=enargite. Ele=electrum. Ep=epidote. Gn=galena. HS=high sulphidation. Hydroth=hydrothermal. Ill=illite. IS=intermediate sulphidation. Jas=jasperoid. LS=low sulphidation. Kln=kaolinite. Kfs=potassium felspar. Kut=kutnohorite. Mar=marcasite. Mgt=magnetite. Msc=muscovite. Moly=molybdenite. Or=orthoclase. Pmp:pumpellyite. Po=Pyrrhotite. Pol=polybasite. PPyg=proustite-Pyrargyrite. Py=Pyrite. Prl=Pyrophillite. Pot=potassic. Phy=Prllic. Prop=propilitic. Rho=rhodochrosite. Ser=Sericite. Sid=siderite. Sm=smectite. Sph=sphalerite. Stib=stibnite. Stk=stockwork. Sulph=sulphide. Ttr=tetrahedrite. Qz=quartz. Vn=vein. Vug=vuggy.

References for Tables 3-4:
[1] Hardjana and Sweeney (2011). [2]Hardjana (2012). [3]Swift and Alwan (1990). [4] Wisanggono et al. (2011). [5] Lubis et al. (1994). [6]van Leeuwen and Pieters (2011). [7]BHP-Utah Pacific Inc.,unpub data. [8]Kavalieris et al. (1992). [9] Kavalieris et al. (1990) [10]Sillitoe (1994). [11]Garwin et al. (2005). [12]Perelló (1994). [13] Yamamoto et al. (2013). [14] Turner et al. (1994). [15]Querubin and Walters (2012). [16]Musri et al. (2011). [17] Mclean (2010). [18]Internal Report PT CPM unpub data (2013). [19]Newcrest Mining (2004).

3.4 The geology of the Latimojong region

The Latimojong Metamorphic Complex (Fig. 13) is situated in the Western Sulawesi arc, as part of a Late Cretaceous accretionary complex (Wakita 2000; van Leeuwen and Muhardjo 2005; Kadarusman et al. 2007; White et al. 2017). It consists of high-pressure low temperature metamorphic rocks (phyllite, chlorite phengite schist, metasandtone), tectonically mixed with chert and ophiolitic rocks (metabasite, volcaniclastic). The unit is moderately to strongly folded. According to Bergman et al. (1996), Soesilo (1998) and Parkinson (1998), the Latimojong Complex underwent high-pressure metamorphism followed by the obduction of the Lamasi Complex.

The Lamasi Complex, part of the East Sulawesi Ophiolite (ESO) (Parkinson 1998; Kadarusman et al. 2004; White et al. 2017), is situated east of the Latimojong Complex. It is composed of dioritic plutons, basaltic sheeted dykes, pillow lavas, greenstones and tuff (Bergman et al. 1996)(Fig. 13). The Lamasi Complex is intensely deformed, metamorphosed by ocean-floor metamorphism, and bounded by thrust faults. Generally, the mafic components from the Lamasi Complex have depleted Sr-Nd isotopes, MORB-like geochemistry, and possibly represent obducted MORB or back-arc oceanic crust (Bergman et al. 1996). Isotopic data (K-Ar, ^{40}Ar-^{39}Ar, Rb-Sr and Sm-Nd) suggest Cretaceous to Eocene formation ages (Priadi et al. 1994; Bergman et al. 1996; Parkinson 1998). The timing of ESO obduction onto the Sundaland craton is dated at 30 Ma, based on the K-Ar age of the metamorphic sole (Parkinson 1998). In contrast, White et al. (2017) suggested that the timing of ophiolite obduction was between Early and Middle Miocene, and the Lamasi Complex may represent Eocene-Oligocene arc/back-arc volcanic rocks.

The development of an accretionary complex of the Latimojong Metamorphic Complex began during the Cretaceous. This complex was deformed and uplifted above sea level before the Eocene (White et al. 2017). During this period, the Latimojong Metamorphic Complex was deformed and metamorphosed into greenschist- to blueschist-facies rocks. The collision between different parts of Sulawesi causing ophiolite emplacement (Parkinson 1998), which may be interpreted as an arc-continent collision between the micro-continental Sula Spur

and North Arm of Sulawesi in the Early Miocene (Bergman et al. 1996; van Leeuwen and Muhardjo 2005; Watkinson et al. 2011).

Soesilo (1998) have distinguished several deformational phases in the Latimojong Complex. First, (i) initial deformation and metamorphism of siliciclastic sedimentary, volcanic rocks and carbonate materials. Metamorphism started from zeolite to pumpellyite - actinolite facies. Metamorphism occured at a temperature of 310 - 350°C and pressure of 3 - 4.5 kbar, corresponding to depth of > 9 km. (ii) Ductile deformation, blueschist- to greenschist-facies metamorphism of metasedimentary and metavolcanic rocks, characterized by the pumpellyite-actinolite and glaucophane in metavolcanic rocks. The estimated temperature and pressure are > 350° C and > 6 kbar and further increase up to 550° C of the early amphibolite facies. The last stage is (iii) brittle deformation with the formation of chlorite and calcite as a crack filling.

White et al. (2017) presented an updated geological map and revised stratigraphy of the Latimojong region, including biostratigraphic ages, whole-rock data and age dating of zircon extracted from igneous rock (Fig.14). They propose to distinguish between the Latimojong Formation and the Latimojong Metamorphic Complex (previously this region was named as the Latimojong Complex). The Latimojong Formation consists of Upper Cretaceous weakly deformed, unmetamorphosed sediments or very low-grade metasediments, while the Latimojong Metamorphic Complex is an accretionary complex of low- to high-grade metamorphic rocks tectonically mixed with cherts and ophiolitic rocks. The stratigraphy of the Latimojong region is shown in Figure 14. Additional comments are added based on the results of this study.

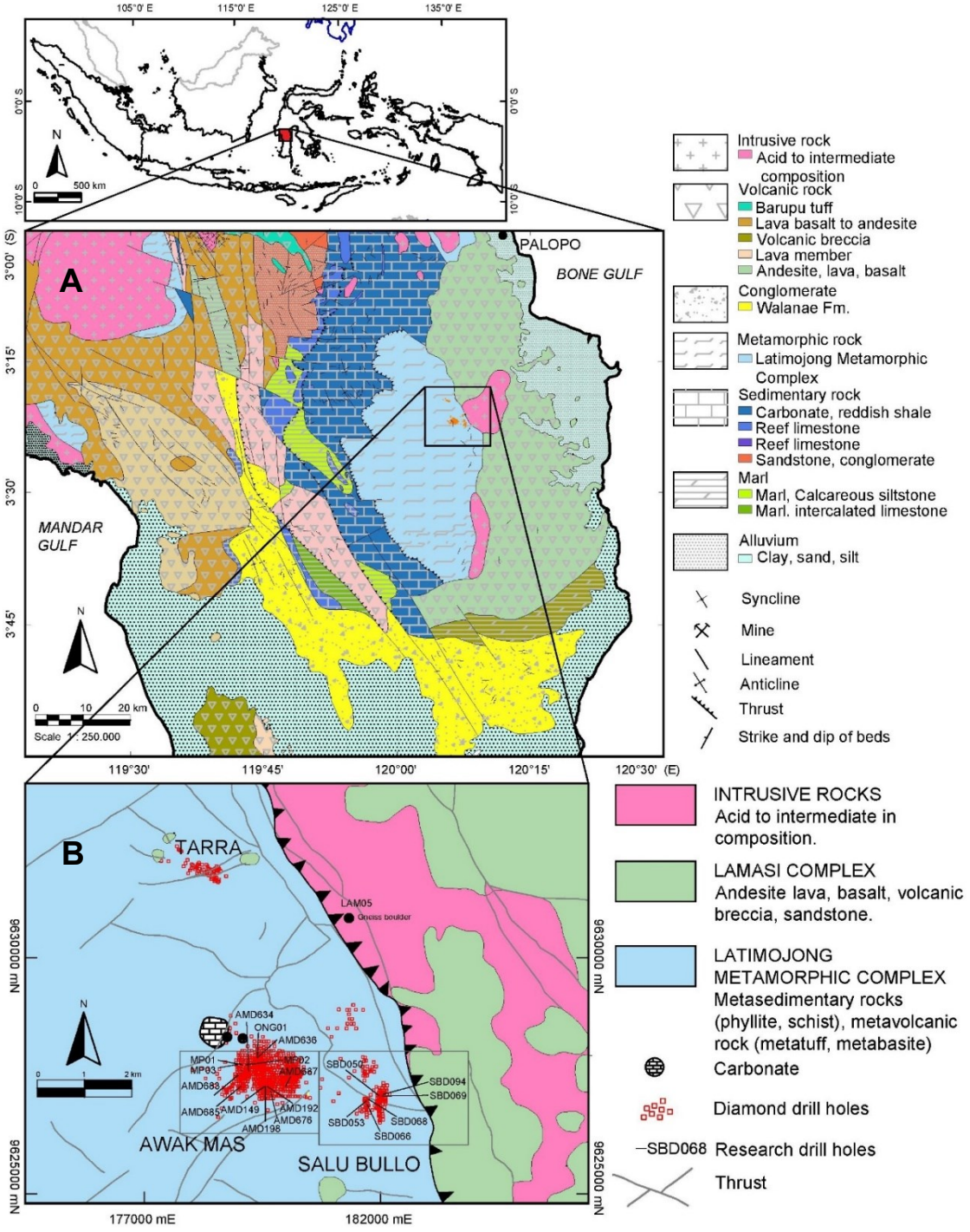

Fig. 13. Geological map of the Latimojong area. (A) Simplified geological map of the Latimojong metamorphic complex and its surrounding (modified after Djuri et al., 1998). Research area is highlighted by square line. (B) General map of the Latimojong metamorphic complex in South Sulawesi with location of the studied ore deposits (Tetra Tech 2013).

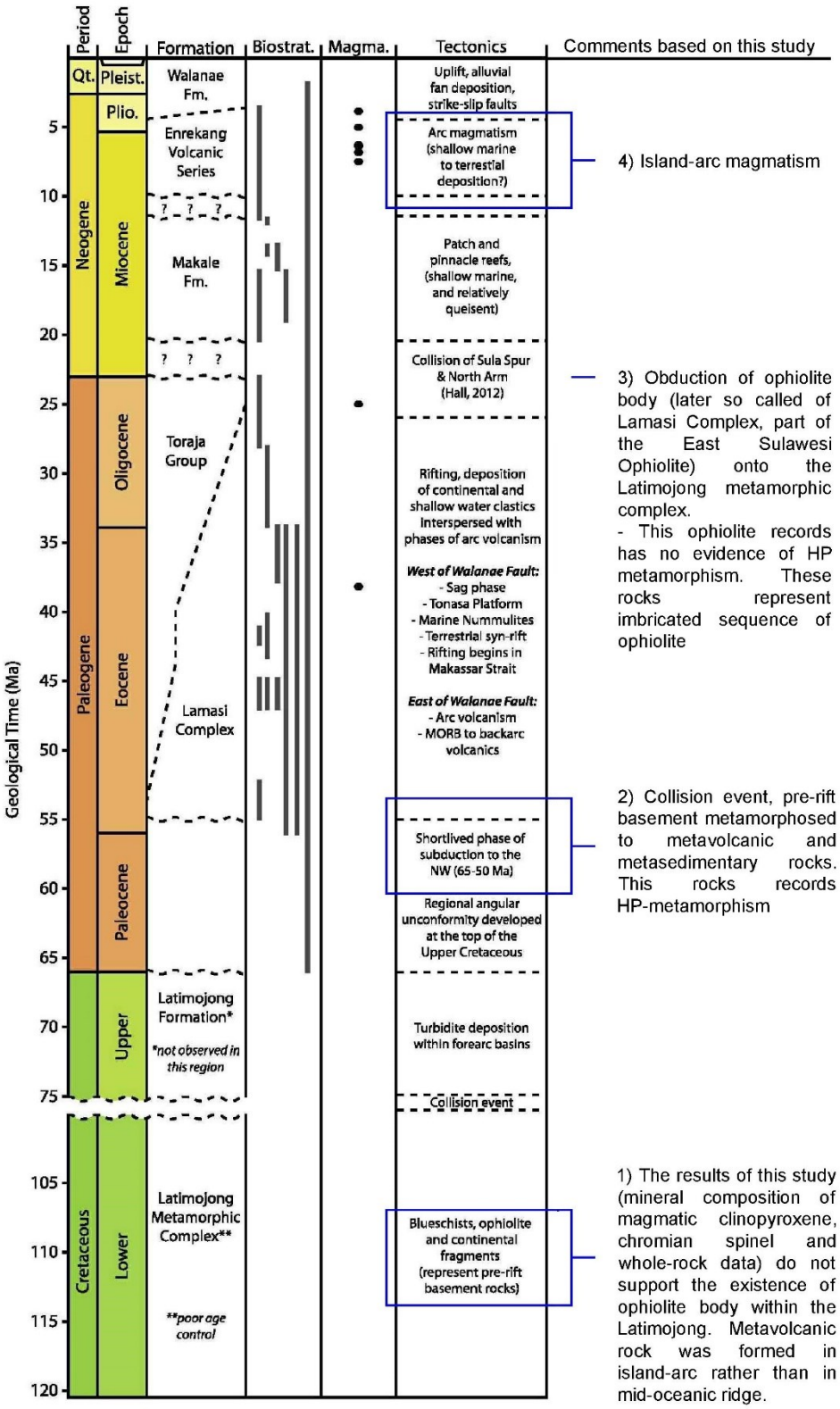

Fig. 14. Stratigraphic chart for Latimojong Mountains (after White et al. 2017). Comment sections on the right side of the stratigraphical unit are compiled based on the results of this study.

3.5 Historical exploration

This chapter was summarized from unpublished Technical Reports on Awak Mas and Salu Bullo Gold Project (Tetra Tech 2013, 2013). Exploration in this area has been carried out by several companies since 1987. The discovery of the deposit was based on artisanal mining activity, which then was followed by semi detailed exploration during 1988 to 1990. During the years, geochemical and soil sampling, geological photos, airborne survey, GIS database, regional mapping and detailed structural mapping had been done in the area. During this earlier time, the company was owned by Asminco and New Hope Consolidated Industries.

In 1991, 77 bore holes were conducted to define the Awak Mas target. It was continued from 1993 to 1997 resulting in 791 bore holes (diamond and reverse circulation drilling). During this period, individual studies were conducted and resulted in a feasibility study in 1996 with resources of 3 million tonnes. Due to a fall in gold price in late 1997, an extension of the feasibility study period was granted by the government and gave the opportunity to find another prospect around Awak Mas. These resulted in the definition of the Tarra, Kandeapi and Salu Bullo deposits.

From 1991 to 1998, the ownership of the company changed to the Battle Mountain Gold Company (1991); Lone Star Exploration NL-LSE, Gasgoyne Gold Mine NIL-GGM and JCI Limited-JCI (1994, combining the interest of GGM-NIL-LSE into Masmindo Mining Company-MMC); Placer Dome Inc.-Placer joint ventures with MMC (1998), and Placer withdraw in 1999.

During 1998, the priority target of regional exploration was the Salu Bulo Prospect, with an estimated resources of approximately 160,000 to 230,000 ounces (4,500 to 6,500 kg) gold. The Tarra Prospects were also explored by traverse mapping, trenching, channel sampling, and drilling. From 1998 to 2004, no exploration program had been done. The operation re-started in 2004, with the aims of arranging the old data into a single database. Vista Gold acquired 100% of interest and formed the company Masmindo Dwi Area (MDA).

The exploration program continued in 2006, focusing in the Rante and the Lematik area with total of 470.20 meters intercepts. In late 2009, the ownership

was changed into One Asia and the project completed 75 holes with total 5,137.60 meters intercepts. The total drilling in the Awak Mas project since 1991 and its satellite prospects adds up to 1,012 holes with a total of 118,081.30 meters as of September 2011. Total resources in the Awak Mas deposit are 47.3 Mt at 1.4 ppm Au (One Asia press release, 2015)(Table 5).

Table 5. Resource statement of Awak Mas deposits per March 2015

Deposit	Resources				Grade (ppm)
	Measured (Mt)	Indicated (Mt)	Inferred (Mt)	Total (Mt)	
Awak Mas	12.0	35.0	0.3	47.3	1.4
Sallu Bullo	2.2	3.4	0.5	6.1	2.1
Tarra			7.4	7.4	1.3
Total				60,8	1.5

Note: resources calculation were based on JORC code 2012 with cut off grade 0.5 ppm Au (One Asia Press Release, 2015).

3.5.1 The Awak Mas gold deposit

The mineralization at Awak Mas is associated with quartz veins, brecciation and silicification within foliated meta-sediments and along fault zones. Albite – silica – pyrite - carbonate alteration generally accompanies and envelopes quartz veins. Gold mineralization is associated with fine-grained pyrite within alteration zones. Two main styles of mineralization are: (i) steeply dipping, structurally controlled quartz veins and stockworks with prominent brecciation and silica alteration, and (ii) foliation parallel zones of quartz veins and stockworks.

The steeply dipping zones along pre-mineral faults serve as conduits to hydrothermal fluids. The second style formed in an upper level, in near a surface environment where hydrothermal fluids migrate laterally into permeable beds or foliated (bedding parallel) zones.

A soil up to 15 m thick covers bedrock in the Awak Mas region. The bedrock generally consists of light to dark grayish metasedimentary rock, mainly of phyllite, carbonaceous phylite, chlorite phengite schist, hematitic mudstone, metasiltstone and metasandstone. Layering dips overall 15-50° northward. The veins have an extent of 700 to 910 meters. The shallow veins are generally thicker than the deeper part. The average thickness of shallow veins ranges from 5 to 60 meters, while the deeper parts range from 5 to 10 meters.

There are five main veins at Awak Mas and these veins are segregated by three major faults. The five domains of Awak Mas, from west to the east are Mapacing, Ongan, Lematik, Tanjung and Rante (Figs. 15 - 17). Major structures in the Awak Mas district are three north-south trending discrete sub vertical fault zones (Chinese, Garlic, and Discovery Faults) up to 40 m wide cutting the project area (Fig. 16). Faulting varies from syn- to post mineralization with multiple episodes of movement including early dextral phases noted by displacement of mineralized domains, and later sinistral displacement. Sheared intervals and minor conjugate faults occur between the major structures.

The Chinese Fault displays moderately strong fracturing with sheared intervals, characterized by cataclastic textures, and/or mylonites with fragmented host rock and quartz materials; fault gouge and slicken-slides are observed locally. The fault indicates early stage(s) of overall dextral oblique displacement. The Chinese Fault transects mineralization resulting in non-continuity of grade across the structure.

The Garlic Fault extends through the central part of the Awak Mas area and splays towards its southern extent. It is characterized by high angle, dip slope movement. The Discovery Fault is sub-parallel to the Chinese Fault and Garlic Fault, and separates the mineralization into the east and south-east part of the Awak Mas deposit. Figures 15 - 17 show the main structures and the section through the five main domain at Awak Mas.

Fig. 15. Geological domains in Awak Mas deposits (looking northwest)

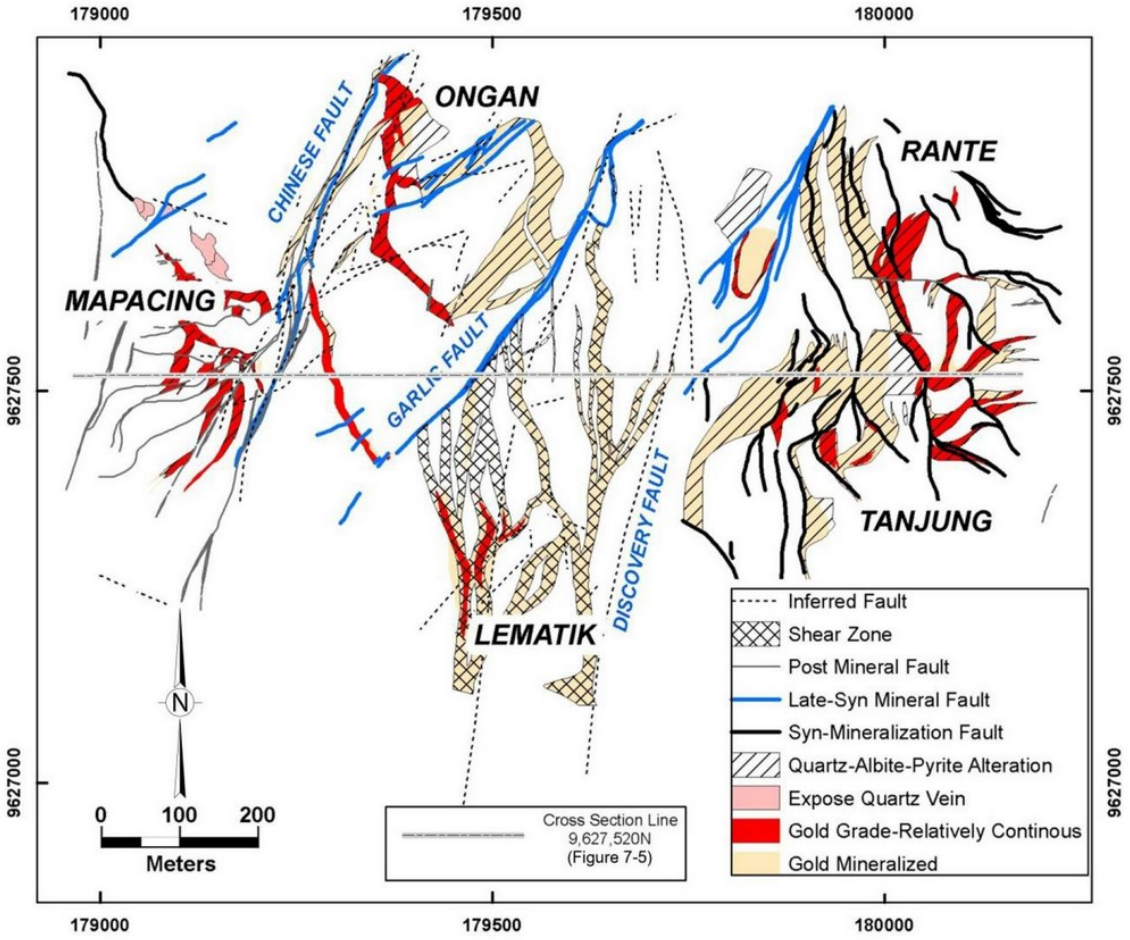

Fig. 16. Regional structure and mineralization in the Awak Mas (Querubin and Walters 2012)

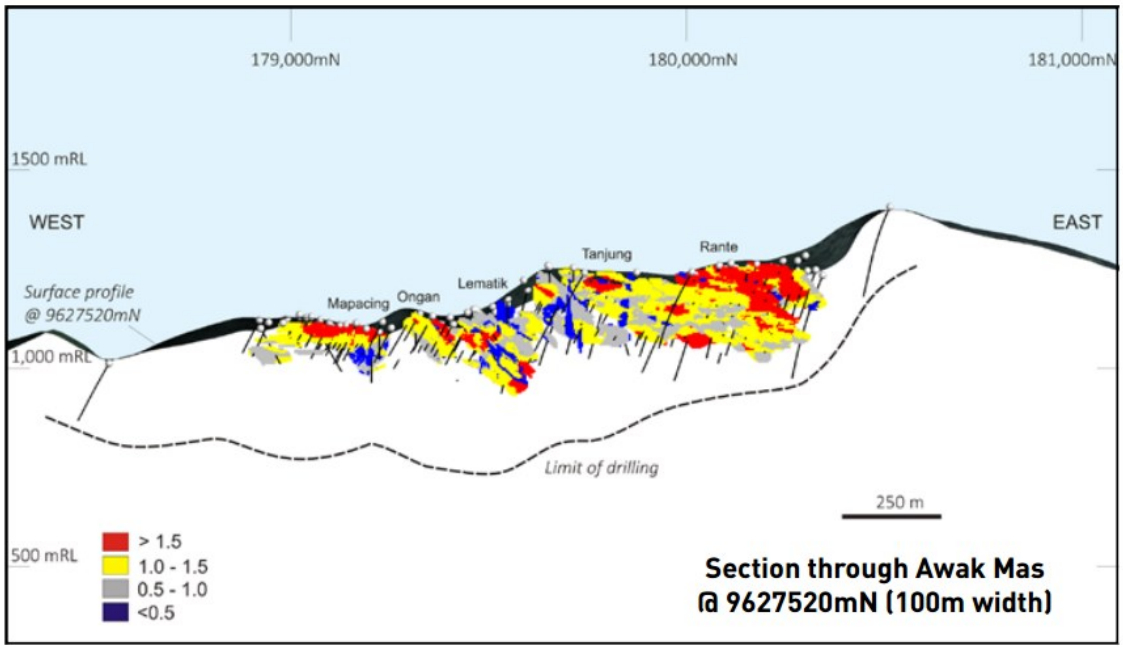

Fig. 17. Cross section through the Awak Mas along 9627520 mN (Cube 2017)

3.5.2 The Salu Bullo gold deposit

The Salu Bullo gold deposit is considered to be analogous to the Awak Mas deposit, but with a more dominant sub-vertical structural control. The host rock is metabasite and metatuff and this deposit is associated with strong albite alteration. Mineralization overprints ductile deformation and is related with (i) quartz vein stockworks and (ii) quartz – albite – pyrite - chlorite alteration. Four main ore veins in subsequent order from north to south are: Freddie, Bandoli, Biwa and Lelating veins (Fig. 18).

The structural geology is mainly controlled by the accretion of ophiolite rocks onto metasedimentary sequences by the major, north-northwest striking Lamasi-Latimojong thrust (Figs. 18-19). It comprises of a thick-metasedimentary sequence underlain by metavolcanic rocks of the Latimojong metamorphic complex. The metasedimentary rocks generally consist of chlorite phengite schist, phyllite, hematitic mudstone and metasiltstone, as illustrated in Figure 19. The metavolcanic rocks are metabasite, clinopyroxene-phyric basalt and volcaniclastic rocks. Mafic metavolcanic rocks and hematite mudstone alteration are abundant in Salu Bullo and occurs as an important indicator to differ between the Awak Mas and Salu Bullo.

According to the recent feasibility study (Cube 2017), both deposits (Awak Mas and Salu Bullo) were classified as high level, low sulphidation or intrusion related hydrothermal systems. The mineralising fluids have been introduced via structural conduits and have been overprinted by a strong sub-vertical fracture control. In addition to the conformable styles of mineralization, the late stage hydrothermal overprint has deposited gold in some of the major sub vertical structures. The gold mineralisation is characterized by breccias, vuggy quartz infill, and stockwork quartz veins with distinct sub-vertical feeder structures.

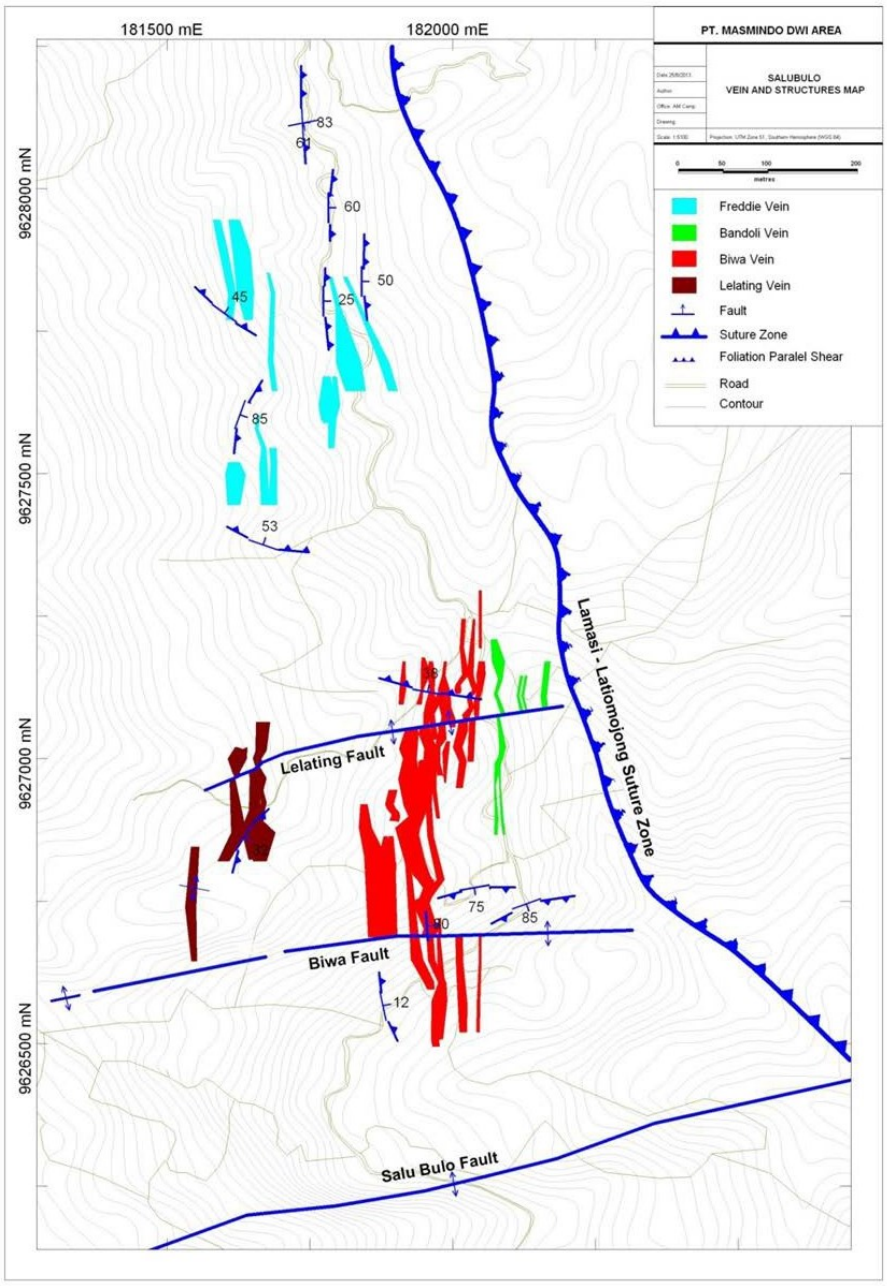

Fig. 18. Main veins of the Salu Bullo deposit (Tetra Tech 2013).

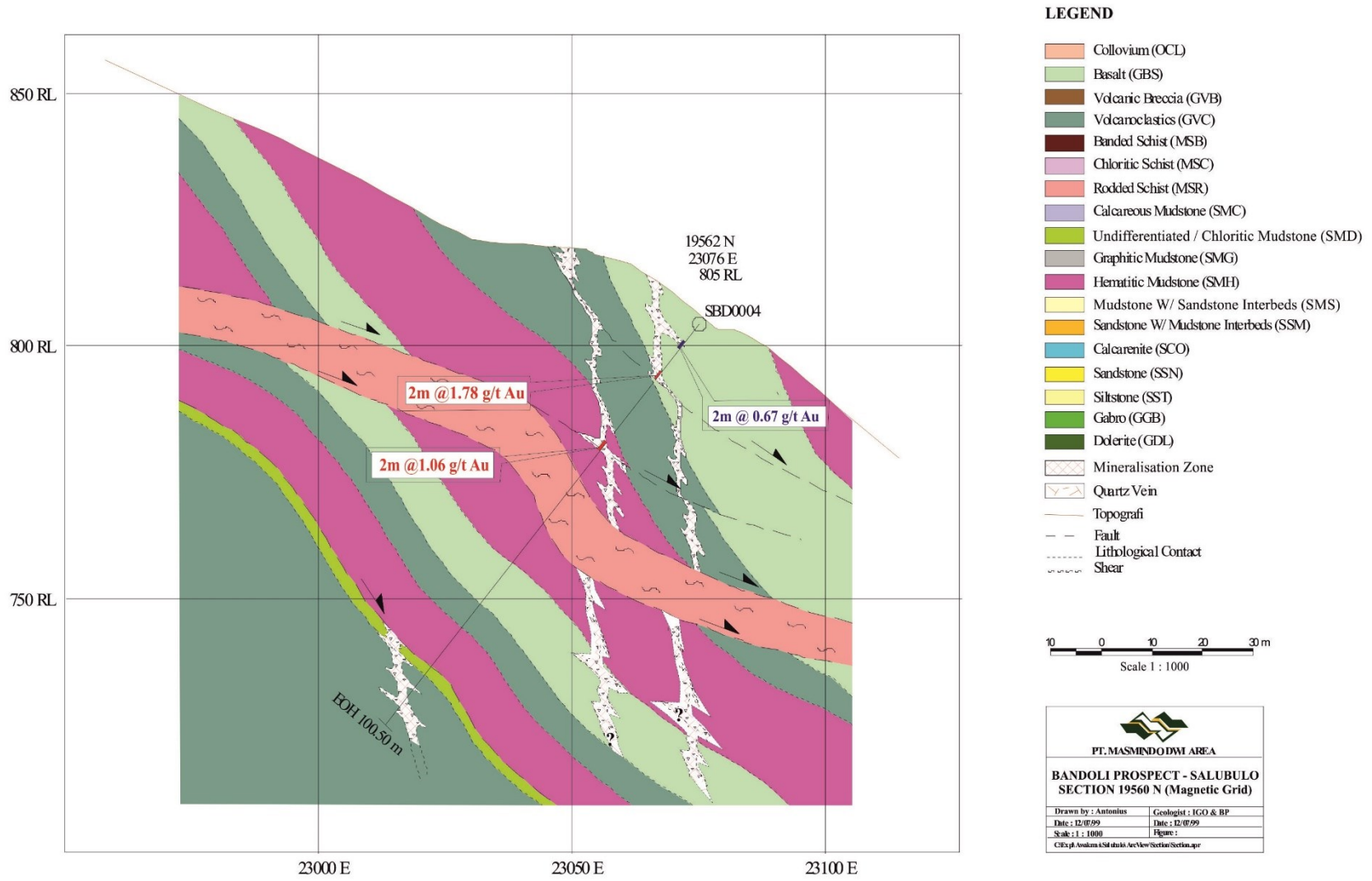

Fig. 19. Cross section along SBD004 of the Bandoli vein, Salu Bullo (One Asia Resources, unpublished report).

4. METHODS AND ANALYTICAL TECHNIQUES

Representative samples were used for petrographical, mineralogical, geochemical and fluid inclusion study. The analytical approach applied is based on the following techniques:

4.1. Sample collection

Geological mapping and sampling were conducted in the Awak Mas and Salu Bullo regions on 11 - 17 January 2015 and 16 – 21 February 2016. The dense forest, steep topography and extensive weathering render geological observation rather difficult. Quartz veins with visible sulphides, various host rocks and samples from artisanal mining were collected. The sample location was recorded using a Garmin Etrex 30 GPS receiver.

Fourteen drill holes from previous diamond core drilling were observed in detail and logged to understand the lithology of the research area. Quarter-core samples were collected by cutting core samples from remnant half core samples (original drill core samples were split in half for initial analysis by the company). The quarter core samples were transported from the mine site to the Chair of Geology and Economic Geology, Montanuniversität Leoben in February 2015 and 2016. Drill hole descriptions are shown separately in Appendix A and Appendix B.

4.2. Petrography

4.2.1. Sample preparation

Thirteen thin sections (75 x 24 x 10 mm) covered by a cover slip attached to the rock with epoxy and nineteen polished sections mounted in resin (diameter of 25 µm) were prepared in Bandung, Indonesia. However, chemical compositions of minerals cannot be obtained from covered thin sections, therefore, more polished thin sections were prepared in Leoben, Austria. In total, twenty-eight polished thick sections mounted in resin and one hundred one polished thin sections were produced.

Polished thick sections have a diameter of 25 mm and polished thin sections have a dimensions of 24 x 32 x 16 mm. Polished thin sections were ground by hand with 800 – 1000 – 1200 grit silicon carbide, followed by fine polishing with

diamond compound 9 – 3 – 1 – 0.5 µm. The interference colors of quartz are used as an indicator to estimate the thickness of thin sections. For a routine mineralogical observation, thin sections are ~30 µm thick.

Thin sections for a LA-ICP-MS were produced separately using a similar procedure with a thickness at around 100 µm. Nineteen doubly-polished sections (~150 µm thickness) of the quartz and carbonate veins were produced for fluid inclusions study. Appendix A-C show the list of samples and analytical methods for this study, respectively.

4.2.2. Optical microscopy

Optical microscope investigations were carried out on thin, polished and double polished sections. Petrographic descriptions of vein and host rock were performed at the Chair of Resource Mineralogy and Chair of Geology and Economic Geology at the Department of Applied Geosciences and Geophysics, Montanuniversität Leoben using an Olympus BX60 microscope.

4.2.3. Scanning Electron Microscope – Energy Dispersive X-ray (SEM-EDX)

The mineralogical composition of was determined using a scanning electron microscope Zeiss EVO MA 10 equipped with a secondary electron (SE) and a back-scattered electron (BSE) detector at the Chair of Geology and Economic Geology, Montanuniversität Leoben, Austria. Scanning electon microscope (SEM) was equipped with Bruker Nano Xflash 430M energy dispersive X-ray (EDX) detector. The instrument operated at 15 - 20 keV accelerating voltage, a 100 nA beam current, a 30 µm aperture size and a 10 - 11 mm free working distance.

4.2.4. Electron microrpobe analyses (EMPA)

Selected mineral grains were subsequently analysed using an electron microprobe (EMPA) at the Eugen F. Stumpfl Laboratory, Montanuniversität Leoben, Austria. The instrument was operated in WDS mode at 15 keV accelerating voltage, 10 nA beam current and with a beam diameter of 1 µm. The

analyses of sulphide, sulphosalt and gold were carried out at 20 keV. Table 6 - 8 shows the list of reference materials for electron microprobe analyses.

Table 6. Reference materials for electron microprobe analyses of silicates.

Observation minerals	Reference materials	Elements	Diffracting Crystals	Peak counting time	Background counting time
Chlorite					
	Albite	Na, Al	TAP	20s	10s
	Wollastonite	Ca	PETJ	20s	10s
	Sanidine	K	PETH	20s	10s
		Si	PETJ	20s	10s
	Phlogopite	Mg	PETJ	20s	10s
	Kaersutite	Fe	LIFH	20s	10s
	Rutile	Ti	LIFH	20s	10s
	Rhodonite	Mn	LIFH	20s	10s
	Synthetic Cr_2O_3	Cr	LIFH	20s	10s
Other silicates (mica, pyroxene, albite, amphibole, pumpellyite, epidote)					
	Sanidine	Na	TAP	20s	10s
		K	PETH		
	Albite	Al	TAP	20s	10s
		Si	PETH		
	Wollastonite	Ca	PETJ	20s	10s
				20s	10s
	Kaersutite	Mg	TAP	20s	10s
	Almandine	Fe	LIFH	20s	10s
	Rutile	Ti	LIFH	20s	10s
	Rhodonite	Mn	PETJ	20s	10s

Table 7.Reference materials for electron microprobe analyses of sulphide, sulphosalt and gold.

Observation minerals	Reference materials	Elements	Diffracting Crystals	Peak counting time	Background counting time
Pyrite					
	Skutterudite	Co		20s	10s
		As		40s	20s
	Pyrite	Fe, S		20s	10s
	Millerite	Ni		40s	10s
	Chalcopyrite	Cu		20s	10s
Sulphosalt					
	Arsenopyrite	As		20s	10s
	Stibnite	S		20s	10s
		Sb		20s	10s
	Synthetic Bi_2Te_3	Bi		20s	10s
	Chalcopyrite	Cu		20s	10s
	Synthetic Ag	Ag		20s	10s
	Sphalerite	Zn		20s	10s

Observation minerals	Reference materials	Elements	Diffracting Crystals	Peak counting time	Background counting time
	Synthetic Pd_3HgTe_3	Hg		20s	10s
	Pyrite	Fe		20s	10s
Gold					
	Calaverite	Au		20s	10s
	Synthetic Ag	Ag		20s	10s
	Pyrite	Fe		20s	10s
	Chalcopyrite	Cu		20s	10s
	Synthetic Pd_3HgTe_3	Hg		20s	10s
	Synthetic Bi_2Te_3	Bi		20s	10s

Table 8.Reference materials for electron microprobe analyses of chromian spinel.

Observation minerals	Reference materials	Elements	Diffracting Crystals	Peak counting time	Background counting time
Chromian spinel					
	Kaersutite	Mg	TAP	20s	10s
	Chromian	Al	TAP	20s	10s
	spinel	Fe	LIFH	20s	10s
	Ilmenite	Ti	PETJ	20s	10s
	Willemite	Si	PETJ	20s	10s
		Zn	LIFH	20s	10s
	Synthetic Cr_2O_3	Cr	LIFH	20s	10s

4.2.5. X-ray fluorescence spectrometry

Major, minor and trace element analyses were performed on ten bulk samples. The element concentration was determined on fused glass bead in boric acid binder using 2.5 grams of the dried and milled sample. A sequential wavelength dispersive X-Ray fluorescence (XRF) spectrometer (Axios-Panalytical) was used at the Department of General and Analytical Chemistry, Montanuniversität Leoben. Total loss on ignition (LOI) was gravimetrically estimated after overnight heating at 950°C. The following elements were analysed by XRF: Si, Na, Mg, Al, P, K, Ca, Ti, V, Cr, Mn, Fe, Cu, Zr.

4.2.6. Inductively Coupled Plasma Mass Spectrometry (ICP-MS) techniques

Inductively coupled plasma mass spectrometry (ICP-MS) was used for the determination of the total elemental composition of samples. The Na_2O_2 sintering technique (Meisel et al. 2002) was used for total digestion. Fine grained samples

(100 mg) and 600 mg sodium peroxide are added into glassy carbon crucibles. Samples were heated at 460°C for 30 minutes followed by heating at 480°C for 30 minutes. The samples were allowed to cool down to room temperature and kept in Teflon beakers. Milli-Q destilled water (Siemens water technology) was added in the crucibles until reaction ended. Crucibles were stirred on magnetic stirrer with a small Teflon coated magnet at about 80°C in order to remove O_2 and unreacted Na_2O_2. Glass lids were used to cover the Teflon beaker during the stirring process. The final solution was centrifuged at 4,000 rpm for 5 min.
The clear supernatant solution was then poured into 100 mL volumetric flasks. Undisolved hydroxides were dissolved in 3 mol/l hydrochloric acid (*ca.* 3 mL). Two ml of concentrated hydrochloric acid was added for rinsing the crucibles. The rinsing solution was added to the volumetric flask. The dissolved residue and the acidified supernatant were combined in a labelled flasks, and then diluted up to 50 ml. One ml of the final solution was diluted up to 5 ml with 1% HNO_3. The clear solution was ready for measurements. Reference material to calibrate the results are: OU7, HARZ, BCR2, DBC1 and MTA1. Analyses were performed at the Department of General and Analytical Chemistry, Montanuniversität Leoben.

4.2.7. Raman spectroscopy of carbonaceous material and fluid inclusions

Nine samples of carbonaceous materials from carbonaceous phyllite and carbonaceous breccia were separated chemically from all other mineral phases (Rantitsch et al. 2004). Measurement of carbonaceous material spectra was performed using a Jobin Yvon LABRAM Raman spectrometer equipped with a Nd-YAG laser (wavelength 532 nm) and a 10x objective. To obtain a better signal to noise ratio, five scans with an acquisition time of 30 s in the 700–2,000 cm^{-1} region were summed to composite spectra. Ten spectra were recorded for each sample. The numerical analysis spectra focuses on four bands in this range, including the G band (centered ~ 1,580 cm^{-1}) and three defect bands, ~1,350 cm^{-1} (D1 band), ~1,620 cm^{-1} (D2 band) and 1,500 cm^{-1}(D3 band). Numerical analysis of the Raman spectrum was performed using the itterative fitting approach “IFORS” of (Lünsdorf et al. 2014). The IFORS software simultaneously fits the

signal and baseline functions without the need for user interaction and therefore, eliminate user subjectivity.

Vapour, liquid and entrapped solid phases of single inclusions within quartz were analysed using the same laser Raman probe. The laser spot on the samples was focused approximately to a diameter of 1 µm. For the analyses of CO_2, N_2, and CH_4 vapour phases, spectra were recorded from 1,000 to 3,800 cm^{-1} using a single 20-s integration time per spectrum. All inclusions for microthermometric analyses were observed carefully using Raman spectroscopy to confirm the composition of the vapour phases.

4.2.8. Laser Ablation-ICP-MS

Laser-Ablation Inductively-Coupled Mass Spectrometry (LA-ICP-MS) was used on selected samples to provide quantitative trace element data for albite and sphalerite. In-situ laser ablation of albite was performed on 100 µm polished thick sections. For sphalerite, rock samples were mounted in epoxy resin and were polished with 3000 grit, 5000 grit and 12000 grit abrasive paper.

The point measurements was performed using an ESI NWR213 Nd:YAG laser system coupled to an Agilent 8800 Triple Quadrupole ICP-MS (ICP-QQQ) at the Chair of Geology and Economic Geology, Montanuniversität Leoben. The measurement of albite was performed on a spot size with diameter of 80 µm. For calibration and data monitoring, synthetic glasses doped with trace element (NIST SRM 612) and synthetic glasses from natural rocks (USGS glasses BCR2G) were used. The albite was analyzed for ^{85}Rb, ^{88}Sr, ^{89}Y, ^{139}La, ^{140}Ce, ^{141}Pr, ^{146}Nd, ^{147}Sm, ^{153}Eu, ^{157}Gd, ^{159}Tb, ^{163}Dy, ^{165}Ho, ^{166}Er, ^{169}Tm, ^{172}Yb and ^{175}Lu. The measurement of sphalerite was performed on a spot size of 20 µm and 10s ablation time because sphalerite has a small and irregular grain size. The sphalerite was analyzed for ^{51}V, ^{52}Cr, ^{55}Mn, ^{57}Fe, ^{59}Co, ^{60}Ni, ^{63}Cu, ^{71}Ga, ^{74}Ge, ^{75}As, ^{82}Se, ^{95}Mo, ^{107}Ag, ^{111}Cd, ^{115}In, ^{118}Sn, ^{121}Sb, ^{201}Hg, ^{205}Tl, ^{208}Pb and ^{209}Bi. MUL-ZnS-1 was used for calibration (Onuk et al. 2016).

A beam of 80 µm with laser frequency of 10 Hz and fluence of 2 J cm^{-2} pulse were used to analyze pyrite grains. Internal standardization was based on ^{57}Fe using stoichiometric iron values of pyrite. The following isotopes were measured:

^{59}Co, ^{61}Ni, ^{65}Cu, ^{67}Zn, ^{75}As, ^{82}Se, ^{107}Ag, ^{121}Sb, ^{130}Te, ^{197}Au and ^{209}Bi. All data are in ppm, except ^{130}Te (in cps). MASS-1, which is a pressed powder pellet doped with 50-70 ppm trace elements (Ag, As, Bi, Pb, Re, Sb, Se, Sn and Te) supplied by the United States Geological Survey (USGS) was used for internal standard for quality control. FeS-1 from Dany Savard (UQAC) was used for calibration. The LA-ICP-MS configuration for measuring pyrite, sphalerite and feldspar is listed in Table 9.

Table 9. LA-ICP-MS configuration for pyrite, sphalerite and albite .

Gas blank	30s	He	750 mL
Laser on	30s	Fluent laser	4.5 J cm^{-2}
Laser pulses	600	Frequency	10 Hz
Oxidate formation	< 0.3%	Double judge	0.6%

4.2.9. Microthermometry

Nineteen double-polished sections, which represent the various hydrothermal alteration systems with and without gold mineralization were examined petrographically, and of these nine samples were selected for microthermometric analyses.

A transmitted light microscope was used to obtain information on the relative formation chronology and paragenetic sequences of the fluid inclusions (FIs). Microthermometric data were collected using a Linkam THSMG 600 heating and freezing stage equipped with a microscope with objective magnification of 100x. Calibration was done by using synthetic fluid inclusions with the melting point of CO_2 at −56.6 °C, the melting point of water at 0.0 °C and the critical homogenization temperature of water at 374.0 °C. The precision within the low temperature range is estimated to be 0.1°C.

The volume fraction of fluid inclusion was determined by measuring the vapour bubble diameter at room temperature using the 100x magnification objective lens. Calculation of perimeter and area of vapour was obtained by drawing the fluid inclusion along the perimeters of the inclusion and vapour bubble using ImageJ software (Bakker and Diamond 2006). For optimal measurements, large, regular and near-surface inclusions were considered to minimize the error. For irregular

shaped inclusions, volume fractions were calculated using the *PVTX* properties as an input of the BULK software (Bakker 2003).

The software packages *CLATHRATES* (Bakker 1997) and *FLUIDS* (version 1) (Bakker 2003) were used to calculate fluid properties of fluid inclusions from Raman spectroscopy, microthermometry and volume fraction based on optical measurements. Program *ICE* from the package *CLATHRATES* (Bakker 1997) was used to calculate bulk fluid properties based on T_m(ice), T_m(clathrate), gas composition and volume-fraction composition. The properties of low-density gas mixtures are calculated with the equations from Peng and Robinson (1976). Furthermore, the equation of state of Duan et al. (1992a, 1992b, 1995) was selected for fugacity calculations in clathrate equilibria. The isochores that results from the output of *ICE* and *BULK* software were further calculated using software *ISOC* (Bakker 2003). The equation of state of Anderko and Pitzer (1993) and Duan et al. (1995) were used to calculate the isochores in the H_2O-CO_2-CH_4-NaCl fluid system.

4.2.10. Crush leach analysis on bulk samples

Sixty three quartz and fourteen carbonate samples were selected for crush-leach analyses as described in Banks and Yardley (1992), Banks et al. (2000) and Gleeson (2003). Quartz samples were treated with HNO_3 in a sand bath to remove possible contaminations. 1- to 2-mm quartz and carbonate grains were cleaned by boiling and washing three times in milli-Q water. About 1 g dried samples was transferred into an agate mortar, 5 mL of milli-Q water was added and samples were crushed for 2 minutes for carbonate and 3 minutes for quartz. The solutions were filtered through 0.2 µm nylon filters prior to analyses. The leachates were analysed for F^-, Cl^-, Br^-, I^-, SO_4^{2-} by ion chromatography with a micro membrane suppressor Dionex DX-500. Cations (Li^+, Na^+, K^+, Mg^{2+}, Ca^{2+}) were analysed in the aliquots of the same solution by a Dionex DX-120 system. All measurements were conducted at the Chair of Geology and Economic Geology, Montanuniversität Leoben.

4.2.11. Stable isotope geochemistry

Sixteen carbonate samples were measured for the oxygen and carbon isotope geochemistry at the at the Fritz Ebner Isotopic Laboratoy, Chair of Petroleum Geology, Montanuniversität Leoben. Samples were prepared by using a dentist drill. 0.2 mg of rockpowder was drilled and transferred into autosampler vial and sealed with butyl-rubber septa. Analyses was carried out with Thermo Scientific DELTA-V isotopic ratio mass spectrometer (IRMS) employing a Finnigan Gas Bench II. Carbon and oxygen isotope measurements were performed by addition of anhydrous H_3PO_4 to the samples heated at 70°C using a GC PAL on-line system. The results are reported relative to the VSMOW standard for both $\delta^{13}C$ and $\delta^{18}O$. The reproducibility was better than 0.2‰.

The approach devised for this research is shown in Figure 20.

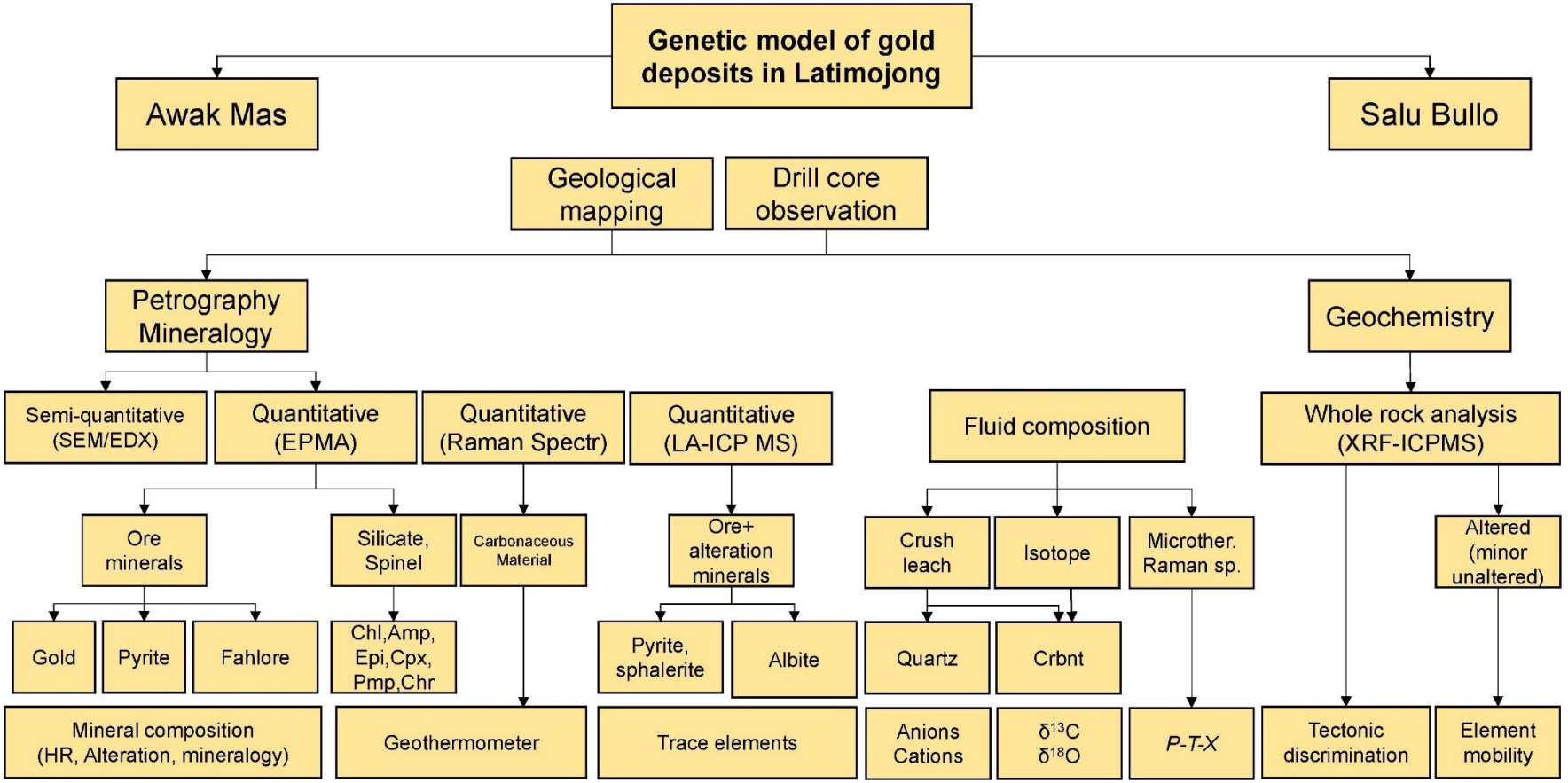

Fig. 20 Flowchart of research methodology presented in this thesis

5. PETROGRAPHY, MINERAL COMPOSITIONS AND GEOCHEMISTRY OF THE METASEDIMENTARY AND MAFIC METAVOLCANIC ROCKS

5.1 Introduction

Almost 50 mineral species have been identified in metasedimentary and metavolcanic rocks of the Latimojong metamorphic complex. Observations are based on geological mapping, macroscopic characterisation, observations of thin, double-polished and polished section samples. In total, almost 150 samples were studied. The mineralogy was confirmed using SEM-EDX and/or EMPA. Some of the minerals were characterised using Raman spectroscopy (i.e. anatase, tourmaline) during the observation of vapour phases of fluid inclusions. Table 10 presents a list of the minerals in the Awak Mas and Salu Bullo deposits. The ore and rock-forming mineral names are abbreviated according to Whitney and Evans (2010).

Table 10. List of minerals mentioned in this manuscript.

No	Symbol	Mineral Name	Relative abundance	EMPA
1	Act	Actinolite	Abundant	√
2	Ab	Albite	Abundant	√
3	Ant	Anatase	Trace	-
4	Ank	Ankerite	Minor	-
5	Ap	Apatite	Minor	-
6	Au	Gold	Trace	√
7	Aug	Augite	Minor	√
8	Bdy	Baddeleyite	Trace	-
9	Bi	Native bismuth	Trace	-
10	Bis	Bismuthinite	Trace	-
11	Brt	Barite	Trace	-
12	Bn	Bornite	Trace	-
13	Cal	Calcite	Abundant	-
14	Car	Carrolite	Trace	√
15	Ccp	Chalcopyrite	Minor	-
16	Chm	Chamosite	Trace	√
17	Chr	Chromian spinel	Trace	√
18	Clc	Clinochlore	Abundant	√
19	Cob	Cobaltite	Trace	-
20	Cv	Covellite	Minor	-
21	Dol	Dolomite	Abundant	-
22	Di	Diopside	Minor	√
23	Eng	Enargite	Minor	√
24	Ep	Epidote	Minor	√
25	Fam	Famatinite	Minor	√
26	Gn	Galena	Minor	-

No	Symbol	Mineral Name	Relative abundance	EMPA
27	Goy	Goyazite	Trace	-
28	Gr	Graphite	Minor	-
29	Hem	Hematite	Minor	-
30	Kao	Kaolinite	Trace	-
31	Kfs	K-Feldspar	Trace	-
32	Luz	Luzonite	Minor	√
33	Mnz	Monazite	Trace	-
34	Or	Orthoclase	Trace	-
35	Ph	Phengite	Minor	√
36	Pmp	Pumpellyite	Minor	√
37	Chl	Pycnochlorite	Abundant	√
38	Py	Pyrite	Abundant	√
39	Qz	Quartz	Abundant	-
40	Chl	Ripidolite	Abundant	√
41	Rt	Rutile	Minor	-
42	Ser	Sericite	Minor	-
43	Sd	Siderite	Minor	-
44	Sp	Sphalerite	Minor	-
45	Spn	Sphene (titanite)	Trace	-
46	Ttr	Tetrahedrite*	Minor	-
47	Tur	Tourmaline	Trace	-
48	Tnt	Tennantite	Minor	√
49	Xtm	Xenotime	Trace	-
50	Zrn	Zircon	Trace	√

√ quantitatively measured using EMPA; - confirmed by SEM-EDX and/or Raman spectroscopy

5.2 Presentation of results

All rocks were petrographically and mineralogically studied in polished thin or thick sections. The list of samples and the results of investigations are available in Appendix B. The lithological descriptions are reported separately for (1) Awak Mas (Chapter 5.3) and (2) Salu Bullo (Chapter 5.4 and 5.5). Vein descriptions will be presented in Chapter 5.6. The mineral chemistry of rock forming and trace minerals is presented all together in Chapter 5.8. Chapter 5.9 deals with the results of whole-rock analysis using XRF and ICP-MS. Appendix A-C show the petrographical observations, analytical methods and borehole profile from the Awak Mas and Salu Bullo.

5.3 Metasedimentary rocks of Awak Mas region

The metasedimentary unit in the Awak Mas region includes phyllite, carbonaceous phyllite, chlorite phengite schist, metasandstone-metasiltstone.

5.3.1 Phyllite

Phyllite is low-grade foliated metamorphic rock. These rocks are mylonitic and consist of a fine-grained matrix of white mica + quartz + siderite + albite ± carbonaceous materials.

Carbonaceous phyllite contains thin carbonaceous layers (less than 1 cm)(Fig. 21A). Carbonaceous phyllite is often deformed (Figs. 21B) with notable angular lithic clasts of quartz, chlorite and calcite. The constituent minerals are graphite, quartz, albite, white mica, with small amounts of siderite, apatite and opaque minerals. Framboidal pyrite (Py1) is preserved along foliation. Carbonaceous phyllite is often mineralized with gold, galena, mercurian tetrahedrite, sphalerite and trace amounts of native bismuth. Deformed carbonaceous phyllite is altered by chlorite.

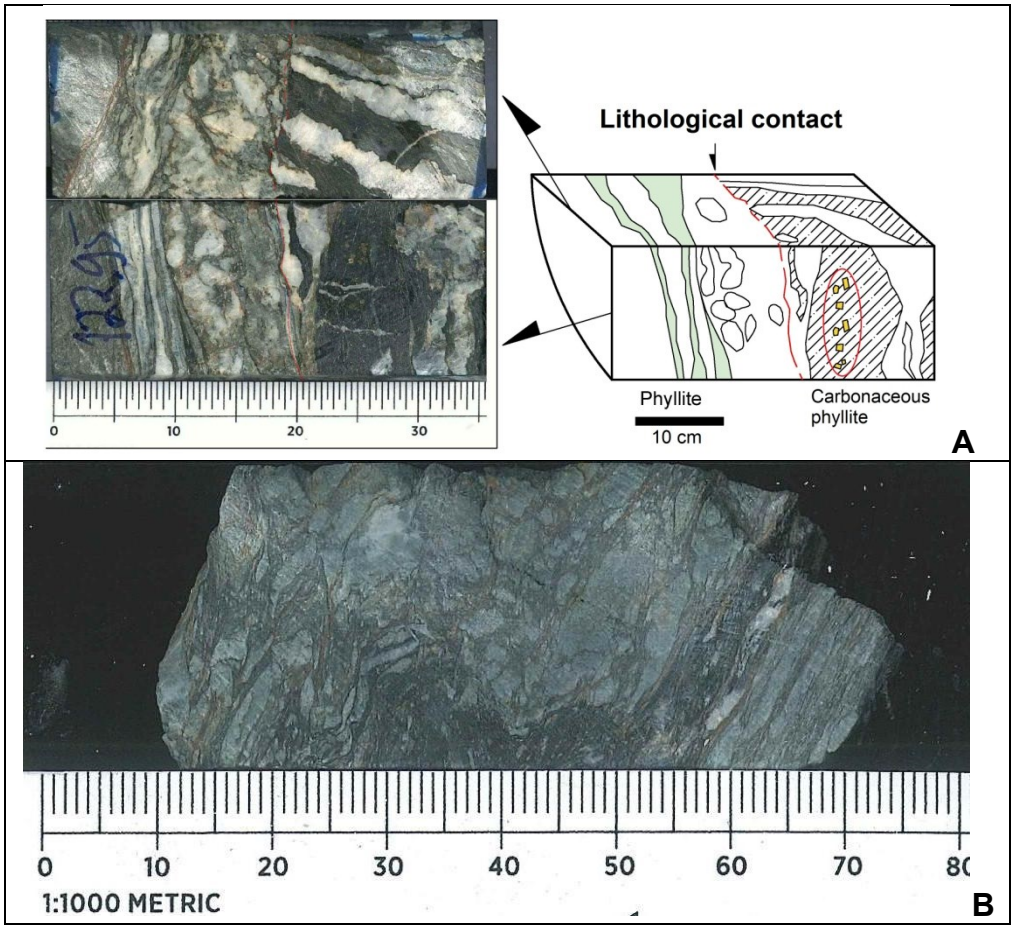

Fig. 21. Hand specimen photograph of phyllite. (A) Lithological contact between phyllite and carbonaceous phyllite. Red ellipsoid in Fig. 21A shows sulphides hosted in graphite band. A192-122.95. (B) Highly deformed carbonaceous phyllite.

The chlorite-phengite schist is highly a deformed rock, composed of chlorite, phengite, with porphyroclasts of quartz, Fe-chlorite (chamosite)(Figs. 22A-B) and pyrite. The foliation is intense and phengite shows remarkable parallelism. In addition, the rock is segregated into chlorite-rich and phengite-rich domains parallel to schistosity. Minor apatite, calcite and rutile are observed as accessory minerals. The abundance of chlorite and albite as well as the absence of quartz and muscovite may imply a protolith with a mafic composition. Opaque minerals are pyrite, chalcopyrite and galena.

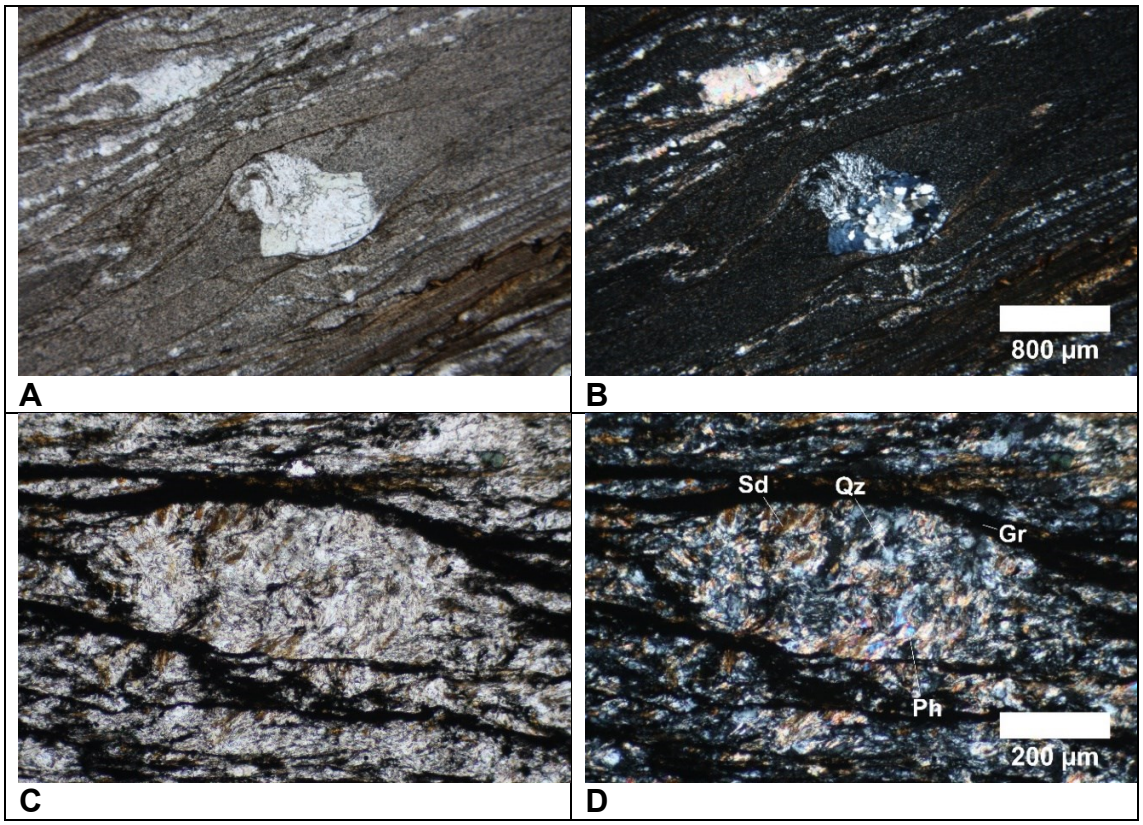

Fig. 22. Photomicrograph of the chlorite and carbonaceous phyllite. (A-B) Coarser quartz grains have sutured boundaries. Minor phengite is at the bottom right of the image. Chamosite and quartz show rotational fabrics. A685-171. A PPL and XPL images are shown in Figures 22A and 22B, respectively. (C-D) Carbonaceous phyllite consisting of fine-grained mica (phengite, Ph), siderite (Sd), quartz (Qz) in a graphite matrix. A687-53.60. A PPL and XPL images are shown in Figures 22C and 22D, respectively.

Generally, phyllite is composed of well-orientated quartz, white mica, siderite and albite. Augen, mottled and flaser textures are commonly observed. White mica has phengitic composition is widely found in pelitic metamorphic rocks. Rutile, apatite, zircon, monazite, xenotime and tourmaline occur as accessory minerals in matrix. Some of the apatite has a coarse grain size up to 1mm in diameter. Monazite and zircon are less than 40 µm and 80 µm, respectively. Sulphide and sulphosalt minerals are preserved both parallel to, or cutting foliation. Sulphides comprise pyrite, chalcopyrite, sphalerite and galena. Additional ore minerals are tetrahedrite$_{ss}$, famatinite, electrum and native bismuth. Framboidal pyrite was also commonly observed in this lithology. The latter mineral represents the first generation of pyrite that was formed in anoxic condition and reducing environment. Figure 23 shows photographs of a phyllite outcrop and the borehole sample. Photomicrograph of phyllite is indicated in Figure 24.

Fig. 23. Photograph of phyllite (A) Field photograph at Awak Mas (courtesy of Agus Haris Widayat). (B) Borehole photograph of phyllite.

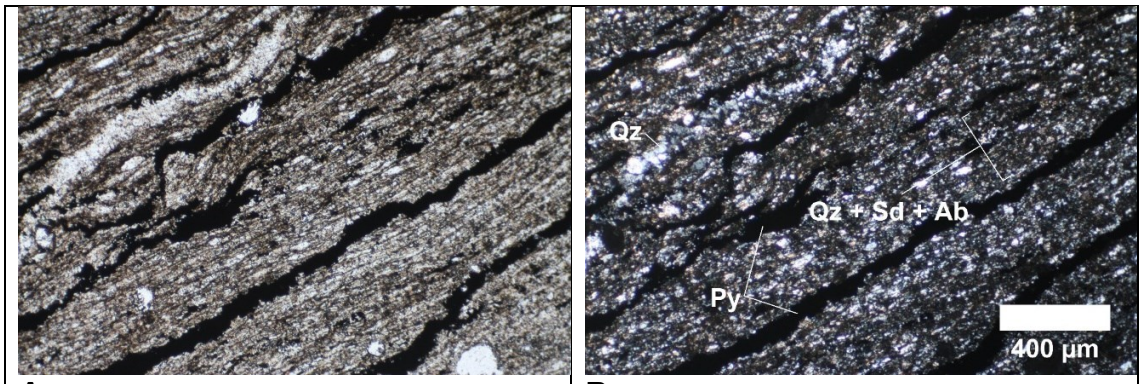

Fig. 24. Photomicrograph of phyllite (ONG01). (A) PPL image. (B) XPL image.

5.3.2 Metasandstone - metasiltstone

Metamorphosed quartz sandstone is a massive crystalline rock composed of essentially quartz (Figs. 25A-B), with the grain size between 63 µm and 2 mm. The metasiltstone is a fine-grained metamorphic rock that mainly consists of quartz with a grain size less than 63 µm (Figs. 25C-D). In both rocks, polygonal textures develop in quartz. The metasandstone and metasiltstone mainly consist of quartz, albite and minor hematite, and are commonly altered by carbonate and/or sericite.

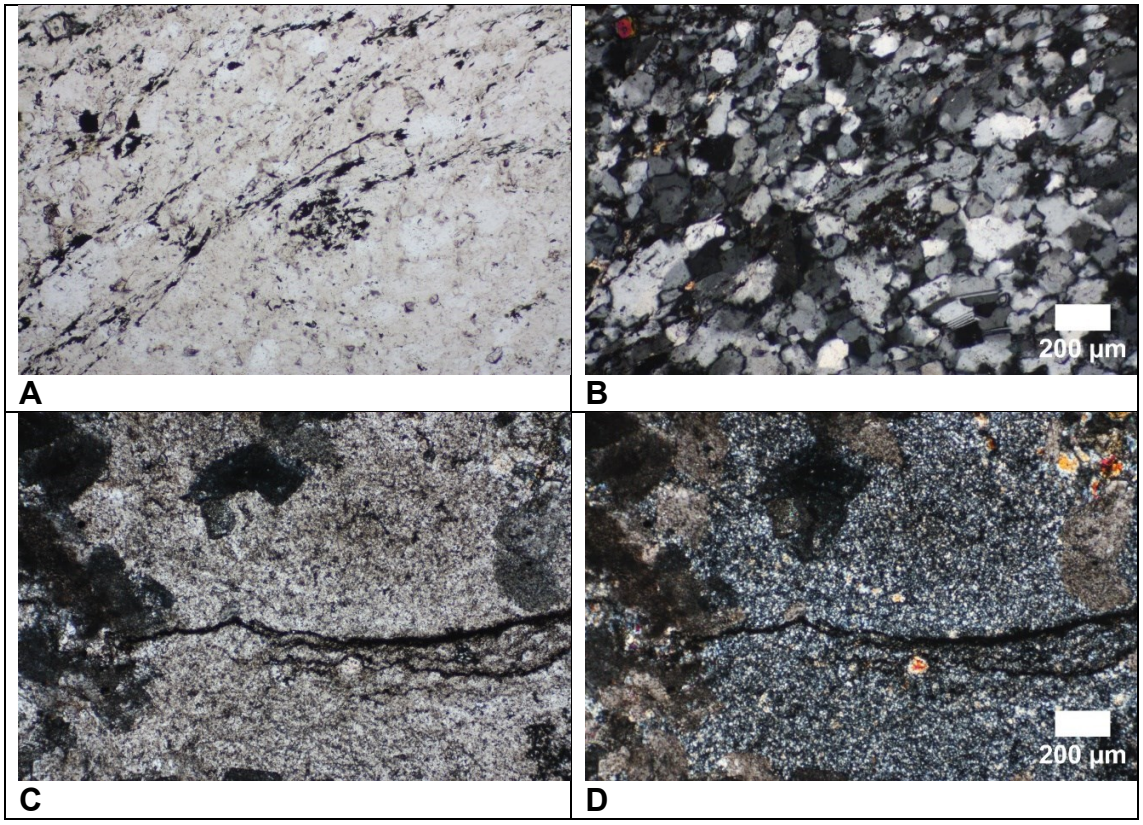

Fig. 25. Photomicrograph of metasandstone and metasiltstone. (A-B) A PPL and XPL images of metasandstone showing grain size grading. A tabular crystal of zircon with high interference colour is at the top left of the image. A685-20. (C-D) A XPL image of metasiltstone with carbonate alteration. A634-26.10.

5.3.3 Carbonate block

Boulders of carbonate measuring more than five meters containing abundant foraminifera are located on the eastern side of the Latimojong Mountain, near the core shed of PT Masmindo Dwi Area (Fig. 26). White et al. (2017) reported isolated foraminifera samples in the eastern part of Latimojong Mountains (not in Awak Mas region), which probably refer to similar carbonate blocks. Those authors argue that the foraminifera give the evidence of shallow/marine reef condition at ca. 54 – 52 Ma and represent a marine incursion during the Early Eocene. These rocks originate from the Toraja Group (approximately 20 km to the west of the Latimojong), and was deposited in a reef and inner neritic setting, overlying the metamorphic basement of Latimojong.

A B

Fig. 26. Photograph of carbonate (olistolite?) (A) Carbonate bodies have a size of more than 5 meters. As a comparison is a semi-permanent house and oil barrel. (B) Carbonate slump contains abundant foraminifera.

5.4 Metavolcanic rocks of the Salu Bullo region

As mentioned in the previous chapter, the most striking host rocks difference between the Awak Mas and Salu Bullo is the presence of mafic metavolcanic rocks, which are restricted to the upper part of the sequence at Salu Bullo. These are clinopyroxene-phyric metabasite (Fig. 27A), chlorite-actinolite schist or greenschist (Fig. 27B), metatuff (Fig. 27C) and meta-andesites (Fig. 27D). Volcanoclastic materials are included in this description because most magmatic components (clinopyroxene, chromian spinel) are often still preserved.

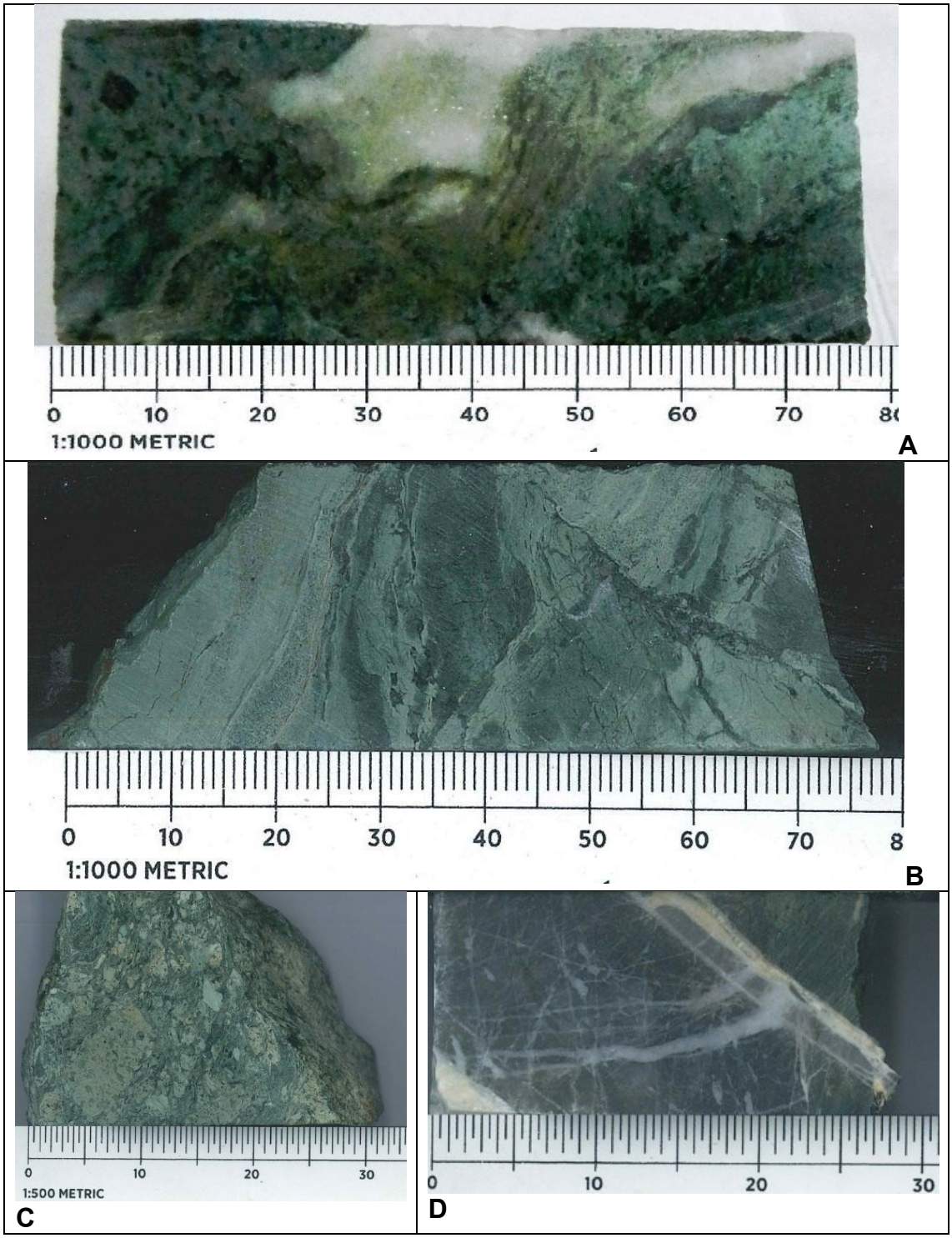

Fig. 27. Photograph of green metavolcanic rocks at Salu Bullo. (A) Clinopyroxene phyric metabasite. S68-47. Black-dot mineral on top left is clinopyroxene. (B) Greenschist. S68-84.50. (C) Metatuff. S53-50.20. (D) Meta-andesite crosscut by late calcite – albite veinlets. S69-112. Greenschist at the top right is composed chlorite-actinolite.

5.4.1 Metabasite

Green metavolcanic rocks (metabasites) contain macroscopically visible clinopyroxene, in addition to pumpellyite, chlorite and albite as main constituents (Fig. 27). The low- to medium-grade metavolcanic rocks are characterized by the presence of: (1) pumpellyite + actinolite + chlorite + albite + sphene - calcite, (2) epidote + actinolite + chlorite + white mica + albite + quartz + sphene - calcite.

The basalts in the Salu Bullo underwent metamorphic conditions ranging from blueschist- to greenschist-facies metamorphism. The basalts have been classified here on the basis of texture, type and abundance of mafic minerals. The basalts are classified into (1) clinopyroxene-phyric metabasite (Figs. 28A-B); (2) plagioclase-phyric metabasite (Figs. 28C-D); (3) epidote-actinolite metabasite (greenschist)(Figs. 28E-F), and (4) metatuff (Fig. 28H).

Clinopyroxene- or plagioclase-phyric metabasites retain some relic igneous textures, including primary magmatic minerals such as pyroxene (augite), plagioclase, Fe-Ti oxide and chromium spinel. Primary clinoyproxene is commonly observed as a coarse grain, sometimes up to 1 mm. Clinopyroxene is partially altered by chlorite or actinolite. Chromium spinel forms euhedral - subhedral grains with variable size ranging from <10 μm up to 80 μm in diameter; they occur as inclusions in clinopyroxene phenocrysts. Plagioclase is altered to pure-albite, chlorite, epidote or sericite. This rock type has no evidence of high-pressure metamorphism, unlike other metabasite types. In accordance with White et al. (2017), this lithology may represent younger rocks (probably from the Lamasi Complex) that were tectonically juxtaposed with the older metamorphic sequences.

The greenschist described in this study is a mafic metavolcanic rock commonly composed of pumpellyite + epidote + actinolite + quartz + albite + sphene + calcite (Fig. 28E-F). Chromian spinel is highly deformed, anhedral, generally less than 50 μm in diameter and commonly surrounded by chlorite and pumpellyite (Fig. 28G). This lithology is part of the Latimojong metamorphic complex and records high-pressure low-temperature metamorphism in this area.

Metatuff is characterized by a variable concentration of components, including tuff (Fig. 28H) and bioclastic materials (Figs. 29A-B). These rocks have green-

hued to gray colors, are fine-grained with veins filled with late-stage calcite, quartz or albite. Thin sections show that the volcanoclastic rocks are metamorphosed to greenschist facies and commonly contain abundant chlorite, quartz, albite, with minor actinolite, augite, sericite and clay minerals. The vesicles in basalts are filled with secondary chlorite, calcite, quartz and clay minerals. Magmatic minerals including chromian spinels and clinopyroxene are often still preserved, therefore, this rock type can be best classified as tuffitic metabasite (Fig. 28H).

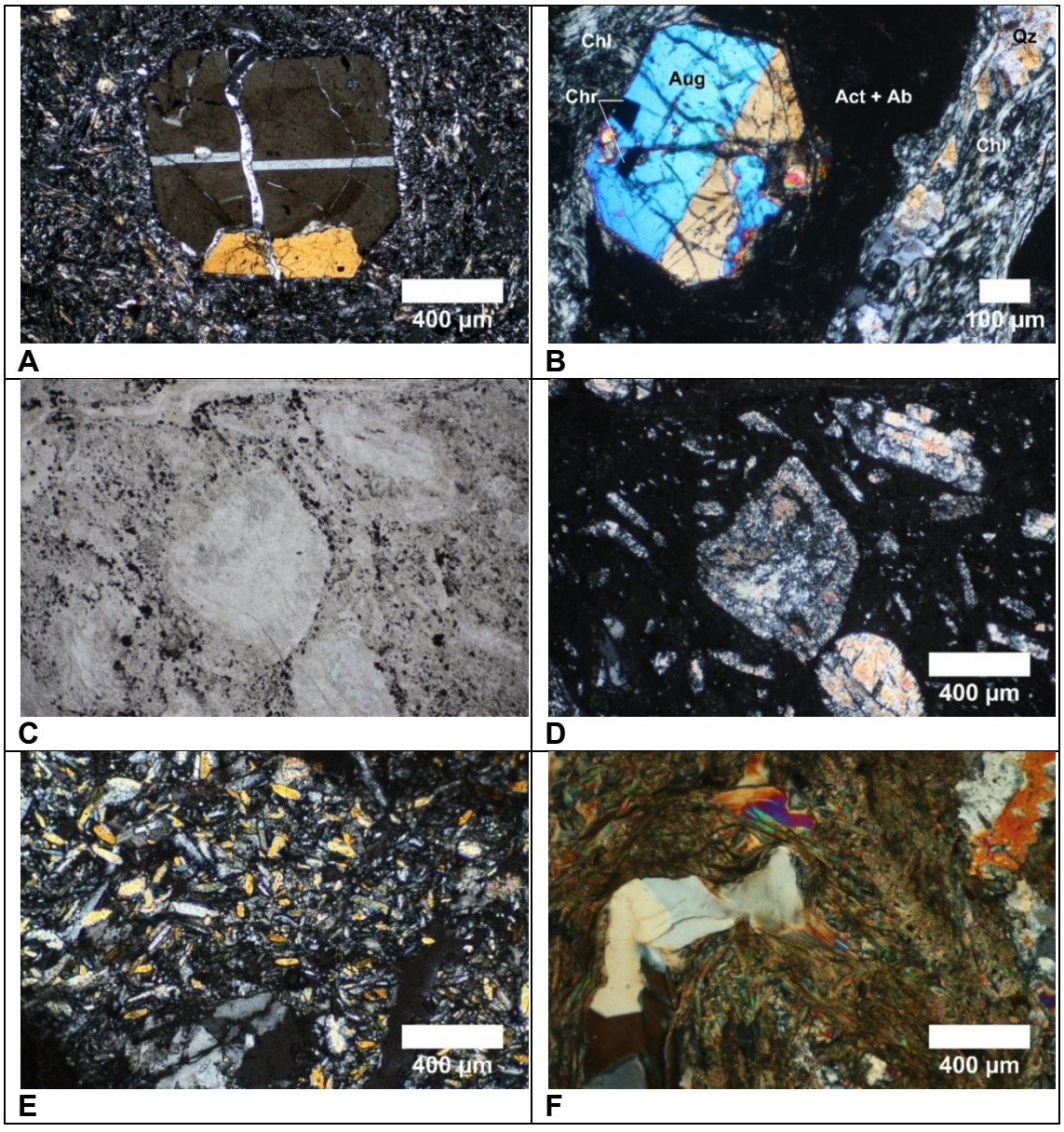

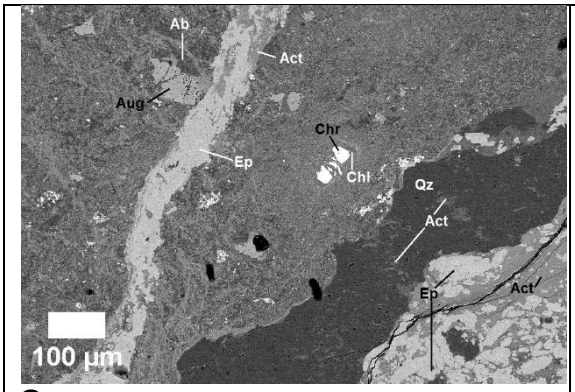

G

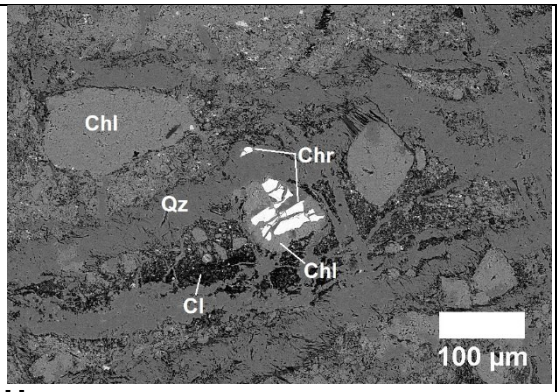

H

Fig. 28. Photomicrograph of metavolcanic rocks. (A) A XPL image of clinopyroxene-phyric metabasite. The groundmass is composed of albite, chlorite and actinolite. Chlorite occur as a fracture-filling material in augite. S68-47. (B) Two magmatic chromian spinel grains trapped in the rim of augite. S68-34.90. (C) A PPL image of plagioclase-phyric basalt. S68-57.60. (D) A XPL image of Fig. 28C. Plagioclase is altered to sericite. (E) Greenschist mainly consist of epidote (yellow to colorless interference colors) with minor quartz. S53-10.90. (F) Ductile deformation of quartz in greenschist. S68-34.90. (G) A BSE image of epidote-actinolite metabasite. Layer of silica (quartz) marks the contact between clinopyroxene-phyric metabasite (left) and greenschist (right). Chromian spinel (Chr) grains is restricted in clinopyroxene-phyric metabasite. S68-34.90. (H) Metatuff hosts detrital chromian spinel. Spinel is pseudomorphed by chlorite, quartz and clay mineral. S68-63.40.

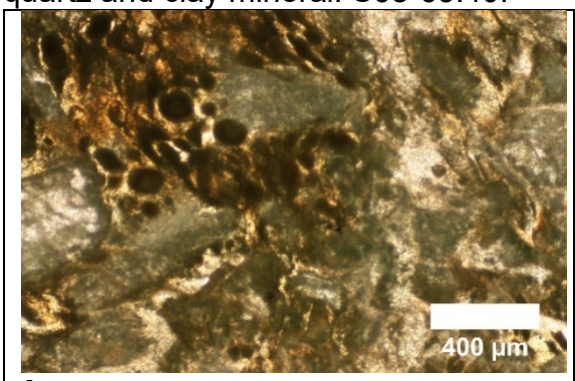

A

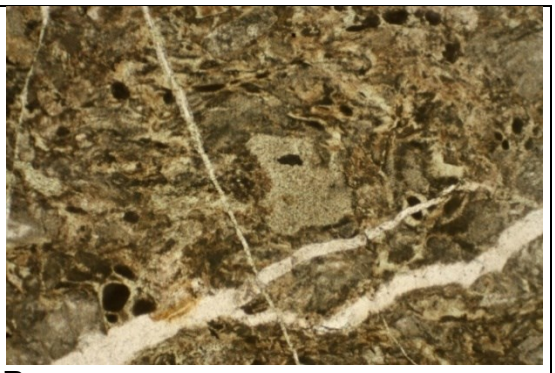

B

Fig. 29. Photomicrograph of metatuffs. (A-B) Chlorite and calcite occurs as a fracture filling within a bioclastic grainstone. S50-83.05.

5.4.2 Meta-andesite

Meta-andesite is a medium greenish-gray fine grained rock in which no quartz can bee seen macroscopically. Thin sections show that meta-andesite consists mainly of albite, minor quartz, calcite, siderite-ankerite (confirmed by EDS) and hematite. Albite is altered to sericite. The meta-andesite sometimes preserves

augite relics and epidote, and can be best classified as basaltic meta-andesite. Photomicrograph of meta-andesite is shown in Figure 30.

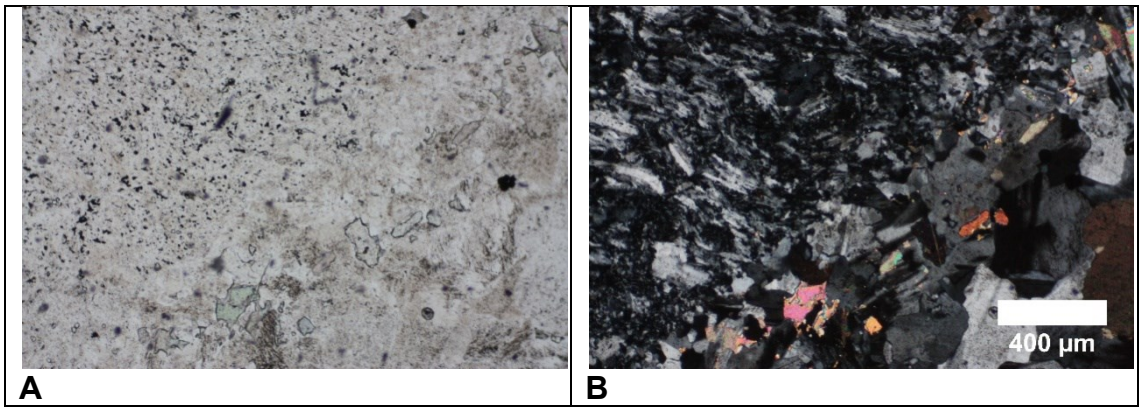

Fig. 30. Photomicrograph of meta-andesite (A) A PPL image of meta-andesite. This rock is consists of fine-grained albite and quartz with minor hematite. Dark minerals are hematite and minor pyrite. (B) A XPL image of Fig. 30A.

5.4.3 Orthogneiss

A boulder of orthogneiss (2 meter in diameter) crops out in the detachment zone of Latimojong and Lamasi (coordinates S3°20'08.8" E120°07'59.5"), as shown in a regional geological map of the studied area (Figure 13). The orthogneiss has green porphyroblasts (probably amphibole) and shows a ductile textures (Fig. 31). However, high-grade metamorphic rocks (i.e. orthogneiss) are not present in the boreholes.

There are some scenarios for the formation of ductile shear fabrics in this area. First, field observation suggests that the orthogneiss probably represent a metamorphic sole of the Lamasi Complex, part of the East Sulawesi Ophiolite (ESO). The rocks are covered by a thick sequence of soil and metavolcanic rocks within the ophiolite unit. Alternatively, White et al. (2017) suggested that the meta-igneous rocks such as amphibolite, meta-gabbro and meta-granitoids were tectonically juxtaposed within parts of the Latimojong Metamorphic Complex and represent younger rocks.

Fig. 31. Photomicrograph of orthogneiss (?). Sketch of superimposed fabrics of orthogneiss including deformation and lineation. Green mineral is probably amphibole.

In order to illustrate the regional geology of the Salu Bullo area, borehole sections through the metavolcanic rocks and its metamorphic basement had been studied systematically (combination of petrography, ore mineralogy and geochemistry). The result are shown in Figure 32.

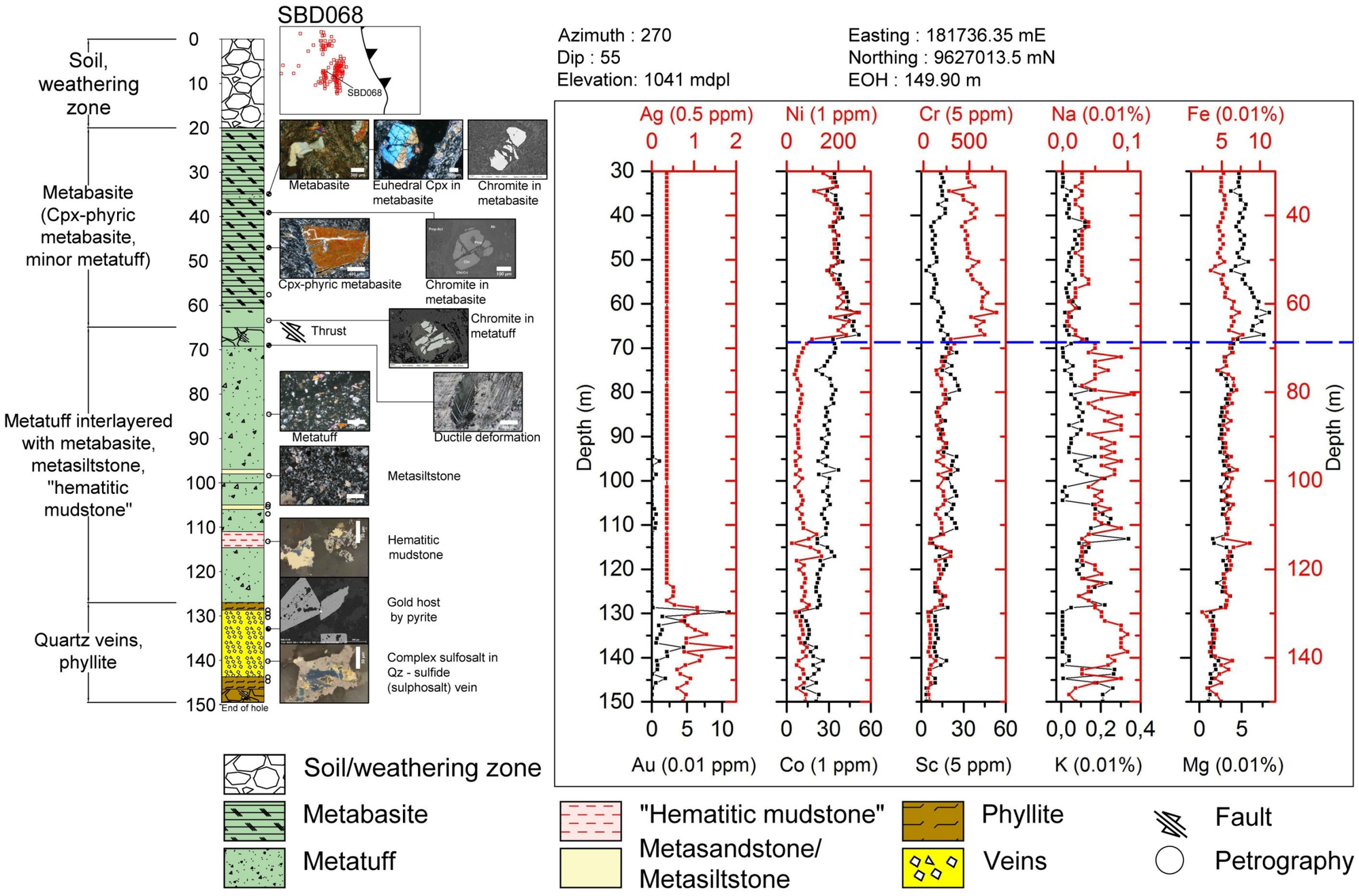

Fig. 32. Borehole section through the metavolcanic rocks of Latimojong and metamorphic basement. A thick soil and overburden covers the metavolcanic rocks. Metatuffitic rocks are characterized by low Ni-Cr and high Na-K. On the right side of the diagram is the whole rock geochemistry data provided by the mining company.

5.5 Metasedimentary rocks of the Salu Bullo region

5.5.1 Hematitic mudstone

The red to brown fine-grained rock (marked by yellow lines, Fig. 33A) is referred as hematitic mudstone. The mineralogy comprises albite + quartz + calcite + rutile + apatite + monazite with abundant sulphide (pyrite, chalcopyrite, sphalerite) and sulphosalt (tetrahedrite$_{ss}$), galena, sphalerite and gold. This lithology has high gold grades up to 8.94 ppm Au (pink circle, Fig. 33A). It may be inferred that the hematitic mudstone is a product of intensive hydrothermal alteration.

5.5.2 Metasandstone-metasiltstone

These rocks are part of the basement of the Latimojong Mountains and are similar to rocks cropping out in Awak Mas. Metasandstone and metasiltstone are dominated by quartz with minor albite and carbonate (mainly calcite)(Fig. 33D-E).

A

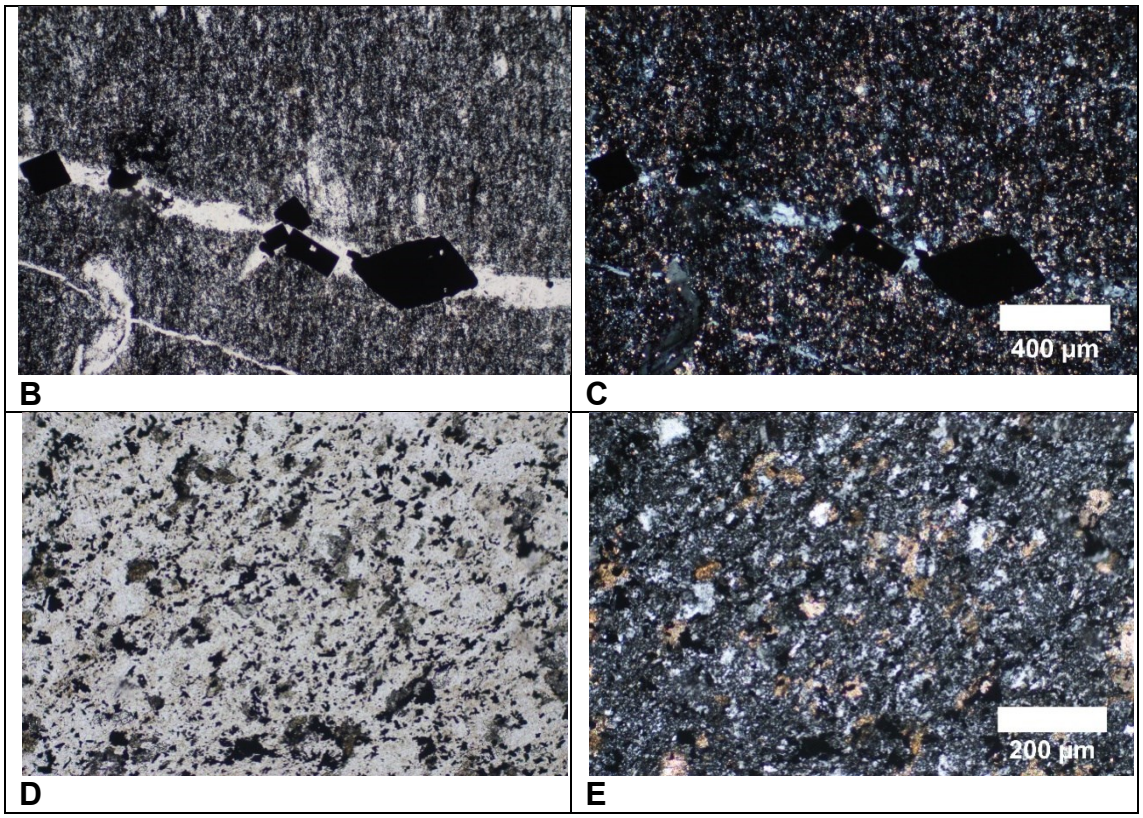

Fig. 33. Photograph of metasedimentary rocks of Salu Bullo. (A) Borehole photograph of SBD069 showing mineralized hematitic mudstone with grade up to 8.94 ppm Au. (B) A PPL image of very fine-grained rock containing quartz and albite with minor calcite. S69-24.50. (C) A XPL image of Fig. 33B. (D) A PPL image of metasiltstone showing bedding. S68-105.40. (E) A XPL image of Fig. 33D.

5.6 Vein description

The presence of oxide and sulphide - sulphosalt assemblages is a diagnostic feature to distinguish three vein types. These are quartz-hematite-Au veins, quartz-sulphide-sulphosalt Au veins and barren veins.

5.6.1 Quartz – pyrite - Au veins

The first type of gold mineralization is found in stockworks of pyrite accompanied by minor hematite (Fig. 34A). Galena and sphalerite are minor sulphides. Gold is enclosed in coarse-grained (>100 µm) pyrite. Based on crosscutting relations, quartz - pyrite Au veins are often cut by later generations of barren veins. Minor calcite-hematite veinlets are sometimes present and cut other lithologies, but this vein type is barren. Hematite is tabular, disseminated, homogenous without any exsolution textures. Rutile and sphene occur commonly in this vein type, associated typically with a silica + albite alteration

5.6.2 Quartz – sulphide (sulphosalt) – Au veins

The second type of gold mineralization is characterized by disseminated pyrite with Cu-As-Sb-Zn-Fe-(Pb) minerals The grain size of gold ranges from 2 μm to 50 μm, averaging about 10μm. Almost all gold occurs as inclusions in pyrite with less free gold in quartz. Breccia quartz veins consist of angular light brown tuff (Fig. 35A) and mineralized schist (Fig. 35B) fragments. This type of vein often hosts high gold grades.

5.6.3 Barren veins

Barren veins consist of open-space fillings by quartz and/or albite + carbonate (mainly dolomite). Exploration data reveal that veins containing less than 0.5ppm of Au are of no economic interest. Barren veins are widespread in all mineralization stages (Fig. 34C).

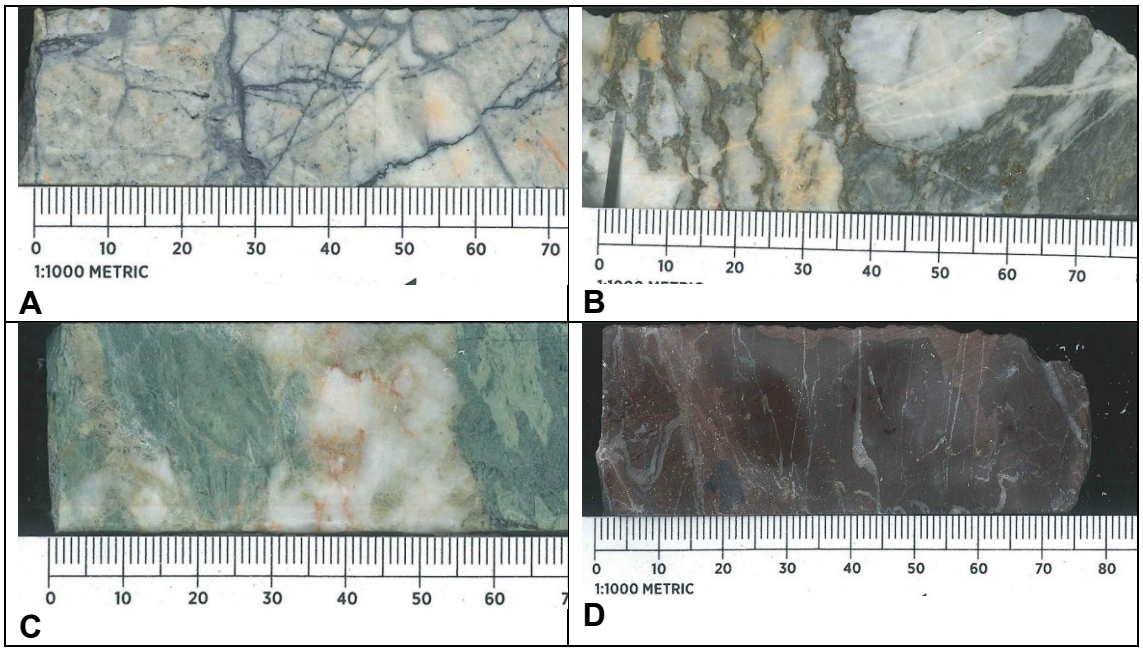

Fig. 34. Diamond drill core photographs of the host rock lithology. (A) Quartz-hematite Au veinlet. (B) Breccia composed of quartz clasts, containing coarse grained sulphides. (C) Barren quartz-carbonate veins cross cut the metatuff. (D) Mineralized hematitic mudstone crosscut by carbonate veinlet. Silica and hematite alteration. S69-24.50.

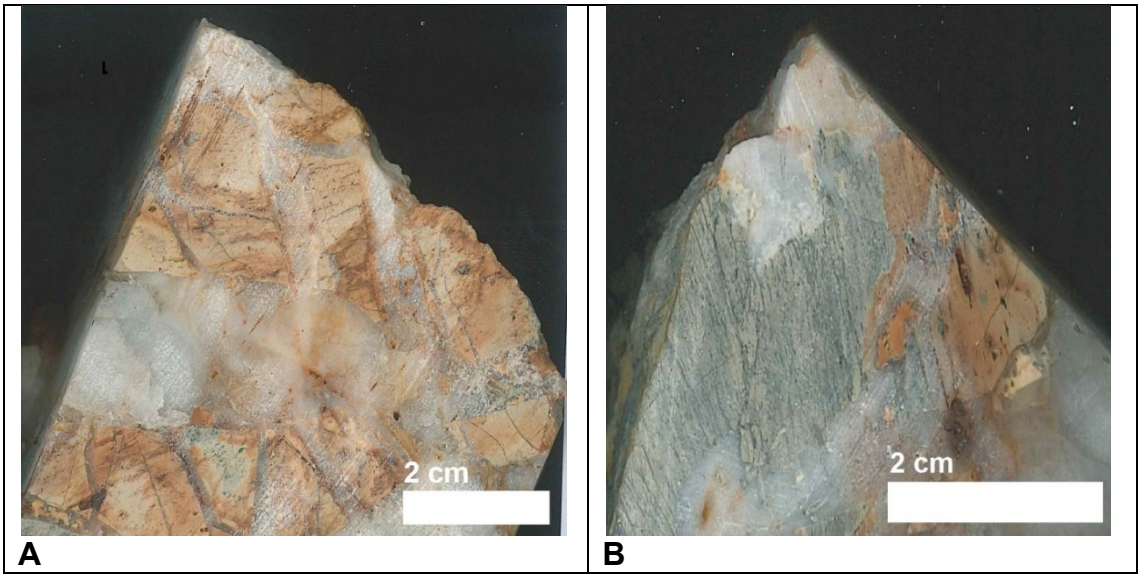

Fig. 35. Breccia quartz vein from Awak Mas consists of metatuff and mineralized phyllite. Both photos were taken from the same sample with different orientation. A microphotograph of this sample is shown in Fig. 24. ONG-01

5.6.4 Other vein types

Beside the ores described above, gold with high-grades also occurs in the oxidation zone near the surface at Salu Bullo (Fig. 36) and in thin quartz veins within the carbonaceous phyllite at Awak Mas (Fig. 37). Processes of surficial oxidation have extensively altered iron sulphides, so that much of the gold has been released from the sulphides. The gold grade reaches up to 13 ppm. These oxidized ores also contain abundant free gold, mainly in quartz. In carbonaceous phyllite at Awak Mas, sulphides commonly occur within graphite layers. Sulphides mainly consists of pyrite, chalcopyrite, galena, tetrahedrite with minor sphalerite. Native bismuth is rare. Gold content is generally less than 1 ppm.

Fig. 36. Bore hole photograph of SBD069 at Salu Bullo showing intense surficial oxidation near the surface. Some samples have a high gold grade with assays up to 13 ppm. The pink circles show gold content > 5 ppm. The yellow bar indicates the samples interval. Gold-silver grades are based on fire-assay analyses and are provided by mining company.

Fig. 37. Borehole photograph of AMD198 at Awak Mas showing thin quartz veins (generally less than 10 cm) within a thick layer of carbonaceous phyllite. Gold-silver grades are based on fire-assay analyses and are provided by the mining company.

Based on the field and petrographical observations compiled above, the sequence of lithologies from east to west is summarized in Figure 38. From the east, mafic to intermediate igneous rocks of the Lamasi Complex are exposed in the eastern Latimojong Mountains. These rocks suffered ocean-floor metamorphism but have no signatures of high pressure low-moderate temperature metamorphism. In contrast, the Latimojong metamorphic complex is an accretionary complex that experienced blueschist-greenschist facies metamorphism and tectonically mixed with metavolcanic rocks.

The Salu Bullo mainly consists of an imbricated assemblage of mafic metavolcanic rocks with minor metasedimentary rocks. The protoliths of mafic metavolcanic rocks are inferred to be ash fall materials (tuffitic), basalts and andesites, which had been metamorphosed into metatuff, metabasites and meta-andesites, respectively. The Awak Mas consists of a thick sequence of metasedimentary rocks, mainly composed of schist and phyllite with minor volcanic components. It is unclear whether the orthogneiss separates the metamorphic complex from the ophiolite. The orthogneiss probably represents the metamorphic sole of the ophiolite, or the younger rocks which had been tectonically juxtaposed during the obduction.

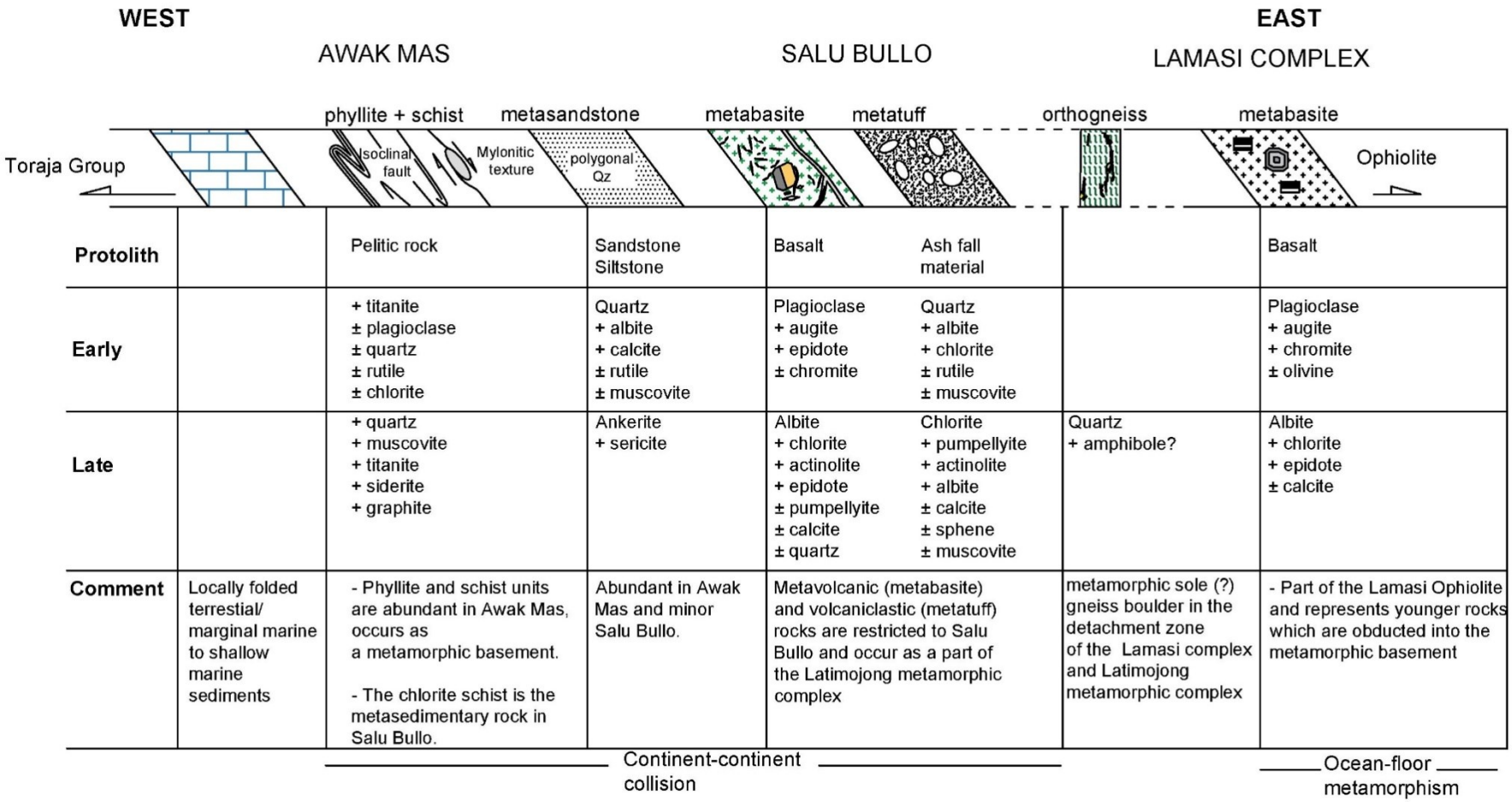

Fig. 38. Mineral assemblages of metasedimentary and metavolcanic rocks from the Awak Mas and Salu Bullo regions.

5.7 Mineral chemistry

5.7.1 Clinopyroxene

Metabasites and metatuff contain abundant primary magmatic pyroxene. The clinopyroxene generally is euhedral to subhedral with simple and lamellar twinning (Fig. 39A). Some concentric zoning can be observed using refracted light microscope and more prominent in back-scattered electron images.

In clinopyroxene-phyric basalt, grains of pyroxene are partially altered by chlorite, albite, sericite and/or actinolite (Fig. 39B). In contrast, clinopyroxene is fresh in metabasite. Some of the clinopyroxene megacrysts are filled by chalcopyrite and chromian spinel. Chalcopyrite and chromian spinel often occur as inclusions within clinopyroxene phenocrysts. The inclusions in clinopyroxene are generally less than 10 µm with subhedral to euhedral crystals.

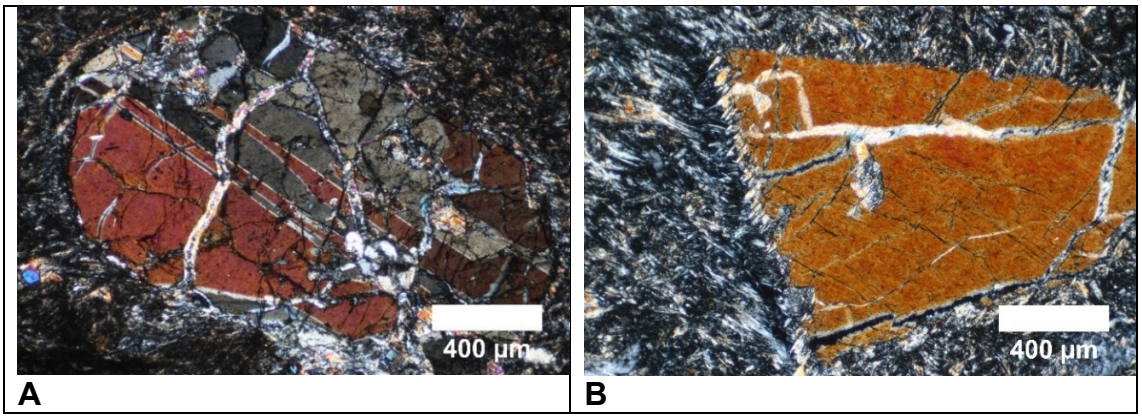

Fig. 39. Photomicrograph of altered clinopyroxene. (A) Simple twin basal section of clinopyroxene in a clinopyroxene-phyric basalt. S68-47. (B) A XPL image showing subhedral clinopyroxene phenocryst in a fine-grained groundmass containing albite, sericite and chlorite. S68-47.

Fifty-six spot analyses were performed on clinopyroxene and calculated using the spreadsheet PX-NOM (Sturm 2002). In cases of concentric zoning, rim and core were analysed separately. Clinopyroxene is of augite ($Wo_{40-44}En_{44-51}Fs_{7-15}$) composition (Morimoto 1988)(Fig. 40A). Representative clinopyroxene compositions are listed in Tables 11-12 and Appendix D.

In order to compare clinopyroxene composition of different lithologies, a plot of *Mg*-number vs. Ti, Al has been constructed (Fig. 42B). Metabasites have variable *Mg*-number (74-88) and low Ti (< 0.01 a.p.f.u.). Metatuff is similar to metabasites by having variable *Mg*-number ranging from 66 to 87 and low Ti content.

Clinopyroxene-phyric basalt of S68-47 display a large variation and higher Ti values than the metabasites and tuff metabasite (up to 0.05 a.p.f.u.)(Table 11). Figure 41B has been constructed in order to illustrate considerable scatter Ti and Al contents of clinopyroxene. The EDS line scan on zoned clinopyroxene grain indicates that clinopyroxenes are augite with cores having higher MgO and TiO_2 content than rims (Fig. 41).

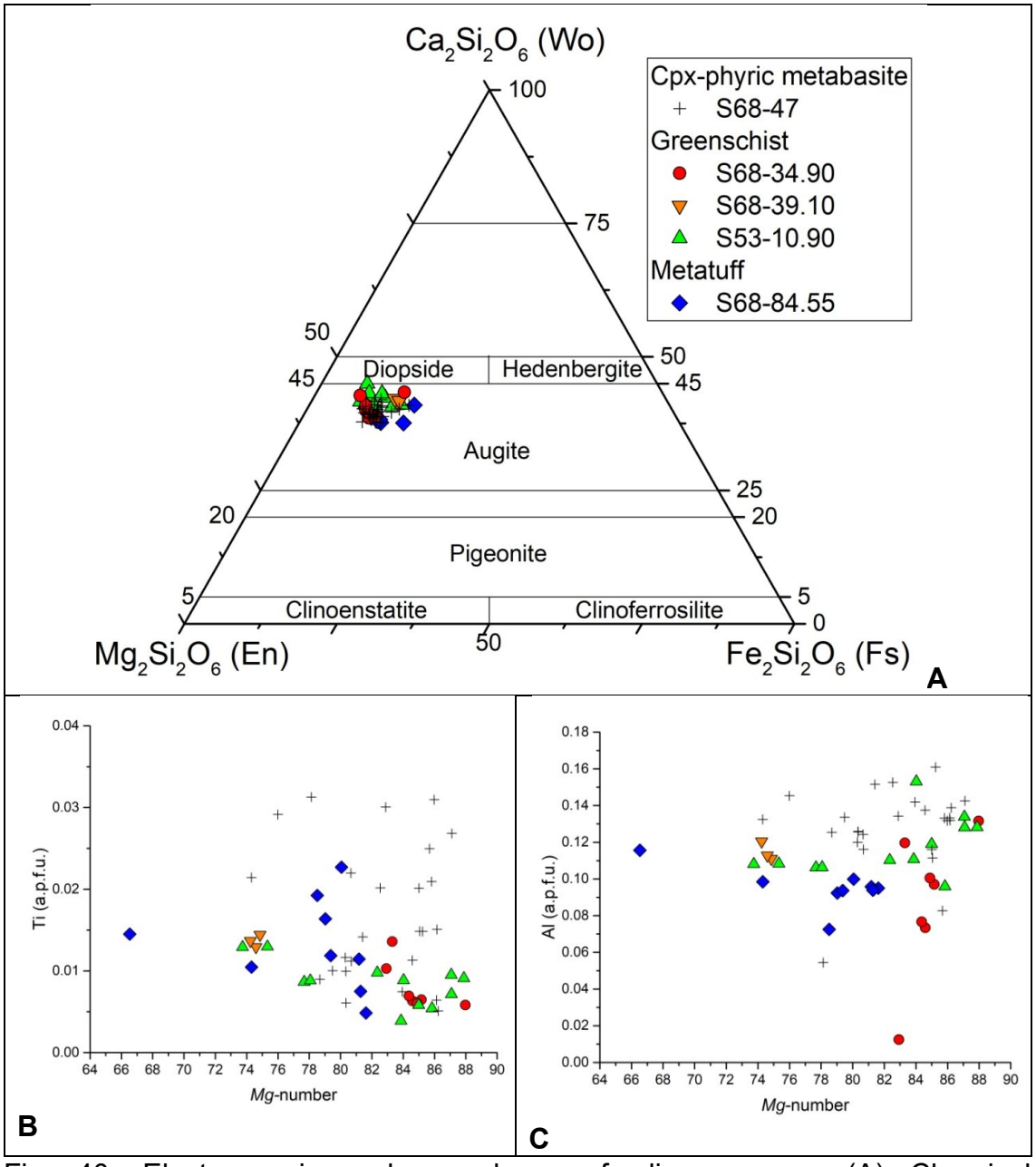

Fig. 40. Electron microprobe analyses of clinopyroxene. (A) Chemical composition of clinopyroxene on the wollastonite-enstatite-ferrosilite triangular diagram. All primary pyroxenes fall into the field of augite. Diagram after Morimoto (1988). (B) A plot of *Mg*-number vs. Ti of clinopyroxenes. (C) *Mg*-number vs. Al of clinopyroxenes.

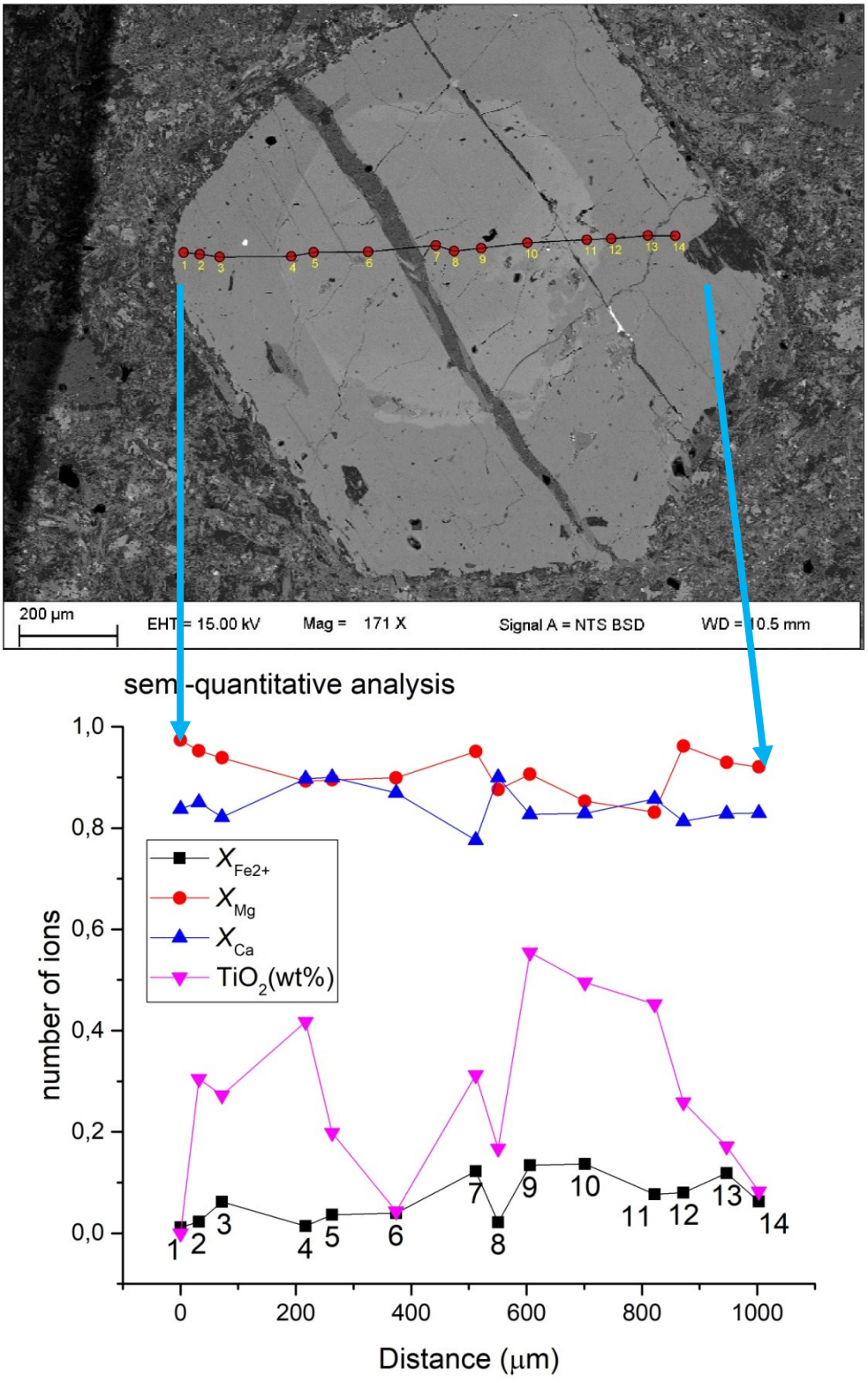

Fig. 41. Semi-quantitative line mapping of clinopyroxene (S68-47).

Table 11. Representative analyses of clinopyroxene (wt%).

Sample no	**S68-34.90**		**S68-39.10**		**S68-84.55**		**S53-10.90**		**S68-47**	
Number of analyses	8		3		9		12		25	
	mean	SD	mean	SD	mean	SD	mean	SD	Mean	S.D:
SiO_2	53.57	1.32	52.01	0.06	52.13	0.99	52.67	0.34	52.46	0.73
TiO_2	0.25	0.14	0.49	0.03	0.62	0.38	0.31	0.10	0.61	0.30
Al_2O_3	2.11	0.87	2.63	0.12	2.22	0.29	2.69	0.37	2.94	0.50
FeO	5.70	0.70	9.24	0.13	8.23	1.66	6.32	1.91	6.41	1.32
MnO	0.17	0.05	0.20	0.02	0.21	0.06	0.23	0.10	0.17	0.06
MgO	17.40	0.78	15.20	0.10	16.47	1.29	16.39	0.80	16.94	0.81
CaO	19.71	1.36	19.99	0.18	18.67	0.59	20.18	0.59	19.21	0.56
Na_2O	0.18	0.09	0.24	0.01	0.27	0.14	0.28	0.15	0.21	0.07
K_2O	0.01	0.03	0.00	0.00	0.01	0.01	0.01	0.01	0.01	0.01
Total	99.32	0.98	99.99	0.41	98.83	1.00	99.07	0.98	98.96	0.80
Normalisation on the basis of 6 oxygens										
Si	1.97	0.04	1.93	0.01	1.94	0.01	1.95	0.02	1.94	0.02
Ti	0.01	0.00	0.01	0.00	0.02	0.01	0.01	0.00	0.02	0.01
Al	0.09	0.04	0.11	0.01	0.10	0.01	0.12	0.02	0.13	0.02
Fe^{3+}	-0.03	0.04	0.02	0.01	0.00	0.03	-0.01	0.02	-0.03	0.03
Fe^{2+}	0.21	0.04	0.27	0.01	0.25	0.05	0.21	0.05	0.23	0.03
Mn	0.01	0.00	0.01	0.00	0.01	0.00	0.01	0.00	0.01	0.00
Mg	0.95	0.04	0.84	0.01	0.91	0.06	0.90	0.04	0.93	0.04
Ca	0.78	0.04	0.79	0.00	0.75	0.02	0.80	0.02	0.76	0.02
Na	0.01	0.01	0.02	0.00	0.02	0.01	0.02	0.01	0.01	0.00
K	0.00	0.00	0.00	0.00	0.00	0.00	0.00	0.00	0.00	0.00
Total	4.00	0.00	4.00	0.00	4.00	0.00	4.00	0.00	4.00	0.00
Mg-number	85	1.69	75	0.31	78	4.88	82	4.89	83	3.51
En	0.49	0.03	0.44	0.00	0.48	0.03	0.47	0.02	0.49	0.02
Fs	0.11	0.02	0.14	0.01	0.13	0.02	0.11	0.03	0.12	0.02
Wo	0.40	0.02	0.42	0.00	0.39	0.01	0.42	0.01	0.40	0.01

Table 12. Chemical parameters (mean and range) of augite in the Salu Bullo obtained by electron microprobe

	S68-34.90	**S68-39.10**	**S68-47**	**S68-84.55**	**S53-10.90**
Mg-number	84.5 (82.6-88)	74.6 (74.2-74.9)	82.5 (74.3-87.9)	78.6 (66.5-86.5)	82.3 (73.7-87.9)
En	0.49 (0.42-0.51)	0.44 (0.44)	0.49 (0.43-0.52)	0.49 (0.42-0.54)	0.47 (0.44-0.5)
Fs	0.11 (0.07-0.14)	0.14 (0.13-0.14)	0.11 (0.08-0.16)	0.13 (0.08-0.17)	0.11 (0.07-0.15)
Wo	0.4 (0.39-0.43)	0.42 (0.41-0.42)	0.4 (0.38-0.42)	0.39 (0.36-0.41)	0.42 (0.4-0.45)
Ca (a.p.f.u.)	0.78 (0.74-0.87)	0.79 (0.79-0.8)	0.77 (0.72-0.81)	0.74 (0.7-0.78)	0.8 (0.77-0.85)
Na (a.p.f.u.)	0.01 (0.01-0.03)	0.02 (0.02)	0.01 (0.01-0.03)	0.02 (0.01-0.05)	0.02 (0.01-0.05)
Ti (a.p.f.u.)	0.01 (0-0.01)	0.01 (0.01)	0.01 (0.01-0.05)	0.01 (0.01-0.04)	0.01 (0-0.01)

5.7.2 Chromian spinel

Chromian spinel is a trace mineral observed in metabasite and metatuff. In total, forty grains of chromian spinel were observed. Chromian spinel grains are subhedral to anhedral, showing different microstructures of alteration including (a) homogenous or zoned cores surrounded by chlorite (Fig. 42B) and (b) chromian spinel in clinopyroxene phenocryst (Fig. 42C). Some chromian spinels show the typical ferrian-chromian spinel alteration along grain boundaries with silicate. The chemical composition of chromian spinel was determined using electron microprobe. The composition of chromian spinel from the Latimojong Complex has never been investigated before. Information about the geochemical composition of spinel is available in other parts of Sulawesi, including the East Sulawesi Ophiolite (Kadarusman et al. 2004), Barru Block, southeast Sulawesi (Maulana et al. 2015) and southeast and east arms of Sulawesi (Zaccarini et al. 2016). Those authors described chemical composition of chromian spinel from the mantle rocks.

On each chromian spinel grain at least two measurements were performed to provide average values of Cr, Fe, Al, Mg, Ti, Zn and Si. Spinels are grouped into (i) silicate matrix hosted spinel and (ii) augite phenocryst hosted spinel.

(i) Type-1: silicate matrix hosted spinel grains.(Chl + Pmp + Ep + Ab)

- Cr_2O_3 from 30.84 to 58.10 wt% (average of 46.96 wt%),
- Al_2O_3 from 9.89 to 21.68 wt% (average of 15.37 wt%),
- FeO from 16.78 to 36.70 wt% (average of 25.52 wt%),
- MgO from 7.76 to 15.01 wt % (average of 11.20 wt%)
- TiO_2 from 0.14 to 1.67 wt%.(average of 0.45 wt%)
- Cr# from 64.1 to 73.2 and Fe^{2+}# from 32.1 to 49.7.

(ii) Type-2: augite phenocryst hosted spinel inclusions.

- Cr_2O_3 from 29.90 to 51.57 wt% (average of 41.59 wt%),
- Al_2O_3 from 12.96 to 23.26 wt% (average of 16.96 wt%),
- FeO from 25.83 to 31.34 wt% (average of 28.98 wt%),
- MgO from 9.29 to 12.03 wt % (average of 10.43 wt%)
- TiO_2 from 0.2 to 1.16 wt%.(average of 0.60 wt%)
- Cr# < 67 with small Fe^{2+}# variation (50.6 – 52).

The ZnO and SiO_2 in both spinel types was generally below the detection limit of the electron microprobe (detection limit Zn=500 ppm, Si=300 ppm), with a maximum content of 1.18 wt% ZnO. The results are shown in Tables 22-24 and Appendix D.

The spinel is also found as blebs associated with chalcopyrites along cracks of clinopyroxene (Fig. 43A). The clinopyroxene (augite) phenochryst has concentric zoning (Fig. 43A) and spinel is observed in the outer rim (Figs. 43B-C). Spinel grains are 4 µm and 13 µm in diameter and in this case, only grains that are bigger than 10 µm were analysed using electron microprobe. The latter grain (Fig. 53C) has 14 wt% Al_2O_3, 44.7 wt% Cr_2O_3 and 29.7 wt% FeO contents. The Cr# [100 x Cr/(Cr + Al)] is 68 and Fe^{2+}# [100 x Fe^{2+}/(Fe^{2+} + Mg^{2+})] is 55.

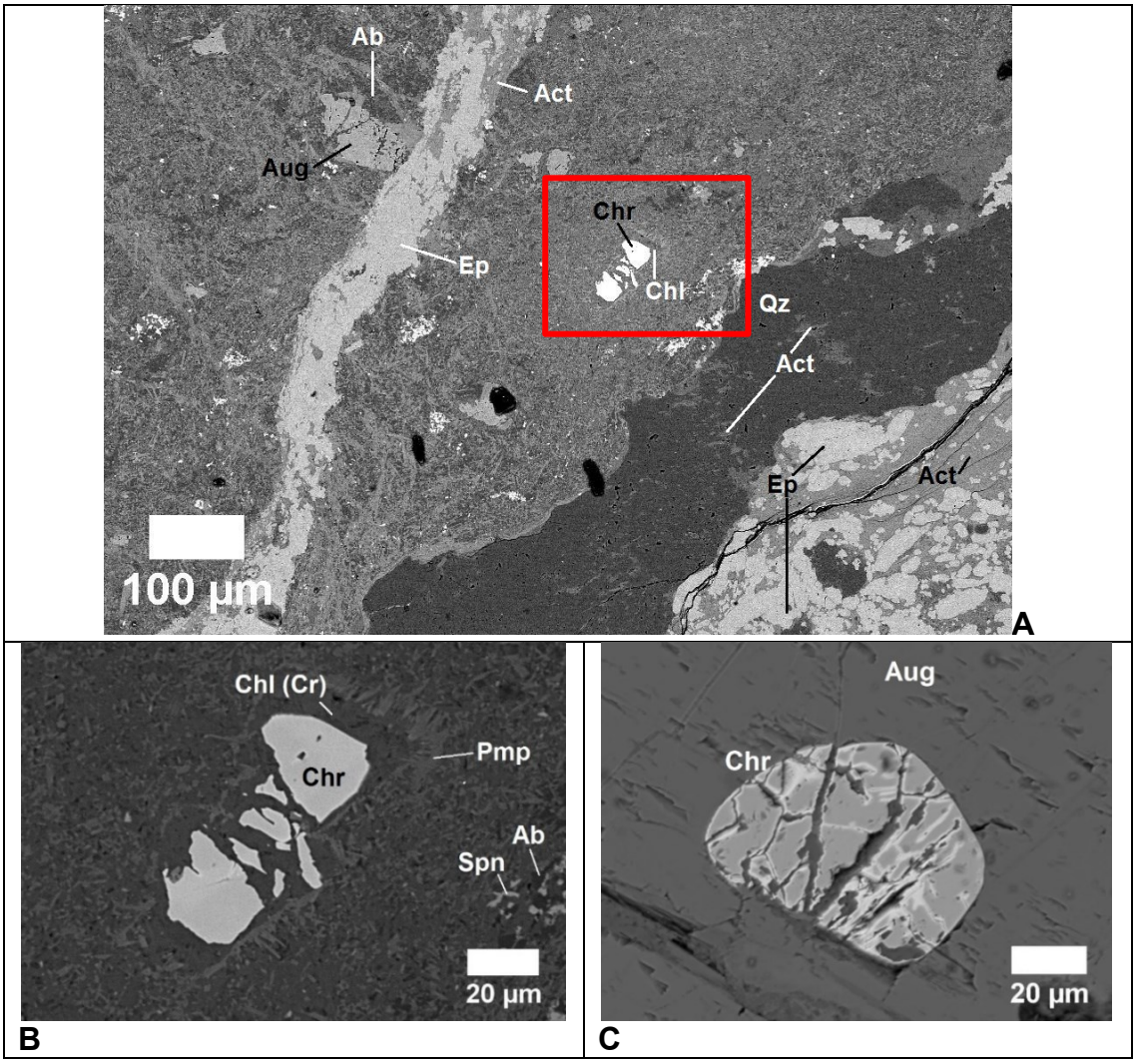

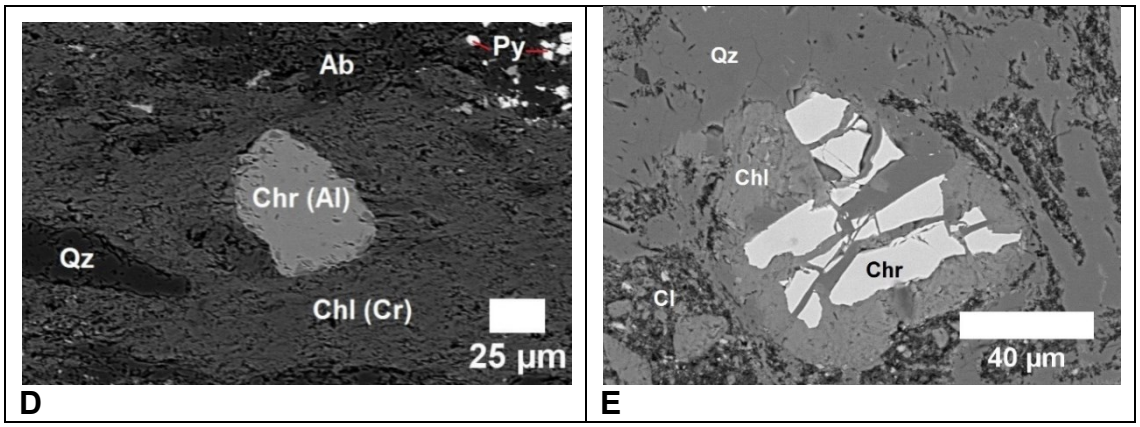

Fig. 42. BSE images of chromian spinel. (A) Chromian spinel in clinopyroxene phyric basalt. S68-47. (B) Fig. 42B is the enlargement image from the inset square of Fig. 42A. Chromian chlorite alteration (dark grey) developed in the rim of chromian spinel. (C) Zoned chromian spinel in augite phenocryst. S68-47. (D) High-Al chromian spinel host in chlorite phengite schist. A687-79.80. (E) Chromian spinel in volcaniclastic basaltic tuff in the Salu Bullo. Clay materials (Cl), quartz (Qz) and chlorite (Chl) are the main components of tuff metabasite. S68-63.40.

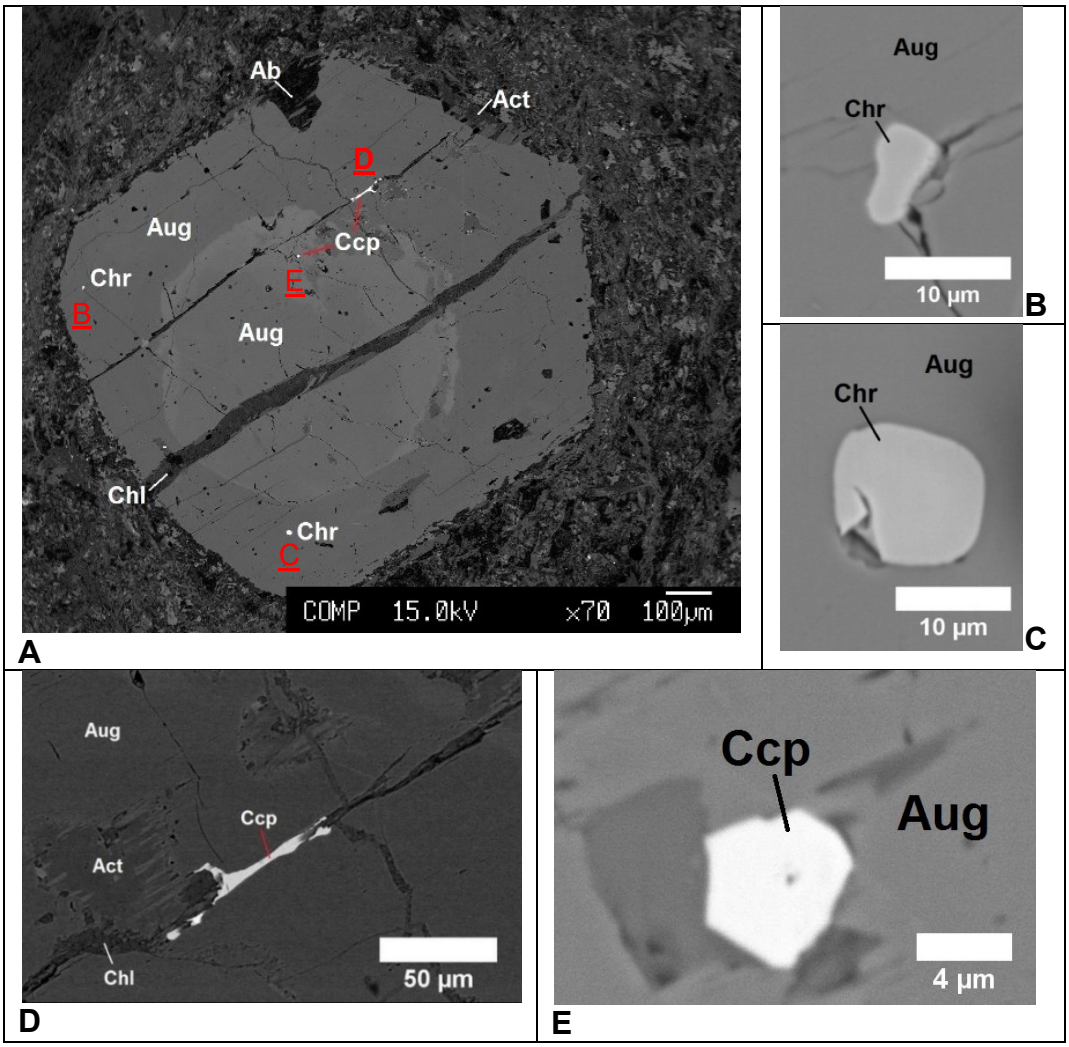

Fig. 43. BSE images of chromian spinel hosted by clinopyroxene. (A) Concentric zoning in augite grain.S68-47. Inset is enlarged in Fig. 43B-E as indicated by underlined text. (B-E) Rounded grains of chromian spinel are observed in augite matrix. (D) Anhedral grain of chalcopyrite and chlorite are precipitated in a crack. Augite is partially replaced by actinolite. (E) Subhedral grain of chalcopyrite in the matrix of augite.

Homogenous clinoyproxene phenocrysts host chromian spinel with variable compositions. These spinels are less than 100 µm in size, forming subhedral to anhedral grains. Quantitative analysis on spinel A (Fig. 44A-B) indicates that spinel has 18.5 wt% Al_2O_3, 0.7 wt% TiO_2, 38.9 wt% Cr_2O_3 contents and Cr# of 59. In contrast, spinel B has 13 wt% Al_2O_3, 0.14 wt% TiO_2, 51 wt% Cr_2O_3 contents and Cr# of 73. In order to illustrate the variation, a quantitative map analyses was performed in this section (Fig. 44C). Selected chromian spinel analyses are listed in Tables 12 - 14.

Solid inclusions of silicates in chromian spinel are observed in some grains. The silicate inclusions have a rounded shape (<20 µm in diameter) and are distributed randomly in the spinel host. This silicates are identified as phlogopite and pargasite (Fig. 45). In other spinel grains, inclusions are secondary with respect to chromian spinel and are associated with cracks. These secondaty silicate inclusions are identified as chlorite and pumpellyite and probably formed during high-pressure metamorphism. Cr-contents in all inclusions are generally high (Cr_2O_3 > 3 wt%).

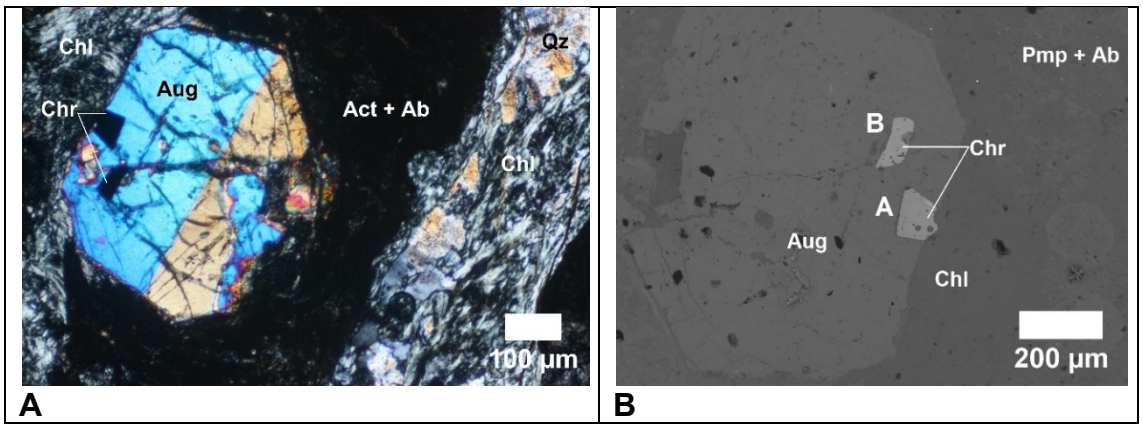

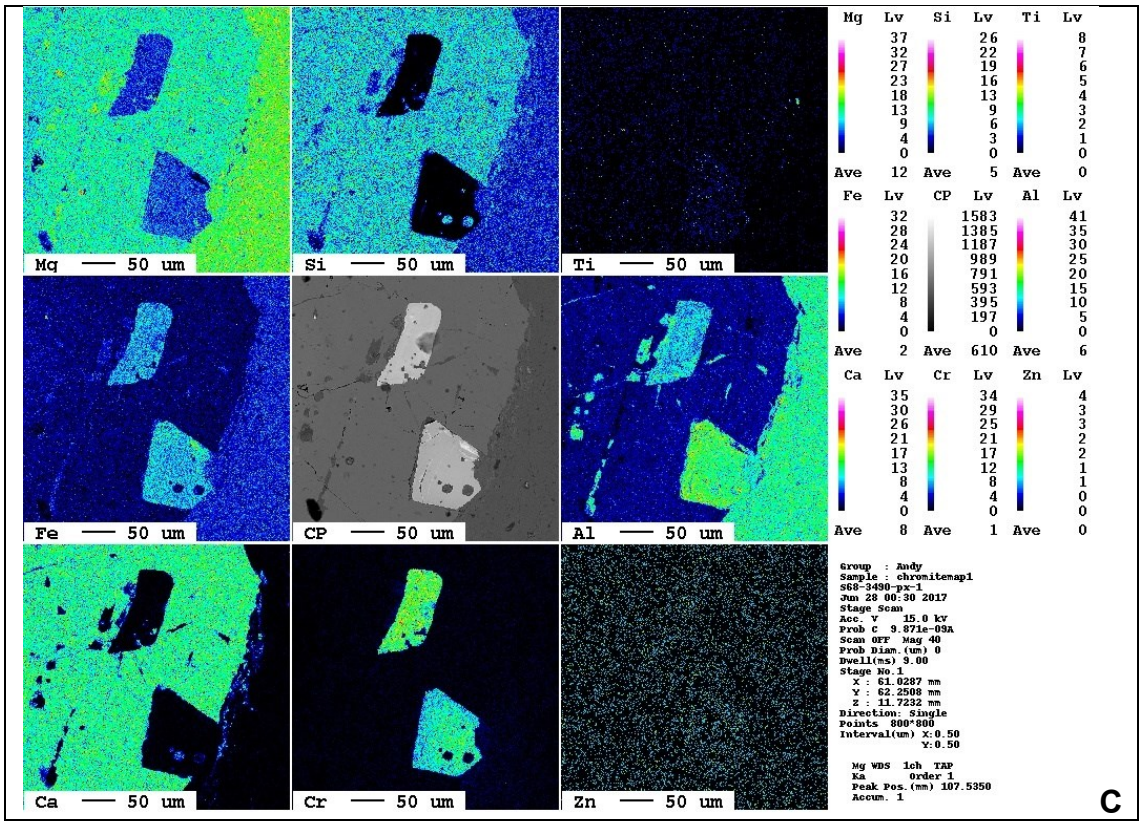

Fig. 44. Photomicrograph of chromian spinel hosted by clinopyroxene. (A) A XPL image of augite phenocrysts hosting two grains of chromian spinel. (B) A BSE image of Fig. 44A. (C) Quantitative element map of spinel. Variable composition of Cr and Al in spinels are clearly observed.

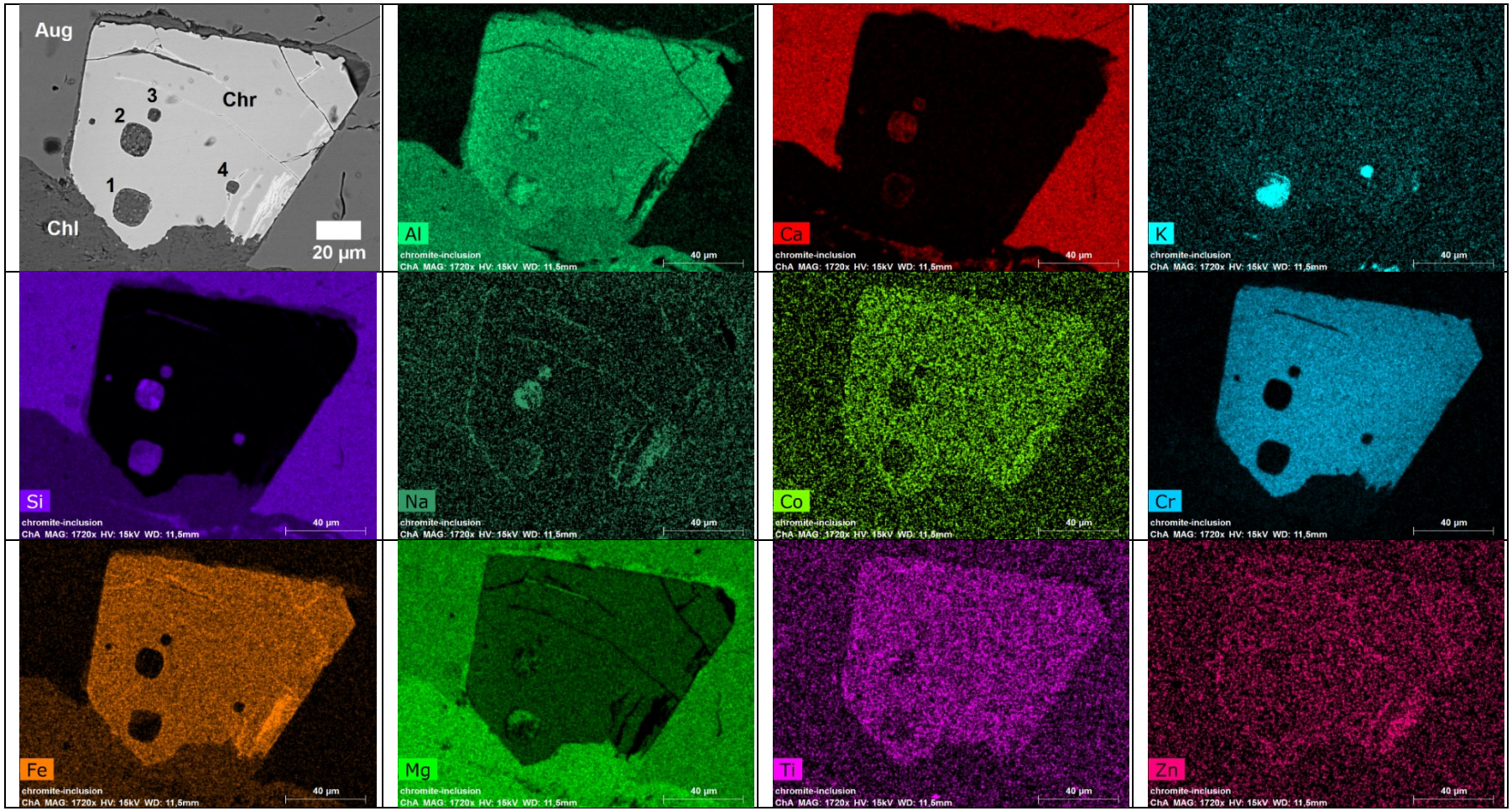

Fig. 45. Semi-quantitative analysis map of chromian spinel hosts in clinopyroxene from Figure 44. Silicate inclusions has variable Ca-K-Na-Al contents. Inclusions in chromian spinels has been numbered from 1-4. Minerals number 1 and 4 are mica (K_2O=8.35%,SiO_2=51.87%, Al_2O_3=20.9%,MgO=6.7%,FeO=5.5%,Cr_2O_3=3.3%,CaO=2.6%,TiO_2=0.83%), minerals number 2 and 3 are amphibole (Na_2O=1.55%,SiO_2=52.1%, Al_2O_3=17.7%,MgO=10.2%,FeO=4.5%, CaO=13.96%).

Table 13. Representative quantitative analyses on chromian spinel in silicate matrix (type-1) using electron microprobe

Sample number	**S68-34.90**		**S68-63.40**		**S68-47**		**S53-10.90**		**A687-79.80**	
Number of analyses	**11**		**11**		**38**		**33**		**5**	
	Mean	**S:D.**	**Mean**	**S:D.**	**Mean**	**S:D.**	**Mean**	**S:D.**	**Mean**	**S:D.**
Cr_2O_3	53.06	2.87	45.04	6.82	43.84	7.37	48.02	4.72	54.45	0.48
Al_2O_3	12.99	1.47	16.78	3.47	16.15	2.78	15.08	2.81	13.47	0.16
TiO_2	0.21	0.05	0.42	0.18	0.64	0.42	0.31	0.16	0.46	0.02
FeO	22.18	1.52	25.65	2.80	27.85	4.36	25.18	1.81	17.00	0.15
MgO	11.48	0.55	11.45	1.09	10.93	0.99	10.81	0.74	14.76	0.20
ZnO	0.09	0.06	0.11	0.07	0.14	0.18	0.10	0.06	0.04	0.06
SiO_2	0.07	0.04	0.05	0.03	0.07	0.13	0.11	0.09	0.06	0.04
Total	100.08	0.63	99.50	0.99	99.63	0.73	99.61	0.91	100.25	0.42
Formula units based on 32 oxygens and Fe^{2+}/Fe^{3+} assuming full site occupancy										
Cr	10.84	0.60	9.10	1.49	8.90	1.59	9.81	1.05	10.84	0.08
Al	3.95	0.43	5.04	0.98	4.87	0.78	4.58	0.80	4.00	0.04
Ti	0.04	0.01	0.08	0.03	0.12	0.08	0.06	0.03	0.09	0.00
Fe^{3+}	1.10	0.16	1.65	0.46	1.91	0.70	1.45	0.36	0.97	0.10
Fe^{2+}	3.71	0.22	3.87	0.36	4.12	0.39	4.02	0.24	2.62	0.08
Mg	4.42	0.21	4.35	0.36	4.17	0.34	4.16	0.25	5.54	0.08
Total	24.07	0.00	24.09	0.02	24.11	0.04	24.08	0.02	24.06	0.00
Fe^{2+}#	45.6	2.7	32.1	1.0	47.1	4.3	49.7	4.3	49.2	3.0
Fe^{3+}#	6.9	1.0	6.1	0.6	10.5	3.0	12.2	4.6	9.2	2.3
Cr#	73.2	3.3	73.0	0.2	64.1	8.3	64.2	7.7	68.1	6.1

Fe^{2+}# = 100 x $Fe^{2+}/[(Fe^{2+}+Mg^{2+})]$; Fe^{3+}# = 100 x $Fe^{3+}/[(Cr+Al+Fe^{3+})]$; and Cr# = 100 x Cr/[(Cr+Al)]

Table 14. Representative quantitative analyses on chromian spinel host in augite (type-2) using electron microprobe.

Sample number	**S68-34.90**		**S68-47**		**S53-10.90**	
Number of analyses	**7**		**6**		**2**	
	Mean	**S.D.**	**Mean**	**S.D.**	**Mean**	**S.D.**
Cr_2O_3	42.04	6.24	39.78	7.37	45.46	0.11
Al_2O_3	17.23	2.94	17.21	4.65	15.25	0.23
TiO_2	0.57	0.24	0.70	0.32	0.41	0.01
FeO	10.40	0.73	10.42	1.24	10.54	0.01
MgO	28.86	1.95	29.61	1.38	27.51	0.13
ZnO	0.15	0.07	0.11	0.04	0.12	0.05
SiO_2	0.06	0.07	0.09	0.02	0.12	0.07
Total	99.30	0.84	97.93	0.57	99.40	0.37
Formula units based on 32 oxygens and Fe^{2+}/Fe^{3+} assuming full site occupancy						
Cr	8.55	1.39	8.21	1.73	9.30	0.03
Al	5.21	0.83	5.24	1.24	4.65	0.05
Ti	0.11	0.05	0.14	0.06	0.08	0.00
Fe^{3+}	1.96	0.45	2.20	0.35	1.84	0.02
Fe^{2+}	4.30	0.16	4.31	0.25	4.17	0.02
Mg	3.98	0.23	4.02	0.35	4.06	0.02
Total	24.10	0.02	24.12	0.02	24.09	0.00
Fe^{2+}#	52	2.37	52	3.64	51	0.20
Fe^{3+}#	12	2.94	14	2.40	11.65	0.13
Cr#	61.9	7.37	60.7	10.89	66.7	0.29

Fe^{2+}# = 100 x $Fe^{2+}/[(Fe^{2+}+Mg^{2+})]$; Fe^{3+}# = 100 x $Fe^{3+}/[(Cr+Al+Fe^{3+})]$; and Cr# = 100 x Cr/[(Cr+Al)]

Table 15. Chemical parameters (mean and range) of chromian spinel obtained by electron microprobe

Sample	**S68-34.90**	**A687-79.80**	**S68-63.40**	**S68-47**	**S53-10.90**
Number of analyses	**11**	**5**	**11**	**38**	**33**
	----------chromian spinel in silicate matrix----------				
Cr_2O_3	53.1(48.4-56.6)	54.5(53.7-55.1)	45.1(34.3-54.7)	43.8(30.8-54.6)	48(37.7-58.1)
Al_2O_3	13(11-4-15.2)	13.5(13.3-13.6)	16.8(10.9-21.7)	16.1(10.6-21.2)	15.1(9.9-20.5)
TiO_2	0.2(0.14-0.2)	0.46(0.44-0.48)	0.42(0.18-0.71)	0.64(0.16-1.67)	0.31(0.17-0.87)
ZnO	b.d.l.	b.d.l.	b.d.l.	b.d.l - 1.67	b.d.l.
$Fe^{2+}/(Fe^{2+}+Mg^{2+})$	46(42-50)	32(31-33)	47(40-54)	50(38-64)	49(39-54)
$Fe^{3+}/(Cr+Al+Fe^{3+})$	7(6-9)	6(6-7)	10(7-15)	12(5-22)	9(5-15)
Cr/(Cr+Al)	73(68-77)	73	64(51-77)	68(50-77)	68(55-80)

Sample	**S68-34.90**	**S68-47**	**S53-10.90**
Number of analyses	**7**	**6**	**2**
	---------chromian spinel in clinopyroxene----------		
Cr_2O_3	42(36.4-51.6)	39.8(29.9-45.2)	45.4-45.5)
Al_2O_3	17.2(13-20)	17.2(13.9-23.3)	15.3(15.1-15.4)
TiO_2	0.57(0.2-0.77)	0.7(0.44-1.16)	0.41(0.4-0.41)
ZnO	b.d.l.	b.d.l.	b.d.l.
$Fe^{2+}/(Fe^{2+}+Mg^{2+})$	52(59-55)	52(47-56)	50-51
$Fe^{3+}/(Cr+Al+Fe^{3+})$	12(8-15)	14(12-17)	12
Cr/(Cr+Al)	62(55-73)	61(46-68)	66-67

5.7.3 Chlorite

The upper part of the Salu Bullo region consists of metavolcanic rocks, containing abundant chlorite minerals. The chlorite occurs as filled vesicles or as veinlets, mostly in mafic host rock or chlorite phengite schist. In optical microscope, the chlorite has blue and green birefringence colours (Fig. 46A-B). In Awak Mas, chlorite occurs as porphyroclast in schist (Figs. 46C-D) or as a secondary alteration minerals (Fig. 46F). In total, eighty-two electron microprobe analyses were obtained from seven samples. The quantitative analyses of chlorite are listed on Tables 16-18 and Appendix D. Figure 46 presents the photomicrograph and BSE image of chlorite from the Awak Mas and Salu Bullo deposits. Some samples (S53-50.20; greenschist) containing elevated amount of Cr_2O_3 up to 0.78 wt% (Fig. 46F).

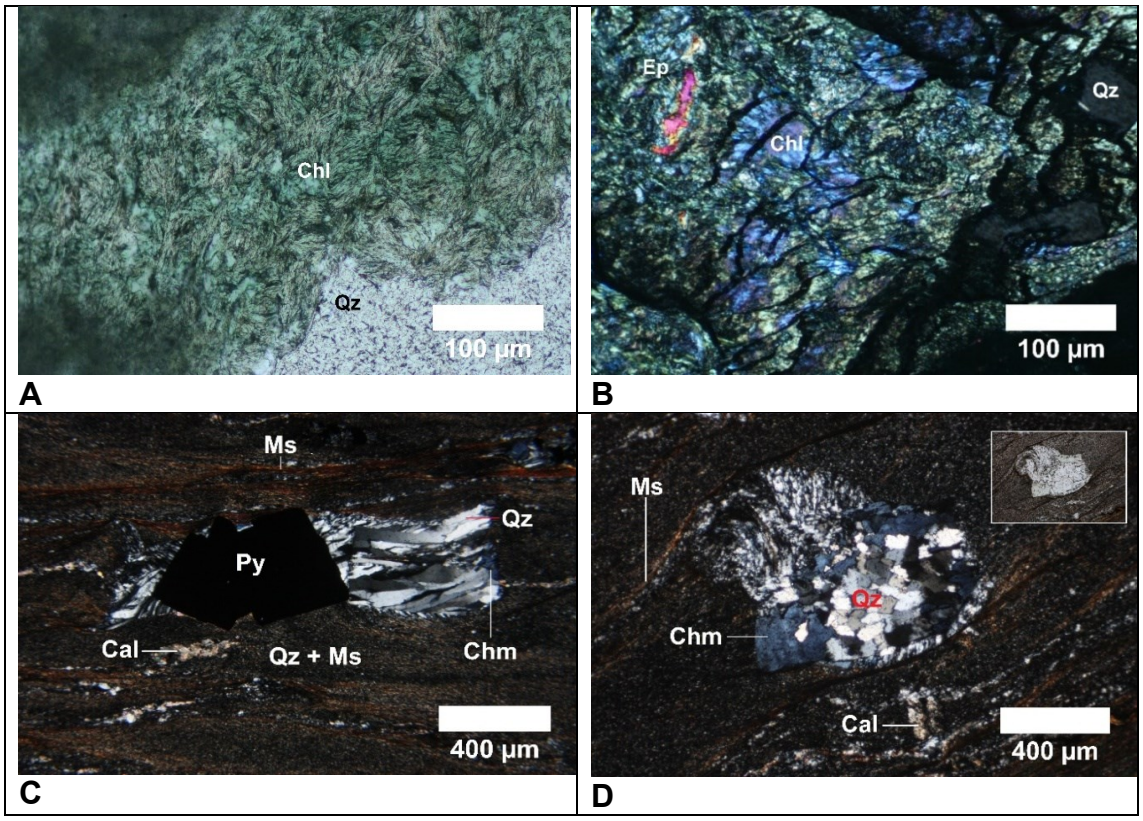

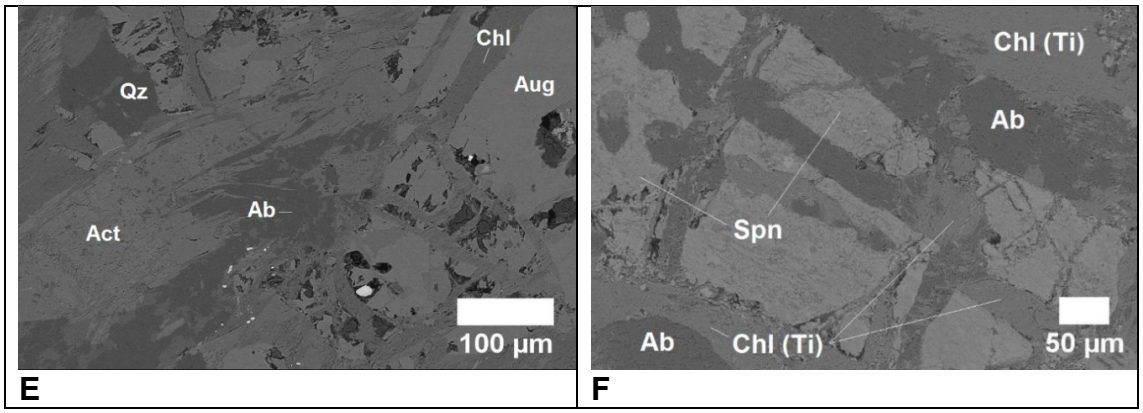

Fig. 46. Photomicrographs of chlorites. (A) Radiating crystals of chlorite showing pale green colours, PPL, S50-39.10. (B) Blue interference colours indicate iron-rich chlorite. XPL. S50-80.30. (C) Iron-rich chlorite and quartz occur as tails from pyrite porphyroblasts. A687-171. (D) Ductile deformation from Awak Mas indicated by the rotation of chlorite-quartz porphyroblast. Inset shows PPL image of Fig. 46D. A687-171. (E) Chlorite as veinlets filling fractures in augite. (F) Titanian chlorite in altered chlorite albite schist.

Chlorite compositions of Salu Bullo are generally Mg-rich with X_{Mg} values ranging from 0.43 to 0.74 (average of 0.67) with low X_{Mn} values (less than 0.03). Silica contents vary from.5.14 to 5.99 cations per 28 oxygens (Tables 16-17); compositions plot into pycnochlorite and ripidolite fields of the classification of Hey (1954)(Fig. 47A). However, according to Deer et al. (2009), the earlier names of pycnochlorite and ripidolite (and some other chlorite terminology) are obsolete. These authors suggested the usage of end-member compositions as accepted by the International Mineralogical Association (I.M.A.). The appropriate terminology of the observed chlorite are chlinochlore - $Mg_6(Mg_4Al_2)[Si_6Al_2O_{20}](OH)_{16}$ and chamosite - $Fe^{2+}(Fe^{2+}{}_4Al_2)[Si_6Al_2O_{20}](OH)_{16)}$ (Fig. 47B). Chlorite in Salu Bullo has a high magnesium and low titanium contents. In contrast, the Awak Mas chlorite is enriched in iron and titanium (Table 17).

Table 16. Representative electron microprobe analyses on Mg-rich chlorite (wt%) in the Salu Bullo

Sample number	S53-50.20		S50-39.10		S68-69		S68-47.00		S66-122.50		S68-34.90		S68-84.55-2	
Number of analysis	13		15		10		12		6		10		2	
	Mean	S.D.	Mean	S.D.	Mean	S.D.	Mean	S.D.	Mean	S.D.	Mean	S.D.	Mean	S.D.
Lithology	Metabasite		Metabasite		Metabasite		Cpx-phyric basalt		Metabasite		Metabasite		Metatuff	
SiO_2	30.18	0.84	30.37	1.05	29.50	0.68	30.36	0.70	26.92	1.00	29.80	0.48	28.14	0.50
TiO_2	0.02	0.02	0.01	0.01	0.02	0.02	0.07	0.21	0.02	0.03	0.04	0.13	0.16	0.22
Al_2O_3	18.46	0.66	18.01	1.06	18.68	0.63	18.49	0.61	20.31	0.37	17.76	0.82	18.70	0.67
FeO	16.34	0.31	17.67	0.73	19.52	1.31	16.38	1.03	26.15	1.63	15.91	0.73	25.71	0.62
MnO	0.20	0.03	0.24	0.03	0.91	0.24	0.29	0.22	0.85	0.19	0.22	0.03	0.32	0.01
MgO	23.78	0.49	22.79	0.66	21.58	1.25	24.24	1.18	14.41	1.51	24.36	0.82	18.24	0.17
CaO	0.06	0.04	0.10	0.06	0.05	0.10	0.06	0.03	0.02	0.01	0.13	0.11	0.26	0.26
Na_2O	0.02	0.02	0.02	0.02	0.01	0.01	0.01	0.01	0.03	0.02	0.01	0.02	0.02	0.02
K_2O	0.01	0.01	0.01	0.01	0.01	0.03	0.01	0.01	0.03	0.02	0.01	0.02	0.02	0.00
Cr_2O_3	0.18	0.22	0.04	0.06	0.01	0.02	0.02	0.02	0.00	0.00	-	-	-	-
Total	89.25	1.21	89.25	1.84	90.29	0.30	90.02	1.27	88.73	0.99	88.23	1.46	91.56	0.14
Normalisation on the basis 28O														
Si	5.92	0.10	5.99	0.11	5.84	0.10	5.91	0.13	5.61	0.10	5.91	0.12	5.66	0.11
Al^{iv}	2.08	0.10	2.01	0.11	2.16	0.10	2.09	0.13	2.39	0.10	2.09	0.12	2.34	0.11
Al^{vi}	2.19	0.08	2.18	0.12	2.20	0.08	2.15	0.08	2.62	0.05	2.07	0.09	2.10	0.06
Ti	0.00	0.00	0.00	0.00	0.00	0.00	0.01	0.03	0.00	0.00	0.01	0.02	0.02	0.03
Cr	0.03	0.04	0.01	0.01	0.00	0.00	0.00	0.00	0.00	0.00	0.00	0.00	0.00	0.00
Fe^{3+}	0.07	0.08	0.10	0.08	0.03	0.03	0.06	0.07	0.12	0.05	0.02	0.03	0.00	0.00
Fe^{2+}	2.61	0.12	2.82	0.26	3.21	0.26	2.62	0.19	4.44	0.40	2.64	0.14	4.41	0.15
Mn	0.03	0.00	0.04	0.01	0.15	0.04	0.05	0.04	0.15	0.04	0.04	0.01	0.06	0.00
Mg	6.95	0.15	6.70	0.13	6.36	0.32	7.03	0.28	4.47	0.40	7.20	0.14	5.46	0.05
Ca	0.01	0.01	0.02	0.01	0.01	0.02	0.01	0.01	0.00	0.00	0.03	0.02	0.06	0.06
Na	0.01	0.01	0.01	0.02	0.01	0.01	0.01	0.01	0.02	0.01	0.01	0.02	0.01	0.01
K	0.01	0.00	0.01	0.01	0.01	0.01	0.00	0.00	0.01	0.01	0.01	0.01	0.01	0.00
T-corrected(°C)	260	11	254	12	272	12	260	14	308	13	260	12	300	12
Mg-number	72	0.58	70	1.45	66	2.78	72	2.10	49	4.23	73	1.20	55	1.09

Table 17. Representative electron microprobe analyses on Fe-rich chlorite (wt%) in the Awak Mas.

Sample number	A687-157.98		A192-155.70		A685-171-2	
number of analysis	5		5		4	
	Mean	S.D.	Mean	S.D.	Mean	S.D.
Lithology	Chlorite phengite schist		Carbonaceous phyllite		Chlorite phengite schist	
SiO_2	27.44	2.00	24.98	0.93	24.36	0.39
TiO_2	1.67	2.40	0.38	0.59	0.48	0.43
Al_2O_3	18.87	2.89	21.41	0.68	22.11	0.36
FeO	26.37	1.51	33.12	0.42	34.94	1.35
MnO	1.65	0.10	0.52	0.21	1.03	0.13
MgO	14.31	1.03	11.22	0.64	9.11	0.98
CaO	0.05	0.06	0.03	0.03	0.02	0.02
Na_2O	0.07	0.04	0.04	0.05	0.08	0.02
K_2O	0.07	0.07	0.09	0.02	0.03	0.02
Cr_2O_3	-	-	-	-	-	-
Total	90.49	0.39	91.78	1.99	92.156	0.51
Normalisation on the basis 28O						
Si	5.63	0.36	5.22	0.08	5.14	0.05
Al^{iv}	2.37	0.36	2.78	0.08	2.86	0.05
Al^{vi}	2.23	0.48	2.52	0.08	2.66	0.10
Ti	0.25	0.37	0.06	0.09	0.08	0.07
Cr	0.00	0.00	0.00	0.00	0.00	0.00
Fe^{3+}	0.20	0.20	0.01	0.02	0.01	0.01
Fe^{2+}	4.34	0.53	5.87	0.32	6.20	0.29
Mn	0.29	0.02	0.09	0.04	0.18	0.02
Mg	4.38	0.28	3.50	0.12	2.87	0.30
Ca	0.01	0.01	0.01	0.01	0.00	0.00
Na	0.05	0.03	0.03	0.04	0.06	0.02
K	0.03	0.04	0.05	0.01	0.02	0.01
T-corrected	307	40	359	9	372	7
Mg-number	49	3.20	37	1.89	32	3.16

The chlorite geothermometer of Kranidiotis and MacLean (1987)

Table 18. Chemical parameters (mean and range) of Mg-rich chlorite in the Salu Bullo and Fe-rich chlorite in the Awak Mas.

Salu Bullo

Sample	**S66-122.50**	**S68-84.55**	**S68-69**	**S68-47**	**S53-50.20**	**S68-39.10**	**S68-34.90**
Number of analyses	6	2	10	12	13	15	10
Elevation (m)	948.26	971.14	984.48	1002.5	1005.88	1008.97	1012.41
Depth (m)	106.90	118.53	56.52	38.50	41.12	32.03	28.59
wt% K_2O	0.01-0.05	0.02	0-0.09	0-0.01	0-0.03	0-0.04	0.08-0.13
wt% TiO_2	0.02(0-0.08)	0.16(0-0.3)	0.02(0-0.06)	0.01(0-0.05)	0.02(0-0.06)	0.01(0-0.03)	0-0.04
Mg-number	49.5(43.4-53.3)	55.4(54.6-56.1)	66.2(61.9-71.8)	72.2(70-73.6)	72.1(71.1-72.9)	69(66-72.2)	71.6(69.3-73.1)
T (°C)	308(296-325)	300(291-308)	272(252-289)	257(234-280)	260(236-276)	253(227-272)	260(243-276)

Awak Mas

Sample	**A685-171**	**A687-157.90**	**A192-155.70**
Number of analyses	4	5	5
Elevation (m)	1033.91	1043.25	1059.51
Depth (m)	148.09	136.75	135.19
wt% K_2O	0.03(0.02-0.06)	0.03 (0.02-0.06)	0.09 (0-0.13)
wt% TiO_2	0.48(0.09-1.10)	1.67(0.01-5.47)	0.38 (0-1.36)
Mg-number	31.6(27-32)	47.4(45.5-52.9)	37.3(34.1-39)
T (°C)	372(362-376)	321(269-346)	359(347-373)

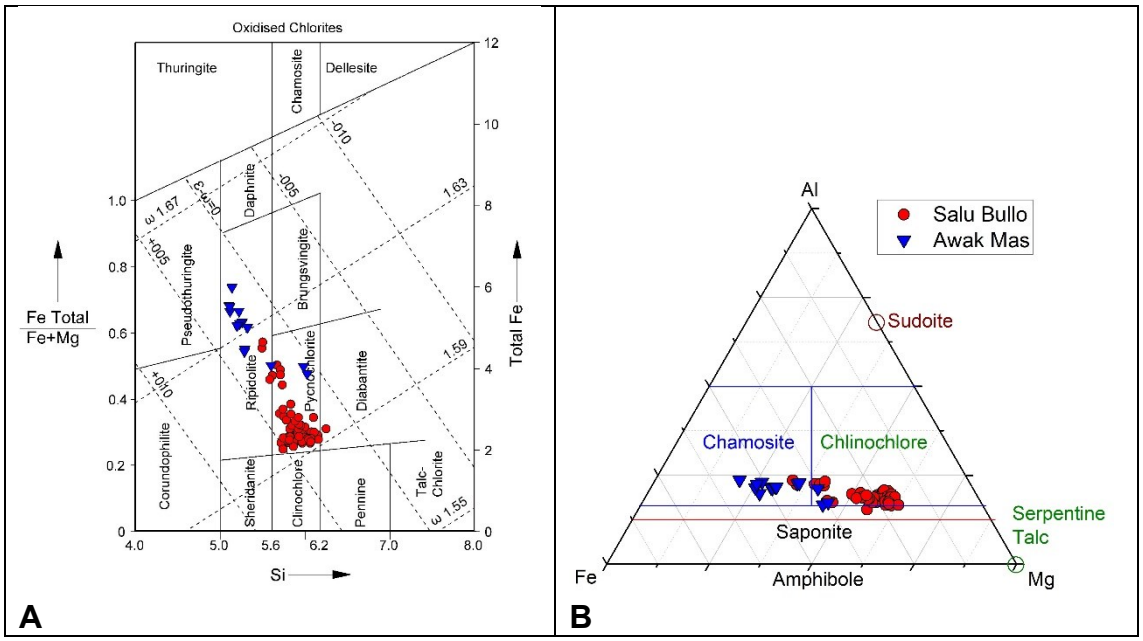

Fig. 47. Composition of chlorites obtained by electron microprobe. (A) Chemical composition of chlorite after Hey (1954). (B) Ternary diagram of the relative atomic proportions of Al, Fe, and Mg shows that chlorite from Salu Bullo falls into chlinochlore field, while chlorite in Awak Mas is classified as chamosite.

5.7.4 Muscovite

White mica defines the primary schistosity in phyllite, and often occurs as a fine-grained sericite in hydrothermally altered rock. White micas are abundant minerals in Awak Mas (Figs. 48A-C) and are rarely present in the Salu Bullo deposit. Twenty-four spot analyses of white mica were performed using electron microprobe and the results indicate a phengite composition. The phengite is a muscovite in which the Si: Al ratio is greater than 3:1 and in which the increasing of Si is accompanied by substitution of Mg^{2+} or Fe^{2+} for Al in octahedral sites.

Figure 48D illustrates that the Si contents of carbonaceous phyllite of the Awak Mas ar lower than the metavolcanic rocks of the Salu Bullo. In contrast, the Awak Mas mica has higher Al contents than the white mica from Salu Bullo. The average Si contents of the white mica from the Awak Mas and Salu Bullo are 3.4 and 3.6, respectively. Tables 18-19 and Appendix D list representative compositions of phengitic muscovite from Awak Mas and Salu Bullo.

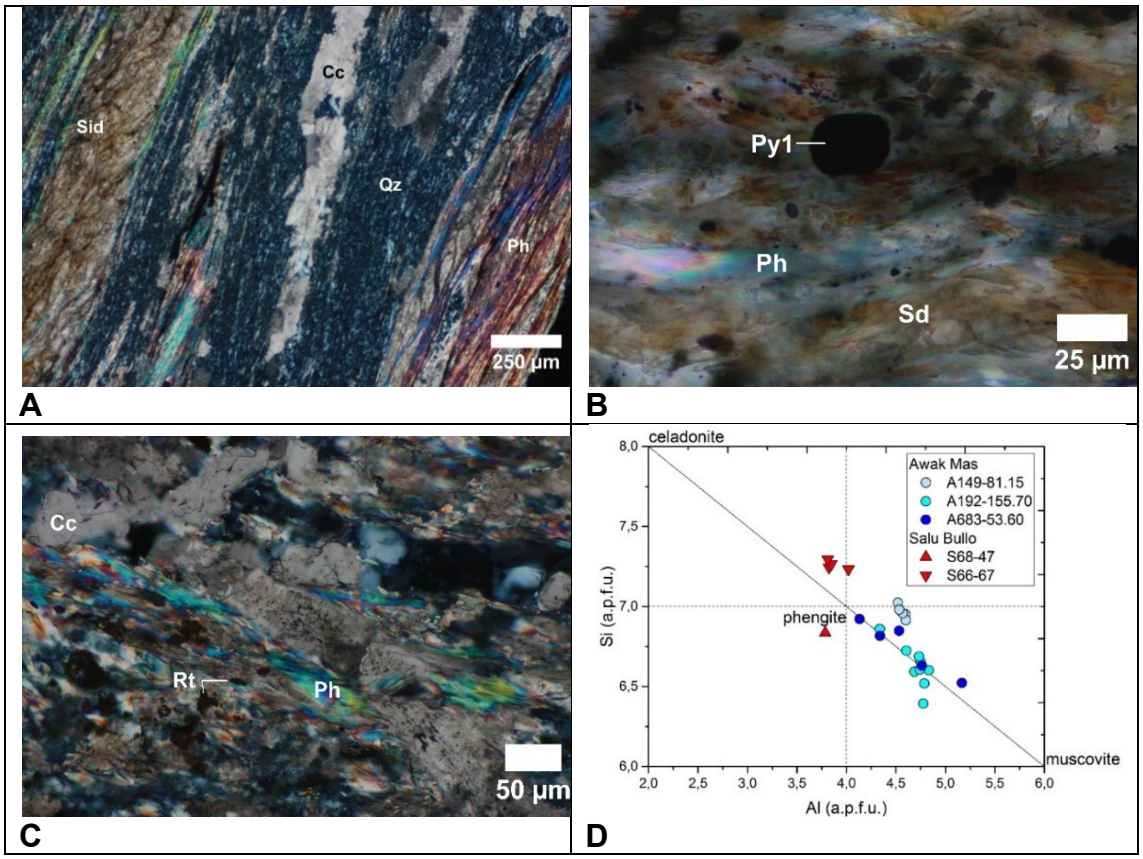

Fig. 48. Photomicrograph of phyllite and classification of mica minerals. (A) A XPL image of phyllite. (B) Framboidal pyrite (Py1) observed within the foliation. (C) Fine-grained phengite in phyllite. (D) Classification of the representative white mica phases in the diagram Si vs Al. Three samples from Awak Mas are phyllite (A149-81.15) and carbonaceous phyllite (A192-155.70 and A683-53.60). Sample S68-47 is clinopyroxene-phyric metabasite and S66-67 is metatuff containing some sulphide.

Table 19. Representative composition of phengite (wt%).

Sample number	**A192-155.70**		**A683-53.60**		**A149-81.15**		**S66-67**		**S68-47**
number of analyses	9		5		6		3		1
	Mean	S.D.	Mean	S.D.	Mean	S.D.	Mean	S.D.	Mean
Lithology	Carbonaceous phyllite		Carbonaceous phyllite		Phyllite		Metatuff		Clinopyroxene phyric metabasite
SiO_2	50.47	1.25	49.63	2.51	50.62	50.62	51.49	51.49	50.50
TiO_2	0.49	0.32	0.45	0.51	0.10	0.10	0.10	0.10	0.00
Al_2O_3	30.33	0.98	28.59	2.29	28.59	28.59	23.32	23.32	23.73
FeO	3.05	1.33	2.36	0.79	3.29	3.29	5.57	5.57	4.43
MnO	0.02	0.01	0.01	0.02	0.03	0.03	0.19	0.19	0.03
MgO	2.06	0.32	1.98	0.76	1.65	1.65	3.20	3.20	6.06
CaO	0.04	0.04	0.11	0.06	0.03	0.03	0.04	0.04	0.06
Na_2O	0.21	0.06	0.20	0.10	0.21	0.21	0.19	0.19	0.07
K_2O	9.99	0.88	9.44	1.33	9.36	9.36	10.26	10.26	10.49
Total	96.66	1.17	92.78	3.60	93.89	93.89	94.35	94.35	95.34
Normalisation on the basis of 22 negative charges									
Si	6.63	0.13	6.75	0.17	6.93	6.93	7.26	7.26	6.84
Ti	0.05	0.03	0.05	0.05	0.01	0.01	0.01	0.01	0.00
Al	4.69	0.15	4.59	0.40	4.61	4.61	3.88	3.88	3.79
Fe^{+3}	0.00	0.00	0.00	0.00	0.00	0.00	0.00	0.00	0.00
Fe^{+2}	0.34	0.15	0.27	0.09	0.00	0.00	0.00	0.00	0.50
Mn	0.00	0.00	0.00	0.00	0.00	0.00	0.03	0.03	0.00
Mg	0.40	0.06	0.40	0.16	0.34	0.34	0.67	0.67	1.22
Ca	0.01	0.01	0.02	0.01	0.01	0.01	0.01	0.01	0.01
Na	0.05	0.02	0.05	0.03	0.06	0.06	0.05	0.05	0.02
K	1.67	0.15	1.64	0.21	1.64	1.64	1.85	1.85	1.81
Mg-number	56.1	8.8	59.5	7.1	99.6	1	96.9	0.4	70.8

Table 20. Chemical parameters (mean and range) of Mg-rich mica in the Salu Bullo and Awak Mas deposits

	S68-47	**A192-155.70**	**A683-53.60**	**A149-81.15**
Elevation (m)	1002.5	1059.1	1079.91	1119.87
Number of analyses	1	9	5	5
K/(K+Ca+Na)	0.99	0.97 (0.95-0.98)	0.97 (0.94-0.99)	0.96 (0.95-0.98)
wt% K_2O	10.49	9.99 (8.39-10.95)	9.44 (7.36-10.93)	9.30 (9.09-9.62)
Si (a.p.f.u)	6.84	6.63 (6.39-6.86)	6.75 (6.52-6.92)	6.97 (6.91-7.02)
Al (a.p.f.u)	3.79	4.69 (4.34-4.83)	4.59 (4.13-5.17)	4.56 (4.52-4.60)
Mg-number	70.8	56.1(42.7-65.7)	59.5(49.3-66.1)	98.8(97.5-99.9)
Pressure (kbar)*	8.2 (7.8-8.5)-	7.3 (4.2-9.7)	7.9 (4.6-11.1)	11.1 (10.4-13.1)
Temperature (°C)	257 (234-280)[1]	360 (327-377)[2]	395 (361-405)[2]	372(339-393)[3]

[1]Chlorite geothermometry from the same sample (this study).
[2]Graphite thermometry from the same sample (this study).
[3]Temperature of phyllite (A192-155.50) based on Raman spectrocopic analysis on carbonaceous materials (this study)

5.7.5 Actinolite

Amphibole is observed only in mafic protolith at Salu Bullo. Amphibole has moderate to high positive relief, splintery radiating crystals, and often occurs as fine-grained matrix of metabasites (Fig. 49A). Some of the amphibole forms inclusions in quartz crsytal (Fig. 49B). Fifteen spot analyses were performed on amphibole. Only amphibole with total oxide contents of 97-99 wt% and calculated Si content <8.05 a.p.f.u. are used in this study (Table 19). SiO_2 contents vary from 55.47 to 58.04 wt% (average of 57.16). TiO_2 and Al_2O_3 contents are generally less than 2 wt% (TiO_2: 0.00 -1.64; Al_2O_3: 0.45 - 1.72 wt%). Amphibole has a high Mg-number of 78 – 81 (average of 79). Using the nomenclature of Leake et al. (1997; 2004), all analyzed amphibole can be classified as calcic amphibole with further subdivisions of actinolite (Fig. 50). Actinolite from Salu Bullo has Ca ≥ 1.5 and low Na + K in the A-site (<0.5).

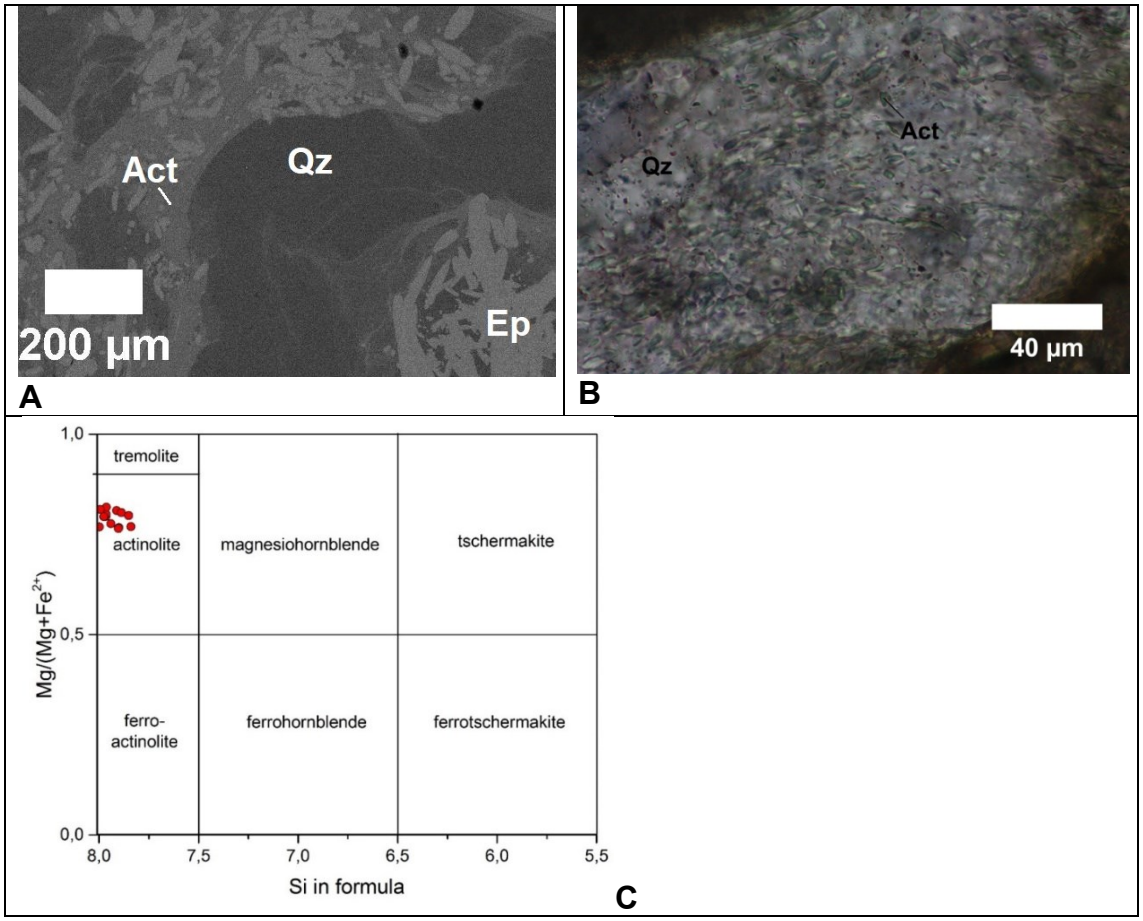

Fig. 49. Mineral assemblages in metabasite. (A) A BSE image shows epidote in a fine-grained matrix of actinolite. (B) The first overgrowth of acicular actinolite in quartz. (C) Chemical composition of calcic amphiboles based on electron microprobe analyses. Diagram after Leake et al. (1997).

Table 21. Representative analyses of actinolite (wt%).

Sample no	**S53-10.90**	**S68-39.10**	**S53-10.90**	**S53-10.90**	**S53-10.90**	**S68-34.90**	**S68-34.90**	**S68-34.90**	**S68-34.90**	**S68-34.90**
Point no	21	16	4	10	23	7	9	12	24	11
SiO_2	56.85	57.29	57.66	58.04	57.69	56.04	56.66	56.91	55.47	58.04
TiO_2	0.02	0.00	0.00	0.06	0.00	0.25	0.00	0.64	0.53	0.25
Al_2O_3	1.35	0.45	1.72	1.01	0.73	0.72	0.56	1.00	0.86	0.54
FeO	8.68	9.81	8.20	8.88	8.52	9.54	8.66	10.15	10.16	8.57
MnO	0.26	0.22	0.13	0.27	0.34	0.29	0.17	0.28	0.20	0.15
MgO	19.24	18.30	19.49	19.29	18.63	18.60	19.49	18.49	19.01	19.48
CaO	11.63	12.57	12.06	12.14	12.23	11.65	11.74	11.65	11.38	11.74
Na_2O	0.15	0.24	0.30	0.20	0.12	0.13	0.29	0.28	0.30	0.26
K_2O	0.04	0.01	0.027	0.051	0.049	0.05	0.03	0.03	0.01	0.01
Total	98.21	98.89	99.58	99.94	98.32	97.27	97.60	99.43	97.91	99.03
Normalisation on the basis of 23 oxygens, assuming all ferrous iron										
Si	7.96	8.00	7.91	7.96	8.04	7.94	7.96	7.90	7.84	8.01
Ti	0.00	0.00	0.00	0.01	0.00	0.03	0.00	0.07	0.06	0.03
Al	0.22	0.07	0.28	0.16	0.12	0.12	0.09	0.16	0.14	0.09
Fe^{2+}	1.02	1.14	0.94	1.02	0.99	1.13	1.02	1.18	1.20	0.99
Mn	0.03	0.03	0.02	0.03	0.04	0.03	0.02	0.03	0.02	0.02
Mg	4.02	3.81	3.99	3.95	3.87	3.93	4.08	3.83	4.00	4.01
Ca	1.75	1.88	1.77	1.79	1.83	1.77	1.77	1.73	1.72	1.74
Na	0.04	0.06	0.08	0.05	0.03	0.04	0.08	0.07	0.08	0.07
K	0.01	0.00	0.00	0.01	0.01	0.01	0.01	0.00	0.00	0.00
Total	17.05	17.00	16.99	16.98	16.925	16.79	16.83	16.79	16.77	16.79
Mg-number	80	77	81	80	80	78	80	76	77	80

Representative analyses of actinolite (cont.)

Sample no	**S68-47**	**S68-47**	**S68-47**	**S68-47**	**S68-47**
Point no	4	6	7	8	16
SiO_2	57.38	57.56	56.88	57.75	57.21
TiO_2	1.42	0.85	1.64	0.68	0.00
Al_2O_3	0.30	0.58	0.46	0.39	0.31
FeO	8.62	8.81	8.87	7.94	8.23
MnO	0.17	0.17	0.18	0.14	0.11
MgO	19.87	19.03	19.52	20.04	20.01
CaO	11.88	11.58	11.85	11.92	11.82
Na_2O	0.15	0.27	0.21	0.16	0.17
K_2O	0.03	0.05	0.03	0.02	0.02
Total	99.82	98.89	99.63	99.04	97.88
Normalisation on the basis of 23 oxygens, assuming all ferrous iron					
Si	7.89	7.98	7.85	7.96	7.99
Ti	0.15	0.09	0.17	0.07	0.00
Al	0.05	0.10	0.07	0.06	0.05
Fe^{2+}	0.99	1.02	1.02	0.92	0.96
Mn	0.02	0.02	0.02	0.02	0.01
Mg	4.07	3.93	4.02	4.12	4.17
Ca	1.75	1.72	1.75	1.76	1.77
Na	0.04	0.07	0.05	0.04	0.04
K	0.00	0.01	0.00	0.00	0.00
Total	16.77	16.78	16.64	16.66	16.70
Mg-number	80	79	80	82	81

Table 22. Chemical parameters (mean and range) of actinolite in the Salu Bullo obtained by electron microprobe

	S53-10.90	**S68-34.90**	**S68-47**	**S68-39.10**
Si (a.p.f.u.)	8(7.9-8.04)	7.93(7.84-8.01)	7.93(7.85-7.99)	8
Ca (a.p.f.u.)	1.8(1.75-1.88)	1.75(1.72-1.77)	1.75(1.72-1.77)	1.88
Na (a.p.f.u.)	0.07(0.04-0.08)	0.07(0.04-0.08)	0.05(0.04-0.07)	0.06
Mg-number	79.3(76.9-80.9)	78.3(76.4-80.2)	80.5(79.4-81.8)	77

5.7.6 Pumpellyite and epidote

The problem of identifying calcium-aluminium silicates (pumpellyite, prehnite and epidote) in low-grade metabasites has been pointed out by Frey and Robinson (1999). Using petrographic methods, these minerals might be hard to distinguish from one to another, because their refractive indices covary with their Fe contents (Deer et al. 2001). Absorption colour for prehnite is colourless, epidote is yellow to colourless (varies with Fe content) and pumpellyite is green to colourless (varies with Fe content). In refracted light, pumpellyite occurs as blue needles to colourless showing high relief. They are restricted to mafic metavolcanic rocks. However, these minerals (in particular pumpellyite and epidote) often occur as fine-grained aggregates within groundmass (pumpellyite - Fig. 51, epidote - Fig. 52).

To unravel this problem, the pumpellyite is distinguished from prehnite and epidote by its diagnostic small, but always present, Mg peak (Frey and Robinson 1999). Prehnite and epidote cannot be differentiated by EDS, and WDS analyses may be necessary for quantitative differentiation. The chemical formula for those minerals is given bellow. follows:

a. pumpellyite - $Ca_2(Al,Fe^{++},Mg)Al_2(SiO_4)(Si_2O_7)(OH)_2.(H_2O)$;

b. prehnite $Ca_2Al_2Si_3O_{12}(OH)$; and

c. epidote – $Ca_2(Al_2,Fe)(SiO_4)(Si_2O_7)O(OH)$. Epidote is an end member of solid solution with clinozoisite - $Ca_2Al_3(SiO_4)(Si_2O_7)O(OH)$, where the iron of epidote is replaced by aluminium to the end member of clinozoisite.

Raman spectroscopy is also an efficient method to distinguish the epidote - clinozoisite and pumpellyite. Figure 53 illustrates spectra obtained by laser Raman spectroscopy, comparable to clinozoisite spectra from the RRUF database.

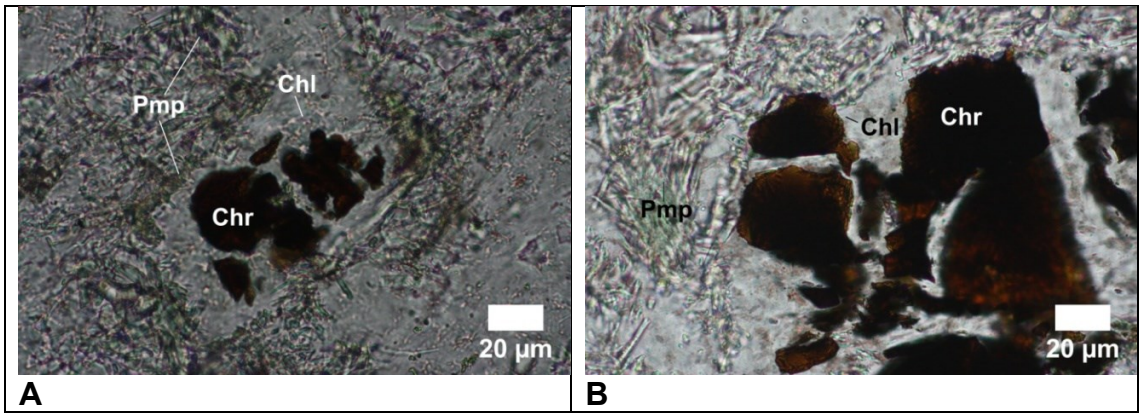

Fig. 50. Photomicrograph of pumpellyite from sample S53-10.90.

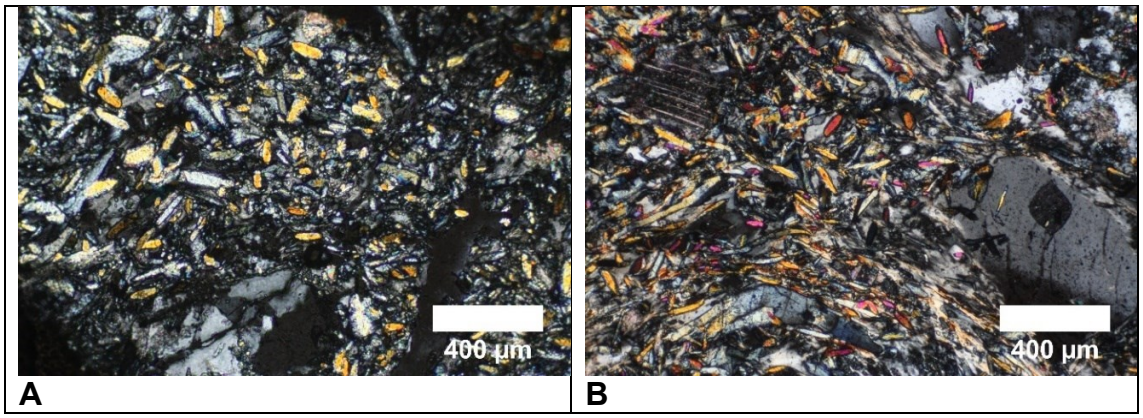

Fig. 51. Photomicrograph of epidote from sample S53-10.90.

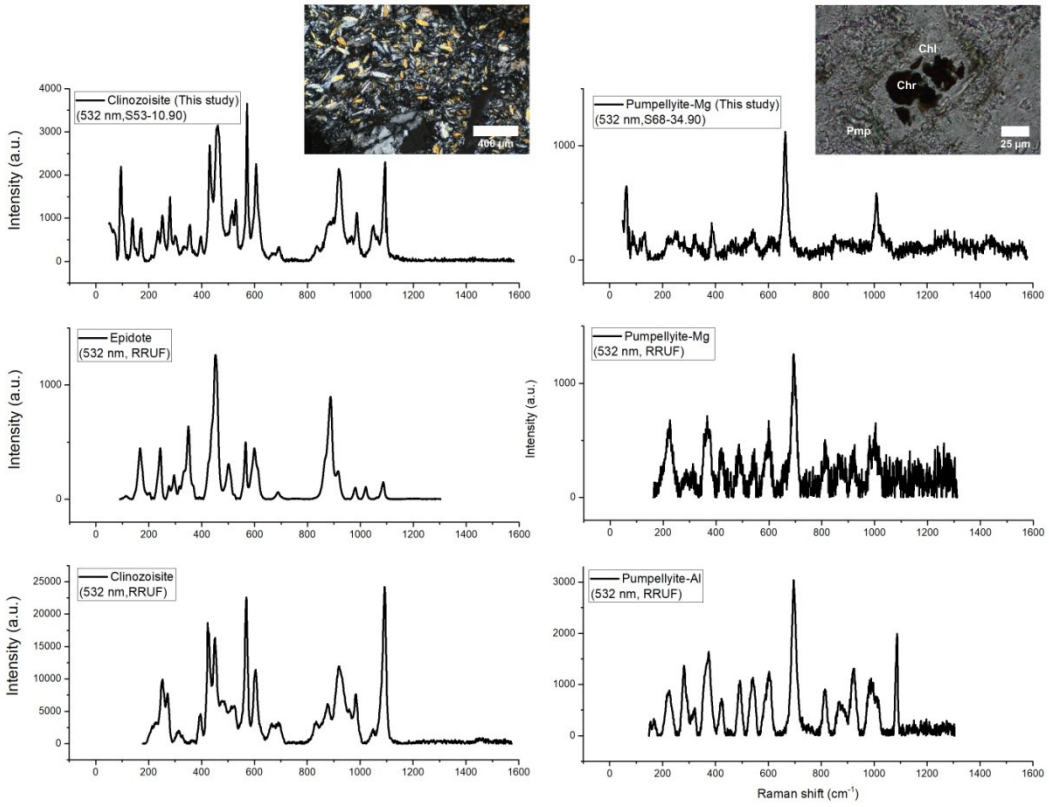

Fig. 52. Raman spectra of epidote from sample S53-10.90 and S68-34.90. References are epidote, clinozoisite, zoisite and pumpellyite-Al from RRUF database.

Mineral analyses were obtained in four samples of the metabasites from the Salu Bullo. Twenty-four spot analyses were performed on epidote and pumpellyite. Representative analyses of epidote and pumpellyite are listed in Tables 22 -24.

Epidote and pumpellyite was calculated on the basis 12.5 and 24.5 oxygens, respectively. In general, epidote has a lower Mg-number (*Mg*-number less than 2, Table 23) than pumpellyite (*Mg*-number ranging from 6 to 42.6, Table 24). Average epidote compositions vary from X_{Fe} = 0.62 to 0.98, X_{Al} = 2.05 to 2.20 and may reflect the composition of clinozoisite. Pumpellyite has 4.02 and 4.43 Al atom per formula unit (Table 24).

The calculated stoichiometry of pumpellyite and epidote are not ideal. The results show sligthly higher-Si and lower-Ca (Table 25). This is probably because all pumpellyite data were obtained from fine-grained materials within the chlorite matrix (Fig. 50A-B). However, it is believed that corresponding results are close to the stoichiometry of Al-pumpellyite and Al-epidote (clinozoisite).

Table 23. Representative analyses of epidote (wt%)

Sample No	**S68-34.90**	**S68-34.90**	**S68-34.90**	**S68-34.90**	**S68-34.90**	**S68-34.90**	**S68-34.90**	**S68-34.90**	**S94-80.30**	**S94-80.30**
	17	18	1	2	4	5	7	9	3	7
SiO_2	39.68	38.42	38.57	38.12	38.95	38.93	38.32	38.58	38.98	38.20
TiO_2	0.00	0.00	0.29	0.14	0.13	0.09	0.31	0.03	0.96	0.00
Al_2O_3	23.25	24.41	22.11	23.04	24.46	23.69	24.01	22.16	21.91	20.82
FeO	11.87	11.07	12.69	11.20	9.31	10.56	10.14	12.26	12.16	14.25
MnO	0.12	0.09	0.08	0.21	0.15	0.40	0.07	0.35	0.03	0.08
MgO	0.75	0.66	0.13	0.05	0.15	0.03	0.01	0.17	0.33	0.02
CaO	20.81	20.90	22.05	21.84	22.29	21.68	22.11	21.74	21.64	19.91
Na_2O	0.01	0.01	0.01	0.05	0	0	0.08	0.03	0.07	0.03
K_2O	0.00	0.00	0.01	0.01	0.01	0.001	0.02	0.01	0.01	0.01
Total	96.49	95.56	95.93	94.65	95.45	95.34	95.07	95.326	96.08	93.32
Normalisation on the basis of 12.5 O. all iron is calculated as Fe^{3+}										
Si	3.12	3.05	3.08	3.08	3.10	3.11	3.07	3.10	3.10	3.13
Ti	0.00	0.00	0.02	0.01	0.01	0.01	0.02	0.00	0.06	0.00
Al	2.16	2.29	2.08	2.19	2.29	2.23	2.27	2.10	2.05	2.01
Fe^{+3}	0.78	0.74	0.85	0.76	0.62	0.70	0.68	0.82	0.81	0.98
Mn	0.01	0.01	0.01	0.01	0.01	0.03	0.00	0.02	0.00	0.01
Mg	0.09	0.08	0.02	0.01	0.02	0.00	0.00	0.02	0.04	0.00
Ca	1.75	1.78	1.89	1.89	1.90	1.85	1.90	1.87	1.84	1.75
Na	0.00	0.00	0.00	0.01	0.00	0.00	0.01	0.00	0.01	0.01
K	0.00	0.00	0.00	0.00	0.00	0.00	0.00	0.00	0.00	0.00
Mg-number	1	0.9	0.6	1.9	1.7	3.7	0.7	2.8	0.3	0.6

Mg-number = 100 x Mg/ (Mg+Fe^{+3})

Representative analyses of epidote (wt%) (cont.)

Sample No	**S94-80.30** 9	**S53-10.90** 3	**S53-10.90** 8	**S53-10.90** 12	**S53-10.90** 13	**S53-10.90** 14	**S53-10.90** 22	**S53-10.90** 24
SiO_2	37.59	38.62	38.83	38.24	37.97	38.20	38.83	39.41
TiO_2	0.05	0.21	0.08	0.18	0.02	0.28	0.27	0.05
Al_2O_3	21.60	22.24	23.26	23.30	22.47	22.05	22.87	23.49
FeO	13.37	12.40	10.96	10.92	12.12	12.29	11.67	9.70
MnO	0.03	0.00	0.34	0.03	0.21	0.05	0.06	0.20
MgO	0.00	0.08	0.06	0.05	0.04	0.07	0.08	0.04
CaO	20.75	22.06	21.67	21.85	21.80	22.00	22.23	21.81
Na_2O	0.01	0.03	0.07	0.00	0.04	0.00	0.00	0.01
K_2O	0.00	0.01	0.01	0.00	0.01	0.00	0.00	0.03
Total	93.39	95.65	95.27	94.57	94.68	94.94	96.01	94.74
Normalisation on the basis of 12.5 O. all iron is calculated as Fe^{3+}								
Si	3.08	3.09	3.11	3.08	3.07	3.08	3.09	3.15
Ti	0.00	0.01	0.00	0.01	0.00	0.02	0.02	0.00
Al	2.09	2.10	2.19	2.21	2.14	2.10	2.14	2.22
Fe^{+3}	0.92	0.83	0.73	0.74	0.82	0.83	0.78	0.65
Mn	0.00	0.00	0.02	0.00	0.01	0.00	0.00	0.01
Mg	0.00	0.01	0.01	0.01	0.00	0.01	0.01	0.00
Ca	1.82	1.89	1.86	1.89	1.89	1.90	1.90	1.87
Na	0.00	0.00	0.01	0.00	0.01	0.00	0.00	0.00
K	0.00	0.00	0.00	0.00	0.00	0.00	0.00	0.00
Mg-number	0.2	0	3.	0.2	1.7	0.4	0.5	2

Mg-number = 100 x Mg/ (Mg+Fe^{+3})

Table 24. Representative analyses of pumpellyite

Sample	**S50-39.10-2**	**S94-80.30-2**	**S94-80.30-4**	**S53-10.90-5**	**S53-10.90-7**	**S68-34.90-10**
No.	5	26	28	39	41	78
SiO_2	37.94	38.70	37.90	40.42	39.18	39.85
TiO_2	0.07	0.10	0.08	0.08	0.10	0.07
Al_2O_3	20.23	22.73	23.19	22.27	22.28	22.48
FeO	7.30	6.18	7.07	10.26	11.35	9.61
MnO	0.17	0.12	0.07	0.10	0.15	0.19
MgO	3.04	1.62	1.55	1.18	0.44	1.61
CaO	21.06	21.22	21.58	21.59	21.79	21.43
Na_2O	0.06	0.09	0.09	0.00	0.00	0.02
K_2O	0.01	0.00	0.00	0.00	0.01	0.01
Total	89.87	90.76	91.54	95.89	95.29	95.27
Normalisation on the basis 24.5 O. all iron is calculated as Fe^{2+}						
Si	6.40	6.40	6.26	6.43	6.34	6.38
Ti	0.01	0.01	0.01	0.01	0.01	0.01
Al	4.02	4.43	4.51	4.18	4.25	4.24
Fe^{+2}	1.03	0.85	0.98	1.37	1.53	1.29
Mn	0.02	0.02	0.01	0.01	0.02	0.03
Mg	0.76	0.40	0.38	0.28	0.11	0.38
Ca	3.81	3.76	3.82	3.68	3.77	3.67
Na	0.02	0.03	0.03	0.00	0.00	0.01
K	0.00	0.00	0.00	0.00	0.00	0.00
Mg-number	42.6	31.8	28.2	17	6.5	23

Mg-number = 100 x Mg/ (Mg+Fe^{+2})

Table 25. Chemical parameters (mean and range) of epidote and pumpellyite in Salu Bullo obtained by electron microprobe

	S68-34.90	**S94-80.30**	**S53-10.90**	**S50-39.10**	**S94-80.30**	**S53-10.90**	**S68-34.90**
	----------Epidote----------			----------Pumpellyite----------			
Ca(a.p.f.u.)	1.85 (1.75-1.9)	1.8 (1.75-1.84)	1.88 (1.86-1.90)	3.81	3.79(3.76-3.82)	3.73(3.68–3.77)	3.67
Fe^{2+}(a.p.f.u.)	-	-	-	1.03	0.92(0.85-0.98)	1.45 (1.37-1.53)	1.29
Fe^{3+}(a.p.f.u.)	0.74 (0.62-0.85)	0.9 (0.81-0.98)	0.77 (0.65-0.83)	-	-	-	-
Al(a.p.f.u.)	2.2 (2.08-2.29)	2.05 (2.01-2.09)	2.16 (2.1-2.22)	4.02	4.47(4.43–4.51)	4.21(4.18-4.25)	4.24
Si(a.p.f.u.)	3.09 (3.05-3.12)	3.1 (3.08-3.13)	3.1 (3.07-3.1)	6.4	6.33(6.26–6.4)	6.39 (6.34-6,43)	6.38
Mg-number	1.6 (0.6-3.7)	0.4 (0.2-0.5)	1.1 (0.02-3.04)	42.6	30(28.2-31.7)	11.7	23

5.7.7 Plagioclase feldspar

Plagioclase feldspars vary in grain size, ranging from 10 µm to 500 µm (Figs. 53A-B). Lamellar twinning in plagioclase feldspar is common, as shown in Figure 53A. In the mafic host rocks, the plagioclase is altered to pure albite. Some basalt samples contain large altered megacrysts of plagioclase that are pseudomorphed by sericite and chlorite (Fig. 53C). Plagioclase feldspar displays minor variation in composition and is albite with X_{An} [Ca/(Ca+Na)] < 0.02 (Fig. 53D). Oligoclase is very rare with (Ca/Ca+Na) of 0.10, where Ca and Na are the number of calcium and sodium cations, respectively, per formula unit. Minor and trace element contents of albite are discussed separately in Chapter 6.5.3.

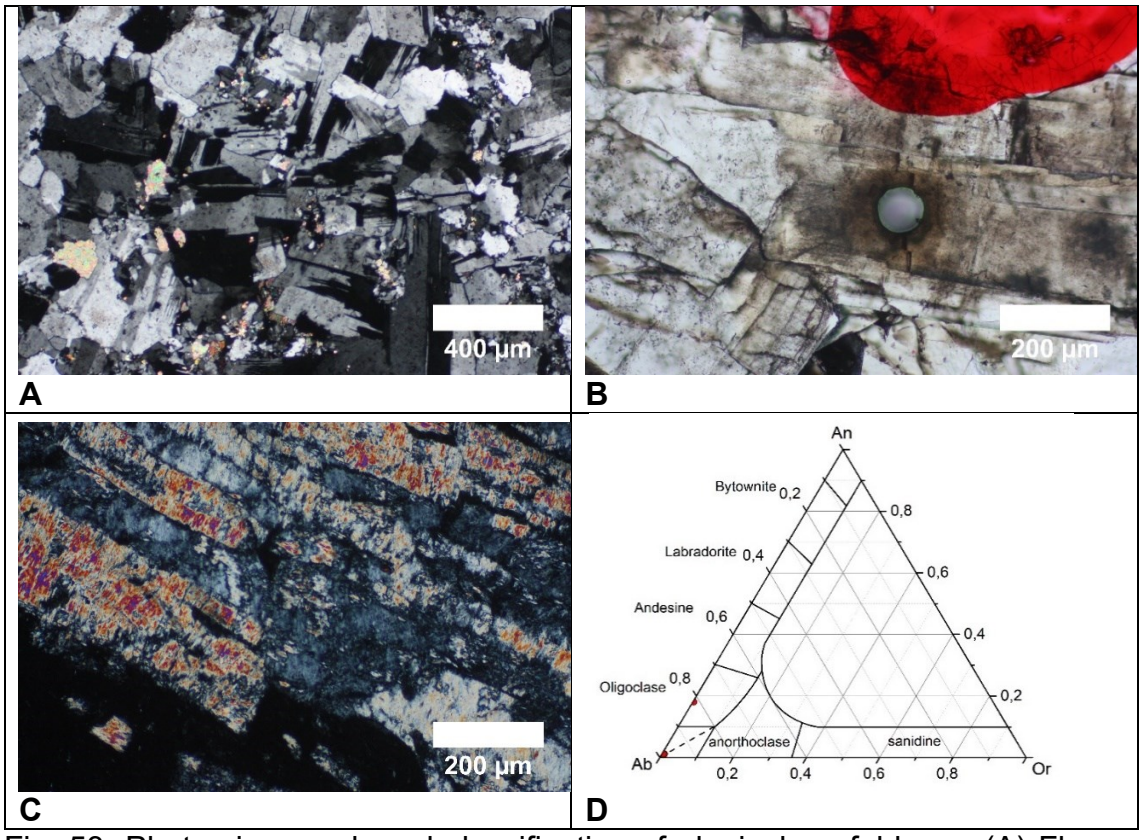

Fig. 53. Photomicrograph and classification of plagioclase feldspar. (A) Flame-shaped twinning in albite. Albitisation is intense near the quartz vein. SBD003. (B) SEM image of albite after analysis by LA-ICP-MS. (C) Sericitization of albite. (D) Chemical composition of plagioclase in the feldspar ternary system.

5.7.8 Carbonate

Carbonate minerals from the Awak Mas and Salu Bullo gold fields were studied using the electron microscope. Different carbonates including siderite, dolomite-ankerite and minor calcite were observed (Fig. 54). Semi-quantitative spot

analyses on carbonate were obtained using SEM-EDX and the results are illustrated in a ternary diagram (Fig. 55).

Ankerite-dolomite is the prominent carbonate alteration mineral in all lithology at Awak Mas and Salu Bullo. Ankerite-dolomite occurs as: (i) primary minerals in dolomite-ankerite schist; (ii) hydrothermal alteration and replacing earlier silicate, mainly quartz and albite (Figs. 54A-B).

Calcite is the second common carbonate mineral. Texturally, calcite occurs as: (i) fibrous (Fig. 54C); (ii) rhombic; (iii) microcrystalline aggregates that replace quartz or albite.

Siderite is present as: (i) primary mineral in phyllite and carbonaceous phyllite (siderite-1); or (ii) alteration from earlier sulphide minerals (siderite-2). Based on the major element compositions obtained using SEM-EDX, siderite-2 is Mg-rich and Ca-poor, whereas siderite-1 has slighly more Ca and lower Mg contents. This different type of siderite (Ca-poor and Ca-rich) are illustrated in Figure 55. In addition, siderite and ankerite usually often co-exist and occur as thin alteration rims surrounding sulphide or sulphosalt (Figs. 54D-E).

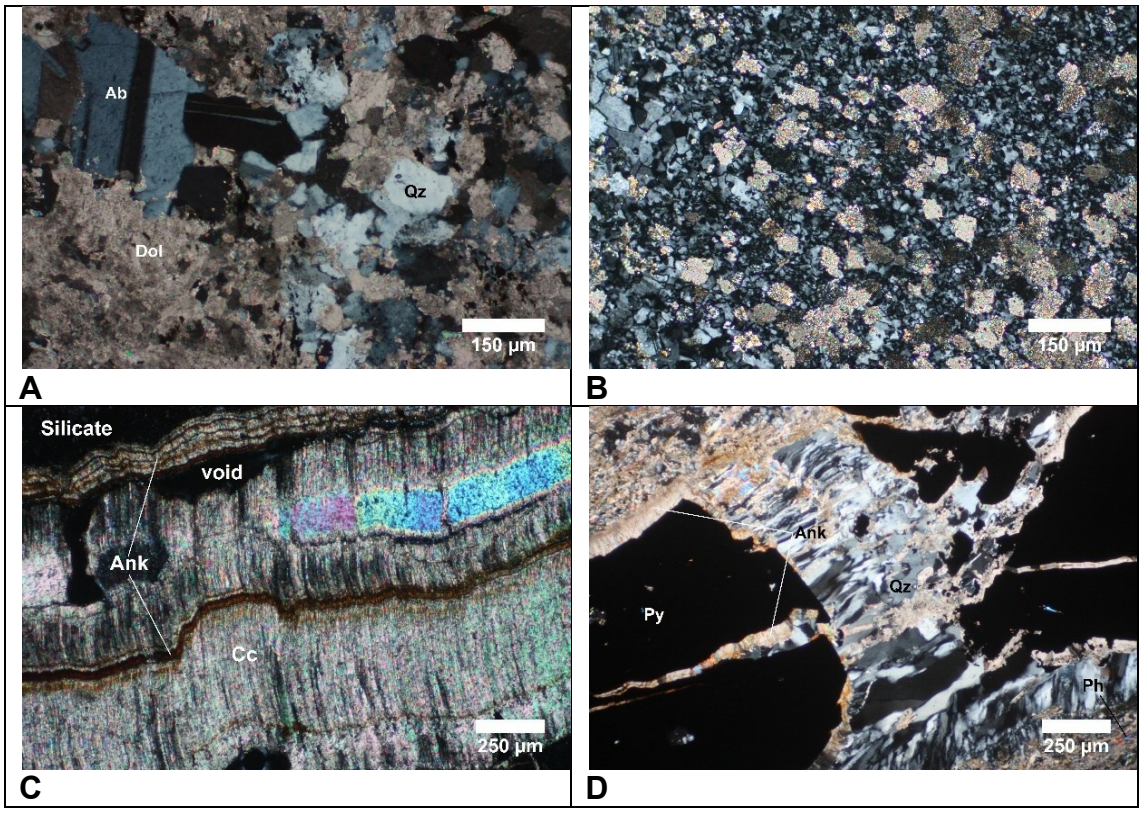

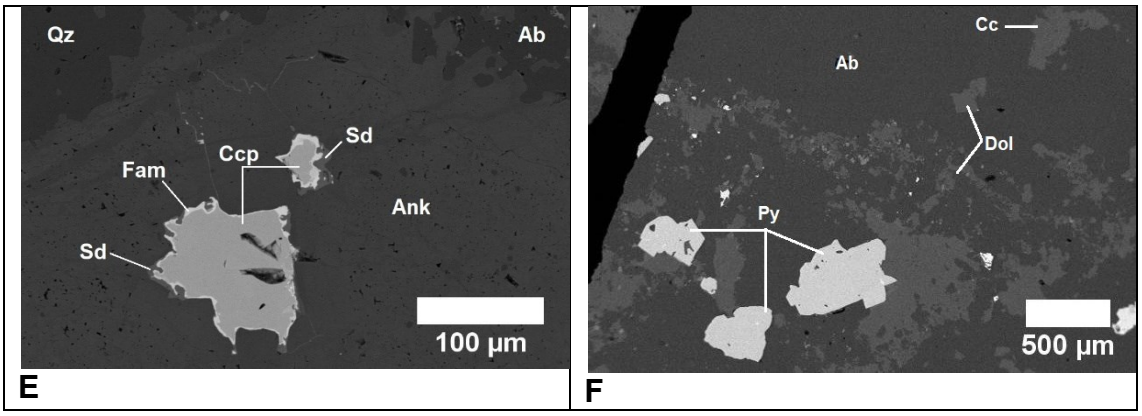

Fig. 54. Photomicrograph and back-scattered images of various carbonate minerals. (A-B) Dolomite alteration. (C) Fibrous calcite as a crack-filling. S66-56. (D) Ankerite surrounding the sulphide minerals. A635-34.70. (E) Siderite in equilibrium with ankerite. S68-143.80. (F) Calcite in equilibrium with dolomite. S69-24.50.

The amount of $MgCO_3$ in calcite in equilibrium with dolomite can be used for estimating metamorphic temperature (Anovitz and Essene 1987). The equation provided an updated correction for the effect of Fe on calcite-dolomite thermometry. In this study, as examples, the coexisting $ankerite_{ss}$ with $siderite_{ss}$ and coexisting calcite in equilibrium with dolomite are observed (Figs. 54E-F). However, the energy dispersive system (EDS systems were not able to detect the amount of trace element contents because the amounts of subsequent elements are below the detection limit of EDS system (i.e. Mg content in calcite). Different technique are required (i.e. WDS of electron microprobe or LA-ICP-MS) to further studied the trace element content in carbonate, in order to unravel the geothermometry based on carbonate minerals.

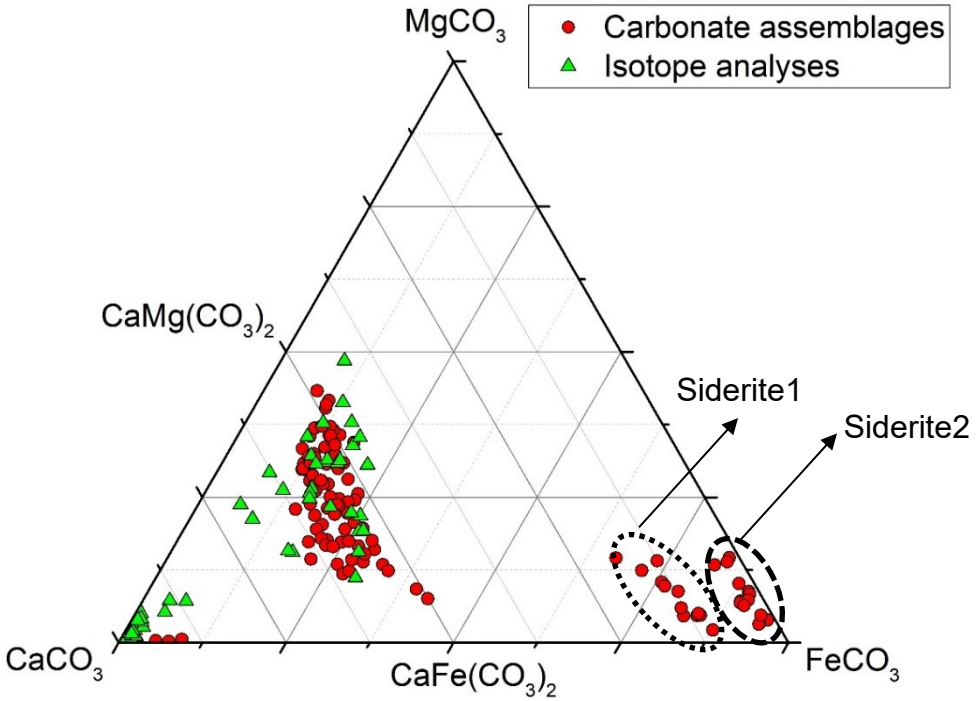

Fig. 55. A ternary diagram of carbonate assemblages at Awak Mas and Salu Bullo. Some samples were separated for isotope analyses.

5.7.9 Accessory and REY-minerals

Variable amounts of accessory minerals were determined in all rocks. These include zircon, apatite, rutile, titanite, crandallite and REY-minerals (monazite, xenotime and baddeleyite). Zircon is abundant within phyllite and schist (Fig. 57A), minor in quartz vein and metasandstone. Some zircon is enclosed in pyrite crystals (A192-86.40)(Fig. 56B). This rock also contains more than ten gold grains ranging from only a few micron up to 50 µm, droplets of galena and monazite (generally less than 10 µm, Fig. 57A), all together trapped as inclusions in pyrite (probably hydrothermal pyrite). In some metasandstone samples (A685-20), zircon occurs as a rounded grain at the border of albite and ankerite (Fig. 56C). No signs of metamict cores and oscillatory zoning were found in zircon.

Fifty small monazite grains were identified in thin sections from Awak Mas and Salu Bullo in the course of this investigation. In total thirty-six grains were measured using the SEM-EDX technique. The grains are generally less than 20 µm in size and euhedral to anhedral in shape (Fig. 56). Monazite commonly observed in carbonaceous phyllite, phyllite and quartz veins, rarely present in metasandstone. In quartz veins, monazite occurs as minute inclusions (lessthan

3 µm in size) in pyrite crystals. Semi-quantitative data of monazite are shown in Table 26.

The monazite-(Ce) has low ThO_2 (0.40 – 3.64 wt% ThO_2) and high Ce_2O_3 (ranging from 26.88 to 42.94 wt% Ce_2O_3), and has an average formula of $Ce_{0.53}La_{0.26}Nd_{0.23}Th_{0.01}P_{0.98}O_4$. The low-contents of ThO_2 are typical of hyrothermal monazite (Krenn et al. 2011), which is not suitable for age dating due to the excess of Pb.

Goyazite ($SrAl_3(PO_4)_2(OH)_5.H_2O$ – crandallite ($CaAl_3(PO_4)_2(OH)_5.H_2O$) are members of the alunite supergroup, known as aluminium phospates and sulphates (APS) (Dill 2001). The REE determined by electron microprobe analysis on APS are mainly represented by La, Nd, Sm and Eu. APS minerals have been observed in several vein and hydrothermal deposits, i.e. sediment-hosted disseminated gold of the Vantage gold deposits, Alligator Ridge- Bald Mountain Mining District, NV, USA (Ilchik 1990).

The APS mineral in the Salu Bullo is goyazite, occuring in breccia veins. The mineral assemblage in this section (S53-103) is albite + rutile + monazite + kaolinite + apatite + titanite. The ore minerals are pyrite + chalcopyrite + tennantite + famatinite + luzonite + galena and gold. The habit of goyazite as shown in Fig. 58E-F is euhedral with hexagonal crystal system.

Three grains of xenotime with 10 µm in width and 20 µm in length, subhedral habit were observed in carbonaceous phyllite (A192-189.40)(Fig. 58G). Baddeleyite with a tabular shape, 50 µm in length was observed in chlorite phengite schist (A687-157.90). The amount of chlorine in apatite is generally less than 0.50 wt%. Apatite has a variable grain size with the biggest grain of 200 µm (Fig. 57H).

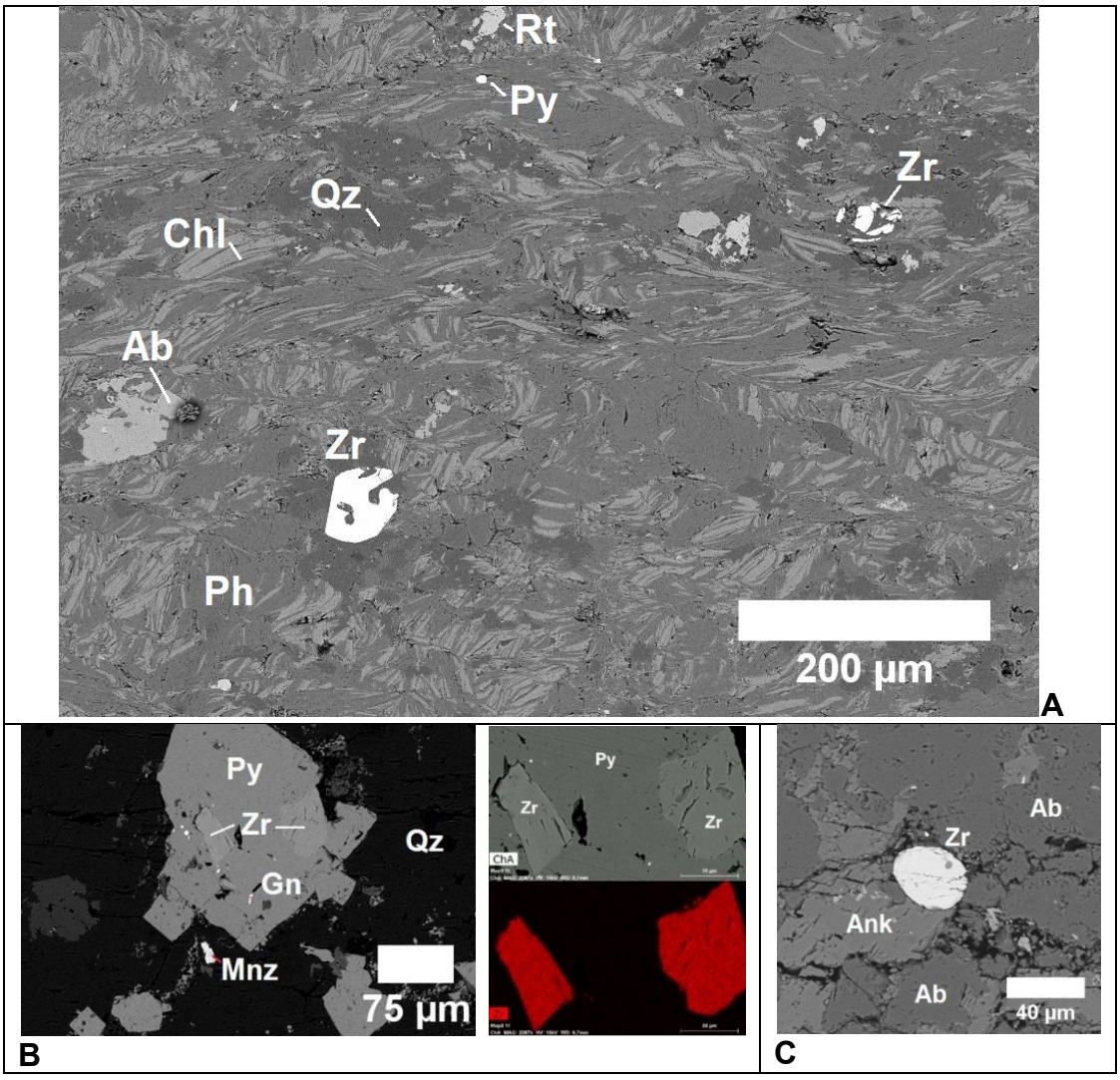

Fig. 56. A BSE images of zircon. (A) Zircon and galena occur as an inclusion in pyrite. Sample A192-86.40. (B) A BSE image of zircon inclusion in pyrite. (C) Rounded zircon at the border of albite and ankerite.

Table 26. Semi-quantitative analyses of monazite from different lithology.

Lithology	Sample	La_2O_3 wt%	Ce_2O_3 wt%	Nd_2O_3 wt%	ThO_2 wt%	P_2O_5 wt%	CaO wt%	La a.p.f.u.	Ce a.p.f.u.	Nd a.p.f.u.	Th a.p.f.u.	P a.p.f.u.
Metasandstone	A685-20 29BRX	24.02	42.94	1.50		31.54		0.34	0.60	0.02	0.00	1.02
Breccia vein	A34-28.3 15	19.53	38.53	14.26	0.41	27.28		0.30	0.58	0.21	0.01	0.95
Breccia vein	S53-103 19	18.07	36.07	15.82		30.03		0.26	0.52	0.22	0.00	1.00
Carbonaceous phyllite	A192-189.40 58	20.47	38.45	14.46		25.77	0.85	0.32	0.59	0.22	0.00	0.92
Carbonaceous phyllite	A192-189.40 57	19.39	37.12	13.30		29.34	0.84	0.29	0.54	0.19	0.00	0.99
Carbonaceous phyllite	A192-189.40 22	19.42	37.66	11.62		30.21	1.10	0.28	0.54	0.16	0.00	1.01
Carbonaceous phyllite	A192-221.65 37	16.70	32.61	22.15	2.38	26.16		0.26	0.50	0.33	0.05	0.93
Carbonaceous phyllite	A192-221.65 22	18.47	36.89	14.33	1.88	28.42		0.27	0.54	0.21	0.03	0.97
Carbonaceous phyllite	A192-225.00 24	18.14	34.48	13.51	1.41	32.46		0.25	0.48	0.18	0.02	1.04
Carbonaceous phyllite	A192-225.00 23	18.68	36.87	13.12	2.69	28.64		0.28	0.54	0.19	0.05	0.98
Carbonaceous phyllite	A192-225.00 21	19.48	38.70	13.07	2.40	26.35		0.30	0.59	0.19	0.05	0.93
Carbonaceous phyllite	A192-225.00 20	18.37	39.09	15.35	1.03	26.16		0.28	0.60	0.23	0.02	0.93
Carbonaceous phyllite	A192-225.00 11	19.30	37.18	12.83	0.46	30.23		0.28	0.53	0.18	0.01	1.00
Carbonaceous phyllite	A192-189.40 92	13.27	32.32	21.82		30.71	1.87	0.19	0.47	0.31	0.00	1.02
Carbonaceous phyllite	A192-189.40 75	14.30	35.49	21.76	0.55	26.30	1.60	0.22	0.55	0.33	0.01	0.94
Phyllite	A192-177.30 37	16.94	35.03	16.93		31.11		0.24	0.50	0.23	0.00	1.02
Phyllite	A192-177.30 26	18.45	35.29	16.07	0.49	29.70		0.27	0.51	0.23	0.01	0.99
Phyllite	A192-177.30 25	18.43	34.17	16.30	0.67	30.43		0.27	0.49	0.23	0.01	1.01
Phyllite	A192-177.30 24	18.73	37.27	17.77		26.22		0.29	0.57	0.26	0.00	0.93
Phyllite	A192-177.30 37	16.94	35.03	16.93		31.11		0.24	0.50	0.23	0.00	1.02
Phyllite	A192-177.30 26	18.45	35.29	16.07	0.49	29.70		0.27	0.51	0.23	0.01	0.99

Lithology	Sample	La_2O_3 wt%	Ce_2O_3 wt%	Nd_2O_3 wt%	ThO_2 wt%	P_2O_5 wt%	CaO wt%	La a.p.f.u.	Ce a.p.f.u.	Nd a.p.f.u.	Th a.p.f.u.	P a.p.f.u.
Phyllite	A192-177.30 25	18.43	34.17	16.30	0.67	30.43		0.27	0.49	0.23	0.01	1.01
Phyllite	A192-177.30 24	18.73	37.27	17.77		26.22		0.29	0.57	0.26	0.00	0.93
Phyllite	A35-24.40 19	12.87	32.77	20.96	1.99	31.41		0.18	0.46	0.29	0.03	1.03
Phyllite	A35-24.40 10	14.09	36.11	20.88		28.92		0.21	0.53	0.30	0.00	0.98
Phyllite	A35-24.40 9	14.22	35.68	16.51	1.99	31.60		0.20	0.50	0.23	0.03	1.03
Phyllite	A34-38.3 15	16.64	36.05	16.79		30.53		0.24	0.51	0.23	0.00	1.01
Phyllite	A34-38.3 9	17.13	36.43	15.85	3.14	27.45		0.26	0.55	0.23	0.06	0.95
Phyllite	A34-38.3 3	16.92	34.21	15.16	3.64	30.07		0.25	0.49	0.21	0.07	1.00
Qz vein	S69-25.80 19	19.82	34.42	13.66		32.10		0.28	0.48	0.19	0.00	1.03
Qz vein	S66-67 10	21.93	26.88	21.05		30.14		0.32	0.39	0.29	0.00	1.00
Qz vein	A149-110.3 23	17.96	31.52	17.48		33.04		0.25	0.43	0.23	0.00	1.05
Qz vein	A35-18.65 7	16.57	39.61	13.23		30.59		0.24	0.56	0.18	0.00	1.01
Qz vein	A35-18.65 7	18.40	41.56	15.71		24.33		0.29	0.66	0.24	0.00	0.89
Qz vein	A35-18.65 1	16.53	39.04	17.44		26.99		0.25	0.59	0.26	0.00	0.94
	max	24.02	42.94	22.15	3.64	33.04	1.84	0.34	0.66	0.33	0.07	1.05
	min	12.87	26.88	1.50	0.40	24.33	0.84	0.18	0.39	0.02	0.00	0.89
	average	17.88	36.05	15.93	1.55	29.18	1.25	0.26	0.53	0.23	0.01	0.98

Formula unit is calculated on the basis of four oxygen atoms.

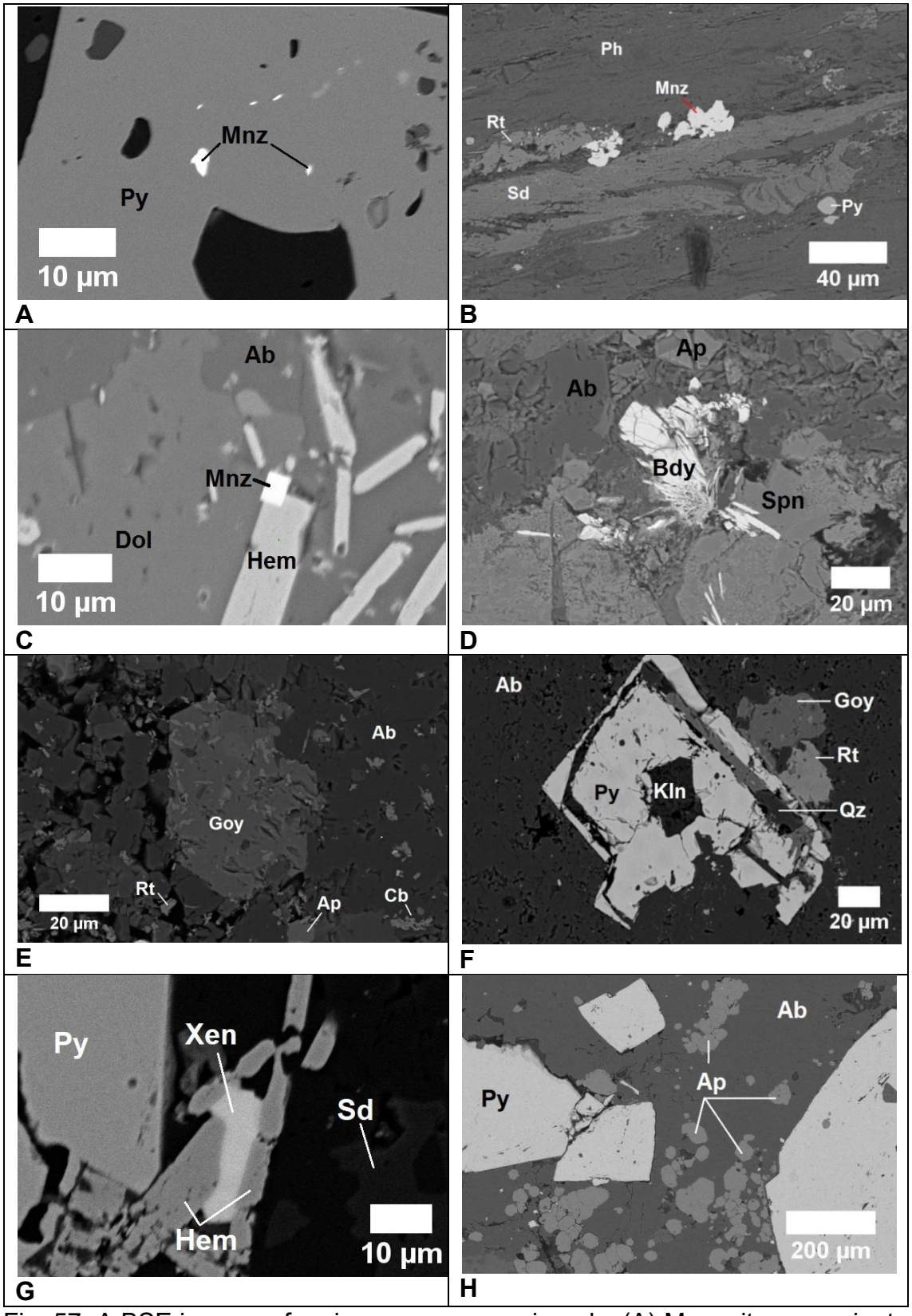

Fig. 57. A BSE images of various accessory minerals. (A) Monazite as a minute inclusion in pyrite. Lithology is quartz-sulphide (sulphosalt) Au vein. S68-143.90. (B) Rutile and monazite in carbonaceous phyllite. A192-189.40. (C) Euhedral monazite grain in carbonaceous phyllite. A192-189.40. (D) Tabular baddeleyite

and anhedral sphene in chlorite-albite schist. A687-157.90 (E-F) Hexagonal goyazite (aluminium-phosphate-sulphate) in breccia quartz vein. S53-103. (G) Elongated xenotime in carbonaceous phyllite. A192-189.40. (H) Anhedral coarse apatite grain in quartz vein. S50-33.90.

5.8 Geochemistry

5.8.1 Major and trace element geochemistry

Major and trace element data of the investigated rocks from the Latimojong metamorphic complex are shown in Table 26. In order to estimate the original mineral phases of the protolith, the major element data of mafic metavolcanic rocks was re-calculated using a CIPW-normative composition (norm4-CIPW excel program, Kurt Hollocher). This excel program includes recalculation of major and trace elements (Sr, Ba, Ni, Cr and Zr) from ppm elements to wt% oxides, and results are plotted in Total Alkali Silica diagrams of Le Maitre (2002). Being aware of the fact that most rocks in the studied area had experienced metamorphism event, the element mobility may change the concentrations of mobile elements and calculation of CIPW-normative composition may differ from the magmatic modal composition (Melcher and Meisel 2004).

According to the major and selected trace element content, the epidote actinolite metabasite (greenschist)(S68-34.90) corresponds to a basalt with normative plagioclase (56.2 vol%), hypersthene (27.1 vol%), diopside (6.9 vol%), hematite (6.3 vol%), olivine (1.2 vol%), orthoclase (0.5 vol%). Other mafic metavolcanic rocks plot in the field of basalt (S68-34.90, S50-83.95) and basaltic andesite (S68-94.40, S50-53.40).

Variation diagrams of MgO against selected major and trace elements have been constructed in order to compare different degrees of hydration between mafic metavolcanic and metasedimentary rocks. Metasedimentary rocks were included as a comparison. Major elements oxides were recalculated on a volatile-free basis (Fig. 58).

Metabasites in three samples have 46.12 – 52.77 wt% SiO_2, 0.03 - 1.1 wt% Na_2O and average 13.05 wt% MgO (10.24 – 15.4 wt%). Metabasites have a variable CaO (0.65 -10.78 wt%) and K_2O (0.1 to 2.74 wt%) contents. The variations in Al_2O_3 (17.1 – 19.5 wt%), Fe_2O_{3T} (10.7 – 10.9 wt%), V (322 – 362 ppm) are small. Chromium and nickel concentrations are high in metabasites, ranging from 598

to 1159 ppm; 180 to 270 ppm, respectively. Metabasites have high *Mg*-numbers (> 48, ranging from 48 – 59), low Rb (1.73 – 26.3 ppm) and Sr (24.33 - 153 ppm). Meta-andesites have higher SiO_2 (57 - 59.31 wt%) and lower MgO (3.9 – 4.5 wt%) contents than metabasites. Concentrations of TiO_2 (0.54 – 0.63), Al_2O_3 (14.5 – 16.6), Fe_2O_{3T} (7.1 – 7.2), MnO (0.14 – 0.17 wt%) and *Mg*-number (35.5 - 38) are similar. In contrast, meta-andesites display a large variation in K_2O (0.02 – 0.21 wt%) and Na_2O (1.73 – 6.73 wt%). Meta-andesites are characterized by low Cr (63 – 74 ppm), Ni (25 – 36 ppm), Rb (1.1 – 6.3 ppm), *mg*-number (<38) and high Sr (95 – 283 ppm).

Metasedimentary rocks (phyllite and carbonaceous phyllite) differs from metavolcanic rocks (metabasites and meta-andesites) in having high SiO_2, Ba, Sr, Zr and low MgO, CaO, *Mg*-number. The carbonaceous phyllites are characterized by high SiO_2 (63.42 – 65.57 wt%), CaO (2.69 – 3.47 wt%), Na_2O (7.5 – 8.29 wt%) and low Fe_2O_{3T} (< 6.3 wt%), Al_2O_3 (13.25 – 15.55 wt%), Sr (~280 ppm), Rb (1.9 – 4.3 ppm). Phyllite shows large variation of SiO_2 (59.5 – 66.4), but similar TiO_2 (0.8 – 1 wt%), K_2O (~3 wt%), MgO (1.8 – 1.9 wt%). This rocks has the highest Rb (108 - 116.3 ppm), Ba (323 - 379 ppm) and Zr (160.2 – 281.55 ppm) concentration among all samples. The phyllites and carbonaceous phyllites have higher As and lower Cr contents than metavolcanic rocks. *Mg*-number of carbonaceous phyllites and phyllites are lower than 25.

Altered metasiltstone has high Al_2O_3 (20.68 wt%), Fe_2O_{3T} (11.32 wt%) and K_2O (4.93 wt%). This sample is located near the mineralized veins (less than 2 meter) and the mineralogy mainly consists of quartz, hematite, sericite and calcite.

All metavolcanic and metasedimentary rock samples have relatively high LOI (ranging between 5.51 and 11.75) that can be explained by the intense hydrothermal alteration in most rocks.The data were plotted in the CaO/Al_2O_3 – MgO - SiO_2 diagram (Schweitzer and Kröner 1985; Bouyo et al. 2015) to indicate the alteration effects in metavolcanic rocks (Fig. 60A). Majority of the samples plots in the field of altered rock, except S50-53.40 and S68-98.40, which has the lowest MgO (3.90 wt%), Fe_2O_3T (7.09 wt%) and the highest CaO (10.42 wt%) contents (Table 24). Most metasedimentary rocks are plot in the field of “not altered” rocks, except S68-105.40 (metasiltstone).

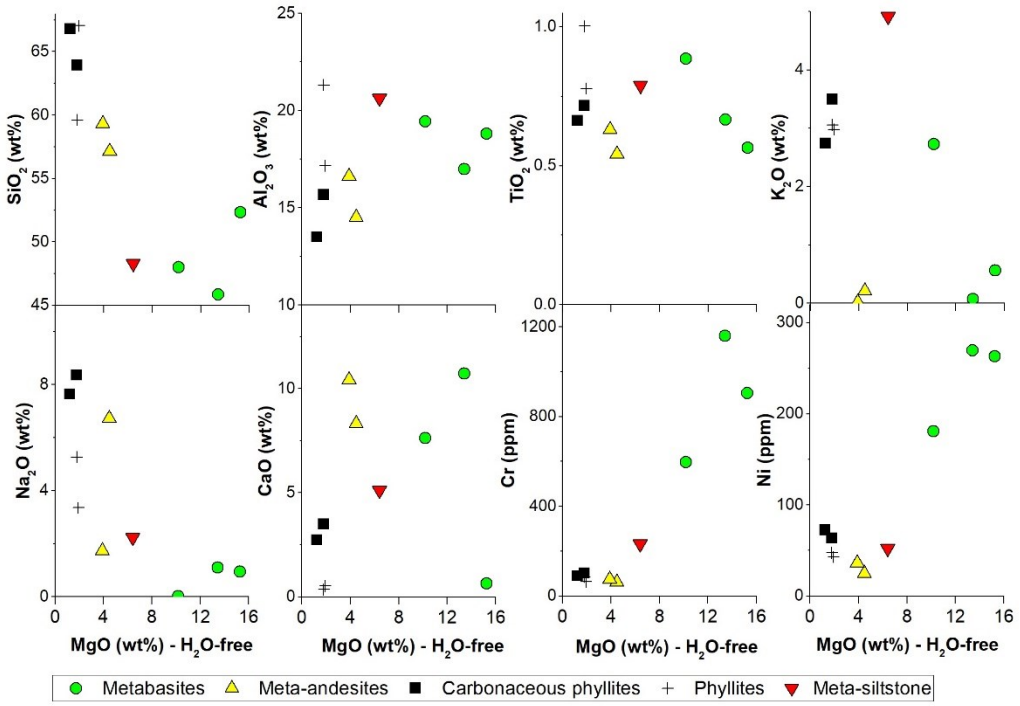

Fig. 58. Variation diagrams of MgO vs SiO_2 wt%, Al_2O_3 wt%, TiO_2 wt%, K_2O wt%, Na_2O wt%, CaO wt%, ppm Cr and ppm Ni for metavolcanic and metasedimentary rocks of Latimojong.

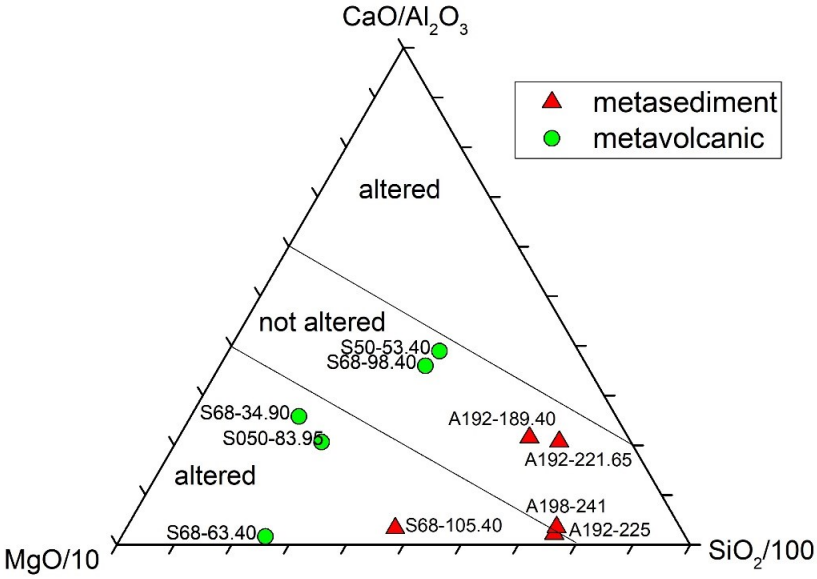

Fig. 59. CaO/Al_2O_3-MgO-SiO_2 diagram showing most metavolcanic samples of the Latimojong Metamorphic Complex were hydrothermally altered.

5.8.2 Trace and rare earth element concentrations

Trace elements and rare earth elements + yttrium (REY) were normalized using primitive mantle (Sun and McDonough 1989) and Cl-chondrite (McDonough and Sun 1995), respectively. Literature data of continental crust (Rudnick and

Fountain 1995), E-MORB and N-MORB (Sun and McDonough 1989), Lamasi Complex and Neogene Volcaniclastic rocks of Sulawesi (Kadarusman et al. 2004), and blueschists-eclogites of Bantimala, South Sulawesi (Maulana et al. 2013) are shown for comparison. Trace-element and extended rare earth patterns are plotted in Figures 60. Only samples obtained using the combination of XRF and ICP-MS methods were plotted.The summaries of rare earth element data are shown in Table 27.

All metavolcanic and metasedimentay rocks of the studied sample suite have a general enrichment of mobile elements on the left-hand side of the diagram (Fig. 60), most probably due to alteration and/or metamorphism. Metabasites from Salu Bullo are characterized by positive anomalies of Cs, Rb, Ba, K, Pb and very low concentrations of Sr, Zr, Hf, Ti (Fig. 60). Sample S68-34.90 (greenschist) shows strong depletion in Nb, Ta (Fig. 60). Sample S68-34.90 has extremely high Nb/Ta ratio (up to 52). Most samples have Nb/Ta ratio of less than 10 (Table 27). The meta-andesites show a strong enrichment of Cs and slight depletion of K. The multi-element diagram of meta-andesites is relatively similar to a metabasites of Latimojong and parallel to N-MORB (Sun and McDonough 1989).

Carbonaceous phyllites and phyllites show different LILE patterns. Carbonaceous phyllites are characterised by strong anomalies of Cs, Rb, Ba, K, low concentrations of Sr. In contrast, LILE components of phyllites are low. All metasedimentary samples display strong enrichment of Pb and depletion of Sr and P. HFSE and REE patterns of carbonaceous, phyllites and metasiltstone are relatively parallel and comparable to continental crust (Rudnick and Fountain 1995).

Table 27. Representative whole-rock and trace element analyses of samples

Sample code	**S68-34.90**	**S68-98.40**	**S50-53.40**	**A192-189.40**	**A192-221.65**	**A192-225.00**	**A192-245.00**	**S68-63.40***	**S050-83.95***	**S68-105.40***
Lithology	**Metabasite**	**Meta-andesite**	**Meta-andesite**	**Phyllite**	**Phyllite**	**Carbonaceous phyllite**	**Carbonaceous phyllite**	**Metabasite**	**Metabasite**	**Meta-siltstone**
in wt %										
SiO_2	46.12	57	59.31	63.42	65.57	59.48	66.41	52.77	48.22	48.41
TiO_2	0.67	0.54	0.63	0.71	0.65	1	0.77	0.57	0.89	0.79
Al_2O_3	17.09	14.48	16.62	15.55	13.25	21.27	17.01	18.98	19.54	20.68
Fe_2O_3T	10.81	7.22	7.09	5.18	6.31	6.89	5.54	10.69	10.88	11.32
MnO	0.2	0.14	0.17	0.25	0.06	0.08	0.11	0.15	0.19	0.23
MgO	13.51	4.48	3.9	1.79	1.22	1.79	1.91	15.4	10.24	6.43
CaO	10.78	8.3	10.42	3.47	2.69	0.36	0.53	0.65	7.66	5.14
Na_2O	1.1	6.7	1.73	8.29	7.5	5.26	3.33	0.96	0.03	2.23
K_2O	0.07	0.21	0.02	0.16	0.09	3.05	2.95	0.57	2.74	4.93
P_2O_5	0.05	0.12	0.1	0.11	0.08	0.13	0.13	0.06	0.08	0.06
SO_3	0.16	0.56	0	0.29	0.75	0.45	0.35	0.02	0.01	0.01
LOI	6.04	11.75	5.51	6.65	6.09	6.76	5.43	9.6	10.34	10.6
∑	100.77	99.87	100.09	99.41	98.48	100.01	99.24	101.02	100.66	100.37
in ppm										
Li	37.67	35.59	22.76	8.61	2	28.66	48.45	-	-	-
Be	0.32	1.23	0.63	1.23	0.93	4.09	2.61	-	-	-
B	23.79	24.44	24.81	9.4	b.d.l.	114.82	91.13	-	-	-
Sc	35.56	22.44	27.83	21.46	13.46	21.26	18.95	20.1	41.55	37.95
V	361.95	254.2	191.9	270.15	37.2	386.15	159.1	322.35	343.95	373.6
Cr	1159.1	62.85	74.2	101.8	90	84.55	63.65	905.05	597.25	232.8
Co	40.78	115.63	194.71	560.42	2203.59	458.63	513.96	59.3	77.75	82.05
Ni	269.71	24.94	36.23	63.47	72.23	47.63	42.84	262.95	180.8	52.15

Sample code	S68-34.90	S68-98.40	S50-53.40	A192-189.40	A192-221.65	A192-225.00	A192-245.00	S68-63.40*	S050-83.95*	S68-105.40*
Lithology	Metabasite	Meta-andesite	Meta-andesite	Phyllite	Phyllite	Carbonaceous phyllite	Carbonaceous phyllite	Metabasite	Metabasite	Meta-siltstone
Cu	85.6	73.8	110.95	180.85	b.d.l.	80.35	55.55	61.35	91.2	96.85
Zn	56.78	51.98	61.52	51.74	35.72	134.31	64.96	79.4	90.9	107.1
Ga	12.02	10.42	16.54	12.78	14.86	29.18	19.64	16	10.7	15.1
As	9.1	8.97	8.62	67.62	18.8	12.86	16.49	-	-	-
Rb	1.73	6.31	1.09	4.27	1.86	116.32	108.01	26.25	7.6	108.7
Sr	24.33	283.37	95.63	281.84	288.87	179.74	79.31	31.4	152.9	246.5
Y	14.11	23.24	24.68	25.2	14.18	32.72	28.92	7.6*	17.75*	22.4
Zr	32.15	73.45	52.95	93.55	87	218.55	160.2	25.3	43.9	38.85
Nb	0.56	0.79	1.14	3.19	11.9	7.05	5.99	6.6*	5*	3.55
Cd	0.11	0.2	0.54	2.93	0.77	0.21	0.32	-	-	-
Sn	1.75	b.d.l.	1	b.d.l.	3.9	5.18	1.78	-	-	-
Sb	8.62	4.33	2.45	19.41	8.96	8.14	5.36	-	-	-
Cs	4.27	1.61	28.21	1.83	0.42	7.48	6.67	-	-	-
Ba	21.01	22.92	17.9	26.5	19.56	379.29	322.99	159.5	37.25	71
La	1.39	2.96	4.24	15.42	17.07	34.57	30.24	5.85	7.35	7.45
Ce	4.06	6.67	9.18	28.51	35.12	71.68	58.49	10.7	b.d.l.	23.9
Pr	0.54	1.1	1.38	3.56	3.61	7.97	6.5	-	-	-
Nd	2.94	5.85	6.93	14.86	13.53	30.19	25.13	-	-	-
Sm	1.12	2.18	2.34	3.52	2.53	6.11	5.16	-	-	-
Eu	0.36	0.62	0.89	0.95	0.56	1.28	1.2	-	-	-
Gd	1.63	2.95	3.17	3.78	2.19	5.47	4.77	-	-	-
Tb	0.34	0.56	0.6	0.68	0.38	0.91	0.79	-	-	-
Dy	2.3	3.73	3.92	4.36	2.5	5.55	4.82	-	-	-
Ho	0.51	0.82	0.86	0.92	0.53	1.14	0.97	-	-	-
Er	1.56	2.44	2.58	2.7	1.64	3.26	2.79	-	-	-

Sample code	S68-34.90	S68-98.40	S50-53.40	A192-189.40	A192-221.65	A192-225.00	A192-245.00	S68-63.40*	S050-83.95*	S68-105.40*
Lithology	Metabasite	Meta-andesite	Meta-andesite	Phyllite	Phyllite	Carbonaceous phyllite	Carbonaceous phyllite	Metabasite	Metabasite	Meta-siltstone
Tm	0.24	0.38	0.39	0.41	0.26	0.49	0.41	-	-	-
Yb	1.62	2.53	2.63	2.68	1.71	3.14	2.62	-	-	-
Lu	0.26	0.4	0.42	0.4	0.25	0.45	0.39	-	-	-
Hf	0.63	1.5	1.71	2.23	2.2	3.37	2.93	-	-	-
Ta	0.01	0.11	0.25	0.78	4.24	1.05	1.12	-	-	-
Au	b.d.l.	b.d.l.	b.d.l.	b.d.l.	0.21	b.d.l.	b.d.l.	-	-	-
Tl	0.01	0.03	0.01	0.05	0.03	0.48	0.45	-	-	-
Pb	1.05	17.73	2.31	30.99	50.49	7.14	11.79	8.6	6.4	17.85
LREE	12.05	22.33	28.14	70.6	74.61	157.28	131.48	-	-	-
HREE	6.82	10.86	11.41	12.13	7.27	14.93	12.78	-	-	-
REE+Y	32.98	56.43	64.23	107.94	96.06	204.92	173.18	-	-	-
LREE/HREE	1.77	2.05	2.47	5.82	10.26	10.54	10.29	-	-	-
Zr/Hf	50.9	48.96	31.05	41.94	39.6	64.88	54.69	-	-	-
Nb/Ta	51.66	7.23	4.57	4.09	2.8	6.7	5.36	-	-	-
Ce/Ce*	1.13	0.89	0.92	0.93	1.08	1.04	1.01	-	-	-
Eu/Eu*	0.81	0.75	1.00	0.79	0.73	0.67	0.74	-	-	-
$(La/Yb)_N$	0.58	0.79	1.10	3.91	6.78	7.48	7.84	-	-	-
$(La/Gd)_N$	0.72	0.84	1.12	3.43	6.54	5.31	5.32	-	-	-
Mg-number	55.55	38.29	35.49	25.68	16.20	20.62	25.64	59.03	48.48	36.23

Abbreviations: b.d.l. (below detection limits); Ce/Ce*= $Ce_N/\sqrt{[(La_N).(Pr_N)}$ Eu/Eu*=$Eu_N/\sqrt{[(Sm_N).(Gd_N)}$ according to Taylor and McLennan (1985); Eu_N, Sm_N, Gd_N = chondrite normalized McDonough and Sun (1995); $(La/Yb)_N$ $(La/Gd)_N$ are normalized concentration ratios in the selected samples. *Mg*-number = [100xMgO/(MgO+$Fe_2O_3^{tot}$)]. Sample with asterisk code (*) were measured using XRF method, other samples were measured using the combination of ICP-MS and XRF methods. (-) = not analysed

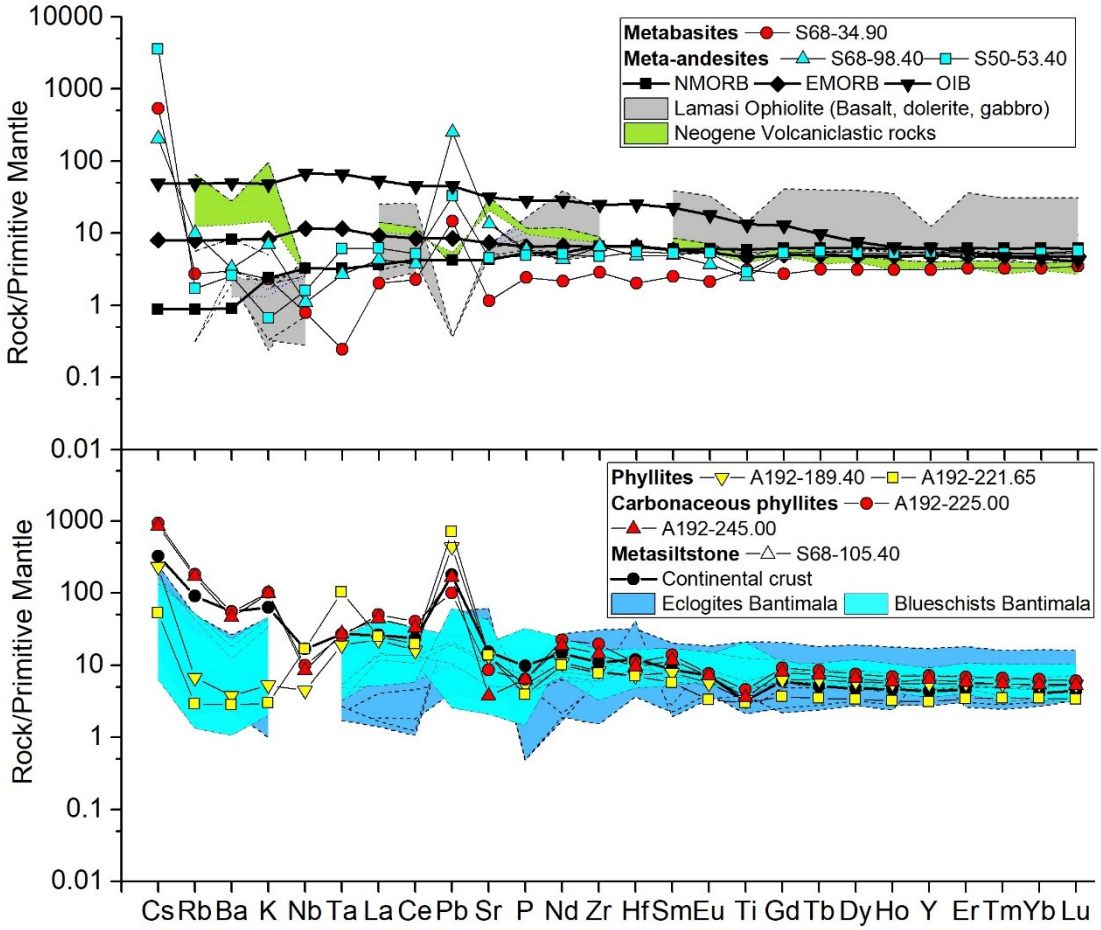

Fig. 60. Geochemical patterns for metavolcanic (A) and metasedimentary (B) rocks within the research area. Primitive mantle normalizing values are from Sun and McDonough (1989). Reference whole rock multielement diagrams. (1) Neogene Volcaniclastic and East Sulawesi Ophiolite (Kadarusman et al. (2004); (2) E-MORB and N-MORB (Sun and McDonough 1989); (3) blueschists and eclogites of Bantimala (Maulana et al. 2013); (4) continental crust (Rudnick and Fountain 1995).

Metabasites and meta-andesites have low REE concentrations (REE+Y ranging from 33 – 64 ppm), low LREE/HREE ratio (1.77 – 2.47) and display flat chondrite-normalized patterns. Metasedimentary rocks from the Latimojong show REE+Y concentrations > 98 ppm and negative Eu anomaly (Eu/Eu* < 0.80). Ce/Ce* of metavolcanic and metasedimentary rocks are close to 1 (Ce/Ce*=0.89-1.13). The metasedimentary rocks of the Latimojong have high LREE/HREE ratios (5.82 – 10.29) and are enriched in LREE (Fig. 61). The $(La/Yb)_N$ of metavolcanic rocks (0.58 - 1.10) is smaller than in metasedimentary rocks (3.91 - 7.84). Most samples have negative Eu anomalies ($Eu/Eu^*=Eu^N/\sqrt{[(Sm^N).(Gd^N)]}$, ranging from 0.67 to

1. Figure 61 displays the Cl-chondrite normalized pattern for metavolcanic and metasedimentary rocks from Latimojong.

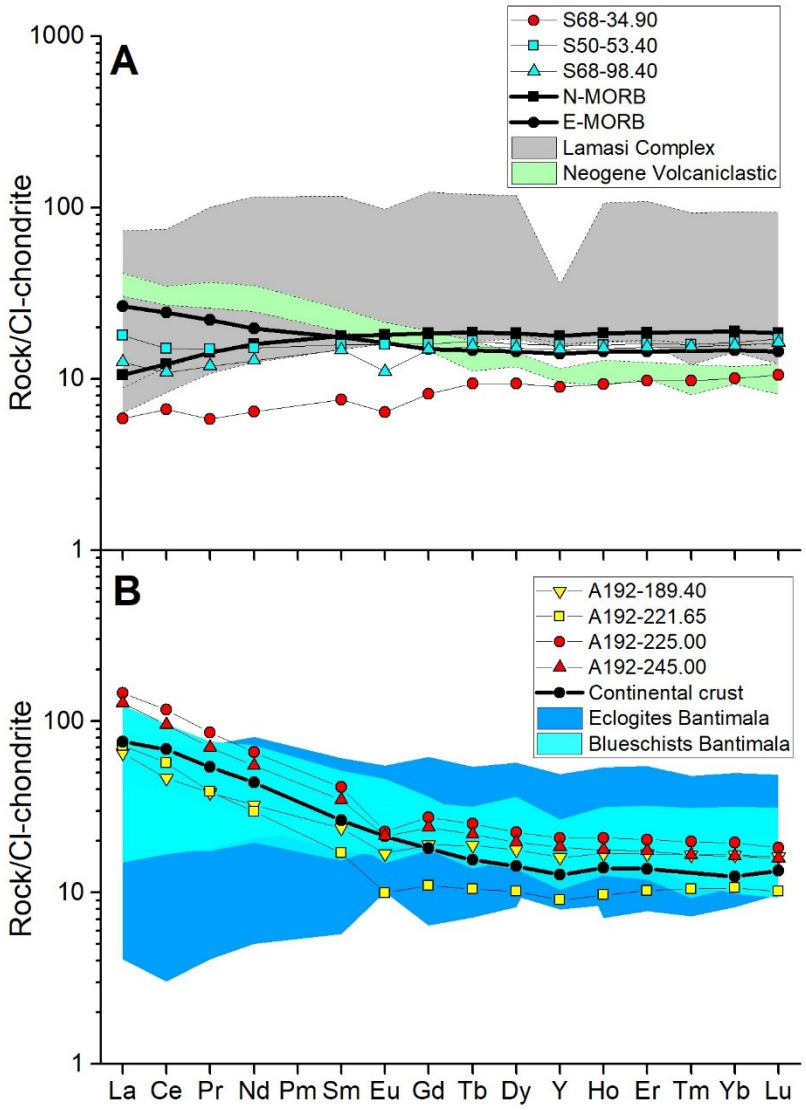

Fig. 61. Rare earth + Y patterns for metavolcanic (A) and metasedimentary (B) rocks within the research area. Cl-Chondrite normalizing values are from McDonough and Sun (1995). Reference whole rock multielement diagrams. (1) Neogene Volcaniclastic and East Sulawesi Ophiolite (Kadarusman et al. (2004); (2) E-MORB and N-MORB (Sun and McDonough 1989); (3) blueschists and eclogites of Bantimala (Maulana et al. 2013); (4) continental crust (Rudnick and Fountain 1995).

6. ORE MINERALOGY AND HYDROTHERMAL ALTERATION

6.1 Introduction

Gold in Awak Mas and Salu Bullo is related with sulphide and sulphosalt minerals, only minor trace gold is observed in quartz in weathering or oxidation zones. This study presents data on ore mineralogy and mineral chemistry of the different mineral assemblages, including gold and its association with sulphide and sulphosalt. Albite is the main alteration mineral in the studied area and the trace element content has been studied using in situ laser ablation-inductively coupled plasma spectrometer (LA-ICP-MS). A combination of geochemical data from the mining company and analyses on plagioclase feldspar in this study are used to compare the effect of plagioclase composition during alteration process.

Previous mineralogical studies in the Awak Mas and Salu Bullo were only based on optical petrography, ore microscopy and XRD analysis. No mineral chemistry of rock-forming and ore-minerals has been reported from this area. The aims of the study are as follows:

1. To provide a detailed overview of the different gold generation found within the Awak Mas and Salu Bulo districts, on their transport and precipitation mechanisms.
2. To obtain the mineral chemistry of gold, sulphides and sulphosalts to understand the metallogenic evolution of the Awak Mas and Salu Bullo gold deposits.
3. To obtain pyrite and sphalerite trace element data in order to understanding the origin of the different pyrite and sphalerite textures.
4. To correlate the exploration data with in situ laser ablation-inductively coupled plasma spectrometer (LA-ICP-MS) on plagioclase feldspar. These data will be used to correlate the effect of REY distributions during hydrothermal alteration.

This chapter will focus on ore mineralogy, mineral chemistry, trace element contents of sulphide and some oxide, hydrothermal alteration and its interpretation.

6.2 Previous mineralogical study

White (1999)(mineralogical consultant, unpublished report) investigated twenty one samples from the Awak Mas drill cores using optical petrography, ore microscopy and XRD analysis. The protoliths of the observed samples are mudstone, siltstone, basalt, diorite, possibly limestone and hyaloclastite. Many are strongly sheared and mylonitised. Rocks are strongly altered and have a widespread propylitic alteration style, which is locally overprinted by phyllic and argillic minerals.

Secondary plagioclase (oligoclase) and carbonate (including calcite, ankerite and siderite) are the most common secondary minerals. Brecciation affects most of the samples and is predominantly related to tectonic processes. Hydrothermal brecciation was distinguished in some samples. Ore minerals are gold, chalcocite, chalcopyrite, pyrrhotite and pyrite. Those authors concluded that the style of alteration, mixed lithologies and intense shearing are indications of a mesothermal system associated with major shear structures. The summary of mineralogical observations is given in Table 28.

Table 28. Summary of lithology, alteration and mineralogy of Awak Mas samples (summarized from White 1999)

Sample Code	Lithology	Alteration and Veining
SBD0001-31.56	Mudstone (Qz)	Intense: Fsp (Pl,Ksp),Ilt,Chl,Cb,Amp,Qz,Opq Vein: Cb,Chl,Qz,Opq
SBD0001-83.25	Mudstone (Qz)	Intense:Ilt*,Chl,Cb,Opz,Ksp,Qz,Ep Vein:Cb,Chl,Qz,Ilt*
SBD0001-97.95	Siltstone (Qz,Plg,Ap)	Intense:Ilt*,Kln*,Cb,Chl,Ep,Qz,Opq Vein:Qz,Cb
SBD0001-59.53	Epidote skarn/ altered diorite?	Intense:Ep,Cb,Plag,Ksp,Qz,Chl,Opz,Ttn Vein:Cb, Qz, Ep
SBD0002-57.25	Protomylonite	Intense:Cc,Qz,Chl,Cb,Pl,Ilt,Opq Vein:Cb,Qz,Ep
SBD0003-98.10	Siltstone (Qz,Plg)	Intense:Cb,Kln*,Illt*,Chl,Op, Qz,Ep Vein:Cb,Chl,Opq
SBD0004-70.85	Epidote skarn	Intense:Ep,Qz,Cb,(Cc,Ank),Op,Qz,Pl,Opq Vein:Qz,Cb,Pl,Chll
SBD0001-67.35	Diorite (Plag)	Strong:Amph,Chl,Qz,Ep,Tt,Opq Vein:QZ,Cb,Plag,Chl
SBD0002-20.75	Mylonite (Ap)	Intense:Cb,Chl,Qz,Opq,Ttn,Chal,Sm?
SBD0002-49.56	Pillow Basalt	Intense:Ep,Cl,Pl,Ksp,I*,Cb,Chl,Opq,Qz Vein:Qz,Cb,Ep,Chl
SBD0002-86.87	Basalt(Plag,Aug)	Intense:Chl,Cb,Ksp,Qz,Ep,Opq Vein:Qz,Ep,Cb,Chl,Opq
SBD0008-57.26	Mudstone?	Intense:Pl,Qz,Cb,Kln*,Py,Tt,Hem Vein:Qz,Cb,Pl,Ksp,Py,Po
SBD0011-46.50	Mudstone	Intense: Ank,Pl,Py Vein:Pl,Qz,Ank,Py,Ccp,(Au)
SBD0005-56.71	Basalt/Limestone?	Intense:Cb,Prh,Ep,Pl,Chl,Hem,Lim

Sample Code	Lithology	Alteration and Veining
		Vein:Cb
SBD0004-87.40	Mylonite	Intense:Cb,Dck,Pl,Qz,Ilt,Py,Hem,Lim,Ccp
		Vein:Cb,Pl
SBD0006-70.70	Mylonite	Intense:Ilt*,Cb,Qz,Chl,Py,Ccp,Lim,Cct
SBD0008-60.49	Mudstone	Intense:Pl,Cb,Qz,Py,Hem,(Au)
		Vein:Cb,Qz,Pl,Chl,Py,(Au)
SBD0006-83.88	Mylonite	Intense:Qz,Cb,Chl,Ilt,Py,Pl,Lim,Ttn,Ccp
SBD0006-60.10	Mudstone	Intense:Pl,Cb,Chl,Py,Lim
		Vein:Pl,Cb
SBD0006-67.25	Mudstone	Intense:Pl,Cb,Qz,Py,Hem,Lim
		Vein:Cb,Kln*,Qz,Pl,Py,Hem,Ccp
SBD0019-51.00	Mudstone?	Intense:Cb,Pl,Py,Hem,(Au)
		Vein:Qz,Cb,Py,Kln*,Plg

Abbreviations according to Whitney and Evans (2010). Amph: amphibole. Ank: ankerite. Ap: apatite. Au: gold. Aug: augite. Cb: unidentified carbonate. Cc: calcite. Chal: chalcedony. Cct: chalcocite. Chl: chlorite. Ccp: chalcopyrite. Dck: dickite. Ep: epidote. Hem: hematite. Ilt: illite. Kln: kaolinite. Ksp: potassium feldspar. Lim: limonite. Opq: unidentified opaque phase. Pl: plagioclase. Prh: prehnite. Py: pyrite. Pyrr: pyrrhotite. Q: quartz. Ser: sericite. Sid: siderite. Sm: smectite. Ttn: titanite. *: clay phase unconfirmed by XRD.(…): phase present only as inclusions.

Purvis and Pontifex (2013)(mineralogical consultant, unpublished report) described the host rocks of nine drill core and outcrop samples from Salu Bullo: (i) extremely fine-grained rocks and laminated sediments, possibly mudstone, chert or carbonate, and (ii) albite-chlorite altered basalt or andesite. Secondary oxides are mainly fine-grained Fe-oxide such as hematite and limonite, whereas ore minerals consist of pyrite with minor chalcocite, covellite, digenite, sphalerite and gold. In more porous rock, malachite and azurite were observed locally. The mineralogical summary is listed on Table 29.

Table 29. Summary of lithology and mineralogy of Salu Bullo samples (summarized from Purvis and Pontifex 2013)

Sample Code	Depth (m)	Lithology	Mineralogy
SBD036	32	Mudstone/ shale and or microcrystalline carbonate dark coloured by apparent earthy hematite	Ab+Qz+Cb+Py+Hm+Lim+ Kln+Cl+Cb
SBD039	122.5	Laminated cherty and/or silicified mudstone	Qz+Cb+Ab+Py
SBD045	32.8	Quartz veins in an earthy-hematite-flooded sediment	Qz+Hm+Cb+Ab+Py+Au (Cct/Cv)
SBD50	44.5	Net-veined and brecciated hematite/ limonite-flooded dark extremely fine laminated sediment (?mudstone or carbonate)	Qz+Ab+Fe Dol+Py+Ccp+Sp
SBD056	121.5	Veined and brecciated albitised felsic volcanic (?original trachyte)	Qz+Ab+Cb+Fe Dol+Py+Au

Sample Code	Depth (m)	Lithology	Mineralogy
SBD066	71.1	Basalt or andesite, with heterogenous textures, altered to albite-chlorite leucoxene	Ab+Chl+Cb+Lcx
SBD066	79.4	Phyllocsilicate-carbonate- albite schist, with a vein of carbonate and minor quartz. Tentatively identified as a metamorphosed and altered andesite	Ser+Tlc(?)+Ab+Qz+Cb
SBD068	132.3	Blocks dominated by aggregates of albite and carbonate within microcrystalline material rich in albite, quartz, carbonate and hematite	Qz+Ab+Fe Dol+Opq
Kombong		Heterogenous massive crystalline aggregate with local volcanic textures within albite+carbonate +limonite	Ab+Fe Dol+Spn+Lim+ Cc+Dig+Cv+Mlc

Abbreviations according to Whitney and Evans (2010). Ab:albite. Au: gold. Cb: unidentified carbonate. Cct: chalcocite. Chl: chlorite. Ccp: chalcopyrite. Cv: covellite. Fe Dol: iron-rich dolomite. Hem: hematite. Kln: kaolinite. Lcx:leucoxene. Lim: limonite. Mlc:malachite. Opq: unidentified opaque phase. Pl: plagioclase. Prh: prehnite. Py: pyrite. Qz: quartz. Ser: sericite. Spn: sphene (titanite).

6.3 Mineral chemistry

6.3.1 Native gold and electrum

Based on ore microscopy, two types of gold can be distinguished. Gold type-I includes gold as an inclusion in pyrite, commonly associated with other sulphide and/or sulphosalt minerals. Gold type-I is related to structurally controlled quartz veins, breccias, within a graphitic layer of schist or in hematitic mudstone. The gold type-I occur mainly as small (less than 50 μm, average of 10 μm) grains in length and associated with disseminated pyrite grains (Fig. 62). Sub-microscopic gold (less than 1 μm in diameter) was observed in some samples (Fig. 62E) as an inclusion in a pyrite crystal. The composition of gold has been confirmed using SEM-EDX or EMPA.

Gold type-II includes free gold hosted by quartz (Fig. 62F). Gold has irregular grains, less than 30 μm in diameter. This gold type-II is less common and is related with the intensive weathering process near the surface. Most pyrite and other sulphides were also altered to secondary iron oxide, which in turn released gold from pyrite into the surrounding silicate or secondary iron oxide. Gold type II

was observed in sample SB-02 (outcrop sample). No gold was found in carbonate (calcite, dolomite-ankerite and siderite).

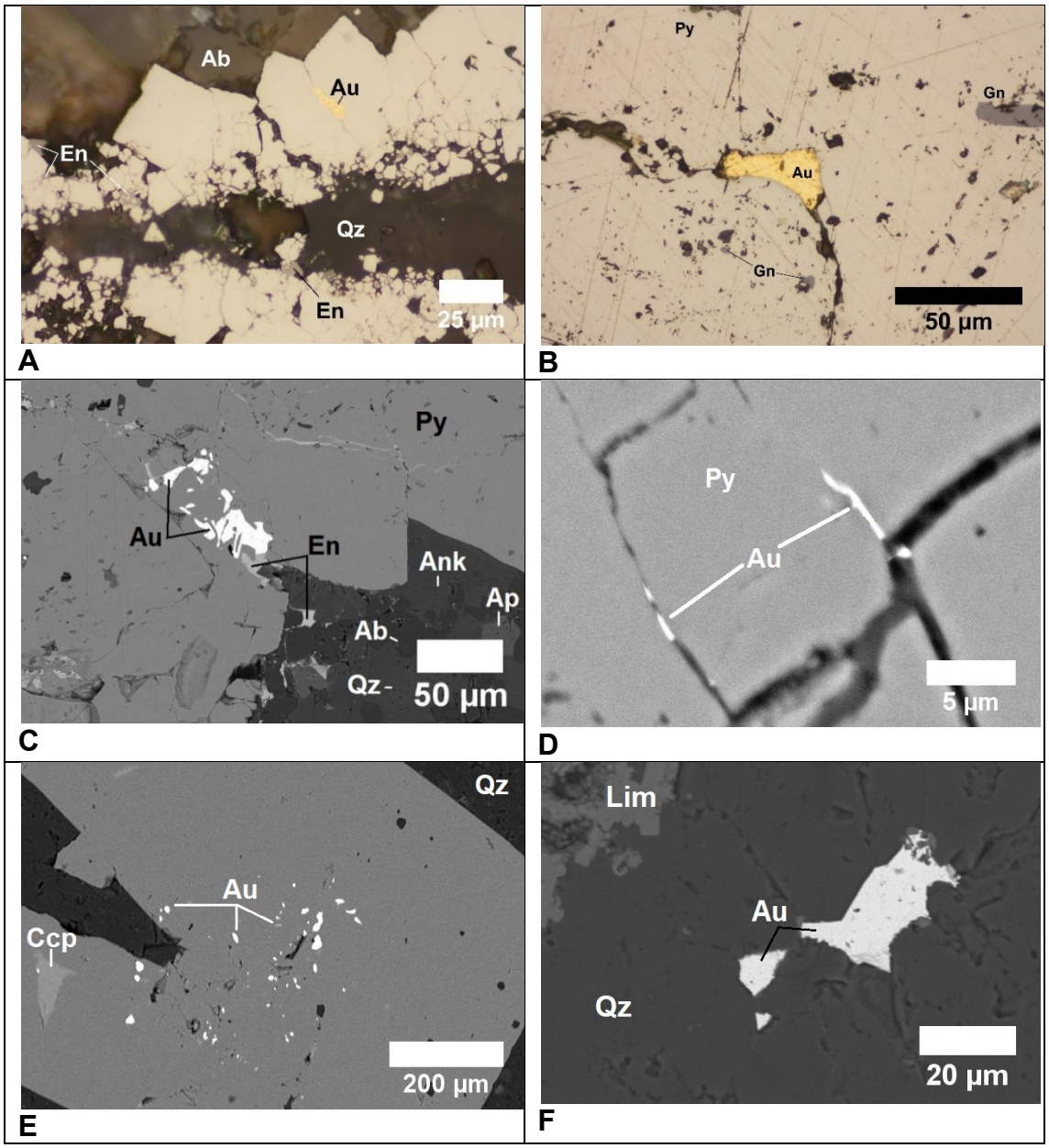

Fig. 62. Photomicrographs of gold. (A-D) Gold hosted in pyrite cracks. Pyrite crystal is generally bigger than 1 mm in size. (E) Blebs of gold hosted in pyrite. S94-34.35. (F) Free-grained gold hosted by quartz. SB-02.

The Au, Ag, Cu, Hg, Bi and Fe concentrations of gold were determined using electron microprobe. Eighty-seven electron microprobe analyses carried out. The amount of Cu, Bi and Hg was generally less than 0.05 wt%. Iron content of gold likely results from fluorescence of the host mineral (pyrite). This problems occured during the quantification of irregular and small (<5 µm) gold grains. For

calculation and data presentation, the Au and Ag contents obtained from EMPA were normalized to 100%. Gold consists of 84.2 to 90.9 wt% Au (average of 86.6 wt%) and 9.1 to 15.8 wt% Ag (average of 13.4 wt%). There are no significant differences in gold fineness from different type of host rocks (i.e. hematitic mudstone, breccia, mica schist, phyllite). A summary of electron microprobe analysis on gold is provided in Table 30, Figure 63 and Appendix D.

Table 30. Representative electron microprobe analyses of gold. The analyses were presented in wt% and normalized to 100%.

Sample	Description		Au	Ag	Host mineral
Salu Bullo					
S69-25	Gold within pyrite in	Minimum	84.55	9.06	Pyrite
(n=37)	hematitic mudstone	Maximum	90.94	15.45	
		Average	85.65	14.35	
		S.D.	1.10	1.10	
S69-25.80	Gold within pyrite in	Minimum	89.80	10.11	Pyrite
(n=2)	hematitic mudstone	Maximum	89.89	10.20	
		Average	89.84	10.16	
		S.D.	0.06	0.06	
S68-132.90	Breccia quartz vein within	Minimum	84.24	15.44	Pyrite
(n=2)	phyllite	Maximum	84.56	15.76	
		Average	84.40	15.60	
		S.D.	0.23	0.23	
S94-34.35	Gold within pyrite in	Minimum	86.57	12.64	Pyrite
(n=8)	hematitic mudstone	Maximum	87.36	13.43	
		Average	87.02	12.98	
		S.D.	0.24	0.24	
S53-101	Breccia quartz vein	Minimum	88.18	10.49	Quartz
(n=13)		Maximum	89.51	11.82	
		Average	88.73	11.27	
		S.D.	0.44	0.44	
S68-107	Quartz vein within chlorite	Minimum	86.47	13.32	Pyrite
(n=3)	schist	Maximum	86.68	13.53	
		Average	86.57	13.43	
		S.D.	0.10	0.10	
S68-140.20	Quartz vein within chlorite	Minimum	86.06	13.47	Pyrite
(n=3)	schist	Maximum	86.53	13.94	
		Average	86.23	13.77	
		S.D.	0.26	0.26	
SB-02	Quartz vein in oxidized	Minimum	86.84	13.01	Quartz
(n=4)	and abandoned tunnel	Maximum	86.99	13.16	
		Average	86.89	13.11	
		S.D.	0.07	0.07	
Awak Mas					
A149-90.65	Quartz veins within mica	Minimum	91.45	7.56	Pyrite

Sample	Description		Au	Ag	Host mineral
(n=3)	schist	Maximum	92.41	8.56	
		Average	91.82	8.19	
		S.D.	0.52	0.52	
A635-21	Quartz veins within	Minimum	88.28	11.71	Pyrite
(n=2)	phyllite	Maximum	88.29	11.72	
		Average	88.29	11.71	
		S.D.	0.00	0.00	
A192-86.40	Quartz veins within phyllite	Minimum	93.03	6.36	Pyrite
(n=4)		Maximum	93.64	6.97	
		Average	93.26	6.74	
		S.D.	0.27	0.27	
A635-16	Quartz veins within phyllite	Minimum	88.38	11.26	Pyrite
(n=4)		Maximum	88.74	11.62	
		Average	88.55	11.45	
		S.D.	0.17	0.17	
A685-20	Breccia quartz veins within	Minimum	89.47	8.32	Pyrite
(n=2)	phyllite	Maximum	91.68	10.53	
		Average	90.57	9.43	
		S.D.	1.56	1.56	

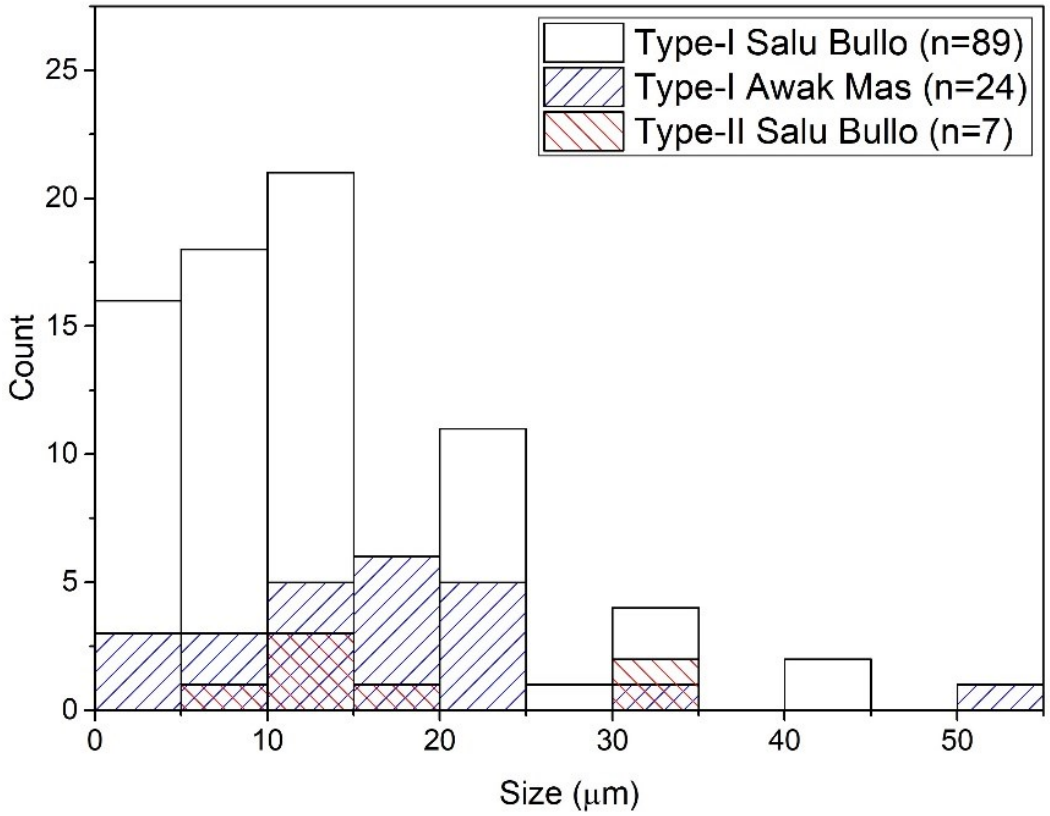

Fig. 63. Histogram showing apparent grain size distribution of gold in Awak Mas and Salu Bullo based on microscopic data. Length refers to the maximum length of gold in SEM image.

6.3.2 Sulphosalt group minerals

The sulphosalt group of minerals has been recognized for its diversity of substitution. The general formula for sulphosalts, as described by (Johnson et al. 1986, 1988) can be written as $^{IV}M1_6{}^{III}M2_6[^{III}X^{IV}Y_3]_4Z$, where *M*1 represents Cu or Ag, *M*2 represents Cu, Fe, Zn, Hg or Cd, *X* represents Sb, As, Bi or Te, and *Y* and Z are S or Se. The end-members include tetrahedrite (Sb-end member), freibergite (Ag-end member), goldfieldite (Te-end member) and tennantite (As-end member)(Foit and Hughes 2004). Tetrahedrite and tennantite solid solutions ($tetrahedrite_{ss}$) are the most common minerals of the sulphosalt group (Johnson et al. 1986).

The studied sulphosalts at Awak Mas and Salu Bullo are tetrahedrite or tennantite, associated with chalcopyrite, pyrite and enargite/luzonite-famatinite (Hakim and Melcher 2016). The sulphosalts are hosted in a wide variety of rocks, including quartz veins, breccia veins, hematitic mudstone, and mica schist. Chalcopyrite occurs as anhedral grains and is often replaced by covellite. Tetrahedrite shows medium grey, tennantite shows greenish grey and covellite has indigo blue colour and has a strong anisotropy. Tetrahedrite also occurs as an indicator mineral for gold in both deposits. However, tetrahedrite has a small grain size (less than 100 μm in length) and can only be distinguished using reflected light microscope. Stibnite was observed only in one sample as a crack filling (~10 μm) in albite. Arsenoyprite, native arsenic, native antimony are absent. Sample S68-143.80 (Figs. 64A-B) shows a complex paragenesis of sulphosalt and sulphide minerals. This sample is located less than 50 cm from the fault zone and is hydrothermally altered by silica, siderite and albite. The primary ore mineral is chalcopyrite, which in turn is replaced by complex assemblages of tetrahedrite-tennantite, covellite, pyrite and carrolite. Covellite replacing chalcopyrite, while carrolite (<5 μm in diameter) is replaced by pyrite. All ore minerals mentioned above are partially rimmed by thin (2-5 μm) siderite.

Ramdohr (1969) described that in the oxidation zone, the alteration of sulphosalt is sometimes complicated and most oxidation begins with the formation of chalcocite and covellite with a highly varied and beautiful textures. Occasionally, a small amount of limonite, cuprite, abundant azurite and malachite can form.

Compositional zoning of sulphosalt and enargite-luzonite from Awak Mas and Salu Bulo samples is not visible in the transmitted light microscope. Chemical zoning is more evident in BSE images and occurs as irregular patchy zoning pattern (Figs. 64C-D and H). Figures 64E-G shows the net-texture of chalcopyrite and partial replacement of chalcopyrite by tennantite and enargite/luzonite. This sample contains abundant gold inclusions, chalcopyrite and galena. All inclusions (gold, chalcopyrite and galena) are typically less than 5 µm and hosted in coarse pyrite crystals (up to 1 mm in diameter)(Fig. 64E). On the same polished-thin section, a chemical zoning of enargite-luzonite can be observed using scanning electron microscopy, the observation was made at a very high contrast (Fig. 64I).

6.3.3 Schwazite and mercurian tetrahedrite

Schwazite is an old terminology for a mercury-rich variety of tetrahedrite from the locality of Schwaz in Tyrol, Austria. The name schwazite was introduced by Kenngot (1853) who reported a tetrahedrite yielding 15.57 wt% Hg. However, tetrahedrite samples from Schwaz-Brixlegg usually are not rich in mercury (Arlt and Diamond 1998; Krismer et al. 2011). In addition, the terminology of schwazite is exhausted and mercurian tetrahedrite is more acceptable. The highest Hg and Ag contents of mercurian tetrahedrite were reported from the epithermal deposit of Steens-Pueblo Mining District, Oregon. The chemical composition is $Ag_{6.00}[(Ag_{4.00})\ (Cu_{0.62}Hg_{0.60}Zn_{0.40}Fe_{0.12}Co_{0.05}Cd_{0.04})]\ (Sb_{2.35}As_{1.72})\ S_{13.09}$ (Foit and Ulbricht 2001), where all Cu is entirely substituted by Ag.

Electron microprobe analyses of sulphosalts indicated that some tetrahedrite grains containing elevated contents of mercury up to 17.11 wt%. The mercurian tetrahedrites investigated in this study (n=12) are hosted in mineralized quartz veins (S68-132.90, S68-143.80) and mica schist (A635-24.40, A635-34.7, A149-90.65). Under reflected light, there is no significant optical difference between tetrahedrite and mercurian tetrahedrite. Ramdohr (1969) described that mercurian tetrahedrite (or schwazite) has a dull cream colour, with correspondingly high reflectivity.

Figure 65 illustrates different occurences of mercurian tetrahedrite in quartz veins and phyllite. Mercurian tetrahedrite from the Awak Mas and Salu Bullo occurs as:

(a) free-grains (irregular habit, less than 15 μm in size) hosted by albite (Figs. 65C-E); (b) enclosing framboidal pyrite or along pyrite cracks (Figs. 65F-G); and (c) inclusion in chalcopyrite or pyrite (Figs. 65H-I). Although Ramdohr (1969) mentioned that the mercurian rich tetrahedrite is always altered by surface processes and often contains massive cinnabar and native mercury, however, as mentioned earlier, native cinnabar and native mercury were not observed in samples from Awak Mas and Salu Bullo.

A total of sixty-six electron microprobe analyses were carried out on tetrahedrite, enargite/luzonite and famatinite. Representative compositions are listed on the Tables 31-32 and Appendix D. The structural formulae were calculated on the basis of 13 sulfur atoms per formula unit for fahlores and on the basis of 4 sulfur atoms per formula unit for enargite/luzonite – famatinite.

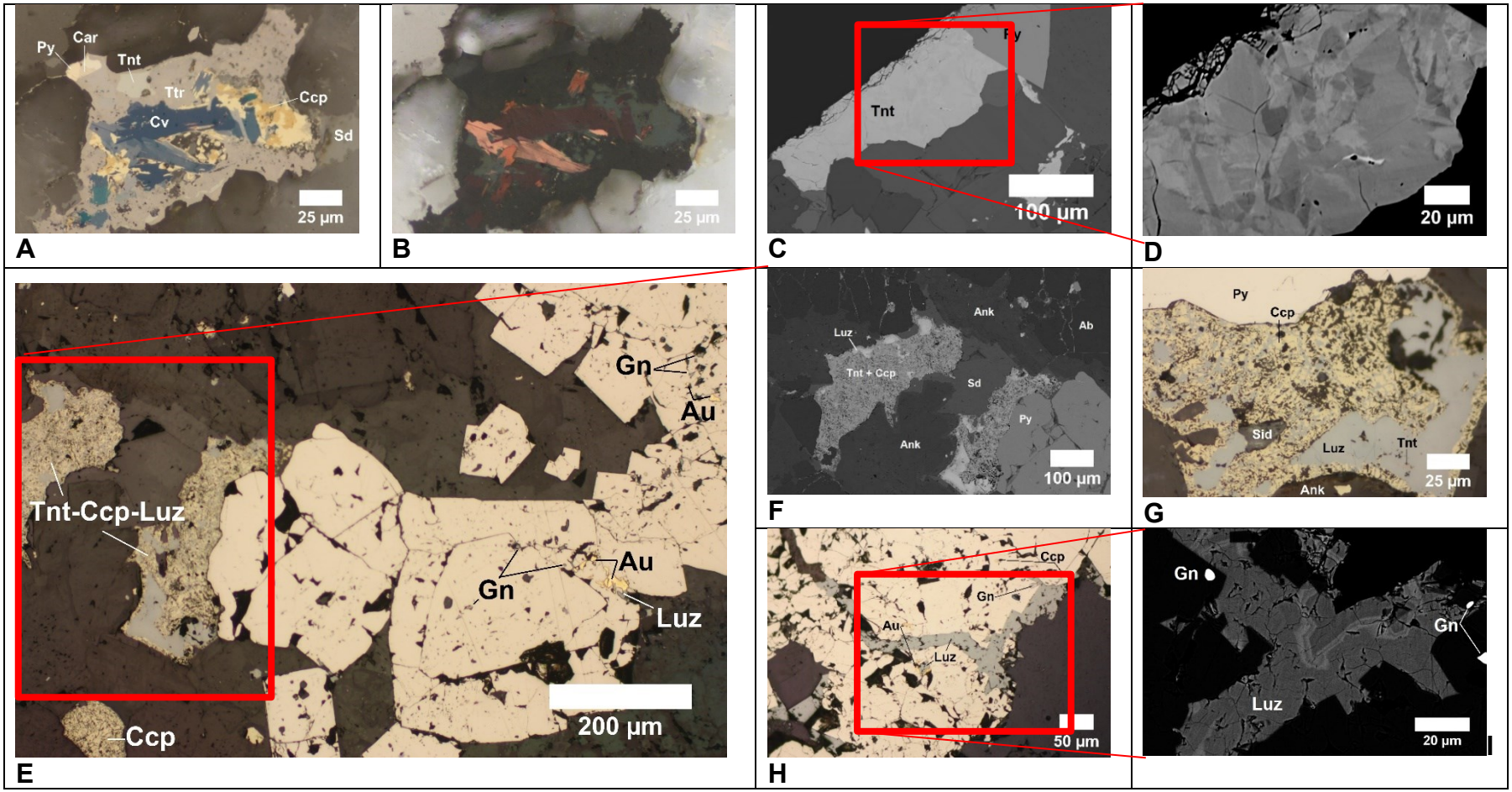

Fig. 64. Photomicrograph of sulphosalt. (A) Complex mineralogical assemblages involving sulphide–sulphosalt+carrolite rimmed by a thin layer of siderite. S68-143.80. (B) A XPL image of Fig. 64A. (C-D) The BSE image shows the intensive zoning of tennantite. (E-G) Reaction textures within the tennantite and chalcopyrite results on the net-texture showing partial replacement of chalcopyrite by tennantite. S53-103. (H-I) High-contrast BSE image shows the rims of luzonite along the fractured pyrite. S53-103.

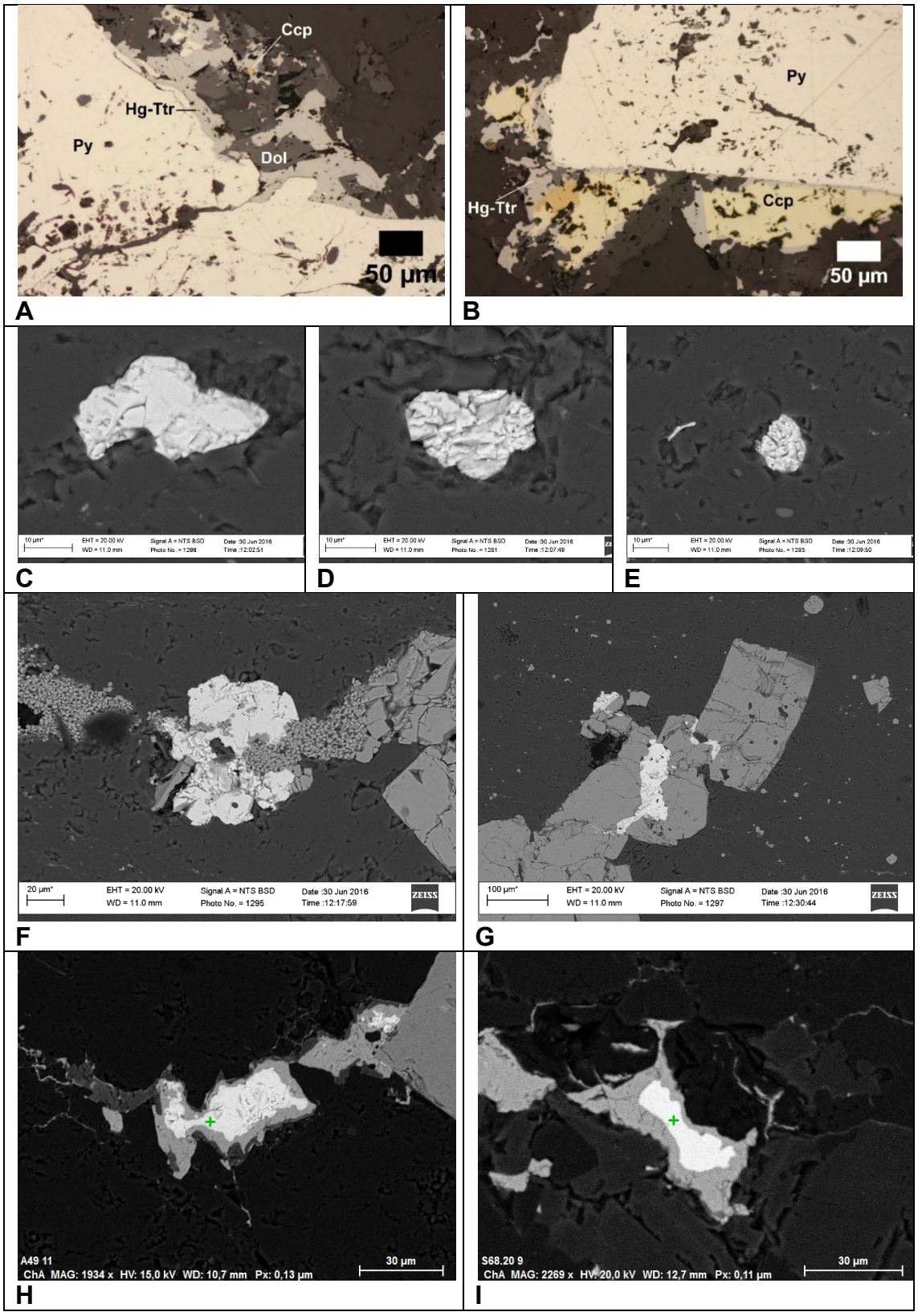

Fig. 65. Photomicrographs of mercurian tetrahedrite. (A-B) A PPL photomicrograph of mercurian tetrahedrite associated with pyrite and chalcopyrite. Host rock is mica schist. A635-34.70. (C-E) Mercurian tetrahedrite occurs as a free-grains hosted in albite. Host rock is mica schist. A635-24.40. (F)

Mercurian tetrahedrite enclosed framboidal pyrite. A635-24.40. (G) Interstitial mercurian tetrahedrite within pyrite cracks. (H-I) Mercurian tetrahedrites occur as an inclusion in chalcopyrite (H) and pyrite (I). Figure H represents sample A149-90.65 and Figure I represents sample S68-132.90.

The general composition of fahlores can be described with the elements Cu, As, Sb, S with minor Hg, Fe and Zn. The mercurian tetrahedrite is characterized by high Sb and low As-Cu-Zn (Figs. 66A-C). The Ag and Bi contents are generally less than 0.1 wt% (Fig. 66D). The enargite/luzonite-famatinite in this study has a wide As-Sb substitution, ranging from Sb-rich [$Cu_{3.07}(Sb_{0.64}As_{0.38})S_4$] to As-rich [$Cu_{3.02}As_{0.79}Sb_{0.21}S_4$](Fig. 66H). The mercurian tetrahedrite has 1.93 to 17.56 wt% Hg, corresponds to 0.16 to 1.63 atoms per formula unit (Fig. 66). In order to illustrate the composition of solid solution in sulphosalts, variation diagram of are shown in Figure 66. Literature data have been plotted as fields of comparison.

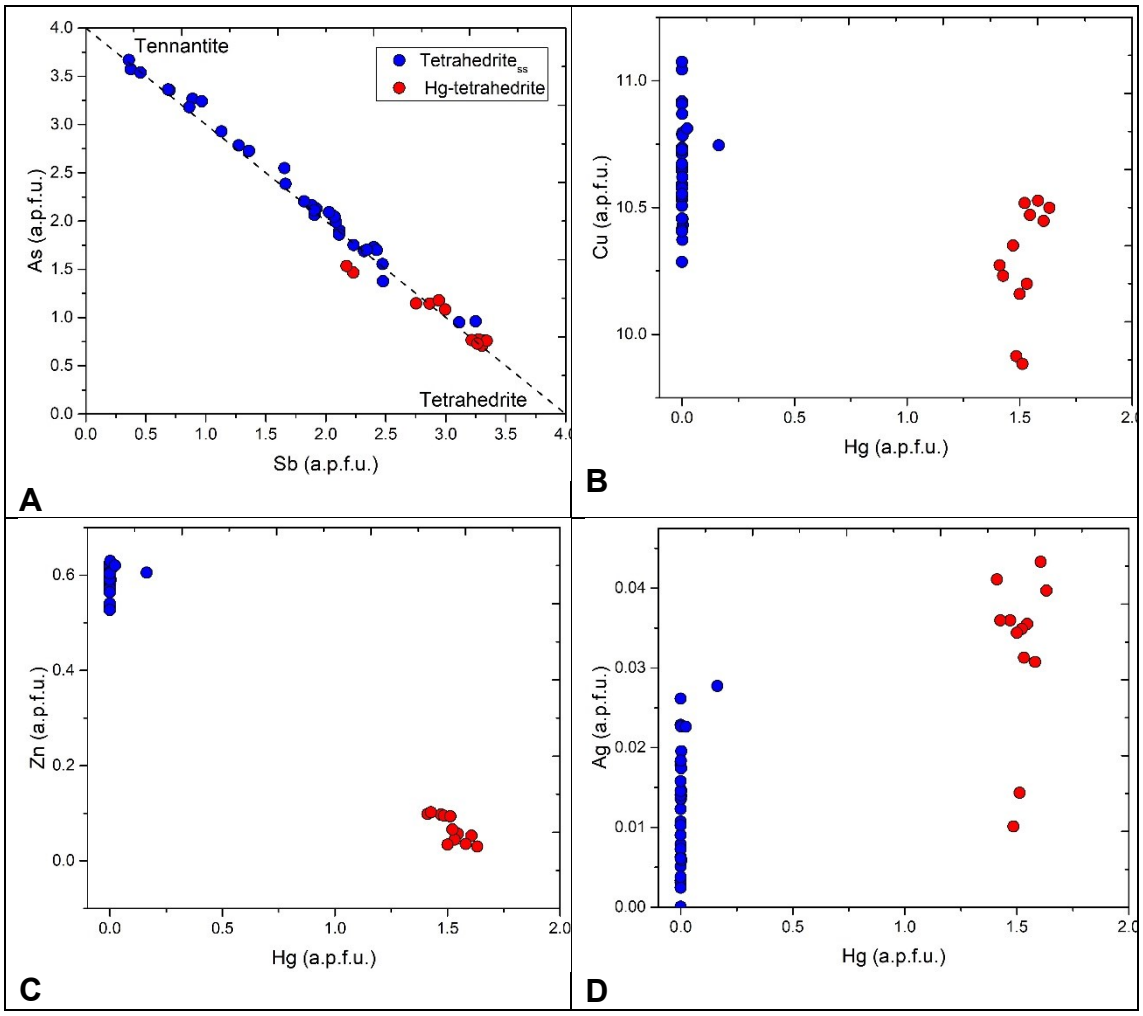

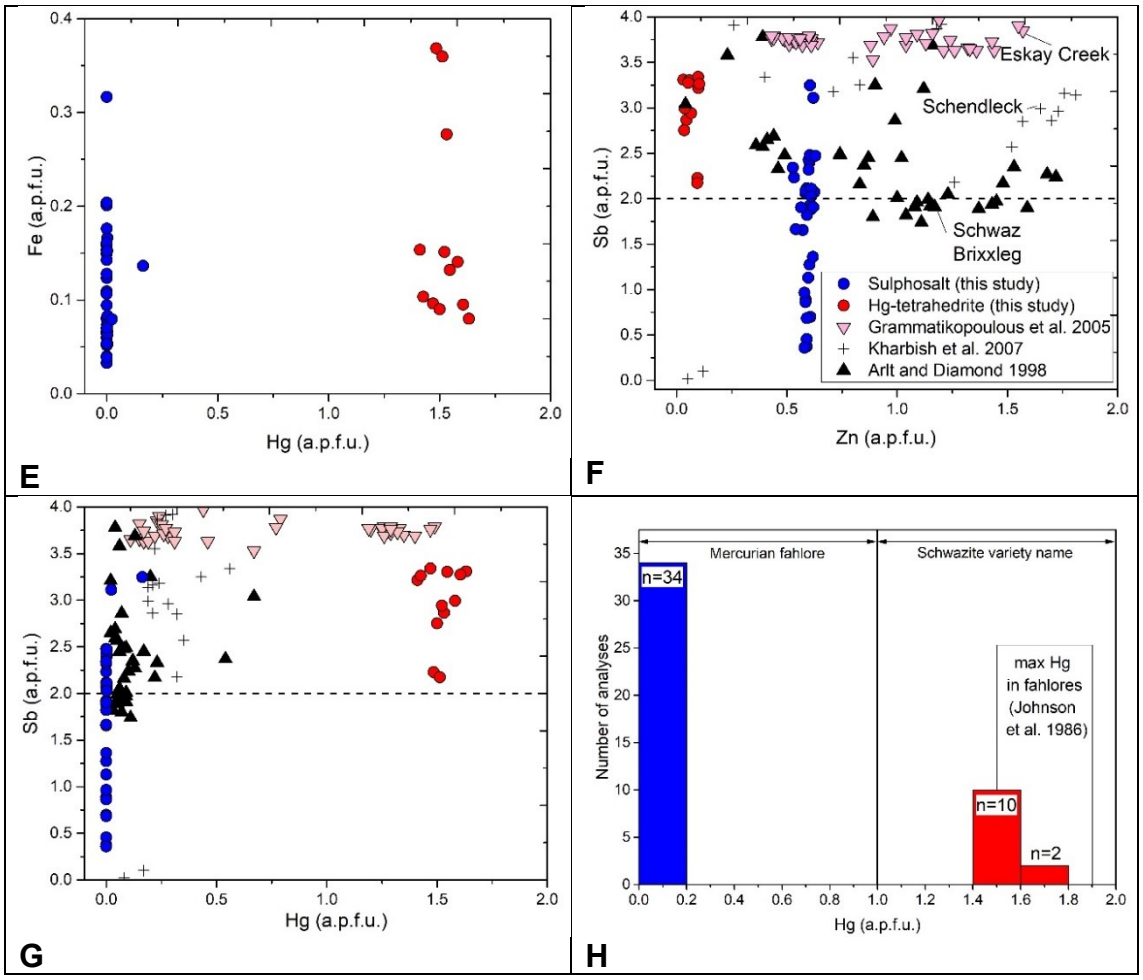

Fig. 66. Bivariate plots of fahlore compositions. Data from Arlt and Diamond (1998), Grammatikopoulos et al. (2005) and Kharbish et al. (2007) are plotted for comparison. (A-G) Hg vs. As, Sb, Fe, Ag and Zn. (H) Mercury contents of fahlores from Latimojong.

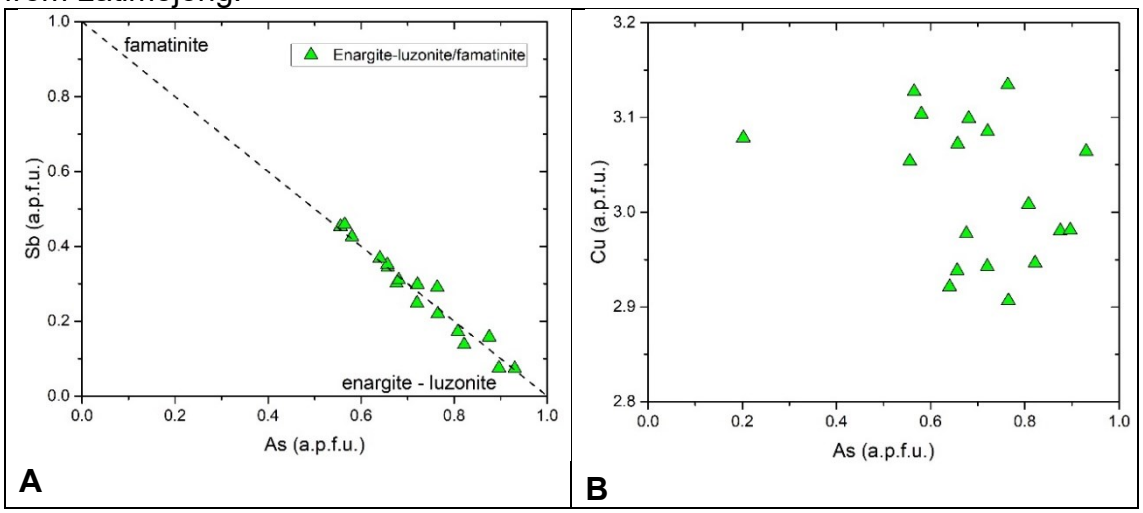

Fig. 67. Bivariate plots of enargite-luzonite compositions.

Table 31. Representative electron microprobe analyses of sulphosalts.

Sample	sam4-18		A35-34.7		sam1-23		S94-34.35		A49-90.65	
Spot	2		10		3		32		1	
	Average	S.D.	Average	S.D.	Average	S.D.	Average	S.D.	Average	S.D.
As	6.39	0.21	3.71	0.86	3.71	0.46	11.84	3.65	4.44	-
S	23.72	0.02	22.79	0.28	24.33	0.23	27.28	0.68	26.01	-
Sb	15.25	0.26	20.80	1.27	23.71	0.52	13.04	5.14	23.64	-
Bi	0.05	0.01	0.11	0.05	0.11	0.05	0.10	0.04	0.17	-
Cu	35.80	0.05	36.02	0.31	39.45	0.71	44.29	1.53	42.88	-
Ag	0.08	0.02	0.21	0.02	0.24	0.06	0.08	0.05	0.15	-
Zn	0.35	0.00	0.22	0.10	2.29	0.03	2.51	0.11	2.53	-
Hg	17.11	0.24	16.70	0.71	2.28	0.31	0.01	0.01	0.29	-
Fe	1.16	0.02	0.40	0.18	0.44	0.11	0.40	0.23	0.28	-
Total	99.90	0.18	100.95	0.63	96.56	0.66	99.55	1.09	100.38	-
Chemical formula										
As	1.50	0.05	0.91	0.20	0.85	0.10	2.40	0.68	0.95	-
S	13.00	0.00	13.00	0.00	13.00	0.00	13.00	0.00	13.00	-
Sb	2.20	0.04	3.13	0.22	3.34	0.11	1.65	0.67	3.11	-
Bi	0.00	0.00	0.01	0.00	0.01	0.00	0.01	0.00	0.01	-
Cu	9.90	0.02	10.37	0.14	10.63	0.18	10.65	0.19	10.81	-
Ag	0.01	0.00	0.04	0.00	0.04	0.01	0.01	0.01	0.02	-
Zn	0.09	0.00	0.06	0.03	0.60	0.01	0.59	0.03	0.62	-
Hg	1.50	0.02	1.52	0.07	0.19	0.03	0.00	0.00	0.02	-
Fe	0.36	0.01	0.13	0.06	0.14	0.03	0.11	0.06	0.08	-
Total	28.57	0.00	29.16	0.23	28.80	0.21	28.42	0.21	28.63	-
As+Sb+Bi	3.71	0.01	4.04	0.07	4.19	0.07	4.06	0.07	4.07	-
Sb/(As+Sb+Bi)	0.59	0.01	0.77	0.05	0.77	0.02	0.41	0.17	0.76	-

Table 32. Representative electron microprobe analyses of enargite/luzonite-famatinite.

	enargite/luzonite						famatinite					
Sample	sam1-24		sam2-5		sam3-15		sam5-19		sam1-24		sam2-8	
Spot	2		7		2		3		2		2	
	average	S.D.	average	S.D.	average	S.D.	average	S.D.	average	S.D.	average	S.D.
As	13.08	1.07	14.64	2.42	14.64	1.57	12.83	1.09	6.69	4.59	10.23	0.23
S	31.00	0.02	31.66	0.64	32.47	0.46	31.41	0.08	29.89	1.04	30.58	0.11
Sb	8.83	0.42	6.33	3.61	5.92	2.33	8.66	1.96	18.14	7.04	12.83	0.63
Bi	0.07	0.01	0.12	0.03	0.10	0.01	0.10	0.03	0.10	0.03	0.09	0.01
Cu	47.87	0.42	47.32	1.36	47.39	0.72	45.77	0.54	45.41	1.32	47.21	0.09
Ag	0.08	0.07	0.05	0.06	0.02	0.02	0.04	0.01	0.07	0.03	0.01	0.01
Zn	0.04	0.01	0.05	0.01	0.05	0.00	0.04	0.02	0.02	0.03	0.06	0.02
Hg	0.01	0.02	0.01	0.02	0.01	0.01	0.02	0.03	0.01	0.01	0.00	0.00
Fe	0.47	0.04	0.78	0.84	0.65	0.22	0.24	0.20	0.71	0.55	0.08	0.00
Total	101.45	1.20	100.97	1.20	101.24	0.25	99.11	1.15	101.04	0.60	101.09	0.37
Chemical formula												
As	0.72	0.72	0.79	0.12	0.77	0.07	0.70	0.06	0.38	0.25	0.57	0.01
S	4.00	4.00	4.00	0.00	4.00	0.00	4.00	0.00	4.00	0.00	4.00	0.00
Sb	0.30	0.30	0.21	0.12	0.19	0.08	0.29	0.07	0.64	0.27	0.44	0.02
Bi	0.00	0.00	0.00	0.00	0.00	0.00	0.00	0.00	0.00	0.00	0.00	0.00
Cu	3.12	3.12	3.02	0.06	2.94	0.00	2.94	0.04	3.07	0.02	3.12	0.02
Ag	0.00	0.00	0.00	0.00	0.00	0.00	0.00	0.00	0.00	0.00	0.00	0.00
Zn	0.00	0.00	0.00	0.00	0.00	0.00	0.00	0.00	0.00	0.00	0.00	0.00
Hg	0.00	0.00	0.00	0.00	0.00	0.00	0.00	0.00	0.00	0.00	0.00	0.00
Fe	0.04	0.04	0.06	0.06	0.05	0.02	0.02	0.01	0.06	0.04	0.01	0.00
Total	8.18	8.18	8.08	0.04	7.96	0.02	7.95	0.05	8.15	0.08	8.14	0.03
As+Sb+Bi	1.02	1.02	1.00	0.02	0.97	0.01	0.99	0.02	1.01	0.04	1.03	0.02
Sb/(As+Sb+Bi)	0.29	0.29	0.21	0.12	0.20	0.08	0.29	0.06	0.56	0.35	0.57	0.21

sam1:S68-143.80; sam2: S69-25; Samp3: S68–132.90 and Samp4:S69-25.80, respectively.

6.4 Sulphide

6.4.1 Pyrite

Three pyrite generations are observed (Fig. 68). The first phase (Py1) comprises finely disseminated grains of diagenetic, framboidal pyrite within grey to dark mica schist. The size of Py1 ranges from 10-50μm. Some framboidal pyrite is partially replaced by galena (Figs. 68A and E). The second phase pyrite (Py2) shows euhedral to subhedral cubic shapes, ranging from 20μm up to several hundred micron (Fig. 68F). The second pyrite consists of pyrite bands that are coarse grained and parallel bedding. The third phase (Py3) of pyrite is a late hydrothermal pyrite, mainly occurs as large cubes up to millimetre size; it is idiomorphic, crosscutting bedding or disseminated and associated with quartz veins (Fig. 68G). Hydrothermal pyrite (Py3) often overgrowths on earlier pyrite generations.

Most pyrite close to the surface has undergone weathering stages (Fig. 68I). It shows a radial texture from core to rim. Replacement of pyrite by hematite is commonly observed in samples close to the surface, or in samples taken close to the fault zone. Some pyrite grains have a simple zoning (Py_{sz}) with an inclusion-rich layer in between core and rim (Figs. 68J-K). The central pyrite generations are clear and inclusion-free. The most common mineral inclusions in zoned pyrite are galena, chalcopyrite, monazite, rutile and electrum. Less common inclusions consist of sphalerite, titanite, monazite and zircon.

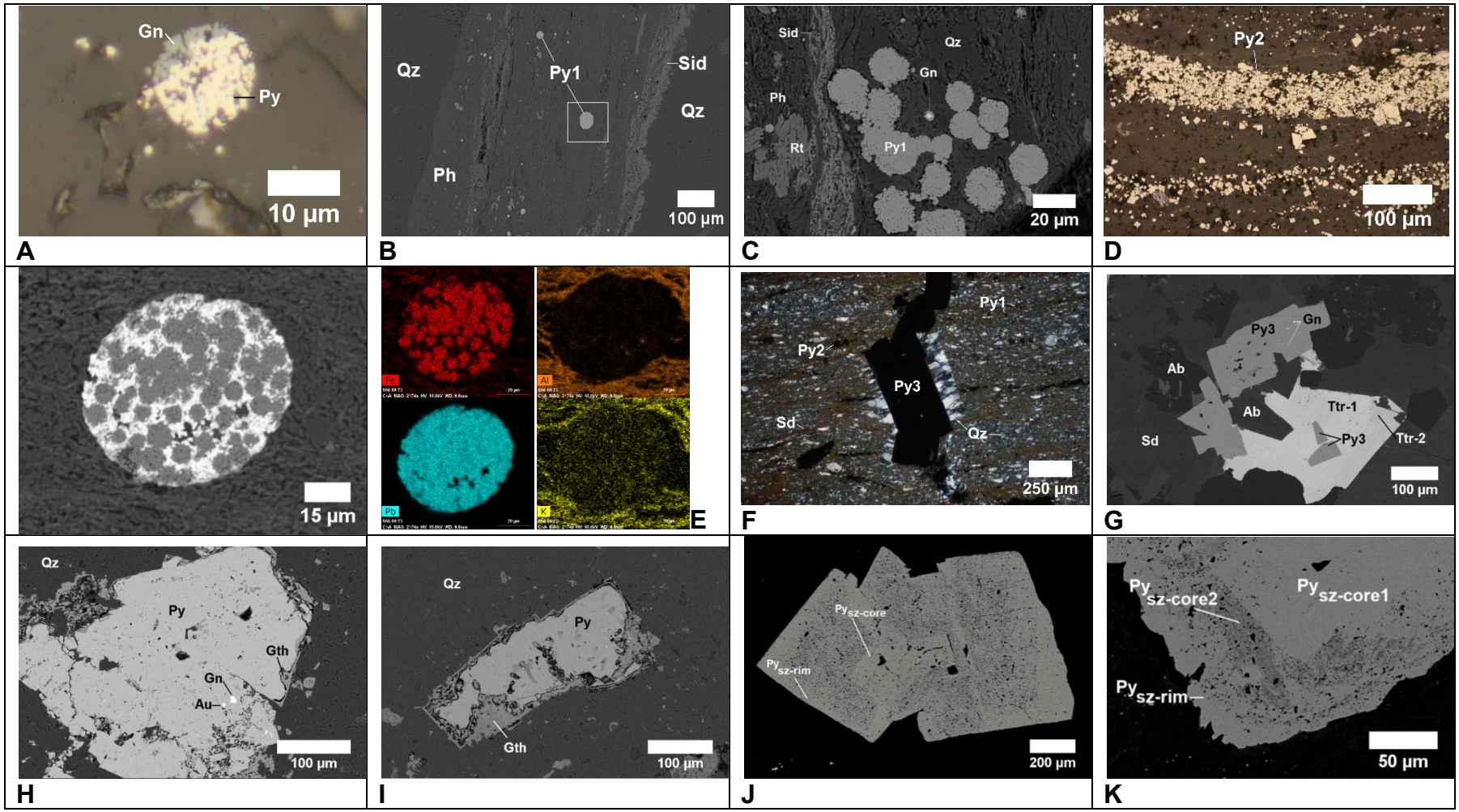
Gn
Py
10 µm
A
Qz
Py1
Sid
Qz
Ph
100 µm
B
Sid
Qz
Gn
Ph
Rt
Py1
20 µm
C
Py2
100 µm
D
15 µm
Fe
Al
Pb
K
E
Py1
Py2
Py3
Sd
Qz
250 µm
F
Py3
Gn
Ab
Ab
Ttr-1
Sd
Py3
Ttr-2
100 µm
G
Qz
Py
Gth
Gn
Au
100 µm
H
Qz
Py
Gth
100 µm
I
Py sz-core
Py sz-rim
200 µm
J
Py sz-core2
Py sz-core1
Py sz-rim
50 µm
K

Fig. 68. Photomicrographs and back-scattered images (BSE) of pyrite. (A) Replacement of a framboid by galena. A687-40.10. (B) Framboidal pyrite preserved in phengite schist. A192-155.70. (C) Framboidal pyrite in phengite schist. Some framboids contain inclusions of galena. A192-189.70. (D) Pyrite2 forms bands of pyrite that are parallel bedding. A635-24.40. (E) Semi-quantitative element map showing the replacement of framboids by galena. A192-225. (F) Three generations of pyrite observed in phyllite. Framboidal texture of Pyrite (Py_1) and euhedral texture of Pyrite (Py_2) are parallel to foliation; Py_3 crosscuts foliation. Photomicrograph in parallel nicols. A635-24.40. (G) BSE image of a tetrahedrite crystal enclosing pyrite. Tetrahedrite-1 (Ttr1) has higher Sb-content than Ttr2. S69-25. (H-I) Idiomorphic crystals of pyrite altered to goethite during weathering. Some gold and galena occur as included in pyrite. Outcrop sample SB-02. (J-K) Textures of simple zoned pyrite. Figures I-J represent sample A687-171 and S68-39.10, respectively. Py_{SZ} = simple zoned pyrite.

6.4.2 Trace elements contents in pyrite by electron microprobe

The Co, Ni, As, Cu, Fe and S contents in pyrite from the Salu Bullo deposit were analysed using electron microprobe. One hundred twenty one spots and twelve quantitative element maps were obtained (Fig. 69, Table 33 and Appendix D). Average detection limits obtained in this study are 140 ppm As, 110 ppm S, 130 ppm Fe, 300 ppm Cu, 250 ppm Co and 195 ppm Ni.

Trace element contents in pyrite are summarized in Table 33. Pyrite in metabasite has a high variation in arsenic and cobalt contents (As = b.d.l. up to 5,220 ppm, Co = b.d.l. up to 8,070 ppm; Table 33 and Fig. 69); i.e. pyrite in S68-39.10 has high As (average of 1,832 ppm As) and Co (average of 2,714 ppm Co) contents. In hematitic mudstone, pyrite is characterized by high average values of Ni and Co (9,209 ppm Ni and 5,740 ppm Co) and low As (average of 600 ppm As). In quartz veins, high variation in As, Co and Ni (207 – 1,991 ppm As; 239 – 346 ppm Co; 213 – 3,853 ppm Ni) contents is observed. Copper content in most of the samples is below the detection limit of electron microprobe. The maximum copper content in pyrite is only 680 ppm Cu. In summary, pyrite from Salu Bullo is characterized by low arsenic and copper contents. The maximum content of Co and Ni in pyrite are 30,870 and 29,640 ppm, respectively. To highlight the heterogenous distribution of the elements within pyrite grains, line scans and quantitative quantitative maps of different type of pyrite from the Salu Bullo deposit have been carried out using electron microprobe (Figures 69-71).

Table 33. Mean value of trace elements in pyrite from the Salu Bullo. All data are in ppm except S and Fe in wt%.

Sample No.		As (ppm)	S (wt%)	Fe (wt%)	Cu (ppm)	Co (ppm)	Ni (ppm)	Total	Co/Ni	Formula
S68-39.10 (n=10)	Maximum	5,220	53.73	47.53	b.d.l.	8,070	1,710	99.93	4.89	$Fe_{1.02}Co_{0.01}S_2$
Metabasite	Minimum	b.d.l.	51.35	45.50	b.d.l.	b.d.l.	b.d.l.			
	Average	1,832	52.77	46.67	b.d.l.	2,714	507			
	S.D.	1,960	0.87	0.81	0	3,288	541			
S68-98.95 (n=4)	Maximum	300	53.56	47.19	b.d.l.	176,78	320	99	N.A.	$Fe_{1.01}S_2$
Metabasite	Minimum	b.d.l.	52.47	46.73	b.d.l.	b.d.l.	b.d.l.			
	Average	207	53.20	46.88	b.d.l.	b.d.l.	209			
	S.D.	83	0.49	0.22	0	0	88			
S68-107 (n=10)	Maximum	1,780	53.64	47.69	b.d.l.	1,010	12,040	100.06	0.27	$Fe_{1.01}Ni_{0.01}S_2$
Quartz vein	Minimum	b.d.l.	53.05	46.14	b.d.l.	b.d.l.	b.d.l.			
	Average	434	53.31	47.08	b.d.l.	299	3,853			
	S.D.	479	0.25	0.55	0	267	4,299			
S68-113.20 (n=6)	Maximum	1,960	53.17	47.56	530	b.d.l.	b.d.l.	99.96	N.A.	$Fe_{1.03}S_2$
Metasiltstone	Minimum	b.d.l.	51.28	46.54	b.d.l.	b.d.l.	b.d.l.			
	Average	835	52.40	47.10	308	b.d.l.	b.d.l.			
	S.D.	698	0.75	0.44	150	0	0			
S68-130.30 (n=6)	Maximum	680	54.23	47.41	680	5,530	7,230	99.96	0.07	FeS_2
Breccia vein	Minimum	b.d.l.	53.91	46.18	b.d.l.	b.d.l.	290			
	Average	285	54.15	47.10	290	1,069	2,448			
	S.D.	225	0.12	0.46	191	2,185	2,627			
S68-136.50 (n=4)	Maximum	450	53.83	47.68	b.d.l.	450	6030	100.13	0.07	$Fe_{1.01}Ni_{0.01}S_2$
Quartz vein	Minimum	b.d.l.	53.58	46.93	b.d.l.	b.d.l.	b.d.l.			
	Average	222	53.71	47.32	b.d.l.	245	3074			
	S.D.	166	0.10	0.33	0	137	3390			
S68-140.20 (n=14)	Maximum	690	53.1	47.6	b.d.l.	b.d.l.	1720	99.95	N.A.	$Fe_{1.06}S_2$

Sample No.		As (ppm)	S (wt%)	Fe (wt%)	Cu (ppm)	Co (ppm)	Ni (ppm)	Total	Co/Ni	Formula
Quartz vein	Minimum	b.d.l.	47.4	46.4	b.d.l.	b.d.l.	b.d.l.			
	Average	249	51.1	47.1	b.d.l.	b.d.l.	339			
	S.D.	184	2.5	0.4	0	0	494			
S68-143.80 (n=5)	Maximum	600	53.52	47.50	b.d.l.	700	3500	99.74	0.2	$Fe_{1.01}S_2$
Quartz vein	Minimum	b.d.l.	53.38	46.47	b.d.l.	b.d.l.	460			
	Average	414	53.47	46.96	b.d.l.	346	2340			
	S.D.	188	0.06	0.42	0	242	1165			
S69-25 (n=16)	Maximum	860	54.12	47.79	b.d.l.	30,870	29,640	98.78	10.45	$Fe_{0.98}Ni_{0.02}Co_{0.01}S_2$
Hematitic mudstone	Minimum	b.d.l.	52.23	43.63	b.d.l.	b.d.l.	b.d.l.			
	Average	364	53.51	46.04	b.d.l.	5,740	9,209			
	S.D.	267	0.45	1.42	0	10,148	9,339			
S69-25.80 (n=10)	Maximum	1,280	54.32	47.96	550	b.d.l.	10,840	98.77	N.A.	$Fe_{1.02}S_2$
Hematitic mudstone	Minimum	b.d.l.	53.11	46.63	b.d.l.	b.d.l.	b.d.l.			
	Average	384	53.53	47.57	246	b.d.l.	1,905			
	S.D.	348	0.37	0.44	107	0	3,456			
S69-32.80 (n=9)	Maximum	640	54.24	47.97	500	b.d.l.	560	98.68	N.A.	$Fe_{1.01}S_2$
Quartz vein	Minimum	b.d.l.	53.70	46.86	b.d.l.	b.d.l.	b.d.l.			
	Average	364	53.99	47.34	244	b.d.l.	213			
	S.D.	224	0.19	0.41	96	0	155			
S69-64.40 (n=9)	Maximum	740	53.92	47.68	b.d.l.	740	8820	98.62	0.08	$Fe_{1.01}S_2$
Quartz vein	Minimum	b.d.l.	52.99	45.73	b.d.l.	b.d.l.	b.d.l.			
	Average	421	53.54	46.88	b.d.l.	239	1820			
	S.D.	247	0.33	0.64	0	188	3321			
S94-80.30 (n=5)	Maximum	260	53.71	47.56	b.d.l.	b.d.l.	650	98.31	N.A.	$Fe_{1.02}S_2$
Metabasite	Minimum	b.d.l.	51.63	46.18	b.d.l.	b.d.l.	b.d.l.			
	Average	176	52.83	46.98	b.d.l.	b.d.l.	240			

Sample No.		As (ppm)	S (wt%)	Fe (wt%)	Cu (ppm)	Co (ppm)	Ni (ppm)	Total	Co/Ni	Formula
	S.D.	64	0.87	0.58	0	0	229			
S53-33.90 (n=23)	Maximum	5,040	53.35	47.57	b.d.l.	b.d.l.	580	99.92	N.A.	$Fe_{1.05}S_2$
Quartz vein	Minimum	b.d.l.	47.66	43.13	b.d.l.	b.d.l.	b.d.l.			
	Average	1,991	51.49	46.88	b.d.l.	b.d.l.	170			
	S.D.	1,486	1.11	0.86	0	0	102			

- b.d.l. : below detection limit.
- The values below the limit of detection were calculated using the mehod of Croghan and Egeghy (2003) by dividing the detection limit by the square root of 2 (b.d.l./√2).

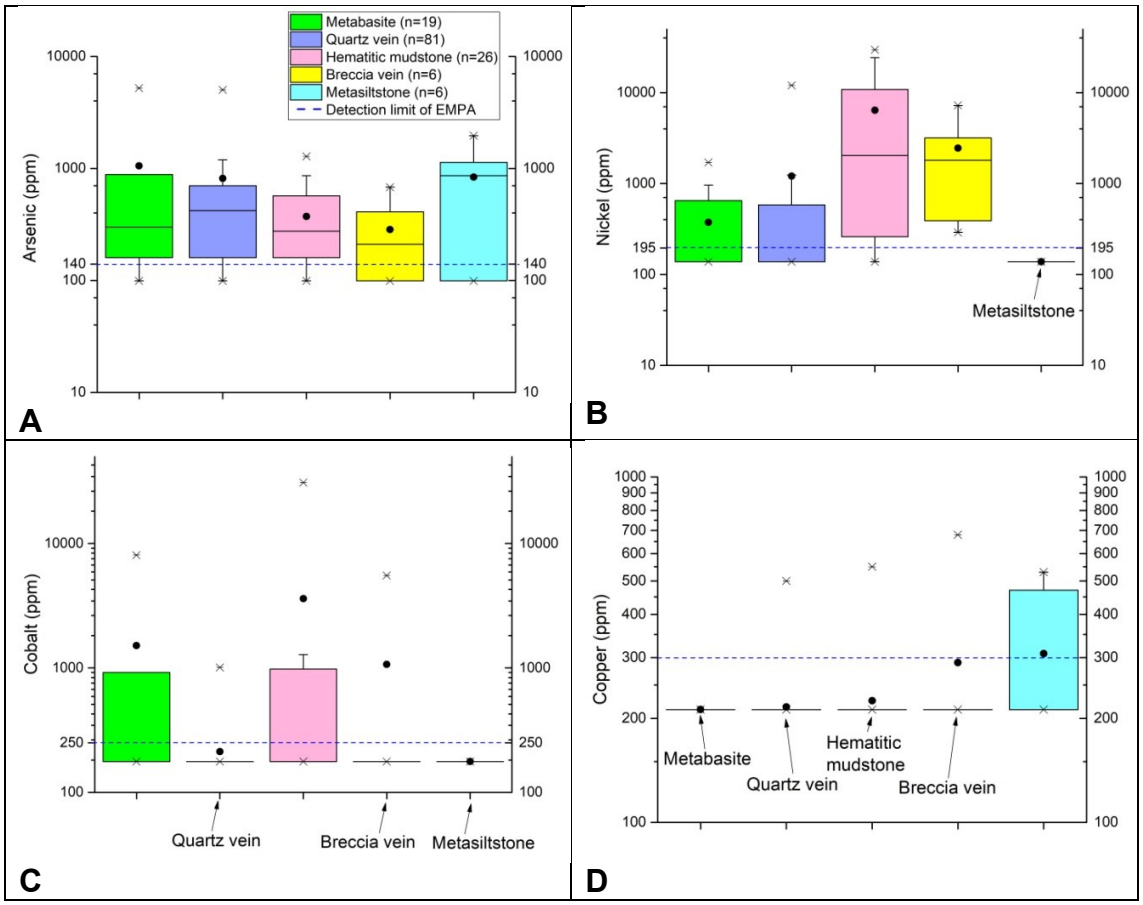

Fig. 69 Box and whisker plot of Ni, As, Co, Cu content in pyrite from the Salu Bullo gold field. The horizontal line represents the median, the solid black dot represents the mean, and the box represents the 25th to 75th percentile of the data. Whiskers are drawn to the last data point that it is 1.5 times the length for the box maximum and minimum. Open circle are ouliers.

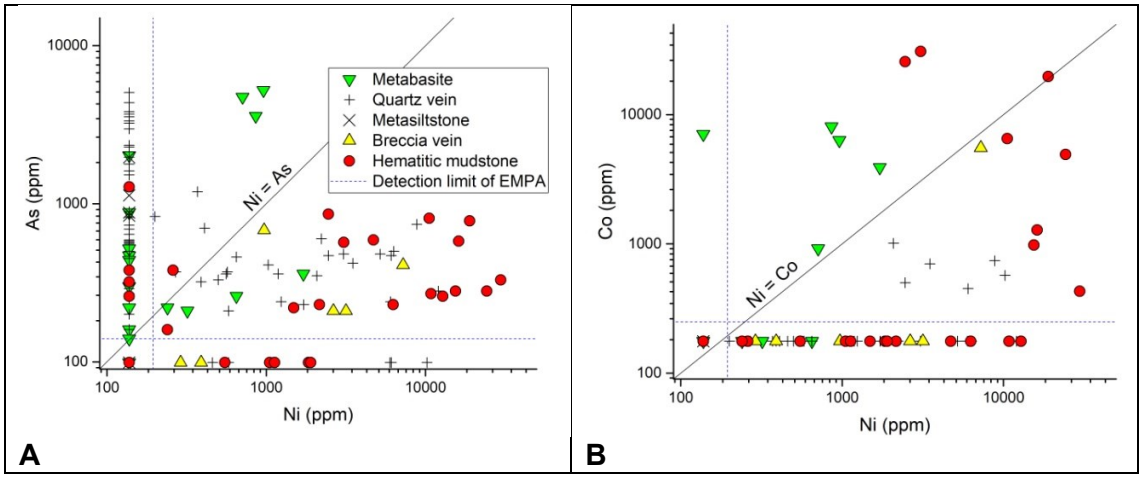

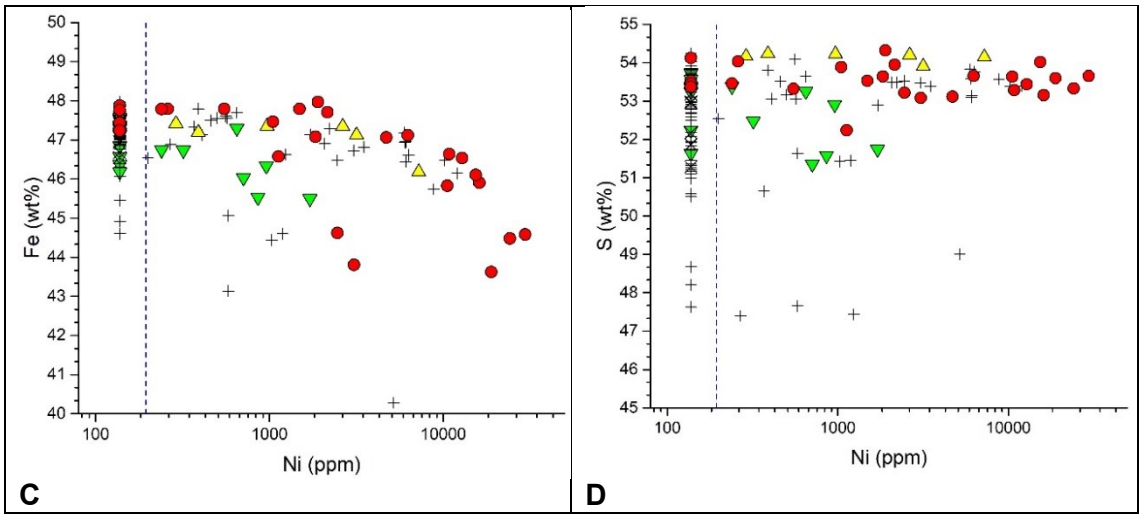

Fig. 70 Composition of pyrite from the Salu Bullo deposit.

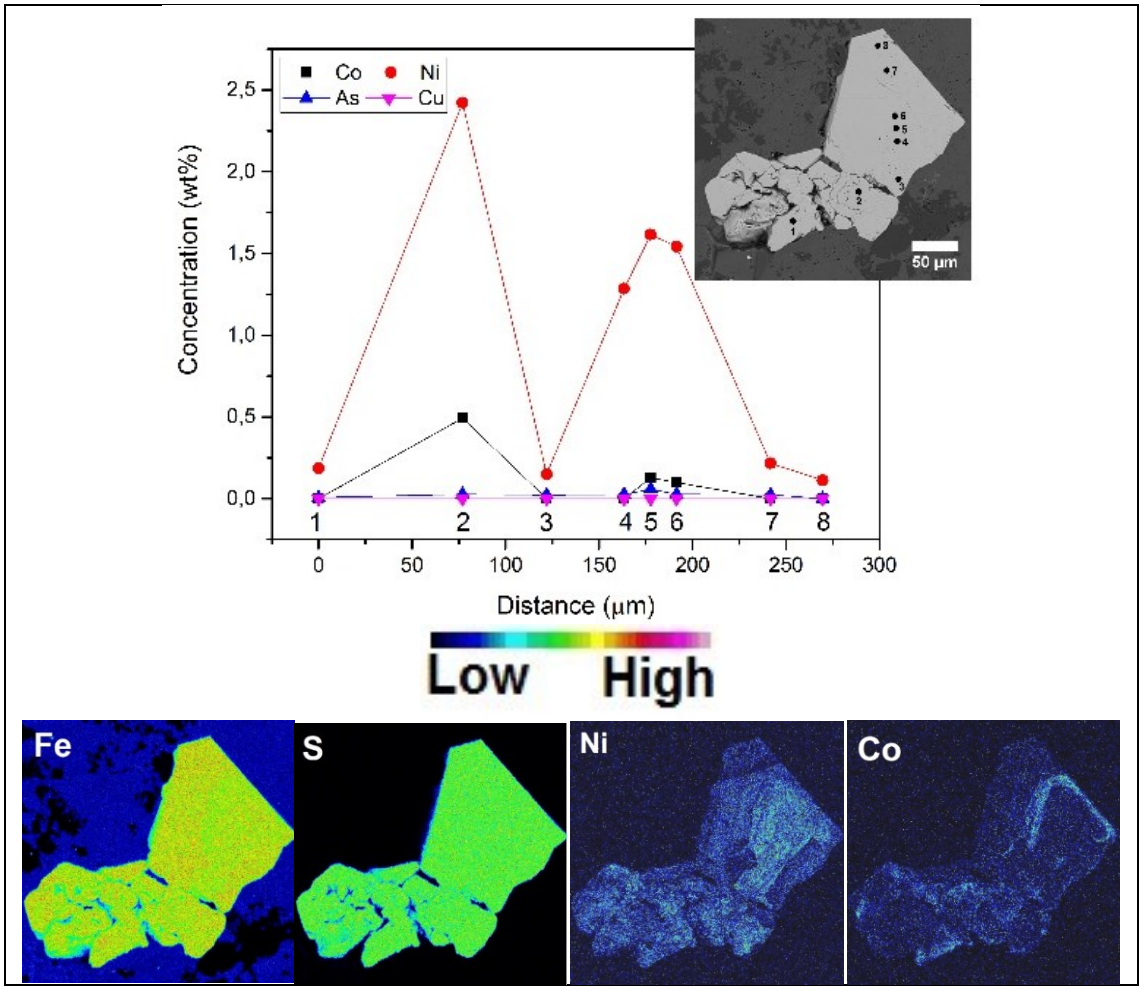

Fig. 71. Line scan and quantitative element map of pyrite. Pyrite has high concentration up to 2,300 ppm Ni up to 500 ppm Co on the core. S69-25.

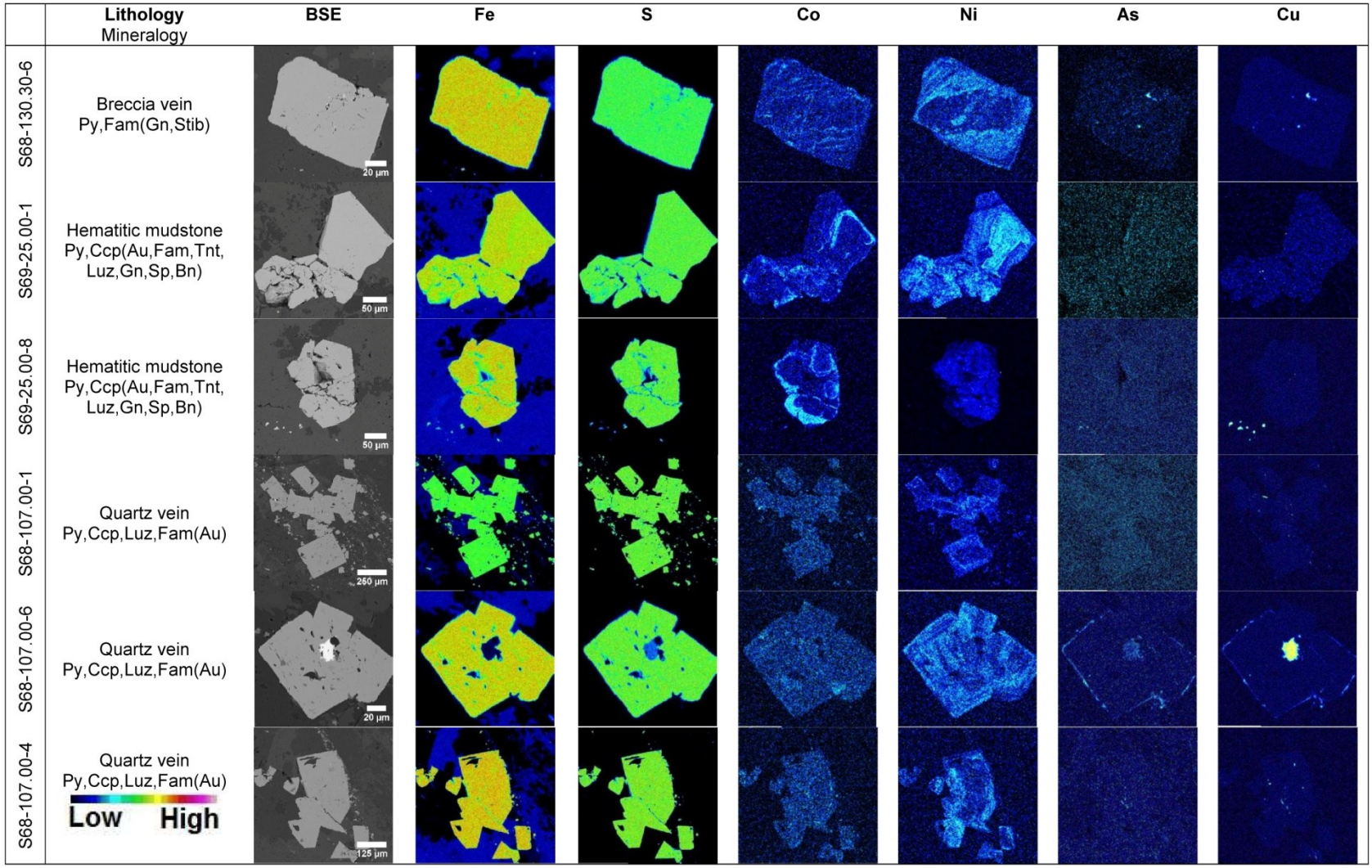

Fig. 72. Electron microprobe element maps of pyrite from Salu Bullo deposit. Ni and Co enrichment are represented in light blue. Arsenic rim surrounding pyrite was observed in S68-107.00-6.

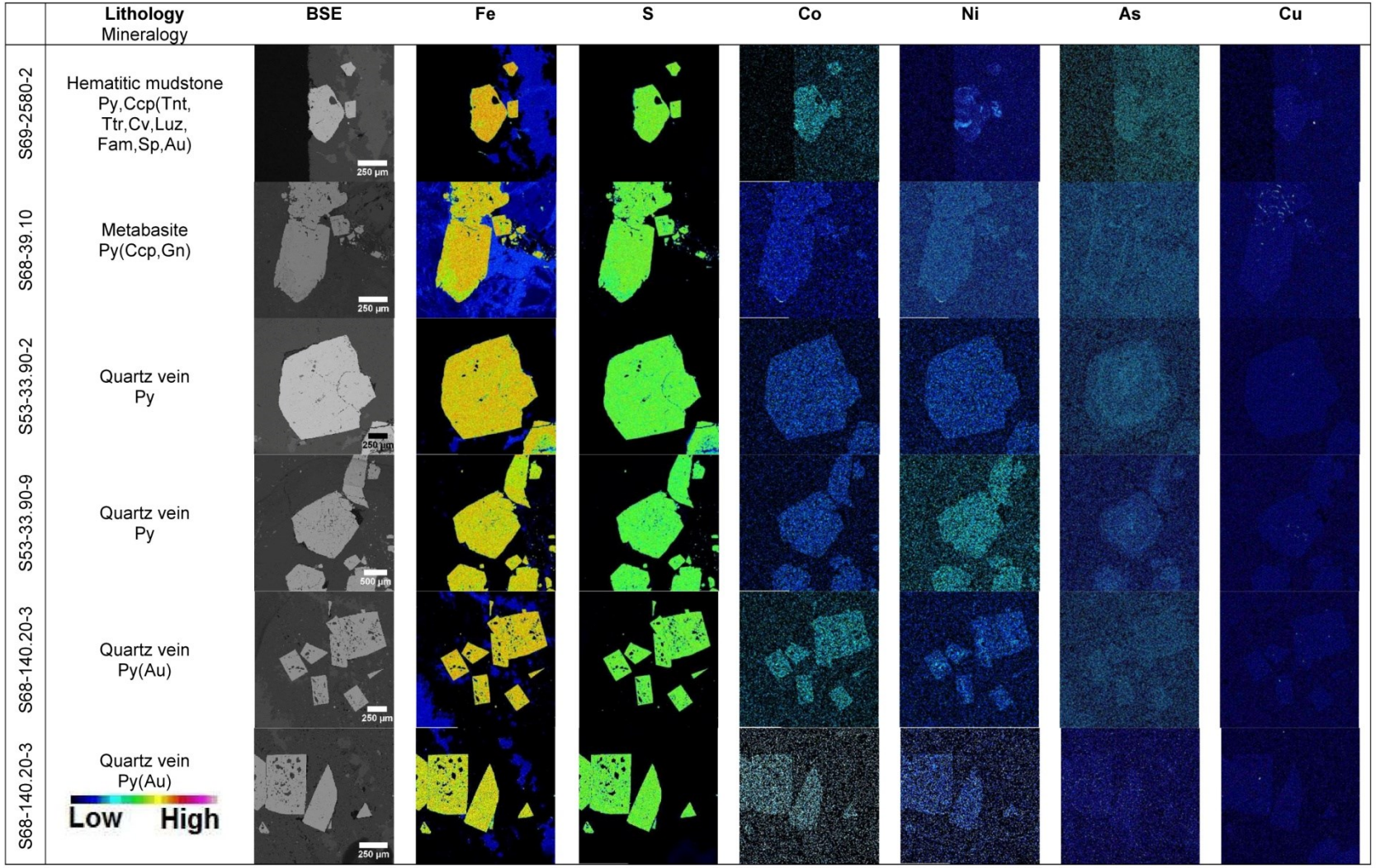

Fig. 73. Electron microprobe element maps of pyrite from Salu Bullo deposit without any enrichment in trace elements.

Cobalt and nickel are heterogenously distributed in pyrite grains, as indicated by quantitative element maps by electron microprobe (Fig. 72). The EMPA maps show concentric, oscillatory zoning parallel to crystal faces. Arsenic form thin layers in or near the rim of pyrites (Fig. 72, sample S68-107.00-6). Some pyrite grains are homogenous without any enrichment in trace elements (Fig. 73).

6.4.3 Trace element contents in pyrite by LA-ICP-MS

Quantitative LA-ICP-MS analyses in pyrite were performed by ablating spots of 80 µm size. Due to the small grain size (<40 µm), trace element contents of pyrite type-1 (framboidal pyrite) and pyrite hosted in metavolcanic rocks could not be performed. Pyrite grains were ablated mainly from mineralized quartz veins and metasedimentary rocks, including hematitic mudstone, phyllite and carbonaceous phyllite. LA-ICP-MS data on are summarized in Figures 74-75, Table 34 and Appendix E.

Based on silver and bismuth contents, pyrite2 can be further grouped: (i) pyrite2a has high Ag, Bi, low Ni, and (ii) pyrite2b has low Ag, Bi and nigh Ni. The median content of silver, bismuth and cobalt for pyrite2a are 1,900 ppm, 1,865 ppm and 33.4 ppm, respectively. Pyrite 2b has low Ag and Bi (median of 1.23 ppm Ag, 0.5 ppm Bi) and high Co(median of 38.7 ppm)(Table 34, Fig. 74).

Pyrite2 has lower As contents (Py2a median of 72 ppm As, n=5; Py2b median of 36 ppm As, n=27) than pyrite3 (median of 156 ppm As, n=46). Nickel and cobalt contents in both pyrite types scatter, ranging from 1 to 2,000 ppm for Co and 7 to 7,000 ppm for Ni. This high variability is similar to the result obtained from the electron microprobe in the previous chapter, which indicates that some pyrite grains are chemically zoned.

Pyrite3 has low Ag and Bi (typically <4 ppm) content, high Co (between 4 and 1,304 ppm), and high variation in arsenic content, ranging from several ppm up to 5,020 ppm (median of 156 ppm As).Selenium contents of pyrite2 and pyrite 3 are typically between 3 and 60 ppm (median of 20 ppm). Gold contents of pyrite2 and pyrite3 are typically less than 1.5 ppm (median of py2=0.11 ppm Au, py3=0.07 ppm Au). Spots with higher Au generally have higher As contents as well.

Table 34. Mean value of trace elements in pyrite from Awak Mas and Salu Bullo by LA-ICP-MS. All data are in ppm.

Element		Isotope	Pyrite2a (n=5)				Pyrite2b (n=27)				Pyrite3 (n=46)			
			Median	Min	Max	SD	Median	Min	Max	SD	Median	Min	Max	SD
Co	(ppm)	^{59}Co	33.4	8.00	332	140	38.7	1.47	2150	488	146	4.27	1304	373
Ni	(ppm)	^{61}Ni	770	542	5700	2216	822	35	23490	4428	401	7.61	7160	1579
Cu	(ppm)	^{65}Cu	22.67	18.57	39.40	8.29	18.2	0.07	193	49.81	9.95	0.071	735	154
Zn	(ppm)	^{67}Zn	4.5	2.90	15.00	5.06	2.6	0.07	128	29.19	2.90	0.071	348	58.89
As	(ppm)	^{75}As	72.7	21.22	135	45.39	36.0	4.83	1290	243	156.1	11.170	5020	1218
Se	(ppm)	^{82}Se	19.12	16.82	20.00	1.28	19.3	10.86	58.11	9	22.63	3.560	56	12.42
Ag	(ppm)	^{107}Ag	1901	1.23	2725	1109	1.23	0.07	3739	948	0.284	0.071	5.21	0.98
Sb	(ppm)	^{121}Sb	9.65	5.62	18.88	6.31	3.99	0.07	1404	264	0.647	0.071	1584	290
Au	(ppm)	^{197}Au	0.236	0.160	0.320	0.068	0.105	0.071	1.300	0.250	0.071	0.071	1.33	0.20
Bi	(ppm)	^{209}Bi	1865	1061	4809	1453	0.5	0.071	40	7.48	0.880	0.071	61.5	9.49

All values below the detection limits were treated using an arbitrary value by dividing the detection limit by the square root of 2 (b.d.l./√2). Arbitrary value of 0.07 was used

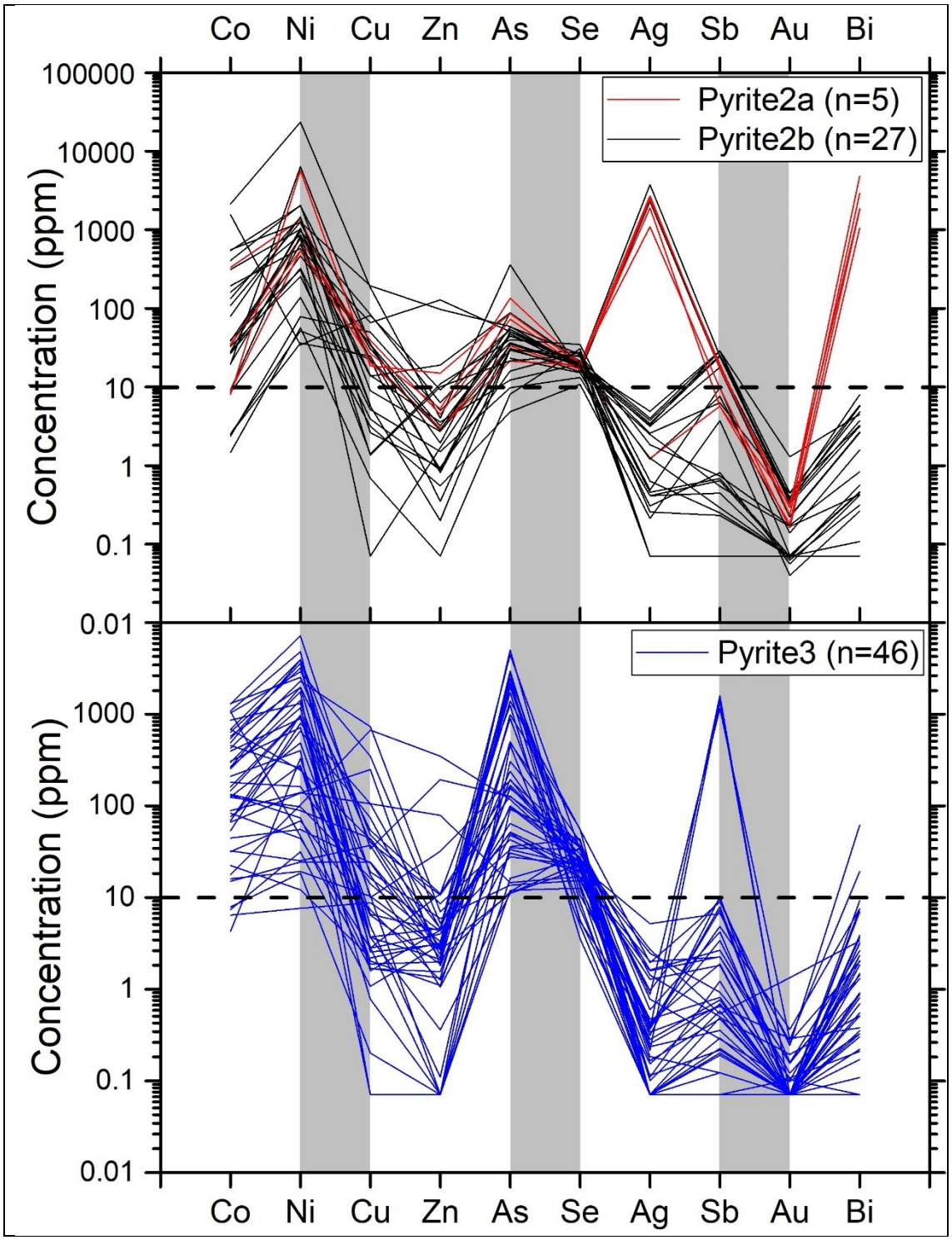

Fig. 74. Multi-element diagram of pyrite from Awak Mas and Salu Bullo. All values below detection limit were treated using an arbitrary value by dividing the detection limit by the square root of 2 (b.d.l./√2).

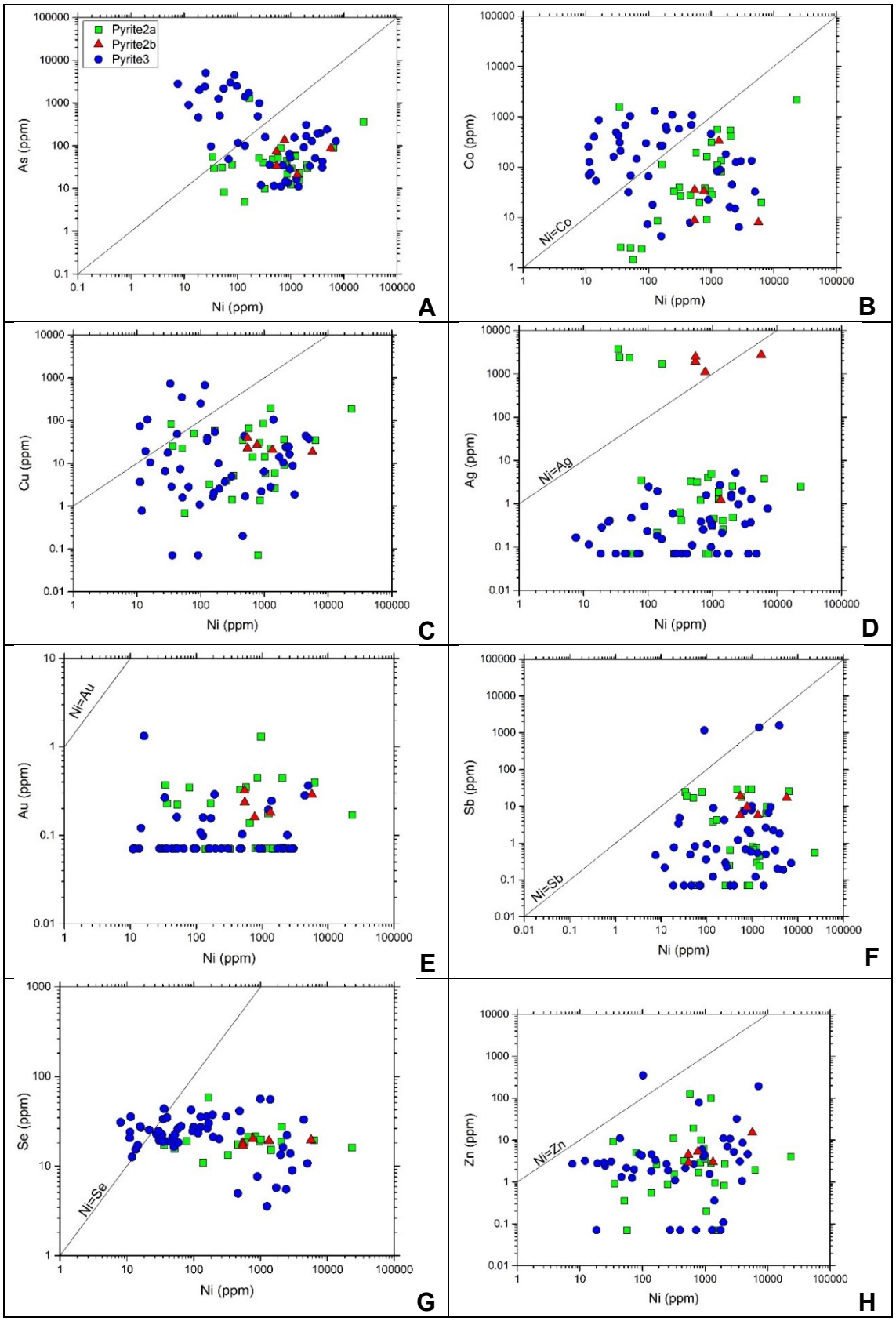
Pyrite2a
Pyrite2b
Pyrite3
As (ppm)
Ni (ppm)
A
Co (ppm)
Ni=Co
Ni (ppm)
B
Cu (ppm)
Ni (ppm)
C
Ag (ppm)
Ni=Ag
Ni (ppm)
D
Au (ppm)
Ni=Au
Ni (ppm)
E
Sb (ppm)
Ni=Sb
Ni (ppm)
F
Se (ppm)
Ni=Se
Ni (ppm)
G
Zn (ppm)
Ni=Zn
Ni (ppm)
H

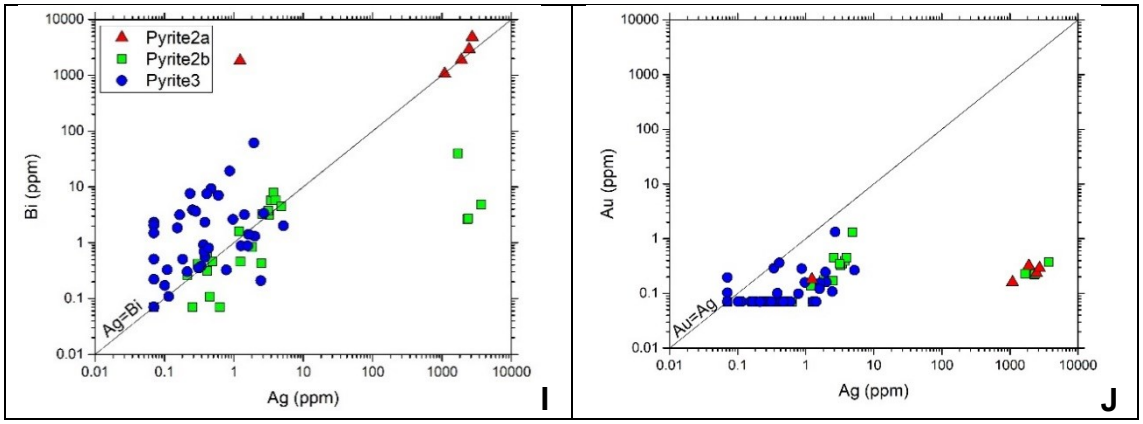

Fig. 75. Binary diagrams of: (A) As, (B) Co, (C) Cu, (D) Ag, (E) Au, (F) Sb, (G) Se, (H) Zn versus Ni, (I) Bi, and (J) Au versus Ag in pyrite obtained using LA-ICP-MS.

6.4.4 Copper minerals

Chalcopyrite in the Awak Mas and Salu Bullo deposits occurs at different textural types: (i) as inclusion in pyrite, (ii) as free grain in silicates (quartz, albite, pumpellyite) or carbonates, or (iii) as randomly dispersed blebs in sphalerite ("chalcopyrite disease" of Barton Jr. and Bethke 1987). Chalcopyrite is often replaced by tetrahedrite-tennantite and covellite (Fig. 76). Bornite is a trace mineral (less than 5 µm in length) and is replaced by pyrite.

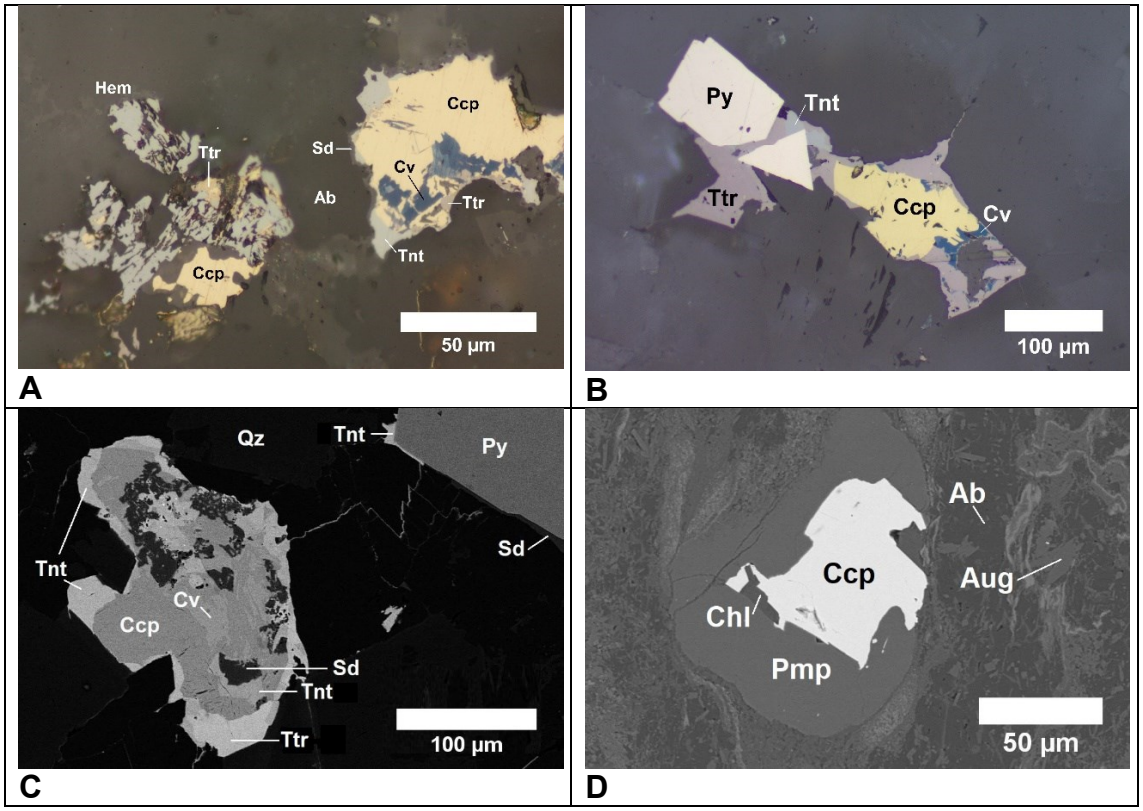

Fig. 76. Photomicrograph of copper minerals (A) Replacement of chalcopyrite by tetrahedrite-tennantite and covellite. On the left side of the image is euhedral hematite with interstitial chalcopyrite. (B-C) Multiple replacement processes involving Cu-Fe-As-Sb-S minerals (chalcopyrite-tetrahedrite-tennantite-covellite). All copper minerals are rimmed by thin (<5 μm) siderite. S69-25. (D) Chalcopyrite rimmed by pumpellyite, chlorite, albite and augite. Host rock is metabasite. S68-39.10.

6.4.5 Sphalerite

In general, ore minerals from the Awak Mas and Salu Bullo deposits lack sphalerite. From almost hundred fifty polished-thin sections, only nine grains of sphalerite were identified in nine samples. Host rocks of sphalerite are phyllite, hematitic mudstone and quartz veins. Sphalerite is enclosed in pyrite and rarely observed as a free grain. It is associated with galena and monazite. Some grains of sphalerite hosted in carbonaceous phyllite have blebs of chalcopyrite ("chalcopyrite disease")(Fig. 77A).

6.4.6 Trace element in sphalerite

A preliminary study of trace elements in sphalerite from the Latimojong Complex was conducted using LA-ICP-MS. From the limited number of materials, four out of nine grains were selected and ablated. None of them has chalcopyrite disease, as has been confirmed using SEM-EDX. All grains have irregular habit ranging from 10 to 50 μm (Figs. 77B-D).

Sphalerite is low in Fe (0.4 – 4.3%). The average concentration of In, Ge, Cd and Ga in sphalerite are 63 ppm; 0.9 ppm; 1.7 ppm and 6 ppm, respectively. Sphalerite contains less than 0.2 wt% Cd. Mercury content ranges from 320-530 ppm and nickel from 5 to 160 ppm. Mean concentration is 87 ppm for manganese (maximum of 280 ppm), 74 ppm for cobalt (maximum of 220 ppm), and 2,650 ppm for copper (maximum of 4,110 ppm). A higher concentration of silver (up to 2,500 ppm Ag) was found in sample S68-105.40, where irregular sphalerite (~50 μm in diameter) occurs together with galena and gold (both < 1 μm), all forming inclusions in a pyrite crystal (Fig. 77C).

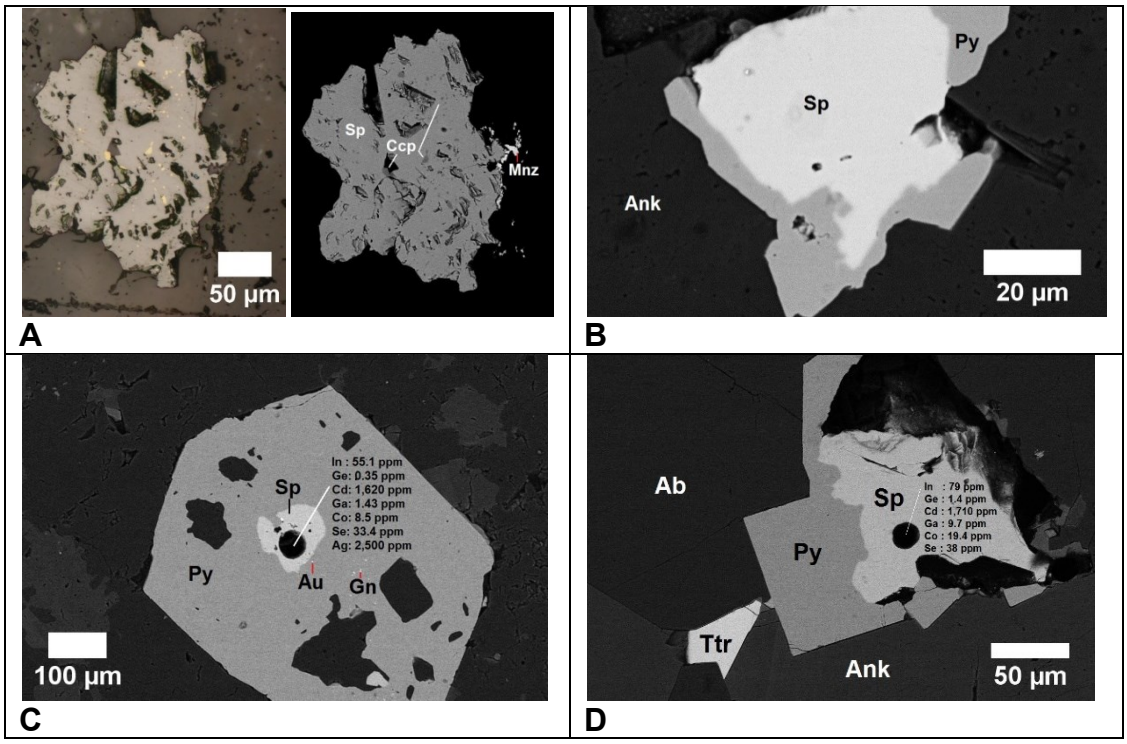

Fig. 77. Photomicrograph of sphalerite. (A) Chalcopyrite (yellow) blebs in a single crystal of sphalerite (grey). Reflected light. A192-189.40. (B) Blebs of gold. galena (bright minerals) and sphalerite occur as inclusions in pyrite. S69-25.80. (C) Sphalerite grain of sample S68-105.40 has high concentration of silver (up to 2,500 ppm). (D) BSE-image of ablated sphalerite with relatively high-Cd content.

Significant amounts of silver may be incorporated in the sphalerite lattice (Taylor and Radtke 1969) although further development on sphalerite studies indicates that higher concentration are almost always related to microscopic or submicroscopic inclusions of discrete Ag-minerals (Cook et al. 2009). In addition, the latter authors suggest that sphalerite is not as significant host for lattice-bound gold.

The sphalerite grains studied from Salu Bullo has high silver content is correlated with the existence of submicroscopic grain of gold. It is reasonable to expect that submicroscopic gold, or the so called invinsible gold in pyrite, was ablated together with sphalerite and resulted in the high silver content. This postulation might be correct because iron (4.3 wt% Fe) and nickel (160 ppm Ni) contents are extremely high (Table 35). Both elements are probably related to the pyrite host under the ablated sphalerite. Such a high Ni-content is commonly observed in pyrite from Salu Bullo.

Table 35. Minor and trace elements in sphalerite from the Salu Bullo deposit. Data are in ppm (except Fe).

Sample	Ag	As	Bi	Cd	Co	Cu	Cr
S68-105.40	2,500	7	2.80	1,620	8.50	1,800	b.d.l.
S68-128.70	4.1	0.60	0.02	1,642	47.60	4,110	b.d.l.
S69-25.00	7.6	b.d.l.	1.27	1,710	19.40	3,300	14.00
S69-24.50	16	17	1.70	1,740	220.00	1,380	9.70

Sample	Fe (wt%)	Ga	Ge	In	Hg	Mn	Mo
S68-105.40	4.3	1.43	0.35	55	431	280	0.09
S68-128.70	0.43	3.84	1.21	69	450	20	b.d.l.
S69-25.00	1.52	9.70	1.40	79	320	33	b.d.l.
S69-24.50	1.1	10.00	0.50	50	530	16	b.d.l.

Sample	Ni	Pb	Tl	Sb	Se	Sn	V
S68-105.40	160	70	0.16	16.50	33	0.90	1.70
S68-128.70	4.80	1.08	0.01	b.d.l.	10	0.62	0.06
S69-25.00	8.50	50	0.34	8.40	38	3.00	100
S69-24.50	60	23	0.04	2.20	19	0.60	b.d.l.

6.4.7 Galena

Galena forms irregular grains, commonly included in pyrite, quartz and calcite(Fig. 78A). Galena grains are <2 to 30µm in diameter (Fig. 78). Commonly small inclusions (<2 µm) or irregular grains occur large (>200 µm) pyrite crystals (Fig. 78C). Triangular pits, as typically seen in galena, are observed only in outcrop samples (sample MP01). Replacement of framboidal pyrite by galena is less common (Figs. 68A, E).

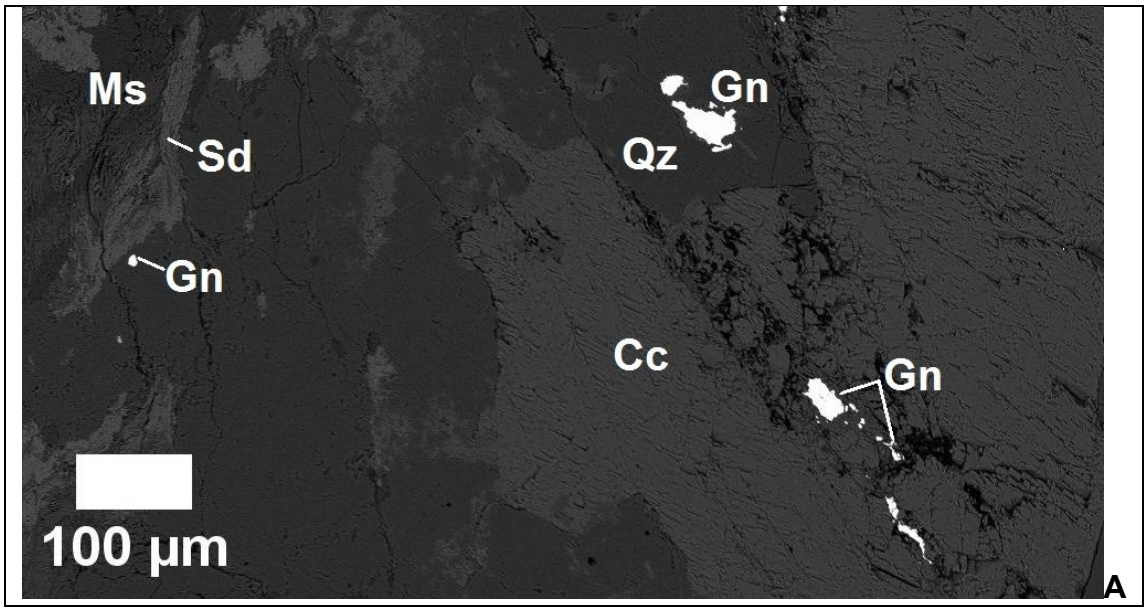

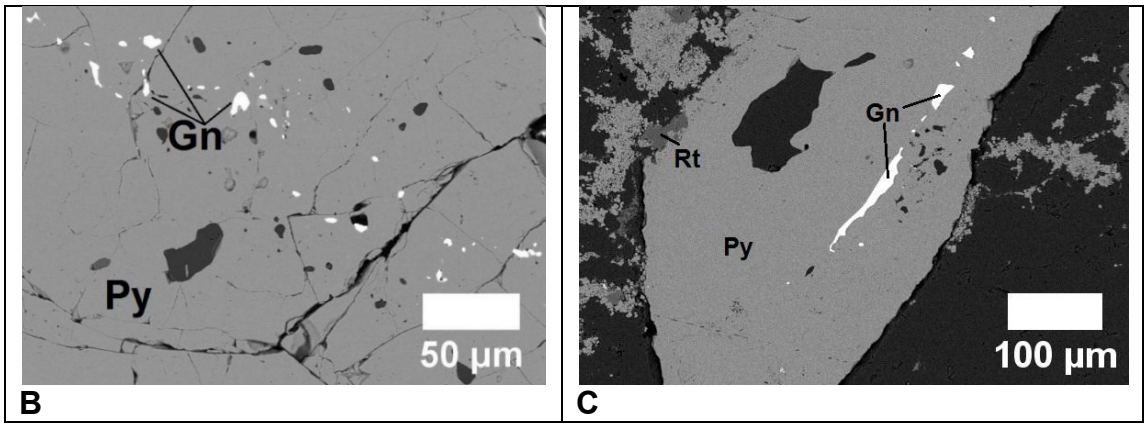

Fig. 78. A BSE images of galena. (A) Anhedral galena hosted by quartz and calcite. A192-189.40. (B) Irregular blebs of galena hosted by massive pyrite. (C) “A knife like” galena included in pyrite. A192-221.65.

6.4.8 Carrolite

One carrolite grain was observed in sample S68-143.80. It has a pale cream color under reflected light and occurs in association with pyrite, tetrahedrite-tennantite, chalcopyrite and covellite (Fig. 64A). Carrolite was quantified using the electron microprobe as $Cu_{0.97}Co_{1.30}Ni_{0.80}Fe_{0.03}S_{4.00}$. Three electron microprobe analyses of carrolite are shown in Table 36.

Table 36. Representative electron microprobe analyses of carrollite from the Salu Bullo deposit.

Sample	S68-143.80-1	S68-143.80-2	S68-143.80-3
As	0.00	0.00	0.06
S	41.23	41.01	41.24
Co	24.13	24.79	24.61
Cu	19.84	19.61	19.80
Ni	14.97	15.01	15.11
Fe	0.51	0.48	0.66
Total	100.67	100.89	101.48
As	0.00	0.00	0.00
S	4.00	4.00	4.00
Co	1.27	1.32	1.30
Cu	0.97	0.97	0.97
Ni	0.79	0.80	0.80
Fe	0.03	0.03	0.04

6.4.9 Sulfarsenides

Sulfarsenides include minerals that belong to the arsenopyrite – cobaltite – gersdorffite (FeAsS – CoAsS – NiAsS) solid solution series. Only cobaltite was detected at Awak Mas and Salu Bullo (Fig. 79A). A total of six grains of cobaltite

was observed in sample A687-157.90 (chlorite schist). Irregular grains range from 5 to 20 micron in size. None of them is associated with gold. The cobaltite was measured using SEM-EDX EVO MA 10 and the analyses are normalized to 100% (Table 37). The cobalt content is between 26.88 and 32.65 wt% (average of 26.88 wt% Co), arsenic between 35.43 and 42.44 wt% (average of 39.96 wt% As) and the average content of iron is 7.18 wt% (ranging from 4.82 to 11.46 wt% Fe). The average results correspond to $Co_{0.78}Fe_{0.19}Ni_{0.05}As_{0.82}S$. A graphical geothermometer based on the composition of Co, Fe, Ni – As – S in the sulfarsenide system is shown in Figure 79B (Klemm 1965), suggesting temperature of 400-500°C.

Table 37. Representative semi-quantitative analyses of cobaltite from the Awak Mas.

Sample	**Cob-1**	**Cob-1**	**Cob-1**	**Cob-1**	**Cob-1**	**Cob-2**	**Cob-2**
Point	**18**	**38**	**39**	**21**	**22**	**18**	**15**
As	38.26	42.26	42.44	38.18	41.24	41.92	35.43
S	21.04	19.22	19.37	20.38	22.6	19.32	26.24
Co	32.49	31.07	30.07	32.65	29.97	27.1	26.88
Ni	1.84	2.63	2.18	0	0	4.96	0
Fe	6.38	4.82	5.94	8.79	6.18	6.69	11.46
Total	100.01	100	100	100	99.99	99.99	100.01
As	0.78	0.94	0.94	0.80	0.78	0.93	0.58
S	1.00	1.00	1.00	1.00	1.00	1.00	1.00
Co	0.84	0.88	0.84	0.87	0.72	0.76	0.56
Ni	0.05	0.07	0.06	0.00	0.00	0.14	0.00
Fe	0.17	0.14	0.18	0.25	0.16	0.20	0.25

Cob-1: A687-157.90; Cob-2: S66-37.50:

The cobaltite shows a minor range of substitutions of Co by Fe and Ni. which falls within the solid solution at an average temperature around 400°C (Fig. 79B) of Klemm (1965). Considering that the gold at Awak Mas and Salu Bullo are not associated with sulfarsenides (cobaltite) and the microthermometric data from gold veins are generally less than 260°C, there is a strong possibility that the temperature of Klemm (1965) are too high and probably related to the greenschist metamorphism.

6.4.10 Bismuth phases

In sample A192-225 from the Awak Mas bore hole, one grain of a bismuth phase was observed as an inclusion (less than 2 µm) the kaolinite and quartz (Fig. 79C).

In the Salu Bullo deposit, a probable tellurobismuthinite (Bi_2Te_3)(?) with a size of 3 µm is hosted by chalcopyrite and hematite. Due to the small size of the grain, a stoichiometric calculation is difficult. The presence of bismuth is important because these minerals are associated with kaolinite and hematite (Fig. 79D), suggesting a late paragenetic position and oxidative process (Ciobanu et al. 2009).

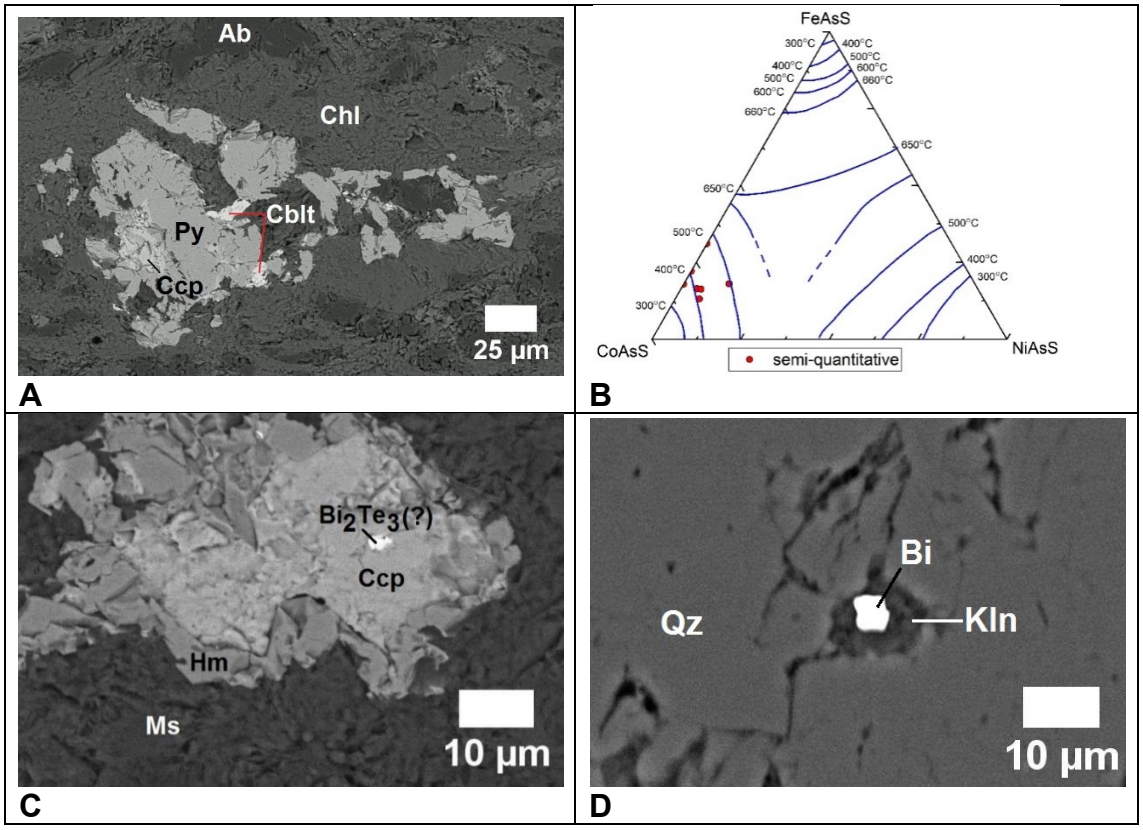

Fig. 79. A BSE image of cobaltite and bismuth phases. (A) Irregular cobaltite grains from the chlorite schist of the Awak Mas deposit. (B) FeAsS – CoAsS – NiAsS ternary diagram indicating a compositional variation of cobaltite from the Awak Mas and Salu Bullo of Klemm (1965). A BSE image of bismuthinite as inclusion in chalcopyrite (C) and in quartz (D).

In summary, the simplified mineral paragenesis and abundance of rock-forming and ore mineral are illustrated in Figure 80.

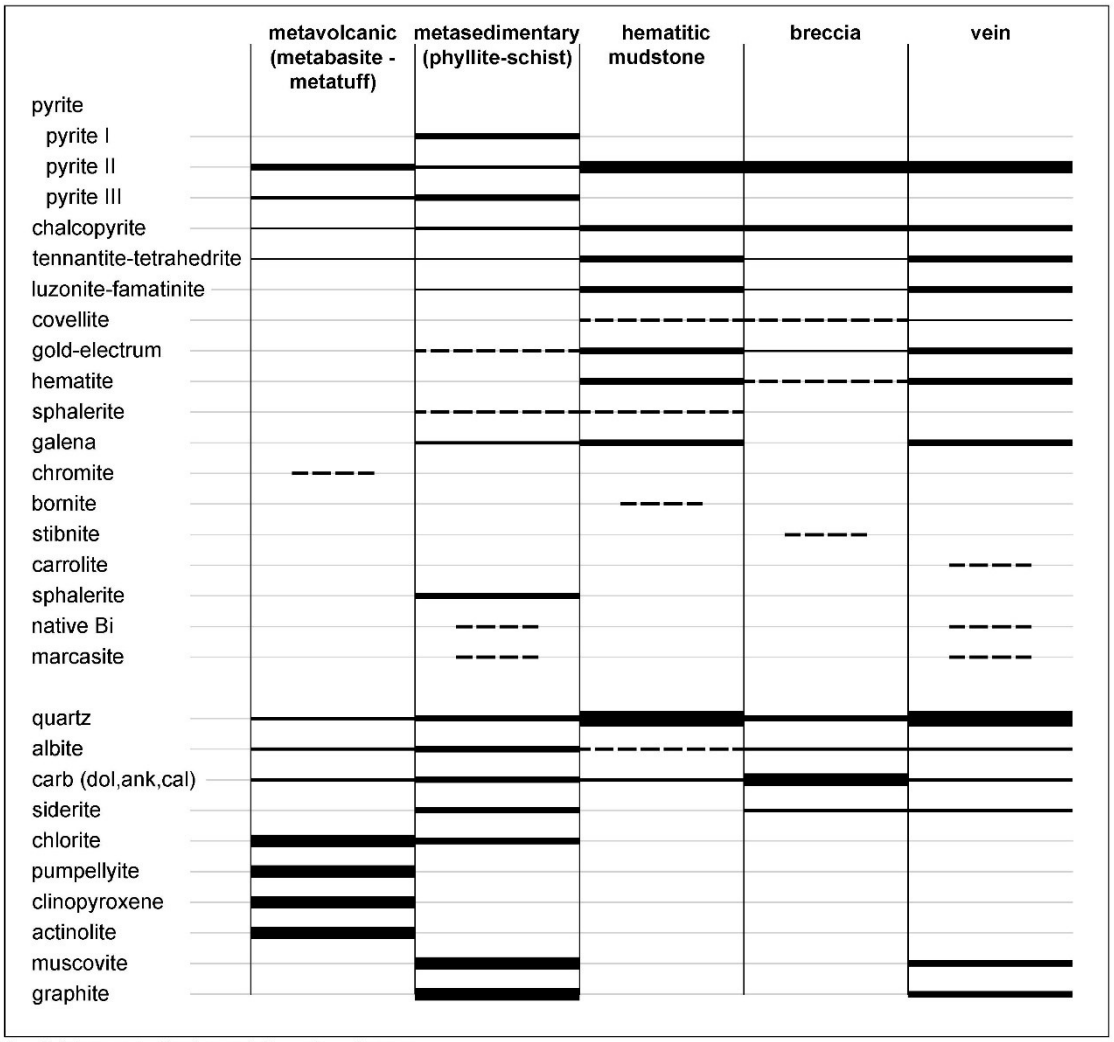

Line thickness indicates relative abundances
Pyrite I: framboidal pyrite, Pyrite II = euhedral pyrite, parallel foliation, Pyrite III = hydrothermal pyrite

Fig. 80 Simplified paragenetic sequence of main ore and alteration minerals in the Awak Mas and Salu Bullo deposit.

6.5 Hydrothermal alteration

6.5.1 Mineralogy

All rocks from drill core are moderately to intensely hydrothermally altered. Most of the alteration products are strongly influenced by the host rock composition. Silica, carbonate, white mica and albite alteration are distinguished. Silicification is characterized by the replacement of initial minerals by quartz. This type of alteration is often accompanied by sulphide (mainly pyrite-chalcopyrite) and extends from the veins outward into the host rock. Silicification is observed mainly around breccia fragments, with little of this alteration extending into intact host rock.

Ankeritic alteration is the most prominent carbonate alteration in all lithologies at Awak Mas and Salu Bullo. Ankeritic alteration is strongly controlled by structures, including foliation, microshears, fractures and faults.

Sericitization and carbonatiozation (dolomite-ankerite) are mainly observed in mafic metavolcanic rocks (Fig. 81). The proximal alteration consists mainly of albite and silica with most distal alteration being chlorite and calcite, accompanied by a lack of hydrothermal sulphide minerals.

Minor siderite is also present as thin rims around sulphides. Albite alteration is observed in host rocks of all compositions. Argillic alteration (kaolinite) is less common. Intense host-rock alteration is found less than 5 meter from veins and faults.

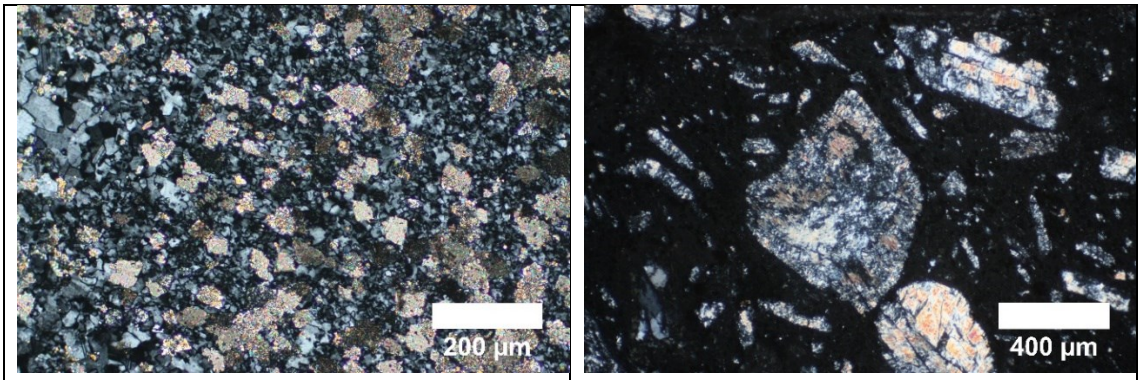

Fig. 81. Alteration minerals in Salu Bullo. (A) Dolomitisation of hematitic mudstone. S69-24.50. (B) Sericitization of plagioclase in basalt (S68-57.60).

6.5.2 Correlation coefficient analysis

In 2009, the mining company drilled 102 diamond drill holes with a total length of 9.738 m. Drill core (HQ – 63.5 mm in diameter) was generally sampled in every 1 - 1.8 m intervals. Core samples were split in half, with half core sent for assay and remaining half stored as reference core. The assay samples were crushed and a 200-500g split was pulverised. A fourty gram (40g) aliquot was analysed using the fire assay method (FAA40_AAS) at Geoservices LTD GeoAssay Laboratory at Bekasi, Indonesia. Thirty-three elements were further analyzed using ICP-MS method with Aqua Regia digestion. This exploration data has been validated for JORC reporting and is also used for this study. Data were filtered and correlation coefficient analysis was performed. Only data from Salu Bullo

were used because exploration data on Awak Mas were limited to gold and silver without any other trace element contents.

Gold and trace element data from Salu Bullo were selected in order to illustrate the correlation of elements during hydrothermal alteration. The values below the limit of detection (b.d.l.) were calculated using the mehod of Croghan and Egeghy (2003) by dividing the detection limit by the square root of 2 (b.d.l./√2).

Spearman rank correlations were used to calculate correlation coefficients (r) for selected elements. The Spearman rank correlation coefficient is suitable to populations that are not normally distributed and/or include outliers data (Rollinson 1993). A matrix of 73 samples of quartz veins from the Salu Bullo core is presented in Figure 82 and Table 38. Other lithologies were included in some diagrams for comparison. The result shows that gold has significant positive correlation with Ag, As, Cd, S and Sb. Other elements such as Al, Ba, Bi, Ca, Co, Cr, Cu, Fe, K, Mg, Mn, P and Zn are depleted relative to gold (Fig. 82A). Figures 82B-M illustrate distribution of several elements including major elements (Ca, Na, Mg, Fe) and trace elements in all litologies.

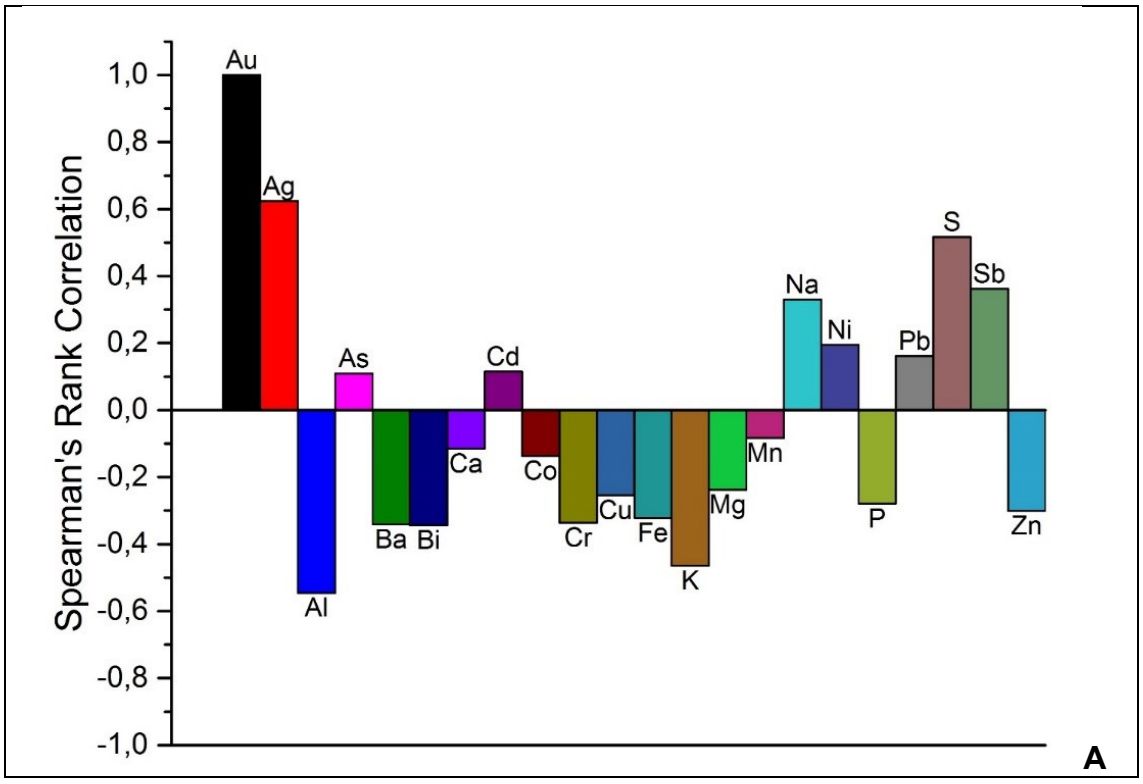

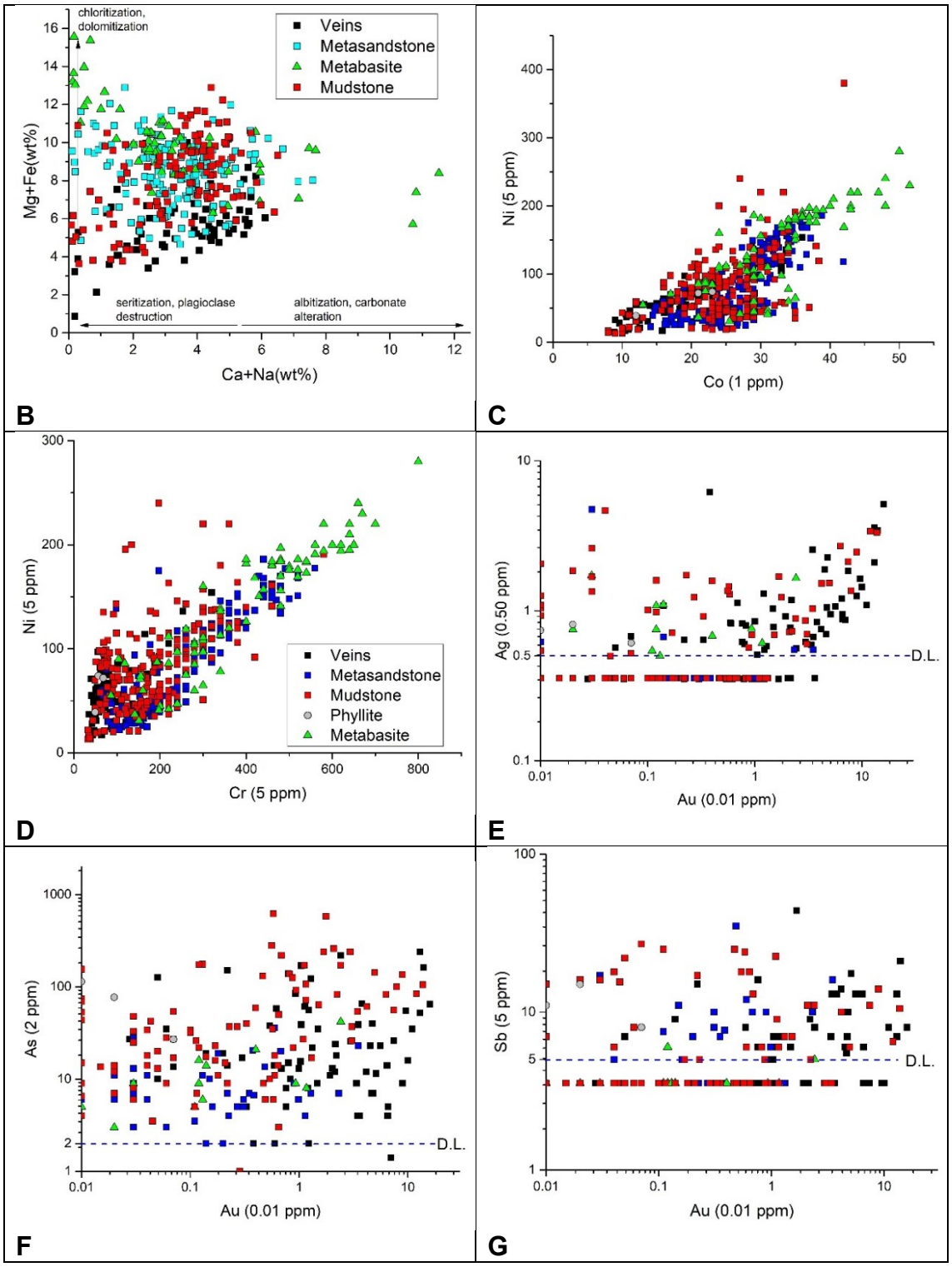
chloritization, dolomitization
Veins
Metasandstone
Metabasite
Mudstone
Mg+Fe(wt%)
Ca+Na(wt%)
seritization, plagioclase destruction
albitization, carbonate alteration
B
Ni (5 ppm)
Co (1 ppm)
C
Ni (5 ppm)
Cr (5 ppm)
Veins
Metasandstone
Mudstone
Phyllite
Metabasite
D
Ag (0.50 ppm)
Au (0.01 ppm)
D.L.
E
As (2 ppm)
Au (0.01 ppm)
D.L.
F
Sb (5 ppm)
Au (0.01 ppm)
D.L.
G

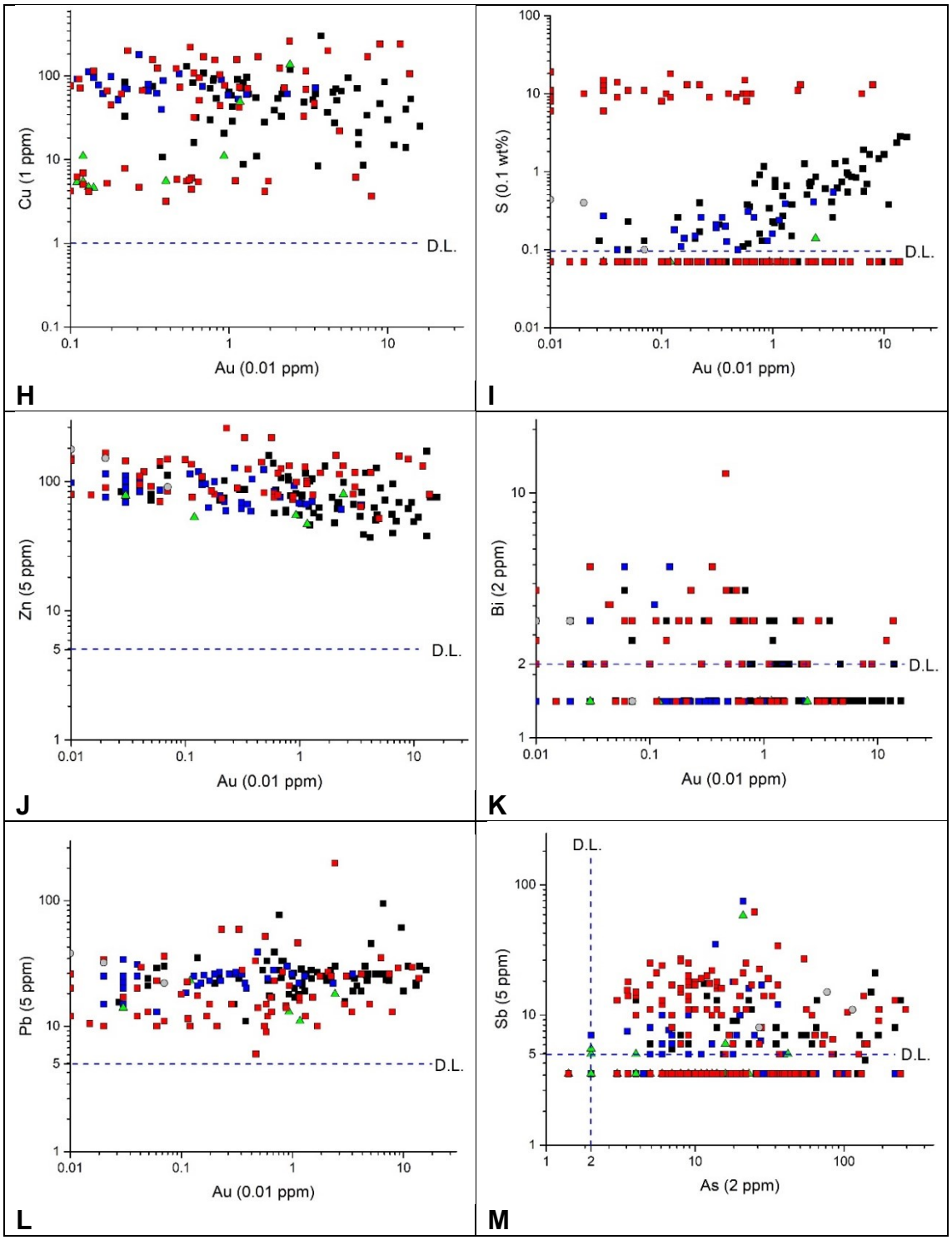

Fig. 82. Histogram and bivariate plots of quartz veins at Salu Bullo. (A) Spearman's correlation coefficient analyses for Salu Bullo. (B-K) Bivariate plot of different elements obtained from the exploration data of Salu Bullo. Number in bracket represents detection limit of element from the instruments (AAS and ICP-MS).

Table 38. Spearman's correlation coefficients for Salu Bullo veins where n=73.

	Au	Ag	Al	As	Ba	Bi	Ca	Cd	Co	Cr	Cu	Fe	K	Mg	Mn	Na	Ni	P	Pb	S	Sb	Zn
Au	1.00	0.62	-0.55	0.11	-0.34	-0.34	-0.12	0.12	-0.14	-0.34	-0.25	-0.32	-0.46	-0.24	-0.08	0.33	0.19	-0.28	0.16	0.52	0.36	-0.30
Ag		1.00	-0.48	-0.13	-0.19	-0.23	0.16	-0.17	-0.10	-0.26	-0.06	-0.18	-0.44	-0.06	0.02	0.20	0.14	-0.11	0.31	0.37	0.29	-0.30
Al			1.00	0.43	0.64	0.47	-0.35	0.41	0.53	0.45	0.49	0.59	0.90	0.00	0.43	-0.16	0.25	0.55	-0.19	-0.63	-0.16	0.76
As				1.00	0.26	0.17	-0.43	0.89	0.29	-0.04	0.30	0.26	0.45	-0.28	0.36	0.20	0.31	0.36	-0.19	-0.10	0.22	0.50
B					0.13	0.56	-0.13	0.16	0.33	0.21	0.24	0.31	0.18	-0.19	0.41	0.30	0.48	0.42	0.28	-0.23	0.00	0.37
Bi						1.00	-0.06	0.19	0.52	0.33	0.51	0.62	0.41	-0.02	0.58	0.09	0.44	0.63	0.20	-0.25	-0.05	0.57
Ca							1.00	-0.45	0.05	0.40	0.11	0.15	-0.44	0.79	-0.09	-0.13	-0.09	-0.25	0.21	0.23	0.01	-0.26
Cd								1.00	0.37	0.06	0.17	0.33	0.48	-0.25	0.39	0.18	0.43	0.31	-0.21	-0.24	0.20	0.50
Co									1.00	0.72	0.60	0.87	0.48	0.27	0.50	-0.08	0.72	0.36	0.17	-0.21	0.15	0.59
Cr										1.00	0.56	0.75	0.34	0.63	0.35	-0.17	0.42	0.13	0.09	-0.34	0.07	0.40
Cu											1.00	0.66	0.46	0.25	0.61	-0.21	0.48	0.41	0.31	-0.25	0.05	0.51
Fe												1.00	0.51	0.38	0.53	-0.08	0.55	0.43	0.20	-0.26	0.05	0.63
K													1.00	-0.13	0.46	-0.20	0.29	0.54	-0.22	-0.65	-0.10	0.74
Mg														1.00	-0.14	-0.31	-0.01	-0.34	0.04	0.08	-0.10	-0.02
Mn															1.00	0.12	0.68	0.77	0.26	-0.39	0.15	0.68
Na																1.00	0.09	0.26	-0.20	0.16	0.04	-0.07
Ni																	1.00	0.38	0.18	-0.18	0.22	0.48
P																		1.00	0.09	-0.49	-0.07	0.63
Pb																			1.00	0.14	0.28	0.09
S																				1.00	0.20	-0.43
Sb																					1.00	0.08
Zn																						1.00

6.5.3 Trace elements in plagioclase feldspar

Spot analyses of plagioclase feldspar from the metavolcanic rocks and veins from Salu Bullo show distinct fields for the mineralized quartz vein and barren host rocks. Mineralized quartz veins are characterized by high content of Rb (15.40 – 20.80 ppm). Metabasites have the highest concentration of Sr (362 – 1200 ppm), Y (9 – 33.50) and are enriched in LREE-HREE. The sample with the highest REE concentrations (metabasite) has no clear Eu-anomaly (Eu/Eu* 0.87 – 1.24) and Ce-anomaly (Ce/Ce* 0.89 – 1.13)(Table 39).

Three types of rare earth element pattern are distinguished by differences in REE slope, as well as the presence and size of Eu-anomaly. Quartz veins are La-enriched and show downward sloping patterns with pronounced positive Eu-anomaly (Eu/Eu*. 2.48 – 2.53). Metasiltstone, metasandstone and hematitic mudstone have similar “hump shaped” patterns; however, ΣREY content of metasandstone is higher than in two other lithologies. Metasiltstone has ΣREY content up to 83 ppm, whereas the ΣREY content of metasandstone and hematitic mudstone are generally lower than 1.5 ppm (Fig. 83)(Table 39).

The correlation of Ce- and Eu-anomalies with the distance from the mineralized veins is illustrated in Figure 84. The results demonstrate progressive increasing values of the Ce-anomaly and decreasing Eu-anomaly with increasing distance from the vein. However, the change of Ce-anomaly relative to distance is not as significant as Eu-anomaly. One albite type close to vein has the highest Eu-anomaly (Fig. 84). Figures 84C-D illustrates a scatter plot of Ce-anomaly versus Eu-anomaly. Ce-anomalies in all samples are generally less than 1.21 but Eu-anomalies and Ce/Lu_N are relatively scattered in distribution.

Table 39. Representative LA-ICP-MS analyses of albite

Lithology	Vn	Vn	Vn	Vn	Vn	Vn	Ms	Ms	Ms	Ms	Ms
Sample code	S53-103 -a1	S53-103 -a2	S53-103 -b1	S53-103 -b2	S69-2 5-1	S69-25 -2	S68-130.30 -1	S68-94.95 -1	S68-94.95 -2	S68-94.95 -3	S68-94.95 -4
Rb	15.4	16.4	20.8	17.7	16.2	16	0.0355	0.234	0.207	0.156	0.0616
Sr	33.6	40.1	47	77.2	92.5	41.4	65	71.4	100.6	97.8	107.8
Y	0.707	0.761	1	0.82	0.8	0.72	0.65	0.14	0.55	0.7	0.132
La	0.722	0.743	0.959	0.79	0.752	0.72	0.04	0.0203	0.0291	0.0169	0.0102
Ce	1.21	1.28	1.59	1.32	1.26	1.22	0.105	0.086	0.122	0.0563	0.035
Pr	0.138	0.145	0.18	0.146	0.14	0.135	0.0167	0.0146	0.0274	0.011	0.0062
Nd	0.528	0.538	0.689	0.583	0.544	0.517	0.101	0.087	0.172	0.068	0.043
Sm	0.11	0.104	0.135	0.109	0.101	0.102	0.047	0.0266	0.08	0.0354	0.0142
Eu	0.086	0.084	0.1087	0.084	0.087	0.081	0.019	0.0097	0.0235	0.012	0.0031
Gd	0.096	0.107	0.125	0.098	0.104	0.09	0.082	0.037	0.1	0.073	0.0207
Tb	0.0146	0.0162	0.0206	0.0153	0.017	0.0148	0.016	0.0054	0.0157	0.0158	0.0037
Dy	0.106	0.112	0.142	0.108	0.112	0.103	0.115	0.0287	0.101	0.108	0.0179
Ho	0.0229	0.0236	0.0299	0.0242	0.0249	0.0216	0.021	0.0065	0.0188	0.03	0.0055
Er	0.076	0.0726	0.108	0.084	0.086	0.076	0.054	0.0145	0.052	0.103	0.0125
Tm	0.0124	0.0119	0.0164	0.0131	0.0138	0.0123	0.0084	0.00255	0.0079	0.0175	0.00216
Yb	0.094	0.098	0.125	0.109	0.101	0.096	0.062	0.0086	0.043	0.124	0.0092
Lu	0.0149	0.0163	0.0213	0.0196	0.0179	0.0169	0.01	0.00191	0.0077	0.025	0.00223
Eu/Eu*	2.55	2.43	2.55	2.48	2.59	2.58	0.93	0.94	0.80	0.72	0.55
Ce/Ce*	0.93	0.94	0.93	0.94	0.94	0.95	0.98	1.21	1.05	1.00	1.06
$(La/Yb)_N$	5.22	5.15	5.21	4.92	5.06	5.09	0.44	1.60	0.46	0.09	0.75
$(La/Gd)_N$	6.31	5.83	6.44	6.77	6.07	6.72	0.41	0.46	0.24	0.19	0.41
Ce/Lu_N	2.00	1.93	1.84	1.66	1.73	1.78	0.26	1.11	0.39	0.06	0.39
ΣREY	3.9378	4.1126	5.2499	4.3232	4.1606	3.9256	1.3471	0.48936	1.3501	1.3959	0.31759

Representative LA-ICP-MS analyses of albite (cont)

Lithology	Hm	Hm	Mst	Mst	Mst	Mst
Sample code	S69-24.50 -2	S69-24.50 -1	S68-113.20 -1	S68-105.25 -5	S68-105.25 -6	S68-105.25 -2
Rb	0.0471	0.0167	0.317	0.321	0.107	0.191
Sr	84	4.9	570	362	1200	1080
Y	0.62	0.187	9	33.4	25	16.8
La	0.019	0.0166	1.45	10.6	0.794	0.9
Ce	0.055	0.043	3.2	11.6	3.96	4
Pr	0.016	0.0085	0.52	1.02	0.9	0.88
Nd	0.085	0.048	3.1	4.28	5.56	5.2
Sm	0.042	0.024	1.17	1.76	2.49	1.99
Eu	0.017	0.0056	0.54	0.752	0.87	0.69
Gd	0.051	0.03	1.51	3.15	3.72	2.92
Tb	0.022	0.0045	0.226	0.75	0.624	0.46
Dy	0.13	0.026	1.3	5.6	3.78	2.78
Ho	0.026	0.0047	0.25	1.25	0.793	0.53
Er	0.071	0.0157	0.64	3.82	2.25	1.32
Tm	0.0087	0.00212	0.085	0.569	0.31	0.163
Yb	0.055	0.0118	0.5	3.63	1.96	0.95
Lu	0.0078	0.0024	0.066	0.531	0.322	0.146
Eu/Eu*	1.12	0.64	1.24	0.97	0.87	0.87
Ce/Ce*	0.76	0.88	0.89	0.85	1.13	1.09
$(La/Yb)_N$	0.23	0.96	1.97	1.98	0.28	0.64
$(La/Gd)_N$	0.31	0.46	0.81	2.83	0.18	0.26
Ce/Lu_N	0.17	0.44	1.19	0.54	0.30	0.67
ΣREY	1.2255	0.42992	23.557	82.712	53.333	39.729

Abbreviations: Hm:hematitic mudstone; Ms:metasandstone; Vn:Quartz vein, Mst:metasiltstone. $Ce/Ce^* = Ce_N/\sqrt{[(La_N).(Pr_N)}$ $Eu/Eu^* = Eu_N/\sqrt{[(Sm_N).(Gd_N)}$ according to Taylor and McLennan (1985); Eu_N. Sm_N. Gd_N = chondrite normalized McDonough and Sun (1995); $(La/Yb)_N$ $(La/Gd)_N$ are normalized concentration ratios in the selected samples

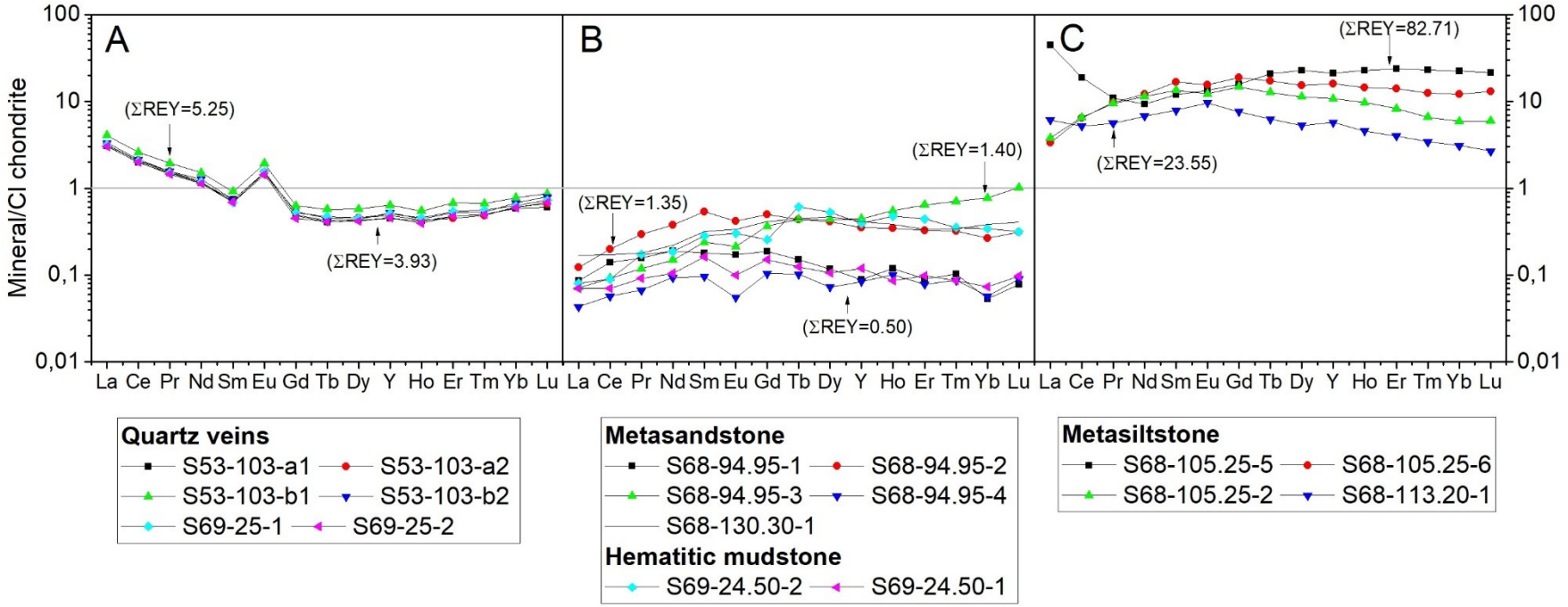

Fig. 83. Cl-Chondrite normalized REY fractionation trends for albite. Number in brackets are ΣREY ranges in ppm

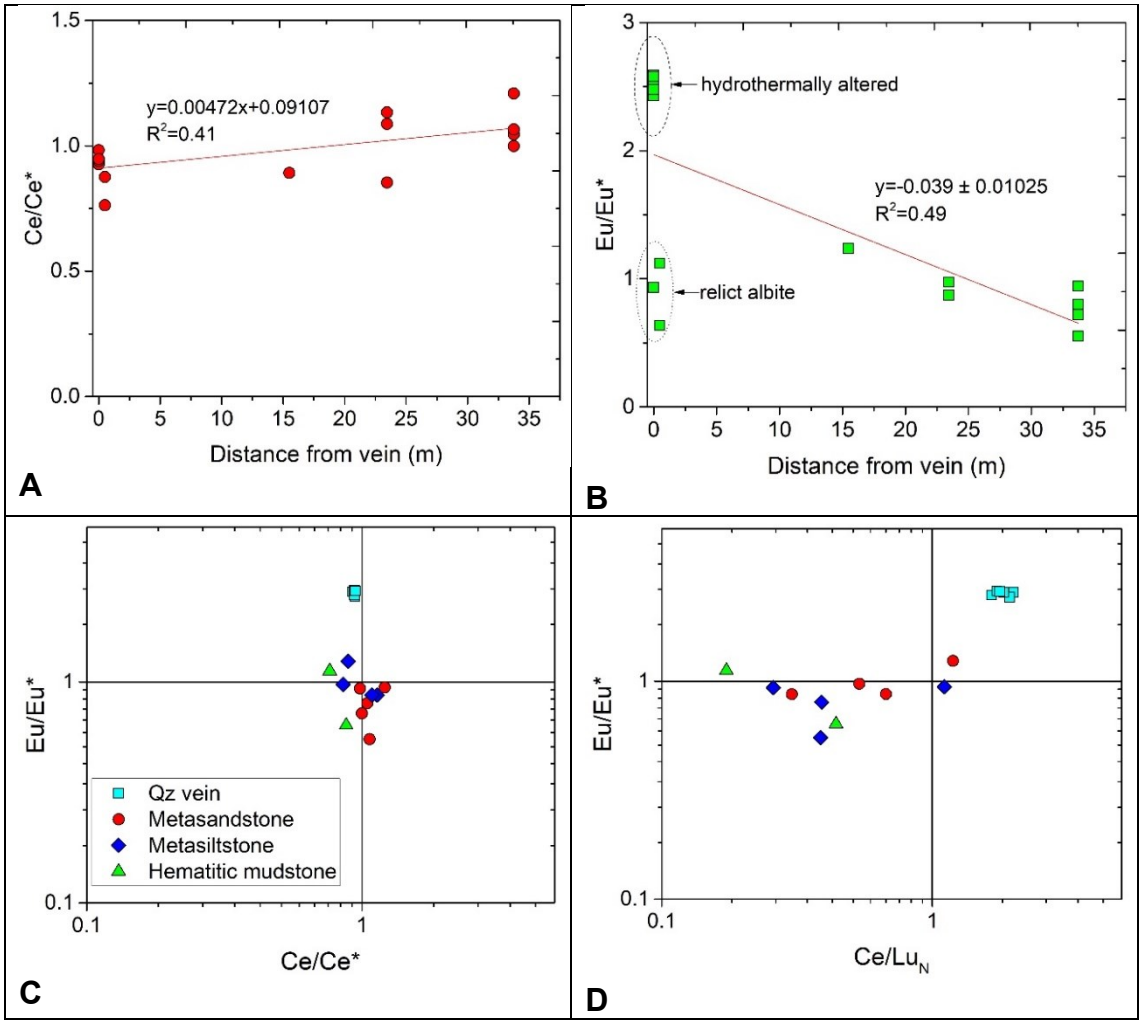

Fig. 84. Plots representing REY distributions in albite. (A) Ce/Ce* vs. distance from vein. illustrating slightly progressive development of Ce-anomaly with increasing distance from vein. (B) Eu/Eu* vs. distance from vein. illustrating the decreasing of Eu-anomaly with increasing distance from vein. (C) Ce/Ce* vs. Eu/Eu* discriminates veins and host rocks. (D) Ce/Lu_N vs. Eu/Eu*. Normalization values after McDonough and Sun (1995). $Ce/Ce^*=Ce_N/[(La_N*Pr_N)^{0.5}]$. $Eu/Eu^*=Eu_N/[(Sm_N*Gd_N)^{0.5}]$.

7. FLUID INCLUSION AND STABLE ISOTOPE

7.1 Introduction

Gold in Awak Mas and Salu Bullo is associated with (i) quartz - pyrite – (hematite) - Au veins and (ii) quartz – sulphide – (sulphosalt) – Au veins. In this chapter, fluid inclusion microthermometry is used to determine the *P-T* conditions and fluid evolution during vein mineralization. Crush leach analysis of quartz and carbonate unravel the chemical factors controlling the ore-forming processes. The carbon and oxygen isotopes of carbonate were studied in order to (1) illustrate the alteration effect between altered and unaltered samples, and (2) to compare the oxygen isotope data as thermometer with those obtained through the chlorite, microthermometric and crush-leach data of fluid inclusion.

7.2 Sampling and analytical methods

Representative vein and host rock samples from the Salu Bullo and Awak Mas gold fields were collected from outcrops and 12 drill cores. Nineteen double-polished sections (Table 40), which represent the various hydrothermal alteration systems with and without gold mineralization were examined petrographically, and of these nine samples were selected for microthermometric analysis.

Sixteen samples of carbonate were chosen from different lithology, including altered and non-altered samples. Carbonates were sampled using a dental drill and stored in a plastic vials. Compositions of samples were evaluated using a SEM-EDS EVO MA 10 to understand the different chemical composition of carbonate.

Table 40. Description samples used for fluid inclusion methods

Sample	Location	Description	Mineralogy	Analytical method
S053-101	SB	Breccia veins	Qz+Ab+Sid+ (Spn+Mnz+Py+ Ccp+Fam +Ttr+ Gn+Au)	1
S053-103	SB	Breccia veins	Qz+Ab+Cb (Ap+Rt+Mnz+ Hem+Spn+Goy+Py+Ccp +Tnt+Fam+Luz+Gn+Au)	1
S050-33.90	SB	Silicified volcaniclastic	Qz+Cb (Ap+Mnz+Py)	1
S069-24.50	SB	Qz veins within hematitic mudstone	Qz+Ab+Sid (Mnz+Rt+Hem+Ap +Py+Ccp+Fam+Luz+Sp+Gn+Au)	1
S069-25	SB	Qz veins within hematitic mudstone	Qz+Ab+Sid (Mnz+Hem+Kln+Ph +Py+Ccp+Fam+Tnt+Luz+Gn+Bn+ Au)	1
S050-80.30	SB	Qz veins within metavolcanic rock	Chl+Qz+Cb (Amp)	1
S068-132.90	SB	Sulphide-sulphosalt-Au Qz veins	Qz+Ab (Kln+Mnz+Hem+Py+ Ccp+Hg Ttr+Luz+Au)	1
SBD03	SB	Outcrop	Qz+Chl+Lim (Py)	1
S68-107	SB	Qz veins within phyllite	Qz+Sid+Ank (Ser+Ab+Sid+Hem+ Py+Luz+Fam+Au)	1
A192-155.70	AM	Graphitic mica schist	Qz+Ms+Ab (Mnz+Rt+Ap+Py+Gn)	1
A192-177.20	AM	Breccia veins	Cb+Ab+ (Rt+Mnz+Py+Gn+Ccp)	1
A198-241	AM	Graphitic mica schist	Cb+Ab+ (Rt+Mnz+Py+Au)	1
A683-46.80	AM	Qz-Cb veins with chlorite alteration	Qz+Cb+Chl (Py)	1
ONG01.1	AM	Qz veins outcrop within Phyllite	Qz+Ab+Sid (Py)	1
GRS08	SB	Barren Qz veins in greenstone. outcrop	Qz	1+2
A687-235	AM	Qz-Cb veins within phyllite	Qz+Dol (Py)	1+2
A687-235-dol	AM	Dolomite separated from Qz-Cb veins	Dol (Py)	1+2
MP01.1	AM	Pyrite-Au Qz veins outcrop	Qz (Py+Hem)	1+2
MP02	AM	Quartz veins in syn-mineralized fault	Qz (Ank+Py+Hem+Gn)	1+2
MP03	AM	Pyrite-Au Qz veins outcrop	Qz (Py+Hem+Gn)	1+2

Sample	Location	Description	Mineralogy	Analytical method
A685-5	AM	Sulphide-sulphosalt-Au Qz veins	Qz (Py+Ttr+Au)	1+2
A676-7310	AM	Sulphide-sulphosalt-Au Qz veins	Qz (Py+Ttr+Au)	1+2
A685-20	AM	Sulphide-sulphosalt-Au Qz veins	Qz (Py+Gn+Ttr+Au)	1+2

Abbreviations after (Whitney and Evans 2010); Alteration minerals are underlined.
Analytical method: 1: Raman spectroscopy on fluid inclusions; 2: Microthermometry

7.3 Fluid inclusion petrography

Fluid inclusions were observed in quartz, dolomite and plagioclase (albite). The focus in this study are the fluid inclusions trapped in quartz and dolomite, because most inclusions in albite occur as cloudy, irregular inclusions less than 5 µm in diameter, which may be regarded as secondary inclusions. Petrography and microthermometry results on quartz and carbonate are shown in Appendix F.

7.3.1 Fluid inclusions in pyrite-Au quartz veins

Pyrite-Au quartz veins are represented by samples MP01.1, MP02 and MP03 (Table 40). Based on the compositions, three different types are distinguished: low salinity aqueous inclusions with CO_2 (type I), H_2O-NaCl (type II) and H_2O-NaCl containing solid phases (type-III).

Quartz: inclusion type I. The inclusions contain vapour CO_2-liquid H_2O at room temperature with sizes between 5 and 15 µm (Fig. 85A-C). Inclusions occur isolated and scattered in quartz, which may imply a primary origin (Fig. 85A). H_2O with minor amounts of CO_2 and probably minor N_2 are the main volatiles (Fig. 86A). Quartz from this type is characterised by strong deformation textures and shows polygonal grains with grain boundaries meeting at 120-degree angles. Negative crystal-shaped inclusions are less common (Fig. 85B).

The volume fraction of vapour is about 0.14-0.15 with CO_2 mole fraction less than 0.15 (χ^{vap}= 0.10 to 0.144)(Fig. 85B-C). Minor N_2 was detected in some of the inclusions along with low-ordered graphite (Fig. 86A).

Quartz: inclusion type II. Type II inclusions are one-phase (L_{H2O}) or two-phase (V_{H2O} + L_{H2O}) liquid-rich aqueous inclusions (Fig. 85D and Fig. 86B). They generally have round, irregular to elliptical shapes. Inclusions are 5 to 40 µm in diameter. These most abundant inclusions occur in clusters and sometimes as trails along healed fractures, which do not cut across the crystal boundaries of quartz. These features suggest a primary or pseudo-secondary origin.

Quartz: inclusion type III. These inclusions are one-phase inclusions with locally small opaque mineral inclusions that were identified as anatase (5 µm in size) using Raman spectroscopy (sample MP02). The inclusions contain about 10 vol.% liquid phase at room temperature (Table 41).

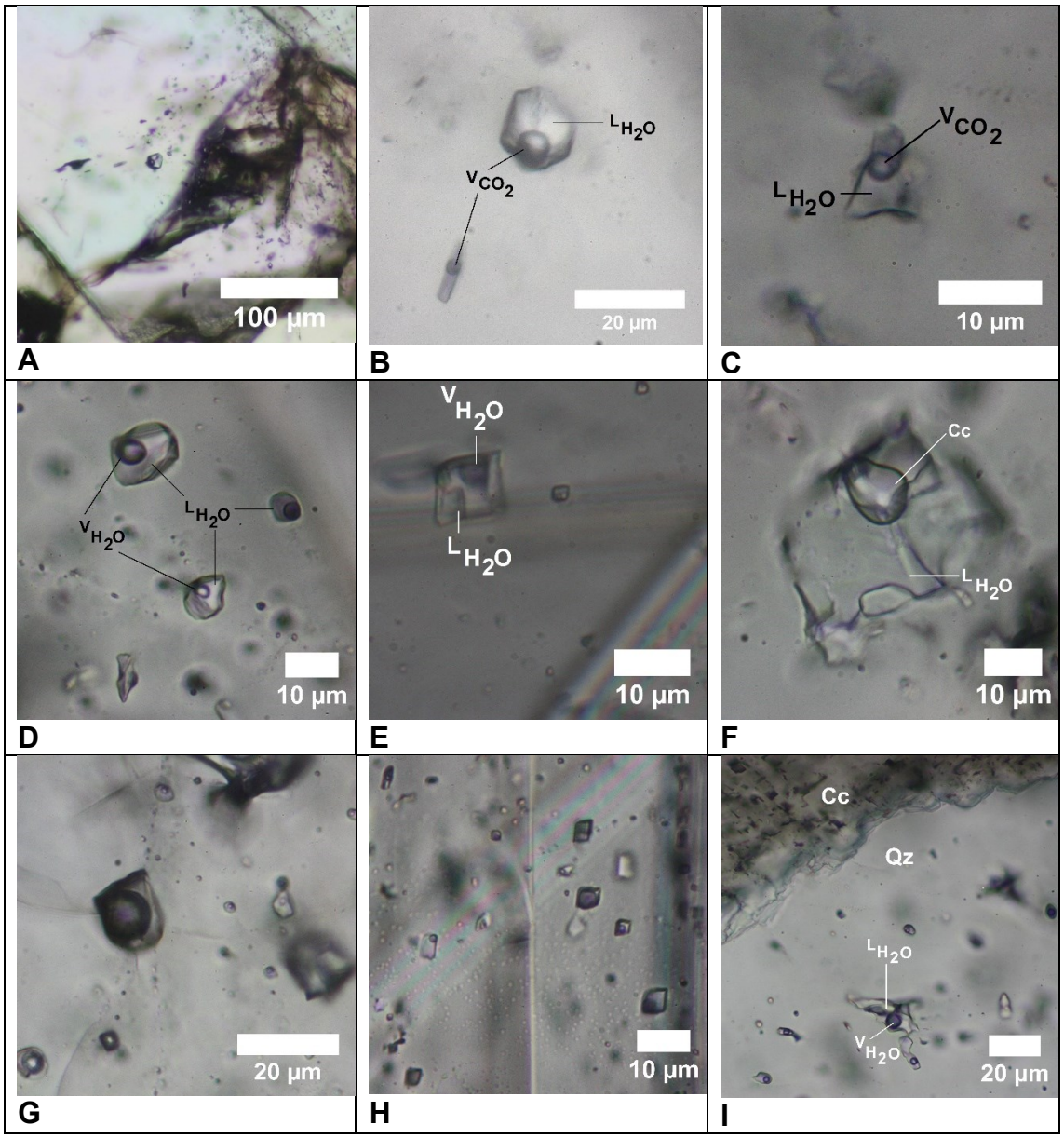

Fig. 85. Photomicrographs of fluid inclusions trapped in quartz at room temperature. (A) Isolated CO_2 bearing fluid inclusion hosted in quartz. (B). Enlargement of Figure 85A. A big isolated fluid inclusion containing liquid H_2O and vapour CO_2 at room temperature which has been confirmed using Raman spectroscopy. Sample S69-25. (C) Type I inclusion hosted in quartz from sample MP02. Boundary between liquid CO_2 and vapour CO_2 is not clearly visible but gas can be detected using Raman spectroscopy. (D) Primary aqueous inclusion of type II hosted in quartz grain from sample MP03. (E) Photomicrograph of type-II inclusions hosted in dolomite (A683-4680) (F) highly irregular shaped inclusion with calcite daughter crystal (inclusion type-III). (G-H) Photomicrograph of fluid inclusion type-II from sample A687-235 with variable volume fractions of the vapour phase hosted in quartz (G) and dolomite (H). (I) Irregular aqueous inclusions host in quartz.

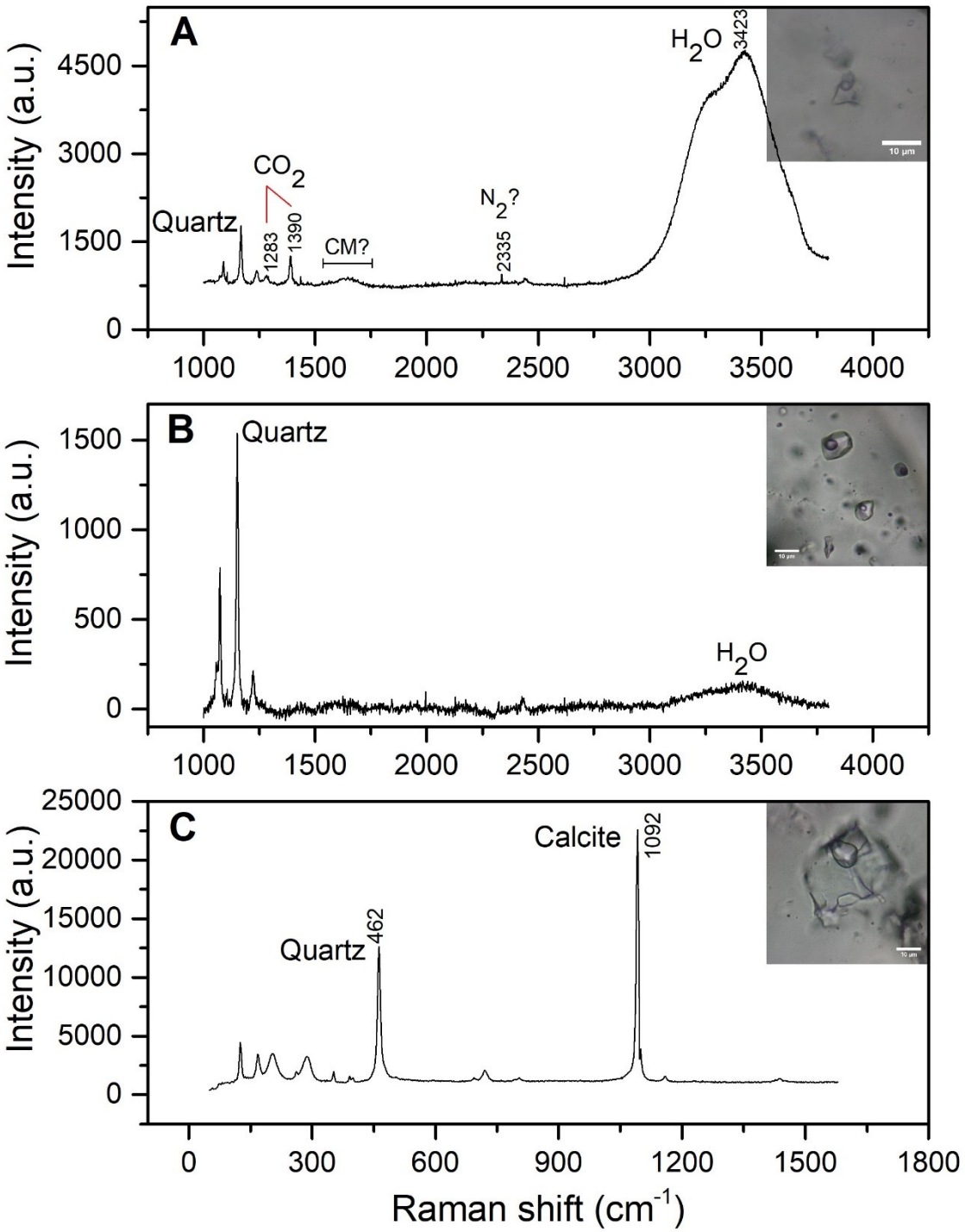

Fig. 86 Raman spectra of fluid inclusions. (A) Aqueous inclusions with minor amounts of salt and CO_2 (type I). Inclusion probably contains trace amounts of CM (carbonaceous material) and N_2. (B) Type II fluid inclusion containing aqueous fluid. (C) Type III fluid inclusion with calcite as a daughter mineral.

Table 41. Summary of microthermometric data for fluid inclusions.

Sample	n	Volume fraction (vap)	Inclusion type	Size (μm)	Bulk density (g/cc)	$T_m(CO_2)$ (°C)	T_m(ice) (°C)	T_m(clat) (°C)	T_h(total) (°C)	Salinity (eq% NaCl)
Barren veins										
GRS08	29	0.15-0.25	II	5 to 20	0.78 to 0.87		-3.80 to -1.60		180.60 to 284.00	2.74 to 6.16
A687-235	22	0.10 – 0.39	II	10 to 40	0.63 to 0.94		-2.40 to -1.30		165.60 to 344.70	2.24 to 4.03
Barren dolomite										
A687-235dol	21	0.12 – 0.46	II	5 to 10	0.55 to 0.89		-2.50 to -1.60		191.30 to 386.90	2.74 to 4.18
Pyrite-Au quartz veins										
MP01.1	25	0.10 – 0.13	II	5 to 10	0.92 to 0.93		-3.30 to -2.90		164.60 to 194.70	4.80 to 5.41
MP02	14	0.10 – 0.15	II,III	10 to 20	0.89 to 0.94		-3.80 to -2.70		157.70 to 211.30	4.49 to 6.16
MP02	5	0.14 – 0.15	I	3 to 8	0.85 to 0.99	-57.50 to -56.60	-3.60 to -2.80	8.60 to 9.90	146.30 to 177.50	4.70 to 5.94
MP3	46	0.10. – 0.18	II	10 to 40	0.87 to 0.93		-5.20 to -0.80		157.80 to 241.70	1.40 to 8.14
Sulphide ± sulphosalt-Au veins										
A685-5	48	0.12 – 0.19	II, III	10 to 20	0.86 to 0.92		-3.60 to -2.40		184.60 to 243.20	4.02 to 5.86
A676-7310	26	0.13 – 0.15	II	10 to 20	0.88 to 0.89		-3.20 to -1.20		158.40 to 212.30	2.07 to 5.26
A685-20	18	0.15 – 0.21	II	5 to 10	0.83 to 0.90		-3.20 to -1.60		175.40 to 257.00	2.73 to 5.26

Inclusion type-I: H_2O-(CO_2)-NaCl, type-II: H_2O-NaCl; type-III: H_2O+NaCl with solid daughter minerals

7.3.2 Fluid inclusions in sulphide ± sulphosalt Au veins

Quartz: inclusion type-II. Observations for this type of inclusions are based on samples A685-5, A676-73.10 and A685-20. The inclusions are relatively large, 5 to 20 µm in diameter and have regular shapes. The volume fraction of vapour ranges from 0.12 to 0.21 (Table 41).

Quartz: inclusions type-III. Type III inclusions are one-phase (L_{H2O}) inclusions with small trapped solid phases; they reach up to 12 µm (Fig. 85F) and have irregular shapes. The inclusions are randomly distributed in the quartz crystals. Solid phases were identified as quartz, calcite or tourmaline by Raman spectroscopy (Fig. 86C). These minerals may be regarded as accidentally trapped crystals.

7.3.3 Fluid inclusions in barren veins.

Quartz: *inclusion type II.* Inclusions in sample GRS08 range from 5 to 20 µm in size and have regular to irregular elongated shapes. Sample A687-235 also contains barren veins. Volume fractions of FI from barren quartz veins in samples GRS08 and A687-235 are highly variable, ranging from 0.15 to 0.25 and from 0.10 to 0.38, respectively (Table 41). Figure 85G illustrates type-II fluid inclusions in quartz with variable volume fractions.

Dolomite: inclusion type II. Fluid inclusions in dolomite are regular shaped inclusions between 5 and 10 µm in diameter (Fig. 85E). Sample A687-235-dol contains two-phase (V_{H2O} + L_{H2O}) liquid-rich aqueous inclusions (type II), with a highly variable volume area fraction between 0.12 and 0.46 (Fig. 85H).

7.4 Microthermometic data

7.4.1 Fluid inclusions in pyrite-Au quartz veins

Quartz: inclusion type I. The melting temperature of solid CO_2 in type I inclusions [T_m (CO_2)] ranges between -57.5 and –56.6°C (Fig. 87A). This is close to the triple point of pure CO_2 (-56.6°C) and indicates that the gas phase is mainly composed of CO_2 with some contribution of N_2 (Fig. 87A). Clathrate completely dissolves (T_m clathrate) at temperatures between 8.6 and 9.9°C (Fig. 87B) with the

presence of liquid and vapour CO_2. Homogenization temperatures of aqueous-carbonic CO_2 (T_h CO_2) ranges from 25.4 to 31°C (Fig. 87C).

The final dissolution of ice (T_m ice) occurs in a narrow temperature range between -3.6 and -2.8°C (Fig. 87B). Liquid and vapour phases homogenize from 146.3 to 177.5°C (Fig. 88A). Densities of the bulk type I inclusions are relatively homogenous, between 0.96 and 0.99 g/cm^3 (Table 41), with calculated salinities ranging from 4.70 to 5.94 eq. mass% NaCl (Table 41, Fig. 89).

During quantification of CO_2 inclusions, several difficulties were encountered. The CO_2 bearing FIs are irregular (Fig. 85C) and most of the inclusions are less than 5µm in size. Only sample S69-25 contains regular shaped fluid inclusions (Fig. 85B). Gaseous species could be assessed using laser Raman spectroscopy (Fig. 86A) but observation and quantification using the heating freezing stage remains problematic. The FI are likely of type-I; results are shown in Figures 87A-C and Figure 88A.

Quartz: inclusion type II. The final dissolution temperatures of type II aqueous inclusions are bimodally distributed: (i) from -4.60 to -2.50°C and (ii) from -1.80 to -0.80°C (Fig. 87D). This data corresponds to a wide range of salinities between 1.40 and 7.31 eq. mass% NaCl (Fig. 89). The temperature of homogenization to the liquid phase is between 157.7 and 241.7 °C (Fig. 87A and 88D). Densities of the bulk inclusions range from 0.85 to 0.94 g/cm^3.

7.4.2 Fluid inclusions in sulphide ± sulphosalt-Au quartz veins

Quartz: inclusion type II. The final dissolution temperature of ice in sulphide ± sulphosalt-Au quartz veins has a bimodal distribution with (i) ranging from -3.60 to -2.40°C, and (ii) from -2.40 to -1.20 °C at an average value of -2.76°C (s.d. ±0.78, mode at -2.80, see Fig. 87D), which produces calculated salinities between 2.07 and 5.86 eq. mass% NaCl (Fig. 89). The bulk density is between 0.83 and 0.92 g/cm^3 and the total homogenization is between 158.40 to 243.20 °C, with a mode at 207.40 °C (Fig. 88B).

7.4.3 Fluid inclusions in barren veins

Quartz: inclusion-type II. Final ice dissolution temperatures are at a mode of -2.8 °C (ranging from -3.80 to -1.30 °C, Fig. 87F), corresponding to salinities ranging from 2.24 to 6.16 eq. mass% NaCl (Fig. 89). Total homogenization of vapour phases occurs from 165.60 to 344.70 °C (Fig. 88C). The bulk density of FI in sample 687-235 is highly variable, between 0.63 and 0.94 g/cm^3.

Dolomite: inclusion type II. Type II inclusions hosted in dolomite yield final melting temperatures from -2.50 to -1.60°C (Fig. 87F), corresponding to salinities between 2.74 and 4.18 eq. mass% NaCl. The total homogenization temperatures of FI in dolomite are highly variable, between 191.3 and 386.9°C, with an average of 304.3°C (Fig. 88C). These conditions define the maximum homogenization temperatures in this study. Densities of the bulk inclusions in dolomite range from 0.55 to 0.89 g/cm^3.

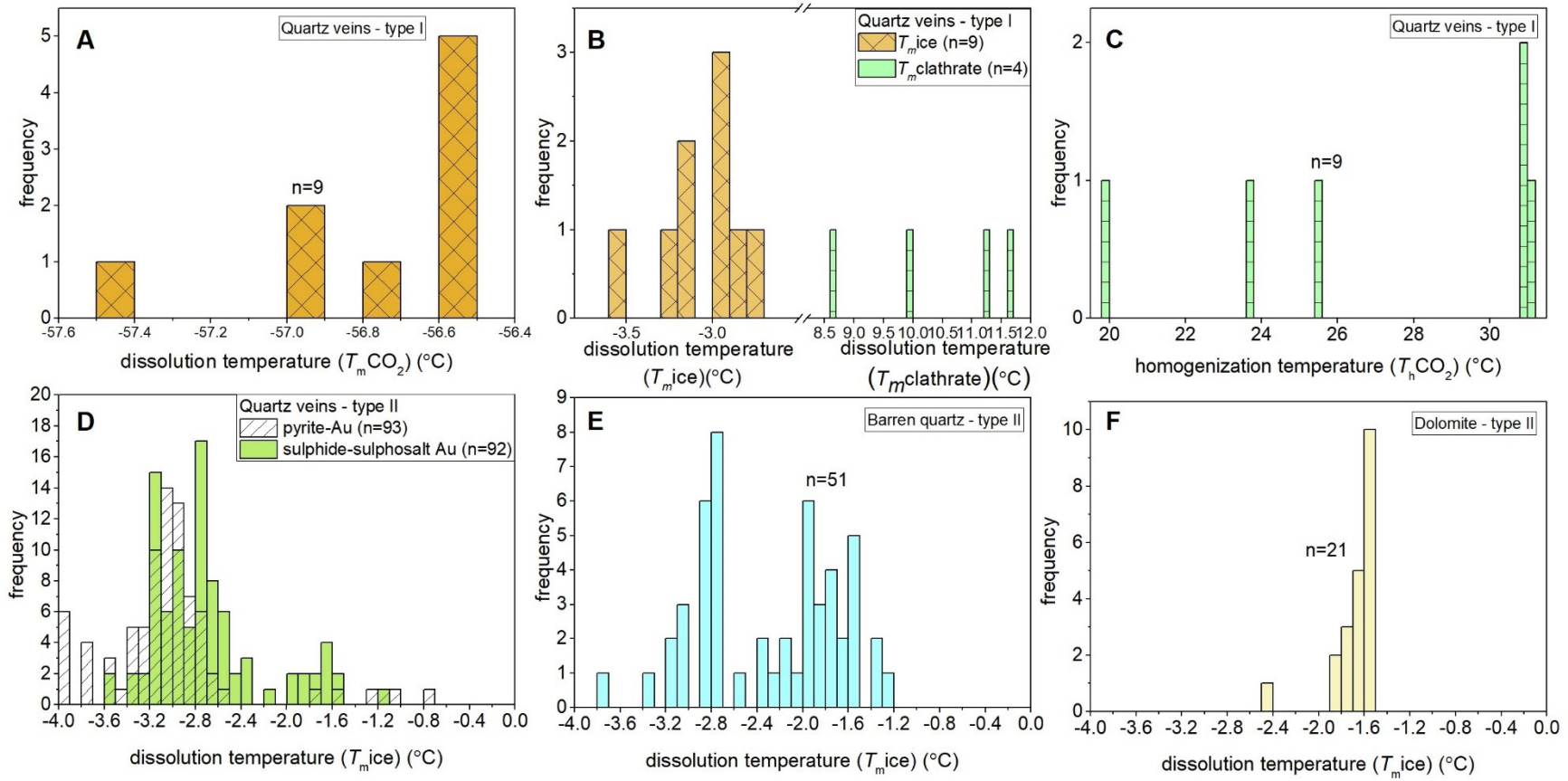

Fig. 87. Histogram showing the microthermometry results. (A) dissolution temperature of CO_2 from fluid inclusion type-I; (B) dissolution temperature clathrate indicate low-concentration of CO_2-gas in system; (C) homogenization temperature of CO_2; (D) dissolution temperature of type I and type II quartz-pyrite-Au veins; (E) dissolution temperature of barren quartz veins; and (F) dissolution temperature of barren dolomite veins.

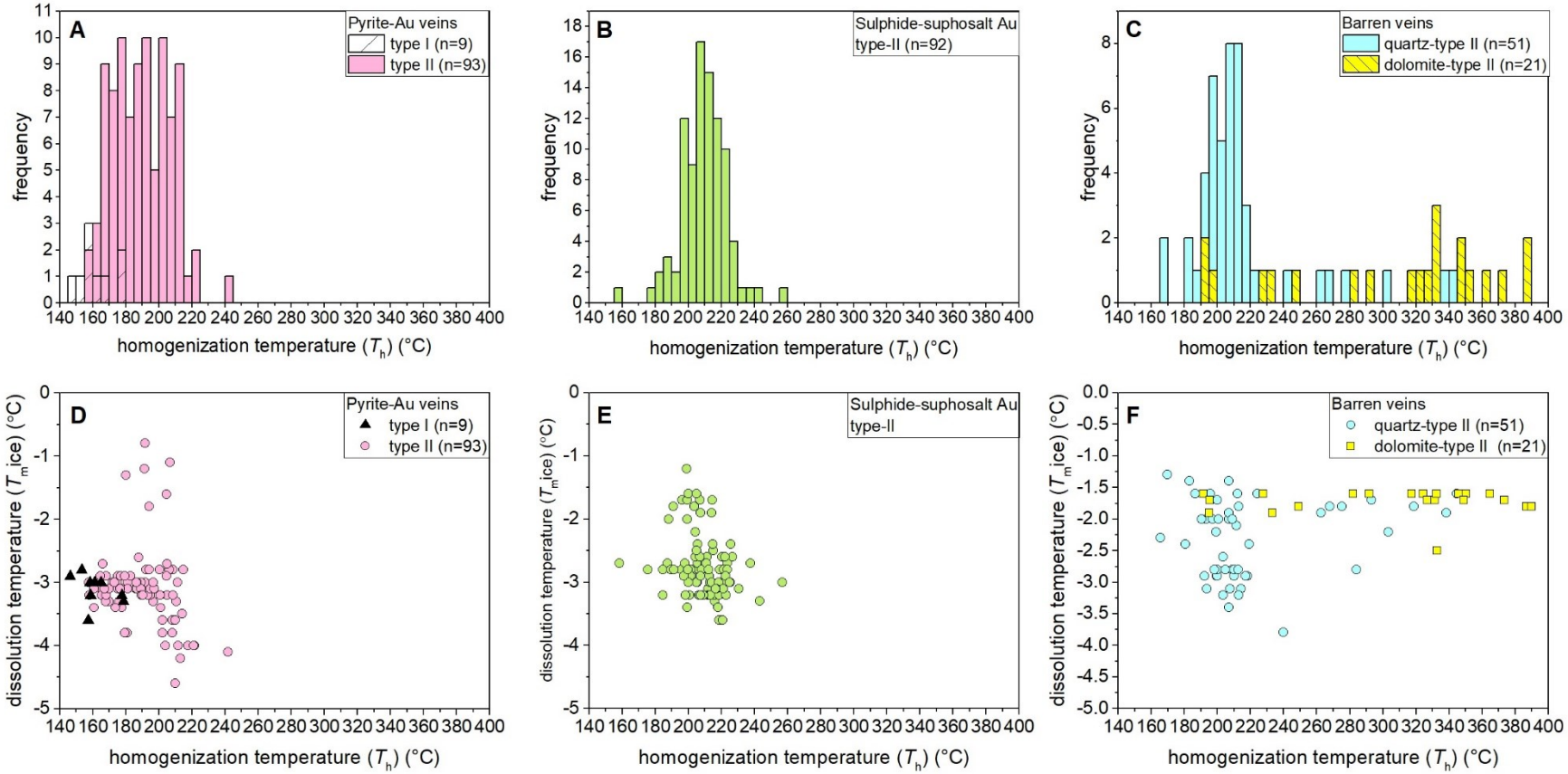

Fig. 88. Histogram showing the homogenization temperature from microthermometry observation (A) type-I and type-II inclusion hosted in quartz-pyrite-Au veins; (B) sulphide-sulphosalt Au veins; (C) barren quartz-dolomite veins. Scatter plot of homogenization temperature versus dissolution temperature of (D) quartz-pyrite-Au veins. (E) sulphide-sulphosalt veins and (F) barren quartz-dolomite veins.

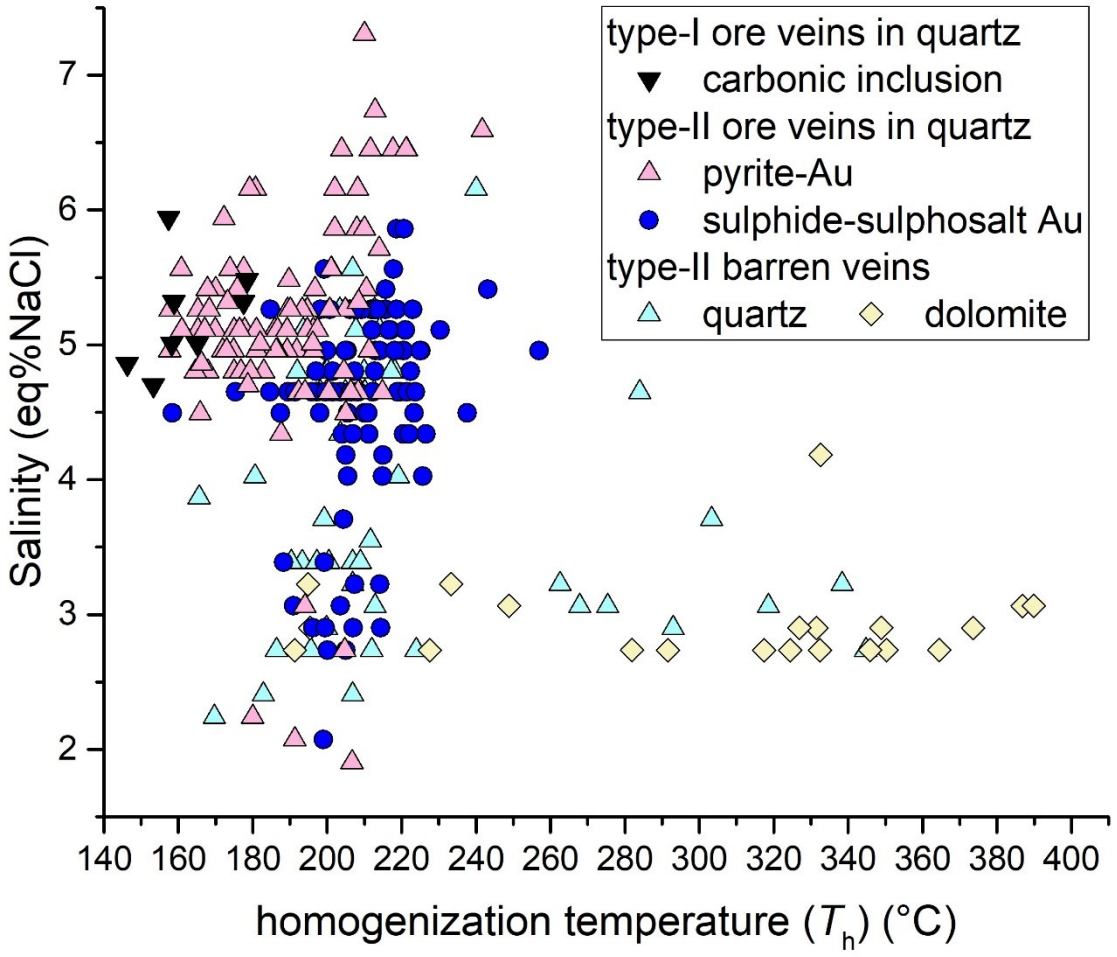

Fig. 89. Scatter plot of homogenization temperature versus salinity of mineralized and barren veins.

7.5 Crush-leach analyses

The chemical composition fluids extracted from quartz and carbonate from the Latimojong Metamorphic Complex is summarized in Appendix G. The ratios of (I/Cl) versus (Br/Cl) discriminate the results into two groups based on lithology (Fig. 90A). Quartz yield log (I/Cl) at an average of -3.59-0.31 (ranging from -4.48 to -3.26), whereas the average composition of barren carbonate is -3.36-0.40 (ranging from -4.50 to -3.01) (Fig. 90A). The ratios of (Na/Cl) versus (Br/Cl) (Fig. 90B) from veins are distributed into two groups: (i) Na/Cl molar ratios < 1.80 with Br ratio ranging from 1068 to 5433, and (ii) Na/Cl molar ratios >1.80 with Cl/Br ratio ranging between 734 and 2874. Furthermore, barren materials are characterized by Na/Cl and Cl/Br molar ratios > 0.68 and < 3,065, respectively (Fig. 90B). The Br/Cl ratios from quartz veins and carbonate in Latimojong range from 0.08 to 4x10^3 molar ratios (average of 0.85 x10^3 molar ratios) and from 0.63

to 5.57x10^3 molar ratios (average of 1.85x10^3 molar ratios), respectively (Fig. 90C).

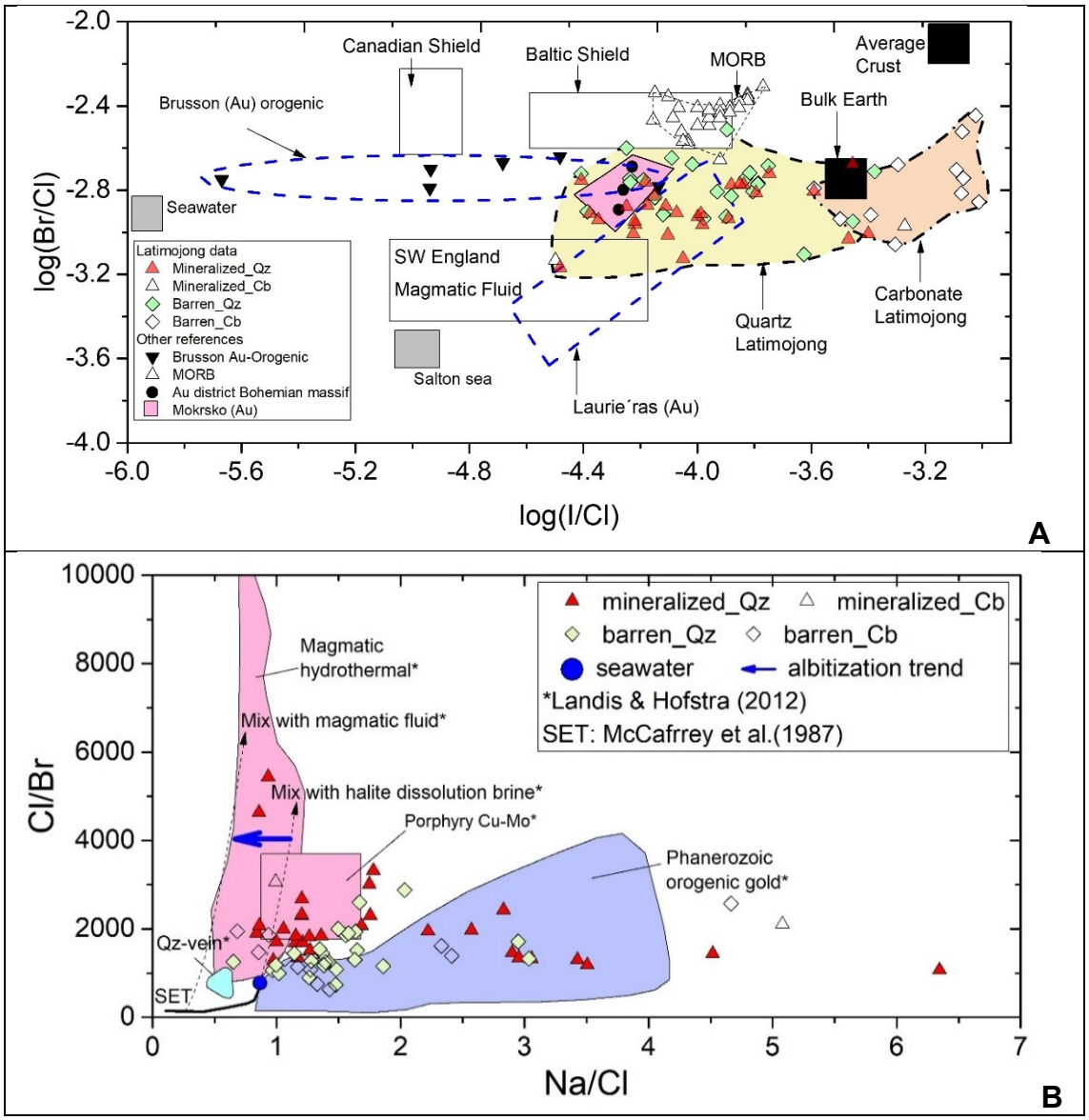

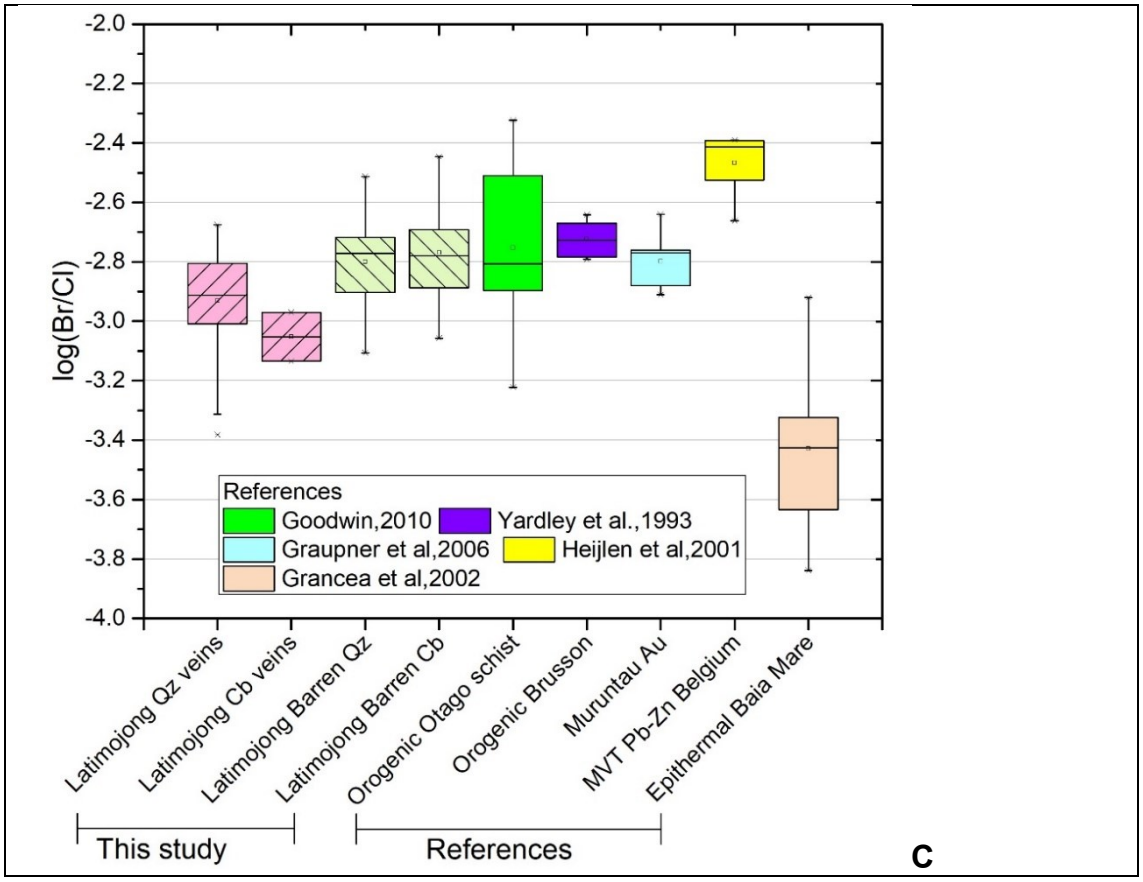

Fig. 90. Halogen data for quartz and carbonate. (A) Log (I/Cl) vs. log (Br/Cl) mole ratios plot for crush leach analyses obtained on gold bearing quartz-carbonate veins from the Latimojong metamorphic complex. Literature data are shown for other crustal fluids (Frape and Fritz 1987; Yardley 1993; Boiron et al. 2001; Boiron et al. 2003; Kendrick et al. 2012). (B) Molar Na/Cl vs. Cl/Br plot of fluid inclusion extracts from quartz and carbonate (Landis and Hofstra 2012). The black line shows the evaporation path along the seawater evaporation trend (SET). (C) The Br/Cl molar ratios of veins in the Latimojong Complex compared to literature data.

7.6 Stable isotope on carbonate

The result of oxygen and carbon isotope analysis are shown in Table 42 and Figure 91. Carbonate samples for isotope analysis are calcite and dolomite–ankerite. Siderite could not be separated from the veins due to the small grain size. The distribution of carbonate samples is illustrated in Table 42.

The stable isotopic compositions of hydrothermal carbonate minerals indicate highly variable $\delta^{13}C$ and $\delta^{18}O$ isotope ratios between -13.30 and +0.42‰ (average of -3.90‰ VPDB) and from 15.95 to 19.76‰ (average of 17.36 ‰ VSMOW), respectively (Table 42). Interestingly, this variation is related with the lithology. Calcites have more restricted $\delta^{13}C$ values (-2.34 - +1.18) and wider

range of $\delta^{18}O$ values (16.78 – 24.30‰) than dolomites (Fig. 91A). Dolomites have $\delta^{18}O$ values of 15.94 – 19.75‰ and $\delta^{13}C$ values from -13.30 to -2.51‰ (Fig. 91B) The carbon and oxygen isotopes of unaltered samples (calcite) are relatively high ($\delta^{13}C$ from -2.34 to +1.18‰ VPDB; $\delta^{18}O$ of +22.2 – +24.3‰ VSMOW).

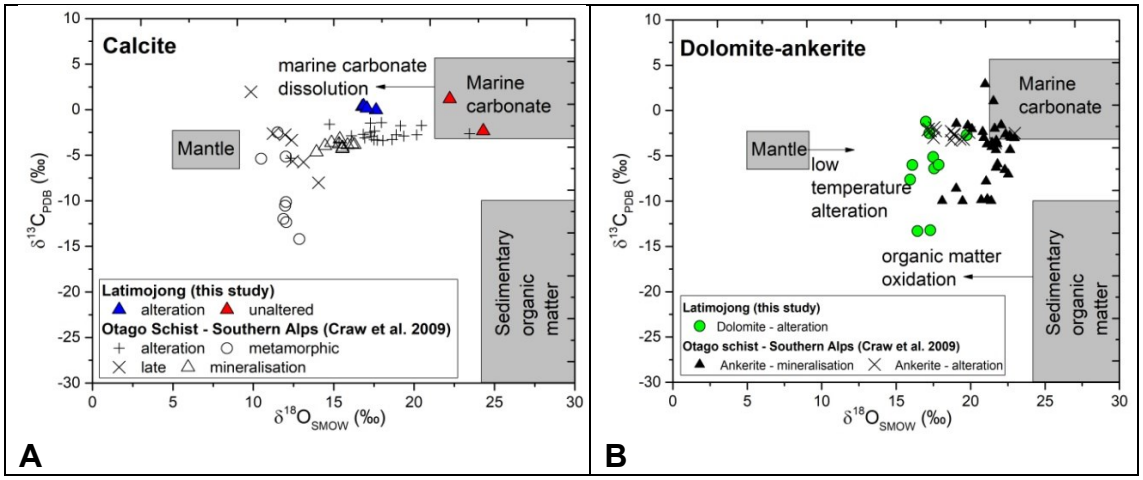

Fig. 91. Oxygen and carbon isotope data for (A) calcite and (B) dolomite-ankerite. Data from Craw et al. (2009) were used as comparison. Gray fields are from Xu et al. (2016).

7.7 Crush-leach data on carbonates

Carbonate materials for stable isotope were analyzed using crush-leach methods. Altered samples are characterized by low F (<44 ppm) and high Cl (> 2,000 ppm) contents (Table 43). The composition of Br, SO_4 and Li are varies (Br between 0.94 and 19 ppm; SO_4 between 158 and 4,470 ppm; Li between 0.76 and 17.85 ppm)(Table 43). Altered samples have high natrium (from 1,072 to 5,443 ppm) and low potassium (from 126 to 784 ppm) contents (Table 43).

Unaltered sample has significantly high F (50.95 ppm) and low Cl (1,255 ppm) concentrations. The Na and Ca contents of unaltered sample are less than the altered samples (Table 43). In contrast, the K content of unaltered sample is greater (~ 1,500 ppm) than altered sample (125 – 780 ppm).

Table 42. Mineral composition and oxygen-carbon isotope of carbonates from the Awak Mas and Salu Bullo.

Sample code for isotopic analysis*	Sample No.	Elevation (m)	X_{Mg}	X_{Ca}	X_{Fe}	X_{Mn}	Mineral	$\delta^{18}O$ (‰) (VSMOW)	$\delta^{13}C$ (‰) (VPDB)
Altered materials									
AN11	S69-25	930.78	0.23	0.52	0.15	0.10	Dol	17.56	-6.41
AN12	S50-23.60	925.56	0.01	0.99	0.00	0.00	Cc	16.78	0.32
AN13	S54-78.30	925.56	0.01	0.97	0.00	0.02	Cc	17.63	-0.05
AN14	S94-27.60	894.86	0.02	0.98	0.00	0.00	Cc	16.86	0.42
AN16	S94-40.55	894.82	0.47	0.41	0.09	0.02	Dol	17.00	-1.23
AN17	S54-72.90	1,000.87	0.02	0.98	0.00	0.00	Cc	17.06	0.14
AN18	A149-36.20	1,158.92	0.20	0.53	0.25	0.02	Ank	17.49	-5.13
AN19	T05-81.90	804.52	0.36	0.47	0.17	0.01	Dol	17.86	-6.00
CB27	A634-5.5	1,067.52	0.26	0.49	0.22	0.02	Dol	16.44	-13.30
CB28	A634-42	1,030.47	0.17	0.76	0.06	0.02	Dol	19.75	-2.71
CB29	S94-27.65	894.82	0.32	0.54	0.12	0.03	Dol	17.29	-13.21
CB30	S94-40.55	878.94	0.47	0.41	0.09	0.02	Dol	17.23	-2.51
CB31	S94-44.30	876.06	0.42	0.45	0.14	0.00	Dol	15.94	-7.62
CB32	S69-112.50	854.57	0.02	0.76	0.14	0.08	Dol	16.09	-6.01
Unaltered materials									
AN10	S94-116.60	820.68	0.01	0.99	0.00	0.00	Cc	22.22	1.18
AN15	Fossil	930.00	0.05	0.90	0.06	0.00	Cc	24.30	-2.34

*Sample is re-coding for analytical purpose. Original sample number is indicated by column “sample no.”.
Abbreviations after (Whitney and Evans 2010).

Table 43. Crush-leach data on carbonates from the Awak Mas and Salu Bullo.

	Mineral	F^- (ppb)	Cl^- (ppb)	Br^- (ppb)	SO_4^{2-} (ppb)	I^- (ppb)	Li^+ (ppb)	Na^+ (ppb)	K^+ (ppb)	Mg^{2+} (ppb)	Ca^{2+} (ppb)
Altered samples											
AN11	Dol	15.59	1,925.98	0.94	560.58	b.d.l.	0.76	1,071.80	125.29	18.06	227.69
AN13	Cc	23.82	4,953.79	10.37	1,131.70	2.51	17.85	4,092.75	343.00	2549.34	10,702.56
AN14	Cc	28.56	3,556.05	3.49	4,470.13	1.42	7.36	4,048.13	332.26	7481.25	13,920.42
AN16	Dol	23.51	5,011.09	8.57	396.29	0.82	4.20	3,468.07	784.45	83.71	1,662.26
AN17	Cc	43.52	2,822.87	5.09	886.93	2.42	7.83	2,551.34	310.69	1,5715.01	13,816.10
CB27	Dol	9.96	3,528.25	b.d.l.	1,536.40	1.28	8.40	2,964.86	286.55	5,543.07	19,518.91
CB28	Dol	23.59	3,029.51	3.50	260.56	0.96	7.21	1,340.54	654.81	5,454.35	12,691.06
CB30	Dol	9.18	6,318.07	18.96	734.53	5.37	15.43	5,442.67	610.48	1,231.73	12,691.54
CB31	Dol	20.26	3,099.80	4.74	158.43	2.62	3.72	1,723.01	345.22	1,016.21	10,682.80
Unaltered sample											
AN15	Cc	50.95	1,254.99	4.49	3,505.01	1.19	1.20	1,161.27	1,447.97	1,963.29	10,987.49

8. RAMAN SPECTROSCOPY ON CARBONACEOUS MATERIALS

8.1 Introduction

The degree of graphitization of carbonaceous material (CM) has been widely used as an indicator of metamorphic grade. Several studies (Beyssac et al. 2002, Rantitsch et al. 2004, Aoya et al. 2010) pointed out that Raman spectroscopy is an effective method to calculate the evolution of CM during regional metamorphism. During metamorphism, carbonaceous material transforms to anthracite, meta-anthracite, semi-graphite and graphite (Kwiecińska and Petersen, 2004, Rantitsch et al. 2016).

The Raman spectrum of CM is composed of first-order (700 – 2,000 cm^{-1}) and second-order (2,200 – 3,200 cm^{-1}) bands. In the first-order region, the graphite bands occur at ~1,580 cm^{-1} (G band), ~1,350 cm^{-1} (D1 band), ~1,610 cm-1 (D2 band), and ~1,500 cm^{-1} (D3 band). Beyssac et al. (2002) correlated between the defect band [R2 ratio = [D1／(G + D1 + D2) area ratio] and the peak temperature using the following equation: T(°C) = -445 R2 + 641. Lünsdorf and Lünsdorf (2016) introduced the Iterative Fitting of Raman Spectra (IFORS) software to evaluate Raman spectra multiple times. This software was designed for calculating geothermometric constraints from carbonaceous material.

In this study, CM from the carbonaceous phyllites and carbonaceous breccias from Awak was separated and analyzed using laser Raman spectroscopy.

8.2 Materials

The mineralogy of carbonaceous phyllites and carbonaceous breccias are given in Table 44. Samples were studied using optical and electron microscope in order to determine the mineralogy. Ore minerals are pyrite and galena, typically less than 50 µm in size. Framboidal pyrite is commonly observed in carbonaceous phyllites. Some carbonaceous breccias are altered by chlorite and siderite and some samples are gold bearing (A198-241, Table 44).

Table 44. Description carbonaceous material samples

Sample	Location	Description	Mineralogy
A685-104	AM	Carbonaceous breccia	Qz+Ab+Gr+Chl
A683-47.70	AM	Carbonaceous breccia	Qz+Ab+ Gr+Chl
A683-53.60	AM	Carbonaceous breccia	Qz+Chl+Gr (Py)
A192-155.50	AM	Carbonaceous phyllite	Ab+Qz+Ph+Gr+Cb (Mnz+Rt+Ap+Py)
A192-155.70	AM	Carbonaceous phyllite	Ab+Qz+Ph+Gr+Cb (Mnz+Rt+Ap+Py+Gn)
A192-157.30	AM	Carbonaceous phyllite	Ab+Qz+Ph+Gr+Ch (Mnz+Py+Ttr+Bn)
A192-189.40	AM	Carbonaceous phyllite	Qz+Ph+Chl+Gr+Cb (Ap+Rt+Mnz+Py+Sp)
A198-241	AM	Carbonaceous phyllite	Ab+Qz+Ph+Gr+Cb (Ap+Py+Au)

Abbreviations after (Whitney and Evans 2010). Alteration minerals are underlined.

8.3 Result

Figure 92 and Table 45 summarize the data of Raman spectra parameters. The main parameters are the so called Gmax (after graphite), Dmax (defect band) and STA (scaled total area)(Lünsdorf and Lünsdorf 2016). The Dmax and Gmax are the highest pseudo-Voigt values in the D- and G-band, respectively. In addition, D_STA and G_STA represent the parameter the sum of the scaled sum-curve values of the Raman shift interval from 1,000 – 1,800 cm^{-1}.

D_STA was observed between 59.87 and 114.41, whereas G_STA ranges from 86.64 to 138.92 (Table 45). The D1 band was observed between 1,344 and 1,354 cm^{-1}, whereas the G band occurs between 1,581 and 1,600 cm^{-1} (Figs. 92A and B; Table 45). Peak fitting demonstrates the presence of the D2 band at *ca.* 1,610 cm^{-1} (Fig. 92B).

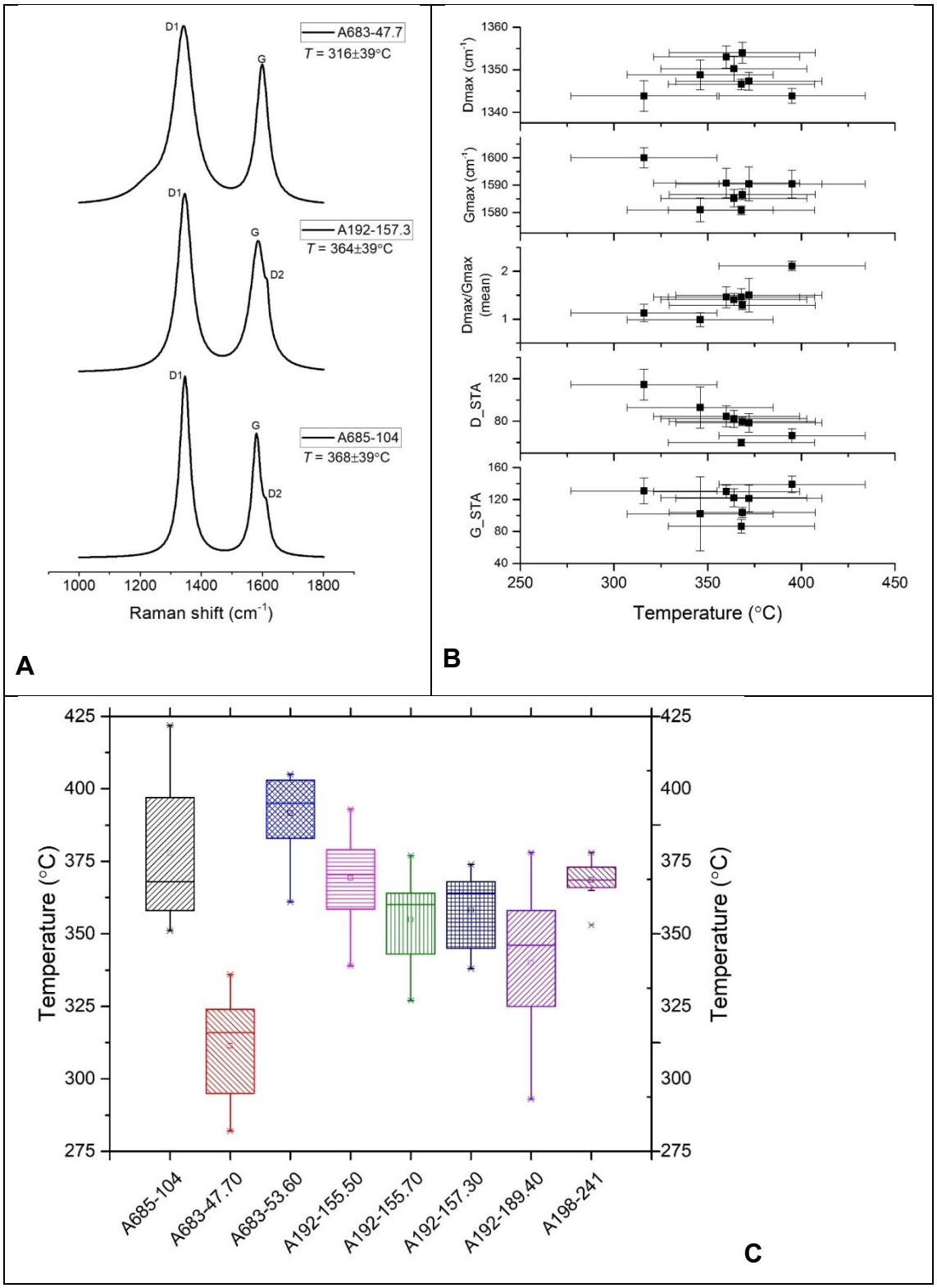

Fig. 92. Output of IFORS software (Lünsdorf and Lünsdorf 2016). (a) The evolution of Raman spectra of carbonaceous material in the study area. (b) Gradual changes in the Dmax/Gmax and D_STA parameter with increasing formation temperature. (c) Summary of formation temperature data of graphitic-mica schist and carbonaceous breccia.

Table 45. Parameter obtained from the decomposition of Raman spectra calculated using Lünsdorf and Lünsdorf (2016).

Sample	n	D_STA	SD	G_STA	SD	Dmax_pos (cm^{-1})	SD	Gmax_pos (cm^{-1})	SD	Dmax/Gmax ratio	SD	Temperature	SD
A685-104	10	59.87	3.28	86.64	8.56	1346.59	1.3	1580.83	1.56	1.46	0.18	368.00	25.67
A683-47.70	11	114.41	14.54	130.84	16.12	1343.85	3.59	1600.01	3.64	1.13	0.18	316.00	17.50
A683-53.60	11	66.35	6.54	138.92	10.22	1343.85	1.74	1590.42	5.08	2.11	0.10	395.00	13.16
A192-155.50	16	78.55	8.89	121.45	16.93	1347.27	2.05	1590.42	6.22	1.50	0.35	372.00	16.00
A192-155.70	9	84.67	9.95	130.02	8.19	1353	2.62	1590.79	5.39	1.46	0.22	360.00	16.00
A192-157.30	10	82.4	7.93	122.24	11.23	1350.2	2.98	1585.2	3.19	1.41	0.13	364.00	13.19
A192-189.40	9	92.85	19.36	101.97	46.39	1348.8	3.48	1581	4.37	0.99	0.15	346.00	28.09
A198-241	10	79.77	3.89	103.84	6.22	1354	2.47	1586.6	1.96	1.29	0.09	368.50	6.82

9. DISCUSSION

9.1 Precursor of metavolcanic rocks

9.1.1 Basalt discrimination based upon clinopyroxene composition

Clinopyroxene is generally considered resistant to alteration and has been used as a discriminant for basalts from different tectonic settings (Le Bas 1962; Nisbet and Pearce 1977; Leterrier et al. 1982; Beccaluva et al. 1989). Clinopyroxene compositions differ between tholeiitic, calc-alkaline basalts and alkali basalts. In alkali basalts, basanites and related rocks, clinopyroxene is more calcic (diopside), whereas in tholeiitic and calc-alkaline basalts, clinopyroxene is augite and pigeonite (low-Ca clinopyroxene), respectively (Juteau and Maury 1999).

A plot of Na_2O-TiO_2-SiO_2 (Beccaluva et al. 1989) discriminates mid-ocean ridge, ocean island and island-arc affinities (Fig. 93A). Figures 93B-D show the data plotted on the Ca-Na-Ti-Al-Cr diagrams (Leterrier et al. 1982). Data plot mostly in island-arc basalt setting and minor mid-oceanic ridge environment (Fig. 93A). They differ from alkali basalt, MORB and OIB by their generally lower contents of Ca, Na, Ti and Al (Figs. 93B - D).

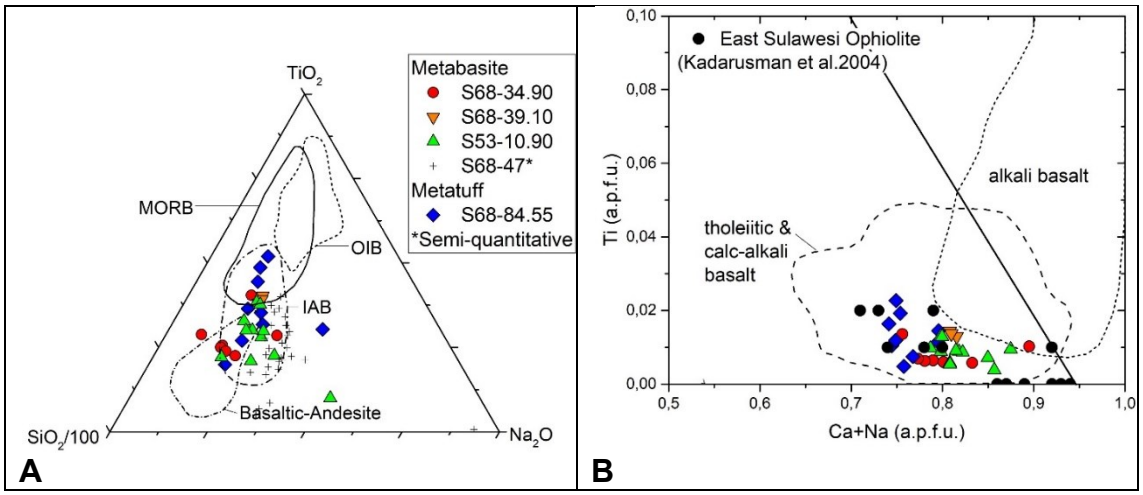

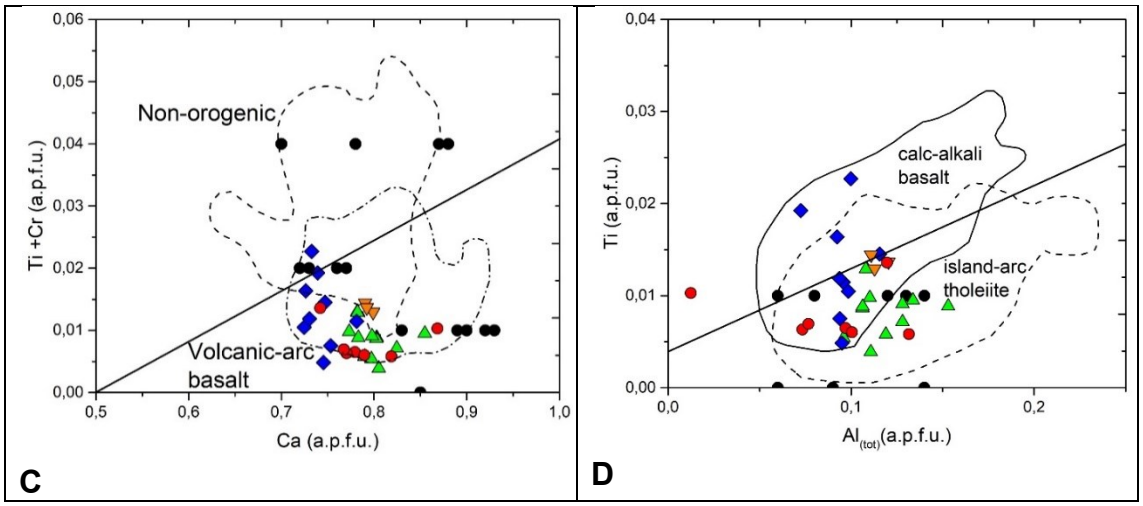

Fig. 93. Electron microprobe analyses results of clinopyroxene from the Latimojong Metamorphic Complex. (A) Tectonic discrimination using ternary diagram of SiO_2-Na_2O-TiO_2, after Beccaluva et al. (1989). (B-D) Tectonic discrimination diagram using clinopyroxene composition after Leterrier et al. (1982).

The metabasite and metatuffite have been generally considered to be related to subduction processes, containing well-preserved relic clinopyroxenes and albitized plagioclases as phenocrysts. These rocks are part of the island-arc basalt rocks which had been amalgamated with meta-sedimentary rocks of Latimojong during Late Cretaceous. Both lithologies had experienced blueschist metamorphism based on the existence of pumpellyite + actinolite + epidote. In addition, most clinopyroxene data plot in volcanic-arc basalt (Fig. 93C) or island-arc tholeiite fields (Figs. 93B-D), which confimed the island-arc basalt environments.

The Lamasi Complex may have been formed in MORB tectonic setings, as suggested by whole-rock geochemistry data suggested by several authors (Bergman et al. 1996; Kadarusman et al. 2004; White et al. 2017). The MORB are interpreted as Eocene-Oligocene arc/backarc volcanic rocks obducted during the Early to Middle Miocene and/or translated by movement along regional faults (Bergman et al. 1996; White et al. 2017).

9.1.2 Magma chemistry constraints from chromian spinel composition

Ophiolite complexes are generally considered to be highly altered because of ocean floor metamorphism. Similar processes took place in the Latimojong Mountains, where most rocks suffered intense hydrothermal alteration and burial metamorphism.

Many studies used chromian spinel in volcanic rocks as a potential discriminant for magma chemistry (Arai 1992; Barnes and Roeder 2001; Kamenetsky et al. 2001). Some of the discriminant diagrams are based on the compositional variation of coexisting olivine-spinel pairs (Arai 1992), however, olivine frequently does not survive during metamorphism. Barnes and Roeder (2001), suggested the ratios of [$Fe^{2+}/(Fe^{2+}+Mg^{2+})$], [$Fe^{3+}/(Cr+Al+Fe^{3+})$], [$Cr/(Cr+Al)$] and TiO_2 contents in spinel to discriminate different compositions in terrestrial mafic and ultramafic rocks. Kamenetsky et al. (2001) proposed that the compositional features of spinel and the differences in TiO_2 and Fe^{2+}/Fe^{3+} between magmatic and mantle spinel can be used in characterizing altered magmatic rocks and the sources of detrital spinels in clastic sedimentary rocks.

Due to strong alteration and metamorphism, spinel does not coexist with olivine in the samples studied. No mantle rock was observed in the Latimojong. Therefore, the discriminant diagram of Arai (1992) which is based on coexisting olivine-spinel pairs of mantle rocks can not be applied.

Various plots of spinel compositions are shown in Figures 94 and are compared with the reference data of Kamenetsky et al. (2001) and Barnes and Roeder (2001).The discrimination between mantle and volcanic spinel is illustrated in Figure 92. Kamenetsky et al. (2001) observed that mantle spinels have lower TiO_2 (<0.2 wt%) and higher Fe^{2+}/Fe^{3+} (>2) over the whole interval in Al_2O_3 (6-56 wt%) than volcanic spinels. Based on the spinel compositions from the metavolcanic rocks, it is inferred that the mafic metavolcanic rocks at Salu Bullo and Awak Mas formed in a suprasubduction zone (SSZ) environment (Fig. 94A). However, some data also plot in the volcanic spinel field. Furthermore, Figure 94A shows that spinels mainly cluster in the island-arc basalt (IAB) field with minor data scattered in the ocean-island basalt (OIB) or mid-ocean ridge (MORB) fields. Similar results were obtained from spinels hosted by clinopyroxene

phenocrysts (Fig. 94B) which indicates that most spinels were derived from basalt in island-arc environment with little overlaps with mid-ocean ridge setting. In the Cr/(Cr+Al) - $Fe^{2+}/(Fe^{2+}+Mg^{2+})$ – TiO_2 diagram (Barnes and Roeder 2001)(Fig. 95), chromian spinel data from Latimojong scatter in the IAB field.

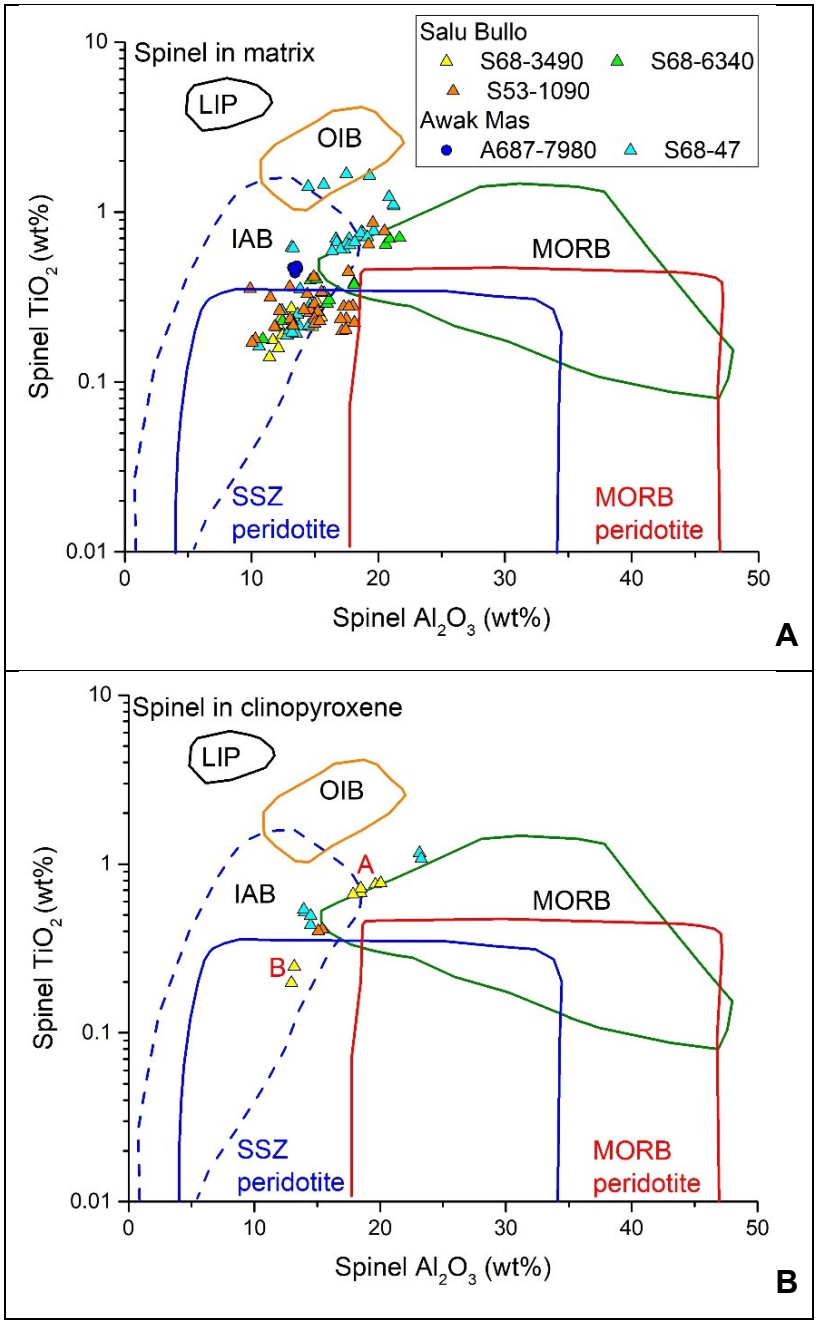

Fig. 94. Al_2O_3 vs. TiO_2 compositional relationships in spinel from Salu Bullo and Awak Mas. (A) A plot of Al_2O_3 vs. TiO_2 in spinel hosted in silicate matrix. (B) A plot of Al_2O_3 vs. TiO_2 in spinel hosted in clinopyroxene. Point “A” and “B” in Fig. 94B are referred to point analyses from the Fig. 44B. Comparison data are based on Kamenetsky et al. (2001).

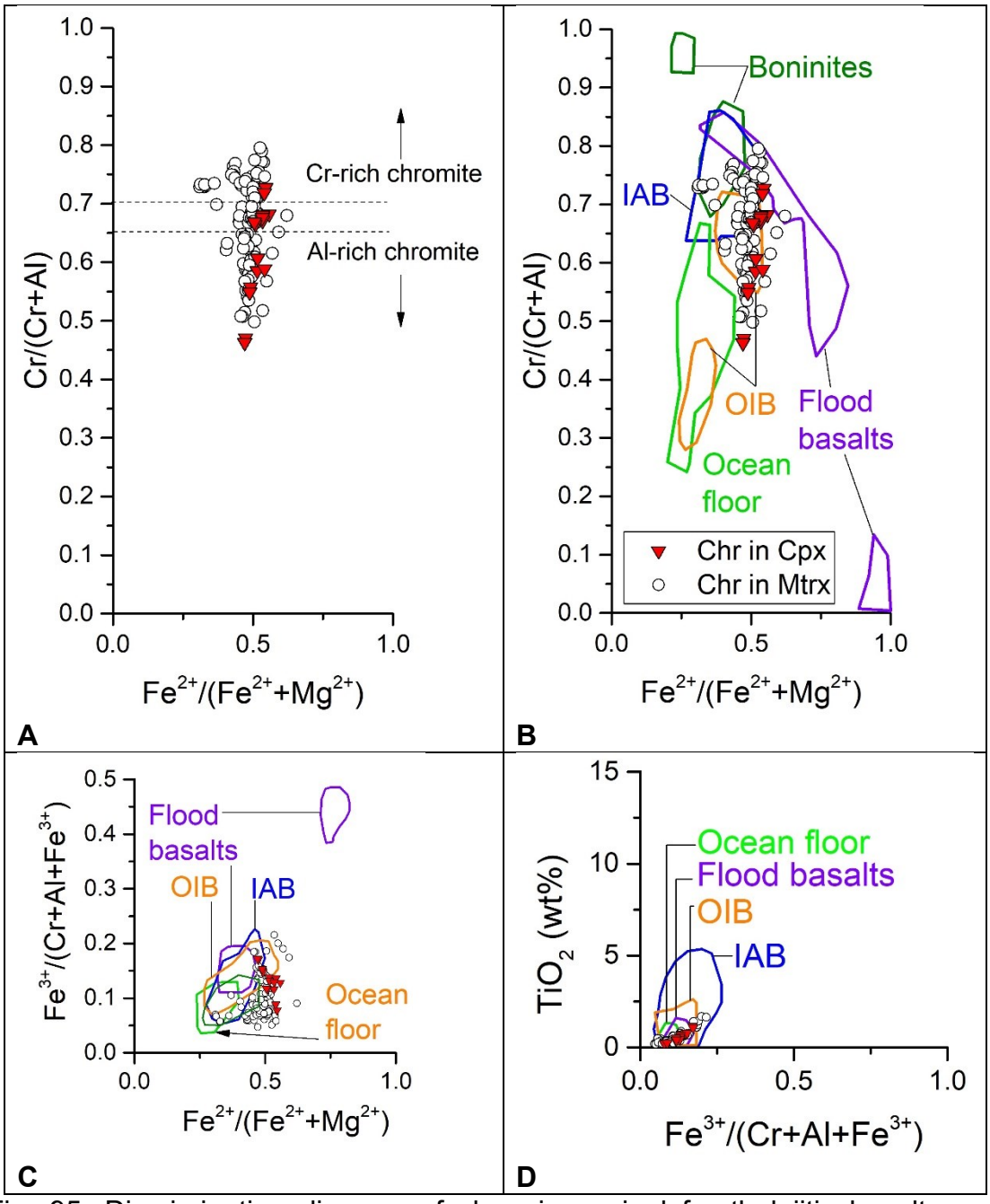

Fig. 95. Discrimination diagram of chromian spinel for tholeiitic basalts and boninites (modified after Barnes and Roeder 2001)

Based on the Al_2O_3 and Cr_2O_3 compositions at Salu Bullo and Awak Mas, two types of spinel are observed: (i) Al-rich chromite (100 x Cr/(Cr+Al) < 65), and (ii) Cr-rich chromite (100 x Cr/(Cr+Al) > 70)(Fig. 95A). Al-rich chromite occurs within augite phenocrysts in clinopyroxene-phyric metabasite and chlorite phengite schist, whereas Cr-rich chromite is associated with metabasite and metatuffite. The large variation of Cr/(Cr+Al) of spinel in this study is similar to the previous

observations made by Kadarusman et al. (2004) and Zaccarini et al. (2016), mentioning that chromian spinels in Sulawesi are bimodal in distribution, Cr-rich and Al-rich. Zaccarini et al. (2016) inferred that bimodal composition and the slight enrichment in TiO_2 observed in some chromitites from different complexes of Sulawesi occurs as a vertical zonation due to the fractionation of a single batch magma with an initial boninitic composition during its ascent, in a suprasubduction zone setting. However, both studies are based on mantle rocks and not on metavolcanic rocks.

It is inferred that the Cr-rich chromites within mafic metavolcanic rocks are derived from a suprasubduction zone (SSZ) environment, whereas Al-rich chromite formed in a mid-ocean ridge (MORB) setting (Zhou and Robinson (1997). The chromian spinel in the Latimojong may have crystallized from a single batch of magma, but at different stages of fractional crystallization. Growing clinopyroxene phenocrysts in an island-arc basalt-type melt trapped floating chromite crystals that developed through time to progressively more Al depleted compositions and forming chromite of higher #Cr (Fig. 44). Al-rich chromite may have been trapped in the clinopyroxene rim by turbulent magma movement where cumulus material has been brought up from deeper parts of the chamber (Hakim and Melcher 2017a). The island-arc basalt was formed during continent-continent collision, while the ophiolite formed in MORB and has been obducted onto the crustal rocks of Latimojong.

Other evidences are the inclusions in chromian spinel that are commonly used to model the source of parental magmas. Silicate inclusions in chromian spinels are abundant and can be classified into two groups: (i) primary silicate inclusions: hydrous-high temperature minerals such as pargasitic amphibole and mica (Fig. 45), and (ii) secondary silicate inclusions of chlorite and pumpellyite, which are related to fissures or cracks. Primary silicate inclusions can be considered to have formed in a magma, whereas secondary silicate inclusions formed later.

Pargasitic inclusions in chromite are frequently reported from ophiolite mantle chromitite, *i.e.* the giant chromite orebodies of the Kempirsai Massif (Melcher et al. 1997). The stability fields of amphibole indicate that pargasitic amphibole in chromite may form at temperatures between 950 and 1050°C at oxygen

fugacitites between the FeO/Fe and the NiO/Ni buffer curves. At a temperature above 1050°C, chromian pargasite melts incongruently to form olivine, chromite and melt. From this evidence, it is interpreted that pargasite inclusions may be trapped during the crystallization of mantle chromite and were not disturbed during the ocean-floor metamorphism or high-pressure metamorphism. In contrast, chlorite and pumpellyite are considered relatively low- to moderate-temperature metamorphic minerals, and are inferred to have formed during pressure dominated greenschist-facies metamorphism.

9.1.3 Interpretation of geochemical data

Several discrimination diagrams employing major and trace element concentrations or ratios have been used to delineate possible tectonic environments. As the rocks have undergone significant alteration, only relatively immobile elements (Zr – Ti – Nb - Y) were considered to trace the former tectonic environment of a suite of basalts. Basalt compositions are plotted into immobile element diagrams, including the Nb/Y vs. Zr/Ti (Winchester and Floyd 1977; Pearce 1996), the Ti-V (Shervais 1982), and the Zr-Zr/Y (Pearce and Norry 1979) diagrams (Fig. 96).

In a Zr/Ti against Nb/Y diagram (Winchester and Floyd 1977; Pearce 1996), the majority of rocks plot into three groups, basalt, andesite + basaltic andesite, and alkali basalt (Fig. 96A). The Ti-V, Zr-Y and Nb-Zr-Y diagrams also indicate that most metavolcanic rocks are classified as island-arc basalt (IAB), with some data overlapping into the mid-oceanic ridge (MORB) field (Figs. 96B-D). The classification of basalts to IAB and MORB is in agreement with petrographical features and discrimination diagrams based on clinoyproxene and chromian spinel compositions (see Chapter 9.1-9.2). In addition, Juteau and Maury (1999) suggested that petrographically, MORB are often subaphyric and IAB usually highly porphyritic (15-50 modal% of phenocrysts, plagioclase being the most abundant), a feature also observed at Salu Bullo.

All basalts from Latimojong have large variation of Nb/Y ratio but similar Zr/Ti ratio (Fig. 96A). The large variation of the Nb/Y ratio reflects different degrees of alkalinity, whereas the Zr/Ti ratio suggests that all samples are at a similar stage

of differentiation. The result of this study shows that mafic metavolcanic rocks show strong island-arc basalt affinity.

It must be mentioned that the discrimination diagram is unlikely to provide unambigous interpretation of the paleotectonic settings, especially for the altered and metamorphosed rocks such as in Latimojong. The tectonic discrimination diagrams thus should be used as an indication but not as conclusive evidence. Therefore, multi-element diagrams are used to compare selected trace element abundances with those of their present-day analogs.

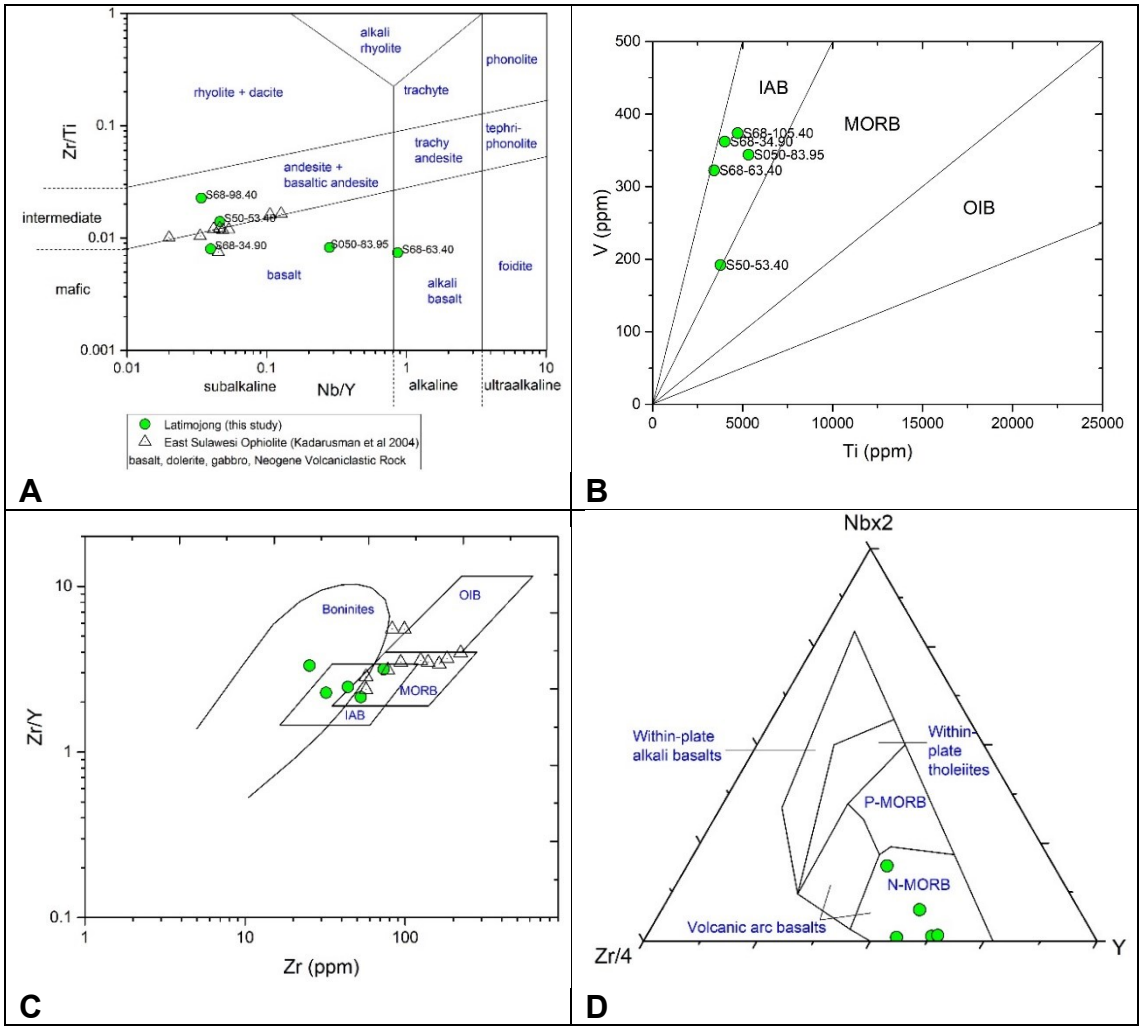

Fig. 96. Basalt discrimination diagrams using trace elements. (A) Zr/Ti versus Nb/Y classification diagram for volcanic rocks (Winchester and Floyd 1977; Pearce 1996). (B) Ti-V discrimination diagram for basalts of Shervais (1982). (C) Zr/Y-Zr diagram of Pearce and Norry (1979). (D) Nbx2-Zr/4-Y diagram (Meschede 1986). Data from East Sulawesi Ophiolite (ESO) (Kadarusman et al. 2004) are plotted for comparison.

In the multi-element diagram (Fig.60A, Chapter 5.8.2), metabasites and meta-andesites show an extreme enrichment of Pb, Large Ion Litophile Elements (LILE)(i.e. Cs, Rb, Ba) with respect to High Field Strength Elements (HFSE), including Nb, Ta, Ti, P, La, Nd, Zr, Hf, Sm and the Light REE (LREE)(La, Ce, ...) and Heavy REE (HREE)(...., Yb, Lu). The elements Nb, Ta, and to a lesser extent Zr and Ti, display negative anomalies in multi-element patterns, typical of island-arc basalt (IAB)(Juteau and Maury, 1999). These data support the model of the Cretaceous Latimojong basalts being a product of volcanic arc basalts related to subduction processes (Pearce et al. 1984; Sun and McDonough 1989). The evidence from clinopyroxene and chromian spinel also supports this model.

Metabasites show strong degree of fractionation compared with meta-andesites, showing that most incompatible and rare-earth elements of metabasites are depleted compared with meta-andesites or MORB (Sun and McDonough 1989). The normalized multi-element pattern of meta-andesites, although similar to the metabasites, are least fractionated than metabasites. Metabasites display weak negative Sr anomalies that may be attributed to plagioclase fractionation processes (Juteau and Maury, 1999).

The phyllites exhibit enrichment of LILE, LREE and HREE relative to primitive mantle. Zheng and Hermann (2014) attributed this pattern to slab dehydration during high-pressure metamorphism at mantle depths. In addition, the carbonaceous phyllites show enrichment of Cs, Rb, Ba and K relative to the phylites. LILE are primarily controlled by phengite, therefore, in more K-rich rocks containing high amounts of phengite, the multi-element diagram will show significant enrichment at the very left side of the diagram.

Figure 60A illustrates the difference betwen metavolcanic rocks of Latimojong and the rocks from East Sulawesi Ophiolite (ESO) and Neogene Volcaniclastic rocks (Kadarusman et al. 2004). No mantle rocks from the East Sulawesi Ophiolite were included in this diagram. Rocks from the ESO do not show such relative enrichment of Pb and depletion of HFSE and REE. In contrast, the metabasites and meta-andesites from Latimojong have a similar Pb enrichment with eclogites and blueschists rocks of Bantimala, South Sulawesi (Fig. 60B) (Maulana et al. 2013). Figure 61B also shows that the rare earth+yttrium pattens

of carbonaceous phyllites and phyllites are similar to that reference. From this evidence, it can be inferred that basalts at Latimojong are derived from a different tectonic setting than ESO and Neogene Volcaniclastic rocks but may have similar protoliths than the Bantimala complex.

According to Kadarusman et al. (2004), the origin of the East Sulawesi Ophiolite (ESO) can be traced back to the proximity of the presently active region of the SW Pacific Superplume. The ESO unit comprises, from base to top, residual mantle peridotite, mafic-ultramafic cumulate, layered isotropic gabbro, sheeted dolerites and basaltic volcanic rocks. Those authors postulated that the ESO originated as an oceanic plateau which immediately was followed by mid-oceanic ridge magmatism. The volcanic arc or suprasubduction zone signatures of some ESO samples indicate that ESO may have been influenced by arc magmatism during emplacement onto the continental margin. In summary, the ESO may have been formed at a different tectonic setting and was later overprinted by magmatism in different environments.

In the pre-Tertiary basement complex of Bantimala and Barru (ca. 200 km to the south of Latimojong Mountains), a wide variety of lithologies of various ages have been reported (Wakita et al. 1996; Maulana et al. 2013). This includes (i) eclogite-blueschist facies metamorphic rock, (ii) amphibolite facies rock, (iii) deep marine sedimentary rocks; (iv) serpentinized ultramafics rocks of ophiolitic affiinity. White et al. (2017) assumed that the Latimojong metamorphic complex is equivalent to the early Late Cretaceous medium-high grade metamorphic rocks exposed in the Bantimala and Barru areas.

Maulana et al. (2013) proposed that eclogite- and blueschist-facies rocks of Bantimala derived from thicker crustal environments (OIB, IAB) which were subducted under blueschist-facies conditions under the southeast margin of Sundaland in the late Jurassic period. Based on the whole-rock composition data, those authors proposed that the eclogites are derived from MORB and cumulate gabbro, whereas blueschists are mainly derived from oceanic basalt and island-arc basalt.

Figure 97 illustrates the tectonic history of the Latimojong Mountains from Early-Late Cretaceous to the present time. The Latimojong is a continental block rifted

from East Asia and was subducted into the eastern Sundaland north of Borneo in the Cretaceous (Hall 2012). The Cretaceous age of the Latimojong Metamorphic Complex is similar to lithologies that have been dated in Barru and Bantimala (Wakita et al. 1996; Parkinson et al. 1998). White mica from Oligocene sandstone in the Latimojong region has been dated to 114±2 Ma using the K/Ar method by Bergman et al. (1996). More support for a Cretaceous age of the Latimojong is summarized by White et al. (2017), i.e. radiolaria obtained in a piece of chert float yield an Aptian-Albian age, and zircon fission track ages of two metasediment samples yield 128-123 Ma. Based on this evidence, the Latimojong formed in the Early-Cretaceous (Figure 97).

Various isotopic data (K-Ar, ^{40}Ar-^{39}Ar,Rb-Sr, Sm-Nd) ranging from 20-201 Ma (Bergman et al. 1996) are reported from of the Lamasi Complex or Lamasi Ophiolite. According to those authors, older ages (162-201 Ma) are interpreted as anomalously high due to excess radiogenic ^{40}Ar. In contrast, younger K-Ar ages (20-24 Ma) are interpreted as reset cooling ages thus dating the ophiolite emplacement. Eocene or Cretaceous ages (46±3 and 120±5 Ma) are interpreted as partially reset higher temperature cooling events. Recently, zircon extracted from the Bua rhyolite and altered andesite of the Lamasi Complex were dated using U-Pb methods by White et al. (2017) to 25.0±0.7 Ma and 38.2±1.3 Ma, respectively. The Bua rhyolite samples contain inherited Paleoproterozoic (2474 Ma) and Archean (2680 Ma) zircon cores, the altered andesite contains inherited ages of Proterozoic to Eocene (1717 Ma, 102 Ma, 101 Ma, 99.6 Ma, 99.2 Ma, 94.2 Ma, 89.6 Ma, 51 Ma, 44 Ma).

It is clear that the basaltic rocks in the Lamasi Complex have “depleted” or MORB-like Sr and Nd isotopic ratios and REE characteristics (Bergman et al. 1996). When considered together, the Lamasi Complex may represent Eocene-Oligocene basalt obducted during the Early to Middle Miocene and/or translated by movement along regional faults (Bergman et al. 1996; White et al. 2017)(Fig. 97). This MORB body is overlying the metamorphic basement, which consist of metasedimentary and metavolcanic rocks.

The results of this study (mineral composition of relic magmatic clinopyroxene, chromian spinel and whole-rock data) do not support the existence of an ophiolite

body within the are under investigation (Table 46, Figure 97). White et al. (2017) speculated that the gabbros and ultramafic rocks of Cretaceous age found in the Latimojong are part of the Latimojong Metamorphic Complex (Fig. 14).

Upper Cretaceous and Paleocene ages rocks were probably erroded, therefore, the stratigraphy between those ages were not observed. The Latimojong rocks represents the basement of Sulawesi and the younger rocks sequences were deposited above an unconformity that developed during Cretaceous (White et al. 2017). During the Paleocene, an angular unconformity is found at the top of Upper Cretaceous unit, possibly due to uplift associated with a short-lived phase of subduction (van Leeuwen and Muhardjo 2005). Continental and shallow water sedimentation occurred during the Miocene into the Oligocene. Furthermore, the collision of the Indo-Australian Plate (e.g. Sula at ca. ~20-25 Ma) with Sulawesi caused uplift and developed another angular unconformity (White et al. 2017).

Widespread magmatic activity in Western-Northern Sulawesi occurred during the Late Cenozoic. Maulana et al. (2016) suggested that the partial melting of lower-middle crust amphibolites in an active subduction environment results in CA-TH (intermediate to felsic calc-alkaline to low-K/ tholeiitic) granitoids in Western-Northern Sulawesi. In contrast, fractional crystallization and crustal contamination have played a significant role in the case of a HK (shoshonitic to high-K) and CAK (felsic high-K calc-alkaline) series.

HK rocks are found throughout Western Sulawesi, CAK rocks occur in the Central and northern part of South Sulawesi, and Late Cenozoic CA-TH rocks are restricted to Northern Sulawesi. This intrusion is probably related to gold mineralization, i.e. gold mineralization hosted by young CAK granitoids (i.e. Palopo gold district, van Leeuwen and Pieters 2011). A discussion related to the genesis of gold mineralization in Latimojong is presented in Chapter 9.3-9.4.

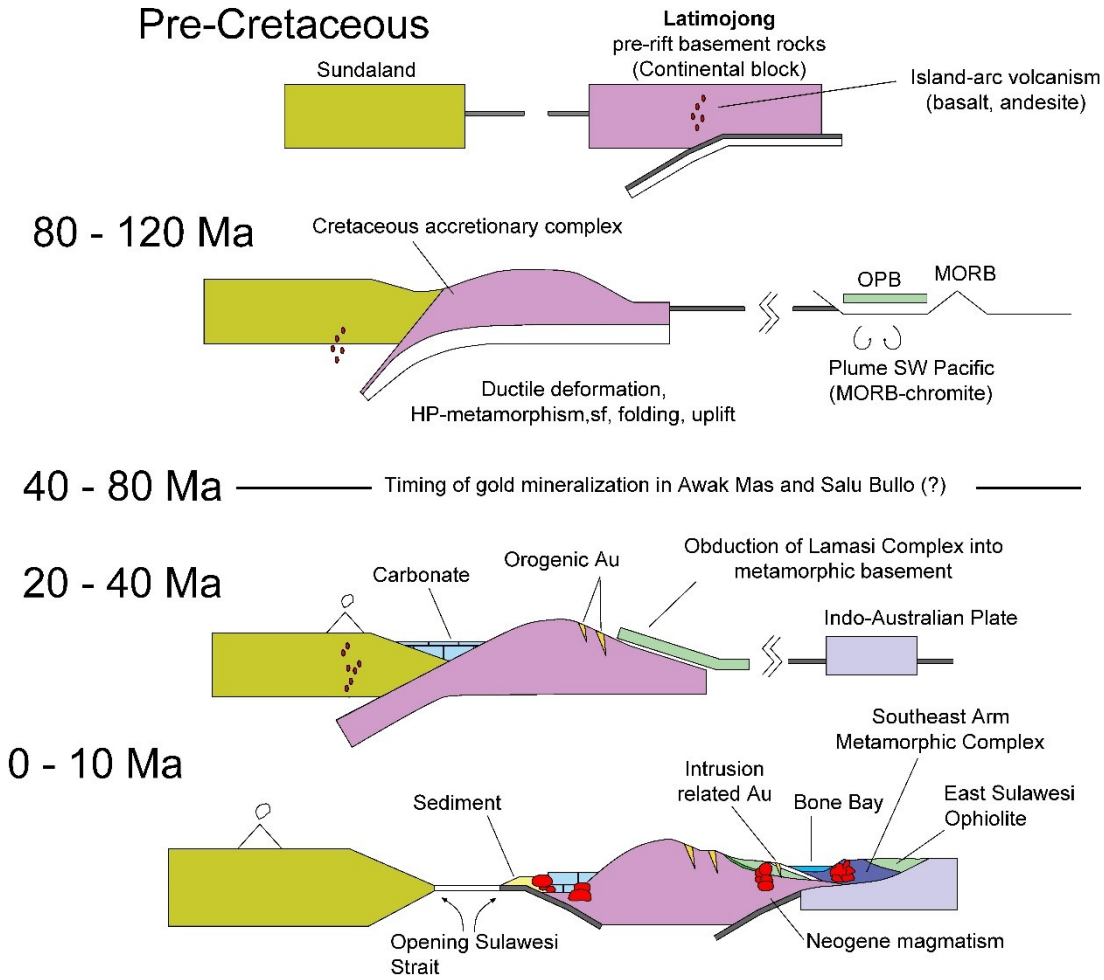

Fig. 97. Schematic cross-sections through the Latimojong from Late-Early Cretaceous to present, as discussed in the text. The figure is based on sketches by Bergman et al. (1996), Guntoro (1999), Kadarusman et al. (2004), Hall (2012). and White et al. (2017).

Table 46. Summary of tectonic setting discrimination based on clinopyroxene and chromian spinel compositions obtained by electron microprobe

Sample	Lithology	Material	Number of analyses	TiO_2 (wt%)*	Tectonic setting**	Consensus
S68-34.90	Greenschist	Cpx	8	0.25 (0.14)	IAB	IAB
		Chr in matrix	11	0.21 (0.05)	IAB	
		Chr in augite	7	0.57 (0.24)	IAB, minor MORB	
S68-47	Cpx-phyric metabasite	Cpx	25	0.61 (0.30)	IAB	MORB interact
		Chr in matrix	38	0.64 (0.42)	IAB + MORB + OIB	with crustal fluids
		Chr in augite	6	0.70 (0.32)	MORB, minor IAB	
S68-63.40	Metabasite	Cpx	-	-	-	IAB
		Chr in matrix	11	0.42 (0.18)	IAB, minor MORB	
		Chr in augite	-	-	-	
S53-10.90	Greenschist	Cpx	12	0.31 (0.1)	IAB	IAB
		Chr in matrix	33	0.31 (0.16)	IAB	
		Chr in augite	2	0.41 (0.01)	IAB	
S68-84.55	Metatuff	Cpx	15	0.38 (0.42)	IAB	IAB
		Chr in matrix	-	-	-	
		Chr in augite	-	-	-	
A687-79.80	Chlorite albite schist	Cpx	-	-	-	
		Chr in matrix	5	0.46 (0.02)	IAB	IAB
		Chr in augite				

*A number in bracket expresses standard deviation of TiO_2.
**Tectonic setting in bracket indicates overlapping fields between different tectonic settings.

9.2 Metamorphic conditions in Latimojong

9.2.1 Chlorite geothermometer

The chlorite geothermometer of Kranidiotis and MacLean (1987), which is based on the calculated $Al^{(IV)}$ and corrected Fe/(Fe+Mg) ratio, indicates temperatures ranging from 227 - 346°C (average of 268°C)(Fig. 98A). Sample A687-157.90 contains abundant titanium content in chlorite (up to 5.47 wt%). Consequently, the high content of titanium in this chlorite will decrease the Al_2O_3 content due to the cation occupancy. As a result, the chlorite geothermometer of Kranidiotis and MacLean (1987) which is based on $Al^{(IV)}$ gives wide range temperatures, ranging from 269 to 346 °C.

Some samples (S53-50.20-metabasite and S50-39.10-epidote actinolite metabasite) contain elevated Cr_2O_3 (up to 0.78 wt%). The high amount of chromium in chlorite correlates well with the presence of chromian spinel as an accessory mineral in mafic rock, which may be interpreted as a mobile element during metamorphism.

Some chlorite phengite schist (A687-157.90) has up to 5.47 wt% TiO_2 in chlorite (average of 1.7 wt% TiO_2, n=5). This sample is characterized by an abundance of Ti-bearing minerals, including sphene and rutile, in which the presence contributes to the high concentration of titanium in chlorite.

Titanium-bearing chlorite has been reported from various localities in subgreenschist and lower greenschist facies rocks (Abdullah Atherton, 1964 in Force 1991). Force (1991) suggests that the predominant titanium carrier in subgreenschist- and lower greenschist- facies rocks is mostly sphene, in upper greenschist-facies rock is biotite and in the lower amphibolite facies hornblende (in mafic rocks) and sphene (all lithologies). The presence of Ti-bearing minerals (sphene and rutile) in the corresponding samples may be regarded as the source of titanium enrichment in chlorite.

Bourdelle and Cathelineau (2015) presented a graphical tool that facilitates the temperature-composition relationships for low-*T* chlorites. A plot of *T*-R^{2+}-Si (R^{2+} refer to divalent cations Fe^{2+} and Mg^{2+}) diagrams indicates temperatures ranging from 200 to 350°C (Fig. 98B).

The chlorite geothermometer estimates (Kranidiotis and MacLean (1987) are consistent with microthermometric temperature of fluid inclusions (Chapter 7) and temperature obtained from carbonaceous materials (Chapter 8). These temperatures will be used in the subsequent discussion regarding the timing of mineralization.

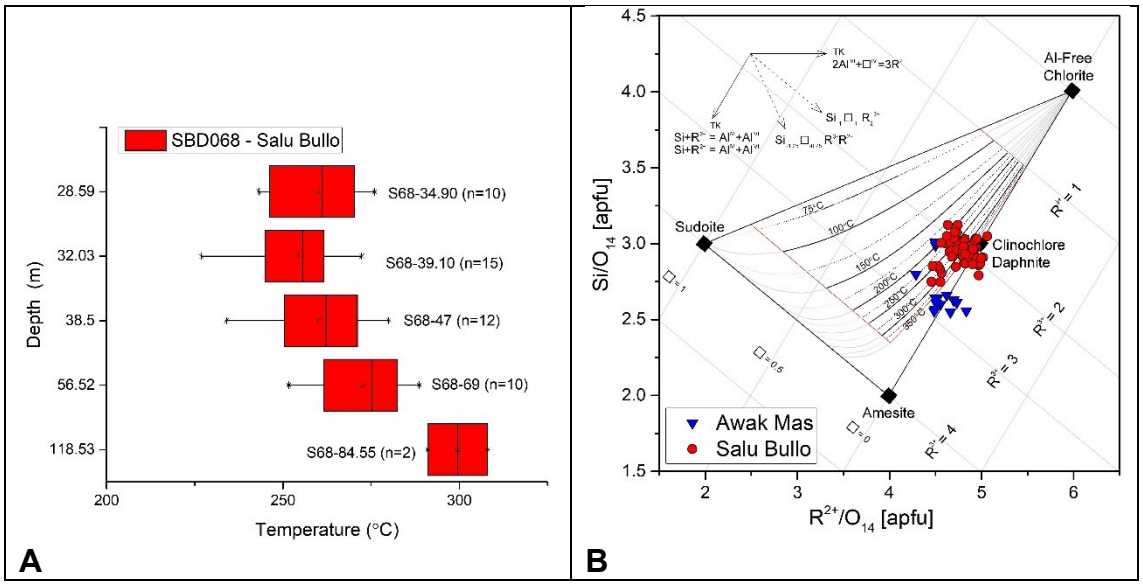

Fig. 98. Geothermometry of chlorites. (A) Geothermoter based on Kranidiotis and MacLean (1987). (B) A graphical representation of the chlorite geothermometer. Diagram after Bourdelle and Cathelineau (2015).

9.2.2 Formation temperature based on carbonaceous materials

The transformation of carbonaceous material to graphite is monitored by Raman spectra on carbonaceous materials (RSCM) in response to rising metamorphic conditions. With increasing structural order, the G and D2 peaks are clearly distinguishable. The D2 band appears on the side of the G band (Fig. 92A), similar to the spectra of semi-graphite of lower greenschist-facies metamorphic samples (Rantitsch et al. (2016), and also a blueschist facies metamorphic sample from the Schistes Lustreés in the Western Alps (Beyssac et al. 2002). With increasing metamorphic rank, both, the D1 and the D2 intensities decrease, whereas the G band increases (Fig. 92A; Lünsdorf and Lünsdorf 2016). The results indicate that the carbonaceous phyllite of the Latimojong Metamorphic Complex is composed of poorly ordered carbonaceous material of the semi-graphite rank. Formation temperature calculations using equations from IFORS software suggest that the metamorphic conditions vary between 316 to 395 °C (±

39°C)(Fig. 92C and Table 45)(Lünsdorf 2015). Interestingly samples containing ore minerals yield higher temperature compared to barren samples (Fig. 92C).

9.3 Gold mineralization

9.3.1 Interpretation of microthermometric data

Most of the fluid inclusion assemblages described in this study are H_2O-NaCl fluids in type-II inclusions. Type-I inclusions were specified only in samples related to early mineralization veins (sample MP02), and are intersected by later vein generation. Quartz forms polygonal grains showing 120 degree angles indicating dynamic recrystallization in quartz at elevated temperature (Pettijohn et al.. (1987). The presence of minor N_2 contributes to the melting of CO_2 below the melting point.

Sample MP02 contains aqueous fluid with salt and minor CO_2 vapour phases of inclusion type-I, which are overprinted by fluid inclusion type-II (Table 41). As mentioned earlier, pre and post-mineralization faulting dominates the structures in the Awak Mas and Salu Bullo gold fields, with late-mineralization faults forming the main veins rather than early-mineralization faults.

In order to illustrate the fluid evolution, a plot of total homogenization versus dissolution temperature has been constructed (Figs. 88D-F, Chapter 7.4). Some aqueous-carbonic inclusions represent the minimum homogenization temperatures observed in this study (146 – 177°C)(Fig. 88D), whereas dolomite yields the maximum homogenization temperature of 387°C (Fig. 88F). Homogenization temperatures of quartz-pyrite-Au veins yield maximum temperatures of 241°C at moderate salinity up to 7.3 eq. mass% NaCl (Fig. 89). Sulphide-sulphosalt veins display an average homogenization temperature of 209°C at low salinity averaging to 4.6 eq. mass% NaCl (Fig. 89). Inclusions in dolomite veins yield interesting results, i.e. a wide range of homogenization temperature (190 to 387°C). The salinity of inclusions in dolomite is relatively low (average of 3.1 eq. mass% NaCl). This variability may reflect the gradual evolution of trapping conditions of dolomite. Mineralized vein data are clustered and yield homogenization temperatures lower than 250°C, whereas barren veins scatter (Figs. 88D-F).

9.3.2 Gold tranport and ore formation

The fineness (N_{Au}) equal to [1000Au/(Au+Ag)] by weight is used to define the composition of Au-Ag alloys or native gold and silver (Fisher 1945; Morrison et al. 1991). The fineness of gold in Awak Mas (N_{Au} of 882 – 936, average of 907, n=15) is similar to the fineness of gold in Salu Bullo (N_{Au} of 842 – 910, average of 866, n=72)(Fig. 99). This result is comparable to the previous information, i.e. Garwin et al. (2005) after Research Information Unit (2002), who described that the Ag/Au ratio of Awak Mas is lower than 1. Harjanto et al. (2016a), based on electron microprobe observations, reported the fineness of gold grains at Awak Mas are 930.

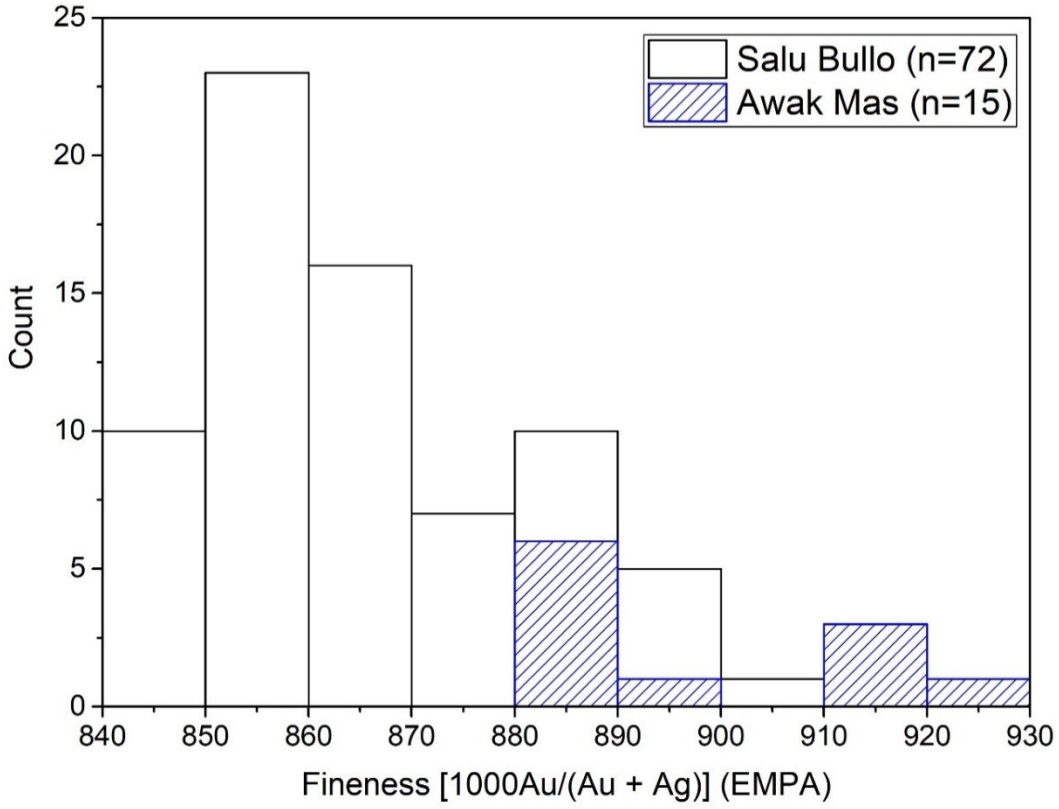

Fig. 99. Box plot and histogram showing grain size distribution of gold in Awak Mas and Salu Bullo. Histogram showing the fineness of gold (n=87). Fineness = 1000Au/(Au + Ag) in wt%. defined by Fisher (1945)

Based on the ore mineral assemblages and the similarity of gold fineness between Awak Mas and Salu Bullo, it is concluded that ore precipitation in both gold districts is a result of a single stage of ore precipitation. The distance of both gold districts is less than 2 km, vein stuctures in both deposits are similar and

directed from north to south. The high fineness of gold in the Awak Mas and Salu Bullo deposits (average N_{Au} of 864) is comparable to other orogenic gold deposits (*i.e.* (Fisher 1945)(Morrison et al. 1991; Goldfarb et al. 2005). The range of values is higher than epithermal deposits in Indonesia (N_{Au} = 420 – 800, (Fisher 1945; Greffie et al. 2002). It is noticeable that epithermal gold deposits usually have a high silver content.

The solubility of gold in hydrothermal fluids depends upon varying factors, including temperature, pressure, redox state, *pH*, the activity of ligands and the mineralogy and composition of Au- and Ag-bearing phases in the source region where metal dissolution takes place (Morrison et al. 1991; Gammons and Williams-Jones 1995). Gammons and Williams-Jones (1995) suggested that hydothermal solutions with low salinity, near-neutral pH, with high dissolved sulphide concentrations will result in relatively high gold solubility and Au/Ag ratios. The interaction of fluids with rocks, which have been preconcentrated in Au with respect to Ag, will produce ore fluids which have higher gold solubility and higher Au/Ag ratio.

Gold generally occurs either in monovalent (aurous gold, Au^{I}) or trivalent (auric gold, Au^{III}) oxidation states. They form stable complexes with ligands, *i.e.* bisulphide (HS^-), chloride (Cl^-), hydroxide (OH^-), cyanide (CN^-). However, the major Au aqueous complexes in hydrothermal fluids are chloride and hydrogen sulphide complex species, $AuCl_2^-$, $Au(HS)_2^-$ and AuHS (Pokrovski et al. 2014).

In a system with a temperature lower than 350 °C, gold solubility is mostly controlled by the bisulphide ion (HS^-) with $AuHS^o$ predominating at lower pH and $Au(HS)_2^-$ at higher pH (Gammons and Williams-Jones 1997). At temperatures higher than 350 °C, gold mostly occurs as $AuCl_2^-$ species.

Based on the homogenization temperature obtained in this study (Chapter 7.4), the bisulphide complex (HS^-) is considered as the main ligand for gold deposition in the Latimojong Complex. Mineral assemblages and fluid inclusion composition within Latimojong are consistent with a relatively reduced fluid. Iron and carbon rich-rocks prove to be important geochemical traps for the release of gold from hydrothermal solutions. This arguments are based on the evidence of the precipitation of gold in iron-bearing host rock (i.e. hematitic mudstones) and

carbonaceous rock (i.e. carbonaceous phyllite, carbonaceous breccias). These are summarized below.

The presence of carbonaceous material in metasedimentary host rocks may facilitate precipitation of gold from fluids by chemical reduction (Goldfarb et al. 2005; Craw et al. 2007). Carbonaceous material in may have acted as a reducing agent for fluid carrying gold as bisulphide complexes, resulting in gold precipitation via Reaction 1 (Hu et al. 2015 and references therein):

$$4Au(HS)_2^- + C + 4H^+ + 2H_2O = 4Au + CO_2 + 4H_2S_{(aq)} \quad (1)$$

Alternatively, those authors suggest that the carbonaceous materials may also be deposited from hydrothermal fluids containing volatile organic compounds during gold deposit formation. Hydrothermal carbonaceous materials precipitates from fluids with sulphides via Reaction 2, causing loss of sulphur from solution which resulting in gold deposition via destabilization of aqueous Au-sulphide complexes:

$$2FeO_{(in\ silicates)} + 4H_2S_{(aq)} + CO_{2(aq)} = 2FeS_{2(s)} + C_{(s)} + 4H_2O_{(l)} \quad (2)$$

A relatively small drop either in *pH* or $f(O_2)$ is inferred to have led to a precipitous drop in HS^- concentration and gold solubility, as a result, deposition of gold is favoured by oxidation and occurs through interaction of the ore-bearing fluid with an iron-bearing host rock (Gammons and Williams-Jones 1997). Fluids carrying gold-bisulphide sulphidize iron-rich wall rock, thereby desulphidizing the fluid causing gold to precipitate where pyrite replaces iron minerals in the wall rock (Reaction 3)(Barnes 1979). Iron-bearing silicates depleting aqueous sulphide, driving gold precipitation from its bisulphide complex (Reaction 4)

$$4FeO_{(rock)} + 7H_2S_{(aq)} + SO_4^{2-} + 2H^+ = 4FeS_{2(s)} + 8H_2O_{(aq)} \quad (3)$$

$$8Au(HS)^-_{2(aq)} + 6H^+_{(aq)} + 4H_2O_{(aq)} = 8Au^0 + 15H_2S_{(aq)} + SO_4^{2-}{}_{(aq)} \quad (4)$$

Iron-bearing host rock is favourable for gold concentration and deposition, as shown by interaction processes in ferrous–iron-bearing rocks at the Muruntau gold deposit (Drew et al. 1996). Goldfarb et al. (2005) mentioned that rocks with high Fe/Fe+Mg are good traps for epigenetic gold deposits, i.e. iron formations, iron-rich tholeiites in Archean greenstone belts, and felsic igneous rock types. In this case, iron form as important ore sinks because of desulphidation reactions with the gold-transporting fluids.

The precipitation of gold from hydrothermal ore fluids in response to changes in the physicochemical conditions may result from a number of processes (Mikucki 1998). These include: (i) adiabatic and conductive cooling of the ore fluids, (ii) interaction between ore fluids and surrounding host rocks, (iii) phase separation in response to decreasing pressures during the rise of the ore fluid, or (iv) by the mixing of two or more different fluids. Fluid mixing reactions controlling gold precipitation were suggested by several workers (Mikucki 1998; Gleeson et al. 2001; Wilkinson 2001; Boiron et al. 2003).

Mikucki (1998) suggested that ore depositional mechanisms in Archean lode-gold systems vary with crustal depth. With decreasing depth of formation, phase separation and fluid mixing appear as the most important gold precipitation mechanism, rather than fluid-rock interaction and wall rock sulphidation. Boiron et al. (2003) also discuss the role of fluid mixing in Hercynian gold systems in western Europe, which show the contribution of shallow and deep-seated fluids. Several of the orogenic deposits in Western Australia formed in a shallow environment via mixing of deeply sourced fluids with surface waters (i.e. Hagemann et al. 1992; Gebre-Mariam et al. 1993, 1993; Groves et al. 1998).

The Racetrack deposit in the Yilgarn block of Western Australia is a shallow orogenic gold system deposited from CO_2-poor fluids in lower greenschist-facies rocks at depths <2.5 km, which has hydrothermal alteration similar to orogenic deposits, whereas the quartz-vein texture and the ore mineralogy are more characteristic of epithermal deposits (Gebre-Mariam et al. 1993). The ore mineralogy consists of arsenopyrite, pyrite, chalcopyrite, sphalerite, galena, freibergite, tetrahedrite, tennantite, electrum and gold, with fluid salinity of 1 – 8 (average 4 eq% NaCl), CO_2 content of < 0.85 molal and homogenization temperatures ranging from 190 – 260 °C. Similar textures were described from the Wiluna deposits; there, $\delta^{18}O_{quartz}$ of 4.4‰ ± 2.3‰ relative to SMOW indicates contribution of near-surface waters in an orogenic gold deposit (Hagemann et al. 1994).

In Latimojong, gold precipitation in carbon- and iron-bearing rocks are found locally. Although those geochemical traps are important for the release of gold from hydrothermal solution in other deposits, veins in Awak Mas and Salu Bullo

are related to major structures, including shear-zone, extensional veins and breccia veins.

9.3.3 Interpretation of halogen data and comparison to other deposit

The halogen ratios (Cl/Br/I) can be used to detect sources of salinity, fluid mixing relations and water-rock reactions, because halogens are strongly fractionated by evaporation and organic activity (Böhlke and Irwin 1992). In Fig. 90A, the values of I/Cl versus Br/Cl are plotted for all investigated samples. Literature data have been plotted as fields for comparison.

The log Br/Cl values of the gold deposit in Latimojong (-3.38 to 2.51) overlap with the ore fluids circulating in orogenic deposits of Brusson, NW Italy (Yardley 1993), Mokrsko (Boiron et al. 2001) and Laurie´ras, Bohemian massif (Boiron et al. 2003)(Fig. 90A). Data overlap only somewhat at the low-end of their range with the magmatic deposits in SW England (Böhlke and Irwin 1992) and MORB fields (Kendrick et al. 2012).

In Figure 90B, Na/Cl/Br diagrams based on Landis and Hofstra (2012) demonstrate that the halogen data of Latimojong scatter over a large range and plot into several fields. They are similar to metamorphic fluids from Phanerozoic orogenic gold deposit, magmatic fluids from porphyry Cu-Mo deposits, with some data shifting into the albitization field. The introduction of sodium-rich minerals through an albitization process may be regarded as metasomatic alteration during the cooling process and metal deposition. Data points also differ from residual evaporative brines of Mississippi Valley-type (MVT) Pb-Zn deposits; therefore, dissolution or precipitation of halite are considered to be less important factors in the present study(Landis and Hofstra 2012).

The Br/Cl diagram (Fig. 90C) supports the evidence of different fluid sources in the Latimojong Complex. The Br/Cl values from this study are comparable to orogenic gold deposits of Otago schist, New Zealand (Goodwin 2010), Muruntau (Graupner et al. 2006) and porphyry Cu deposits in USA (Kendrick et al. 2001). In contrast, the values are different to carbonate-hosted Zn-Pb deposits in Poland (Heijlen et al. 2003) and the Baia Mare epithermal gold polymetallic district, Romania (Grancea et al. 2002).

It is concluded that the halogen ratios of fluids trapped within quartz veins are in agreement with metamorphic fluids. Metamorphic reactions in the metasedimentary rocks during the retrogression stage are considered as the main source of ascending fluids for the formation of the economic Au-mineralization at Latimojong.

While single inclusion analysis always is preferrable, bulk analyses methods are sufficiently sensitive for many ions and halogens of interest. Bulk extraction techniques suffers several complications: (i) solid inclusions can swamp the signal from fluid inclusions, (ii) leaching larger sample volumes yield result from multiple, possibly unrelated fluid inclusion generations (Banks and Yardley 1992), therefore, the results of this study can be checked further using laser ablation techniques, or by the selection crystals with only one type of fluid inclusions.

9.3.4 Sulphosalt composition and thermodynamic implications

This study has documented a wide range of element substitutions in sulphosalts, mainly between As – Sb (Fig. 66). Sulphosalts from Awak Mas and Salu Bullo can be described as tetrahedrite and tennantite.The formulae vary significantly in their tetrahedrite (Ttd) content, [Ttd-content = Sb/(As+Sb+Bi)], ranging from 0.41 to 0.77. Samples with high-Cu content (44.29 wt% ~10.65 a.p.f.u) correspond to the lowest Ttd-content and inversely the lowest Cu-content (35.80 wt% ~ 9.9 a.p.f.u.) has the highest Ttd-content (Table 31).

Sulphosalts with high mercury contents (up to 1.5 a.p.f.u.) tend to enriched in Sb, Fe, Ag with low As, Cu, Zn (Table 31 and Fig. 66). The highest mercury contents from Awak Mas show a stoichiometric formula of $(Cu_{10.37}Ag_{0.04})(Hg_{1.52}Fe_{0.13}Zn_{0.06})(Sb_{3.13}As_{0.91}Bi_{0.01})S_{13}$ (Hakim and Melcher 2016) The high variation of Sb in sulphosalts in this study is comparable with the Schendleck deposit in Austria (Kharbish et al. 2007), however, it differs in term of Zn content (Fig. 66F). The Schendleck has a variable Zn content up to 2 a.p.f.u, whereas the Zn contents in Awak Mas and Salu Bullo are generally less than 0.60 a.p.f.u (Fig. 66F). Mercurian tetrahedrite at Awak Mas and Salu Bullo has low Zn content compared to other occurences, including Schwaz-Brixxleg and

Schendleck in Austria (Arlt and Diamond 1998; Kharbish et al. 2007) and Eskay Creek in Canada (Grammatikopoulos et al. 2005)(Fig. 66F).

Early mineral assemblages contain chalcopyrite, tetrahedrite-tennantite, sphalerite and galena, whereas later assemblages are dominated by pyrite, covellite, enargite/luzonite-famatinite, hematite, and less commonly bismuthinite. Late minerals (secondary copper and Fe-oxide minerals) were commonly observed in: (i) weathering zone (< 30 meter from surface), and (ii) less than 2 meter the fault zones.

The coexistence of tetrahedrite-pyrite, which would indicate low sulfur activity, bound the range of sulfur activity and temperature during mineral deposition (Fig. 100). More locally, there is an indication of paragenetic evolution to a higher sulphidation state with chalcopyrite replacement by covellite, coexisting enargite/luzonite-famatinite with pyrite and replacement of pyrite by hematite, or goethite pseudomorphed after pyrite. The fahlores in Latimojong are typically accompanied by minor enargite and/or luzonite (the high- and low-temperature polymorphs, respectively, of $Cu_3(As,Sb)S_4$, Arlt and Diamond 1998). These secondary copper mineral (*i.e.* covellite) and Fe-oxides (*i.e.* hematite, goethite), which would indicate high sulfur activity, bound the upper boundary of mineral stabilities (Fig. 100).

Two origin would best meet the available mineralogical evidence for late-stage: (i) a low temperature, late-stage hydrothermal fluids might be responsible for metasomatic introduction of Bi during kaolinisation and secondary copper replacement in the last stage of ore deposition in response to Miocene magmatism in Sulawesi. However, this evidence is difficult to be applied in Awak Mas and Salu Bullo because from hundred of thin-polished section samples, bismuthinite and bismuth phases were observed only in two samples (Bismuth phases, Chapter 6.4.10). Along with tungsten bearing minerals, tellurium- and bismuth-bearing mineral phases are widely recognized in many intrusion-related gold deposits (e.g. Thompson et al. 1999) and orogenic gold deposits (e.g. Goldfarb et al. 2005), as well as in the granitoid or metasedimentary host rocks. In metasedimentary rocks, bismuth most typically correlates with anomalous lead, suggesting substitution of bismuth into the the galena structure.

The second option is (ii) the descending meteoric waters oxidize the primary sulphide ore minerals and react with hypogene sulphides and sulphosalts. The latter point may be suitable for ore mineral deposition in Awak Mas and Salu Bullo, because gold and sulphosalts (tetrahedrite-tennantite) correlate positively. A gradual decrease of temperature and sulfur fugacity in the early stage is the principal mechanism triggering precipitation of native gold and As-Sb bearing minerals. When gold is associated with oxide minerals, the sulphide must have been oxidized, resulting in free gold grains.

The mineral stabilities of sulphides and sulphosalts are consistent with petrographic observations, which suggest that both mineral groups formed as function of increasing sulfur activity and decreasing temperature. First, low sulfur fugacity minerals formed. As temperature decreased, some sulphides and sulphosalts were in contact with local oxidizing meteoric water. This interpretation is reasonable because weathering and alteration processes in this area is extensive (up to 30 meters below surface). The formation of a crack network could facilitate the penetration of oxidizing meteoric water into the deeper part of the deposits.

High-sulphidation state minerals including enargite/luzonite-famatinite in Latimojong are rare. The breakdown of tetrahedrite-tennantite to enargite/luzonite-famatinite may be caused by local variations in sulphur fugacity, fS_2, and/or decreasing temperature. The secondary copper minerals are a product of oxidization by local acidic meteoric water and probably were not related with gold deposition. Figure 100 illustrates the evolution curve of the hydrothermal fluids in the Awak Mas and Salu Bullo deposit.

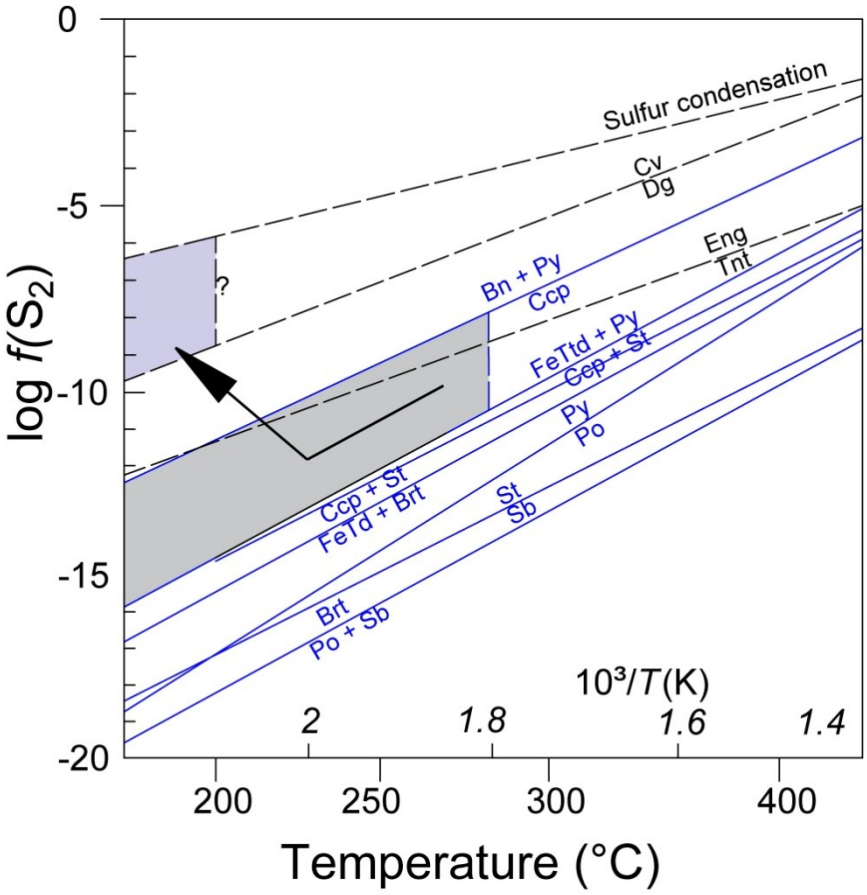

Fig. 100. Phase equilibria in the system Cu-Fe-Sb-S as a function of temperature and sulfur fugacity. Thermodynamic data for sulphides from Barton and Skinner (1979) and sulphosalts from Seal et al. (1990). Black arrow represents the likely changes in temperature and sulfur activity with time due to intensive weathering in the studied area. Fields are limited to temperatures below 280°C based on fluid inclusion homogenization temperatures of sulphide-(sulphosalt) Au quartz veins (see Chapter 7.4). Temperature for covellite-digenite field in the studied samples is not available. Mineral abbreviations: Bn: bornite; Brt: berthierite; Ccp: chalcopyrite; Cv: covellite; Dg: digenite; Eng: enargite; FeTtd: Fe-tetrahedrite; Po: pyrrhotite; Py: pyrite; Sb: native antimony; St: stibnite.

9.3.5 Implications from pyrite geochemistry

Many studies of trace elements have related the ratio of Co/Ni to the genetic type of ore deposits (hydrothermal vs. syngenetic/diagenetic)(Loftus-Hills and Solomon 1967)(Bajwah et al. 1987; Brill 1989; Gregory et al. 2015; Gregory et al. 2016). Bajwah et al. (1987) shows that the majority of pyrite formed from hydrothermal fluid has Co/Ni ratios greater than 2, with sedimentary pyrite (exhalative deposit) having pyrite with lower ratios (Fig. 101). Gregory et al. (2015) suggests that sedimentary pyrite has a characteristic composition of: 0.01

< Co/Ni < 2; 0.01 < Cu/Ni < 10; 0.01 < Zn/Ni < 10; 0.1 < As/Ni < 10; Ag/Au > 2; 1 < Te/Au < 1,000; Bi/Au > 1; Sb/Au > 100; and As/Au > 200.

Elemental mapping of pyrite with the electron microprobe reveals significant variation in the distribution of chemical elements, indicating selective availability of the elements during the periods of growth. Furthermore, the Co/Ni ratio in pyrite indicates two main groups of pyrite. The first group with Co/Ni ratio lower than 1, corresponds to samples from quartz veins and metasandstone; the second group in the metabasite has Co/Ni ratio between 1 and 10 (Fig. 101). Arsenic/nickel ratios in pyrite2a-2b are less than 1, in contrast, As/Ni ratios of pyrite 3 are highly varied.

Cobalt, nickel and arsenic enrichment in pyrite may indicate that these elements are available during particular phases of metamorphism (Craig 2001). Gregory et al. (2015) proposed that high Co content of pyrite in metabasite is likely due to the large amount of mafic host rock, which would increase the total amount of Co available during diagenesis. These elements (nickel and cobalt) are incorporated into pyrite and substitute for Fe in the structure of pyrite (Table 33).

Pyrite2 has low arsenic content, only some grains are enriched in silver and bismuth (Fig. 74). Bivariate plots show that bismuth and gold corelate well with silver with the majority of analyses yielding Ag/Bi and Ag/Au ratios close to 1 (Figs. 75I-J). There is a data spread of pyrite 2a which show high silver (>1,000 ppm Ag) with low gold (0.1 – 0.5 ppm Au) content. High Ag and Bi contents in pyrite are most probably due to the occurence of microinclusions of Ag-Bi bearing minerals and/or galena inclusions in pyrite (Fig. 78).

The hydrothermal pyrite (pyrite3) crosscutting and/or overgrowing earlier pyrite generations is enriched in arsenic (Fig. 74). Abraitis et al. (2004) indicated that As-rich pyrites typically appear to have formed at relatively low temperature and are incorporated in the pyrite through the hydrothermal fluids. Alternatively, arsenic and other trace elements released from the structure of pyrite2 during the metamorphism and incorporated in the hydrothermal pyrite (pyrite3) (Gregory et al. 2016).

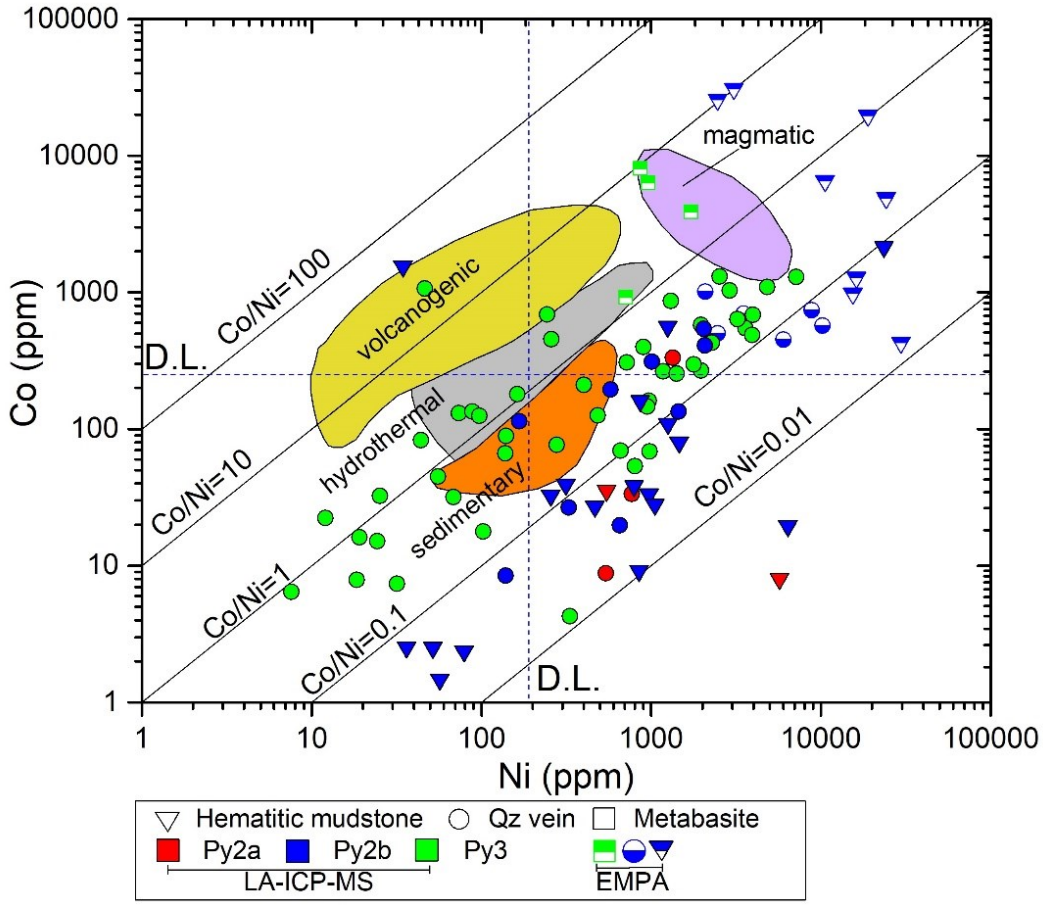

Fig. 101. Bivariate plots of Ni-Co of pyrite from Awak Mas and Salu Bullo. Shown for comparison are pyrite from orebodies of different origins according to Bajwah et al. (1987) and Brill (1989). Average detection limit (D.L.) of electron microprobe for Ni and Co are 195 and 250 ppm, respectively (broken lines).

Carrolite is observed locally in one sample of quartz veins and is in equilibrium with pyrite, chalcoyprite, tetrahedrite-tennantite and covellite (Figs. 64A-B). Bertolani (1962) in Augustithis (1995) reported the presence of cobalt minerals (probably siegenite or carrollite) associated with the ophiolites of Corchia (Parmessan Appennines). The presence of Co minerals from those area, together with chalcopyrite and intergrowth of sphalerite-pyrrhotite, suggest a pneumatolytic-hypothermal genesis. Although carrolite from Salu Bullo is observed in a quartz veins within mafic host rocks, a correlation between ophiolite and cobalt bearing minerals is unknown.

Carrolite in sedimentary Cu-Co deposit in the in Katanga Copperbelt (Congo) is observed as first sulphide phase, associated with bornite, digenite, chalcocite and authigenic quartz (Dewaele et al. 2006). Those authors proposed that the

association of the cobalt mineralization and copper mineralization with diagenesis minerals (dolomite) indicates that both precipitated during diagenesis process.

9.3.6 Interpretation of REY patterns of albite

REY are typically in the +3 oxidation state, but Eu can occur in the +2 oxidation state in strongly reducing environments (Tostevin et al. 2016). Large positive Eu-anomalies in quartz veins (Fig. 83) may indicate slightly reducing hydrothermal fluids (Meyer et al. 2012) and implying significant plagioclase fractionation. Modern seawater contains a large positive Y anomaly (mass ratio of Y and Ho) (Tostevin et al. 2016). There are no signatures of any Ce and Y anomalies in the Cl-chondrite patterns in all studied samples.

In order to illustrate the effects of plagioclase fractionation relative to the distance from veins, Figures 84A and B are constructed. Figure 84A shows the increasing Ce-anomaly with increasing distance from the vein, whereas Figure 84B illustrates the decreasing Eu-anomaly with increasing distance from vein. Discriminant diagrams of Kontonikas-Charos et al. (2014) were also used to characterize the alteration and redistribution of REY from the albite in the magmatic-hydrothermal system (Figs. 84C-D). A plot of of Eu/Eu* *vs.* Ce/Ce* and Eu/Eu* *vs.* Ce/Lu_N efficiently discriminates the REY fractionation trends among the sample. Using these diagrams, the quartz vein shows strong positive Eu-anomaly (2.43-2.59), whereas other lithologies generally have Eu/Eu* and Ce/Lu_N less than 1. These trends (Ce- and Eu anomalies, Eu/Eu*vs. Ce/Lu_N) may be interpreted as albitization process during hydrothermal alteration, with samples closer to the vein more affected by this process.

The evidence from Spearman's correlation (Fig. 82A) also supports this interpretation. Positive correlation between the Au and Na are generally considered to indicate albitization process. Gold has a positive correlation with Ag, As, Cd, Pb, S and Sb. It supports the petrographical observation, that gold has a strong relation with As-Sb-S-bearing minerals, including chalcopyrite, tetrahedrite-tenanntite and enargite/luzonite-famatinite; as well as with Cd-Pb bearing minerals, *i.e.* galena. In addition, the depletion in Al, Fe, Mg, K, Mn is related to the replacement of Al- Fe- Mg – Mn - K silicate bearing minerals within

the alteration zones, in particular in the vicinity of veins that contain abundant quartz and sulphide minerals.

Bivariate plots of Figure 82B shows that Ca+Na of whole rock data in quartz veins correlate positively with Mg+Fe. It can be interpreted that veins were likely altered by various types of minerals, including albite, carbonate (calcite, dolomite-ankerite, siderite) and chlorite, which contributes to the enrichment of Ca, Na, Mg and Fe in quartz veins. High Mg + Fe and low Ca + Na characterize most rocks at Salu Bullo.

Figures 82E-L illustrates the distribution of gold *vs.* other trace elements. Gold has a strong correlation with Ag, As, Sb, Cu and S. Bismuth has a weak correlation with gold. Bivariate plots of gold and other trace elements in hematitic mudstone show that this lithology has a high content of gold and other trace elements. Petrographical observation supports the interpretation that hematitic mudstone often contains significant sulphide and sulphosalts, which is commonly associated with gold. Iron-bearing rocks prove to be important geochemical traps for the release of gold from hydrothermal solutions. The hematitic mudstone has the potential to be the future target for mineral exploration in the area.

9.3.7 Origin of carbonates

Carbonates within the metasedimentary and metavolcanic rocks of the Latimojong Mountains have the following stable isotope characteristics: $\delta^{13}C$: -13.30 to +1.18‰ VPDB; $\delta^{18}O$: +16 to +24.3‰ VSMOW. The average $\delta^{13}C$ values for calcite and dolomite-ankerite in the Awak Mas and Salu Bulo gold deposits are -0.91‰ for calcite and -5.49‰ for dolomite. According to Ohmoto and Rye (1979), the carbonate minerals from Awak Mas and Salu Bullo have $\delta^{13}C$ values that overlap with several possible fields, including fresh water limestone, marine limestone, and reduced carbon in sedimentary and metamorphic rocks. Some data were also overlaps with the range of mantle (-5 ± 2‰, Deines 1980), however, the oxygen values of mantle are lower than the the result of this study (Fig. 91). There are several possibilities for a mixed carbon-oxygen in the hydrothermal veins of the Awak Mas and Salu Bullo gold deposits.

1. The isotopic composition of altered host rock is shifted towards lighter values during interaction with hydrothermal fluids, resulting in distinctive isotopic ratios between hydrothermally altered and unaltered host rock (Hakim and Melcher 2017b).
2. Two samples of unaltered materials (calcite) plots in the marine carbonate field (Fig. 91A). This can be explained by the occurrence of foraminifera in this sample, which most likely represent a carbonate block derived from the Toraja Group (20 km to the west of the Latimojong Mountains). According to White et al. (2017) and references therein, this nummulitic limestones were deposited on tilted fault blocks during the early stages of graben development between the Eocene and Oligocene. Therefore, the isotopic values of unaltered materials is different with other observed data.
3. The source of carbon in the dolomites (Fig. 91B) is probably from the surrounding metasedimentary rocks which formed through metamorphic rock reactions, similar to the Muruntau gold district, Uzbekistan (Graupner et al. 2006). The halogen data (Cl/Br/I, Chapter 7.5) of the fluids trapped at Awak Mas and Salu Bullo are in agreement with metamorphic fluids with minor meteoric fluids, which contribute to the ore-bearing fluids circulating during the formation of the economic Au mineraliization.

9.3.8 Geothermometry of carbonates

Different geothermometers using cations in fluid leachates were applied (Table 47). These are the Na-K geothermometer of Giggenbach (1988); the Na-Li, Na-K and Mg-Li geothermometer of Kharaka and Mariner (1989, 2012). The Na-K geothermometer yields highly variable result (Table 47), for example the Na-K of Kharaka and Mariner (1989, 2012) yield 220-257°C for calcite, 92-450°C for dolomite-ankerite and 150-430°C for quartz. Some samples have been excluded from calculations because give unrealistic calculated temperature (e.g. sample FOS-fossil- has 1,400 ppb K. 1,100 ppb Na and 1.2 ppb Li, which gives Na-K temperature of >600°C, in contrast, Na-Li and Mg-Li geothermometer give low temperature of 150°C and 40°C, respectively).
Figure 102 has been constructed in order to illustrate the correlation between the cations geothermometer. The results show that Na-K and Na-Li

geothermometers yield higher temperature than Mg-Li geothermometer. Petrographical observations suggest that dolomite-ankerite and siderite are associated with ore minerals (gold, sulphide and sulphosalts), whereas calcite is observed as crack- or vesicle-filling. These late calcite veins are typically barren and crosscut mineralized quartz veins. The calculated temperatures (Na-K, Na-Li) are comparable to the microthermometric results. Dolomite-ankerite and quartz, which yields calculated temperature >400°C. may be interpreted as a metamorphic temperature of the greenschist facies in the Latimojong.

Table 47. Various geothermometers based on cation data.

		Na-K[1]	Na-K[2]	Na-Li[1]	Mg-Li[1]
Calcite	min	219.4	217.0	178.6	56.5
(n=3)	max	257.3	248.5	233.3	98.4
	average	232.7	228.0	207.3	72.7
	S.D.	21.4	17.8	27.4	22.5
Dolomite-Ankerite	min	92.4	105.8	77.4	29.8
(n=13)	max	454.7	401.2	248.5	136.6
	average	258.2	247.4	156.1	82.0
	S.D.	89.1	72.9	57.7	26.0
Quartz	min	148.6	156.2	102.8	50.1
(n=46)	max	430.0	383.0	236.2	133.7
	average	294.5	277.5	164.6	93.6
	S.D.	69.1	55.9	30.9	22.9

[1]Kharaka and Mariner (1989, 2012) [2]Giggenbach (1988).

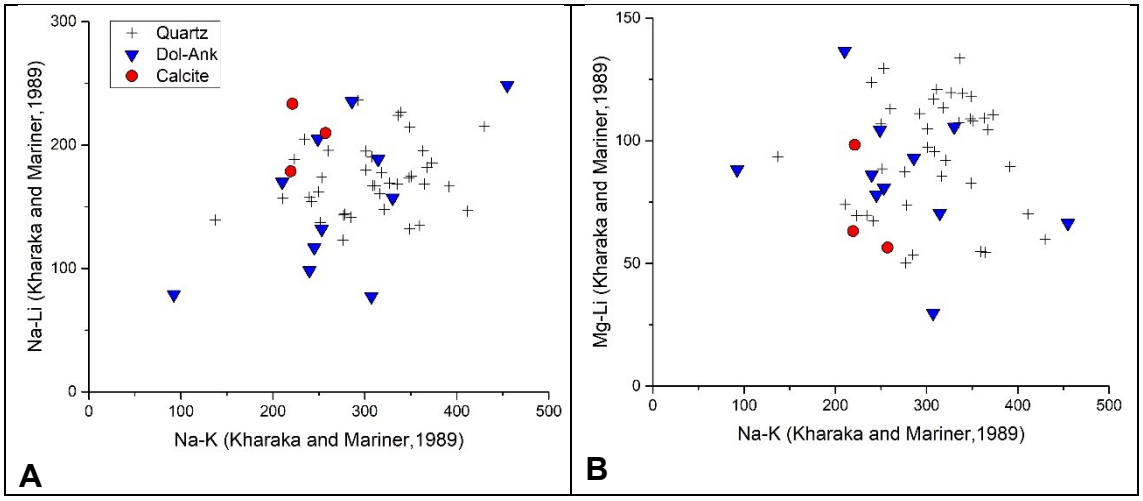

Fig. 102. Bivariate plots of (A) Na-Li, and (B) Mg-Li *vs.* Na-K geothermometers obtained from crush leach data.

9.3.9 Mineralization related to metamorphism

Progressive metamorphism of sedimentary rocks has been shown to mobilize elements, including Au, As, to form world-class orogenic gold deposits, such as in metasedimentary schist belt in southern New Zealand (Pitcairn et al. 2006; Large et al. 2011). The gold trace elements were released from those rocks into metamorphic fluids that are generated by metamorphic dehydration reactions (Large et al. 2011). These authors considered that carbonaceous metasedimentary rocks are required to form large deposits in metasedimentary host rocks (Carlin-type and Orogenic gold deposits). Gold and arsenic are introduced early into black shale and turbidites during sedimentation and diagenesis, and later concentrated to ore grades by hydrothermal, tectonic or magmatic processes.

Pitcairn et al. (2015) studied the effects of increasing metamorphic grade on the concentration of Au and related elements (As, Sb, Se and Hg) in metabasaltic samples in the Otago and Alpine schists. The results prove that metasedimentary rocks are more suitable source rocks for fluids and metals in orogenic gold deposits than metabasaltic rocks, as they show mobility during metamorphism of all elements commonly enriched in this style of deposit. Similarly, the Macraes gold of the Otago schist belt in southern New Zealand, does not show evidence for magmatism in the later stages of metamorphism when mineralization occurred (Goodwin et al. 2017). These authors suggest that the fluids and metals were mobilized from metasedimentary host rocks during metamorphism from pumpellyite-actinolite facies to amphibolite facies.

According to geochemical data obtained by XRF and ICP-MS from this study (Chapter 5.8), the metasedimentary rocks within the Latimojong may contents up 0.21 ppm Au, 67.62 ppm As and 19.41 ppm Sb (Table 27). Refractory gold can be observed in carbonaceous phyllites as inclusion blebs in pyrite. This fluids (retrograde fluids) infiltrate along the cracks or shear-zone, and graphite layers occur as a geochemical traps of the mineralising fluid. It still unclear whether metasedimentary rocks in Latimojong can also be the source rocks for the mineralising fluids and metals. Carbon occurs in sediments in a reduced form as

organic matter, oil, gas, or graphite, but can be oxidised to form carbonate species, CO_2 gas, and minerals (Yardley and Bodnar 2014).

Archibald et al. (1996) in van Leeuwen and Pieters (2011) inferred that the flysch sequence at Awak Mas district is unlikely to be a source of the gold owing to the low gold contents generally inherent to this sediment type. In addition, Neogene potassic igneous rocks may contribute to the potassic-rich alteration (sericite). These authors suggested that the source of fluids in Latimojong is the basement blueschist and associated serpentinites and/or adjacent ophiolites. Intense albite metasomatism accompanied by low-moderate temperature seafloor hydrothermal alteration is inferred to have leached the gold from the basaltic-gabbroic rocks (Archibald et al. 1996).

However, the mineralization history of Latimojong is comparable to gold deposits in the Otago and Alpine schists, New Zealand. The maximum pressure and temperature of metamorphism for the Otago schists are estimated at 450°C and between 4.5 and 8 kbar (Pitcairn et al. 2010). Locally, amphibolite-facies conditions have been reached. In comparison, the Latimojong Complex underwent pressure-dominated pumpellyite-actinolite to greenschist-facies metamorphism. However, high-grade metamorphic rocks are not present on the bore holes in Latimojong.

9.4 Genetic model

Phengite barometry and chlorite geothermometry in combination with temperature estimation on carbonaceous materials is used to establish a possible *P-T* path, assuming that coarse white mica and semi-graphite reflect the maximum *P-T* conditions in the studied area. Isochores obtained from fluid inclusions were included to illustrate the timing of mineralization related to metamorphism.

Petrographic observations indicate that white mica in metamorphic rocks from the studied samples is not equilibrated with the rest of the minerals of the rocks. The mineral assemblage is Ph + Qz + Ab + Gr in carbonaceous phyllite and Chl + Pmp - Ph with augite relic in clinopyroxene phyric basalts. The equilibrium problems of white mica in nature are commonly observed and had been indicated by Massonne and Schreyer (1987). Those authors indicated that homogenization

and re-equilibration of phengitic micas is an extremely sluggish process within geologic times scales; therefore, white mica still could be the key to unraveling the earlier stages of the metamorphic rock.

White mica in carbonaceous phyllites with Si contents of 3.19 - 3.48 a.p.f.u. (average of 3.37 a.p.f.u.) and temperature of 300-400°C (Raman spectroscopic analyses of carbonaceous materials) yields a pressure of ca. 3.45 - 12.3 kbar (average of 7.9 kbar) (Massonne and Schreyer 1987). This high pressure may represent the collision between the Indo-Australian and Eurasian plates during the Late Cretaceous. Elevated pressure signatures are also recorded by the mineral assemblage of some greenschist samples (Pmp + Act + Epi). The latter mineral asemblage is important in petrogenetic studies in this region, since it represents key minerals of the blueschist facies and likely the metamorphic peak in the Latimojong Metamorphic Complex. This will be discussed below.

In a low-grade metamorphic terrain, rocks containing albite + quartz may have, in addition, chlorite + pumpellyite in more ferroan compositions, chlorite + actinolite in magnesian bulk compositions, and prehnite in a bulk composition relatively lower in aluminium and ferric iron (Beiersdorfsser and Day 1995). The first appearance of calcic amphibole as overgrowth on relict clinopyroxene and as acicular crystals in quartz marks the beginning of the Pmp + Act + Epi facies. The minerals prehnite, laumontite, lawsonite, and glaucophane are absent in all samples.

The absence of these minerals provides important information, because those minerals bound the stability field of Pmp + Epi + Act. Prehnite and laumontite are restricted to low pressures; lawsonite and glaucophane are restricted to high pressures. With increasing temperature, the dissapearance of pumpellyite and prehnite and the appearance of albite - chlorite - actinolite - epidote - sphene mark the transition to greenschist facies assemblages.

According to the stability field of Pmp + Epi + Act suggested by Beiersdorfsser and Day (1995), and the absence of prehnite, laumontite, lawsonite and glaucophane correspond over to a wide pressure range, from 4 to 9 kbar at temperature between 200 – 350 °C.

Blueschist facies metamorphism within the temperature range 300–400°C is then followed by cooling and isothermal decompression to a maximum of 3 kbar (based on the ore fluids isochores), giving rise to gold precipitation. The brittle faults acted as fluid conduits for ore precipitation at shallow depth during retrogression. During the retrogression stage, hydrothermal alteration affected large volumes of rocks; therefore, most rocks studied were highly metamorphosed and hydrothermally altered. This observation is based on the mineralogy of host rock, which indicates that most host rocks have typical greenschist facies mineral assemblages of quartz + albite + calcite ± chlorite ± sphene. The pumpellyite - actinolite facies is observed only in more mafic host rocks, with mineral assemblages of Pmp + Act + Chl + Ep + Cal ± Spn ± Qz, sometimes with relic clinopyroxene.

Figure 103 illustrates the trapping conditions of pyrite - Au quartz veins, sulphide ± sulphosalt-Au quartz veins and barren veins. The isochores of the pyrite - Au stage are slightly above those of the sulphide-± sulphosalt-Au stage. The estimated trapping conditions of the pyrite - Au veins are at about 180 – 250 °C and <1.27 kbar. The sulphide ± sulphosalt veins are at similar temperatures and slightly lower pressures of less than 0.84 kbar. Both veins have similar dip directions and thus are parallel. The presence of minor amounts of CO_2 in inclusion type I results in flatter slopes which overlap with the sulphide ± sulphosalt Au isochore field (Fig. 103). Trapping conditions of the barren veins are at about 300 - 374°C and <1.15 kbar. The parallel isochores may reflect a gradual evolution of trapping conditions for each fluid generation.

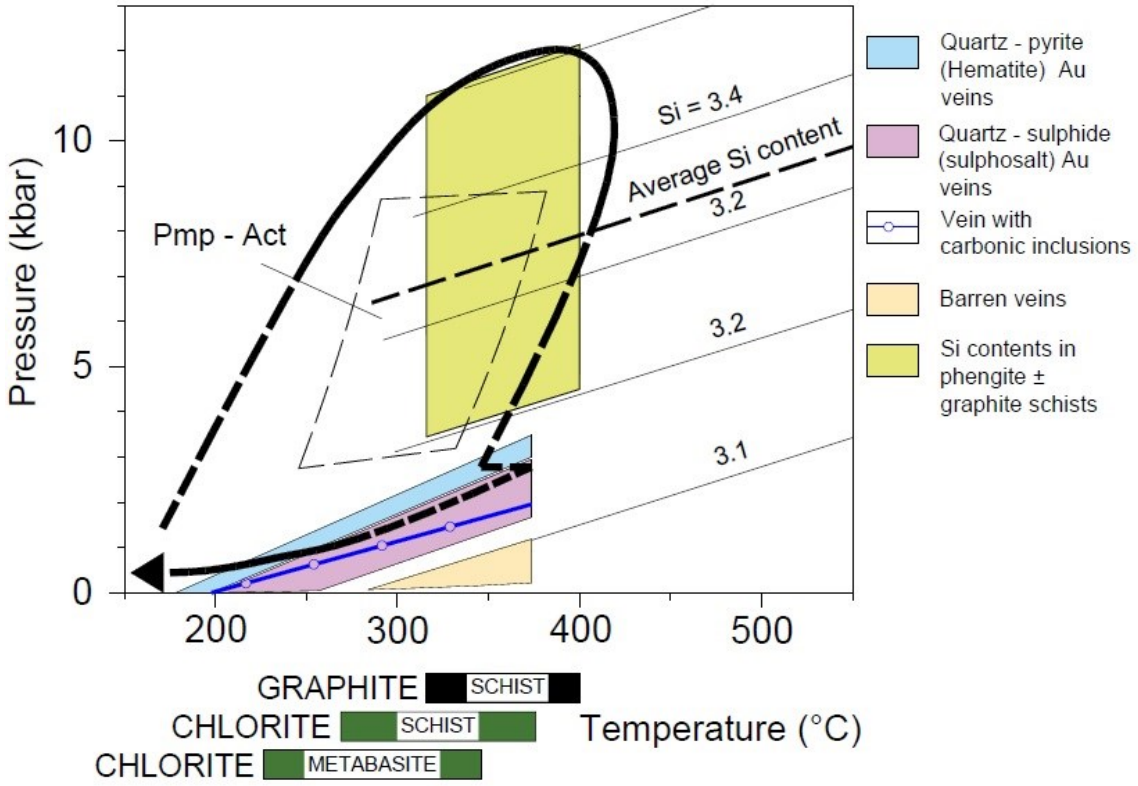

Fig. 103. General *P-T* reconstruction of the conditions prevailing in the Latimojong Complex using the phengite barometer diagram from Massonne and Schreyer (1987), graphite geothermometry based on IFORS software (Lünsdorf and Lünsdorf 2016), chlorite geothermometry according to Kranidiotis and MacLean (1987). The stability field of pumpellyite-actinolite based on Liou et al. (1987).

The fluid pressure estimation corresponds to depths less than 4.8 km, assuming lithostatic overburden. Based on the classification of orogenic gold by Groves et al. (1998), the gold deposits within the Latimojong belong to the epizonal orogenic gold group. This epizonal level of orogenic gold emplacement is consistent with the high As-Sb concentrations, the dominance of brittle structures and the open-space filling textures (Goldfarb et al. 2005). It is postulated that the fluid circulated in the studied area is a product of metamorphic dehydration, which going upwards along the crack, brittle and faults.

There are no earlier reports of the relative timing of gold ores to structural evolution in the studied area. Archibald et al. (1996) inferred that the gold mineralization took place between 8-6 Ma. This postulation is based on cross-cutting relationships, radiometric dating and superimposition of fluid temperatures on fission track uplift curves data from Bergman et al. 1996.

Based on this study, veins must be post-peak metamorphic; i.e., younger than ~80 Ma. On the other hand they must be older than the obduction of the Lamasi Complex (~30 Ma according to (Parkinson 1998), because the mineralization is bounded by a big thrust system (Kandeappi thrust). Hence, the age of the gold deposits in the Latimojong is post-Late Cretaceous but older than Miocene-Oligocene. Despite this earlier interpretation, there is still uncertainty about the timing of gold mineralization.

The timing of mineralization can potentially be dated using radioactive minerals, including monazite, xenotime and zircon. In the Awak Mas and Salu Bullo gold fields, monazite is abundant, whereas xenotime, baddeleyite and rutile are minor. Those minerals are associated with mineralized ore veins, and have irregular grain shapes. The size of minerals is generally less than 30 micron in diameter, therefore, mineral separation needed for age dating. In-situ geochronological investigations on these minerals should provide more clarity about the timing of mineralization.

In summary there is evidence for post-orogenic gold deposits (Groves et al. 1998; Goldfarb and Groves 2015). The Latimojong is similar to those described from other localities, including New Consort, South Africa (Otto et al. 2007), Renco, Zimbabwe; (Kolb et al. 2015), the Tauern gold deposit, Eastern Alps (Paar 1994; Pohl and Belocky 1999; Günther and Paar 2000; Raith et al. 2015); the Brusson deposit, NW Italy (Yardley 1993) and the Otago and Alpine schists, New Zealand; (Craw et al. 2009; Pitcairn et al. 2015). Furthermore, there are some small gold provinces in metamorphic belts that are younger than 50 Ma (Goldfarb et al. 2005), including orogenic deposits in the European Alps, Greater Caucasus of the Georgia Republic and Southern Alps of New Zealand

In the Eastern Alps, gold is typically associated with arsenopyrite, pyrite and chalcopyrite, sometimes with sulphosalt and tellurides (Raith et al. 2015). In Macraes gold deposit, New Zealand (Craw and MacKenzie 2016), arsenopyrite, antimony and tungsten minerals are the most significant additions to the hydrothermally rocks. However, arsenopyrite and tungsten are absent in Latimojong.

It is suggested that there is no contribution of the intrusive rocks in Western Sulawesi during Neogene magmatism to the gold mineralization, as the halogen data do not fit to magmatic sources. The fluids circulating in the Latimojong are comparable to deep-seated fluids with some contribution of shallow water, probably meteoric water. Although the sulphosalt mineralogy may indicate a component of HS-epithermal mineralization, typical alteration assemblages (i.e. high-sulphidation: alunite, barite, kaolinite, diapore, pyrophyllite; low-sulphidation: adularia, illite) are absent (Hakim et al. 2017). Moderate salinity of fluid inclusions and the presence of aqueous-carbonic inclusions ($CO_2 \pm N_2$) also argue against the epithermal model. Furthermore, the deposit is characterised by low-silver content (Au:Ag ratio is 9:1) and the ratios do not change significantly with depth (Hakim and Melcher 2016) which is not typical for an epithermal gold model.

Finally, Figure 104 illustrates the possible mechanism of gold precipitation in the Latimojong metamorphic complex. Gold mineralizations in Latimojong (Awak Mas and Salu Bullo) are not related with intrusion and are different from the Palopo gold district, where a monzonite intrusion is available as the heat souce for mineralisation (van Leeuwen and Pieters 2011). It is speculated that the melts and fluids in Palopo gold district derived from the same magma sources with the intrusion. Features of gold deposits in the Latimojong are summarized in Table 48.

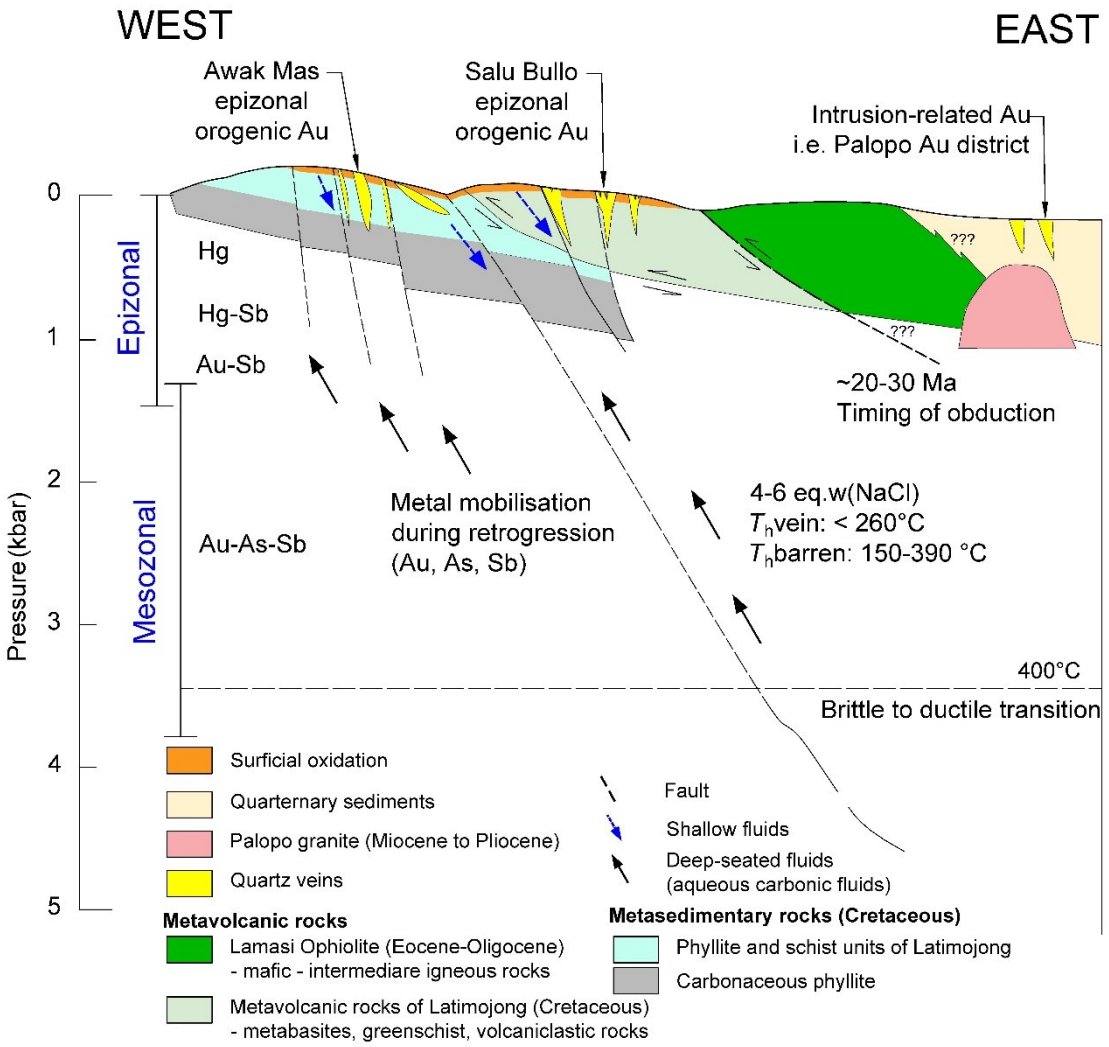

Fig. 104. Mechanism of structurally-controlled ore precipitation in the Latimojong metamorphic complex during retrograde metamorphism. The deposits are interpreted to have formed in a shallow environment (epizonal) via fluid-mixing between a deep-seated fluid with meteoric water.

Table 48. Characteristic of Awak Mas and Salu Bullo gold deposits

	Awak Mas-Salu Bullo Epizonal Orogenic Au deposits	**Orogenic Deposit**	**High Sulphidation Epithermal Deposit**
Tectonic setting	Veins precipitated in oblique normal faults, extensional faults, extensional shears and fractures of continental crust and mafic metavolcanic rocks	Continental margin; compressional to transpressional regime; veins typically in metamorphic rocks on seaward side of continental arc	Oceanic arc, continental arc, or back-arc extension of continental crust, extensional environments, but commonly in compressional regimes
Host rock	Metasedimentary rocks: phyllite, carbonaceous phyllite, chlorite schist, carbonaceous breccia, metasandstone Metavolcanic rocks: metatuff, metabasite.	Deformed metamorphic terranes of all ages	Calc-alkaline volcanic rock (and associated sediments) which are strongly leached, typically leaving a vuggy silica residue, subsequently recrystallized to quartz
Mineralogy	Vein-I: Quartz + pyrite + (hematite + galena) Vein-II: Quartz + pyrite + tennantite + tetrahedrite + enargite/luzonite ± sphalerite ± galena Barren: Albite + white mica + dolomite-ankerite	Qz-dominant vein system, $\leq$ 3-5% sulfide minerals, $\leq$ 5-15%, albite, white mica or fuchsite, chlorite, scheelite and albite	Enargite, tennantite-tetrahedrite and covellite, ± sphalerite ± galena (“acid-sulfate” type). Zonation is common, including alunite, kaolinite/dickite, pyropyllite ± dickite/diaspore ± pyrite ± baryte
Vein texture	Disseminated, brecciated veins	Stockwork, breccia	Massive, vuggy silica texture, disseminated
Alteration	Albitization, chloritization, sericitization, dolomitization, silicification.	Carbonation, sericitization, sulphidation, skarn-like assemblages in higher temperature deposits	Quartz ± alunite ± pyrophyllite ± dickite ± kaolinite
Metamorphic grade	Greenschist- to blueschist-facies	Varies from subgreenschist – greenschist – amphibolite facies, greenschist is the most common facies	Unrelated to metamorphism
Temperature of formation (°C)	Mineralization: $\leq$ 250 Barren: 150-400	200 – 700	100 – 300

	Awak Mas-Salu Bullo Epizonal Orogenic Au deposits	Orogenic Deposit	High Sulphidation Epithermal Deposit
Depth of emplacement (km)	Epizonal (< 6 km)	2-20	surface - 2
Ore fluid composition	3-8 eq. wt% NaCl (average of 5 eq. wt% NaCl), ($\chi^{vap}CO_2$= 0.10 to 0.144)	3-10 eq. wt% NaCl, $\geq$ 5 mol% CO_2; traces of CH_4 and N_2	< 1-20 eq. wt% NaCl; early acidic condensate
Fluid source	Halogen data support the evidence of fluid mixing between deep-seated fluid with meteoric fluid	Deep sourced crustal fluid	Hydrothermal fluid with little contribution of meteoric water
Au:Ag	8-9, gold has high fineness (800-950)	1 – 10 , high gold fineness	0.02-1
Other key features	Hosted in deformed metasedimentary or metavolcanic rocks, disseminated sulfide mineralization; minor volcanic rocks. Different vein types: (i) quartz-pyrite (hematite)-Au veins, (ii) sulfide-sulfosalt quartz vein; (iii) breccia quartz veins; (iv) hematitic mudstone and carbonaceous phyllite; (v) barren dolomite-quartz veins.	Hosted in deformed metamorphic terranes, $\leq$ 3-5% sulfide minerals; individual deposit of $\geq$ 1-2 km vertical extent; spatial association with transcrustal fault zones and granitic magmatism.	Veins and replacements are similar age as ore-hosting or nearby volcanic rocks; disseminated ore common
Magmatism	No evidence for involvement of magmatic-hydrothermal fluids during Neogene magmatism. Au-As-Sb were mobile during metamorphism, which may have originated from metasedimentary rocks, or precipitated in a shear-zone.	Only few examples to support formation of orogenic gold deposit from magmatic-hydrothermal fluids. Fluids may have exsolved from a melt emplaced into the upper or middle crust, therefore, magmatic fluid not typical for this type of mineral deposit	Important. Acid fluids responsible for leaching, resulting in advanced argillic alteration.

References: compilation from White and Hedenquist (1995), Groves et al. (1998), Simmons et al. (2005), Goldfarb and Groves (2015).

10. CONCLUSION

Petrographical, mineralogical, and geochemical methods of metasedimentary and metavolcanic rocks in Latimojong have been used to construct the geologic setting of Awak Mas and Sau Bullo prospects, as well as a genetic model for gold mineralization. The host rocks of the deposits are metasediments and metabasites, which underwent blueschist- to greenschist facies metamorphism. Based on relic magmatic clinopyroxene and chromian spinel compositions, in combination with whole-rock geochemical data, the protolith of the metabasites are basalts formed in an island-arc environment. Metasedimentary rocks have LILE enrichment and high LREE/HREE ratios relative to primitive mantle, which may be intepreted as a slab dehydration process during high-pressure metamorphism at mantle depths. It is unclear whether the orthogneiss observed in the fieldnseparates the metamorphic complex from the ophiolite. The orthogneiss probably represents part of the metamorphic sole of the ophiolite.

Pumpellyite + epidote + actinolite + chlorite ± calcite are the main minerals of mafic metavolcanic rocks, and white mica + graphite + quartz + chlorite siderite + sphene are the mineral assemblages of the metasedimentary rocks. The chlorite at Salu Bullo is chlinochlore, Mg-rich (Mg# 43-74), indicating formation temperatures between 260 and 309°C. In contrast, chlorite at Awak Mas is characterized by iron-rich chlorite (chamosite), low Mg-number (Mg# 32 – 49) and indicating temperatures from 307 to 372°C. The formation temperature of chlorite consistently increases with depth. These formation temperatures are also consistent with a geothermometer based Raman Spectra of Carbonaceous Materials (RSCM) which yield temperatures in the range of 316 to 395°C. Interestingly, carbonaceous samples containing ore minerals yield higher temperature compared to barren samples. Cation geothermometers calculated from fluid leachate data yield highly variable temperatures, i.e. the Na-K geothermometer yields 219-257°C for calcite, 92-455°C for dolomite-ankerite, and 150-430°C for quartz.

Geochemical modelling indicates that metavolcanic and metasedimentary rocks from the accretionary complex in the Central Sulawesi are comparable to

blueschist- and eclogite- facies rocks at Bantimala, South Sulawesi. The results of this study do not support the existence of ophiolite rocks within the mineralized area in the Latimojong Metamorphic Complex.

Gold is the only economic mineral at Awak Mas and Salu Bullo. Gold grains are usually small (average of 10 μm), mainly hosted by late hydrothermal pyrite. Gold occurs within pyrite cracks, as an inclusion in pyrite (sometimes less than 1 micron in size), and in some outcrop samples, gold occurs as free-grains in quartz. Both gold types (inclusions in pyrite and free-grains) have high fineness (850 – 935) and are classified as electrum.

Tetrahedrite-tennantite solid solution with wide Sb/(Sb+As+Bi) ratio is associated with gold. Sulphosalts are enriched in copper, antimony and arsenic, and some samples carry exceptionally mercurian-rich tetrahedrite (up to 17.11 wt% Hg). Silver and bismuth content in sulphosalts are below the detection limit of the electron microprobe.

The trace element contents in pyrite from the Awak Mas and Salu Bullo deposits were determined by electron microprobe and LA-ICP-and MS show enrichment in Co, Ni and As. Pyrite shows concentric, oscillatory zoning parallel to crystal faces. Gold concentrations in pyrite are low, commonly below detection limit (<0.1 ppm). The resuls of LA-ICP-MS on sphalerite indicating that sphalerite in Salu Bullo carries low Fe and Ni, but significant In and Cd. Pyrite and sphalerite have high Ag and Bi contents, which are most probably due to the occurence of microinclusions of Ag-Bi bearing minerals and/or galena inclusions. Galena also occurs replacing framboidal pyrite.

Spearman coefficient correlation rank from whole-rock analysis obtained from the mining company illustrate that gold has a positive correlation with Ag, As, Cd, Pb, S, and Sb. This supports the interpretation that gold is strongly related to As-Sb-S-bearing minerals (i.e. tetrahedrite, tennantite and enargite/luzonite-famatinite), and Pb-Cd-S bearing mineral (i.e. galena and sphalerite).

Albite, dolomite-ankerite, chlorite, and white mica are the dominant alteration minerals. Samples closer to the veins have high-Eu and low-Ce anomalies, which significantly decrease with increasing distance. This might be explained by the

albitization process during hydrothermal alteration, where Eu will fractionate into the albite, resulting in a strong positive-Eu anomaly.

Gold deposits formed from H_2O-CO_2-NaCl (type I), H_2O-NaCl (type II, type III) fluids. The estimated trapping conditions of the gold are between 180 to 250°C at pressures ca. 0.84 to 1.3 kbar. Trapping conditions of the barren veins are at about 300 - 374°C and <1.15 kbar. The fluid pressure estimation corresponds to a depth lower than 5 km, assuming lithostatic conditions. The gold deposits within the Latimojong are classified as epizonal orogenic gold, consistent with the high As-Sb concentrations, the dominance of brittle structures and the open-space filling textures. Considering the homogenization and salinity data, the bisulphide complex (HS^-) is considered as the main ligand for gold deposition. Iron-rich and carbonaceous rocks prove to be the important geochemical traps for the release of gold from hydrothermal solution.

Halogen ratios in fluid inclusions in mineralized rocks provide evidence for the fluid mixing of deep-seated and meteoric water. The late influx of meteoric water was probably favoured by the connection of fluid reservoirs with faults responsible for rapid uplift of the metamorphic complex into shallow crustal levels. Phase separation in response to decreasing pressures during the rise of the ore fluid and fluid mixing appear to be most important factors of gold precipitation in the open space of secondary faults.

The mineralization was induced by the onset of rapid uplift after Miocene continental collision, before the obduction of the Lamasi Ophiolite Complex over the Latimojong Metamorphic Complex. Metamorphic reactions in the metasedimentary rocks during the retrogression stage are considered as the main source of ascending fluids to form the Au-mineralization at Latimojong. The deposit formed during a retrogression event following isothermal decompression and post-dates regional metamorphism.

References

Abidin HZ (1998) Tectonic history and mineral deposits of the East-Central Kalimantan volcanic belt, Indonesia: A comparative study of the Kelian, Muyup and Masupa Ria gold deposits/by Hamdan Zainal Abidin

Abraitis PK, Pattrick R, Vaughan DJ (2004) Variations in the compositional, textural and electrical properties of natural pyrite: A review. International Journal of Mineral Processing 74:41–59. doi: 10.1016/j.minpro.2003.09.002

Anderko A, Pitzer KS (1993) Equation-of-state representation of phase equilibria and volumetric properties of the system NaCl-H2O above 573 K. Geochimica et Cosmochimica Acta 57:1657–1680. doi: 10.1016/0016-7037(93)90105-6

Angeles CA, Prihatmoko S, Walker JS (2002) Geology and Alteration-Mineralization Characteristics of the Cibaliung Epithermal Gold Deposit, Banten, Indonesia. Resource Geology 52:329–339. doi: 10.1111/j.1751-3928.2002.tb00143.x

Anovitz LM, Essene EJ (1987) Phase Equilibria in the System CaCO3-MgCO3-FeCO3. Journal of Petrology 28:389–415. doi: 10.1093/petrology/28.2.389

Arai S (1992) Chemistry of Chromian Spinel in Volcanic Rocks as a Potential Guide to Magma Chemistry. Mineral. Mag. 56:173–184. doi: 10.1180/minmag.1992.056.383.04

Arif J, Baker T (2004) Gold paragenesis and chemistry at Batu Hijau, Indoneisa: Implications for gold-rich porphyry copper deposits. Miner Deposita 39:523–535. doi: 10.1007/s00126-004-0433-0

Arlt T, Diamond LW (1998) Composition of tetrahedrite-tennantite and "schwazite" in the Schwaz silver mines, North Tyrol, Austria. Mineral. Mag. 62:801

Augustithis S-SP (1995) Atlas of the Textural Patterns of Ore Minerals and Metallogenic Processes. De Gruyter, Berlin

Bajwah ZU, Seccombe PK, Offler R (1987) Trace element distribution, Co: Ni ratios and genesis of the big cadia iron-copper deposit, new south wales, australia. Mineral. Deposita 22. doi: 10.1007/BF00204522

Bakker RJ (1997) Clathrates: Computer programs to calculate fluid inclusion V-X properties using clathrate melting temperatures. Computers & Geosciences 23:1–18. doi: 10.1016/S0098-3004(96)00073-8

Bakker RJ (2003) Package FLUIDS 1. Computer programs for analysis of fluid inclusion data and for modelling bulk fluid properties. Chemical Geology 194:3–23. doi: 10.1016/S0009-2541(02)00268-1

Bakker RJ, Diamond LW (2006) Estimation of volume fractions of liquid and vapor phases in fluid inclusions, and definition of inclusion shapes. American Mineralogist 91:635–657. doi: 10.2138/am.2006.1845

Banks D, Yardley B (1992) Crush-leach analysis of fluid inclusions in small natural and synthetic samples. Geochimica et Cosmochimica Acta 56:245–248. doi: 10.1016/0016-7037(92)90129-7

Banks D, Gleeson S, Green R (2000) Determination of the origin of salinity in granite-related fluids: Evidence from chlorine isotopes in fluid inclusions. Journal of Geochemical Exploration 69-70:309–312. doi: 10.1016/S0375-6742(00)00076-5

Barnes SJ, Roeder PL (2001) The range of spinel compositions in terrestrial mafic and ultramafic rocks. Journal of Petrology 42:2279–2302

Barnes HL (1979) Solubilities of ore minerals. Geochemistry of hydrothermal ore deposits 2:404–460

Barton PB, Skinner BJ (1979) Sulfide mineral stabilities: Geochemistry of Hydrothermal Ore Deposits, 2nd edn. Wiley, New-York

Barton Jr. PB, Bethke PM (1987) Chalcopyrite disease in sphalerite: Pathology and epidemiology. American Mineralogist 72:451–467

Basuki A, Aditya Sumanagara D, Sinambela D (1994) The Gunung Pongkor gold-silver deposit, West Java, Indonesia. Journal of Geochemical Exploration 50:371–391. doi: 10.1016/0375-6742(94)90032-9

Beccaluva L, Macciotta G, Piccardo GB, Zeda O (1989) Clinopyroxene composition of ophiolite basalts as petrogenetic indicator. Chemical Geology 77:165–182. doi: 10.1016/0009-2541(89)90073-9

Beiersdorfsser RE, Day HW (1995) Mineral paragenesis of pumpellyite in low-grade mafic rocks. In: Schiffman P, Day HW (eds) Low-grade metamorphism of mafic rocks, vol 296. Geological Society of America, Boulder, Colo., pp 5–28

Bergman SC, Coffield DQ, Talbot JP, Garrard RA (1996) Tertiary Tectonic and magmatic evolution of western Sulawesi and the Makassar Strait, Indonesia: Evidence for a Miocene continent-continent collision. Geological Society, London, Special Publications 106:391–429. doi: 10.1144/GSL.SP.1996.106.01.25

Beyssac O, Goffé B, Chopin C, Rouzaud JN (2002) Raman spectra of carbonaceous material in metasediments: A new geothermometer. Journal of Metamorphic Geology 20:859–871. doi: 10.1046/j.1525-1314.2002.00408.x

Böhlke J, Irwin J (1992) Laser microprobe analyses of Cl, Br, I, and K in fluid inclusions: Implications for sources of salinity in some ancient hydrothermal fluids. Geochimica et Cosmochimica Acta 56:203–225. doi: 10.1016/0016-7037(92)90127-5

Boiron M-C, Barakat A, Cathelineau M, Banks DA, Durisová J, Morávek P (2001) Geometry and P–V–T–X conditions of microfissural ore fluid migration: The Mokrsko gold deposit (Bohemia). Chemical Geology 173:207–225. doi: 10.1016/S0009-2541(00)00276-X

Boiron M-C, Cathelineau M, Banks DA, Fourcade S, Vallance J (2003) Mixing of metamorphic and surficial fluids during the uplift of the Hercynian upper crust: Consequences for gold deposition. Chemical Geology 194:119–141. doi: 10.1016/S0009-2541(02)00274-7

Bourdelle F, Cathelineau M (2015) Low-temperature chlorite geothermometry: A graphical representation based on a *T*–R^{2+} –Si diagram. Eur.J.Mineral. 27:617–626. doi: 10.1127/ejm/2015/0027-2467

Bouyo MH, Zhao Y, Penaye J, Zhang SH, Njel UO (2015) Neoproterozoic subduction-related metavolcanic and metasedimentary rocks from the Rey Bouba Greenstone Belt of north-central Cameroon in the Central African Fold Belt: New insights into a continental arc geodynamic setting. Precambrian Research 261:40–53. doi: 10.1016/j.precamres.2015.01.012

Brill BA (1989) Trace-element contents and partitioning of elements in ore minerals from the CSA Cu–Pb–Zn deposit, Australia. Can. Mineral 27:263–274

Carlile J, Davey G, Kadir I, Langmead R, Rafferty W (1998) Discovery and exploration of the Gosowong epithermal gold deposit, Halmahera, Indonesia. Journal of Geochemical Exploration 60:207–227. doi: 10.1016/S0375-6742(97)00048-4

Carlile JC, Mitchell A (1994) Magmatic arcs and associated gold and copper mineralization in Indonesia. Journal of Geochemical Exploration 50:91–142. doi: 10.1016/0375-6742(94)90022-1

Carlile JC, Digdowirogo S, Darius K (1990) Geological setting, characteristics and regional exploration for gold in the volcanic arcs of North Sulawesi, Indonesia. Journal of Geochemical Exploration 35:105–140. doi: 10.1016/0375-6742(90)90037-B

Ciobanu CL, Cook NJ, Pring A, Brugger J, Danyushevsky LV, Shimizu M (2009) 'Invisible gold' in bismuth chalcogenides. Geochimica et Cosmochimica Acta 73:1970–1999. doi: 10.1016/j.gca.2009.01.006

Clark LV (2013) The geology and genesis of the Kencana epithermal AU-AG deposit, Gosowong Goldfield, Halmahera Island, Indonesia, University of Tasmania

Cook NJ, Ciobanu CL, Pring A, Skinner W, Shimizu M, Danyushevsky L, Saini-Eidukat B, Melcher F (2009) Trace and minor elements in sphalerite: A LA-ICPMS study. Geochimica et Cosmochimica Acta 73:4761–4791. doi: 10.1016/j.gca.2009.05.045

Coutts BP, Susanto H, Belluz N, Flint D, Edwards A (1999) Geology of the deep ore zone, Ertsberg East skarn system, Irian Jaya: Pacrim'99 Congress, Bali, Indonesia, 1999. Proceedings: Melbourne, Australasian Institute of Mining and Metallurgy:539–547

Craig JR (2001) Ore-mineral textures and the tales they tell. The Canadian Mineralogist 39:937–956. doi: 10.2113/gscanmin.39.4.937

Craw D, Mackenzie DJ, Pitcairn IK, Teagle D, Norris RJ (2007) Geochemical signatures of mesothermal Au-mineralized late-metamorphic deformation zones, Otago Schist, New Zealand. Geochemistry: Exploration, Environment, Analysis 7:225–232. doi: 10.1144/1467-7873/07-137

Craw D, Upton P, Mackenzie DJ (2009) Hydrothermal alteration styles in ancient and modern orogenic gold deposits, New Zealand. New Zealand Journal of Geology and Geophysics 52:11–26. doi: 10.1080/00288300909509874

Craw D, MacKenzie D (2016) Macraes orogenic gold deposit (New Zealand): Origin and development of a world class gold mine. SpringerBriefs in world mineral deposits. Springer, Switzerland

Darman H, Sidi FH (2000) An outline of the geology of Indonesia. Indonesian Association of Geologists, Jakarta

Davies AGS, Cooke DR, Gemmell JB, Simpson KA (2008a) Diatreme Breccias at the Kelian Gold Mine, Kalimantan, Indonesia: Precursors to Epithermal Gold Mineralization. Economic Geology 103:689–716. doi: 10.2113/gsecongeo.103.4.689

Davies AGS, Cooke DR, Gemmell JB, van Leeuwen T, Cesare P, Hartshorn G (2008b) Hydrothermal Breccias and Veins at the Kelian Gold Mine, Kalimantan, Indonesia: Genesis of a Large Epithermal Gold Deposit. Economic Geology 103:717–757. doi: 10.2113/gsecongeo.103.4.717

Deer WA, Howie RA, Zussman J (2001) Rock-forming minerals. Volume 4A, Framework silicates: Feldspars / W.A. Deer, R.A. Howie, J. Zussman, 2nd ed. Geological Society, London

Deer WA, Howie RA, Zussman J (2009) Layered silicates excluding micas and clay minerals, 2nd ed. Rock-forming minerals, v. 3B. Geological Society, London

Deines P (1980) The carbon isotopic composition of diamonds: Relationship to diamond shape, color, occurrence and vapor composition. Geochimica et Cosmochimica Acta 44:943–961. doi: 10.1016/0016-7037(80)90284-7

Dewaele S, Muchez P, Vets J, Fernandez-Alonzo M, Tack L (2006) Multiphase origin of the Cu–Co ore deposits in the western part of the Lufilian fold-and-thrust belt, Katanga (Democratic Republic of Congo). Journal of African Earth Sciences 46:455–469. doi: 10.1016/j.jafrearsci.2006.08.002

Dill HG (2001) The geology of aluminium phosphates and sulphates of the alunite group minerals: A review. Earth-Science Reviews 53:35–93. doi: 10.1016/S0012-8252(00)00035-0

Drew LJ, Berger BR, Kurbanov NK (1996) Geology and structural evolution of the Muruntau gold deposit, Kyzylkum desert, Uzbekistan. Ore Geology Reviews 11:175–196. doi: 10.1016/0169-1368(95)00033-X

Duan Z, Møller N, Weare JH (1992a) An equation of state for the CH4-CO2-H2O system: I. Pure systems from 0 to 1000°C and 0 to 8000 bar. Geochimica et Cosmochimica Acta 56:2605–2617. doi: 10.1016/0016-7037(92)90347-L

Duan Z, Møller N, Weare JH (1992b) An equation of state for the CH4-CO2-H2O system: II. Mixtures from 50 to 1000°C and 0 to 1000 bar. Geochimica et Cosmochimica Acta 56:2619–2631. doi: 10.1016/0016-7037(92)90348-M

Duan Z, Møller N, Weare JH (1995) Equation of state for the NaCl-H2O-CO2 system: Prediction of phase equilibria and volumetric properties. Geochimica et Cosmochimica Acta 59:2869–2882. doi: 10.1016/0016-7037(95)00182-4

Elburg M, Foden J (1999) Sources for magmatism in Central Sulawesi: Geochemical and Sr–Nd–Pb isotopic constraints. Chemical Geology 156:67–93. doi: 10.1016/S0009-2541(98)00175-2

Fisher NH (1945) The fineness of gold, with special reference to the Morobe gold field, New Guinea. Economic Geology 40:449–495. doi: 10.2113/gsecongeo.40.7.449

Foit FF, Ulbricht ME (2001) Compositional variation in mercurian tetrahedrite tennantite from the epithermal deposits of the Steens and Pueblo Mountains, Harney County, Oregon. The Canadian Mineralogist 39:819–830. doi: 10.2113/gscanmin.39.3.819

Foit FF, Hughes JM (2004) Structural variations in mercurian tetrahedrite. American Mineralogist 89:159–163. doi: 10.2138/am-2004-0118

Force ER (ed) (1991) Geology of titanium-mineral deposits. Special paper, vol 259. Geological Society of America, Boulder, Colo.

Frape SK, Fritz P (1987) Geochemical Trends for Groundwaters from the Canadian Shield. Geological Association of Canada 33:19–38

Frey M, Robinson D (1999) Low-grade metamorphism. Blackwell Science, Oxford

Gammons CH, Williams-Jones AE (1995) Hydrothermal geochemistry of electrum; thermodynamic constraints. Economic Geology 90:420–432. doi: 10.2113/gsecongeo.90.2.420

Gammons CH, Williams-Jones AE (1997) Chemical mobility of gold in the porphyry-epithermal environment. Economic Geology 92:45–59. doi: 10.2113/gsecongeo.92.1.45

Garwin S, Hall R, Watanabe Y (2005) Tectonic setting, geology, and gold and copper mineralization in Cenozoic magmatic arcs of Southeast Asia and the West Pacific. Economic Geology 100th Anniversary Volume:891–900

Garwin SL (2000) The Setting, Geometry and Timing of Intrusion-related Hydrothermal Systems in the Vicinity of the Batu Hijau Porphyry Copper-gold Deposit, Sumbawa, Indonesia. University of Western Australia

Gebre-Mariam M, Groves DI, McNaughton NJ, Mikucki EJ, Vearncombe JR (1993) Archaean Au−Ag mineralisation at Racetrack, near Kalgoorlie, Western Australia: A high crustal-level expression of the Archaean composite lode-gold system. Mineral. Deposita 28:375–387. doi: 10.1007/BF02431597

Gemmell JB (2007) Hydrothermal Alteration Associated with the Gosowong Epithermal Au-Ag Deposit, Halmahera, Indonesia: Mineralogy, Geochemistry, and Exploration Implications. Economic Geology 102:893–922. doi: 10.2113/gsecongeo.102.5.893

Giggenbach WF (1988) Geothermal solute equilibria. Derivation of Na-K-Mg-Ca geoindicators. Geochimica et Cosmochimica Acta 52:2749–2765. doi: 10.1016/0016-7037(88)90143-3

Gleeson SA (2003) Bulk analyses of electrolytes in fluid inclusions: In: Samson I, Anderson A, Marshall D (eds) Fluid Inclusions: analysis and interpretation. Mineralogical Association of Canada, Short Course 32, pp 233-247

Gleeson SA, Wilkinson JJ, Stuart FM, Banks DA (2001) The origin and evolution of base metal mineralising brines and hydrothermal fluids, South Cornwall, UK. Geochimica et Cosmochimica Acta 65:2067–2079. doi: 10.1016/S0016-7037(01)00579-8

Goldfarb RJ, Groves DI (2015) Orogenic gold: Common or evolving fluid and metal sources through time. Lithos 233:2–26. doi: 10.1016/j.lithos.2015.07.011

Goldfarb RJ, Baker T, Dube B, Groves DI, Hart C, JR, Gosselin P (2005) Distribution, character, and genesis of gold deposits in metamorphic terranes. Economic Geology 100th anniversary volume 40

Goodwin NRJ, Burgess R, Craw D, Teagle DAH, Ballentine CJ (2017) Noble gases fingerprint a metasedimentary fluid source in the Macraes orogenic gold deposit, New Zealand. Miner Deposita 52:197–209. doi: 10.1007/s00126-016-0648-x

Goodwin NRJ (2010) A combined noble gas and halogen study of orogenic gold mineralisation in the Alpine and Otago Schists, New Zealand, University of Manchester

Grammatikopoulos TA, Roth T, Valeyev O (2005) Compositional variation in Hg–Ag-rich tetrahedrite from the polymetallic Eskay Creek deposit, British Columbia, Canada. N. Jb. Miner. Abh. 181:281–292. doi: 10.1127/0077-7757/2005/0025

Grancea L, Bailly L, Leroy J, Banks D, Marcoux E, Milési J, Cuney M, André A, Istvan D, Fabre C (2002) Fluid evolution in the Baia Mare epithermal gold/polymetallic district, Inner Carpathians, Romania. Mineralium Deposita 37:630–647. doi: 10.1007/s00126-002-0276-5

Graupner T, Niedermann S, Kempe U, Klemd R, Bechtel A (2006) Origin of ore fluids in the Muruntau gold system: Constraints from noble gas, carbon isotope and halogen data. Geochimica et Cosmochimica Acta 70:5356–5370. doi: 10.1016/j.gca.2006.08.013

Greffie C, Bailly L, Milesi J-P (2002) Supergene Alteration of Primary Ore Assemblages fromLow-Sulfidation Au-Ag Epithermal Deposits at Pongkor, Indonesia, andNazareno, Peru. Economic Geology 97:561–571. doi: 10.2113/gsecongeo.97.3.561

Gregory DD, Large RR, Halpin JA, Baturina EL, Lyons TW, Wu S, Danyushevsky L, Sack PJ, Chappaz A, Maslennikov VV, Bull SW (2015) Trace Element Content of Sedimentary Pyrite in Black Shales. Economic Geology 110:1389–1410. doi: 10.2113/econgeo.110.6.1389

Gregory DD, Large RR, Bath AB, Steadman JA, Wu S, Danyushevsky L, Bull SW, Holden P, Ireland TR (2016) Trace Element Content of Pyrite from the Kapai Slate, St. Ives Gold District, Western Australia. Economic Geology 111:1297–1320. doi: 10.2113/econgeo.111.6.1297

Groves D, Goldfarb R, Gebre-Mariam M, Hagemann S, Robert F (1998) Orogenic gold deposits: A proposed classification in the context of their crustal distribution and relationship to other gold deposit types. Ore Geology Reviews 13:7–27. doi: 10.1016/S0169-1368(97)00012-7

Günther W, Paar WH (2000) Schatzkammer Hohe Tauern: 2000 Jahre Goldbergbau. Serie "Sonderpublikationen" der Schriftenreihe des Landespressebüros, vol 165. Pustet, Salzburg

Guntoro A (1999) The formation of the Makassar Strait and the separation between SE Kalimantan and SW Sulawesi. Journal of Asian Earth Sciences 17:79–98. doi: 10.1016/S0743-9547(98)00037-3

Hadjana I (2012) The Discovery, Geology, and Exploration of the High Sulphidation Au-Mineralization System in the Bakan District, North Sulawesi. Majalah Geologi Indonesia 27:143–157

Hagemann SG, Groves DI, Ridley JR, Vearncombe JR (1992) The Archean lode gold deposits at Wiluna, Western Australia; high-level brittle-style mineralization in a strike-slip regime. Economic Geology 87:1022–1053. doi: 10.2113/gsecongeo.87.4.1022

Hagemann SG, Gebre-Mariam M, Groves DI (1994) Surface-water influx in shallow-level Archean lode-gold deposits in Western, Australia. Geol 22:1067. doi: 10.1130/0091-7613(1994)022<1067:SWIISL>2.3.CO;2

Hakim AYA, Melcher F (2015) Mineralogical Study of the Awak Mas Deposit: A Contribution to the Ore Genesis of Disseminated Gold Deposits in South Celebes, Indonesia. Mitteilungen der Österreichischen Mineralogischen Gesellschaft 161:43 (abstract)

Hakim AYA, Melcher F (2016a) The composition of gold and mercurian rich tetrahedrite from the sedimentary hosted disseminated gold in Latimojong mountain, South Sulawesi, Indonesia. 1st Postgraduate conference on Geology of Ore Deposits. Freiberg 1:12 (abstract)

Hakim AYA, Melcher F (2016b) The Sallu Bulo Mesothermal Gold Deposit in South Sulawesi, Indonesia. GeoTirol 2016:98 (abstract)

Hakim AYA, Melcher F (2017a) Magmatic chromian spinel in metabasite from the Latimojong Mountains, Sulawesi, Indonesia. Mitteilungen der Österreichischen Mineralogischen Gesellschaft 163:42 (abstract)

Hakim AYA, Melcher F (2017b) Timing of mineralization and origin of hydrothermal carbonate at the gold deposits within the Latimojong Complex, Indonesia. 2nd Postgraduate conference on Geology of Ore Deposits. Hannover 2:22 (abstract)

Hakim AYA, Sulistijo B (2013) Integrated Exploration Method to Determine Cu Prospect in Seweden District, Blitar, East Java. Procedia Earth and Planetary Science 6:64–69. doi: 10.1016/j.proeps.2013.01.009

Hakim AYA, Heriawan MN, Indriati T, Dharma DB, Sanjaya M (2013) Mineralogical observation of Fe-skarn deposit in Lhoong prospect, Nanggroe Aceh Darussalam, Indonesia. International Symposium on Earth Sciences and Technology 2013. Fukuoka:274–279

Hakim AYA, Melcher F, Prochaska W, Bakker RJ, Rantitsch G (2017) The origin and evolution of fluids associated with gold deposits in the basement of Sulawesi, Indonesia. Proceedings of the 14th SGA Biennial Meeting, 20-23 August 2017, Québec City, Canada:355–358. doi: 10.13140/RG.2.2.13179.41767

Hall R (2002) Cenozoic geological and plate tectonic evolution of SE Asia and the SW Pacific: Computer-based reconstructions, model and animations. Journal of Asian Earth Sciences 20:353–431. doi: 10.1016/S1367-9120(01)00069-4

Hall R (2012) Late Jurassic–Cenozoic reconstructions of the Indonesian region and the Indian Ocean. Tectonophysics 570-571:1–41. doi: 10.1016/j.tecto.2012.04.021

Hardjana I (2012) The Discovery, Geology, and Exploration of the High Sulphidation Au-Mineralization System in the Bakan District, North Sulawesi. Majalah Geologi Indonesia 27:143–157

Harijoko A, Sanematsu K, Duncan RA, Prihatmoko S, Watanabe K (2004) Timing of the Mineralization and Volcanism at Cibaliung Gold Deposit, Western Java, Indonesia. Resource Geology 54:187–195. doi: 10.1111/j.1751-3928.2004.tb00199.x

Harjanto E, Meyer FM, Idrus A (2015) Geology and mineralization of Awak Mas gold deposit and challenges for new exploration targeting in the metamorphic rock terrain of eastern Indonesia. In: 13th Biennial SGA Meeting

Harjanto E, Meyer FM, Idrus A, Widyanarko H, Endrasari NL (2016a) An update of key characteristics of Awak Mas mesothermal gold deposit, Sulawesi Island, Indonesia. MGEI Annual Meeting 2016. 4-6 October 2016

Harjanto E, Meyer FM, Idrus A (2016b) Hydrothermal alteration and gold mineralization of the meta-sedimentary rock hosted gold deposit Awak Mas, Sulawesi Island, Indonesia. In: 35TH International Geological Congress. Cape Town, South Africa

Heijlen W, Muchez P, Banks DA, Schneider J, Kucha H, Keppens E (2003) Carbonate-Hosted Zn-Pb Deposits in Upper Silesia, Poland: Origin and Evolution of Mineralizing Fluids and Constraints on Genetic Models. Economic Geology 98:911–932. doi: 10.2113/gsecongeo.98.5.911

Hey MH (1954) A new review of the chlorites. Journal of the Mineralogical Society 30:277–292

Hu S, Evans K, Craw D, Rempel K, Bourdet J, Dick J, Grice K (2015) Raman characterization of carbonaceous material in the Macraes orogenic gold deposit and metasedimentary host rocks, New Zealand. Ore Geology Reviews 70:80–95. doi: 10.1016/j.oregeorev.2015.03.021

Idrus A, Kolb J, Meyer FM (2007) Chemical Composition of Rock-Forming Minerals in Copper?: Gold-Bearing Tonalite Porphyries at the Batu Hijau Deposit, Sumbawa Island, Indonesia: Implications for Crystallization Conditions and Fluorine?Chlorine Fugacity. Resource Geology 57:102–113. doi: 10.1111/j.1751-3928.2007.00010.x

Idrus A, Nur I, Warmada IW, Fadlin F (2011) Metamorphic Rock-Hosted Orogenic Gold Deposit Type as a Source of Langkowala Placer Gold, Bombana, Southeast Sulawesi. Indonesian J. Geosci. 6. doi: 10.17014/ijog.v6i1.114

Idrus A, Prihatmoko S, Hartono HG, Idrus F, Ernowo E, Franklin F, Moetamar M, Setiawan I (2014a) Some Key Features and Possible Origin of the Metamorphic Rock-Hosted Gold Mineralization in Buru Island, Indonesia. Indonesian J. Geosci. 1. doi: 10.17014/ijog.v1i1.172

Idrus A, Prihatmoko S, Hartono HG, Idrus F, Setiawan I (2014b) Some Key Featurws and Possible Origin of the Metamorphic Rock-hosted Gold Mineralization in Buru Island, Indonesia. Indonesian Journal on Geoscience 1:9–19

Ilchik RP (1990) Geology and geochemistry of the Vantage gold deposits, Alligator Ridge-Bald Mountain mining district, Nevada. Economic Geology 85:50–75. doi: 10.2113/gsecongeo.85.1.50

Imai A, Ohno S (2005) Primary Ore Mineral Assemblage and Fluid Inclusion Study of the Batu Hijau Porphyry Cu-Au Deposit, Sumbawa, Indonesia. Resource Geology 55:239–248. doi: 10.1111/j.1751-3928.2005.tb00245.x

Imai A, Watanabe K (2007) Origin of Ore-forming Fluids Responsible for Gold Mineralization of the Pongkor Au-Ag Deposit, West Java, Indonesia: Evidence from Mineralogic, Fluid Inclusion Microthermometry and Stable Isotope Study of the Ciurug?Cikoret Veins. Resource Geology 57:136–148. doi: 10.1111/j.1751-3928.2007.00013.x

Imai A, Shinomiya J, Soe MT, Setijadji LD, Watanabe K, Warmada IW (2007) Porphyry-Type Mineralization at Selogiri Area, Wonogiri Regency, Central Java, Indonesia. Resource Geology 57:230–240. doi: 10.1111/j.1751-3928.2007.00019.x

Johnson NE, Craig JR, Rimstidt JD (1986) Compositional trends in tetrahedrite. The Canadian Mineralogist 24:385–397

Johnson NE, Craig JR, Rimstidt JD (1988) Crystal chemistry of tetrahedrite. Am. Mineral 73:389–397

Juteau T, Maury R (1999) The oceanic crust, from accretion to mantle recycling. Springer-Praxis series in geophysics. Springer; Praxis, London

Kadarusman A, Miyashita S, Maruyama S, Parkinson CD, Ishikawa A (2004) Petrology, geochemistry and paleogeographic reconstruction of the East Sulawesi Ophiolite, Indonesia. Tectonophysics 392:55–83. doi: 10.1016/j.tecto.2004.04.008

Kadarusman A, Massonne H-J, van Roermund H, Permana H, Munasri (2007) P-T Evolution of Eclogites and Blueschists from the Luk Ulo Complex of Central Java, Indonesia. International Geology Review 49:329–356. doi: 10.2747/0020-6814.49.4.329

Kamenetsky VS, Crawford AJ, Meffre S (2001) Factors controlling chemistry of magmatic spinel: An empirical study of associated olivine, Cr-spinel and melt inclusions from primitive rocks. Journal of Petrology 42:655–671

Katili JA (1974) Geological environment of the Indonesian mineral deposits: A plate tectonic approach. Geological Survey of Indonesia, Publikasi Teknik. Seri Geologi Ekonomi 7:1–17

Kavalieris I, Walshe JL, Halley S, Harrold BP (1990) Dome-related gold mineralization in the Pani volcanic complex, North Sulawesi, Indonesia; a study of geologic relations, fluid inclusions, and chlorite compositions. Economic Geology 85:1208–1225. doi: 10.2113/gsecongeo.85.6.1208

Kavalieris I, van Leeuwen TM, Wilson M (1992) Geological setting and styles of mineralization, north arm of Sulawesi, Indonesia. Journal of Southeast Asian Earth Sciences 7:113–129. doi: 10.1016/0743-9547(92)90046-E

Kendrick MA, Burgess R, Pattrick R, Turner G (2001) Fluid inclusion noble gas and halogen evidence on the origin of Cu-Porphyry mineralising fluids. Geochimica et Cosmochimica Acta 65:2651–2668. doi: 10.1016/S0016-7037(01)00618-4

Kendrick MA, Woodhead JD, Kamenetsky VS (2012) Tracking halogens through the subduction cycle. Geology 40:1075–1078. doi: 10.1130/G33265.1

Kharaka YK, Mariner RH (1989, 2012) Chemical Geothermometers and Their Application to Formation Waters from Sedimentary Basins. In: Naeser ND, McCulloh TH (eds) Thermal history of sedimentary basins: Methods and case histories. Springer-Verlag, New York, pp 99–117

Kharbish S, Götzinger M, Beran A (2007) Compositional variations of fahlore group minerals from Austria. Austrian Journal of Earth Sciences 100:44–52

Klemm DD (1965) Synthesen und Analysen in den Dreiecksdiagrammen FeAsS-CoAsS-NiAsS und FeS2-CoS2-NiS2. Neues Jahrbuch für Mineralogie Abhandlungen 103:205–255

Kolb J, Dziggel A, Bagas L (2015) Hypozonal lode gold deposits: A genetic concept based on a review of the New Consort, Renco, Hutti, Hira Buddini, Navachab, Nevoria and The Granites deposits. Precambrian Research 262:20–44. doi: 10.1016/j.precamres.2015.02.022

Kontonikas-Charos A, Ciobanu CL, Cook NJ (2014) Albitization and redistribution of REE and Y in IOCG systems: Insights from Moonta-Wallaroo, Yorke Peninsula, South Australia. Lithos 208-209:178–201. doi: 10.1016/j.lithos.2014.09.001

Kranidiotis P, MacLean WH (1987) Systematics of chlorite alteration at the Phelps Dodge massive sulfide deposit, Matagami, Quebec. Economic Geology 82:1898–1911. doi: 10.2113/gsecongeo.82.7.1898

Krenn E, Putz H, Finger F, Paar WH (2011) Sulfur-rich monazite with high common Pb in ore-bearing schists from the Schellgaden mining district (Tauern Window, Eastern Alps). Mineralogy and Petrology 102:51–62. doi: 10.1007/s00710-011-0170-x

Krismer M, Vavtar F, Tropper P, Kaindl R, Sartory B (2011) The chemical composition of tetrahedrite-tennantite ores from the prehistoric and historic Schwaz and Brixlegg mining areas (North Tyrol, Austria). Eur.J.Mineral. 23:925–936. doi: 10.1127/0935-1221/2011/0023-2137

Landis GP, Hofstra AH (2012) Ore Genesis Constraints on the Idaho Cobalt Belt from Fluid Inclusion Gas, Noble Gas Isotope, and Ion Ratio Analyses. Economic Geology 107:1189–1205. doi: 10.2113/econgeo.107.6.1189

Large RR, Bull SW, Maslennikov VV (2011) A Carbonaceous Sedimentary Source-Rock Model for Carlin-Type and Orogenic Gold Deposits. Economic Geology 106:331–358. doi: 10.2113/econgeo.106.3.331

Le Bas MJ (1962) The role of aluminum in igneous clinopyroxenes with relation to their parentage. American Journal of Science 260:267–288. doi: 10.2475/ajs.260.4.267

Le Maitre RW (ed) (2002) Igneous rocks: A classification and glossary of terms ; recommendations of the International Union of Geological Sciences, Subcommission on the Systematics of Igneous Rocks, 2nd ed. Cambridge University Press, Cambridge

Leake BE, Woolley AR, Arps CES, Birch WD, Gilbert MC, Grice JD, Hawthorne FC, Kato A, Kisch HJ, Krivovichev VG, others (1997) Report. Nomenclature of Amphiboles: Report of the Subcommittee on Amphiboles of the International Mineralogical Association Commission on New Minerals and Mineral Names. Mineralogical Magazine 61:295–321

Leake BE, Woolley AR, Birch WD, Burke EAJ, Ferraris G, Grice JD, Hawthorne FC, Kisch HJ, Krivovichev VG, Schumacher JC, Stephenson NCN, Whittaker EJW

(2004) Nomenclature of amphiboles: Additions and revisions to the International Mineralogical Association's amphibole nomenclature. Mineral. Mag. 68:209–215. doi: 10.1180/0026461046810182

Leterrier J, Maury RC, Thonon P, Girard D, Marchal M (1982) Clinopyroxene composition as a method of identification of the magmatic affinities of paleo-volcanic series. Earth and Planetary Science Letters 59:139–154. doi: 10.1016/0012-821X(82)90122-4

Li S, Yang X, Sun W (2015) The Lamandau IOCG deposit, southwestern Kalimantan Island, Indonesia: Evidence for its formation from geochronology, mineralogy, and petrogenesis of igneous host rocks. Ore Geology Reviews 68:43–58. doi: 10.1016/j.oregeorev.2015.01.008

Loftus-Hills G, Solomon M (1967) Cobalt, nickel and selenium in sulphides as indicators of ore genesis. Mineralium Deposita 2:228–242

Lowder GG, Dow JAS (1978) Geology and exploration of porphyry copper deposits in North Sulawesi, Indonesia. Economic Geology 73:628–644. doi: 10.2113/gsecongeo.73.5.628

Lubis H, Prihatmoko S, James LP (1994) Bulagidun prospect: A copper, gold and tourmaline bearing porphyry and breccia system in northern Sulawesi, Indonesia. Journal of Geochemical Exploration 50:257–278. doi: 10.1016/0375-6742(94)90027-2

Lünsdorf NK, Dunkl I, Schmidt BC, Rantitsch G, Eynatten H von (2014) Towards a Higher Comparability of Geothermometric Data obtained by Raman Spectroscopy of Carbonaceous Material. Part I: Evaluation of Biasing Factors. Geostand Geoanal Res 38:73–94. doi: 10.1111/j.1751-908X.2013.12011.x

Lünsdorf NK (2015) Geothermometry by Raman spectroscopy of dispersed organic matter. PhD thesis University Göttingen

Lünsdorf NK, Lünsdorf JO (2016) Evaluating Raman spectra of carbonaceous matter by automated, iterative curve-fitting. International Journal of Coal Geology 160-161:51–62. doi: 10.1016/j.coal.2016.04.008

MacDonald GD, Arnold L (1994) Geological and geochemical zoning of the Grasberg Igneous Complex, Irian Jaya, Indonesia. Journal of Geochemical Exploration 50:143–178. doi: 10.1016/0375-6742(94)90023-X

Marcoux E, Milési J-P (1994) Epithermal gold deposits in West Java, Indonesia: Geology, age and crustal source. Journal of Geochemical Exploration 50:393–408. doi: 10.1016/0375-6742(94)90033-7

Massonne H-J, Schreyer W (1987) Phengite geobarometry based on the limiting assemblage with K-feldspar, phlogopite, and quartz. Contr. Mineral. and Petrol. 96:212–224. doi: 10.1007/BF00375235

Mathur R, Ruiz J, Titley S, Gibbins S, Margotomo W (2000) Different crustal sources for Au-rich and Au-poor ores of the Grasberg Cu–Au porphyry deposit. Earth and Planetary Science Letters 183:7–14. doi: 10.1016/S0012-821X(00)00256-9

Maulana A (2009) Petrology, Geochemistry and Metamorphic Evolution of the South Sulawesi Basement Complexes, Indonesia. Australian National University

Maulana A, Christy AG, Ellis DJ, Imai A, Watanabe K (2013) Geochemistry of eclogite- and blueschist-facies rocks from the Bantimala Complex, South Sulawesi, Indonesia: Protolith origin and tectonic setting. Island Arc 22:427–452. doi: 10.1111/iar.12037

Maulana A, Christy AG, Ellis DJ (2015) Petrology, geochemistry and tectonic significance of serpentinized ultramafic rocks from the South Arm of Sulawesi, Indonesia. Chemie der Erde - Geochemistry 75:73–87. doi: 10.1016/j.chemer.2014.09.003

Maulana A, Imai A, van Leeuwen T, Watanabe K, Yonezu K, Nakano T, Boyce A, Page L, Schersten A (2016) Origin and geodynamic setting of Late Cenozoic granitoids in Sulawesi, Indonesia. Journal of Asian Earth Sciences 124:102–125. doi: 10.1016/j.jseaes.2016.04.018

McDonough WF, Sun S-s (1995) The composition of the Earth. Chemical Geology 120:223–253. doi: 10.1016/0009-2541(94)00140-4

Meinert LD, Hefton KK, Mayes D, Tasiran I (1997) Geology, zonation, and fluid evolution of the Big Gossan Cu-Au skarn deposit, Ertsberg District, Irian Jaya. Economic Geology 92:509–534. doi: 10.2113/gsecongeo.92.5.509

Meisel T, Schöner N, Paliulionyte V, Kahr E (2002) Determination of Rare Earth Elements, Y, Th, Zr, Hf, Nb and Ta in Geological Reference Materials G-2, G-3, SCo-1 and WGB-1 by Sodium Peroxide Sintering and Inductively Coupled Plasma-Mass Spectrometry. Geostandards and Geoanalytical Research 26:53–61. doi: 10.1111/j.1751-908X.2002.tb00623.x

Melcher F, Meisel T (2004) A Metamorphosed Early Cambrian Crust-Mantle Transition in the Eastern Alps, Austria. Journal of Petrology 45:1689–1723. doi: 10.1093/petrology/egh030

Melcher F, Grum W, Simon G, Thalhammer TV, Stumpfl EF (1997) Petrogenesis of the Ophiolitic Giant Chromite Deposits of Kempirsai, Kazakhstan: A Study of Solid and Fluid Inclusions in Chromite. Journal of Petrology 38:1419–1458. doi: 10.1093/petroj/38.10.1419

Meschede M (1986) A method of discriminating between different types of mid-ocean ridge basalts and continental tholeiites with the Nb-Zr-Y diagram. Chemical Geology 56:207–218. doi: 10.1016/0009-2541(86)90004-5

Meyer EE, Quicksall AN, Landis JD, Link PK, Bostick BC (2012) Trace and rare earth elemental investigation of a Sturtian cap carbonate, Pocatello, Idaho: Evidence for ocean redox conditions before and during carbonate deposition. Precambrian Research 192-195:89–106. doi: 10.1016/j.precamres.2011.09.015

Middleton TW (2003) The Dairi Zinc-Lead Project, North Sumatra, Indonesia. http://www.smedg.org.au/Tiger/DairiZinc.htm

Mikucki EJ (1998) Hydrothermal transport and depositional processes in Archean lode-gold systems: A review. Ore Geology Reviews 13:307–321. doi: 10.1016/S0169-1368(97)00025-5

Milesi JP, Marcoux E, Nehlig P, Sunarya Y, Sukandar A, Felenc J (1994) Cirotan, West Java, Indonesia; a 1.7 Ma hybrid epithermal Au-Ag-Sn-W deposit. Economic Geology 89:227–245. doi: 10.2113/gsecongeo.89.2.227

Morimoto N (1988) Nomenclature of Pyroxenes. Mineralogy and Petrology 39:55–76. doi: 10.1007/BF01226262

Morrison GW, Rose WJ, Jaireth S (1991) Geological and geochemical controls on the silver content (fineness) of gold in gold-silver deposits. Ore Geology Reviews 6:333–364. doi: 10.1016/0169-1368(91)90009-V

Mulja T, Collins M, Wong HH, Rizal R, Brown T, Zainuddin M (2003) An integrated mineral exploration programme in the Takengon tenement, Aceh magmatic arc, north Sumatra. Geochemistry: Exploration, Environment, Analysis 3:321–335. doi: 10.1144/1467-7873/03-017

New B (2006) Controls of Copper and Gold Distribution in the Kucing Liar Deposit, Ertsberg Mining District, West Papua, Indonesia. James Cook University

Nisbet EG, Pearce JA (1977) Clinopyroxene composition in mafic lavas from different tectonic settings. Contr. Mineral. and Petrol. 63:149–160. doi: 10.1007/BF00398776

Ohmoto H, Rye RO (1979) Isotopes of sulfur and carbon: Geochemistry of Hydrothermal Ore Deposits, 2nd edn. Wiley, New-York

Onuk P, Melcher F, Mertz-Kraus R, Gäbler H-E, Goldmann S (2016) Development of a Matrix-Matched Sphalerite Reference Material (MUL-ZnS-1) for Calibration of In Situ Trace Element Measurements by Laser Ablation-Inductively Coupled Plasma-Mass Spectrometry. Geostand Geoanal Res 41:545. doi: 10.1111/ggr.12154

Otto A, Dziggel A, Kisters AFM, Meyer FM (2007) The New Consort Gold Mine, Barberton greenstone belt, South Africa: Orogenic gold mineralization in a

condensed metamorphic profile. Miner Deposita 42:715–735. doi: 10.1007/s00126-007-0135-5

Paar WH (1994) Erze und Lagerstätten: Mineral und Erz in den Hohen Tauern. Naturhistorisches Museum Wien:89–102

Parkinson C (1998) Emplacement of the East Sulawesi Ophiolite: Evidence from subophiolite metamorphic rocks. Journal of Asian Earth Sciences 16:13–28. doi: 10.1016/S0743-9547(97)00039-1

Parkinson CD, Miyazaki K, Wakita K, Barber AJ, Carswell DA (1998) An overview and tectonic synthesis of the pre-Tertiary very-high-pressure metamorphic and associated rocks of Java, Sulawesi and Kalimantan, Indonesia. Isl Arc 7:184–200. doi: 10.1046/j.1440-1738.1998.00184.x

Pearce JA (1996) A user's guide to basalt discrimination diagrams. Trace element geochemistry of volcanic rocks: applications for massive sulphide exploration. Geological Association of Canada, Short Course Notes 12:113

Pearce JA, Norry MJ (1979) Petrogenetic implications of Ti, Zr, Y, and Nb variations in volcanic rocks. Contr. Mineral. and Petrol. 69:33–47. doi: 10.1007/BF00375192

Pearce JA, Lippard SJ, Roberts S (1984) Characteristics and tectonic significance of supra-subduction zone ophiolites. Geological Society, London, Special Publications 16:77–94. doi: 10.1144/GSL.SP.1984.016.01.06

Peng D-Y, Robinson DB (1976) A New Two-Constant Equation of State. Ind. Eng. Chem. Fund. 15:59–64. doi: 10.1021/i160057a011

Perelló J (1994) Geology, porphyry Cu-Au, and epithermal Cu-Au-Ag mineralization of the Tombulilato district, North Sulawesi, Indonesia. Journal of Geochemical Exploration 50:221–256. doi: 10.1016/0375-6742(94)90026-4

Pettijohn FJ, Potter PE, Siever R (1987) Sand and Sandstone, 2nd edn. Springer, New York, NY

Pitcairn IK, Teagle DAH, Craw D, Olivo GR, Kerrich R, Brewer TS (2006) Sources of Metals and Fluids in Orogenic Gold Deposits: Insights from the Otago and Alpine Schists, New Zealand. Economic Geology 101:1525–1546. doi: 10.2113/gsecongeo.101.8.1525

Pitcairn IK, Olivo GR, Teagle DAH, Craw D (2010) Sulfide evolution during prograde metamorphism of the otago and alpine schists, New Zealand. The Canadian Mineralogist 48:1267–1295. doi: 10.3749/canmin.48.5.1267

Pitcairn IK, Craw D, Teagle DAH (2015) Metabasalts as sources of metals in orogenic gold deposits. Miner Deposita 50:373–390. doi: 10.1007/s00126-014-0547-y

Pohl W, Belocky R (1999) Metamorphism and metallogeny in the Eastern Alps. Mineralium Deposita 34:614–629. doi: 10.1007/s001260050223

Pokrovski GS, Akinfiev NN, Borisova AY, Zotov AV, Kouzmanov K (2014) Gold speciation and transport in geological fluids: Insights from experiments and physical-chemical modelling. Geological Society, London, Special Publications 402:9–70. doi: 10.1144/SP402.4

Pollard PJ, Taylor RG, Peters L (2006) Ages of Intrusion, Alteration, and Mineralization at the Grasberg Cu-Au Deposit, Papua, Indonesia. Economic Geology 100:1005–1020. doi: 10.2113/gsecongeo.100.5.1005

Prendergast K, Clarke GW, Pearson NJ, Harris K (2006) Genesis of Pyrite-Au-As-Zn-Bi-Te Zones Associated with Cu-Au Skarns: Evidence from the Big Gossan and Wanagon Gold Deposits, Ertsberg District, Papua, Indonesia. Economic Geology 100:1021–1050. doi: 10.2113/gsecongeo.100.5.1021

Priadi B, Polve M, Maury RC, Bellon H, Soeria-Atmadja R, Joron JL, Cotten J (1994) Tertiary and quaternary magmatism in Central Sulawesi: Chronological and petrological constraints. Journal of Southeast Asian Earth Sciences 9:81–93. doi: 10.1016/0743-9547(94)90067-1

Querubin CD, Walters S (2012) Geology and Mineralization of Awak Mas: A Sedimentary Hosted Gold Deposit, South Sulawesi, Indonesia. Majalah Geologi Indonesia 27:69–85

Raith JG, Leitner T, Paar WH (2015) Orogenic-type copper-gold-arsenic-(bismuth) mineralization at Flatschach (Eastern Alps), Austria. Mineralogy and Petrology 109:531–553. doi: 10.1007/s00710-015-0391-5

Ramdohr P (1969) The ore minerals and their intergrowths, Third edition. Pergamon Press, Oxford, England

Rantitsch G, Grogger W, Teichert C, Ebner F, Hofer C, Maurer E-M, Schaffer B, Toth M (2004) Conversion of carbonaceous material to graphite within the Greywacke Zone of the Eastern Alps. Int J Earth Sci (Geol Rundsch) 93:959–973. doi: 10.1007/s00531-004-0436-1

Rantitsch G, Lämmerer W, Fisslthaler E, Mitsche S, Kaltenböck H (2016) On the discrimination of semi-graphite and graphite by Raman spectroscopy. International Journal of Coal Geology 159:48–56. doi: 10.1016/j.coal.2016.04.001

Rollinson HR (1993) Using geochemical data: Evaluation, presentation, interpretation. Longman Scientific & Technical, Harlow

Rosana MF, Matsueda H (2002) Cikidang Hydrothermal Gold Deposit in Western Java, Indonesia. Resource Geology 52:341–352. doi: 10.1111/j.1751-3928.2002.tb00144.x

Rudnick RL, Fountain DM (1995) Nature and composition of the continental crust: A lower crustal perspective. Rev. Geophys. 33:267. doi: 10.1029/95RG01302

Saing S, Takahashi R, Imai A (2016) Fluid Inclusion and Stable Isotope Study at the Southeastern Martabe Deposit: Purnama, Barani and Horas Ore Bodies, North Sumatra, Indonesia. Resource Geology 66:127–148. doi: 10.1111/rge.12093

Schweitzer J, Kröner A (1985) Geochemistry and petrogenesis of early Proterozoic intracratonic volcanic rocks of the Ventersdorp Supergroup, South Africa. Chemical Geology 51:265–288. doi: 10.1016/0009-2541(85)90137-8

Seal RR, Essene EJ, Kelly WC (1990) Tetrahedrite and tennantite; evaluation of thermodynamic data and phase equilibria. The Canadian Mineralogist 28:725–738

Setiabudi BT, Campbell IH, Martin CE, Allen CM (2007) Platinum Group Element Geochemistry of Andesite Intrusions of the Kelian Region, East Kalimantan, Indonesia: Implications of Gold Depletion in the Intrusions Associated with the Kelian Gold Deposit. Economic Geology 102:95–108. doi: 10.2113/gsecongeo.102.1.95

Setijadji LD, Basuki NI, Prihatmoko S (eds) (2010) Kalimantan mineral resources: an update on exploration and mining trends, synthesis on magmatism history and proposed models for metallic mineralization. Proceedings PIT IAGI LOMBOK 2010, The 39th IAGI Annual Convention and Exhibition

Shervais JW (1982) Ti-V plots and the petrogenesis of modern and ophiolitic lavas. Earth and Planetary Science Letters 59:101–118. doi: 10.1016/0012-821X(82)90120-0

Sillitoe RH (1994) Indonesian mineral deposits — introductory comments, comparisons and speculations. Journal of Geochemical Exploration 50:1–11. doi: 10.1016/0375-6742(94)90020-5

Simandjuntak TO, Barber AJ (1996) Contrasting tectonic styles in the Neogene orogenic belts of Indonesia. Geological Society, London, Special Publications 106:185–201. doi: 10.1144/GSL.SP.1996.106.01.12

Simmons SF, White NC, John DA (2005) Geological characteristics of epithermal precious and base metal deposits. Economic Geology 100th anniversary volume 29:485–522

Soeria-Atmadja R, Priadi B, van Leeuwen TM, Kavalieris I (1999) Tectonic setting of porphyry Cu-Au, Mo and related mineralization associated with contrasted Neogene magmatism in the Western Sulawesi Arc. Isl Arc 8:47–55. doi: 10.1046/j.1440-1738.1999.00221.x

Soesilo J (1998) Metamorphism in the Latimojong Complex, South Sulawesi and its tectonic significances. Unpublished Magister thesis, Institute of Technology Bandung

Sturm R (2002) PX-NOM—an interactive spreadsheet program for the computation of pyroxene analyses derived from the electron microprobe. Computers & Geosciences 28:473–483. doi: 10.1016/S0098-3004(01)00083-8

Sukamto R (1978) The structure of Sulawesi in the light of plate tectonics. Proceedings of Regional Conference on Geology and Mineral Resources of SE Asia

Sukamto R (1986) Tektonik Sulawesi Selatan dengan acuan khusus ciri-ciri himpunan batuan daerah Bantimala. Dissertation, Institute of Technology Bandung

Sun S-s, McDonough WF (1989) Chemical and isotopic systematics of oceanic basalts: Implications for mantle composition and processes. Geological Society, London, Special Publications 42:313–345. doi: 10.1144/GSL.SP.1989.042.01.19

Surjono SS, Wijayanti HDK (2011) Tectono-Stratigraphic Framework of Eastern Indonesia and its Implication to Petroelum Systems. Jurnal Teknik Geologi

Susanto A, Suparka E (eds) (2012) Hydrothermal Alteration and Mineralization of Porphyry-Skarn Deposits in The Geunteut Area, Nanggroe Aceh Darussalam, Indonesia. Bulletin of the Geological Society of Malaysia, vol 58

Sutopo B (2013) The Martabe Au-Ag high-sulfidation epithermal deposits, Sumatra, Indonesia: Implications for ore genesis and exploration, University of Tasmania

Swift LR, Alwan M (1990) Discovery of gold-silver mineralization at Binabase, Sangihe Island, Indonesia: Proc. Pacific Rim Congress 90 Aust. IMM:533–540

Syafrizal, Imai A, Motomura Y, Watanabe K (2005) Characteristics of Gold Mineralization at the Ciurug Vein, Pongkor Gold-Silver Deposit, West Java, Indonesia. Resource Geology 55:225–238. doi: 10.1111/j.1751-3928.2005.tb00244.x

Tarkian M, Stribrny B (1999) Platinum-group elements in porphyry copper deposits: A reconnaissance study. Mineralogy and Petrology 65:161–183. doi: 10.1007/BF01161959

Taylor CM, Radtke AS (1969) Micromineralogy of silver-bearing sphalerite from Flat river, Missouri. Economic Geology 64:306–318. doi: 10.2113/gsecongeo.64.3.306

Taylor SR, McLennan SM (1985) The continental crust: Its composition and evolution : an examination of the geochemical record preserved in sedimentary rocks / Stuart Ross Taylor, Scott M. McLennan. Geoscience texts. Blackwell Scientific, Oxford

Thompson JFH, Sillitoe RH, Baker T, Lang JR, Mortensen JK (1999) Intrusion-related gold deposits associated with tungsten-tin provinces. Miner Deposita 34:323–334. doi: 10.1007/s001260050207

Tostevin R, Shields GA, Tarbuck GM, He T, Clarkson MO, Wood RA (2016) Effective use of cerium anomalies as a redox proxy in carbonate-dominated marine settings. Chemical Geology 438:146–162. doi: 10.1016/j.chemgeo.2016.06.027

Tuakia MZ, Takahashi R, Imai A (2016) Fluid Inclusion and Sulfur Isotope Studies on the Salu Bulo Prospect, South Sulawesi,Indonesia: A Metasedimentary Rock-Hosted Gold Deposit. In: SEG 2016 Conference Tethyan Tectonics and Metallogeny

Turner SJ, Flindell PA, Hendri D, Hardjana I, Lauricella PF, Lindsay RP, Marpaung B, White GP (1994) Sediment-hosted gold mineralisation in the Ratatotok district, North Sulawesi, Indonesia. Journal of Geochemical Exploration 50:317–336. doi: 10.1016/0375-6742(94)90029-9

van Bemmelen RW (1949) The Geology of Indonesia: General Geology of Indonesia and Adjacent Archipelagoes. US Government Printing Office

van Leeuwen T (1994) 25 years of mineral exploration and discovery in Indonesia. Journal of Geochemical Exploration 50:13–90. doi: 10.1016/0375-6742(94)90021-3

van Leeuwen T, Pieters PE (eds) (2011) Mineral deposits of Sulawesi, Manado, North Sulawesi, Indonesia

van Leeuwen TM, Muhardjo (2005) Stratigraphy and tectonic setting of the Cretaceous and Paleogene volcanic-sedimentary successions in northwest Sulawesi, Indonesia: Implications for the Cenozoic evolution of Western and Northern Sulawesi. Journal of Asian Earth Sciences 25:481–511. doi: 10.1016/j.jseaes.2004.05.004

van Leeuwen TM, Leach T, Hawke AA, Hawke MM (1990) The Kelian disseminated gold deposit, East Kalimantan, Indonesia. Journal of Geochemical Exploration 35:1–61. doi: 10.1016/0375-6742(90)90035-9

Wakita K, Sopaheluwakan J, Miyazaki K, Zulkarnain I, Munasri (1996) Tectonic evolution of the Bantimala Complex, South Sulawesi, Indonesia. Geological Society, London, Special Publications 106:353–364. doi: 10.1144/GSL.SP.1996.106.01.23

Wakita K (2000) Cretaceous accretionary–collision complexes in central Indonesia. Journal of Asian Earth Sciences 18:739–749. doi: 10.1016/S1367-9120(00)00020-1

Warmada IW, Lehmann B, Simandjuntak M (2003) Polymetallic sulfides and sulfosalts of the Pongkor Epithermal Gold-Silver Deposit, West Java, Indonesia. The Canadian Mineralogist 41:185–200. doi: 10.2113/gscanmin.41.1.185

Warmada IW, Lehmann B, Simandjuntak M, Hemes HS (2007) Fluid Inclusion, Rare-Earth Element and Stable Isotope Study of Carbonate Minerals from the Pongkor Epithermal Gold?: Silver Deposit, West Java, Indonesia. Resource Geology 57:124–135. doi: 10.1111/j.1751-3928.2007.000012.x

Watkinson IM, Hall R, Ferdian F (2011) Tectonic re-interpretation of the Banggai-Sula–Molucca Sea margin, Indonesia. Geological Society, London, Special Publications 355:203–224. doi: 10.1144/SP355.10

White NC, Hedenquist JW (1995) Epithermal gold deposits: Styles, characteristics and exploration. SEG newsletter 23:9–13

White LT, Hall R, Armstrong RA, Barber AJ, Fadel MB, Baxter A, Wakita K, Manning C, Soesilo J (2017) The geological history of the Latimojong region of western Sulawesi. Journal of Asian Earth Sciences. doi: 10.1016/j.jseaes.2017.02.005

Whitney DL, Evans BW (2010) Abbreviations for names of rock-forming minerals. American Mineralogist 95:185–187. doi: 10.2138/am.2010.3371

Widi BN, Matsueda H (1998) Epithermal gold-silver-tellurides-deposit of Cineam, Tasikmalaya District, West Java, Indonesia. Directorate of Mineral Resources Indonesia, Special Publication 96:1–19

Wilkinson J (2001) Fluid inclusions in hydrothermal ore deposits. Lithos 55:229–272. doi: 10.1016/S0024-4937(00)00047-5

Winchester JA, Floyd PA (1977) Geochemical discrimination of different magma series and their differentiation products using immobile elements. Chemical Geology 20:325–343. doi: 10.1016/0009-2541(77)90057-2

Wisanggono A, Abaijah P, Akiro K, Pertiwi D, Sauzy RA (2012) Supergene Enriched, Intrusion Related Low Suphidation Deposit, Binebase-Bawone, North Sulawesi, Indonesia. Indonesian Journal on Geoscience 7:241–253

Xu L, Lehmann B, Mao J, Zheng W, Ye H, Li H (2016) Strontium, Sulfur, Carbon, and Oxygen Isotope Geochemistry of the Early Cambrian Strata-bound Barite and Witherite Deposits of the Qinling-Daba Region, Northern Margin of the Yangtze Craton, China. Economic Geology 111:695–718. doi: 10.2113/econgeo.111.3.695

Yardley BWD (1993) Post-Metamorphic Gold-Quartz Veins from N.W. Italy: The Composition and Origin of the Ore Fluid. Mineralogical Magazine 57:407–422. doi: 10.1180/minmag.1993.057.388.05

Yardley BWD, Bodnar RJ (2014) Fluids in the continental crust. Geochemical Perspectives 3:1–2

Yuningsih ET, Matsueda H, Rosana MF (2014) Epithermal Gold-Silver Deposits in Western Java, Indonesia: Gold-Silver Selenide-Telluride Mineralization. Indonesian J. Geosci. 1. doi: 10.17014/ijog.v1i2.180

Zaccarini F, Idrus A, Garuti G (2016) Chromite Composition and Accessory Minerals in Chromitites from Sulawesi, Indonesia: Their Genetic Significance. Minerals 6:46. doi: 10.3390/min6020046

Zheng Y-F, Hermann J (2014) Geochemistry of continental subduction-zone fluids. Earth Planet Space 66:93. doi: 10.1186/1880-5981-66-93

Zhou M-F, Robinson PT (1997) Origin and tectonic environment of podiform chromite deposits. Economic Geology 92:259–262. doi: 10.2113/gsecongeo.92.2.259

LIST OF APPENDICES

APPENDIX A

Petrographical descriptions for samples from Awak Mas and Salu Bullo

	Sample code	Lithology	Mineral Assemblages	Alteration	Ore Minerals	Comment
	Awak Mas					
1	A34-28.30	Breccia Qz veins	Qz+Ab+Cb (Gth+Hem+Rt+Mnz+Ap)	Ab	Py(Gn+Au)	Phyllite+Qz vein+Clastic materials
2	A49-64.00	Breccia Qz veins	Qz+Ab+Cb (Ms+Hem)	Cb+Ser	Py	Cb+Qz veins HR: phengite
3	A685-20	Breccia Qz veins	Qz+Ab+Rt+Cb (Mnz+Lim+Zr+Goy)	Cb	Py (Ccp+Ttr+Sph+Au)	Goyazite, Au+Gn in Py, Runded zircon (20μm)
4	A192-155.70	Carbonaceous phyllite	Gr+Qz+Ms+Ab(Mnz+Rt+Ap)		Py (Gn)	Framboidal pyrite,coarse grain apatite (±1.5 mm)
5	A192-189.40	Carbonaceous phyllite	Gr+Qz+Ms+Chl (Ap+Rt+Sd+Cc+Mnz)		Py (Sp+Fam+Ttr+Mrc+Au)	Framboidal pyrite, irregular Mnz
6	A192-221.65	Carbonaceous phyllite	Gr+Qz+Ab+Cb (Rt+Mnz+Ap+Zr)		Py (Fam+Gn+Au)	
7	A192-225.00	Carbonaceous phyllite	Gr+Qz+Ab+Ms (Sd+Kn+Ap+Mnz+Rt)		Py+Ccp (Bi)	
8	A192-245.65	Carbonaceous phyllite	Gr+Qz+Ab (Cb+Chl+Ms+Xtm)		Gn (Bi)	
9	A198-241.00	Carbonaceous phyllite	Gr+Ab+Qz+Ms (Ap)		Au	
10	A676-68.7	Carbonaceous phyllite	Gr+Qz+Ab+Cb		Py	Framboidal pyrite
11	A683-53.60	Carbonaceous phyllite	Gr+Qz+Ms(Sd+Ser)		Py	Framboidal pyrite, mylonite
12	A687-157.90	Chlorite abite schist	Ab+Chl (Ap+Badly+Spn+Rt)		Py+Ccp (Cobaltite)	Ab-Ap-Spn phenocryst on schist, high Ti content in Chlorite
13	A687-171	Chlorite mica schist	Ms+Chl+Clay (Ap)		Py (Ccp)	Ripidolite
14	A687-171	Chlorite mica schist	Qz+Cc+Chl (Ms)		Py (Gn)	
15	A687-174.5	Dark phyllite	Qz		Py	Fine-grained pyrite parallel foliation
16	A687-79.80	Metabasite	Qz+Chl+Cc (Rt+Ab+Ap+Spn+Pmp+Chr)		Py	Framboidal
17	A49-36.20	Metasandstone	Qz+Cb (Ab)	Cb	Py	
18	A49-67.05	Metasandstone	Qz+Ab+Cb (Hem+Tur)	Cb	Py	
19	A49-76.45	Metasandstone	Qz+Ab (Gth+Rt+Hem)	Hem	Py	Pyrite replacing Hem
20	A49-77.75	Metasandstone	Qz			
21	A49-90.65	Metasandstone	Ab+Cb+ Ms (Hem+Sid+Kln+Rt+Mnz)		Py+Ccp+ (Gn+En+Hg-ttr+Mrc)	Mrc (bluish phleochroism)
22	A34-26.10	Metasiltstone	Qz+Ab (Cb+Ap+Mnz+Rt)	Cb	Py	Apatite >50μm

	Sample code	Lithology	Mineral Assemblages	Alteration	Ore Minerals	Comment
23	PHI-CAMP	Metatuffite Altered bioclastic rock?	Chl+Qz+Cb			Greenrock near Awak Mas campsite
24	A149-110.3	Phyllite	Ab (Rt+Mnz+Ap)			
25	A192-157.30	Phyllite	Qz+Ab+Chl+Ms(Mnz)	Chl	Py(Ttr+Brn)	Framboidal pyrite+ bornite (<10µm)+ Mnzite (<10µm)
26	A34-28.00	Phyllite	Ab+Cb(Rt)		Py	Laminated fine-grained Ab-Cb+sulfide parallel lamination
27	A34-32.80	Phyllite	Cb+Ab (Ap+Mnz+Rt)		Py (Ttr+Fam+Gn)	
28	A34-38.30	Phyllite	Cb+Ab (Rt+Mnz+Ap)		Py	Framboydal pyrite, euhedral pyrite
29	A35-24.40	Phyllite	Ab+Cb (Qz+Mnz+Rt+Ser)	Ab	Py (Hg-Ttr)	Py1: framboidal+ py2: parallel foliation+ py3: cutting foliation; fine-grained qz parallel to foliation
30	A35-26.00	Phyllite	Qz+Cb		Py	Hematite
31	A35-33.85	Phyllite	Qz+Cb+Ms	Cb	Py	Layered Dol-Qz-Ms cut by Qz veinlets; mylonite texture
32	A35-34.70	Phyllite	Qz+Cb+Rt+Ms+Sid+Kn (Tur)	Cb	Py+Hg-Ttr+Ccp (Gn)	Siderite rim around sulphide
33	A49-81.55	Phyllite	Ms+Qz+Ab (Cb+Hem+Lim+Rt)	Ser	Py	Framboidal pyrite
34	A676-66.2	Phyllite	Ph+Qz (Sid+Rt)		Py	
35	A687-40.10	Phyllite	Qz+Ab+Act+Ms		Py+Ccp (Gn)	Framboidal Py partly replaced by Gn
36	A192-177.20	Quartz vein	Cb+Ab+(Rt+Mnz)		Py (Gn+Ccp)	HR: phyllite
37	A192-86.40	Quartz vein	Qz+Cb (Mnz+Zr+Rt+Xtm)		Py (Gn+Au)	Gold sit on pyrite
38	A192-8640	Quartz vein	Qz (Ab+Rt)	Cb	Py (Au)	
39	A35-16.00	Quartz vein	Qz+Ab+Cb (Ap+Rt+Mnz)		Py Gn+Hg-Ttr+Au)	Hg-Ttr next to pyrite+ irregular Rt in pyrite
40	A35-18.65	Quartz vein	Qz+Ab+Cb (Mnz+Ap+Rt)		Py	sulfide parallel to foliation+ cut by Ab, Mnz in Py, HR: phyllite
41	A35-21.00	Quartz vein	Qz+Cb+Ab (Ap+Zir+Hem)		Py (Gn+Au)	Sulphide parallel foliation, HR: phyllite
42	A35-21.90	Quartz vein	Qz+Ab+Cb		Py	
43	A35-30.85	Quartz vein	Qz+Ab+Cb (Ap+Rt+Brt+Kln+Hem)		Py (Gn)	Qz veins cut altered phyllite, barite, siderite rims pyrite, HR: phyllite
44	A49-110.30	Quartz vein	Qz+Ab (Hem)		Py (Ccp)	Ccp in Py

	Sample code	Lithology	Mineral Assemblages	Alteration	Ore Minerals	Comment
45	A49-125.00	Quartz vein	Qz (Sid+Mnz+Rt)	Ser	Py	
46	A49-125.80	Quartz vein	Qz+Cb+Ab	Cb	Py (Cv+Au)	Coarse grain of gold sit in pyrite
47	A49-48.65	Quartz vein	Qz+Ab+Cb (Hem)		Py	
48	MP01	Quartz vein	Qz (Sid)	Cb	Py	Coarse grained quartz (>100 micron)+ recrystallize Qz
49	ONG01	Quartz vein	Qz		Py	Fine-grained pyrite parallel foliation (HR: phyllite)
50	ONG05	Quartz vein	Qz+Ab (Lim)		Py	
51	A35-15.90	Quartz vein+phyllite	Ab+Qz+Ms (Ap+Rt+Xen)		Py (Gn+Hg-Ttr)	sulfide parallel foliation+ small Mnz (20μm)+Ap>100μm, HR: phyllite
	Salu Bullo					
1	S68-130.30	Breccia Qz veins	Qz+Ab+Cb (Kln+Hem+Mnz+Rt)	Ab	Py(Fam+Gn+Stib)	
2	S69-25.80	Breccia Qz veins	Qz+Ab (Sid+Ap+Mnz+Hem)	Cb	Py+Ccp+(Tnt+Ttr+Cv+Luz+Fam+Sph+Au)	
3	S66-135.5	Clinopyroxene-phyric metabasite	Cpx+Chl+Act+Ab+(Qz+Cb)			
4	S68-47	Clinopyroxene-phyric metabasite	Aug+Chl+Ab (Pmp+Chr)		Ccp	Abundant augite, Ccp in augite crack
5	S66-109	Green phyllite	Ab+Hem+Mnz (Rt+Mnz+Dol)	Kln+Cb	Py+Ccp (Gn)	Galena in hematite
6	S50-25.00	Hematitic mudstone	Cb+Qz+Ab+Hem	Dol		Qz+Cb veins
7	S69-24.50	Hematitic mudstone	Qz+Cb (Ab+Mnz+Rt+Hem+Ap)		Py+Ccp (Fam+Luz+Au+Sph+Gn)	Cb veinlets
8	S69-25.00	Hematitic mudstone	Qz (Ab+Sid+Mnz+Hem+Kln+Ap)	Ser+Hem	Py+Ccp (Au+Fam+Tnt+Luz+Gn+Sph+Brn)	Breccia textures, veinlet of hematite
9	S69-25.80	Hematitic mudstone	Cb+Ab+Ap+Hem+Mnz		Py+Ccp (Luz+Cv+Sph+Gn+Au)	
10	S94-19.10	Hematitic mudstone	Ab+Cb+Qz	Ser+Hem		Cb veinlets
11	S94-34.35	Hematitic mudstone	Qz+Ab (Cb)	Hem	Py+(Hg-Ttr+Gn+Au)	
12	S50-80.30	Metabasite	Chl+Qz+Cb (Amp)		Py	
13	S50-83.95	Metabasite	Cb+Chl (Qz+Lim+Ms+Ep+Act)	Ser+Cb		Cb veinlets
14	S50-9.90	Metabasite	Cb+Qz+Ab (Ms+Lim)	Ser+Cb		
15	S53-10.90	Metabasite	Chl (Aug+Act+Cc+Act+Chl+Pmp+Chr+Qz)	Ser	Py+Ccp (Gn)	

	Sample code	Lithology	Mineral Assemblages	Alteration	Ore Minerals	Comment
16	S66-122.50	Metabasite	Chl+Ms+Ab+ (Act+Qz+Kln+Sid+Rt)		Py+Ccp	
17	S66-127.5	Metabasite	Chl+Cpx+Ab+Act (Qz)			
18	S66-127.50	Metabasite	Ab+Pmp+Aug+Chl (Ap+Qz)		Py (Ccp)	
19	S66-131.5	Metabasite	Chl+Ms+Ab (Qz)		Py	
20	S66-23.5	Metabasite	Chl+Qz+Cc (Act+Pmp)		Gn	
21	S68-34.90	Metabasite	Chl (Pmp+Cc+Aug+Act+Qz)	Cc		
22	S68-39.10	Metabasite	Cc+Qz+Chl (Pmp+Aug+Ab+Rt+Ap+Chr+K-Na Fsp)	Ser	Py+Ccp (Gn)	Lithological contact between metabasite-metatuffite
23	S68-69	Metabasite	Ab+Chl+Ph (Qz+Cc+Ap+Pmp+Rt)	Cb	Ccp	
24	S68-98.40	Metabasite	Qz+Cb+Hem (Chl)		Py	
25	S94-116.60	Metabasite	Chl (Rt+Pmp+Ap+Qz)			
26	S94-119.80	Metabasite	Chl+Ab+Cb (Rt+Sid+Kln+Qz)		Py+Ccp (Luz+Tnnt)	
27	S94-14.60	Metabasite	Ab+Cb+Qz	Ser		
28	S53-86.90	Metasandstone	Qz+Hem+Rt (Mnz)	Cb	Py	Hematite veinlet; Coarse-grained Mnz (>50 μm) in Cb
29	S68-105.40	Metasandstone	Qz+Cb+Hem	Ser+Dol	Py	
30	S69-68.80	Metasandstone	Qz+Cc (Ab+Ser+Hem+Apat)	Cb+Ser		Platy hematite
31	S94-64.30	Metasandstone	Cb+Qz+Ab (Kln+Ap+Rt)	Cb	Py	Strong Cb alteration
32	S94-86.20	Metasandstone	Cb+Qz (Hem)	Cb		
33	S68-105.25	Metasiltstone	Qz+Ab (Hem+Dol+Amp+Sid)	Dol	Py+Ccp (Fam)	Qz lamination altered by dolomite
34	S53-50.20	Metatuffite	Qz+Act+Chl+Chl (Spn+Ap+Sid)		Py+Ccp	Pyrite with high-Ni content
35	S66-56	Metatuffite	Ank+Cc+Lm		Py (Cv)	Zoning in Cc
36	S66-67	Metatuffite	Cc+Ab+Qz (Hem+Mnz)	Ser	Py+Ccp (Ag-Bi-Te phases)	
37	S68-57.60	Metatuffite	Ab+Amp+Chl+Qz+Aug	Ser		Porphyroblast Ab altered into sericite
38	S68-63.40	Metatuffite	Ab+Amp+Chl+Qz+Aug	Chl, Ser		Albite altered by chlorite and sericite
39	S68-84.55	Metatuffite	Chl+Aug+Cb (Qz)	Cb	Py	Qz-carb veinlets
40	S94-80.30	Metatuffite	Qz+Cb (Chl+Ms+Pmp+Spn)	Cb	Py+Ccp	Ccp inclusion in Py. Qz+Cb veinlets
41	S50-109.40	Metatuffite	Chl (Qz+Cb)	Ser	Py+Ccp	Porphyroblast Ab altered into sericite
42	S53-106	Phyllite	Ab+ Qz+Sid (Dol+Goy+Rt+Kln)		Py (Au)	

	Sample code	Lithology	Mineral Assemblages	Alteration	Ore Minerals	Comment
43	S66-114.50	Phyllite	Sd+Mnz+Rt+Ap	Ser		
44	S66-37.50	Phyllite	Sid+Qz (Ap)	Ser	Py+Sph+Ccp	
45	S68-144.70	Phyllite	Qz+Cb+Ab(Ap+Mnz)	Cb	Py+Ccp (Tnt+Ttr+Gn+En)	Lamination consist of Qz-Cb
46	S50-33.90	Quartz vein	Qz+Cb (Ap+Mnz)	Cb	Py	
47	S50-81.50	Quartz vein	Qz+Cb+Ab (Lim)		Hem	
48	S53-101	Quartz vein	Qz+Ab (Sid+Spn+Mnz)		Py (Ccp+ Fam+ Ttr+Gn+Au)	Au in pyrite (d=10μm+ 8μm+ 5.9μm+ 5.7μm)
49	S53-103	Quartz vein	Qz+Ab+Cb (Ap+Rt+Mnz+Hem+Spn+Goy)		Py (Ccp+Tnt+Ttr+ Fam+Lu+Gn+Au)	relic of rutile in albite
50	S53-8690	Quartz vein	Qz+Ab+Cb (Hem+Lim)	Cb	Py	Qz veins cut by hematite veinlets
51	S66-67	Quartz vein	Qz+Cc+Hem		Ccp+(Bi-Te phases)	
52	S68-107.00	Quartz vein	Qz+Sid+Ank (Ser+Ab+Sid+Hem)		Py+Ccp (Luz+fam+Au)	Mylonite texture
53	S68-128.70	Quartz vein	Qz+Sid+Ank (Hem)		Py	
54	S68-128.70	Quartz vein	Qz+Cb+Ab (Hem+Mnz+Sid)		Py (Sph+Fam)	
55	S68-129.50	Quartz vein	Qz+Sid+Ank+Ab		Py (Gn+Fam)	Intergranular qz
56	S68-132.90	Quartz vein	Qz+Ab (Kn+Mnz+Hem+Sid+Ank)		Py+Ccp (Gn+Tnt+Hg-Ttr+Luz+Au)	
57	S68-136.50	Quartz vein	Qz+Sid+Ank+Ab (Hem)		Py (Gn)	Intergranular qz
58	S68-140.20	Quartz vein	Qz+Ab (Sid+Mnz+Rt+Ap+Hem)		Py (Au)	fine-grained crystalline qz vein
59	S68-143.80	Quartz vein	Qz+Cb+Ab (Chl+Rt+Mnz+Hem+Sid)		Py+Ccp (Cv+Tnt+Ttr+Fam+ Luz+Carr)	Polycrystalline Qz, siderite rims sulphide, carrolite
60	S68-144.70	Quartz vein	Qz+Cb+Ab (Ap+Mnz)	Cb	Py+Ccp (Tnt+Ttr+Gn+Fam)	
61	S69-32.80	Quartz vein	Qz+Cb (Ab+Hem+Ap)	Ser	Py+Ccp (Tnt+Ttr+Luz)	
62	S69-64.40	Quartz vein	Qz+Cb+Ab			
63	SBD003	Quartz vein	Qz (Chl+Lim)		Py	
64	S50-33.90	Quartz vein+metabasite	Qz+Cb (Chl+Ms+Cpx)		Py	
65	S68-113.20	Quartz vein+metabasite	Qz+Cb(Ab+Epi+hem)		Py+Ccp (Cv+Ttr+Fam+Luz)	
66	S69-112.50	Quartz vein+metabasite	Ab+Cb+Qz (Chl)		Py	

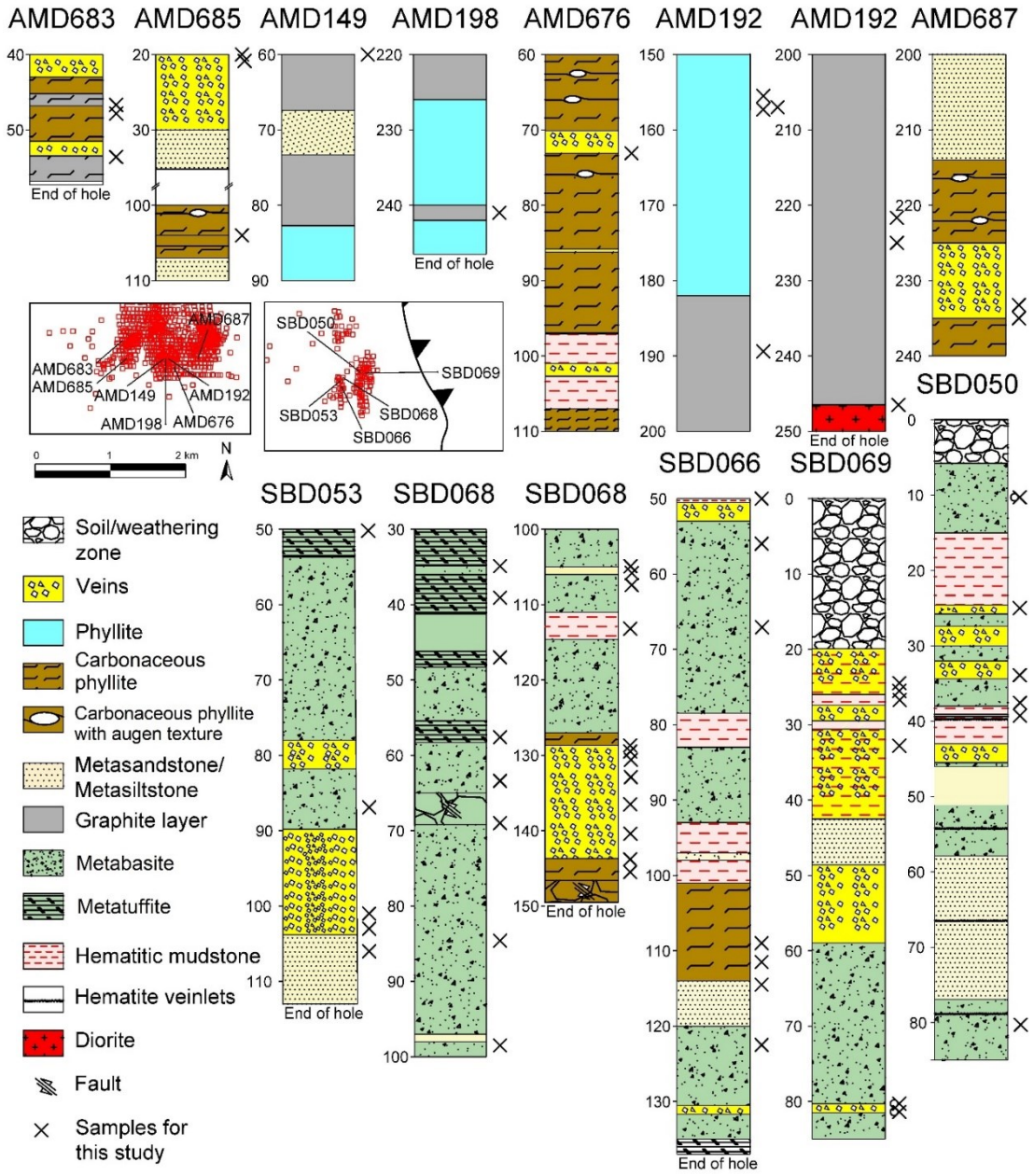

*Bore holes sample distribution for used for this study, includiing sample for fluid inclusion, EMPA on silicate, sulphide, gold, sulphosalt and Raman spectroscopic analyses on carbonaceous material
*Samples analysed using crush leach, LA-ICP-MS, stable isotope and XRF, ICP-MS methods are not shown.

APPENDIX B

Mineralogy, borehole profile and geochemistry of Salu Bullo deposit.

SBD050

From	To	Remark	Type	Petrography	Description	Mineralogy
			Barren	S50-9.9	Metatuff	Cb+Qz+Ab (Ms+Ser)
20.0	23.6	Hematitic mudstone	Barren			
23.6	24.6	Hematitic mudstone	Barren		Chlorite alteration	
24.6	25.7	Qz vein	Vein	S50-25	Veinlet of Qz-Cb-Ab	Cb+Qz+Ab (Hem)
25.7	27.1	Sandstone	Barren		Chlorite alteration	
27.1	30.1	Hematitic mudstone	Barren			
30.1	36.4	Qz vein	Vein	S50-33.90	Qz vein	Qz+Dol (Ap+Mnz)
36.4	38.3	Metavolcanic	Barren			
38.3	42.6	Hematitic mudstone	Barren			
40.3	42.6	Hematitic mudstone	Barren			
42.6	44.6	Qz vein	Vein			
44.6	46.1	Hematitic mudstone	Barren			
46.1	51.1	Metaandstone	Barren			
51.1	53.8	Metavolcanic	Barren			
53.8	57.9	Volcaniclastic	Barren			
57.9	76.5	Metasandstone	Barren			
76.5	81.3	Metavolcanicc	Barren	S50-80.30	Metavolcanic	Qz+Cb+Chl (Amp)
81.3	82.4	Metavolcanic-Qz vein	Barren			
82.4	86.4	Metaandstone	Barren			

Borehole Profile

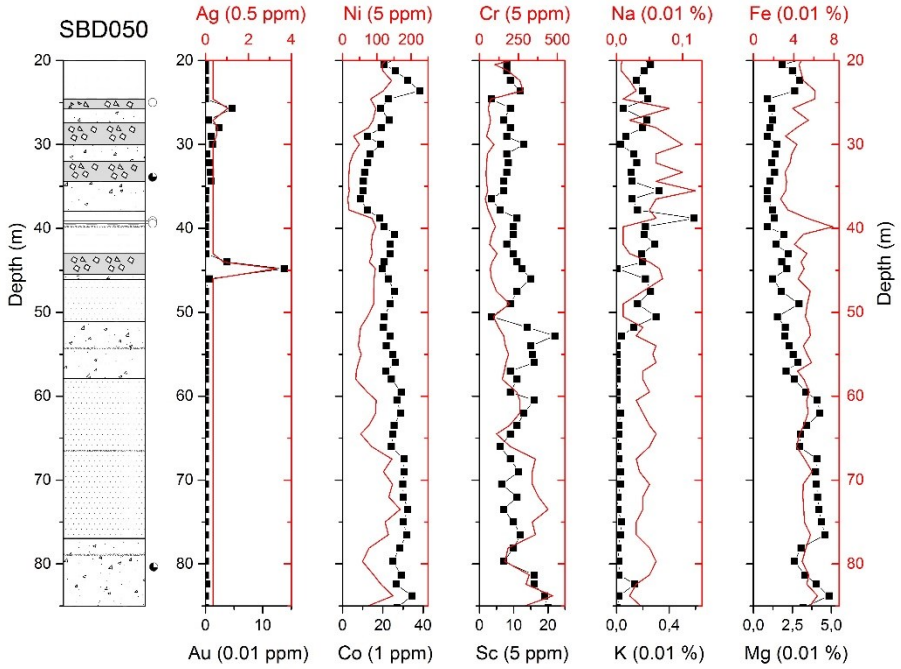

-All values below detection limit (bdl) was treated according to Croghan, 2003 by bdl/√2
-Geochemistry of bore hole were based on exploration data of PT Masmindo Dwi Area and verified for JORC reporting. Gold content determined using fire assay fussion with an Atomic Adsorption Spectrometry technique, other element were determined using FAA40_AAS package of Geoservices ltd. GeoAssay Laboratory (Geoservices) at Cikarang, Indonesia.

SBD053

From	To	Remark	Type	Petrography	Description	Mineralogy
50	53.7	Metatuff		S53-50.20	Metatuff	Sid+Qz+Amp+Chl+Chl (Spn+Ap+Py+Ccp)
53.7	78.7	Metasandstonee				
78.7	81.8	Qz brecia with dissemi- nated Py, intense silica alteration	Vein			
81.80	89.7	Metasandstone, disseminated Py,stringer hematite	Barren	S53-86.9	Sandstone with hematitic veinlet	Qz+Ab+Hem (Cb)
89.7	104.6	Qz breccia	Vein	S53-101	Qz Breccia containing siderite-albite phyllite fragment	Qz+Ab+Sid(Spn+Mnz+ Py+Cpy+Fam+Ttr+Gn+Au)
			Vein	S53-103	Qz Breccia containing siderite-albite phyllite fragment	Qz+Ab+Sid(Ap+Rt+Mnz+ Hem+Spn+Goy+Py+Ccp+Tnt+ Fam+Luz+Gn+Au)
104.6	114.50	Metasandstone	Barren	S53-106	Sandstone with intense carbonate alteration in contact with phyllite.	Qz+Ab+Sid(Py)

Borehole Profile

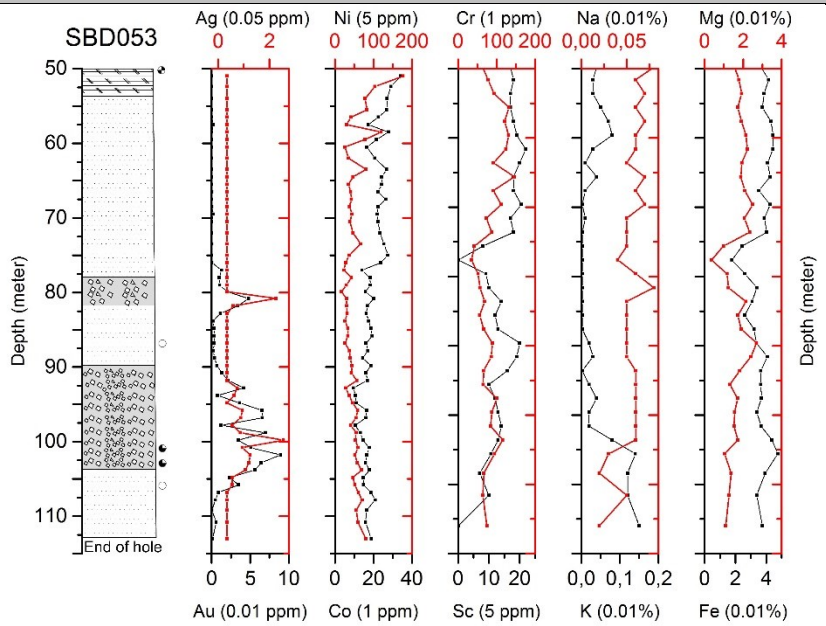

-All values below detection limit (bdl) was treated according to Croghan, 2003 by bdl/√2
-Geochemistry of bore hole were based on exploration data of PT Masmindo Dwi Area and verified for JORC reporting. Gold content determined using fire assay fussion with an Atomic Adsorption Spectrometry technique, other element were determined using FAA40_AAS package of Geoservices ltd. GeoAssay Laboratory (Geoservices) at Cikarang, Indonesia.

SBD066

From	To	Remark	Type	Petrography	Description	Mineralogy
50.5	53	Brecciation, highly altered	Barren			
53	57	Pyroclastic intersect by Cb veining	Barren	S66-56	Pyroclastic cut by Cc vein	Cc+Ank+Lm (Py+Cov)
57	63	Pyroclastic with minor sulphide				
63	78.5	Pyroclastic with Cb-Qz veining, pebbles of Qz-Cb-Fsp	Barrem	S66-67	Metatuff	Cc+Ab+Qz (Hem+ Ph+Mnz+Py+Ccp+ unknown Ag-Te-Bi)
			Barren	S66-69	Metatuff	Cc+Ab+Qz+Chl (Ph+Sd)
78.5	83	Hematitic mudstone with Cb veining	Barren			
83	86	Pyroclastic with Cb veining	Barren			
86	93	Pyroclastic	Barren			
93	97	Hematitic mudstone	Barren			
97	98	Intense lamination in pyroclastic	Barren			
98	101	Hematitic mudstone	Barren			

Borehole Profile

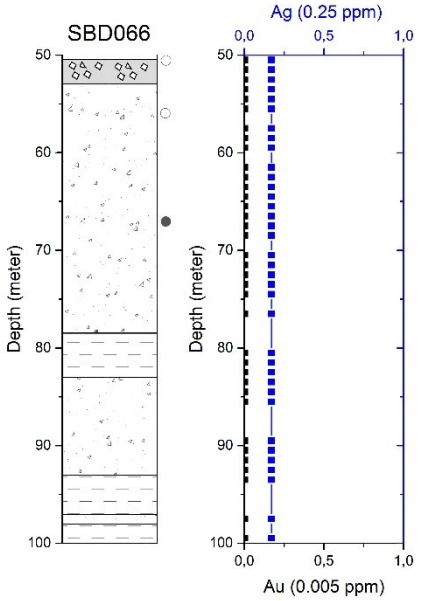

-All values below detection limit (bdl) was treated according to Croghan, 2003 by bdl/√2
-Geochemistry of bore hole were based on exploration data of PT Masmindo Dwi Area and verified for JORC reporting. Gold content determined using fire assay fussion with an Atomic Adsorption Spectrometry technique, other element were determined using FAA40_AAS package of Geoservices ltd. GeoAssay Laboratory (Geoservices) at Cikarang, Indonesia.

SBD066

From	To	Remark	Type	Petrography	Description	Mineralogy
101	108	Phyllite	Barren			
108	114	Phyllite, foliated, crenulated with minor tuff	Barren	S66-109	Phyllite	Ab+Pmp(Hem+Mnz+Rt, Dol+Kln+Py+Ccp+Gn)
114	119	Clastic rock, layering, disrupted but not mylonite, reddish Hematitic mudstone to greenish laminated clast	Barren	S66-114.5	Siderite phyllite	Sd+Ser (Mnz+Ap+Rt)
119	123	Clay	Barren			
123	127	Massive, green, metavolcanic	Barren			
127	130.5	Altered, barren metavolcanic	Barren	S66-127.5	Metavolcanic	Qz+Ab+Di+Chl+Pmp (Ap+ Py+Ccp)
130.5	131.7	Barren Qz vein	Barren			
131.7	137	Metavolcanioc	Barren			
			Barren			

Borehole Profile

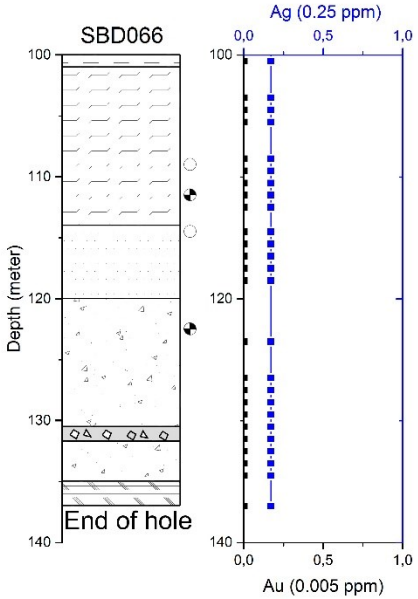

-All values below detection limit (bdl) was treated according to Croghan, 2003 by bdl/√2

-Geochemistry of bore hole were based on exploration data of PT Masmindo Dwi Area and verified for JORC reporting. Gold content determined using fire assay fussion with an Atomic Adsorption Spectrometry technique, other element were determined using FAA40_AAS package of Geoservices ltd. GeoAssay Laboratory (Geoservices) at Cikarang, Indonesia.

Soil
Veins
Mica schist
Phyllite
Phyllite with augen texture
Diorite
Metasandstone
Graphite
Metavolcanic
Metatuff
"Hematitic mudstone"
Hematite veinlets
Raman spectroscopy on fluid inclusions
Microthermometry
Raman spectroscopy on carbonaceous materials
Electron microprobe on mica
Electron microprobe on chlorite
Petrography

SBD068

From	To	Remark	Type	Petrography	Description	Mineralogy
30.0	34.9	Metatuff-metabasite	Barren	S68-34.9	Pyroxene bearing metabasite	Qz+Chl (Pmp+Cc+Aug+Act)
34.9	36.0	Metabasite	Barren	S68-39.1		Qz+Chl (Pmp+Cc+Aug+Act+ Py+Ccp)
36.0	41.25	Metatuff	Barren			
41.25	55.4	Metavolcanic	Barren	S68-47	Cpx phyric basalt (metabasite?)	Aug+Chl+Ab+Pmp (Act+Chr+Ccp)
55.4	58.3	Metatuff	Barren	S68-57.6	Metatuff	Qz+Ab+Chl (Act+Aug+Ser)
58.3	69.3	Metavolcanic	Barren	S68-69	Metabasite	Ab+Chl+Ph (Qz+Cc+Ap +Pmp+Rt+Ccp)
69.3	94.7	Metasandstone	Barren			
94.7	95.7	Qz vein	Vein			
95.7	100	Metasandstone	Barren	S68-98.4	Metasandstone	Qz (Dol+Hem)

Borehole Profile

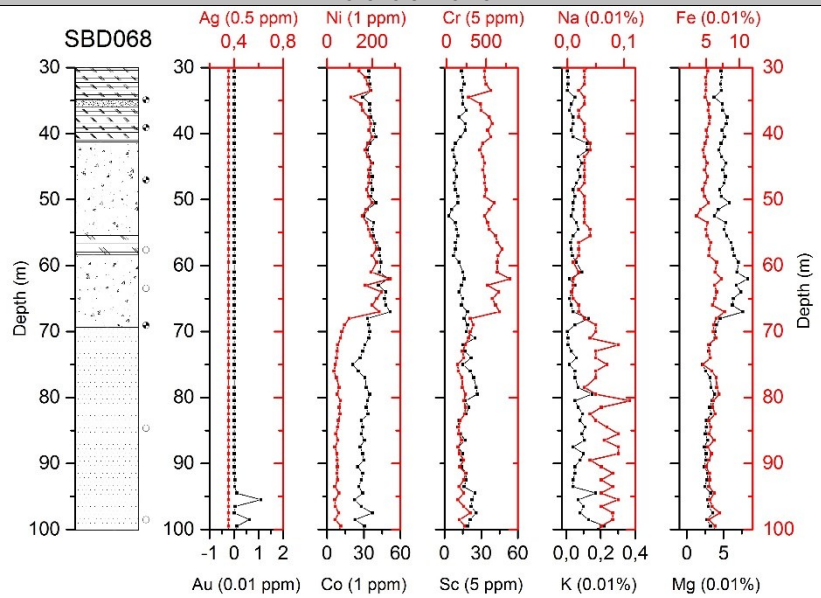

-All values below detection limit (bdl) was treated according to Croghan, 2003 by bdl/√2
-Geochemistry of bore hole were based on exploration data of PT Masmindo Dwi Area and verified for JORC reporting. Gold content determined using fire assay fussion with an Atomic Adsorption Spectrometry technique, other element were determined using FAA40_AAS package of Geoservices ltd. GeoAssay Laboratory (Geoservices) at Cikarang, Indonesia.

SBD068

From	To	Remark	Type	Petrography	Description	Mineralogy
100	105.5	Metasandstone	Barren	S68-105.4	Meta-sandstone	Qz (Dol+Ser+Hem+Py)
105.5	110.8	Qz vein	Vein	S68-107	Qz vein	Qz+Ab (Ser+Ank+Sid+Hem+ Py+Ccp+Luz+Fam+Au)
110.8	128.7	Metasandstone	Barren	S68-113.2	Meta-sandstone	Qz+Ab (Sid+Hem+Py+ Ccp+Cov+Ttr+Fam+Luz)
128.7	143.8	Qz vein	Vein	S68-128.7	Qz vein	Qz+Sid (Py+Hem)
				S68-129.5	Qz vein	Qz+Sid+Ab (Py+Gn+Fam)
				S68-130.3	Qz breccia	Qz+Sid+Ab (Kn+Hem+Mnz+Rt+ Py+Fam+Gn+Stib)
				S68-132.9	Qz vein	Qz+Ab (Kn+Mnz+Hem+ Py+Ccp+Gn+Hg Ttr+Luz+Au)
				S68-136.5	Qz vein	Qz+Sid+Ab (Hem+Py+Gn)
				S68-140.2	Qz vein	Qz+Ab (Sid+Mnz+Rt+Ap+ Hem+Py+Au)
				S68-143.8	Qz vein	Qz+Ab (Sid+Ank+Chl +Rt+Mnz+Rt+ Py+Ccp+Cv+Tnt+Ttr+ Fam+Luz+Carr)
143.8	149.5	Phyllite	Barren	S68-144.7	Phyllite	Qz+Cc+Ab (Ap+Mnz+Py+Ccp +Tnt+Ttr+Gn+Fam)

Geochemistry

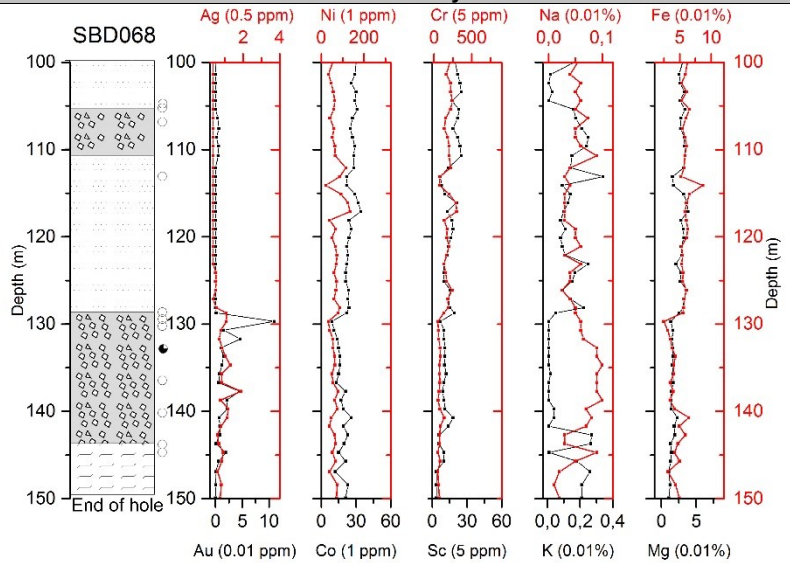

-All values below detection limit (bdl) was treated according to Croghan, 2003 by bdl/√2
-Geochemistry of bore hole were based on exploration data of PT Masmindo Dwi Area and verified for JORC reporting. Gold content determined using fire assay fussion with an Atomic Adsorption Spectrometry technique, other element were determined using FAA40_AAS package of Geoservices ltd. GeoAssay Laboratory (Geoservices) at Cikarang, Indonesia.

SBD069

From	To	Remark	Type	Petrography	Description	Mineralogy
0.0	2.0	Soil, total oxidation= 17.40 m	Barren			
2.0	8.0	Weathered Hematitic mudstone	Barren			
8.0	13.0	Hematitic mudstone	Barren			
13.0	15.5	Qz vein in Hematitic mudstone	Vein			
15.5	19.9	Metasandstone	Barren			
19.9	21.3	Hematitic mudstone	Barren			
21.3	25.9	Qz vein in Hematitic mudstone	Vein	S69-24.5	Qz vein	Qz+Ab+Sd+(Mnz+Rt+ Hem+Ap+Py+Ccp+ Fam+Luz+Sp+Gn+Au)
				S69-25	Qz vein	Qz+Ab+Sd+(Mnz+Hem +Kln+Ph+Py+Ccp+Fam +Tnt+Luz+Gn+Bn+Au)
				S69-25.8	Qz vein	Qz+Ab+Sd(Ap+Mnz+Hem+ Py+Ccp+Tnt+Cov+Luz+Fam+ Sp+Au)
25.9	27.4	Metasandstone	Barren			
27.4	29.5	Qz vein	Vein			
29.5	30.6	Metasandstone	Barren			
30.6	37.1	Qz vein	Vein	S69-32.8	Qz vein	Qz+Ab+Sd(Ap+Mnz+Ser+Hem+ Py+Ccp+Tnt+Ttr+Luz)
37.1	40.0	Qz vein in Hematitic mudstone	Vein			

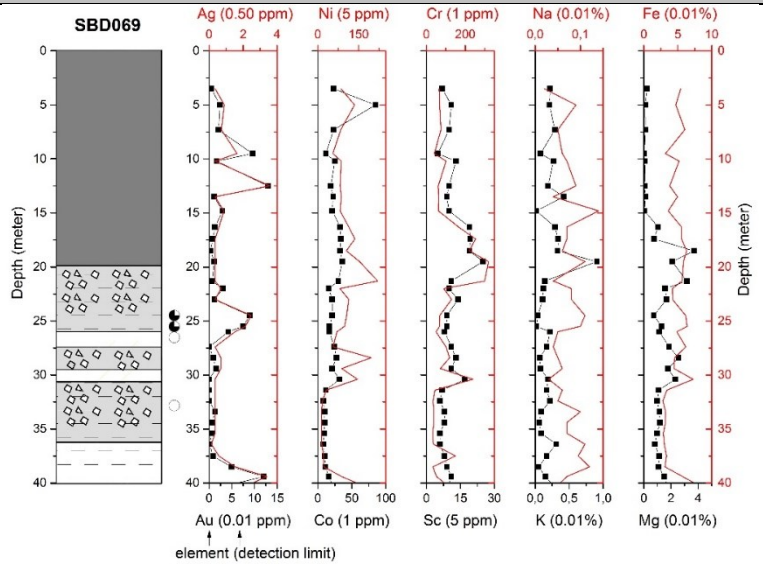

-All values below detection limit (bdl) was treated according to Croghan, 2003 by bdl/√2
-Geochemistry of bore hole were based on exploration data of PT Masmindo Dwi Area and verified for JORC reporting. Gold content determined using fire assay fussion with an Atomic Adsorption Spectrometry technique, other element were determined using FAA40_AAS package of Geoservices ltd. GeoAssay Laboratory (Geoservices) at Cikarang, Indonesia.

SBD069

From	To	Remark	Type	Petrography	Description	Mineralogy
40	42.5	Qz vein in Hematitic mudstone	Vein			
42.5	52.4	Metasandtone	Barren			
52.4	52.9	Coreloss				
52.9	57	Meta-sandstone	Barren-vein			
57.0	80	Metavolcanic, Metasandstone	Barren	S69-64.4	Qz vein	Qz+Cc+Ab
				S69-68.8	Metasandstone	Qz+Cc (Ab+Ph+Hem+Ap)
80	81	Qz vein	Barren			
81	85	Metavolcanic	Barren			

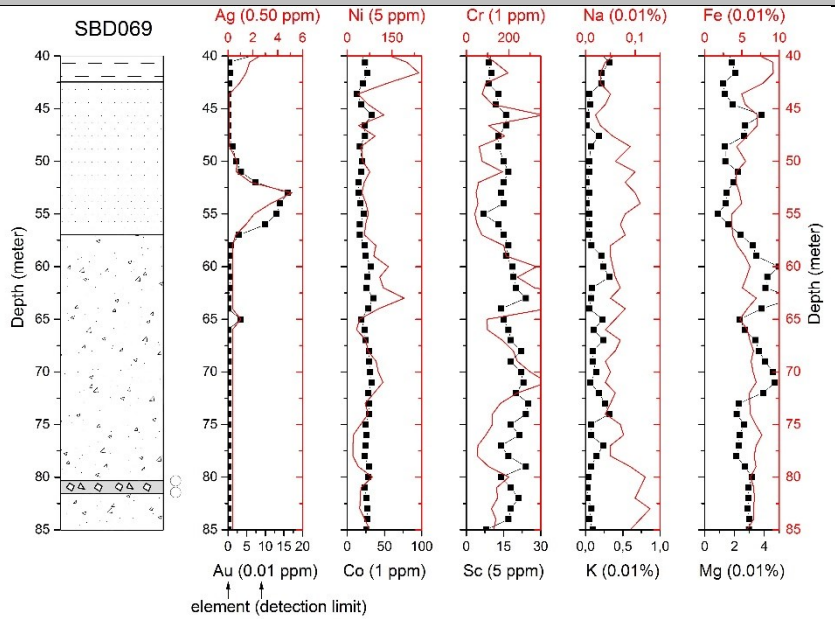

-All values below detection limit (bdl) was treated according to Croghan, 2003 by bdl/√2
-Geochemistry of bore hole were based on exploration data of PT Masmindo Dwi Area and verified for JORC reporting. Gold content determined using fire assay fussion with an Atomic Adsorption Spectrometry technique, other element were determined using FAA40_AAS package of Geoservices ltd. GeoAssay Laboratory (Geoservices) at Cikarang, Indonesia.

APPENDIX C

Methods and analytical techniques

Sample No	S68-34.90	S68-39.10	S68-84.55	S53-10.90	S68-47	S68-63.40	A687-79.80	S53-50.20
Clinopyroxene	EMPA	EMPA	EMPA	EMPA	EMPA			
Chromian spinel	EMPA			EMPA	EMPA	EMPA	EMPA	
Chlorite	EMPA	EMPA	EMPA		EMPA			EMPA
Phengite					EMPA			
Actinolite	EMPA	EMPA		EMPA	EMPA			
Epidote	EMPA			EMPA				
Pumpellyite	EMPA	EMPA		EMPA				
Albite		EMPA		EMPA				
Monazite								
Bdy/ Xtm/ Goy								
Gold								
Sulphosalt								
Pyrite		EMPA						
Sphalerite								
Carrolite								
Cob/ Bi-phases								
Fluid inclusion								
Carbonate								
Graphite								
Whole-rock	XRF					XRF		
Whole-rock	ICP-MS							

Sample No	S68-69	S68-122.50	A687-157.98	A192-155.70	A685-171	A683-53.60	A149-81.15	S66-67
Clinopyroxene								
Chromian spinel								
Chlorite	EMPA	EMPA	EMPA	EMPA	EMPA			
Phengite				EMPA		EMPA	EMPA	EMPA
Actinolite								
Epidote								
Pumpellyite								
Albite			EMPA				EMPA	
Monazite								
Bdy/ Xtm/ Goy			SEM-EDX (Bdly)					
Gold								
Sulphosalt								
Pyrite								
Sphalerite								
Carrolite								
Cob/ Bi-phases			SEM-EDX (Cbt)					
Fluid inclusion				RamanSp				
Carbonate								
Graphite				RamanSp		RamanSp		
Whole-rock								
Whole-rock								

Sample No	S94-80.30	A685-20	A34-28.3	S53-103	A192-189.40	A192-221.65	A192-225	A192-245
Clinopyroxene								
Chromian spinel								
Chlorite								
Phengite								
Actinolite								
Epidote	EMPA							
Pumpellyite	EMPA							
Albite				LA-ICP-MS				
Monazite			SEM-EDX	SEM-EDX	SEM-EDX	SEM-EDX	SEM-EDX	
Bdy/ Xtm/ Goy					SEM-EDX (Xtm)			
Gold		EMPA						
Sulphosalt								
Pyrite	EMPA	LA-ICP-MS		LA-ICP-MS				
Sphalerite								
Carrolite								
Cob/ Bi-phases							SEM-EDX (Bi)	
Fluid inclusion		RamanSp + Microth		RamanSp				
Carbonate								
Graphite					RamanSp			
Whole-rock					XRF	XRF	XRF	XRF
Whole-rock					ICP-MS	ICP-MS	ICP-MS	ICP-MS

Sample No	A192-177.30	A35-24.40	A34-38.3	S69-25.80	A149-110.3	A35-18.65	S53-106	S68-94.95
Clinopyroxene								
Chromian spinel								
Chlorite								
Phengite								
Actinolite								
Epidote								
Pumpellyite								
Albite								LA-ICP-MS
Monazite	SEM-EDX	SEM-EDX	SEM-EDX	SEM-EDX	SEM-EDX	SEM-EDX		
Bdy/ Xtm/ Goy							SEM-EDX (Goy)	
Gold				EMPA				
Sulphosalt				EMPA				
Pyrite				EMPA				
Sphalerite								
Carrolite								
Cob/ Bi-phases								
Fluid inclusion	RamanSp			RamanSp				
Carbonate								
Graphite								
Whole-rock								
Whole-rock								

Sample No	S68-105.25	S68-130.30	S69-24.50	S69-25	S53-103	S68-113.20	S50-53.40	S68-98.40
Clinopyroxene								
Chromian spinel								
Chlorite								
Phengite								
Actinolite								
Epidote								
Pumpellyite								
Albite	LA-ICP-MS	LA-ICP-MS	LA-ICP-MS	LA-ICP-MS	LA-ICP-MS	LA-ICP-MS		
Monazite								
Bdy/ Xtm/ Goy				SEM-EDX (Goy)				
Gold				EMPA				
Sulphosalt								
Pyrite		EMPA	LA-ICP-MS	EMPA, LA-ICP-MS		EMPA		
Sphalerite			LA-ICP-MS	LA-ICP-MS				
Carrolite								
Cob/ Bi-phases								
Fluid inclusion			RamanSp					
Carbonate			Stable isotope					
Graphite								
Whole-rock						XRF		XRF
Whole-rock						ICP-MS		ICP-MS

Sample No	S50-83.95	S68-105.40	S68-132.90	S94-34.35	S53-101	S68-107	S68-140.20	SB-02
Clinopyroxene								
Chromian spinel								
Chlorite								
Phengite								
Actinolite								
Epidote								
Pumpellyite								
Albite								
Monazite								
Bdy/ Xtm/ Goy								
Gold			EMPA	EMPA	EMPA	EMPA	EMPA	EMPA
Sulphosalt			EMPA					
Pyrite					LA-ICP-MS	EMPA LA-ICP-MS	EMPA, LA-ICP-MS	
Sphalerite		LA-ICP-MS						
Carrolite								
Cob/ Bi-phases								
Fluid inclusion			RamanSp		RamanSp	RamanSp		
Carbonate								
Graphite								
Whole-rock	XRF	XRF						
Whole-rock								

Sample No	A149-90.65	A635-21	A192-86.40	A635-16	S68-143.80	A35-34.70	S68-98.95	S68-136.50
Clinopyroxene								
Chromian spinel								
Chlorite								
Phengite								
Actinolite								
Epidote								
Pumpellyite								
Albite								
Monazite								
Bdy/ Xtm/ Goy								
Gold	EMPA	EMPA	EMPA	EMPA				
Sulphosalt	EMPA				EMPA	EMPA		
Pyrite			LA-ICP-MS				EMPA	EMPA
Sphalerite								
Carrolite					EMPA			
Cob/ Bi-phases								
Fluid inclusion								
Carbonate								
Graphite								
Whole-rock								
Whole-rock								

Sample No	S69-32.80	S69-64.40	S50-33.90	ONG-1	S68-128.70	S66-37.50	GRS 08	S50-80.30
Clinopyroxene								
Chromian spinel								
Chlorite								
Phengite								
Actinolite								
Epidote								
Pumpellyite								
Albite								
Monazite								
Bdy/ Xtm/ Goy								
Gold								
Sulphosalt								
Pyrite			EMPA LA-ICP-MS	EMPA, LA-ICP-MS				
Sphalerite	EMPA	EMPA		LA-ICP-MS				
Carrolite								
Cob/ Bi-phases						SEM-EDX (Cbt)		
Fluid inclusion			Raman Sp	Raman Sp			Raman Sp + Microth	Raman Sp
Carbonate								
Graphite								
Whole-rock								
Whole-rock								

Sample No	SBD003	A683-46.80	A687-235	MP01	MP02	MP03	A685-5	A676-73.10
Clinopyroxene								
Chromian spinel								
Chlorite								
Phengite								
Actinolite								
Epidote								
Pumpellyite								
Albite								
Monazite								
Bdy/ Xtm/ Goy								
Gold								
Sulphosalt								
Pyrite								
Sphalerite								
Carrolite								
Cob/ Bi-phases								
Fluid inclusion	RamanSp	RamanSp	RamanSp + Microth	RamanSp + Microth	RamanSp + Microth	RamanSp + Microth	RamanSp + Microth	RamanSp + Microth
Carbonate								
Graphite								
Whole-rock								
Whole-rock								

Sample No	S50-23.60	S94-27.60	S94-40.55	S54-72.90	A149-36.20	T05-81.90	A634-5.5	A634-42
Clinopyroxene								
Chromian spinel								
Chlorite								
Phengite								
Actinolite								
Epidote								
Pumpellyite								
Albite								
Monazite								
Bdy/ Xtm/ Goy								
Gold								
Sulphosalt								
Pyrite								
Sphalerite								
Carrolite								
Cob/ Bi-phases								
Fluid inclusion								
Carbonate	Isotope	Isotope	Isotope	Isotope	Isotope	Isotope	Isotope	Isotope
Graphite								
Whole-rock								
Whole-rock								

Sample No	S94-44.30	S69-112.50	S94-116.60	Fossil -	A685-104	A683-47.70	A192-155.50	A192-157.30
Clinopyroxene								
Chromian spinel								
Chlorite								
Phengite								
Actinolite								
Epidote								
Pumpellyite								
Albite								
Monazite								
Bdy/ Xtm/ Goy								
Gold								
Sulphosalt								
Pyrite								
Sphalerite								
Carrolite								
Cob/ Bi-phases								
Fluid inclusion								
Carbonate	Isotope	Isotope	Isotope	Isotope				
Graphite					Raman Sp	Raman Sp	Raman Sp	Raman Sp
Whole-rock								
Whole-rock								

APPENDIX D

Representative composition of clinopyroxene (1)

Sample number	S68-34.90-10	S68-34.90-20	S68-34.90-23	S68-34.90-18	S68-34.90-17	S68-34.90-16	S68-34.90-19	S68-34.90-22	S50-39.10-14	S50-39.10-13	S50-39.10-19
SiO_2	56.18	51.92	52.67	53.64	54.19	54.27	52.954	52.76	51.94	52.04	52.04
TiO_2	0.37	0.00	0.49	0.24	0.23	0.25	0.217	0.21	0.52	0.47	0.49
Al_2O_3	0.29	2.74	2.75	2.25	1.70	1.78	2.311	3.03	2.53	2.59	2.76
FeO	5.70	6.58	6.30	5.54	5.82	5.90	5.541	4.23	9.10	9.29	9.34
MnO	0.26	0.15	0.13	0.21	0.17	0.09	0.2	0.14	0.20	0.19	0.22
MgO	15.53	17.55	17.65	17.86	17.92	17.87	17.469	17.37	15.19	15.30	15.10
CaO	22.17	18.54	18.78	19.92	19.68	19.59	19.975	20.76	19.81	20.18	19.97
Na_2O	0.38	0.16	0.20	0.15	0.15	0.08	0.162	0.20	0.25	0.23	0.24
K_2O	0.00	0.01	0.00	0.00	0.00	0	0	0.01	0.00	0.00	0.00
Total	100.87	97.64	98.98	99.81	99.87	99.84	98.83	98.71	99.53	100.29	100.17
Si	2.05	1.94	1.94	1.96	1.98	1.98	1.95	1.94	1.93	1.92	1.93
Ti	0.01	0.00	0.01	0.01	0.01	0.01	0.01	0.01	0.01	0.01	0.01
Al	0.01	0.12	0.12	0.10	0.07	0.08	0.10	0.13	0.11	0.11	0.12
Fe^{3+}	-0.11	0.01	-0.02	-0.02	-0.04	-0.05	-0.01	-0.01	0.01	0.03	0.02
Fe^{2+}	0.29	0.19	0.21	0.19	0.21	0.24	0.18	0.14	0.27	0.25	0.27
Mn	0.01	0.00	0.00	0.01	0.01	0.00	0.01	0.00	0.01	0.01	0.01
Mg	0.85	0.98	0.97	0.97	0.98	0.97	0.96	0.95	0.84	0.84	0.83
Ca	0.87	0.74	0.74	0.78	0.77	0.77	0.79	0.82	0.79	0.80	0.79
Na	0.03	0.01	0.01	0.01	0.01	0.01	0.01	0.01	0.02	0.02	0.02
K	0.00	0.00	0.00	0.00	0.00	0.00	0.00	0.00	0.00	0.00	0.00
Total	4.00	4.00	4.00	4.00	4.00	4.00	4.00	4.00	4.00	4.00	4.00
Mg#	83	83	83	85	85	84	85	88	75	75	74
En	0.42	0.51	0.50	0.50	0.50	0.49	0.50	0.50	0.44	0.44	0.44
Fs	0.14	0.10	0.11	0.10	0.11	0.12	0.09	0.07	0.14	0.13	0.14
Wo	0.43	0.39	0.39	0.40	0.39	0.39	0.41	0.43	0.41	0.42	0.42

Representative composition of clinopyroxene (2)

Sample number	S68-47-3-c 55	S68-47-5 57	S68-47-9 61	S68-47-11-r 63	S68-47-12 64	S68-47-22 74	S68-47-23 75	S68-47-27-r1 79	S68-47-27-c3 80	S68-47-27-c4 81	S68-47-27-c5 82
SiO_2	52.05	51.91	53.55	51.57	52.56	52.91	52.31	52.34	51.58	51.36	52.93
TiO_2	1.08	0.53	1.11	0.27	0.06	0.90	0.41	0.00	0.32	1.05	0.00
Al_2O_3	3.07	3.67	1.24	3.22	3.20	1.90	3.14	3.38	2.86	3.33	2.82
FeO	5.94	5.16	7.48	5.92	5.84	5.48	5.66	6.20	8.19	8.88	4.30
MnO	0.25	0.14	0.33	0.15	0.16	0.15	0.13	0.16	0.23	0.21	0.07
MgO	16.15	16.72	14.99	17.38	17.27	18.41	17.42	16.94	16.95	15.77	17.51
CaO	20.19	19.75	19.99	18.83	18.95	18.66	18.97	19.18	18.29	18.81	20.37
Na_2O	0.29	0.17	0.45	0.15	0.17	0.14	0.18	0.23	0.15	0.28	0.23
K_2O	0.01	0.01	0.03	0.00	0.01	0.03	0.00	0.01	0.00	0.01	0.00
Total	99.02	98.05	99.16	97.49	98.21	98.57	98.23	98.44	98.55	99.70	98.23
Si	1.93	1.93	2.00	1.93	1.95	1.95	1.94	1.94	1.92	1.90	1.96
Ti	0.03	0.01	0.03	0.01	0.00	0.02	0.01	0.00	0.01	0.03	0.00
Al	0.13	0.16	0.05	0.14	0.14	0.08	0.14	0.15	0.13	0.15	0.12
Fe^{3+}	-0.03	-0.04	-0.09	0.00	-0.03	-0.03	-0.03	-0.01	0.02	0.01	-0.02
Fe^{2+}	0.22	0.20	0.32	0.19	0.21	0.20	0.20	0.20	0.23	0.27	0.15
Mn	0.01	0.00	0.01	0.00	0.01	0.00	0.00	0.00	0.01	0.01	0.00
Mg	0.89	0.93	0.84	0.97	0.96	1.01	0.96	0.94	0.94	0.87	0.96
Ca	0.80	0.79	0.80	0.75	0.75	0.74	0.75	0.76	0.73	0.75	0.81
Na	0.02	0.01	0.03	0.01	0.01	0.01	0.01	0.02	0.01	0.02	0.02
K	0.00	0.00	0.00	0.00	0.00	0.00	0.00	0.00	0.00	0.00	0.00
Total	4.00	4.00	4.00	4.00	4.00	4.00	4.00	4.00	4.00	4.00	4.00
Mg#	83	85	78	84	84	86	85	83	79	76	88
En	0.47	0.48	0.43	0.51	0.50	0.52	0.50	0.49	0.49	0.46	0.50
Fs	0.11	0.11	0.16	0.10	0.11	0.10	0.11	0.11	0.12	0.14	0.08
Wo	0.42	0.41	0.41	0.40	0.39	0.38	0.39	0.40	0.38	0.40	0.42

Representative composition of clinopyroxene (3)

Sample number	S68-47-27-c6 83	S68-47-27-c7 84	S68-47-27-c9 86	S68-47-27-r10 87	S68-47-28-r11 88	S68-47-28-r12 89	S68-47-28-r13 90	S68-47-28-r14 91	S68-47-28-r15 92	S68-47-28-r16 93	S68-47-28-r17 94
SiO_2	54.17	51.96	51.25	52.05	53.49	53.36	53.11	52.80	52.85	53.51	52.61
TiO_2	0.00	0.96	0.36	0.00	0.23	0.55	0.07	0.18	0.76	1.13	1.55
Al_2O_3	2.90	3.26	3.03	2.98	3.06	3.05	3.16	3.20	3.07	3.07	3.09
FeO	4.45	4.56	7.76	6.12	5.00	5.04	5.15	5.03	5.19	5.10	5.17
MnO	0.09	0.13	0.23	0.21	0.16	0.15	0.13	0.12	0.11	0.11	0.07
MgO	17.51	17.26	16.88	16.96	17.41	17.61	17.56	17.68	17.62	17.55	17.49
CaO	20.04	19.59	18.33	19.01	19.13	19.34	19.11	19.55	19.33	19.69	19.33
Na_2O	0.26	0.26	0.18	0.22	0.15	0.15	0.14	0.19	0.17	0.17	0.17
K_2O	0.00	0.01	0.01	0.01	0.01	0.00	0.01	0.02	0.01	0.02	0.01
Total	99.43	97.97	98.02	97.55	98.64	99.24	98.44	98.77	99.12	100.35	99.51
Si	1.98	1.93	1.92	1.95	1.97	1.96	1.96	1.94	1.94	1.95	1.93
Ti	0.00	0.03	0.01	0.00	0.01	0.02	0.00	0.01	0.02	0.03	0.04
Al	0.13	0.14	0.13	0.13	0.13	0.13	0.14	0.14	0.13	0.13	0.13
Fe^{3+}	-0.07	-0.04	0.03	-0.01	-0.08	-0.07	-0.06	-0.02	-0.05	-0.07	-0.07
Fe^{2+}	0.20	0.18	0.22	0.20	0.24	0.22	0.22	0.17	0.21	0.23	0.23
Mn	0.00	0.00	0.01	0.01	0.00	0.00	0.00	0.00	0.00	0.00	0.00
Mg	0.95	0.96	0.94	0.95	0.96	0.96	0.97	0.97	0.97	0.95	0.96
Ca	0.78	0.78	0.73	0.76	0.76	0.76	0.76	0.77	0.76	0.77	0.76
Na	0.02	0.02	0.01	0.02	0.01	0.01	0.01	0.01	0.01	0.01	0.01
K	0.00	0.00	0.00	0.00	0.00	0.00	0.00	0.00	0.00	0.00	0.00
Total	4.00	4.00	4.00	4.00	4.00	4.00	4.00	4.00	4.00	4.00	4.00
Mg#	88	87	80	83	86	86	86	86	86	86	86
En	0.49	0.50	0.50	0.50	0.49	0.49	0.50	0.51	0.50	0.49	0.49
Fs	0.10	0.09	0.11	0.10	0.12	0.11	0.11	0.09	0.11	0.12	0.12
Wo	0.40	0.41	0.39	0.40	0.39	0.39	0.39	0.40	0.39	0.39	0.39

Representative composition of clinopyroxene (4)

Sample number	S68-47-32-znin-r1 100	S68-47-32-znin-c2 101	S68-47-32-znin-c3 102	S68-47-32-znin-c4 103	S68-47-32-znin-c5 104	S68-47-32-znin-c6 105	S68-47-32-znin-c7 106	S68-47-32-znin-c8 107	S68-47-32-znin-c11 110	S68-47-32-znin-c12 111	S68-47-32-znin-c13 112
SiO_2	53.34	52.20	52.57	52.61	52.42	52.20	52.98	51.47	52.64	52.79	51.89
TiO_2	0.53	0.04	0.00	0.36	0.22	0.79	1.73	0.41	0.40	1.31	0.77
Al_2O_3	2.56	2.85	2.86	2.90	2.90	2.85	2.79	2.70	2.67	2.87	3.04
FeO	5.55	7.03	7.11	7.19	7.23	7.03	7.12	7.19	7.19	7.06	9.42
MnO	0.13	0.21	0.17	0.21	0.18	0.15	0.17	0.16	0.24	0.17	0.29
MgO	17.70	16.67	16.48	16.48	16.59	16.46	16.41	16.45	16.84	16.52	15.28
CaO	18.71	19.91	20.04	19.68	20.05	19.76	19.89	18.79	19.45	20.02	19.14
Na_2O	0.16	0.22	0.21	0.18	0.23	0.21	0.20	0.23	0.20	0.21	0.32
K_2O	0.00	0.01	0.00	0.00	0.01	0.01	0.01	0.01	0.00	0.01	0.00
Total	98.68	99.14	99.43	99.61	99.84	99.46	101.30	97.41	99.63	100.95	100.15
Si	1.97	1.93	1.94	1.94	1.93	1.93	1.93	1.94	1.94	1.92	1.92
Ti	0.01	0.00	0.00	0.01	0.01	0.02	0.05	0.01	0.01	0.04	0.02
Al	0.11	0.12	0.12	0.13	0.13	0.12	0.12	0.12	0.12	0.12	0.13
Fe^{3+}	-0.07	0.03	0.01	-0.01	0.03	-0.01	-0.06	0.00	0.00	-0.03	0.01
Fe^{2+}	0.24	0.18	0.21	0.23	0.20	0.23	0.28	0.23	0.22	0.24	0.29
Mn	0.00	0.01	0.01	0.01	0.01	0.00	0.01	0.01	0.01	0.01	0.01
Mg	0.98	0.92	0.91	0.91	0.91	0.91	0.89	0.92	0.92	0.90	0.84
Ca	0.74	0.79	0.79	0.78	0.79	0.78	0.78	0.76	0.77	0.78	0.76
Na	0.01	0.02	0.02	0.01	0.02	0.01	0.01	0.02	0.01	0.01	0.02
K	0.00	0.00	0.00	0.00	0.00	0.00	0.00	0.00	0.00	0.00	0.00
Total	4.00	4.00	4.00	4.00	4.00	4.00	4.00	4.00	4.00	4.00	4.00
Mg#	85	81	81	80	80	81	80	80	81	81	74
En	0.50	0.49	0.48	0.47	0.48	0.47	0.46	0.48	0.48	0.47	0.45
Fs	0.12	0.10	0.11	0.12	0.10	0.12	0.14	0.12	0.12	0.13	0.15
Wo	0.38	0.42	0.42	0.41	0.42	0.41	0.40	0.40	0.40	0.41	0.40

Representative composition of clinopyroxene (5)

Sample number	S68-47-32-znin-c14 113	S68-47-32-znin-c15 114	S68-47-32-znin-c16 115	S68-47-32-znin-c17 116	S68-47-32-znin-r19 117	S68-84.55-5 125	S68-84.55-8 128	S68-84.55-9 129	S68-84.55-10 130	S68-84.55-11 131	S68-84.55-13 133
SiO_2	53.40	52.25	53.39	52.79	52.40	50.98	51.65	52.80	52.35	52.72	52.47
TiO_2	0.00	0.00	0.73	0.73	0.51	0.00	0.00	0.17	1.53	0.59	0.41
Al_2O_3	2.03	3.37	2.69	3.52	3.48	2.17	2.58	2.18	2.69	2.12	2.20
FeO	5.65	5.78	5.63	6.36	6.95	9.19	9.73	7.02	6.43	8.10	7.06
MnO	0.14	0.14	0.15	0.14	0.14	0.35	0.25	0.21	0.17	0.22	0.17
MgO	17.90	17.18	17.92	16.86	17.08	16.33	15.12	17.48	16.59	17.12	17.08
CaO	19.45	19.31	19.15	18.95	18.22	17.78	18.93	18.80	19.52	18.34	19.77
Na_2O	0.11	0.23	0.16	0.23	0.20	0.35	0.31	0.17	0.23	0.21	0.20
K_2O	0.00	0.01	0.00	0.01	0.01	0.03	0.00	0.00	0.00	0.01	0.02
Total	98.69	98.27	99.83	99.59	98.98	97.19	98.57	98.83	99.51	99.43	99.38
Si	1.97	1.94	1.95	1.94	1.94	1.93	1.94	1.95	1.93	1.95	1.93
Ti	0.00	0.00	0.02	0.02	0.01	0.00	0.00	0.00	0.04	0.02	0.01
Al	0.09	0.15	0.12	0.15	0.15	0.10	0.11	0.10	0.12	0.09	0.10
Fe^{3+}	-0.02	0.00	-0.05	-0.06	-0.04	0.07	0.03	0.00	-0.05	-0.01	0.03
Fe^{2+}	0.20	0.18	0.22	0.25	0.25	0.22	0.28	0.22	0.25	0.26	0.19
Mn	0.00	0.00	0.00	0.00	0.00	0.01	0.01	0.01	0.01	0.01	0.01
Mg	0.98	0.95	0.98	0.92	0.94	0.92	0.85	0.96	0.91	0.94	0.94
Ca	0.77	0.77	0.75	0.75	0.72	0.72	0.76	0.75	0.77	0.73	0.78
Na	0.01	0.02	0.01	0.02	0.01	0.03	0.02	0.01	0.02	0.01	0.01
K	0.00	0.00	0.00	0.00	0.00	0.00	0.00	0.00	0.00	0.00	0.00
Total	4.00	4.00	4.00	4.00	4.00	4.00	4.00	4.00	4.00	4.00	4.00
Mg#	85	84	85	83	81	76	74	82	82	79	82
En	0.50	0.50	0.50	0.48	0.49	0.49	0.45	0.50	0.47	0.49	0.49
Fs	0.10	0.10	0.11	0.13	0.13	0.12	0.15	0.11	0.13	0.13	0.10
Wo	0.39	0.40	0.39	0.39	0.38	0.39	0.40	0.39	0.40	0.38	0.41

Representative analysis of chromian spinel (1)

Sample number	S68-3490-chr-px-1	S68-3490-chr-px-2	S68-3490-chr-px-3	S68-3490-chr-px-4	S68-3490-chr-px-16	S68-3490-chr-px-17	S68-3490-chr-px-18	S68-47-px-24	S68-47-px-25	S68-47-px-44
Cr_2O_3	38.88	39.37	51.57	50.14	36.85	36.37	41.08	44.77	44.15	30.66
Al_2O_3	18.47	18.47	12.96	13.18	19.61	20.05	17.85	13.99	13.93	23.14
TiO_2	0.67	0.72	0.20	0.25	0.76	0.77	0.66	0.52	0.54	1.16
FeO	29.68	30.76	25.83	26.33	29.62	30.23	29.54	29.69	28.67	31.34
MgO	10.53	10.02	9.49	9.60	11.18	11.39	10.58	9.29	9.69	12.03
ZnO	0.06	0.21	0.12	0.17	0.18	0.04	0.24	0.13	0.04	0.15
SiO_2	0.00	0.11	0.19	0.08	0.02	0.00	0.03	0.13	0.09	0.09
Total	98.30	99.66	100.35	99.74	98.21	98.86	99.97	98.52	97.11	98.56
Cr	7.90	7.95	10.66	10.39	7.43	7.26	8.26	9.35	9.31	6.03
Al	5.60	5.56	4.00	4.08	5.90	5.97	5.35	4.36	4.38	6.79
Ti	0.13	0.14	0.04	0.05	0.15	0.15	0.13	0.10	0.11	0.22
Fe^{3+}	2.17	2.14	1.24	1.40	2.30	2.39	2.06	2.01	2.03	2.62
Fe^{2+}	4.29	4.51	4.43	4.41	4.10	4.08	4.29	4.62	4.43	4.01
Mg	4.03	3.82	3.70	3.75	4.25	4.28	4.01	3.66	3.85	4.46
Total	24.11	24.11	24.07	24.08	24.12	24.12	24.10	24.11	24.11	24.14
$Fe^{2+}/(Fe^{2+}Mg^{2+})$	0.52	0.54	0.55	0.54	0.49	0.49	0.52	0.56	0.54	0.47
$Fe^{3+}/(Cr+Al+Fe^{3})$	0.14	0.14	0.08	0.09	0.15	0.15	0.13	0.13	0.13	0.17
Cr/(Cr+Al)	0.59	0.59	0.73	0.72	0.56	0.55	0.61	0.68	0.68	0.47

Representative analysis of chromian spinel (2)

Sample number	S68-47-px-45	S68-47-px-50	S68-47-px-51	S53-1030-px-15	S53-1030-px-16	S68-3490-chr-mtrx-5	S68-3490-chr-mtrx-6	S68-3490-chr-mtrx-7	S68-3490-chr-mtrx-8	S68-3490-chr-mtrx-9
Cr_2O_3	29.90	44.02	45.17	45.54	45.39	56.27	56.54	55.22	54.25	54.08
Al_2O_3	23.26	14.47	14.49	15.41	15.08	11.68	11.42	12.02	12.21	12.12
TiO_2	1.07	0.44	0.49	0.41	0.40	20.54	20.65	20.60	20.74	20.67
FeO	31.14	28.85	27.97	27.60	27.42	12.07	11.89	11.98	11.98	12.07
MgO	11.99	9.75	9.79	10.55	10.53	0.18	0.14	0.21	0.21	0.16
ZnO	0.10	0.13	0.12	0.09	0.15	0.08	0.13	0.02	0.05	0.03
SiO_2	0.10	0.08	0.07	0.07	0.16	0.02	0.06	0.11	0.07	0.05
Total	97.57	97.73	98.09	99.67	99.14	100.83	100.81	100.16	99.51	99.19
Cr	5.93	9.21	9.42	9.28	9.32	11.43	11.53	11.28	11.13	11.12
Al	6.88	4.51	4.50	4.68	4.62	3.54	3.47	3.66	3.74	3.72
Ti	0.20	0.09	0.10	0.08	0.08	0.03	0.03	0.04	0.04	0.03
Fe^{3+}	2.67	2.03	1.83	1.82	1.85	0.94	0.93	0.96	1.03	1.08
Fe^{2+}	3.98	4.42	4.40	4.18	4.16	3.49	3.53	3.51	3.49	3.44
Mg	4.48	3.84	3.85	4.05	4.08	4.62	4.57	4.61	4.63	4.68
Zn	0.00	0.00	0.00	0.00	0.00	0.00	0.00	0.00	0.00	0.00
Total	24.14	24.11	24.09	24.09	24.10	24.06	24.06	24.06	24.06	24.07
$Fe^{2+}/(Fe^{2+}Mg^{2+})$	0.47	0.53	0.53	0.51	0.50	0.43	0.44	0.43	0.43	0.42
$Fe^{3+}/(Cr+Al+Fe^{3})$	0.17	0.13	0.12	0.12	0.12	0.06	0.06	0.06	0.06	0.07
Cr/(Cr+Al)	0.46	0.67	0.68	0.66	0.67	0.76	0.77	0.75	0.75	0.75

Representative analysis of chromian spinel (3)

Sample number	S68-3490-chr-mtrx-10	S68-3490-chr-mtrx-11	S68-3490-chr-mtrx-12	S68-3490-chr-mtrx-13	S68-3490-chr-mtrx-14	S68-3490-chr-mtrx-15	A687-7980-chr-mtrx-19	A687-7980-chr-mtrx-20	A687-7980-chr-mtrx-21	A687-7980-chr-mtrx-22
Cr_2O_3	48.44	54.57	48.52	52.73	52.86	50.20	54.53	53.76	54.24	55.02
Al_2O_3	15.16	12.43	15.50	13.15	12.33	14.81	13.65	13.43	13.26	13.61
TiO_2	24.18	23.03	24.05	23.10	23.17	23.27	16.78	17.15	17.01	17.15
FeO	11.19	10.60	11.14	10.88	10.94	11.49	14.64	15.01	14.95	14.62
MgO	0.29	0.19	0.24	0.27	0.24	0.21	0.46	0.44	0.47	0.48
ZnO	0.18	0.11	0.06	0.09	0.20	0.06	0.00	0.12	0.00	0.07
SiO_2	0.11	0.13	0.02	0.08	0.03	0.10	0.08	0.05	0.12	0.05
Total	99.55	101.05	99.52	100.30	99.76	100.14	100.14	99.96	100.04	100.99
Cr	9.87	11.16	9.86	10.79	10.90	10.16	10.87	10.71	10.81	10.89
Al	4.61	3.79	4.70	4.01	3.79	4.47	4.06	3.99	3.94	4.02
Ti	0.06	0.04	0.05	0.05	0.05	0.04	0.09	0.08	0.09	0.09
Fe^{3+}	1.38	0.97	1.32	1.08	1.19	1.26	0.89	1.11	1.05	0.90
Fe^{2+}	3.86	4.03	3.88	3.94	3.89	3.75	2.66	2.53	2.55	2.71
Mg	4.30	4.08	4.27	4.20	4.25	4.39	5.50	5.64	5.62	5.45
Zn	0.00	0.00	0.00	0.00	0.00	0.00	0.00	0.00	0.00	0.00
Total	24.07	24.06	24.07	24.06	24.07	24.07	24.06	24.07	24.06	24.06
$Fe^{2+}/(Fe^{2+}Mg^{2+})$	0.47	0.50	0.48	0.48	0.48	0.46	0.33	0.31	0.31	0.33
$Fe^{3+}/(Cr+Al+Fe^{3})$	0.09	0.06	0.08	0.07	0.07	0.08	0.06	0.07	0.07	0.06
Cr/(Cr+Al)	0.68	0.75	0.68	0.73	0.74	0.69	0.73	0.73	0.73	0.73

Representative analysis of chromian spinel (4)

Sample number	A687-7980-chr-mtrx-23	S68-6340-chr-mtrx-24	S68-6340-chr-mtrx-25	S68-6340-chr-mtrx-26	S68-6340-chr-mtrx-27	S68-6340-chr-mtrx-28	S68-6340-chr-mtrx-29	S68-6340-chr-mtrx-30	S68-6340-chr-mtrx-31	S68-6340-chr-mtrx-32
Cr_2O_3	54.69	36.19	35.81	34.28	47.06	44.26	46.41	48.14	48.12	47.76
Al_2O_3	13.40	20.59	20.90	21.68	14.65	18.11	18.09	15.98	16.12	15.13
TiO_2	16.94	29.59	29.46	29.63	26.84	22.35	22.13	24.26	23.80	24.66
FeO	14.59	11.53	11.38	11.78	10.20	12.86	12.96	11.91	11.83	11.81
MgO	0.46	0.64	0.70	0.71	0.40	0.38	0.37	0.29	0.31	0.40
ZnO	0.00	0.10	0.18	0.09	0.25	0.03	0.12	0.12	0.02	0.10
SiO_2	0.01	0.00	0.02	0.08	0.06	0.03	0.04	0.08	0.06	0.05
Total	100.08	98.65	98.44	98.23	99.45	98.01	100.12	100.77	100.25	99.91
Cr	10.91	7.21	7.16	6.82	9.68	8.90	9.18	9.62	9.65	9.64
Al	3.99	6.12	6.23	6.43	4.49	5.43	5.33	4.76	4.82	4.56
Ti	0.09	0.12	0.13	0.13	0.08	0.07	0.07	0.06	0.06	0.08
Fe^{3+}	0.91	2.33	2.27	2.39	1.63	1.48	1.32	1.48	1.39	1.60
Fe^{2+}	2.67	4.00	4.05	3.94	4.25	3.31	3.34	3.68	3.69	3.71
Mg	5.49	4.33	4.29	4.41	3.95	4.88	4.83	4.48	4.47	4.49
Zn	0.00	0.00	0.00	0.00	0.00	0.00	0.00	0.00	0.00	0.00
Total	24.06	24.12	24.11	24.12	24.08	24.07	24.07	24.08	24.07	24.08
$Fe^{2+}/(Fe^{2+}Mg^{2+})$	0.33	0.48	0.49	0.47	0.52	0.40	0.41	0.45	0.45	0.45
$Fe^{3+}/(Cr+Al+Fe^{3})$	0.06	0.15	0.14	0.15	0.10	0.09	0.08	0.09	0.09	0.10
Cr/(Cr+Al)	0.73	0.54	0.53	0.51	0.68	0.62	0.63	0.67	0.67	0.68

Representative analysis of chromian spinel (5)

Sample number	S68-6340 -chr-mtrx-33	S68-6340 -chr-mtrx-34	S68-47-m-1	S68-47-m-2	S68-47-m-3	S68-47-m-4	S68-47-m-5	S68-47-m-6	S68-47-m-7	S68-47-m-8
Cr_2O_3	54.74	52.66	48.70	40.00	42.11	47.91	39.41	39.75	43.08	43.40
Al_2O_3	10.91	12.44	13.18	18.69	17.32	13.30	18.60	18.81	16.66	16.73
TiO_2	24.66	24.78	27.31	28.75	28.21	26.98	28.30	28.59	28.84	28.52
FeO	9.53	10.12	10.18	11.04	11.18	10.34	11.58	11.49	11.14	10.96
MgO	0.18	0.23	0.62	0.76	0.60	0.61	0.72	0.75	0.70	0.67
ZnO	0.15	0.05	0.02	0.10	0.15	0.03	0.08	0.18	0.10	0.09
SiO_2	0.08	0.09	0.10	0.07	0.04	0.00	0.01	0.01	0.00	0.02
Total	100.25	100.37	100.12	99.40	99.62	99.17	98.69	99.59	100.51	100.40
Cr	11.42	10.85	10.00	8.02	8.47	9.90	7.92	7.93	8.62	8.71
Al	3.39	3.82	4.04	5.59	5.20	4.10	5.57	5.60	4.97	5.00
Ti	0.04	0.04	0.12	0.15	0.12	0.12	0.14	0.14	0.13	0.13
Fe^{3+}	1.09	1.21	1.67	2.03	2.03	1.71	2.15	2.11	2.07	1.97
Fe^{2+}	4.37	4.21	4.31	4.14	4.05	4.23	3.94	4.00	4.11	4.15
Mg	3.75	3.93	3.94	4.17	4.24	4.03	4.39	4.32	4.20	4.14
Zn	0.00	0.00	0.00	0.00	0.00	0.00	0.00	0.00	0.00	0.00
Total	24.07	24.07	24.09	24.10	24.10	24.09	24.11	24.11	24.11	24.10
$Fe^{2+}/(Fe^{2}+Mg^{2+})$	0.54	0.52	0.52	0.50	0.49	0.51	0.47	0.48	0.49	0.50
$Fe^{3+}/(Cr+Al+Fe^{3})$	0.07	0.08	0.11	0.13	0.13	0.11	0.14	0.13	0.13	0.13
Cr/(Cr+Al)	0.77	0.74	0.71	0.59	0.62	0.71	0.59	0.59	0.63	0.64

Representative analysis of chromian spinel (6)

Sample number	S68-47-m-9	S68-47-m-10	S68-47-m-11	S68-47-m-12	S68-47-m-13	S68-47-m-14	S68-47-m-15	S68-47-m-16	S68-47-m-17	S68-47-m-18
Cr_2O_3	39.18	38.15	36.08	39.64	40.88	42.97	41.20	38.57	39.75	47.07
Al_2O_3	17.71	18.61	19.64	17.48	17.03	16.35	17.74	19.15	18.15	15.74
TiO_2	29.36	29.84	29.98	30.09	29.42	28.66	29.58	30.23	28.52	25.28
FeO	11.78	11.42	11.64	11.14	10.76	10.60	10.85	11.26	11.15	11.04
MgO	0.70	0.75	0.77	0.65	0.60	0.59	0.64	0.71	0.67	0.33
ZnO	0.05	0.14	0.05	0.19	0.08	0.12	0.12	0.23	0.11	0.18
SiO_2	0.08	0.03	0.02	0.03	0.04	0.01	0.07	0.02	0.04	0.05
Total	98.85	98.93	98.18	99.22	98.81	99.31	100.18	100.17	98.39	99.68
Cr	7.88	7.66	7.24	7.99	8.31	8.74	8.25	7.66	8.05	9.56
Al	5.31	5.57	5.88	5.26	5.16	4.96	5.30	5.67	5.48	4.76
Ti	0.13	0.14	0.15	0.13	0.12	0.11	0.12	0.13	0.13	0.06
Fe^{3+}	2.44	2.39	2.48	2.40	2.21	2.01	2.13	2.31	2.13	1.51
Fe^{2+}	3.90	4.04	3.98	4.11	4.19	4.22	4.21	4.13	4.06	3.95
Mg	4.46	4.32	4.40	4.24	4.12	4.06	4.10	4.22	4.26	4.23
Zn	0.00	0.00	0.00	0.00	0.00	0.00	0.00	0.00	0.00	0.00
Total	24.13	24.13	24.13	24.13	24.12	24.10	24.11	24.12	24.11	24.08
$Fe^{2+}/(Fe^{2+}Mg^{2+})$	0.47	0.48	0.47	0.49	0.50	0.51	0.51	0.49	0.49	0.48
$Fe^{3+}/(Cr+Al+Fe^{3})$	0.16	0.15	0.16	0.15	0.14	0.13	0.14	0.15	0.14	0.10
Cr/(Cr+Al)	0.60	0.58	0.55	0.60	0.62	0.64	0.61	0.57	0.59	0.67

Representative analysis of chromian spinel (7)

Sample number	S68-47-m-19	S68-47-mtrx-27	S68-47-mtrx-28	S68-47-mtrx-29	S68-47-mtrx-31	S68-47-mtrx-32	S68-47-mtrx-33	S68-47-mtrx-34	S68-47-mtrx-35	S68-47-mtrx-36
Cr_2O_3	46.33	51.17	51.55	50.87	32.54	32.61	30.84	53.75	54.60	53.55
Al_2O_3	14.64	13.85	13.64	13.76	21.23	21.20	20.85	13.24	13.21	12.39
TiO_2	28.95	23.80	23.83	23.76	32.05	31.83	32.97	21.56	18.94	21.69
FeO	7.76	10.34	10.47	10.55	12.35	12.50	11.07	11.48	13.80	11.93
MgO	0.29	0.35	0.25	0.21	1.08	1.11	1.23	0.23	0.23	0.26
ZnO	1.18	0.09	0.07	0.15	0.12	0.18	0.29	0.13	0.01	0.09
SiO_2	0.22	0.08	0.12	0.13	0.09	0.04	0.81	0.04	0.07	0.09
Total	99.36	99.68	99.92	99.44	99.46	99.46	98.06	100.44	100.87	100.00
Cr	9.80	10.53	10.59	10.49	6.39	6.40	6.24	10.94	10.89	10.94
Al	4.62	4.25	4.18	4.23	6.21	6.20	6.28	4.02	3.93	3.78
Ti	0.06	0.07	0.05	0.04	0.20	0.21	0.24	0.04	0.04	0.05
Fe^{3+}	1.44	1.06	1.12	1.17	2.85	2.85	2.87	0.94	1.07	1.16
Fe^{2+}	5.07	4.14	4.08	4.03	3.93	3.88	4.32	3.71	2.94	3.55
Mg	3.09	4.01	4.05	4.10	4.57	4.62	4.22	4.41	5.19	4.60
Zn	0.00	0.00	0.00	0.00	0.00	0.00	0.00	0.00	0.00	0.00
Total	24.08	24.06	24.07	24.07	24.16	24.16	24.16	24.06	24.07	24.07
$Fe^{2+}/(Fe^{2+}Mg^{2+})$	0.62	0.51	0.50	0.50	0.46	0.46	0.51	0.46	0.36	0.44
$Fe^{3+}/(Cr+Al+Fe^{3})$	0.09	0.07	0.07	0.07	0.18	0.18	0.19	0.06	0.07	0.07
Cr/(Cr+Al)	0.68	0.71	0.72	0.71	0.51	0.51	0.50	0.73	0.73	0.74

Representative analysis of chromian spinel (8)

Sample number	S68-47-mtrx-37	S68-47-mtrx-38	S68-47-mtrx-39	S68-47-mtrx-41	S68-47-mtrx-42	S68-47-mtrx-43	S68-47-mtrx-46	S68-47-mtrx-47	S68-47-mtrx-48	S68-47-mtrx-49
Cr_2O_3	53.09	52.60	54.47	53.65	52.86	50.71	37.43	34.26	40.35	30.86
Al_2O_3	12.81	13.53	12.98	10.61	13.20	14.54	15.70	17.49	14.48	19.31
TiO_2	21.69	22.94	20.99	24.81	24.26	24.59	35.58	35.88	35.21	36.70
FeO	11.41	11.04	11.03	9.59	10.37	10.52	9.64	10.28	9.05	10.76
MgO	0.19	0.19	0.20	0.16	0.20	0.22	1.45	1.67	1.41	1.64
ZnO	0.07	0.21	0.03	0.09	0.11	0.05	0.18	0.05	0.08	0.10
SiO_2	0.06	0.08	0.05	0.10	0.02	0.07	0.00	0.03	0.02	0.07
Total	99.33	100.59	99.74	99.00	101.02	100.70	99.98	99.65	100.59	99.42
Cr	10.93	10.72	11.19	11.32	10.78	10.29	7.62	6.90	8.25	6.16
Al	3.93	4.11	3.98	3.34	4.01	4.40	4.77	5.26	4.41	5.75
Ti	0.04	0.04	0.04	0.03	0.04	0.04	0.28	0.32	0.27	0.31
Fe^{3+}	1.05	1.08	0.74	1.25	1.11	1.20	2.91	3.04	2.67	3.28
Fe^{2+}	3.69	3.88	3.83	4.32	4.14	4.11	4.90	4.76	5.06	4.65
Mg	4.43	4.24	4.28	3.81	3.98	4.03	3.70	3.90	3.49	4.05
Zn	0.00	0.00	0.00	0.00	0.00	0.00	0.00	0.00	0.00	0.00
Total	24.06	24.06	24.06	24.07	24.07	24.07	24.17	24.18	24.15	24.20
$Fe^{2+}/(Fe^{2+}Mg^{2+})$	0.45	0.48	0.47	0.53	0.51	0.50	0.57	0.55	0.59	0.53
$Fe^{3+}/(Cr+Al+Fe^{3})$	0.07	0.07	0.05	0.08	0.07	0.08	0.19	0.20	0.17	0.22
Cr/(Cr+Al)	0.74	0.72	0.74	0.77	0.73	0.70	0.62	0.57	0.65	0.52

Representative analysis of chromian spinel (9)

Sample number	S53-1030-mtrx-1	S53-1030-mtrx-2	S53-1030-mtrx-3	S53-1030-mtrx-4	S53-1030-mtrx-6	S53-1030-mtrx-7	S53-1030-mtrx-8	S53-1030-mtrx-9	S53-1030-mtrx-10	S53-1030-mtrx-11	S53-1030-mtrx-13
Cr_2O_3	47.79	44.85	48.38	38.01	52.16	50.85	49.14	52.68	43.56	48.86	49.25
Al_2O_3	14.58	14.91	14.62	19.23	13.05	13.28	14.42	11.49	17.63	14.14	14.97
TiO_2	26.01	27.46	26.44	29.28	23.88	25.85	25.61	26.08	26.27	21.71	24.17
FeO	10.69	10.22	10.49	11.40	10.48	10.64	10.51	10.08	11.20	13.49	10.65
MgO	0.26	0.42	0.27	0.65	0.23	0.21	0.33	0.31	0.45	0.27	0.29
ZnO	0.06	0.04	0.11	0.07	0.04	0.14	0.03	0.12	0.09	0.12	0.11
SiO_2	0.08	0.04	0.07	0.04	0.14	0.16	0.08	0.10	0.07	0.55	0.16
Total	99.46	97.94	100.38	98.67	99.98	101.14	100.11	100.85	99.26	99.13	99.59
Cr	9.78	9.31	9.84	7.63	10.73	10.34	10.03	10.86	8.79	9.91	10.08
Al	4.45	4.62	4.44	5.76	4.00	4.03	4.39	3.53	5.30	4.27	4.57
Ti	0.05	0.08	0.05	0.12	0.05	0.04	0.06	0.06	0.09	0.05	0.06
Fe^{3+}	1.62	1.85	1.58	2.28	1.15	1.52	1.43	1.46	1.69	1.67	1.22
Fe^{2+}	4.05	4.23	4.15	4.02	4.07	4.08	4.13	4.26	3.96	3.03	4.04
Mg	4.13	4.00	4.02	4.31	4.07	4.08	4.04	3.91	4.26	5.15	4.11
Zn	0.00	0.00	0.00	0.00	0.00	0.00	0.00	0.00	0.00	0.00	0.00
Total	24.08	24.10	24.08	24.12	24.07	24.08	24.08	24.08	24.08	24.09	24.07
$Fe^{2+}/(Fe^{2+}Mg^{2+})$	0.50	0.51	0.51	0.48	0.50	0.50	0.51	0.52	0.48	0.37	0.50
$Fe^{3+}/(Cr+Al+Fe^{3})$	0.10	0.12	0.10	0.15	0.07	0.10	0.09	0.09	0.11	0.11	0.08
Cr/(Cr+Al)	0.69	0.67	0.69	0.57	0.73	0.72	0.70	0.75	0.62	0.70	0.69

Representative analysis of chromian spinel (10)

Sample number	S53-1030-mtrx-14	S53-1030-mtrx-17	S53-1030-mtrx-18	S53-1030-mtrx-19	S53-1030-mtrx-20	S53-1030-mtrx-21	S53-1030-mtrx-22	S53-1030-mtrx-23	S53-1030-mtrx-24	S53-1030-mtrx-25	S53-1030-mtrx-26
Cr_2O_3	47.49	47.37	45.91	47.02	46.67	47.52	46.50	57.71	58.10	48.06	52.36
Al_2O_3	15.22	17.49	18.00	17.13	17.03	13.02	17.28	10.30	10.05	15.53	11.89
TiO_2	24.54	22.93	23.40	23.78	23.27	27.56	24.18	23.81	23.10	24.87	24.26
FeO	10.76	11.42	11.13	11.08	11.45	10.40	11.37	9.80	9.88	10.75	9.96
MgO	0.26	0.24	0.28	0.20	0.24	0.36	0.28	0.18	0.17	0.34	0.21
ZnO	0.10	0.03	0.16	0.18	0.07	0.15	0.19	0.08	0.00	0.14	0.17
SiO_2	0.09	0.08	0.04	0.11	0.10	0.06	0.11	0.09	0.08	0.06	0.12
Total	98.46	99.55	98.93	99.51	98.83	99.08	99.89	101.97	101.37	99.74	98.96
Cr	9.79	9.53	9.29	9.52	9.47	9.84	9.35	11.87	12.02	9.78	10.98
Al	4.68	5.25	5.43	5.17	5.15	4.02	5.18	3.16	3.10	4.71	3.72
Ti	0.05	0.04	0.05	0.04	0.05	0.07	0.05	0.04	0.03	0.07	0.04
Fe^{3+}	1.40	1.11	1.14	1.21	1.26	1.93	1.33	0.88	0.81	1.34	1.20
Fe^{2+}	3.98	3.79	3.89	3.90	3.76	4.17	3.84	4.31	4.26	4.04	4.20
Mg	4.18	4.33	4.25	4.23	4.38	4.06	4.31	3.80	3.85	4.12	3.93
Zn	0.00	0.00	0.00	0.00	0.00	0.00	0.00	0.00	0.00	0.00	0.00
Total	24.07	24.06	24.06	24.06	24.07	24.10	24.07	24.06	24.06	24.07	24.07
$Fe^{2+}/(Fe^{2+}Mg^{2+})$	0.49	0.47	0.48	0.48	0.46	0.51	0.47	0.53	0.53	0.49	0.52
$Fe^{3+}/(Cr+Al+Fe^{3})$	0.09	0.07	0.07	0.08	0.08	0.12	0.08	0.06	0.05	0.08	0.08
Cr/(Cr+Al)	0.68	0.64	0.63	0.65	0.65	0.71	0.64	0.79	0.80	0.67	0.75

Representative analysis of chromian spinel (11)

Sample number	S53-1030-mtrx-27	S53-1030-mtrx-28	S53-1030-mtrx-30	S53-1030-mtrx-31	S53-1030-mtrx-32	S53-1030-mtrx-33	S53-1030-mtrx-34	S53-1030-mtrx-38	S53-1030-mtrx-39	S53-1030-mtrx-40	S53-1030-mtrx-41
Cr_2O_3	53.43	48.12	53.48	38.25	37.68	50.55	44.36	44.77	46.23	50.93	46.43
Al_2O_3	11.83	14.96	12.22	19.58	20.48	9.89	17.68	18.12	17.44	14.98	15.38
TiO_2	24.47	25.12	24.09	28.03	28.57	27.74	25.45	24.09	23.77	24.20	26.88
FeO	10.14	10.55	9.47	11.70	11.44	10.29	11.06	11.43	11.35	10.79	10.61
MgO	0.21	0.24	0.26	0.87	0.77	0.35	0.28	0.22	0.20	0.22	0.23
ZnO	0.10	0.17	0.11	0.18	0.12	0.08	0.20	0.20	0.00	0.00	0.11
SiO_2	0.12	0.12	0.08	0.08	0.16	0.10	0.06	0.10	0.14	0.10	0.11
Total	100.30	99.27	99.72	98.68	99.21	99.00	99.08	98.93	99.14	101.23	99.75
Cr	11.05	9.88	11.15	7.66	7.50	10.63	8.98	9.04	9.34	10.25	9.46
Al	3.65	4.58	3.80	5.85	6.08	3.10	5.34	5.46	5.26	4.50	4.67
Ti	0.04	0.05	0.05	0.16	0.15	0.07	0.05	0.04	0.04	0.04	0.04
Fe^{3+}	1.20	1.42	0.93	2.09	2.06	2.06	1.54	1.38	1.30	1.14	1.73
Fe^{2+}	4.18	4.07	4.40	3.92	4.03	4.18	3.95	3.79	3.81	4.03	4.11
Mg	3.95	4.08	3.72	4.42	4.29	4.08	4.22	4.35	4.32	4.10	4.07
Zn	0.00	0.00	0.00	0.00	0.00	0.00	0.00	0.00	0.00	0.00	0.00
Total	24.07	24.07	24.06	24.10	24.10	24.11	24.08	24.07	24.07	24.06	24.09
$Fe^{2+}/(Fe^{2+}Mg^{2+})$	0.51	0.50	0.54	0.47	0.48	0.51	0.48	0.47	0.47	0.50	0.50
$Fe^{3+}/(Cr+Al+Fe^{3})$	0.08	0.09	0.06	0.13	0.13	0.13	0.10	0.09	0.08	0.07	0.11
Cr/(Cr+Al)	0.75	0.68	0.75	0.57	0.55	0.77	0.63	0.62	0.64	0.70	0.67

Representative EMPA analyses of chlorite (1)

Sample number	S53-50.20-c2-2	S53-50.20-c2-3	S53-50.20-c4-1	S53-50.20-c6-1	S53-50.20-c6-2	S53-50.20-c7-2	S53-50.20-c8-2	S53-50.20-c9-1	S53-50.20-c9-2	S53-50.20-c11-1	S53-50.20-c1-2	S53-50.20-c2-2	S53-50.20-c2-3
SiO_2	29.62	30.81	30.57	31.19	29.65	30.51	29.68	29.24	29.01	30.16	31.96	29.54	30.42
TiO_2	0.00	0.06	0.01	0.00	0.00	0.01	0.03	0.04	0.04	0.02	0.06	0.02	0.01
Al_2O_3	18.55	18.45	18.61	19.08	18.45	17.82	19.57	16.99	18.41	19.19	17.81	18.64	18.38
FeO	16.02	15.75	16.16	16.25	16.38	16.43	16.22	16.19	16.50	16.52	16.91	16.78	16.36
MnO	0.18	0.18	0.21	0.24	0.22	0.19	0.21	0.18	0.17	0.22	0.19	0.22	0.26
MgO	24.09	23.61	23.89	23.36	22.66	23.92	24.35	23.47	23.64	23.99	23.56	23.87	24.68
CaO	0.05	0.09	0.02	0.04	0.07	0.07	0.06	0.06	0.06	0.08	0.16	0.00	0.06
Na_2O	0.00	0.05	0.00	0.00	0.03	0.03	0.05	0.01	0.02	0.01	0.00	0.01	0.01
K_2O	0.01	0.03	0.01	0.01	0.02	0.02	0.01	0.02	0.00	0.01	0.01	0.00	0.00
Cr_2O_3	0.15	0.30	0.36	0.01	0.78	0.36	0.02	0.10	0.15	0.04	0.00	0.01	0.04
Total	88.68	89.32	89.84	90.17	88.25	89.35	90.19	86.30	88.00	90.23	90.67	89.08	90.21
Normalisation on the basis 28 oxygens (with Fe2+/Fe3+ and OH calculated assuming full site occupancy)													
Si	5.85	6.00	5.94	6.01	5.89	5.98	5.76	5.95	5.80	5.85	6.14	5.83	5.91
Al^{iv}	2.15	2.00	2.06	1.99	2.11	2.02	2.24	2.05	2.20	2.15	1.86	2.17	2.09
Al^{vi}	2.17	2.25	2.21	2.36	2.22	2.10	2.24	2.03	2.13	2.24	2.20	2.16	2.11
Ti	0.00	0.01	0.00	0.00	0.00	0.00	0.00	0.01	0.01	0.00	0.01	0.00	0.00
Cr	0.02	0.05	0.06	0.00	0.12	0.06	0.00	0.02	0.02	0.01	0.00	0.00	0.01
Fe^{3+}	0.02	0.16	0.11	0.20	0.12	0.07	0.00	0.00	0.00	0.06	0.20	0.00	0.01
Fe^{2+}	2.62	2.40	2.51	2.41	2.60	2.62	2.63	2.75	2.77	2.62	2.52	2.77	2.64
Mn	0.03	0.03	0.03	0.04	0.04	0.03	0.03	0.03	0.03	0.04	0.03	0.04	0.04
Mg	7.09	6.85	6.92	6.71	6.71	6.99	7.05	7.13	7.04	6.94	6.75	7.02	7.14
Ca	0.01	0.02	0.00	0.01	0.01	0.01	0.01	0.01	0.01	0.02	0.03	0.00	0.01
Na	0.00	0.04	0.00	0.00	0.02	0.02	0.04	0.01	0.01	0.01	0.00	0.01	0.01
K	0.01	0.01	0.00	0.00	0.01	0.01	0.01	0.01	0.00	0.00	0.00	0.00	0.00
Mg#	73	73	72	72	71	72	73	72	72	72	71	72	73
T (°C)	266	250	257	250	263	253	276	256	273	266	236	269	260

Representative analyses of chlorite (2)

Sample number	S68-3910-1-2	S68-3910-2-1	S68-3910-2-2	S68-3910-2-3	S68-39.10-3-1	S68-39.10-3-2	S68-39.10-4-1	S68-39.10-4-2	S68-39.10-4-4	S68-39.10-4-5	S68-39.10-5-1	S68-39.10-5-2	S68-3910--5	S68-3910-17	S68-3910-21
SiO_2	30.59	29.61	32.20	30.40	31.15	30.39	29.80	29.75	30.54	31.60	31.76	30.83	28.49	28.82	29.58
TiO_2	0.02	0.02	0.00	0.00	0.01	0.01	0.03	0.02	0.00	0.00	0.01	0.04	0.04	0.01	0.00
Al_2O_3	17.73	18.94	17.01	18.33	18.45	18.27	17.71	18.45	19.45	18.42	18.68	18.43	14.82	17.80	17.69
FeO	16.09	18.13	17.95	17.94	17.38	17.93	17.18	18.33	16.91	17.39	17.09	17.34	19.12	18.27	18.05
MnO	0.23	0.24	0.22	0.25	0.27	0.22	0.22	0.23	0.26	0.25	0.22	0.19	0.29	0.28	0.25
MgO	23.47	23.05	22.73	22.96	23.19	22.25	23.26	22.35	22.93	23.07	22.71	23.75	20.94	22.27	22.86
CaO	0.04	0.03	0.10	0.02	0.04	0.08	0.18	0.02	0.20	0.15	0.17	0.15	0.05	0.13	0.08
Na_2O	0.00	0.01	0.05	0.05	0.04	0.00	0.05	0.00	0.00	0.03	0.00	0.00	0.00	0.00	0.02
K_2O	0.01	0.01	0.00	0.02	0.00	0.03	0.01	0.01	0.01	0.04	0.01	0.00	0.01	0.00	0.00
Cr_2O_3	0.24	0.01	0.05	0.05	0.13	0.00	0.01	0.00	0.02	0.04	0.01	0.03	0.00	0.00	0.00
Total	88.40	90.05	90.31	90.01	90.65	89.16	88.44	89.15	90.32	90.98	90.64	90.77	83.75	87.57	88.52
Normalisation on the basis 28 oxygens (with Fe2+/Fe3+ and OH calculated assuming full site occupancy)															
Si	6.04	5.82	6.24	5.95	6.02	6.00	5.94	5.90	5.91	6.07	6.10	5.96	6.10	5.84	5.92
Al^{iv}	1.96	2.18	1.76	2.05	1.98	2.00	2.06	2.10	2.09	1.93	1.90	2.04	1.90	2.16	2.08
Al^{vi}	2.17	2.20	2.15	2.19	2.23	2.26	2.10	2.22	2.36	2.26	2.35	2.17	1.84	2.10	2.09
Ti	0.00	0.00	0.00	0.00	0.00	0.00	0.00	0.00	0.00	0.00	0.00	0.01	0.01	0.00	0.00
Cr	0.04	0.00	0.01	0.01	0.02	0.00	0.00	0.00	0.00	0.01	0.00	0.00	0.00	0.00	0.00
Fe^{3+}	0.14	0.01	0.22	0.07	0.15	0.14	0.02	0.07	0.15	0.18	0.25	0.08	0.00	0.00	0.00
Fe^{2+}	2.52	2.97	2.70	2.87	2.66	2.82	2.85	2.97	2.59	2.61	2.49	2.72	3.45	3.12	3.02
Mn	0.04	0.04	0.04	0.04	0.04	0.04	0.04	0.04	0.04	0.04	0.04	0.03	0.05	0.05	0.04
Mg	6.90	6.75	6.57	6.70	6.68	6.55	6.91	6.61	6.62	6.61	6.50	6.85	6.68	6.73	6.82
Ca	0.01	0.01	0.02	0.00	0.01	0.02	0.04	0.01	0.04	0.03	0.03	0.03	0.01	0.03	0.02
Na	0.00	0.01	0.04	0.04	0.03	0.00	0.04	0.00	0.00	0.02	0.00	0.00	0.00	0.00	0.01
K	0.01	0.00	0.00	0.01	0.00	0.01	0.01	0.00	0.01	0.02	0.01	0.00	0.00	0.00	0.00
Mg#	72	69	69	70	70	69	71	68	71	70	70	71	66	68	69
T (°C)	247	272	227	258	250	254	258	264	261	244	241	256	245	270	262

Representative analyses of chlorite (3)

Sample number	S68-69.00-2	S68-69.00-3	S68-69.00-4	S68-69.00-5	S68-69.00-6	S68-69.00-7	S68-69.00-8	S68-69.00-9	S68-69.00-10	S68-69.00-11
SiO_2	30.77	29.14	28.84	30.22	30.13	29.04	29.71	29.22	29.28	28.64
TiO_2	0.02	0.03	0.01	0.00	0.03	0.06	0.02	0.01	0.00	0.00
Al_2O_3	18.07	18.87	20.00	18.25	17.78	19.17	18.37	18.82	18.65	18.82
FeO	16.73	21.31	20.16	18.48	19.00	19.94	19.15	19.39	20.20	20.86
MnO	0.23	1.05	1.00	0.90	1.00	0.92	0.98	0.98	0.96	1.03
MgO	23.94	19.45	20.76	22.26	22.64	21.41	21.87	21.97	20.98	20.52
CaO	0.06	0.33	0.02	0.00	0.00	0.00	0.02	0.01	0.00	0.01
Na_2O	0.00	0.02	0.00	0.02	0.04	0.01	0.02	0.00	0.00	0.03
K_2O	0.00	0.09	0.02	0.01	0.00	0.02	0.00	0.01	0.00	0.00
Cr_2O_3	0.07	0.00	0.00	0.00	0.01	0.00	0.02	0.00	0.00	0.05
Total	89.89	90.27	90.80	90.14	90.62	90.57	90.15	90.40	90.07	89.96
Normalisation on the basis 28 oxygens (with Fe2+/Fe3+ and OH calculated assuming full site occupancy										
Si	5.99	5.83	5.69	5.95	5.93	5.75	5.88	5.78	5.83	5.74
Al^{iv}	2.01	2.17	2.31	2.05	2.07	2.25	2.12	2.22	2.17	2.26
Al^{vi}	2.15	2.28	2.35	2.18	2.05	2.22	2.17	2.16	2.21	2.19
Ti	0.00	0.00	0.00	0.00	0.00	0.01	0.00	0.00	0.00	0.00
Cr	0.01	0.00	0.00	0.00	0.00	0.00	0.00	0.00	0.00	0.01
Fe^{3+}	0.09	0.05	0.03	0.07	0.00	0.00	0.03	0.00	0.02	0.00
Fe^{2+}	2.64	3.51	3.30	2.97	3.14	3.31	3.14	3.23	3.34	3.53
Mn	0.04	0.18	0.17	0.15	0.17	0.15	0.16	0.16	0.16	0.17
Mg	6.95	5.80	6.11	6.53	6.64	6.31	6.45	6.47	6.23	6.13
Ca	0.01	0.07	0.01	0.00	0.00	0.00	0.00	0.00	0.00	0.00
Na	0.00	0.01	0.00	0.01	0.03	0.00	0.01	0.00	0.00	0.02
K	0.00	0.04	0.01	0.01	0.00	0.01	0.00	0.00	0.00	0.00
Mg#	72	62	65	68	68	66	67	67	65	63
T (°C)	252	277	289	259	262	282	267	278	274	285

Representative analyses of chlorite (4)

Sample number	S68-47 -1	S68-47 -2	S68-47 -3	S68-47 -4	S68-47 -5	S68-47 -6	S68-47 -7	S68-47 -8		S68-47 -10	S68-47-27 -c8	S68-47 -31
SiO_2	29.98	30.23	31.25	30.84	31.12	29.75	30.07	31.48	30.63	29.34	30.14	29.51
TiO_2	0.00	0.00	0.00	0.05	0.01	0.00	0.03	0.01	0.00	0.00	0.74	0.00
Al_2O_3	18.58	19.67	17.88	17.88	18.41	18.47	19.23	17.68	18.59	18.49	17.93	19.08
FeO	19.53	16.17	15.68	16.38	16.03	15.97	15.99	15.83	16.31	15.92	16.11	16.66
MnO	0.97	0.21	0.26	0.28	0.21	0.24	0.21	0.16	0.26	0.22	0.21	0.24
MgO	21.22	25.93	24.57	23.83	25.14	23.45	24.91	23.44	24.41	24.56	24.78	24.62
CaO	0.01	0.03	0.08	0.05	0.06	0.08	0.07	0.06	0.07	0.05	0.11	0.02
Na_2O	0.01	0.03	0.00	0.01	0.01	0.00	0.03	0.00	0.00	0.03	0.02	0.00
K_2O	0.00	0.02	0.01	0.01	0.01	0.01	0.01	0.00	0.00	0.01	0.03	0.01
Cr_2O_3	0.00	0.00	0.00	0.02	0.00	0.04	0.00	0.01	0.06	0.00	0.00	0.00
Total	90.31	92.28	89.73	89.33	90.99	88.02	90.52	88.67	90.33	88.61	90.07	90.12
Normalisation on the basis 28 oxygens (with Fe2+/Fe3+ and OH calculated assuming full site occupancy)												
Si	5.92	5.71	6.06	6.03	5.96	5.91	5.81	6.15	5.93	5.79	5.86	5.74
Al^{iv}	2.08	2.29	1.94	1.97	2.04	2.09	2.19	1.85	2.07	2.21	2.14	2.26
Al^{vi}	2.25	2.11	2.15	2.16	2.13	2.24	2.18	2.25	2.17	2.10	1.98	2.13
Ti	0.00	0.00	0.00	0.01	0.00	0.00	0.00	0.00	0.00	0.00	0.11	0.00
Cr	0.00	0.00	0.00	0.00	0.00	0.01	0.00	0.00	0.01	0.00	0.00	0.00
Fe^{3+}	0.09	0.00	0.12	0.11	0.05	0.08	0.00	0.23	0.06	0.00	0.03	0.00
Fe^{2+}	3.13	2.63	2.43	2.57	2.52	2.57	2.59	2.36	2.58	2.68	2.59	2.77
Mn	0.16	0.03	0.04	0.05	0.03	0.04	0.03	0.03	0.04	0.04	0.03	0.04
Mg	6.24	7.31	7.10	6.95	7.18	6.94	7.17	6.83	7.04	7.23	7.19	7.14
Ca	0.00	0.01	0.02	0.01	0.01	0.02	0.01	0.01	0.01	0.01	0.02	0.00
Na	0.01	0.02	0.00	0.01	0.01	0.00	0.02	0.00	0.00	0.02	0.02	0.00
K	0.00	0.01	0.00	0.00	0.00	0.00	0.00	0.00	0.00	0.00	0.01	0.01
Mg#	66	74	74	72	74	72	73	73	73	73	73	72
T (°C)	264	280	244	247	253	260	270	234	258	272	264	278

Representative analyses of chlorite (5)

Sample number	A687-157.98-8	A687-157.98-7	A687-157.98-9	A687-157.98-13	A687-157.98-4	S66-122.50-10	S66-122.50-8	S66-122.50-6	S66-122.50-5	S66-122.50-9	S66-122.50-7
SiO_2	25.34	25.47	29.26	27.64	29.51	25.68	25.87	27.03	27.10	27.50	28.33
TiO_2	0.01	0.10	0.12	5.47	2.62	0.00	0.08	0.00	0.00	0.01	0.01
Al_2O_3	21.78	21.98	18.18	16.70	15.68	20.30	20.75	20.21	19.98	19.87	20.73
FeO	28.09	27.82	25.98	25.13	24.84	27.96	28.38	24.56	25.89	25.21	24.88
MnO	1.75	1.70	1.66	1.63	1.49	0.99	1.03	0.91	0.49	0.84	0.85
MgO	13.22	13.41	14.99	14.32	15.65	12.89	12.21	15.74	14.67	15.12	15.82
CaO	0.01	0.08	0.15	0.00	0.03	0.03	0.01	0.01	0.03	0.03	0.01
Na_2O	0.05	0.06	0.01	0.13	0.08	0.03	0.02	0.05	0.05	0.01	0.04
K_2O	0.02	0.02	0.02	0.08	0.19	0.04	0.05	0.01	0.03	0.01	0.02
Cr_2O_3	0.00	0.00	0.00	0.00	0.00	0.00	0.00	0.00	0.00	0.00	0.00
Total	90.27	90.63	90.38	91.10	90.09	87.91	88.39	88.52	88.27	88.60	90.69
Normalisation on the basis 28 oxygens (with Fe2+/Fe3+ and OH calculated assuming full site occupancy)											
Si	5.29	5.28	5.98	5.60	6.02	5.49	5.50	5.61	5.67	5.71	5.71
Al^{iv}	2.71	2.72	2.02	2.40	1.98	2.51	2.50	2.39	2.33	2.29	2.29
Al^{vi}	2.66	2.66	2.37	1.62	1.82	2.61	2.71	2.57	2.60	2.58	2.65
Ti	0.00	0.02	0.02	0.83	0.40	0.00	0.01	0.00	0.00	0.00	0.00
Cr	0.00	0.00	0.00	0.00	0.00	0.00	0.00	0.00	0.00	0.00	0.00
Fe^{3+}	0.00	0.00	0.21	0.46	0.32	0.05	0.12	0.09	0.14	0.16	0.19
Fe^{2+}	4.94	4.85	4.23	3.79	3.91	4.95	4.92	4.17	4.39	4.22	4.00
Mn	0.31	0.30	0.29	0.28	0.26	0.18	0.19	0.16	0.09	0.15	0.15
Mg	4.11	4.15	4.56	4.32	4.76	4.11	3.87	4.87	4.57	4.68	4.75
Ca	0.00	0.02	0.03	0.00	0.01	0.01	0.00	0.00	0.01	0.01	0.00
Na	0.04	0.05	0.01	0.10	0.06	0.02	0.01	0.04	0.04	0.01	0.03
K	0.01	0.01	0.01	0.04	0.10	0.02	0.03	0.00	0.02	0.00	0.01
Mg#	45	46	51	50	53	45	43	53	50	52	53
T (°C)	346	346	269	310	263	325	325	306	302	297	296

Representative analyses of chlorite (6)

Sample number	S68-34.90-20	S68-34.90-12	S68-34.90-21	S68-34.90-13	S68-34.90-5	S68-34.90-6	S68-34.90-14	S68-34.90-15	S68-34.90-16	S68-34.90-25	S68-84.55-2	S68-84.55-7
SiO_2	29.51	29.56	29.71	29.74	29.32	30.42	30.86	29.73	29.73	29.39	28,49	27,78
TiO_2	0.00	0.00	0.00	0.00	0.00	0.00	0.00	0.42	0.00	0.01	0,31	0,00
Al_2O_3	16.26	18.00	17.88	17.74	18.53	17.02	16.80	18.66	18.60	18.10	18,23	19,18
FeO	15.94	16.80	15.39	16.68	14.64	16.29	16.15	14.82	16.29	16.16	25,27	26,15
MnO	0.23	0.25	0.26	0.27	0.18	0.18	0.21	0.21	0.18	0.22	0,33	0,32
MgO	23.26	24.53	23.50	23.69	24.18	24.20	24.74	26.15	24.71	24.61	18,36	18,12
CaO	0.14	0.09	0.05	0.07	0.10	0.14	0.43	0.11	0.07	0.07	0,45	0,08
Na_2O	0.00	0.00	0.07	0.00	0.00	0.00	0.01	0.00	0.01	0.01	0,00	0,03
K_2O	0.00	0.00	0.01	0.01	0.00	0.06	0.01	0.01	0.00	0.01	0,02	0,02
Cr_2O_3	0.00	0.00	0.00	0.00	0.00	0.00	0.00	0.00	0.00	0.00	0.00	0.00
Total	85.33	89.23	86.86	88.19	86.96	88.29	89.21	90.10	89.59	88.58	91.46	91.66
Normalisation on the basis 28 oxygens (with Fe2+/Fe3+ and OH calculated assuming full site occupancy)												
Si	6.07	5.82	5.96	5.93	5.86	6.04	6.06	5.74	5.81	5.81	5,73	5,58
Al^{iv}	1.93	2.18	2.04	2.07	2.14	1.96	1.94	2.26	2.19	2.19	2,27	2,42
Al^{vi}	2.01	2.00	2.20	2.10	2.23	2.02	1.95	1.99	2.10	2.04	2,06	2,14
Ti	0.00	0.00	0.00	0.00	0.00	0.00	0.00	0.06	0.00	0.00	0,05	0,00
Cr	0.00	0.00	0.00	0.00	0.00	0.00	0.00	0.00	0.00	0.00	0,00	0,00
Fe^{3+}	0.04	0.00	0.08	0.01	0.05	0.03	0.01	0.00	0.00	0.00	0,00	0,00
Fe^{2+}	2.70	2.84	2.50	2.77	2.40	2.68	2.65	2.45	2.70	2.73	4,30	4,51
Mn	0.04	0.04	0.04	0.05	0.03	0.03	0.03	0.03	0.03	0.04	0,06	0,05
Mg	7.13	7.20	7.03	7.04	7.20	7.16	7.25	7.52	7.20	7.25	5,50	5,43
Ca	0.03	0.02	0.01	0.01	0.02	0.03	0.09	0.02	0.02	0.01	0,10	0,02
Na	0.00	0.00	0.05	0.00	0.00	0.00	0.01	0.00	0.00	0.01	0,00	0,02
K	0.00	0.00	0.00	0.00	0.00	0.03	0.00	0.00	0.00	0.01	0,01	0,01
Mg#	72	72	73	72	75	73	73	75	73	73	56	55
T (°C)	244	270	254	259	264	246	243	276	270	270	291	308

Representative analyses of chlorite (7)

Sample number	A192-155.70-5	A192-155.70-6	A192-155.70-10	A192-155.70-11	A685-171-1	A685-171-2	A685-171-3	A685-171-4	A685-171-6
SiO_2	25.24	25.21	25.43	25.66	23.35	24.93	24.07	24.26	24.17
TiO_2	0.00	0.00	1.36	0.52	0.00	0.39	0.36	0.09	1.10
Al_2O_3	21.66	21.73	22.03	21.40	20.26	22.19	21.69	22.57	22.01
FeO	33.37	33.38	32.80	32.54	33.50	33.88	34.85	36.87	34.15
MnO	0.49	0.46	0.31	0.47	0.87	0.98	1.03	1.21	0.89
MgO	11.29	11.57	11.47	11.66	10.11	9.88	9.59	7.69	9.30
CaO	0.03	0.05	0.01	0.00	0.08	0.03	0.01	0.00	0.03
Na_2O	0.02	0.01	0.03	0.00	0.13	0.04	0.10	0.09	0.09
K_2O	0.09	0.08	0.13	0.08	0.08	0.02	0.03	0.03	0.06
Cr_2O_3	0.00	0.00	0.00	0.00	0.00	0.00	0.00	0.00	0.00
Total	92.19	92.48	93.55	92.32	88.36	92.34	91.72	92.79	91.78
Normalisation on the basis 28 oxygens (with Fe2+/Fe3+ and OH calculated assuming full site occupancy)									
Si	5.26	5.23	5.20	5.32	5.11	5.22	5.10	5.14	5.11
Al^{iv}	2.74	2.77	2.80	2.68	2.89	2.78	2.90	2.86	2.89
Al^{vi}	2.59	2.56	2.51	2.55	2.40	2.70	2.55	2.78	2.61
Ti	0.00	0.00	0.21	0.08	0.00	0.06	0.06	0.01	0.17
Cr	0.00	0.00	0.00	0.00	0.00	0.00	0.00	0.00	0.00
Fe^{3+}	0.00	0.00	0.05	0.01	0.00	0.01	0.00	0.00	0.01
Fe^{2+}	5.89	5.89	5.56	5.63	6.37	5.92	6.29	6.57	6.03
Mn	0.09	0.08	0.05	0.08	0.16	0.17	0.18	0.22	0.16
Mg	3.51	3.57	3.50	3.60	3.30	3.08	3.03	2.43	2.93
Ca	0.01	0.01	0.00	0.00	0.02	0.01	0.00	0.00	0.01
Na	0.01	0.01	0.02	0.00	0.11	0.04	0.08	0.07	0.07
K	0.05	0.04	0.07	0.04	0.05	0.01	0.02	0.01	0.03
Mg#	37	38	38	39	34	34	33	27	33
T (°C)	355	358	361	347	373	362	375	376	374

Representative composition of phengite (1/3)

Sample number	A49-81.15 -3	A49-81.55 -1	A49-81.55 -4	A49-81.55 -5	A49-81.15-2	A49-81.55 -7	S66-67 -6	S66-67 -7	S66-67 -9	S66-67 -10
SiO_2	51.68	49.90	50.00	51.36	50.48	50.28	51.37	51.92	51.88	50.80
TiO_2	0.07	0.13	0.10	0.04	0.16	0.10	0.11	0.10	0.02	0.15
Al_2O_3	28.22	27.97	28.23	28.61	30.79	27.71	23.00	23.34	23.00	23.95
FeO	2.99	4.48	3.56	2.72	2.20	3.79	6.18	5.50	5.34	5.25
MnO	0.01	0.00	0.08	0.03	0.03	0.05	0.21	0.19	0.23	0.13
MgO	1.68	1.61	1.81	1.71	1.33	1.75	3.68	3.36	3.35	2.39
CaO	0.04	0.06	0.05	0.00	0.01	0.04	0.09	0.04	0.00	0.03
Na_2O	0.18	0.12	0.21	0.33	0.24	0.19	0.14	0.17	0.19	0.27
K_2O	9.09	9.21	9.39	9.62	9.67	9.20	10.28	10.33	10.43	10.01
Total	93.96	93.48	93.45	94.43	94.92	93.12	95.05	94.94	94.44	92.98
Normalisation on the basis of 22 negative charges										
Si	7.02	6.95	6.91	6.96	6.77	6.98	7.24	7.27	7.29	7.23
Ti	0.01	0.01	0.01	0.00	0.02	0.01	0.01	0.01	0.00	0.02
Al	4.52	4.59	4.60	4.57	4.87	4.53	3.82	3.85	3.81	4.02
Fe^{+3}	0.00	0.00	0.00	0.00	0.00	0.00	0.00	0.00	0.00	0.00
Fe^{+2}	0.00	0.00	0.00	0.00	0.00	0.00	0.00	0.00	0.00	0.00
Mn	0.00	0.00	0.01	0.00	0.00	0.01	0.03	0.02	0.03	0.02
Mg	0.34	0.33	0.37	0.34	0.27	0.36	0.77	0.70	0.70	0.51
Ca	0.01	0.01	0.01	0.00	0.00	0.01	0.01	0.01	0.00	0.00
Na	0.05	0.03	0.06	0.09	0.06	0.05	0.04	0.04	0.05	0.07
K	1.58	1.64	1.66	1.66	1.65	1.63	1.85	1.84	1.87	1.82

Representative composition of phengite (2/3)

Sample	A192-155.70-1	A192-155.70-2	A192-155.70-3	A192-155.70-4	A192-155.70-7	A192-155.70-8	A192-155.70-9	A192-155.70-14	A683-53.60-10	A683-53.60-4
SiO_2	50.92	50.03	50.96	50.34	48.71	50.40	53.09	49.10	47.91	52.21
TiO_2	0.58	0.44	0.00	0.00	0.91	0.76	0.38	0.72	1.16	0.31
Al_2O_3	30.83	31.18	30.60	29.25	30.88	31.31	28.48	29.60	29.20	29.32
FeO	1.92	4.32	1.97	2.67	5.50	1.57	3.11	4.13	1.73	2.90
MnO	0.01	0.03	0.00	0.03	0.03	0.01	0.04	0.03	0.04	0.00
MgO	1.97	2.57	1.96	2.07	2.32	1.69	2.44	1.75	1.22	1.58
CaO	0.01	0.01	0.03	0.03	0.08	0.03	0.01	0.12	0.19	0.07
Na_2O	0.22	0.19	0.16	0.15	0.16	0.20	0.21	0.23	0.33	0.12
K_2O	9.96	8.39	10.76	10.63	9.28	10.39	10.46	9.07	9.35	9.46
Total	96.42	97.15	96.44	95.18	97.87	96.34	98.23	94.76	91.12	95.96
Normalisation on the basis of 22 negative charges										
Si	6.65	6.52	6.69	6.72	6.39	6.60	6.86	6.59	6.63	6.85
Ti	0.06	0.04	0.00	0.00	0.09	0.07	0.04	0.07	0.12	0.03
Al	4.75	4.79	4.73	4.60	4.78	4.83	4.34	4.68	4.76	4.53
Fe^{+3}	0.00	0.00	0.00	0.00	0.00	0.00	0.00	0.00	0.00	0.00
Fe^{+2}	0.21	0.47	0.22	0.30	0.60	0.17	0.34	0.46	0.20	0.32
Mn	0.00	0.00	0.00	0.00	0.00	0.00	0.00	0.00	0.00	0.00
Mg	0.38	0.50	0.38	0.41	0.45	0.33	0.47	0.35	0.25	0.31
Ca	0.00	0.00	0.00	0.00	0.01	0.00	0.00	0.02	0.03	0.01
Na	0.06	0.05	0.04	0.04	0.04	0.05	0.05	0.06	0.09	0.03
K	1.66	1.39	1.80	1.81	1.55	1.74	1.72	1.55	1.65	1.58

Representative composition of phengite (3/3)

Sample	A683-53.60-6	A683-53.60-7	A683-53.60-9	S68-47-40
SiO_2	46.54	49.42	52.08	50.50
TiO_2	0.00	0.00	0.78	0.00
Al_2O_3	31.28	25.04	28.12	23.73
FeO	1.40	3.30	2.46	4.43
MnO	0.00	0.01	0.00	0.03
MgO	1.53	2.99	2.58	6.06
CaO	0.15	0.12	0.04	0.06
Na_2O	0.29	0.17	0.10	0.07
K_2O	7.36	10.12	10.93	10.49
Total	88.55	91.16	97.09	95.34
Normalisation on the basis of 22 negative charges				
Si	6.52	6.92	6.82	6.84
Ti	0.00	0.00	0.08	0.00
Al	5.17	4.13	4.34	3.79
Fe^{+3}	0.00	0.00	0.00	0.00
Fe^{+2}	0.16	0.39	0.27	0.50
Mn	0.00	0.00	0.00	0.00
Mg	0.32	0.62	0.50	1.22
Ca	0.02	0.02	0.01	0.01
Na	0.08	0.05	0.03	0.02
K	1.32	1.81	1.83	1.81

Representative EMPA analyses of pyrite (wt%)

No	As	S	Fe	Cu	Co	Ni	Total	Comment
1	0.20	53.25	46.37	0.00	0.71	0.02	100.55	S50-3910-2-1
2	0.47	51.35	46.03	0.00	0.09	0.07	98.02	S50-3910-2-1lm
3	0.52	52.91	46.33	0.00	0.63	0.10	100.49	S50-3910-2-1lm
4	0.36	51.57	45.53	0.00	0.81	0.09	98.35	S50-3910-2-2
5	0.09	53.33	47.33	0.00	0.00	0.00	100.75	S50-3910-2-3
6	0.05	53.25	47.13	0.00	0.00	0.00	100.42	S50-3910-2-4
7	0.01	53.23	47.38	0.00	0.00	0.00	100.62	S50-3910-2-5
8	0.04	53.36	47.53	0.00	0.00	0.00	100.93	S50-3910-2-6
9	0.05	53.73	47.53	0.00	0.00	0.00	101.32	S50-3910-2-7
10	0.09	53.35	47.05	0.00	0.00	0.00	100.49	S53-3390-1
11	0.44	51.73	47.23	0.00	0.00	0.01	99.40	S53-3390-10
12	0.33	51.95	47.19	0.00	0.00	0.00	99.47	S53-3390-11
13	0.23	51.71	47.07	0.00	0.00	0.00	99.01	S53-3390-12
14	0.07	51.83	47.01	0.00	0.00	0.00	98.91	S53-3390-13
15	0.20	51.32	47.41	0.00	0.00	0.00	98.92	S53-3390-14
16	0.08	51.35	46.87	0.00	0.00	0.02	98.32	S53-3390-15
17	0.23	51.32	47.05	0.00	0.00	0.00	98.61	S53-3390-16
18	0.01	51.21	47.57	0.00	0.00	0.00	98.79	S53-3390-17
19	0.12	50.65	47.33	0.00	0.00	0.04	98.14	S53-3390-18
20	0.15	51.09	47.00	0.00	0.01	0.01	98.26	S53-3390-19
21	0.50	52.50	46.30	0.00	0.00	0.00	99.31	S53-3390-2
22	0.16	51.26	47.11	0.00	0.00	0.00	98.53	S53-3390-20
23	0.32	50.98	47.07	0.00	0.00	0.00	98.38	S53-3390-21
24	0.30	52.78	46.66	0.00	0.00	0.00	99.75	S53-3390-3
25	0.08	52.54	46.54	0.00	0.00	0.02	99.18	S53-3390-4
26	0.06	52.49	47.36	0.02	0.00	0.00	99.92	S53-3390-5
27	0.03	52.07	47.05	0.00	0.00	0.00	99.15	S53-3390-6
28	0.37	51.45	47.08	0.00	0.00	0.00	98.90	S53-3390-7
29	0.38	51.92	47.21	0.00	0.00	0.00	99.51	S53-3390-9
30	0.00	53.37	46.47	0.00	0.06	1.02	100.92	S68-107-1
31	0.18	53.23	47.53	0.00	0.00	0.00	100.94	S68-107-10
32	0.00	53.14	46.96	0.00	0.00	0.61	100.70	S68-107-2
33	0.05	53.64	47.69	0.00	0.00	0.07	101.45	S68-107-3
34	0.03	53.39	46.14	0.00	0.00	1.20	100.76	S68-107-4
35	0.03	53.16	47.55	0.00	0.00	0.05	100.80	S68-107-5
36	0.05	53.10	46.44	0.00	0.00	0.61	100.19	S68-107-6
37	0.04	53.48	46.90	0.00	0.10	0.21	100.73	S68-107-7
38	0.01	53.58	47.57	0.00	0.00	0.00	101.16	S68-107-8
39	0.04	53.05	47.55	0.00	0.00	0.06	100.70	S68-107-9
40	0.01	52.96	47.49	0.01	0.00	0.01	100.47	S68-11320-1
41	0.11	52.17	46.94	0.00	0.00	0.00	99.22	S68-11320-2
42	0.01	51.86	46.54	0.00	0.00	0.00	98.41	S68-11320-3
43	0.20	52.97	47.40	0.05	0.00	0.02	100.64	S68-11320-4
44	0.09	53.17	47.56	0.05	0.00	0.00	100.87	S68-11320-5
45	0.08	51.28	46.68	0.01	0.01	0.00	98.06	S68-11320-6

No	As	S	Fe	Cu	Co	Ni	Total	Comment
46	0.02	54.20	47.34	0.01	0.01	0.26	101.85	S68-130,30-1
47	0.00	54.23	47.19	0.00	0.00	0.04	101.46	S68-130,30-2
48	0.02	53.91	47.13	0.07	0.00	0.32	101.44	S68-130,30-3
49	0.01	54.16	47.41	0.00	0.00	0.03	101.61	S68-130,30-4
50	0.07	54.23	47.35	0.00	0.00	0.10	101.74	S68-130,30-5
51	0.04	54.15	46.18	0.00	0.55	0.72	101.64	S68-130,30-6
52	0.00	53.83	47.18	0.00	0.00	0.60	101.61	S68-136,50-1
53	0.02	53.58	46.93	0.00	0.05	0.60	101.18	S68-136,50-2
54	0.05	53.75	47.68	0.00	0.00	0.02	101.49	S68-136,50-3
55	0.00	53.70	47.49	0.03	0.00	0.01	101.22	S68-136,50-4
56	0.00	52.58	46.38	0.00	0.00	0.00	98.97	S68-140,20-6lm
57	0.03	52.70	47.17	0.00	0.00	0.00	99.89	S68-140,20-6lm
58	0.00	52.67	47.29	0.00	0.00	0.00	99.95	S68-140,20-6lm
59	0.01	52.91	47.25	0.00	0.00	0.00	100.17	S68-140,20-6lm
60	0.00	52.97	47.23	0.00	0.00	0.00	100.20	S68-140,20-6lm
61	0.02	52.89	47.13	0.00	0.00	0.17	100.22	S68-140,20-6lm
62	0.03	52.87	47.57	0.00	0.00	0.00	100.46	S68-140,20-6lm
63	0.03	52.81	47.63	0.00	0.00	0.00	100.47	S68-140,20-6lm
64	0.00	53.10	47.41	0.00	0.00	0.00	100.52	S68-140,20-6lm
65	0.06	53.49	47.29	0.02	0.02	0.22	101.09	S68-143,80-1
66	0.05	53.47	46.72	0.00	0.00	0.31	100.55	S68-143,80-2
67	0.01	53.51	47.50	0.00	0.00	0.05	101.07	S68-143,80-3
68	0.05	53.52	46.47	0.00	0.05	0.25	100.34	S68-143,80-4
69	0.04	53.38	46.81	0.01	0.07	0.35	100.67	S68-143,80-5
70	0.01	53.38	47.19	0.00	0.01	0.01	100.58	S68-98,95-1
71	0.03	53.56	46.85	0.00	0.00	0.01	100.45	S68-98,95-2
72	0.02	53.38	46.74	0.00	0.00	0.02	100.16	S68-98,95-3
73	0.02	52.47	46.73	0.01	0.00	0.03	99.27	S68-98,95-4
74	0.08	53.64	45.83	0.01	0.65	1.06	101.26	S69-2500-1
75	0.08	53.60	43.63	0.00	1.97	1.89	101.16	S69-2500-2
76	0.01	53.88	47.46	0.00	0.00	0.11	101.46	S69-2500-3
77	0.01	54.12	47.44	0.00	0.00	0.01	101.57	S69-2500-4
78	0.02	53.65	47.12	0.00	0.00	0.63	101.42	S69-2500-5
79	0.09	53.22	44.62	0.00	2.57	0.25	100.74	S69-2500-6
80	0.03	53.65	44.58	0.00	0.04	2.96	101.27	S69-2500-7
81	0.06	53.08	43.81	0.00	3.09	0.31	100.34	S69-2500-8
82	0.01	53.64	47.08	0.00	0.00	0.18	100.91	S69-2500-lm-1
83	0.03	53.33	44.48	0.00	0.49	2.42	100.75	S69-2500-lm-2
84	0.02	53.53	47.79	0.00	0.00	0.15	101.49	S69-2500-lm-3
85	0.03	53.44	46.53	0.00	0.00	1.29	101.28	S69-2500-lm-4
86	0.06	53.15	45.91	0.00	0.13	1.62	100.86	S69-2500-lm-5
87	0.03	54.01	46.10	0.00	0.10	1.54	101.78	S69-2500-lm-6
88	0.02	53.95	47.71	0.00	0.00	0.22	101.89	S69-2500-lm-7
89	0.00	52.23	46.58	0.00	0.00	0.11	98.92	S69-2500-lm-8
90	0.04	54.03	47.79	0.00	0.00	0.03	101.89	S69-2580-1
91	0.03	53.43	47.76	0.06	0.00	0.00	101.27	S69-2580-10

No	As	S	Fe	Cu	Co	Ni	Total	Comment
92	0.03	53.28	46.63	0.00	0.00	1.08	101.03	S69-2580-2
93	0.13	53.52	47.24	0.00	0.00	0.01	100.90	S69-2580-3
94	0.01	54.32	47.96	0.00	0.00	0.19	102.49	S69-2580-4
95	0.03	53.45	47.88	0.00	0.00	0.01	101.36	S69-2580-5
96	0.06	53.11	47.06	0.00	0.00	0.47	100.70	S69-2580-6
97	0.01	53.32	47.79	0.00	0.00	0.06	101.17	S69-2580-7
98	0.04	53.37	47.76	0.00	0.00	0.00	101.17	S69-2580-8
99	0.02	53.46	47.78	0.00	0.00	0.02	101.28	S69-2580-9
100	0.00	53.80	47.26	0.00	0.00	0.00	101.06	S69-32,80-10
101	0.06	53.70	47.58	0.00	0.00	0.00	101.34	S69-32,80-2
102	0.05	54.03	46.86	0.00	0.00	0.00	100.94	S69-32,80-3
103	0.03	53.80	47.79	0.00	0.00	0.04	101.66	S69-32,80-4
104	0.06	54.14	47.06	0.05	0.00	0.00	101.31	S69-32,80-5
105	0.04	54.09	47.61	0.00	0.00	0.06	101.79	S69-32,80-6
106	0.00	54.18	47.04	0.03	0.00	0.00	101.25	S69-32,80-7
107	0.00	53.92	46.87	0.00	0.00	0.01	100.80	S69-32,80-8
108	0.06	54.24	47.97	0.00	0.00	0.00	102.26	S69-32,80-9
109	0.07	53.05	47.12	0.00	0.01	0.04	100.30	S69-6440-1
110	0.03	52.99	46.07	0.00	0.00	0.00	99.08	S69-6440-2
111	0.05	53.71	47.46	0.00	0.00	0.00	101.22	S69-6440-3
112	0.02	53.83	47.02	0.00	0.00	0.00	100.87	S69-6440-4
113	0.07	53.57	45.73	0.00	0.07	0.88	100.33	S69-6440-5
114	0.06	53.49	47.26	0.00	0.00	0.00	100.81	S69-6440-6
115	0.00	53.92	46.93	0.00	0.00	0.00	100.85	S69-6440-7
116	0.05	53.76	46.61	0.00	0.00	0.63	101.06	S69-6440-8
117	0.02	53.59	47.68	0.00	0.00	0.00	101.29	S69-6440-9
118	0.02	52.24	46.57	0.00	0.00	0.00	98.83	S94-80,30-1
119	0.02	53.71	47.56	0.02	0.00	0.00	101.31	S94-80,30-2
120	0.01	53.34	47.29	0.00	0.00	0.00	100.65	S94-80,30-3
121	0.03	53.25	47.30	0.00	0.00	0.07	100.64	S94-80,30-5

Representative EMPA analyses of gold

No.	Comment	Au wt%	Ag wt%	Cu wt%	Fe wt%	Total	Normalize to 100% Au	Ag
1	sam2_g_1	86.45	14.88	0.01	0.42	101.76	85.31	14.69
2	sam2_g_2	85.00	14.81	0.00	0.34	100.15	85.16	14.84
3	sam2_g_3	81.72	14.94	0.00	0.40	97.06	84.55	15.45
4	sam2_g_4	84.76	14.49	0.01	1.16	100.41	85.40	14.60
5	sam2_g_5	85.33	14.78	0.00	1.40	101.50	85.24	14.76
6	sam2_g_6	88.19	14.40	0.00	3.49	106.08	85.96	14.04
7	sam2_g_7	84.73	13.87	0.00	2.80	101.40	85.94	14.06
8	sam2_g_8	82.50	14.82	0.03	1.36	98.71	84.77	15.23
9	sam2_g_9	88.48	8.81	0.02	2.68	100.00	90.94	9.06
10	sam2_g_10	85.46	14.34	0.00	2.73	102.53	85.63	14.37
11	sam2_g_11	84.42	14.58	0.00	2.65	101.65	85.27	14.73
12	sam2_g_12	85.24	14.36	0.00	1.62	101.23	85.58	14.42
13	sam2_g_13	84.59	15.04	0.00	2.08	101.71	84.91	15.09
14	sam2_g_14	86.39	14.58	0.00	1.34	102.31	85.56	14.44

No.	Comment	Au wt%	Ag wt%	Cu wt%	Fe wt%	Total	Normalize to 100% Au	Ag
15	sam2_g_15	85.69	14.91	0.00	2.44	103.04	85.18	14.82
16	sam2_g_16	87.15	12.85	0.00	3.92	103.92	87.15	12.85
17	sam2_g_17	84.38	14.54	0.02	2.66	101.60	85.31	14.69
18	sam2_g_18	85.26	14.66	0.00	1.55	101.48	85.33	14.67
19	sam2_g_19	84.75	14.87	0.00	1.56	101.18	85.07	14.93
20	sam2_g_20	86.61	14.82	0.03	1.46	102.93	85.39	14.61
21	sam2_g_21	84.88	14.31	0.00	2.73	101.93	85.58	14.42
22	sam2_g_22	84.32	14.92	0.00	0.32	99.55	84.97	15.03
23	sam2_g_23	84.18	15.09	0.01	0.43	99.71	84.80	15.20
24	sam2_g_24	86.16	14.56	0.03	0.73	101.48	85.54	14.46
25	sam2_g_25	84.05	15.21	0.00	1.55	100.80	84.68	15.32
26	sam2_g_26	85.58	14.75	0.05	1.82	102.19	85.30	14.70
27	sam2_g_27	83.55	15.07	0.03	2.33	100.99	84.72	15.28
28	sam2_g_28	86.97	14.19	0.00	2.26	103.42	85.98	14.02
29	sam2_g_29	82.90	14.96	0.00	0.76	98.61	84.72	15.28
30	sam2_g_30	85.82	14.30	0.00	1.93	102.05	85.71	14.29
31	sam2_g_31	85.09	14.19	0.00	1.37	100.64	85.71	14.29
32	sam2_g_32	84.46	13.72	0.00	1.85	100.03	86.03	13.97
33	sam2_g_33	85.04	14.08	0.02	2.11	101.24	85.80	14.20
34	sam2_g_34	86.68	13.95	0.04	2.52	103.18	86.14	13.86
35	sam2_g_35	86.98	13.78	0.00	2.81	103.58	86.32	13.68
36	sam2_g_36	86.83	12.35	0.00	1.14	100.33	87.55	12.45
37	sam2_g_37	85.90	14.14	0.00	1.86	101.90	85.86	14.14
38	samp4_g_39	90.79	10.22	0.05	1.87	102.92	89.89	10.11
39	samp4_g_40	89.02	10.11	0.01	1.80	100.94	89.80	10.20
40	samp3_g_41	84.67	15.46	0.01	1.11	101.25	84.56	15.44
41	samp3_g_42	85.74	16.04	0.00	1.12	102.91	84.24	15.76
42	S94-34.35-g1	87.01	13.13	0.00	0.22	100.36	86.89	13.11
43	S94-34.35-g2	87.34	12.92	0.00	0.26	100.51	87.12	12.88
44	S94-34.35-g2	85.80	13.31	0.00	3.57	102.68	86.57	13.43
45	S94-34.35-g3	88.58	13.39	0.00	1.02	102.99	86.87	13.13
46	S94-34.35-g4	88.11	13.02	0.00	0.63	101.76	87.13	12.87
47	S94-34.35-g6	88.19	12.76	0.22	0.81	101.97	87.36	12.64
48	S94-34.35-g7	88.47	13.00	0.17	0.88	102.52	87.19	12.81
49	S94-34.35-g8	88.91	13.27	0.00	1.16	103.34	87.01	12.99
50	A49-90.65-g1	93.50	8.74	0.00	0.66	102.89	91.45	8.55
51	A49-90.65-g2	93.70	8.61	0.00	0.71	103.01	91.58	8.42
52	A49-90.65-g3	96.83	7.95	0.00	2.13	106.91	92.41	7.59
53	A35-21-g1	90.81	12.05	0.00	2.26	105.12	88.29	11.71
54	A35-21-g2	91.40	12.13	0.00	2.06	105.59	88.28	11.72
55	A192-86.40-1	93.05	6.97	0.00	0.00	100.02	93.03	6.97
56	A192-86.40-2	93.78	6.77	0.00	0.00	100.55	93.27	6.73
57	A192-86.40-3	91.52	6.22	0.00	0.00	97.74	93.64	6.36
58	A192-86.40-4	90.55	6.71	0.00	0.00	97.26	93.11	6.89
59	A635-16-1	86.94	11.15	0.00	0.00	98.09	88.63	11.37
60	A635-16-2	87.69	11.44	0.00	0.00	99.13	88.46	11.54
61	A635-16-3	87.24	11.48	0.00	0.00	98.72	88.38	11.62
62	A635-16-4	86.11	10.93	0.00	0.00	97.04	88.74	11.26
63	A685-20-1	88.06	8.00	0.00	0.00	96.06	91.68	8.32
64	A685-20-3	88.54	10.43	0.00	0.00	98.97	89.47	10.53

No.	Comment	Au wt%	Ag wt%	Cu wt%	Fe wt%	Total	Normalize to 100% Au	Ag
65	S53-101-10	87.98	11.24	0.00	0.00	99.22	88.67	11.33
66	S53-101-11	87.88	10.88	0.00	0.00	98.76	88.98	11.02
67	S53-101-12	86.48	11.50	0.00	0.00	97.98	88.27	11.73
68	S53-101-13	87.48	10.96	0.00	0.00	98.44	88.87	11.13
69	S53-101-9	87.69	11.59	0.00	0.00	99.28	88.32	11.68
70	S53-101-PET-1	86.57	11.54	0.00	0.00	98.11	88.24	11.76
71	S53-101-PET-2	87.05	11.67	0.00	0.00	98.72	88.18	11.82
72	S53-101-PET-3	87.50	10.89	0.00	0.00	98.39	88.93	11.07
73	S53-101-PET-4	87.44	10.92	0.00	0.00	98.36	88.90	11.10
74	S53-101-PET-5	87.64	10.44	0.00	0.00	98.08	89.35	10.65
75	S53-101-PET-6	86.77	11.49	0.00	0.00	98.26	88.30	11.70
76	S53-101-PET-7	87.75	10.28	0.00	0.00	98.03	89.51	10.49
77	S53-101-PET-8	88.23	10.89	0.00	0.00	99.12	89.01	10.99
78	S68-107-1	84.86	13.04	0.00	0.00	97.90	86.68	13.32
79	S68-107-2	86.23	13.50	0.00	0.01	99.74	86.47	13.53
80	S68-107-3	87.62	13.61	0.00	0.00	101.23	86.56	13.44
81	S68-140.20-1	85.03	13.24	0.00	0.00	98.27	86.53	13.47
82	S68-140.20-2	84.32	13.66	0.00	0.00	97.98	86.06	13.94
83	S68-140.20-3	84.91	13.70	0.00	0.00	98.61	86.10	13.90
84	SB-02-1	85.29	12.76	0.00	0.00	98.04	86.99	13.01
85	SB-02-2	83.43	12.65	0.00	0.00	96.08	86.84	13.16
86	SB-02-3	85.74	12.97	0.00	0.00	98.70	86.86	13.14
87	SB-02-4	85.15	12.87	0.00	0.00	98.02	86.87	13.13

sam1:S68-143.80; sam2: S69-25; Samp3: S68–132.90 and Samp4:S69-25.80, respectively.

Representative EMPA analyses of mercurian tetrahedrite

	sam4-18	**sam4--17**	**sam1-23**	**sam1-001**	**sam1-2**	**A35-34.7-1**	**A35-34.7-2**	**A35-34.7-3**	**A35-34.7-**	**A35-34.7-5**	**A35-34.7-6**	**A35-34.7-7**	**A35-34.7-8**	**A35-34.7-9**	**A35-34.7-10**
As	6.25	6.54	3.41	3.49	4.24	3.07	2.89	3.14	3.17	3.08	2.99	4.75	4.82	4.41	4.80
S	23.70	23.73	24.08	24.37	24.53	22.35	22.71	22.58	23.01	22.55	22.82	23.09	22.76	22.67	23.31
Sb	15.43	15.07	24.29	23.56	23.27	21.61	21.92	21.60	21.62	22.01	21.75	19.33	19.56	19.83	18.74
Bi	0.04	0.06	0.17	0.09	0.08	0.10	0.13	0.20	0.05	0.14	0.12	0.05	0.07	0.03	0.15
Cu	35.83	35.76	39.38	38.77	40.19	35.78	36.26	35.97	36.04	35.59	35.60	35.91	36.50	36.39	36.11
Ag	0.06	0.09	0.29	0.25	0.18	0.23	0.21	0.25	0.24	0.21	0.21	0.19	0.21	0.18	0.21
Zn	0.35	0.35	2.28	2.27	2.33	0.11	0.20	0.19	0.36	0.34	0.36	0.16	0.24	0.13	0.13
Hg	16.94	17.28	2.36	2.54	1.93	17.56	16.90	17.46	15.63	15.96	15.67	17.02	16.68	17.26	16.83
Fe	1.17	1.14	0.33	0.55	0.45	0.24	0.40	0.29	0.47	0.29	0.32	0.86	0.46	0.43	0.28
Total	99.77	100.02	96.59	95.88	97.19	101.05	101.62	101.68	100.60	100.18	99.84	101.36	101.30	101.32	100.56
% atoms	13.00	13.00	13.00	13.00	13.00	13.00	13.00	13.00	13.00	13.00	13.00	13.00	13.00	13.00	13.00
As	1.47	1.53	0.79	0.80	0.96	0.76	0.71	0.77	0.77	0.76	0.73	1.14	1.18	1.08	1.15
S	13.00	13.00	13.00	13.00	13.00	13.00	13.00	13.00	13.00	13.00	13.00	13.00	13.00	13.00	13.00
Sb	2.23	2.17	3.45	3.31	3.25	3.31	3.30	3.27	3.22	3.34	3.26	2.87	2.94	2.99	2.75
Bi	0.00	0.00	0.01	0.01	0.01	0.01	0.01	0.02	0.00	0.01	0.01	0.00	0.01	0.00	0.01
Cu	9.91	9.88	10.73	10.43	10.75	10.50	10.47	10.45	10.27	10.35	10.23	10.20	10.52	10.53	10.16
Ag	0.01	0.01	0.05	0.04	0.03	0.04	0.04	0.04	0.04	0.04	0.04	0.03	0.03	0.03	0.03
Zn	0.09	0.09	0.60	0.59	0.61	0.03	0.06	0.05	0.10	0.10	0.10	0.04	0.07	0.04	0.03
Hg	1.49	1.51	0.20	0.22	0.16	1.63	1.55	1.61	1.41	1.47	1.43	1.53	1.52	1.58	1.50
Fe	0.37	0.36	0.10	0.17	0.14	0.08	0.13	0.10	0.15	0.10	0.10	0.28	0.15	0.14	0.09
Total	28.57	28.58	28.94	28.56	28.89	29.36	29.27	29.31	28.96	29.16	28.90	29.10	29.42	29.40	28.73
As+Sb+Bi	3.70	3.71	4.25	4.11	4.22	4.08	4.02	4.07	3.99	4.11	4.00	4.01	4.13	4.08	3.91
Hg+Fe+Zn+Ag	1.96	1.98	0.96	1.02	0.93	1.78	1.77	1.80	1.70	1.70	1.67	1.88	1.77	1.79	1.66
Cu+Hg+Fe+Zn+Ag	11.87	11.86	11.68	11.45	11.68	12.28	12.24	12.25	11.98	12.05	11.90	12.08	12.29	12.32	11.82

sam1:S68-143.80; sam2: S69-25; Samp3: S68–132.90 and Samp4:S69-25.80, respectively.

Representative EMPA analyses of enargite-luzonite/famatinite

	sam1-24	sam1-3	sam1-4	sam2-5	sam2-6	sam2-7	sam2-8	sam2-9	sam2-10	sam2-11	sam2-12	sam2-13	sam3-15	sam3-16	sam5-19	sam5-20	sam5-21	sam1-22
As	3.45	13.84	9.94	10.39	13.01	12.07	10.07	11.56	17.55	15.21	16.13	16.94	15.75	13.52	14.07	12.01	12.41	12.32
S	29.15	31.01	30.62	30.66	30.89	31.43	30.51	30.91	32.30	32.23	31.54	32.35	32.80	32.15	31.47	31.31	31.43	30.98
Sb	23.12	8.54	13.17	12.38	8.74	10.26	13.27	10.80	2.25	5.24	4.71	2.29	4.28	7.57	6.56	10.45	8.98	9.13
Bi	0.12	0.08	0.08	0.10	0.11	0.11	0.08	0.14	0.08	0.16	0.15	0.12	0.11	0.09	0.14	0.09	0.07	0.06
Cu	44.47	48.17	46.34	47.15	47.22	47.85	47.28	44.74	49.04	48.04	46.58	47.79	47.90	46.88	45.33	45.60	46.38	47.58
Ag	0.05	0.13	0.09	0.00	0.01	0.00	0.02	0.01	0.06	0.15	0.11	0.00	0.04	0.01	0.05	0.03	0.04	0.02
Zn	0.00	0.03	0.04	0.07	0.06	0.04	0.04	0.06	0.06	0.06	0.04	0.04	0.04	0.05	0.06	0.03	0.05	0.04
Hg	0.00	0.00	0.01	0.00	0.00	0.00	0.00	0.00	0.06	0.00	0.02	0.00	0.02	0.00	0.05	0.00	0.00	0.03
Fe	1.10	0.51	0.33	0.08	0.19	0.09	0.09	2.06	0.24	1.89	0.33	0.69	0.49	0.81	0.05	0.25	0.44	0.44
Total	101.5	102.3	100.6	100.8	100.2	101.8	101.4	100.3	101.6	102.9	99.60	100.2	101.4	101.1	97.8	99.8	99.8	100.6
% atoms	4.00	4.00	4.00	4.00	4.00	4.00	4.00	4.00	4.00	4.00	4.00	4.00	4.00	4.00	4.00	4.00	4.00	4.00
As	0.20	0.76	0.56	0.58	0.72	0.66	0.56	0.64	0.93	0.81	0.88	0.90	0.82	0.72	0.77	0.66	0.68	0.68
S	4.00	4.00	4.00	4.00	4.00	4.00	4.00	4.00	4.00	4.00	4.00	4.00	4.00	4.00	4.00	4.00	4.00	4.00
Sb	0.84	0.29	0.45	0.43	0.30	0.34	0.46	0.37	0.07	0.17	0.16	0.07	0.14	0.25	0.22	0.35	0.30	0.31
Bi	0.00	0.00	0.00	0.00	0.00	0.00	0.00	0.00	0.00	0.00	0.00	0.00	0.00	0.00	0.00	0.00	0.00	0.00
Cu	3.08	3.13	3.05	3.10	3.09	3.07	3.13	2.92	3.06	3.01	2.98	2.98	2.95	2.94	2.91	2.94	2.98	3.10
Ag	0.00	0.00	0.00	0.00	0.00	0.00	0.00	0.00	0.00	0.01	0.00	0.00	0.00	0.00	0.00	0.00	0.00	0.00
Zn	0.00	0.00	0.00	0.00	0.00	0.00	0.00	0.00	0.00	0.00	0.00	0.00	0.00	0.00	0.00	0.00	0.00	0.00
Hg	0.00	0.00	0.00	0.00	0.00	0.00	0.00	0.00	0.00	0.00	0.00	0.00	0.00	0.00	0.00	0.00	0.00	0.00
Fe	0.09	0.04	0.02	0.01	0.01	0.01	0.01	0.15	0.02	0.13	0.02	0.05	0.03	0.06	0.00	0.02	0.03	0.03
Total	8.21	8.23	8.09	8.12	8.12	8.08	8.16	8.09	8.09	8.13	8.05	8.01	7.95	7.97	7.90	7.97	7.99	8.13
As+Sb+Bi	1.04	1.06	1.01	1.01	1.02	1.00	1.02	1.01	1.01	0.98	1.04	0.97	0.96	0.97	0.99	1.01	0.98	0.99
Hg+Fe+Zn+ Ag	0.09	0.04	0.03	0.01	0.02	0.01	0.01	0.16	0.02	0.14	0.03	0.05	0.04	0.06	0.01	0.02	0.04	0.04
Cu+Hg+Fe +Zn+Ag	3.17	3.18	3.08	3.11	3.10	3.08	3.14	3.08	3.09	3.15	3.01	3.03	2.98	3.00	2.92	2.96	3.01	3.14

sam1:S68-143.80; sam2: S69-25; Samp3: S68–132.90 and Samp4:S69-25.80, respectively.

Representative EMPA analyses of fahlores

	S94-34.35-1	S94-34.35-2	S94-34.35-3	S94-34.35C3-1	S94-34.35C3-2	S94-34.35C3-3	S94-34.35C3-4	S94-34.35C3-5	S94-34.35C6-1	S94-34.35C6-2	S94-34.35C6-3	S94-34.35C6-4	S94-34.35C7-1	S94-34.35C7-2	S94-34.35C7-3	S94-34.35C8-1
As	18.37	18.12	18.72	16.24	15.91	9.14	10.41	16.14	9.85	9.50	9.83	13.84	10.32	10.58	10.12	8.95
S	28.60	28.50	28.38	27.66	27.83	26.73	26.96	27.71	26.62	26.55	26.75	27.65	26.96	27.17	27.29	26.79
Sb	3.12	3.80	2.98	7.19	7.01	16.52	14.91	7.82	15.99	16.18	16.20	10.29	15.13	14.94	15.19	16.52
Bi	0.12	0.14	0.18	0.10	0.07	0.13	0.07	0.11	0.15	0.07	0.05	0.14	0.07	0.05	0.11	0.09
Cu	46.19	46.38	46.07	44.96	44.88	42.92	42.88	45.36	43.79	43.70	43.69	44.30	43.19	44.21	43.88	42.71
Ag	0.00	0.02	0.08	0.02	0.02	0.04	0.04	0.00	0.09	0.10	0.07	0.05	0.09	0.10	0.13	0.10
Zn	2.65	2.64	2.58	2.54	2.55	2.62	2.55	2.62	2.54	2.58	2.56	2.31	2.50	2.57	2.45	2.56
Hg	0.00	0.00	0.00	0.00	0.00	0.00	0.05	0.00	0.01	0.02	0.00	0.00	0.00	0.00	0.00	0.04
Fe	0.25	0.25	0.23	0.55	0.30	0.25	0.30	0.53	0.26	0.24	0.44	0.40	0.39	0.47	0.73	0.60
Total	99.30	99.85	99.21	99.27	98.57	98.35	98.17	100.29	99.30	98.93	99.60	98.98	98.65	100.08	99.90	98.35
% atoms	13.00	13.00	13.00	13.00	13.00	13.00	13.00	13.00	13.00	13.00	13.00	13.00	13.00	13.00	13.00	13.00
As	3.57	3.54	3.67	3.27	3.18	1.90	2.15	3.24	2.06	1.99	2.04	2.78	2.13	2.17	2.06	1.86
S	13.00	13.00	13.00	13.00	13.00	13.00	13.00	13.00	13.00	13.00	13.00	13.00	13.00	13.00	13.00	13.00
Sb	0.37	0.46	0.36	0.89	0.86	2.12	1.89	0.97	2.06	2.09	2.07	1.27	1.92	1.88	1.91	2.11
Bi	0.01	0.01	0.01	0.01	0.00	0.01	0.01	0.01	0.01	0.01	0.00	0.01	0.01	0.00	0.01	0.01
Cu	10.59	10.67	10.65	10.66	10.58	10.53	10.43	10.74	10.79	10.79	10.71	10.51	10.51	10.67	10.55	10.46
Ag	0.00	0.00	0.01	0.00	0.00	0.01	0.01	0.00	0.01	0.01	0.01	0.01	0.01	0.01	0.02	0.01
Zn	0.59	0.59	0.58	0.59	0.58	0.62	0.60	0.60	0.61	0.62	0.61	0.53	0.59	0.60	0.57	0.61
Hg	0.00	0.00	0.00	0.00	0.00	0.00	0.00	0.00	0.00	0.00	0.00	0.00	0.00	0.00	0.00	0.00
Fe	0.07	0.06	0.06	0.15	0.08	0.07	0.08	0.14	0.07	0.07	0.12	0.11	0.11	0.13	0.20	0.17
Total	28.20	28.33	28.34	28.56	28.29	28.26	28.17	28.70	28.61	28.58	28.58	28.22	28.27	28.47	28.31	28.22
As+Sb+Bi	3.95	4.00	4.04	4.16	4.05	4.03	4.05	4.21	4.13	4.08	4.12	4.07	4.06	4.05	3.98	3.98
Hg+Fe+Zn+Ag	0.66	0.66	0.65	0.74	0.67	0.70	0.70	0.75	0.70	0.70	0.74	0.65	0.71	0.74	0.79	0.79
Cu+Hg+Fe+Zn+Ag	11.25	11.33	11.30	11.40	11.24	11.23	11.13	11.48	11.48	11.50	11.46	11.16	11.22	11.42	11.34	11.25

Representative EMPA analyses of fahlores

Sample number	S94-34.35 C8-2	S94-34.35 C8-3	S94-34.35 C9-1	S94-34.35 C9-2	S94-34.35 C9-3	S94-34.35 C9-4	S94-34.35 C9-5	S94-34.35 C9-6	S94-34.35 C9-7	S94-34.35 C9-8	S94-34.35C 10-1	S94-34.35 -1	S94-34.35C 11-1	S94-34.35C 12-2	S94-34.35C 12-1	S94-34.35C 13-3	A49-90.65 --1
As	8.35	10.79	8.24	12.42	10.19	13.23	14.71	8.09	10.28	8.07	11.70	8.12	17.20	17.30	6.77	7.44	4.44
S	26.53	27.25	26.51	27.12	27.13	27.00	27.94	26.50	27.09	26.62	27.30	26.57	28.51	28.62	27.39	26.63	26.01
Sb	17.30	14.49	18.60	13.12	16.07	10.73	9.23	18.77	15.07	18.03	13.28	18.18	5.82	5.73	19.83	19.24	23.64
Bi	0.11	0.19	0.11	0.09	0.11	0.09	0.03	0.09	0.10	0.10	0.15	0.04	0.13	0.09	0.08	0.11	0.17
Cu	42.30	43.85	41.93	45.15	44.61	45.47	46.47	43.92	44.31	42.27	44.65	42.16	46.64	48.33	42.96	43.12	42.88
Ag	0.13	0.10	0.12	0.06	0.14	0.05	0.07	0.13	0.07	0.18	0.10	0.11	0.03	0.05	0.16	0.16	0.15
Zn	2.57	2.55	2.49	2.40	2.55	2.29	2.31	2.52	2.51	2.52	2.59	2.49	2.21	2.28	2.58	2.63	2.53
Hg	0.00	0.00	0.03	0.00	0.03	0.00	0.00	0.01	0.00	0.00	0.00	0.00	0.00	0.00	0.00	0.02	0.29
Fe	0.56	0.56	0.22	0.12	0.19	0.19	0.20	0.25	0.64	0.57	0.35	0.73	1.21	0.15	0.14	0.54	0.28
Total	97.9	99.8	98.3	100.5	101.0	99.1	100.9	100.3	100.1	98.4	100.1	98.4	101.8	102.6	99.9	99.9	100.4
% atoms	13.00	13.00	13.00	13.00	13.00	13.00	13.00	13.00	13.00	13.00	13.00	13.00	13.00	13.00	13.00	13.00	13.00
As	1.75	2.20	1.73	2.55	2.09	2.73	2.93	1.70	2.11	1.69	2.38	1.70	3.36	3.36	1.38	1.55	0.95
S	13.00	13.00	13.00	13.00	13.00	13.00	13.00	13.00	13.00	13.00	13.00	13.00	13.00	13.00	13.00	13.00	13.00
Sb	2.23	1.82	2.40	1.66	2.03	1.36	1.13	2.42	1.90	2.32	1.67	2.34	0.70	0.69	2.48	2.47	3.11
Bi	0.01	0.01	0.01	0.01	0.01	0.01	0.00	0.01	0.01	0.01	0.01	0.00	0.01	0.01	0.01	0.01	0.01
Cu	10.46	10.55	10.37	10.92	10.78	11.04	10.91	10.87	10.73	10.41	10.73	10.41	10.73	11.07	10.29	10.62	10.81
Ag	0.02	0.01	0.02	0.01	0.02	0.01	0.01	0.02	0.01	0.03	0.01	0.02	0.00	0.01	0.02	0.02	0.02
Zn	0.62	0.60	0.60	0.56	0.60	0.54	0.53	0.61	0.59	0.60	0.60	0.60	0.49	0.51	0.60	0.63	0.62
Hg	0.00	0.00	0.00	0.00	0.00	0.00	0.00	0.00	0.00	0.00	0.00	0.00	0.00	0.00	0.00	0.00	0.02
Fe	0.16	0.15	0.06	0.03	0.05	0.05	0.05	0.07	0.18	0.16	0.09	0.20	0.32	0.04	0.04	0.15	0.08
Total	28.24	28.35	28.19	28.73	28.58	28.74	28.56	28.69	28.53	28.22	28.50	28.27	28.61	28.68	27.81	28.46	28.63
As+Sb+ Bi	3.99	4.04	4.14	4.21	4.13	4.09	4.06	4.13	4.02	4.01	4.06	4.05	4.06	4.05	3.86	4.04	4.07
Hg+Fe +Zn+Ag	0.79	0.76	0.68	0.60	0.67	0.60	0.59	0.70	0.78	0.79	0.71	0.82	0.81	0.55	0.66	0.81	0.75
Cu+Hg+ Fe+Zn+ Ag	11.25	11.32	11.05	11.52	11.46	11.64	11.50	11.57	11.50	11.20	11.44	11.22	11.54	11.63	10.95	11.43	11.56

APPENDIX E

LA-ICP-MS in pyrite

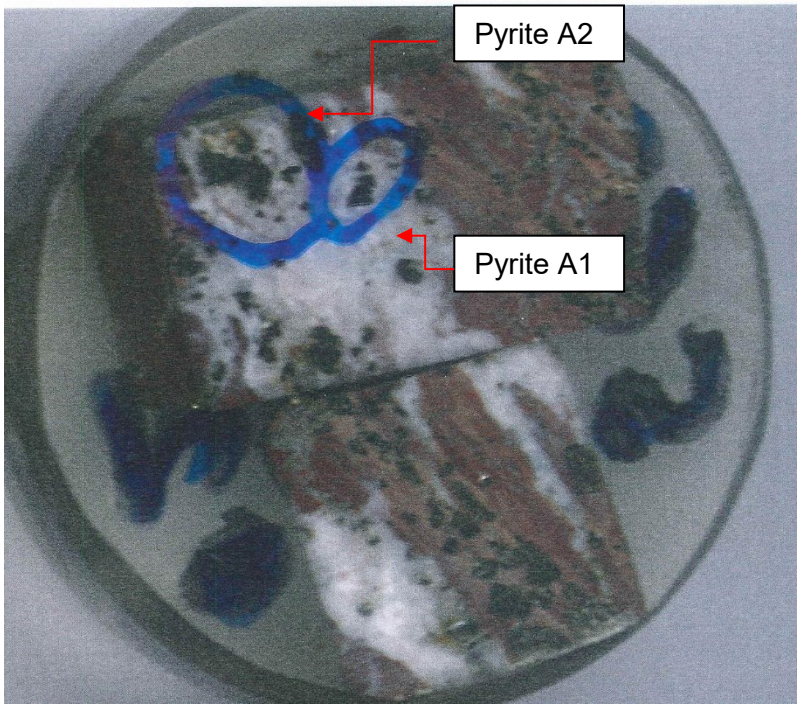

Sample Code: S69-02 or S69-25
Sample Re-code: A

Pyrite A1

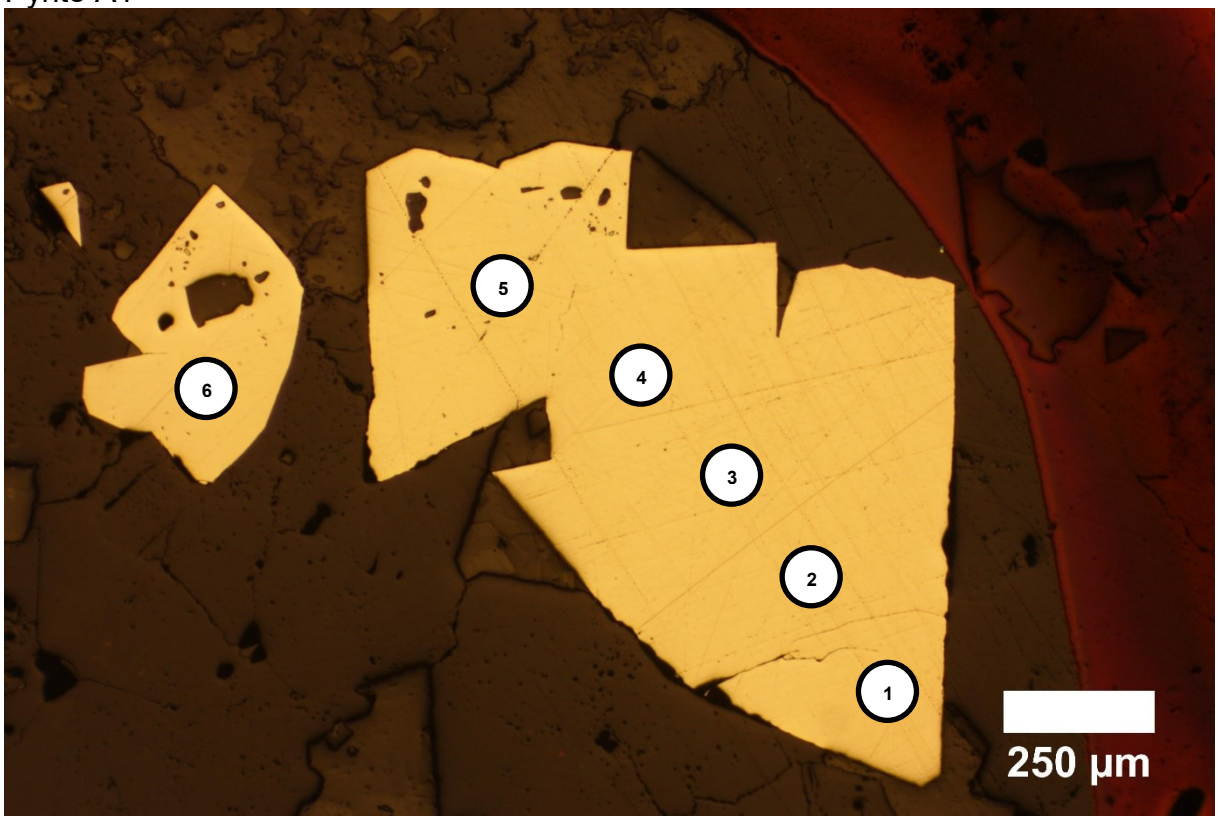

Point for ablation: A1-1, A1-2, A1-3, A1-4, A1-5, A1-6
Pyrite A2

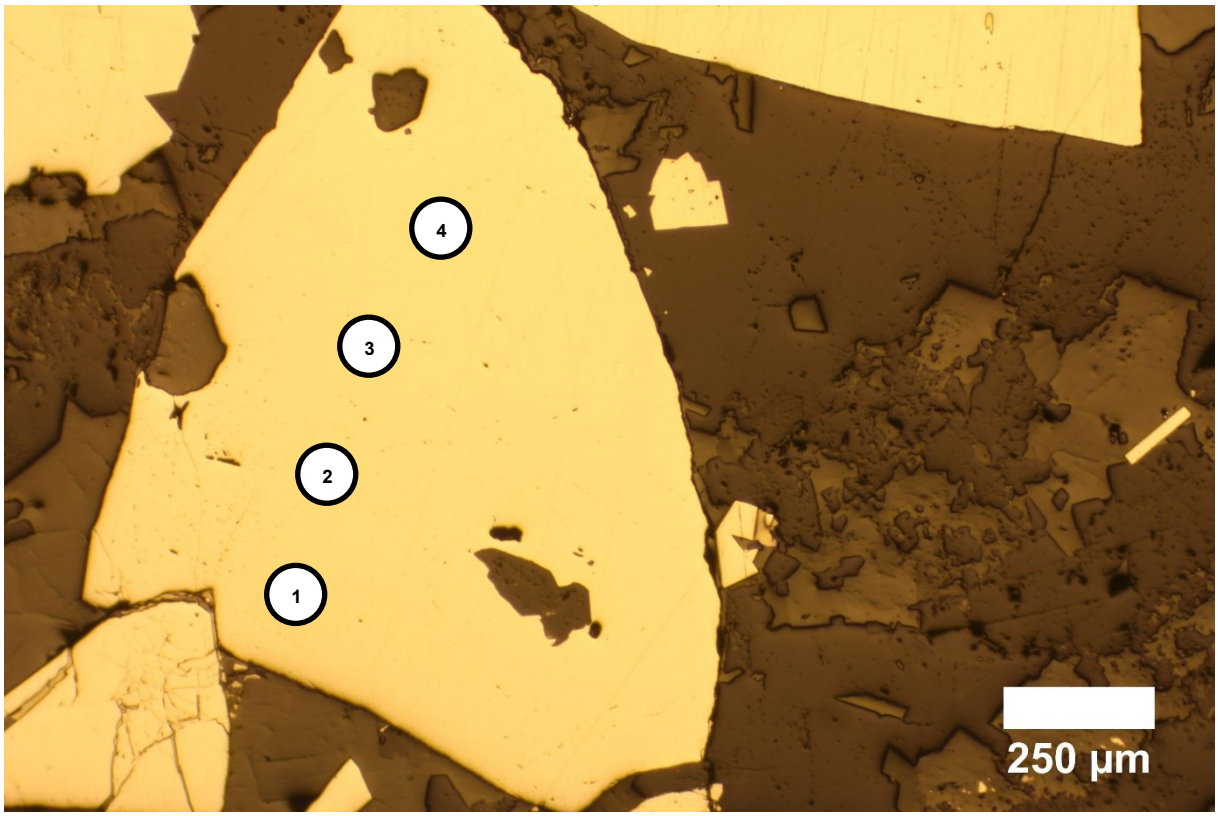

Point for ablation: A2-1, A2-2, A2-3, A2-4

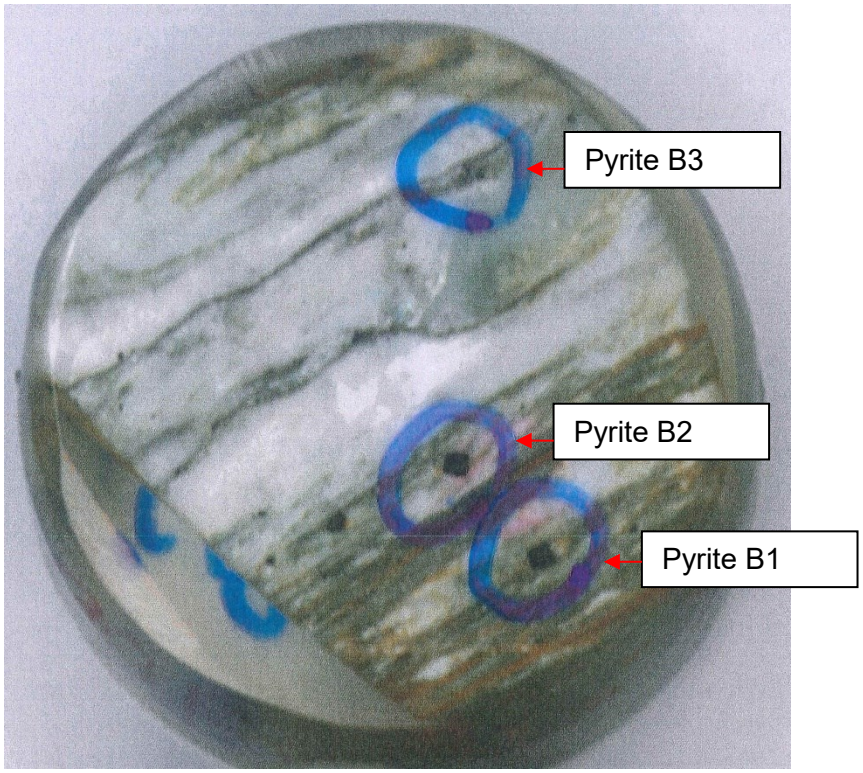

Sample Code: S68-107
Sample Re-code: B

Pyrite B1

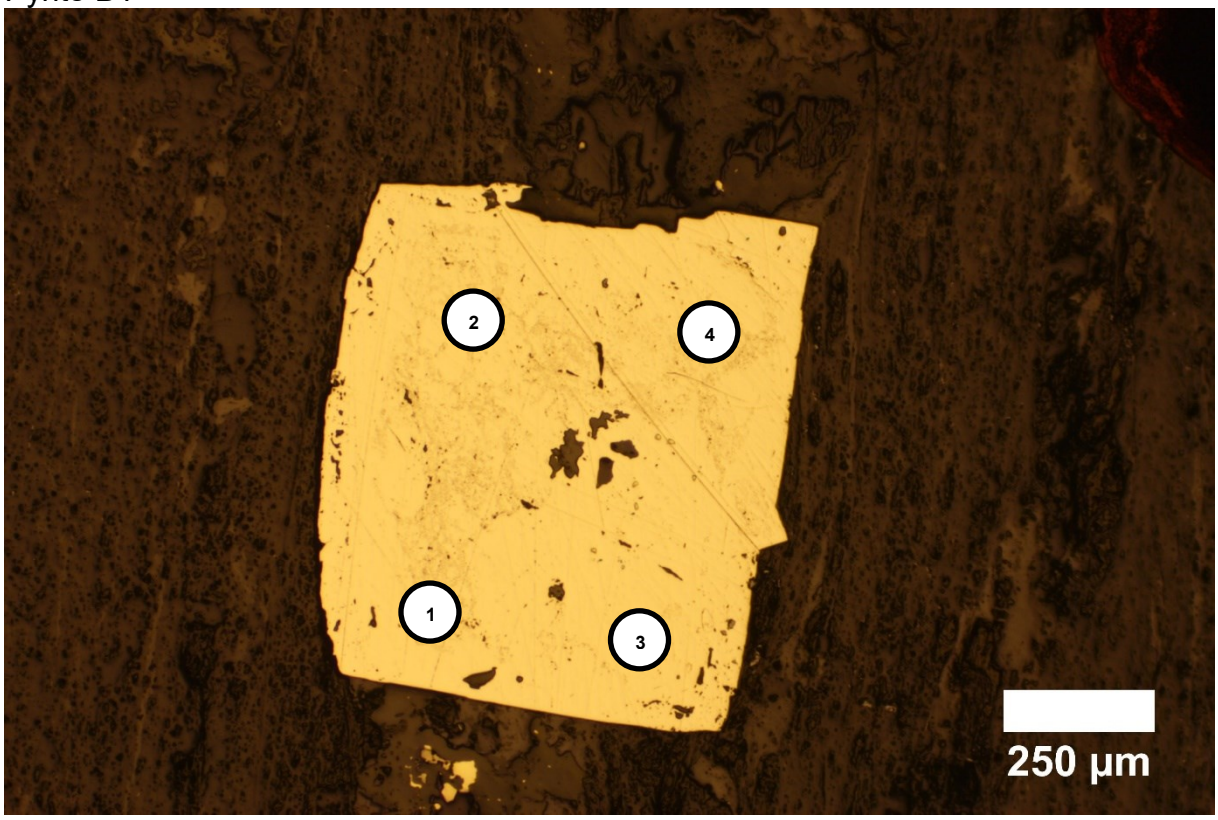

Point for ablation: B1-1, B1-2, B1-3, B1-4

Pyrite B2

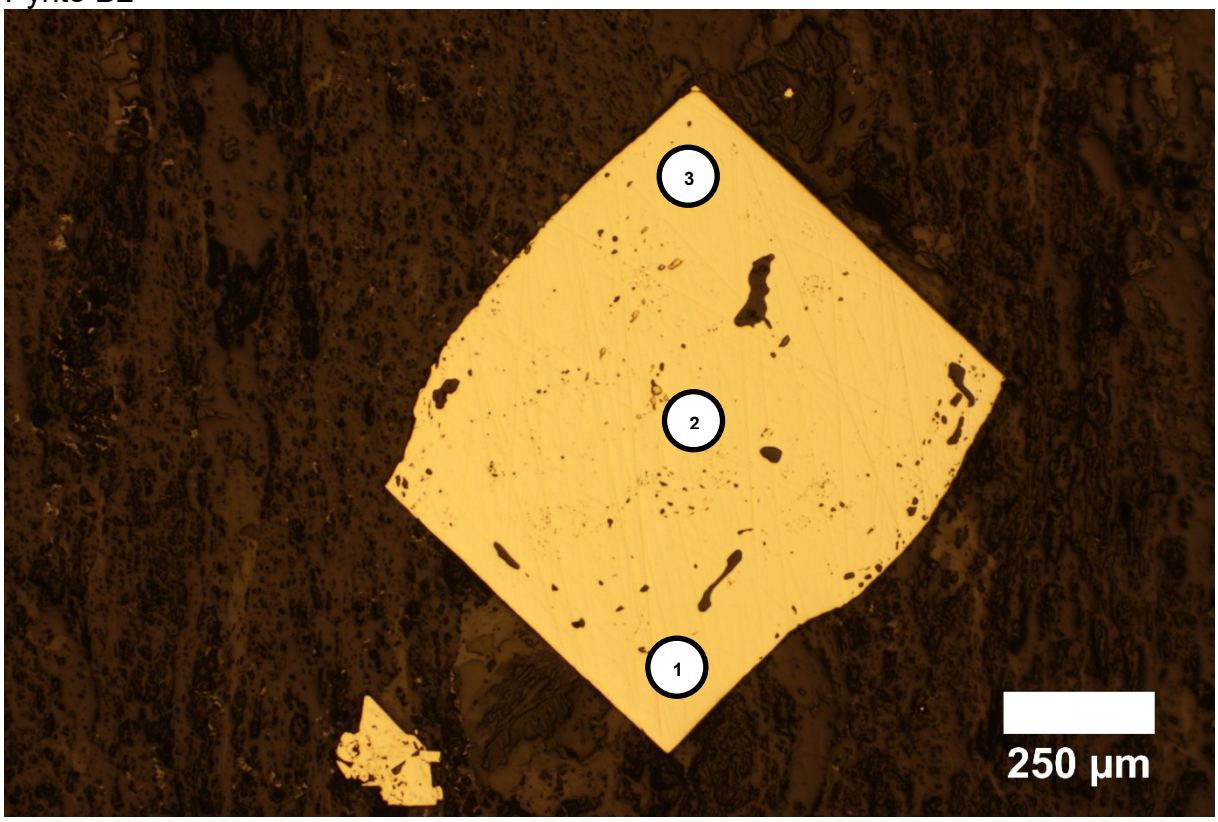

Point for ablation: B2-1, B2-2, B2-3

Pyrite B3

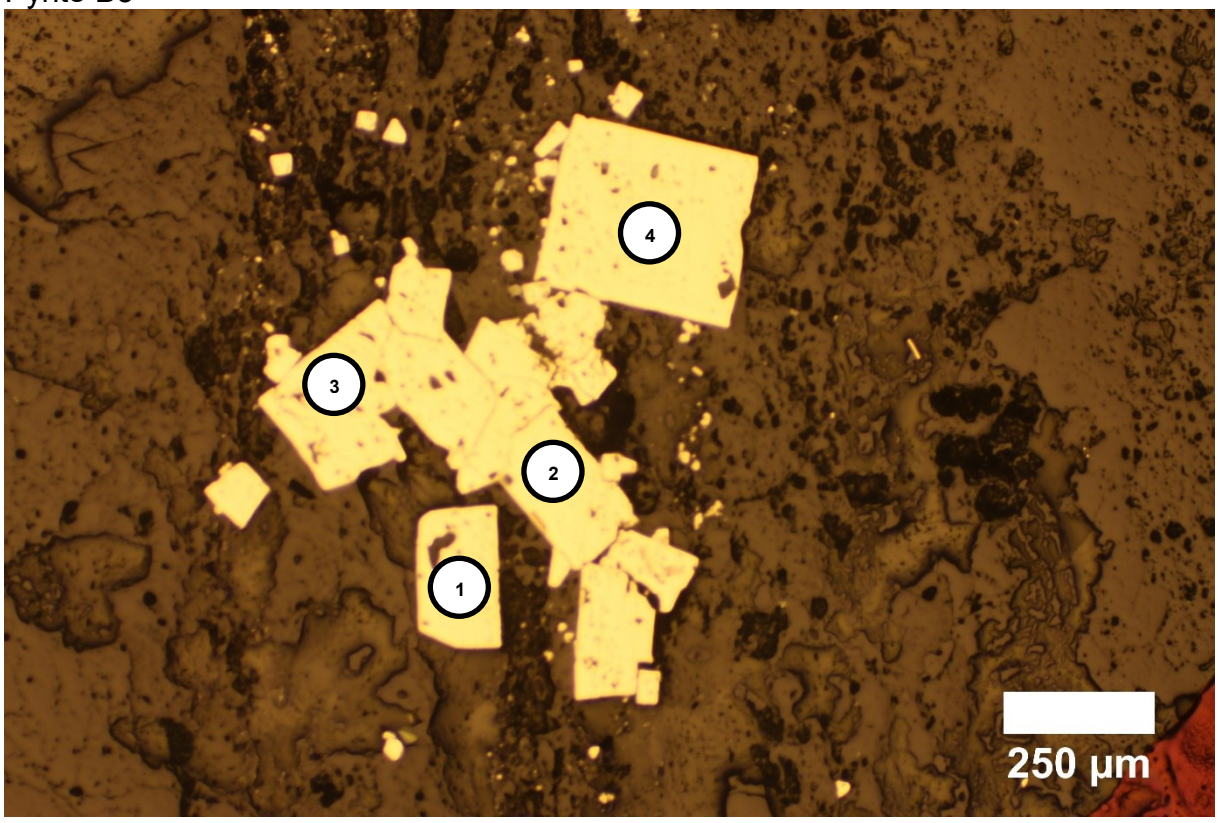

Point for ablation: B3-1, B3-2, B3-3, B3-4

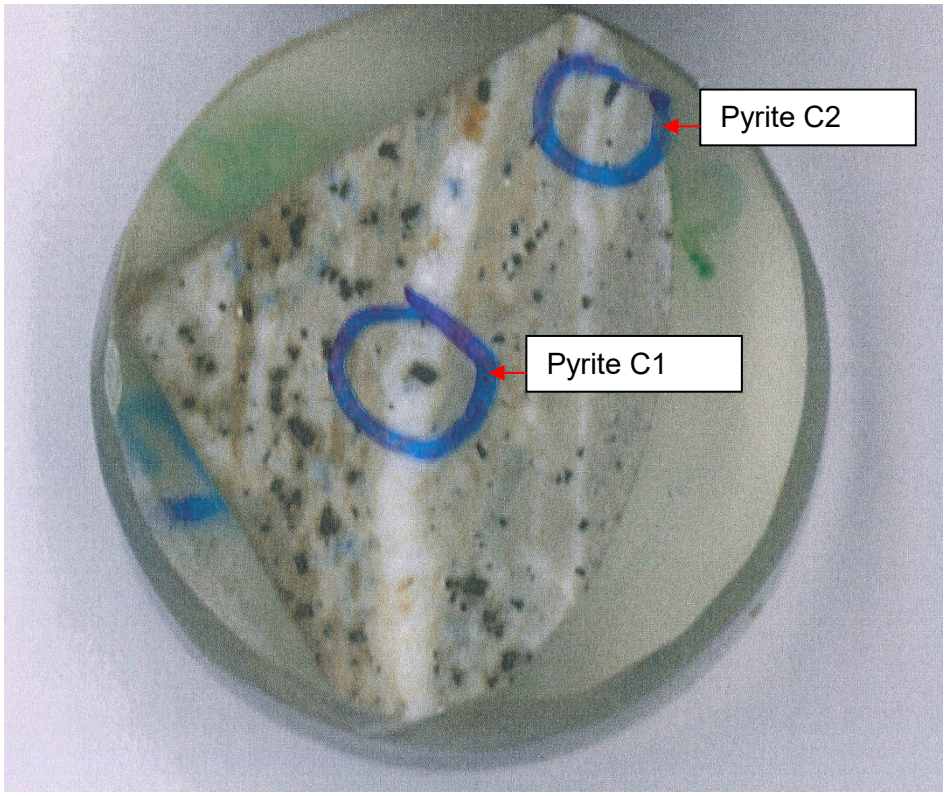

Sample Code: S68-140.20
Sample Re-code: C

Pyrite C1

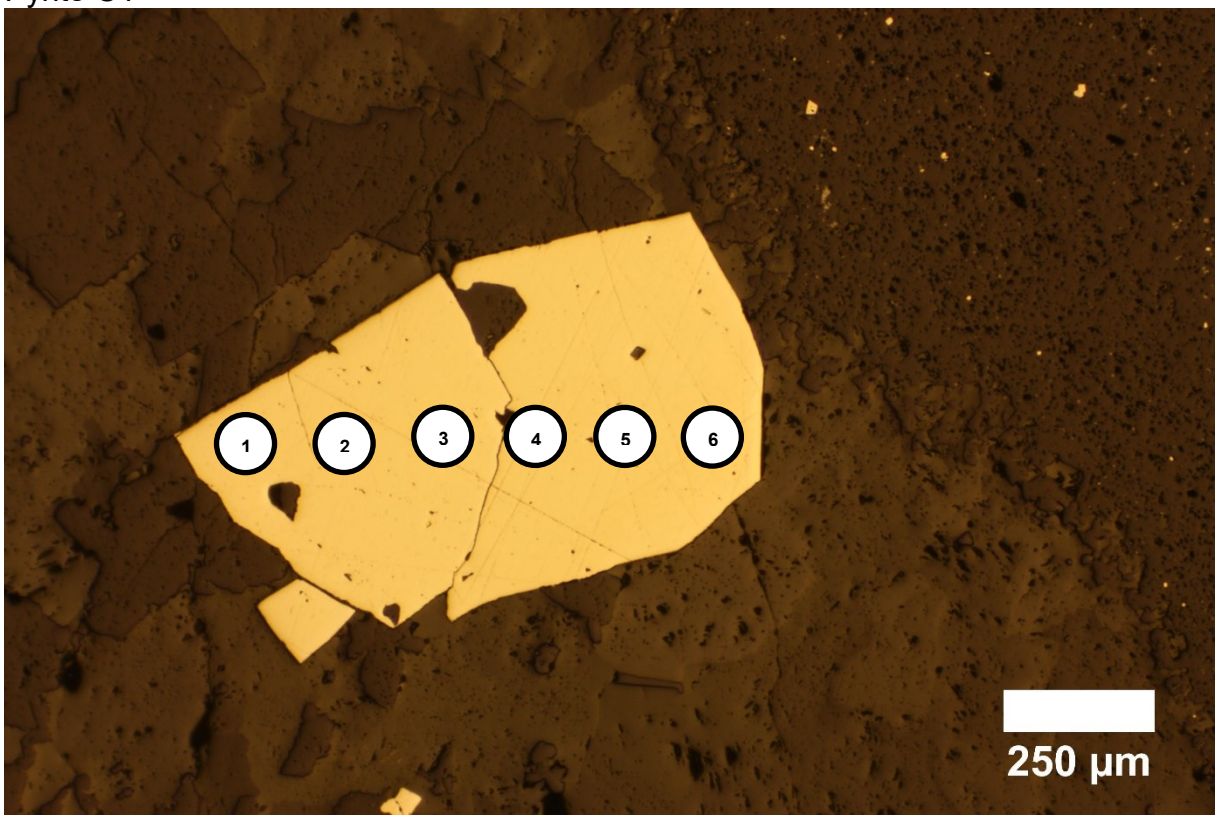

Point for ablation: C1-1, C1-2, C1-3, C1-4, C1-5, C1-6

Pyrite C2

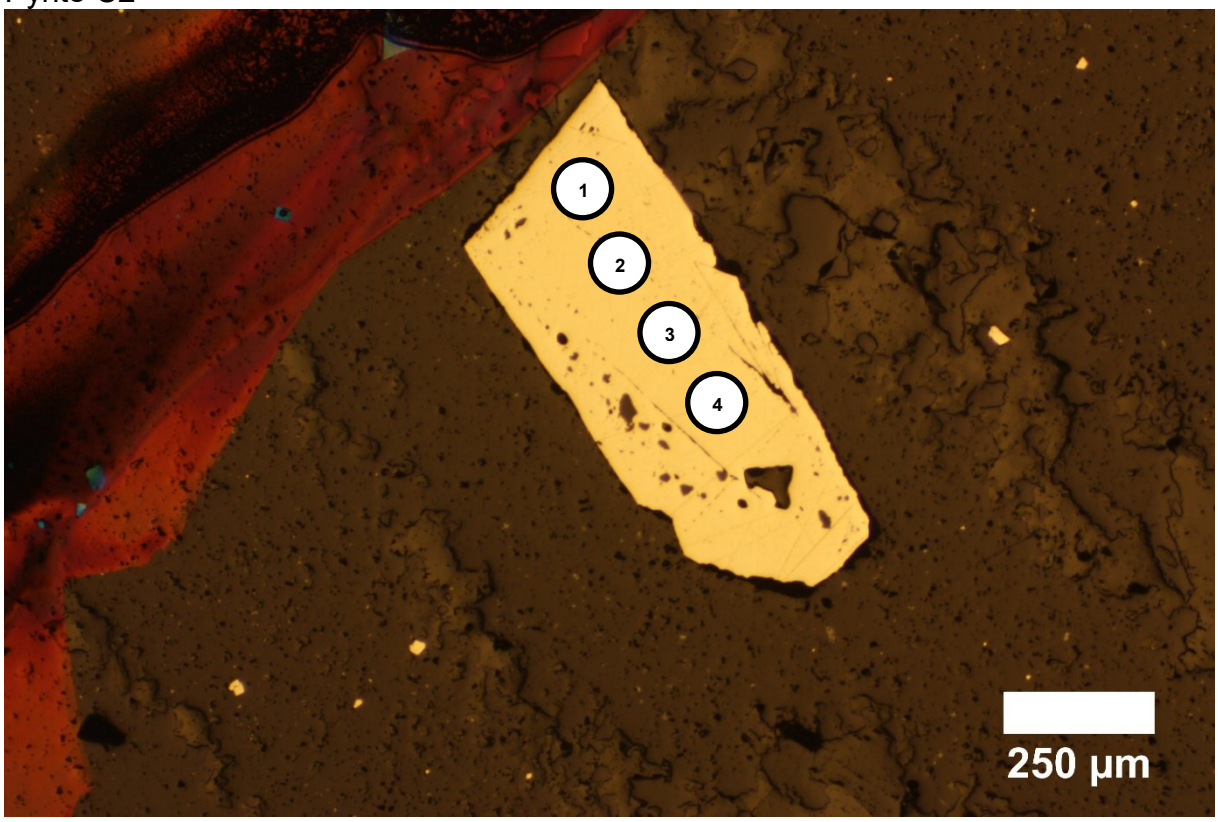

Point for ablation: C2-1, C2-2, C2-3, C2-4

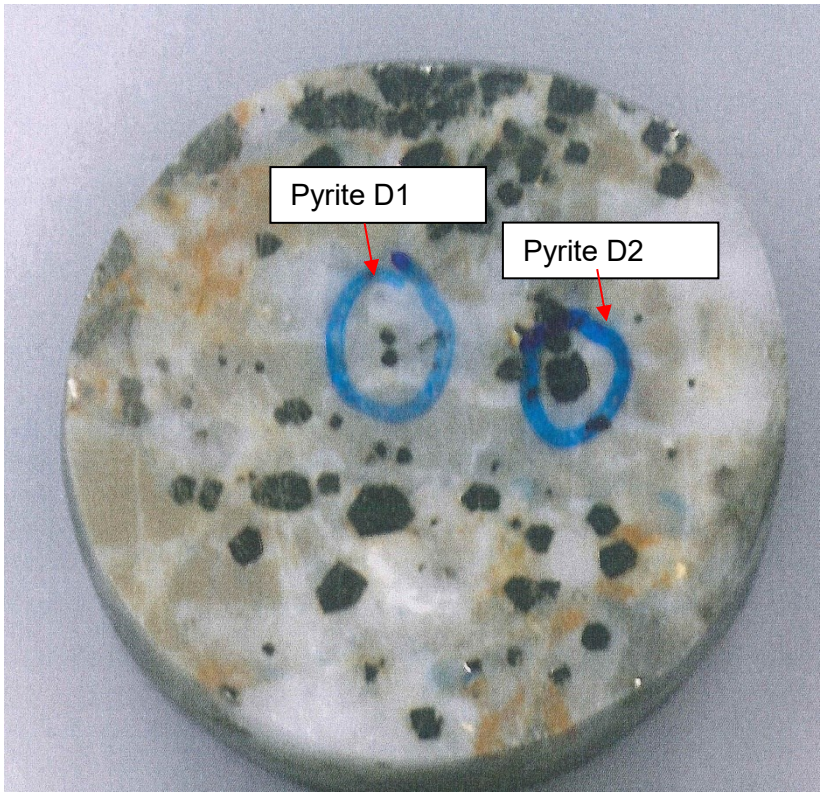

Sample Code: 11 – S50-33.90
Sample Re-code: D

Pyrite D1

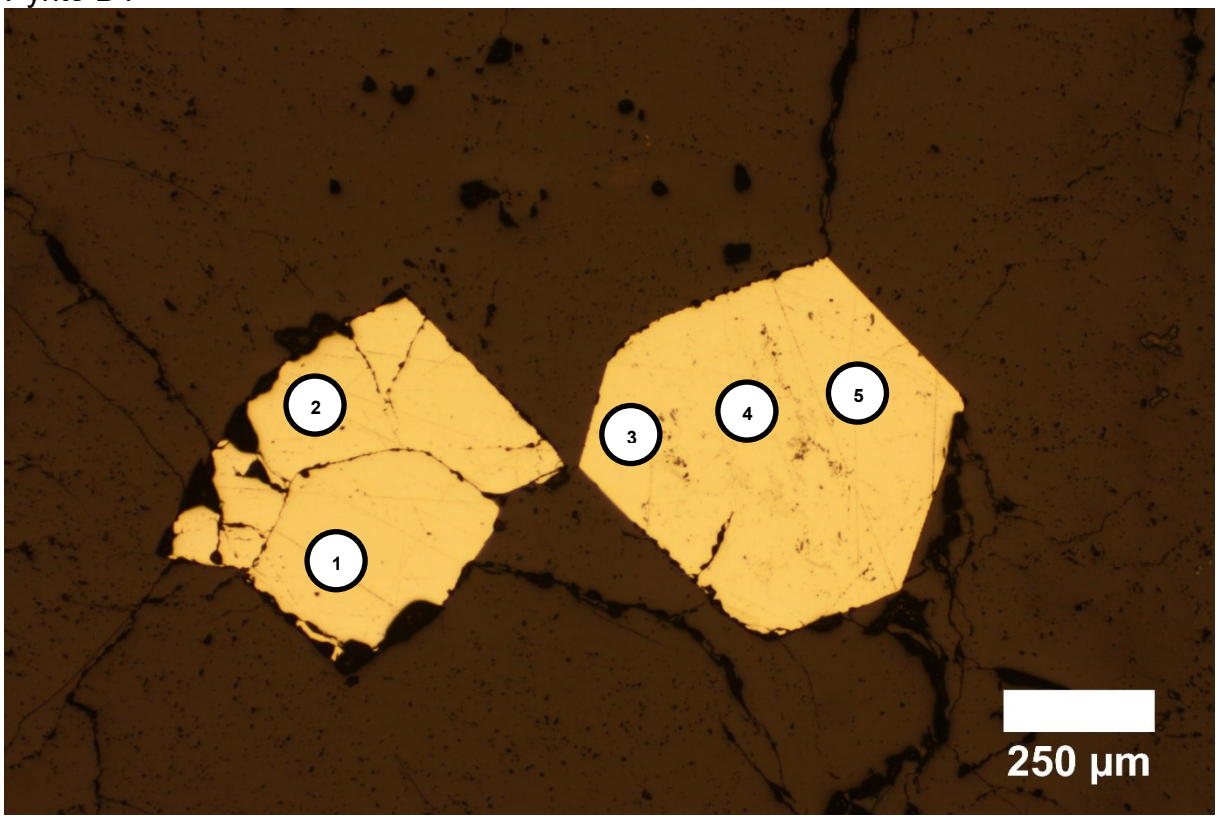

Point for ablation: D1-1, D1-2, D1-3, D1-4, D1-5

Pyrite D2

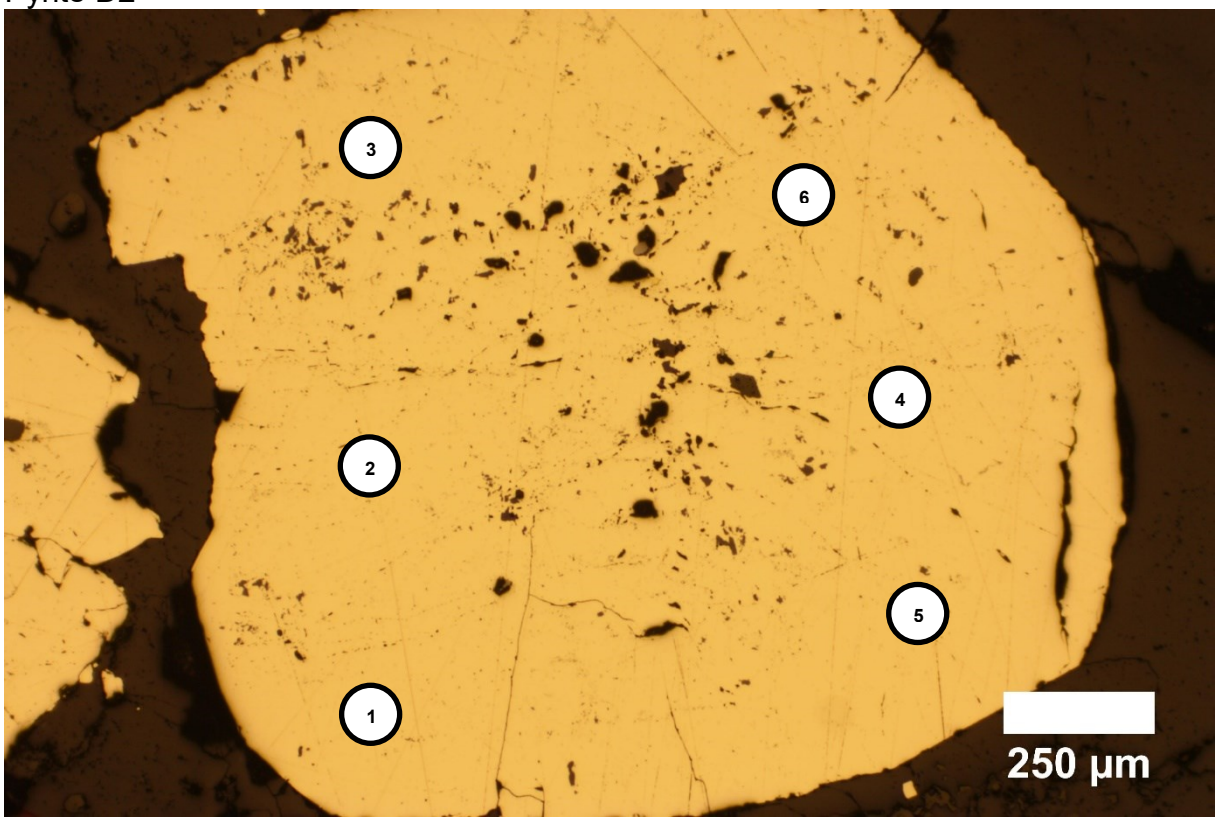

Point for ablation: D2-1, D2-2, D2-3, D2-4, D2-5, D2-6

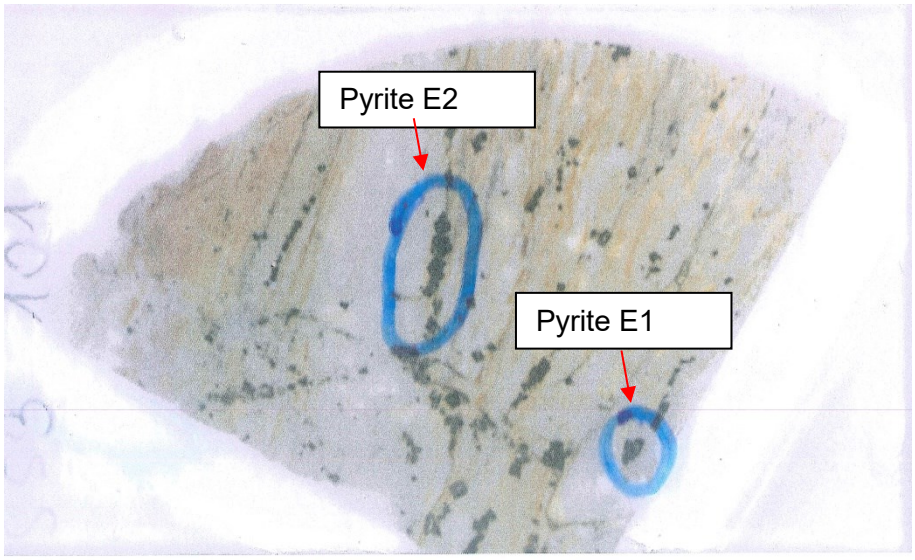

Sample Code: S53-101
Sample Re-code: E

Pyrite E1

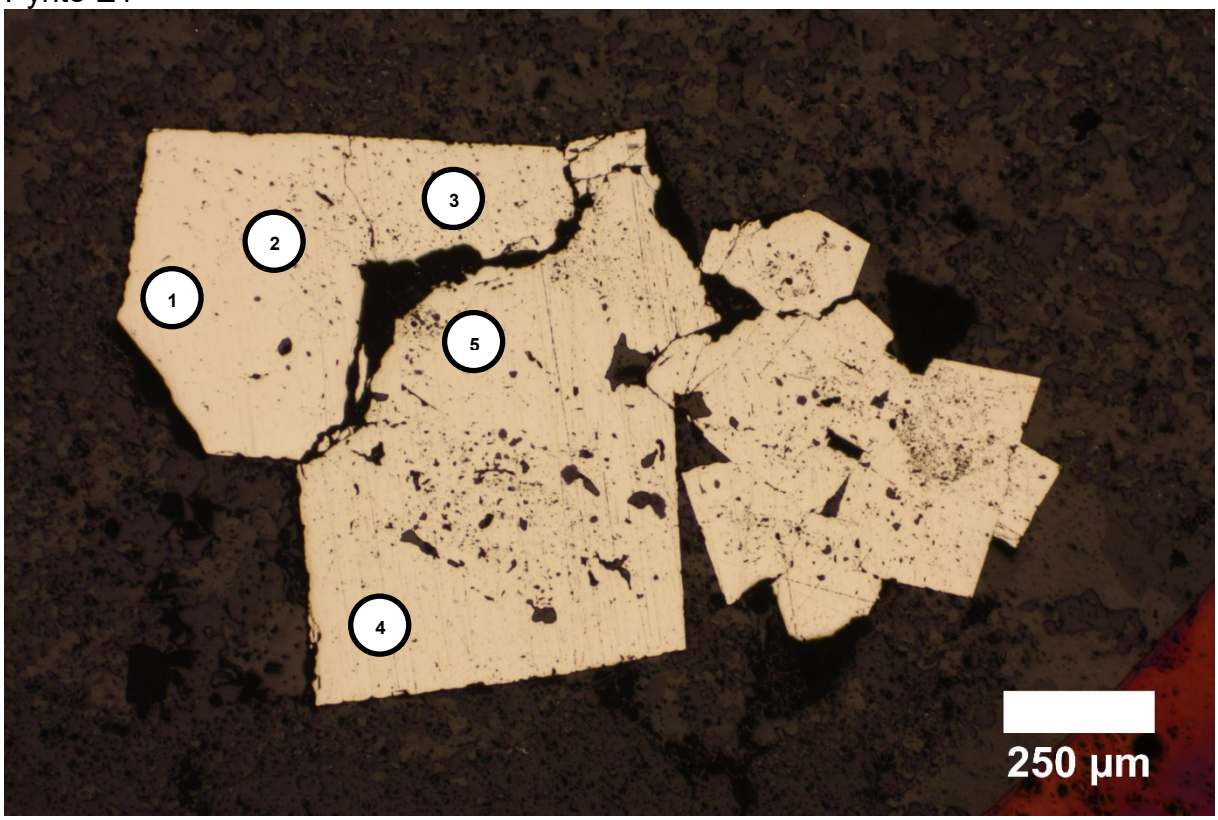

Point for ablation: E1-1, E1-2, E1-3, E1-4, E1-5

Pyrite E2

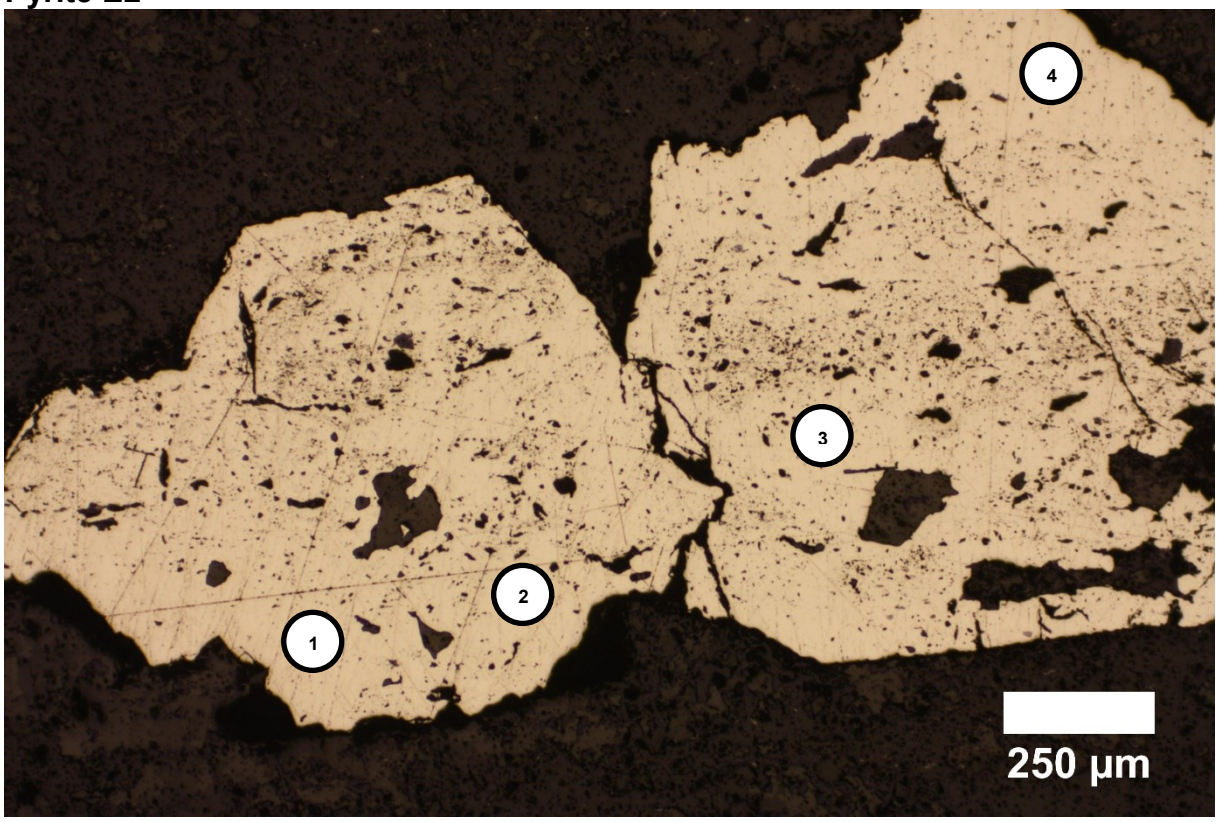

Point for ablation: E2-1, E2-2, E2-3, E2-4

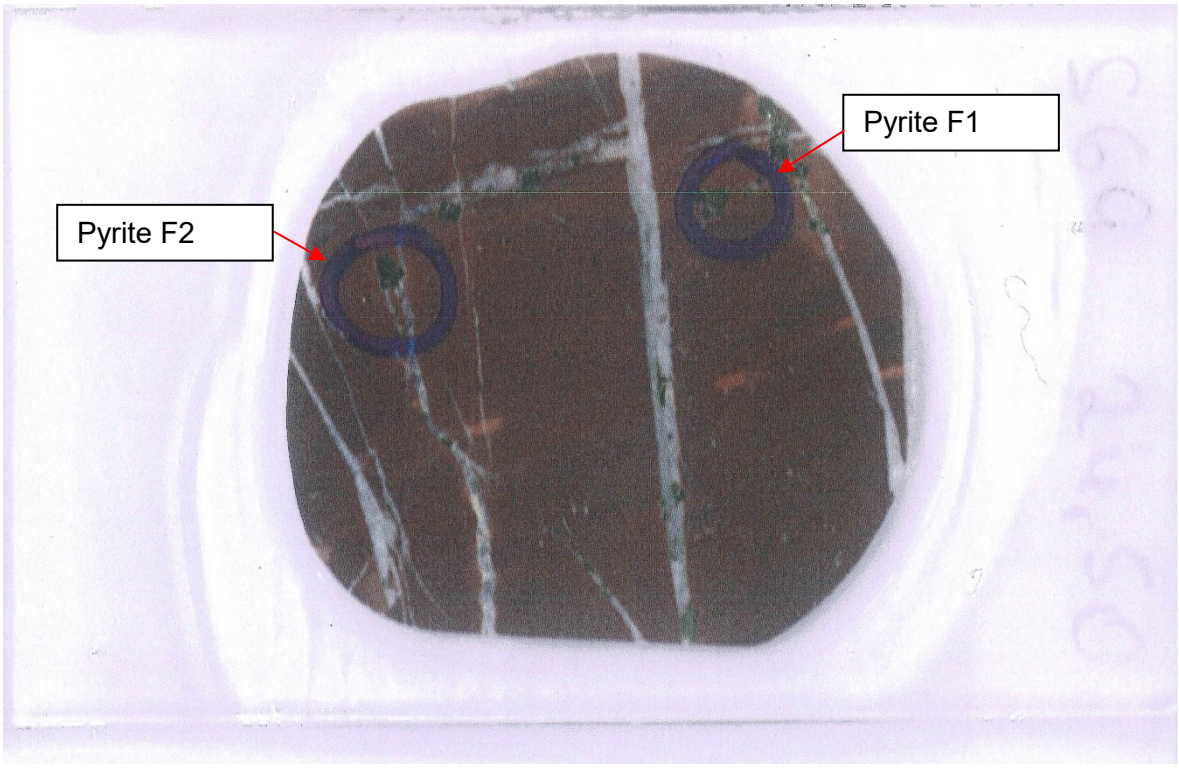

Sample Code: S69-2450
Sample Re-code: F

Pyrite F1

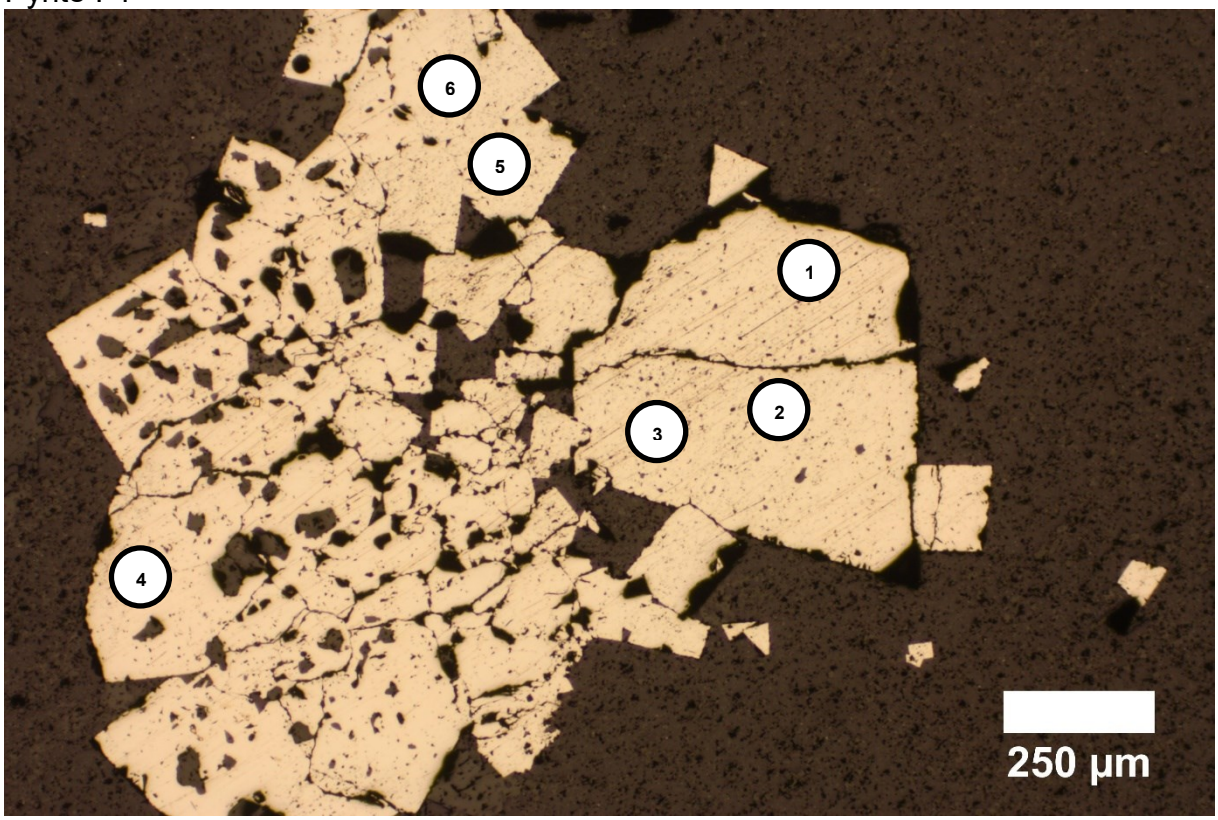

Point for ablation: F1-1, F1-2, F1-3, F1-4, F1-5, F1-6

Pyrite F2

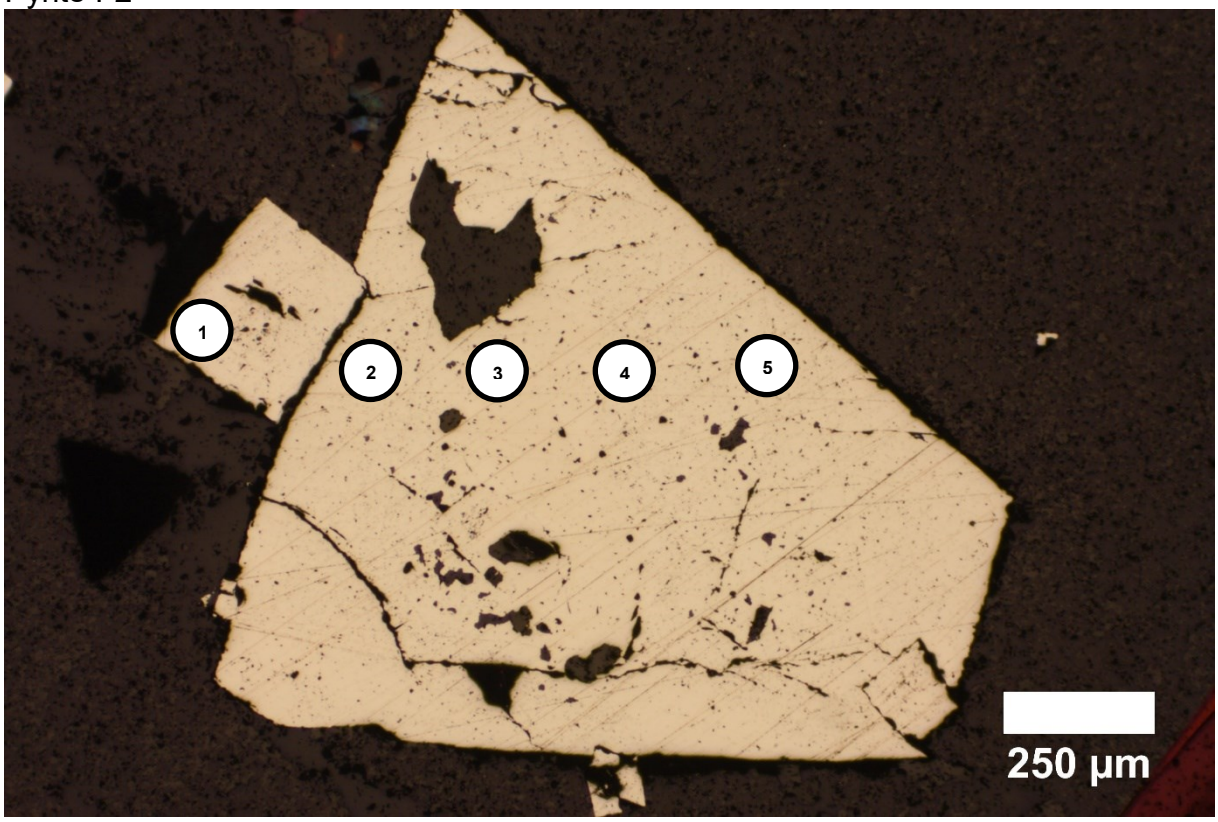

Point for ablation: F2-1, F2-2, F2-3, F2-4, F2-5

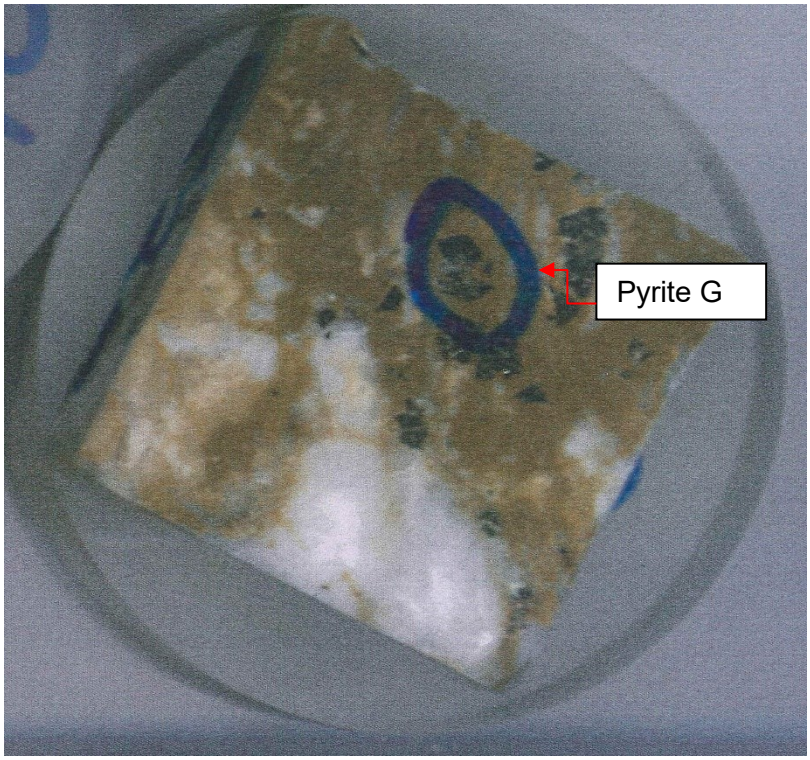

Sample Code: S53-103
Re-code: G

Pyrite G

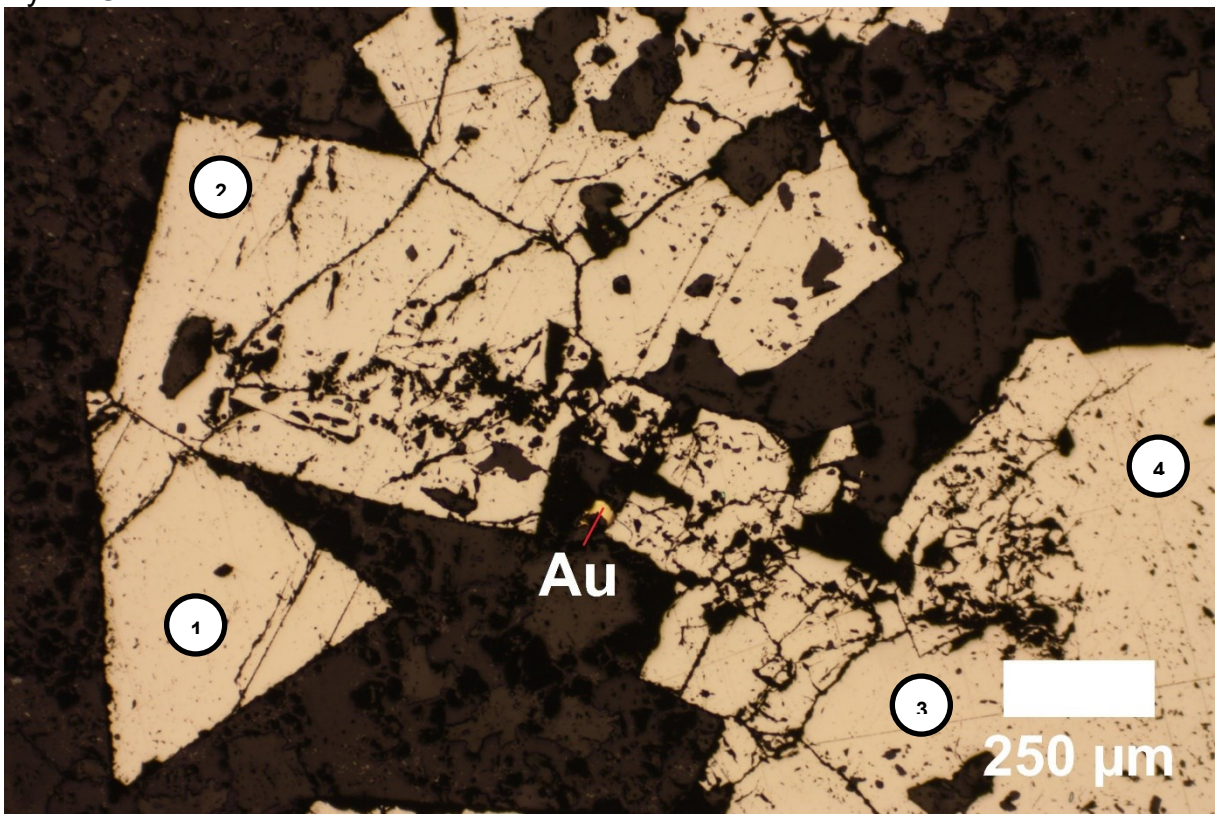

Point for ablation: G1, G2, G3, G4

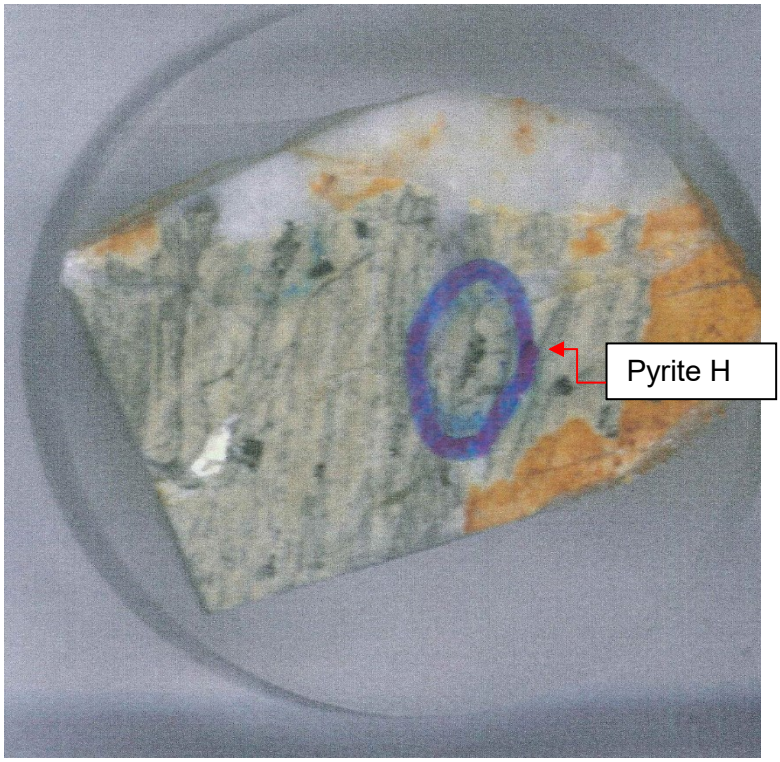

Sample Code: ONG-01
Re-code: H

Pyrite H

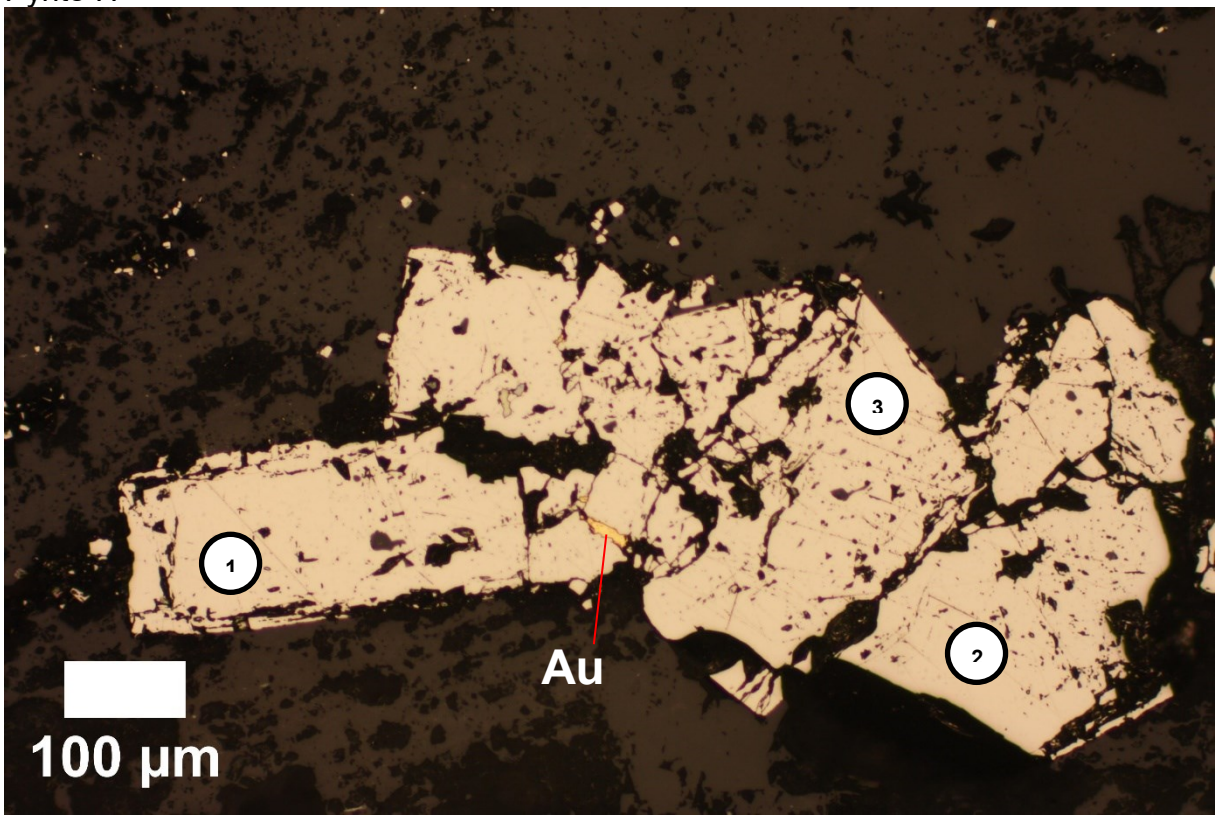

Point for ablation: H1, H2, H3

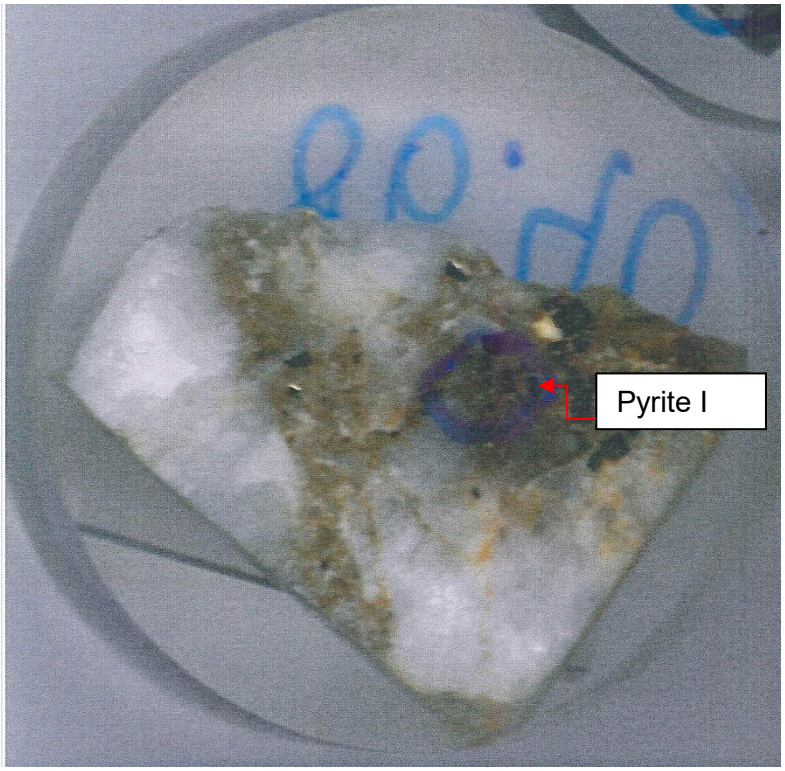

Sample Code: A198-86.40
Re-code: I

Pyrite I1

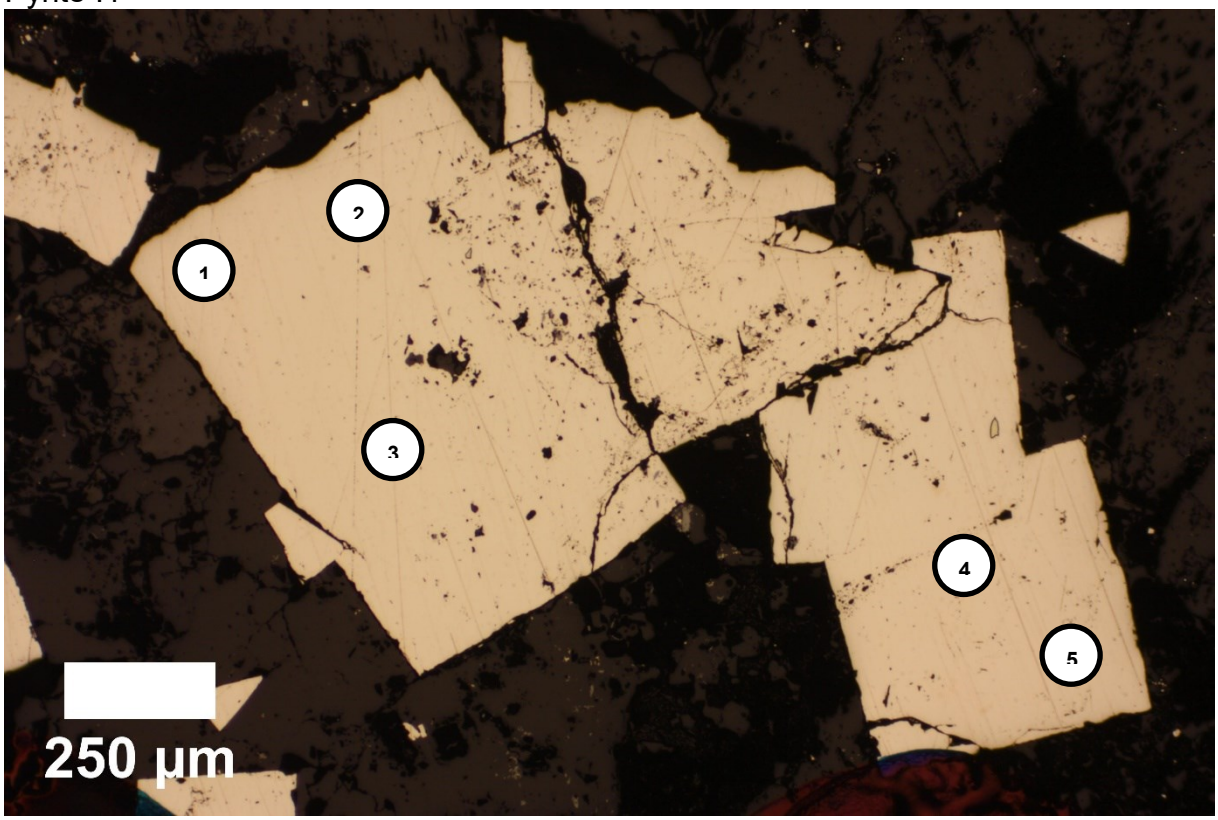

Point for ablation: I1,I2, I3, I4, I5

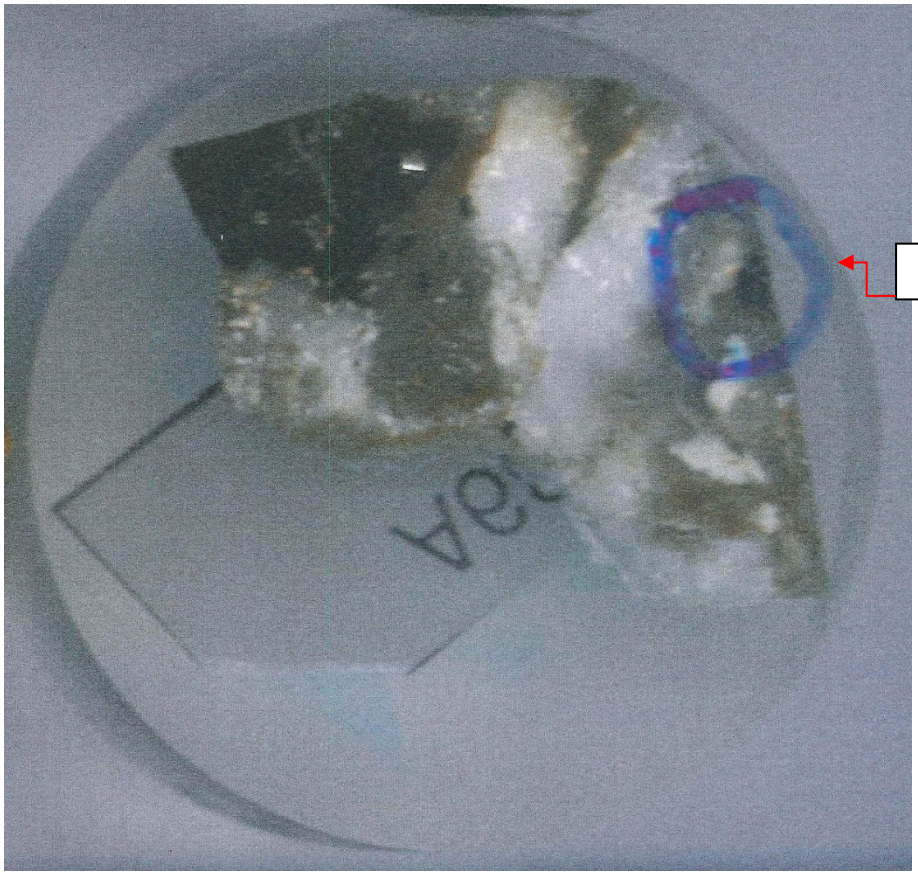

Sample Code: A685-20

Re-code: J

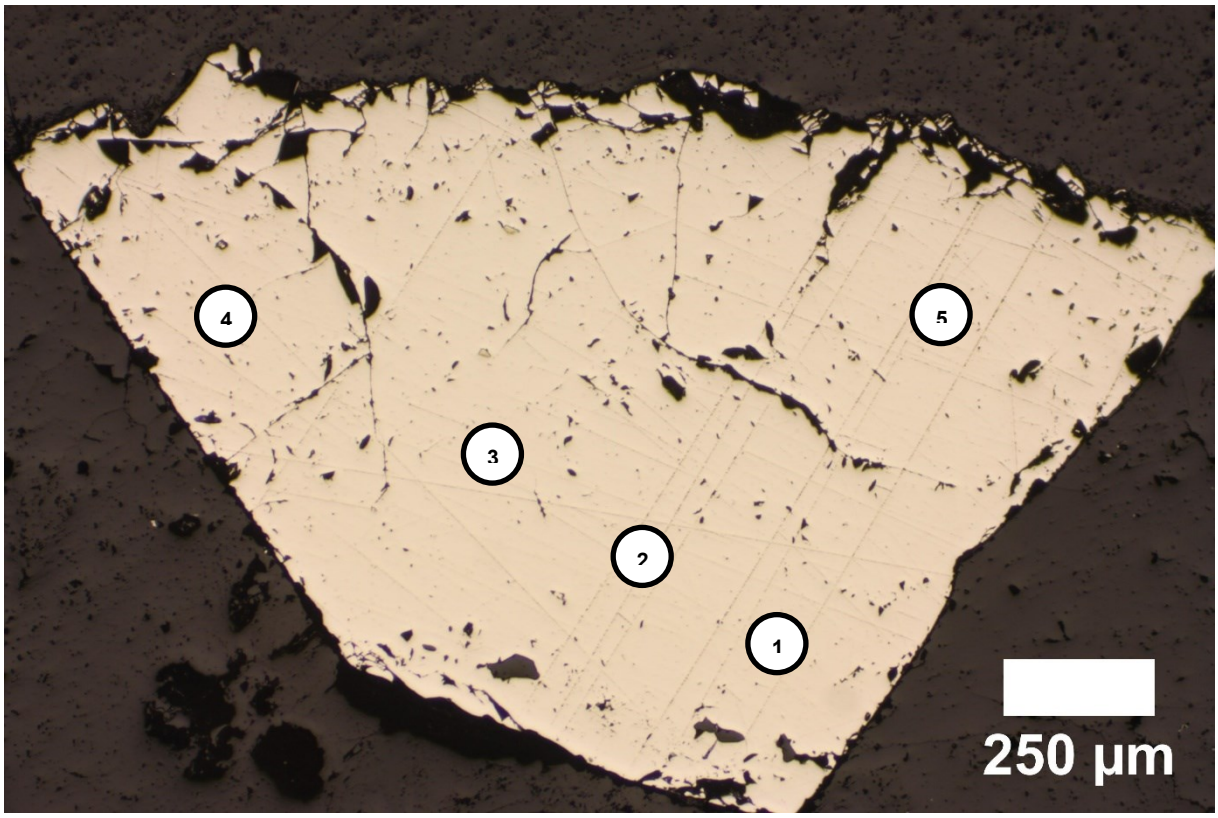

Point for ablation: J1, J2, J3, J4, J5.

LA-ICP-MS in pyrite (1)

Source file	^{59}Co ppm	SD (2σ)	^{61}Ni ppm	SD (2σ)	^{65}Cu ppm	SD (2σ)	^{66}Zn ppm	SD (2σ)	^{75}As ppm	SD (2σ)	^{82}Se ppm	SD (2σ)
Pyrite2a												
S69-24-50-F2-1	35.4	2.8	546	29	22.67	0.94	2.9	3.4	33.4	0.93	16.82	0.49
S69-24-50-F2-4	8	1.1	5700	430	18.57	0.88	15	20	86.2	6.8	19.46	0.56
S69-24-50-F2-5	2.53	0.12	36.3	3.1	24.6	1.1	0.9	0.53	29.36	0.85	17.17	0.47
S53-101-E1-2	332	19	1339	82	20.6	2.7	3	1.5	21.22	0.37	19.12	0.45
ONG-1-2	33.4	3.4	770	130	26.8	9.1	5.3	3.1	135.2	8	20	1
ONG-1-3	8.8	1.1	542	29	39.4	7.2	4.5	1.6	72.7	6.2	17.95	0.58
Pyrite2b												
S69-24-50-F1-1	2.37	0.29	79	11	50	27	5	4.1	36.46	0.96	18.94	0.54
S69-24-50-F1-2	1.556	0.053	34.5	1.3	82	56	9.2	8.6	54.1	1.8	19.3	0.68
S69-24-50-F1-3	19.6	2.9	6390	580	34.4	1.5	1.93	0.83	88.5	6.8	19.3	0.59
S69-24-50-F1-4	27.12	0.84	466	14	34.9	3.6	3.2	1.2	47.3	2.5	17.26	0.62
S69-24-50-F1-5	9.18	0.82	850	150	30.5	1.7	2.9	1.3	44.4	1.3	21.54	0.71
S69-24-50-F1-6	33.3	2.2	970	110	83.9	9.7	6.3	1.7	53.7	2.1	18.78	0.58
S69-24-50-F2-2	2.51	0.1	51.8	3.6	22.49	0.9	0.35	0.44	31.13	0.73	15.55	0.4
S69-24-50-F2-3	2150	140	23490	750	185	94	4	4.6	359	23	15.96	0.5
S53-101-E1-1	255	23	1411	96	3.67	0.39	0.36	0.75	11.08	0.23	20.58	0.56
S53-101-E1-3	542	20	2043	42	35.7	4.1	0.81	0.58	35.5	2	18.7	0.47
S53-101-E1-4	312	16	1013	39	14	18	3.6	5.3	12.19	0.32	19.74	0.52
S53-101-E1-5	195	29	576	95	66	14	128	31	50.7	6	18.26	0.68
S53-101-E2-1	133.8	6.3	1455	24	5.83	0.4	0.07	0.85	23.12	0.82	15.1	0.47
S53-101-E2-2	26.7	2.4	326.4	9.3	5.13	0.72	1.5	3.2	9.77	0.42	13.22	0.4
S53-101-E2-3	408	22	2070	130	9	1.9	2.7	2.5	29.7	2	27.23	0.74
S53-101-E2-4	8.46	0.78	139	11	3.17	0.13	0.55	0.65	4.83	0.31	10.86	0.38
S68-107-B1-4	114.4	6.9	166.8	6.6	56.4	3.1	2.55	0.58	1290	22	58.11	0.83
S69-25-A1-1	39.3	2.1	314	14	1.39	0.42	11	4.4	40.08	0.86	34.73	0.91
S69-25-A1-2	38.19	0.71	794	17	0.07	0.2	1.69	0.96	35	0.86	18.59	0.64
S69-25-A1-4	109	18	1256	90	193	46	97	26	59	15	18.28	0.86
S69-25-A1-5	560	140	1253	38	22.5	9.3	2.8	1.8	57.8	5.2	26.05	0.83
S69-25-A1-6	32.8	1.8	256	16	3.9	1.1	0.88	0.84	50.4	1.9	19.95	0.77
S69-25-A2-1	28	2.6	1051	35	5.7	1.2	0.2	0.6	30	2.4	24.4	1.2
S69-25-A2-2	80	15	1460	190	2.62	0.21	0.95	0.89	15.9	1.3	27.67	0.8
S69-25-A2-3	1.47	0.11	57	4.8	0.69	0.13	0.07	0.67	8.1	0.2	30.8	0.72
S69-25-A2-4	160.7	6.1	862	31	1.36	0.7	10	13	21.61	0.98	25.24	0.65
ONG-1-1	19.7	1.6	653	52	13.8	1.9	19	12	88.4	5.6	21	0.8
Pyrite3												
S53-103-1	161	14	968	36	6.55	0.6	4.38	0.55	27.84	0.69	22.63	0.5
S53-103-2	69.6	4.5	661	31	74	34	2.66	0.66	11.17	0.22	23.9	0.51
S53-103-3	126	12	486	48	3.68	0.85	2.12	0.43	11.44	0.27	35.37	0.59
S53-103-4	1304	83	2530	120	39.5	9.4	10.7	2	127.6	9.5	27.2	1.4
A685-20-1	1097	36	4820	110	3.7	1.2	4.6	4	240.4	5.4	20.05	0.57
A685-20-2	545	19	3603	64	2.54	0.67	3.1	1.6	196	2.9	21.08	0.45
A685-20-3	265	21	1180	100	1.67	0.42	1.55	0.62	156.1	3	35.49	0.84
A685-20-4	4.27	0.16	332.2	8.2	2.03	0.82	1.1	0.63	160.5	4.4	26.34	0.87
A685-20-5	1.069	0.08	46.4	a	1.7	0.56	1.32	0.48	503	19	24.4	1
S68-107-B1-1	690	47	243.7	9.8	43.4	2.3	2.68	0.96	487	14	41.1	1.3
S68-107-B1-2	89	21	140	22	105.4	1.9	4.57	0.57	1396	30	55.4	1.1
S68-107-B1-3	455	15	258	12	6.4	0.57	1.88	0.88	992	35	56	1.9
S68-107-B2-1	131.1	5.5	73.7	3	1.88	0.2	2	1	2.986	0.094	8.95	0.43
S68-107-B2-2	66.2	5.7	138.6	8.6	250	110	1.81	0.75	100.1	7.5	27.19	0.7
S68-107-B2-3	31.8	3.6	68.4	5.6	7.4	4.4	1.25	0.62	48.2	2.6	20.92	0.88
S68-107-B3-1	1032	35	2900	160	350	120	5.23	0.88	50.9	6	16.37	0.48

Source file	^{59}Co ppm	SD (2σ)	^{61}Ni ppm	SD (2σ)	^{65}Cu ppm	SD (2σ)	^{66}Zn ppm	SD (2σ)	^{75}As ppm	SD (2σ)	^{82}Se ppm	SD (2σ)
S68-107-B3-2	488	20	3930	160	17.7	6.9	1.06	0.58	30.6	1.4	19.23	0.47
S68-107-B3-3	399	23	901	23	19.1	7.7	5.9	1	13.67	0.66	15.34	0.39
S68-107-B3-4	428	21	2284	69	735	81	6.99	0.93	33.5	1.4	22.38	0.91
S68-140-20C1-1	683	60	3980	210	48	13	8.6	3.3	42.8	4.1	18.9	1.1
S68-140-20C1-2	1298	74	7160	430	34	12	193	45	127	15	35.3	1.1
S68-140-20C1-3	639	93	3220	180	9.95	0.92	32	9.6	191	21	37.2	1.5
S68-140-20C1-4	267	76	1970	340	54	20	11	13	168	18	30.1	2.5
S68-140-20C1-5	577	64	1970	120	4.9	1.5	0.11	0.58	307	28	35.67	0.74
S68-140-20C1-6	298	60	1780	360	0.07	0.11	0.07	0.52	91.5	5.6	42.2	0.66
S68-140-20C2-1	308	41	719	36	2.84	0.65	0.07	0.53	34.9	2	33.4	1.7
S68-140-20C2-2	864	80	1306	40	10.5	2.9	0.07	0.61	16.2	1.5	26.9	1.2
S68-140-20C2-3	76.7	9.2	278	11	0.78	0.95	0.07	0.54	11.97	0.8	12.61	0.43
S68-140-20C2-4	210	15	401	12	0.07	0.31	0.07	0.58	36	1.1	43.6	1.4
S50-33.90-D1-1	7.9	0.77	18.5	2.2	0.2	1.3	0.07	0.83	460	100	4.95	0.26
S50-33.90-D1-2	83	13	44	18	2.8	1.4	11	12	1250	200	3.56	0.31
S50-33.90-D1-3	44.8	1.2	55.5	2.5	24	10	2.16	0.91	2165	62	16.11	0.64
S50-33.90-D1-4	134	14	88.8	6.7	44.2	2.2	4.6	1.2	4460	100	32.94	0.71
S50-33.90-D1-5	124.7	8.6	97.5	4.8	16.3	1.3	4.3	1.3	2485	79	22.08	0.86
S50-33.90-D2-1	22.4	1.2	12.1	1.4	2.2	0.32	3.2	1	896	55	7.63	0.43
S50-33.90-D2-2	16.1	1	19.2	1.8	10.37	0.9	2.8	1.2	1992	38	13.3	0.52
S50-33.90-D2-3	32.42	0.79	25.3	1.3	37.3	3	2.4	1.1	5020	110	10.69	0.4
S50-33.90-D2-4	180	15	163	12	14.1	1.1	3.3	1.9	1726	74	5.73	0.25
S50-33.90-D2-5	6.42	0.47	7.61	0.7	8.8	1.1	2.7	1.1	2788	61	13.78	0.47
S50-33.90-D2-6	15.1	1.2	24.35	0.92	24.5	1	2.9	1.1	2421	97	5.5	0.26
A198-86-40-1	145.9	5.9	950	37	2.8	1.1	4	2.2	64.7	1.3	27.77	0.67
A198-86-40-2	7.37	0.53	31.8	2.4	1.08	0.46	3.06	0.9	96.4	1.6	24.48	0.62
A198-86-40-3	17.84	0.81	102.4	5.6	670	160	348	42	117	8.2	23.24	0.58
A198-86-40-4	53.5	7.9	802	48	106	30	79	20	14.6	1.3	17.03	0.49
A198-86-40-5	68.5	1.9	980	24	1.59	0.89	4.42	0.98	52.1	2.1	22.31	0.7

LA-ICP-MS in pyrite (cont)

Source file	^{107}Ag ppm	SD (2σ)	^{121}Sb ppm	SD (2σ)	^{130}Te CPS	SD (2σ)	^{197}Au ppm	SD (2σ)	^{209}Bi ppm	SD (2σ)
Pyrite2a										
S69-24-50-F2-1	2.471	0.085	18.88	0.76	6570	250	0.236	0.014	2.914	0.079
S69-24-50-F2-4	2.725	0.072	17.26	0.38	13190	400	0.289	0.015	4.809	0.097
S69-24-50-F2-5	2.406	0.095	19.37	0.73	6480	200	0.226	0.013	2.68	0.12
S53-101-E1-2	1.23	0.057	5.68	0.23	5950	200	0.18	0.0085	1.819	0.057
ONG-1-2	1.094	0.062	9.65	0.38	6760	640	0.16	0.012	1.061	0.081
ONG-1-3	1.901	0.09	5.62	0.18	3930	220	0.32	0.017	1.865	0.09
Pyrite2b										
S69-24-50-F1-1	3.43	0.076	24.48	0.53	10490	300	0.346	0.017	5.72	0.14
S69-24-50-F1-2	3.739	0.098	24.87	0.56	8350	400	0.371	0.012	4.85	0.11
S69-24-50-F1-3	3.74	0.11	25.29	0.66	13230	720	0.393	0.02	7.95	0.25
S69-24-50-F1-4	3.28	0.16	28.9	1.9	5090	180	0.327	0.02	3.17	0.13
S69-24-50-F1-5	4.02	0.11	28.84	0.82	14800	1200	0.448	0.02	5.81	0.18
S69-24-50-F1-6	4.9	0.27	28.76	0.74	10220	780	1.3	1	4.5	0.14
S69-24-50-F2-2	2.304	0.079	17	0.64	6120	210	0.221	0.011	2.62	0.13
S69-24-50-F2-3	2.49	0.85	0.547	0.069	2610	420	0.168	0.052	0.43	0.12
S53-101-E1-1	0.214	0.028	1.404	0.077	3100	120	0.07	0.0036	0.304	0.014
S53-101-E1-3	2.58	0.24	6.33	0.46	8680	630	0.444	0.046	3.22	0.27
S53-101-E1-4	0.304	0.018	0.81	0.054	3630	190	0.07	0.0071	0.42	0.027
S53-101-E1-5	3.17	0.44	17.8	5.3	8850	670	0.348	0.034	3.73	0.75

Source file	^{107}Ag ppm	SD (2σ)	^{121}Sb ppm	SD (2σ)	^{130}Te CPS	SD (2σ)	^{197}Au ppm	SD (2σ)	^{209}Bi ppm	SD (2σ)
S53-101-E2-1	0.411	0.034	0.445	0.062	2670	120	0.07	0.0068	0.314	0.027
S53-101-E2-2	0.413	0.073	0.644	0.038	1240	140	0.07	0.0071	0.562	0.037
S53-101-E2-3	0.488	0.039	9.9	1.9	18220	510	0.07	0.0071	0.462	0.042
S53-101-E2-4	0.213	0.014	3.73	0.43	432	78	0.07	0.0043	0.264	0.01
S68-107-B1-4	1.695	0.088	4.24	0.26	179800	3500	0.229	0.017	39.7	2
S69-25-A1-1	0.63	0.19	0.25	0.1	11020	340	0.07	0.002	0.024	0.0064
S69-25-A1-2	0.002	0.0012	0.0068	0.0063	6570	220	0.07	0.00045	0.0024	0.0013
S69-25-A1-4	1.25	0.29	0.289	0.048	9300	1600	0.07	0.035	0.452	0.076
S69-25-A1-5	1.85	0.37	0.74	0.12	14200	410	0.174	0.033	0.83	0.15
S69-25-A1-6	0.023	0.0062	0.0163	0.0073	4370	370	0.07	0.0012	0.0117	0.0033
S69-25-A2-1	0.457	0.057	0.68	0.19	7710	540	0.07	0.0068	0.108	0.02
S69-25-A2-2	0.256	0.034	0.233	0.03	8080	500	0.07	0.0046	0.087	0.015
S69-25-A2-3	0.0227	0.0047	0.0143	0.0065	6070	220	0.07	0.0013	0.0065	0.0012
S69-25-A2-4	0.0123	0.0034	0.084	0.047	5840	290	0.07	0.00086	0.0109	0.0017
Pyrite3										
S53-103-1	0.367	0.018	8	1	8290	210	0.07	0.006	0.917	0.028
S53-103-2	0.385	0.039	7.34	0.42	7400	170	0.07	0.0056	0.555	0.028
S53-103-3	0.1105	0.0096	1.22	0.1	24800	1400	0.07	0.0028	0.327	0.036
S53-103-4	0.971	0.074	9.7	1.7	40900	4800	0.159	0.019	2.62	0.15
A685-20-1	0.0439	0.0079	0.19	0.031	2660	210	0.07	0.0023	0.055	0.01
A685-20-2	0.049	0.014	0.202	0.061	2250	130	0.07	0.0034	0.064	0.019
A685-20-3	0.028	0.015	0.122	0.025	30850	510	0.07	0.029	0.029	0.012
A685-20-4	0.021	0.026	0.061	0.013	6280	320	0.07	0.0026	0.0192	0.004
A685-20-5	0.0021	0.0022	0.0067	0.0054	7600	1500	0.103	0.014	0.00055	0.0006
S68-107-B1-1	0.599	0.038	4.24	0.19	22800	2100	0.07	0.0088	7.02	0.87
S68-107-B1-2	1.95	0.043	9.01	0.18	165400	3200	0.245	0.01	61.5	1.2
S68-107-B1-3	0.098	0.01	0.293	0.033	71400	4200	0.07	0.0059	2.34	0.22
S68-107-B2-1	0.044	0.013	0.0224	0.0074	549	87	0.07	0.0028	0.0474	0.0079
S68-107-B2-2	0.184	0.051	0.122	0.019	4260	380	0.07	0.0038	0.51	0.09
S68-107-B2-3	0.0089	0.0025	0.0433	0.0084	2180	300	0.07	0.0019	0.221	0.041
S68-107-B3-1	2.01	0.28	2.25	0.13	7360	810	0.161	0.022	1.31	0.14
S68-107-B3-2	0.371	0.037	1.584	0.072	6480	230	0.07	0.007	0.69	0.034
S68-107-B3-3	0.435	0.045	1.88	0.14	4010	170	0.07	0.0065	0.806	0.063
S68-107-B3-4	5.21	0.39	6.7	6.6	11480	470	0.266	0.03	2.02	0.12
S68-140-20C1-1	1.28	0.22	1.82	0.5	8000	1100	0.07	0.0091	0.88	0.12
S68-140-20C1-2	0.78	0.1	0.288	0.044	34200	1900	0.07	0.017	0.325	0.037
S68-140-20C1-3	0.34	0.033	0.647	0.073	60000	10000	0.29	0.041	0.379	0.04
S68-140-20C1-4	1.63	0.46	2.65	0.99	37100	4500	0.156	0.033	1.42	0.33
S68-140-20C1-5	1.42	0.86	0.5	0.12	41800	1100	0.07	0.0066	3.2	1.7
S68-140-20C1-6	0.0023	0.0011	0.0048	0.0072	42800	1100	0.07	0.0018	0.0087	0.0032
S68-140-20C2-1	0.254	0.04	0.676	0.071	31700	2700	0.07	0.0083	3.88	0.39
S68-140-20C2-2	2.71	0.47	0.54	0.12	33100	3600	1.33	0.24	3.38	0.76
S68-140-20C2-3	0.085	0.013	0.227	0.03	1400	140	0.07	0.0039	2.06	0.53
S68-140-20C2-4	0.0115	0.0038	0.055	0.016	17470	600	0.07	0.0034	1.49	0.36
S50-33.90-D1-1	0.0103	0.0038	0.0124	0.0059	4320	210	0.07	0.0013	0.0048	0.0014
S50-33.90-D1-2	0.033	0.011	0.489	0.092	3370	520	0.195	0.041	0.51	0.12
S50-33.90-D1-3	0.472	0.05	0.812	0.078	18300	1100	0.07	0.004	9.31	0.59
S50-33.90-D1-4	0.877	0.038	1.165	0.05	75400	3700	0.282	0.013	19.22	0.69
S50-33.90-D1-5	0.235	0.025	0.357	0.031	31200	2700	0.07	0.0072	7.58	0.84
S50-33.90-D2-1	0.115	0.017	0.217	0.033	2350	210	0.07	0.0038	0.1087	0.0089
S50-33.90-D2-2	0.284	0.018	0.765	0.063	11640	810	0.07	0.006	3.66	0.13
S50-33.90-D2-3	0.409	0.038	4.87	0.53	17450	260	0.364	0.017	7.57	0.58
S50-33.90-D2-4	0.154	0.011	0.69	0.052	1881	94	0.07	0.004	1.84	0.13

Source file	^{107}Ag ppm	SD (2σ)	^{121}Sb ppm	SD (2σ)	^{130}Te CPS	SD (2σ)	^{197}Au ppm	SD (2σ)	^{209}Bi ppm	SD (2σ)
S50-33.90-D2-5	0.166	0.021	0.473	0.063	14160	410	0.07	0.0056	3.16	0.56
S50-33.90-D2-6	0.384	0.013	3.4	0.17	4000	330	0.101	0.013	2.34	0.16
ONG-1-1	1.2	0.25	7.64	0.42	6570	610	0.138	0.015	1.59	0.4
A198-86-40-1	0.101	0.026	0.579	0.097	4710	160	0.07	0.0056	0.171	0.026
A198-86-40-2	0.0142	0.0034	0.065	0.024	3120	210	0.07	0.0019	0.0243	0.0062
A198-86-40-3	2.46	0.45	0.925	0.072	3630	300	0.108	0.015	0.21	0.021
A198-86-40-4	1.59	0.33	2.27	0.43	1070	130	0.121	0.022	0.88	0.23
A198-86-40-5	0.312	0.028	10.2	1.3	1070	72	0.07	0.0059	0.351	0.031

All values below the detection limits were treated using an arbitrary value by dividing the detection limit by the square root of 2 (b.d.l./√2). Arbitrary value of 0.07 was used.

APPENDIX F

Fluid inclusion petrography and microthermometry results.

QUARTZ PYRITE-Au VEINS

Sample: MP03

Inclusion type: II

Microthermometry	T_m(ice)	T_h(LV-L)	Volume area fraction (vap)
fi1	-1.3	180	0.11
fi2	-3.5	214	0.15
fi3	-5.2	203.7	0.15
fi4	-3.6	202	0.14
fi8	-4.6	210	0.15
fi7	-3.3	210.5	0.15
fi6	-4.1	241.7	0.18
fi5	-4.2	212.9	0.15
fi9	-3.8	208.2	0.15
fi13	-1.6	204.7	0.14
fi11	-3.6	208	0.15
fi15	-3.8	202.1	0.14
fi16	-1.1	206.7	0.14
fi14	-3.3	196.7	0.13
fi15	-3	171.9	0.11
fi16	-3.4	177.6	0.11
fi17	-3.3	170	0.11
fi18	-2.7	165.9	0.10
fi19	-3.2	194.7	0.13
fi20	-3.1	165.3	0.10
fi21	-3.4	201.2	0.14
fi22	-3.4	201.1	0.14
fi23	-3.2	204.9	0.14
fi24	-3.2	165.3	0.10
fi25	-3.6	210	0.15
fi35	-0.8	203.9	0.14
fi36	-3.3	175.8	0.11
fi37	-3.2	157.8	0.10
fi29	-4	203.9	0.14
fi30	-4	217.7	0.16
fi48	-4	221.3	0.16
fi32	-2.8	208.3	0.15
fi33	-2.8	214.8	0.15
fi34	-4	221.2	0.16
fi35	-4	211.6	0.15
fi36	-4	211.6	0.15
fi56	-0.8	201.9	0.14
fi38	-2.8	206.3	0.14
fi39	-2.8	200.5	0.14
fi40	-2.9	204.5	0.14
fi41	-1.2	191.3	0.13
fi42	-2.6	187.6	0.12
fi52	-3.2	200.7	0.14
fi53	-3.1	196.3	0.13
fi54	-3.8	180.7	0.12

Microthermometry	T_m(ice)	T_h(LV-L)	Volume area fraction (vap)
fi55	-3	191.8	0.13
fi47	-0.8	191.5	0.12
fi48	-1.8	194	0.13
fi49	-3.1	160.9	0.10
fi50		204.6	
fi51		205	
fi52		210	
fi53		178.1	
fi54		204.8	
fi55		189.3	
fi56		165	
fi57		203.5	
fi58		147.8	
fi59		202.9	
fi60		202.9	
fi61		204.3	
fi62		190.8	
fi63		190.8	
fi64		197.8	
fi65	-2.8		
fi66	-3.1		
fi67	-3.4		

Sample: MP01.1
Inclusion type: II

Microthermometry	T_m(ice)	T_h(LV-L)	Volume area fraction (vap)
fi1	-3	181.1	0.12
fi2	-3	181.1	0.12
fi3	-2.9	168	0.11
fi4	-2.9	175	0.11
fi5	-3.2	193.3	0.13
fi6	-3.3	167.8	0.11
fi7	-3.1	177.8	0.12
fi8	-3.1	185.9	0.12
fi9	-3.2	168.3	0.11
fi10	-3.1	169.9	0.11
fi11	-3	174.8	0.11
fi12	-3	174.8	0.11
fi13	-3.1	175	0.11
fi14	-3.1	167.1	0.11
fi15	-3	173	0.11
fi16	-3	189.2	0.13
fi17	-3	186.6	0.12
fi18	-3.1	194.7	0.13
fi19	-3.1	186.6	0.13
fi20	-2.9	183	0.12
fi21	-2.9	176.8	0.12
fi22	-2.9	164.6	0.10
fi23	-3.1	181	0.12
fi24	-3.1	189.2	0.13

Microthermometry	T_m(ice)	T_h(LV-L)	Volume area fraction (vap)
fi25	-3	186.3	0.12
fi26		176.1	
fi27	-3		

Sample: MP02
Inclusion type: I

Microthermometry	$T_m(CO_2)$	T_m(ice)	T_m(clathrate)	$T_h(CO_2)$	T_h(total)	Volume area fraction (liq) after clathrate melting*
fi1	-57	-3.2	11.6	30.9	177.5	0.84
fi2	-56.6	-3	--	31	165.1	0.85
fi3	-56.6	-3.6	--	30.9	157.4	0.89
fi4	-56.6	-3.3	11.2	--	178.5	0.89
fi5	-57.5	-3	--	23.7	158.3	0.91
fi6	-56.6	-2.9	--	19.9	146.3	0.89
fi7	-56.6	-2.8	8.6	25.4	153.3	0.91
fi8	-56.8	-3.2	9.9	--	158.8	0.87
fi9	-57	-3	--	30.8	161.2	0.86

*Petrographical approach

Sample: MP02
Inclusion type: II

Microthermometry	T_m(ice)	T_h(LV-L)	Volume area fraction (vap)
fi1	-2.8	192.3	0.13
fi2	-3.4	160.8	0.10
fi3	-2.9	179.4	0.12
fi4	-3.4	173.9	0.12
fi5	-3.1	176.5	0.12
fi6	-2.8	194	0.13
fi7	-3.8	179.2	0.12
fi8	-3	157.7	0.10
fi9	-3.1	197.4	0.13
fi10	-3	211.3	0.15
fi11	-2.7	205	0.14
fi12	-3	196.4	0.13
fi13	-3.2	189.4	0.13
fi14	-3.2	190.1	0.13

SULPHIDE-SULPHOSALT Au QUARTZ VEINS

Sample: A685-5
Inclusion type: II

Microthermometry	T_m(ice)	T_h(LV-L)	Volume area fraction (vap)
fi1	-3.2	208.2	0.15
fi2	-2.7	187.5	0.12
fi3	-3.1	212.1	0.15
fi4	-2.8	208.4	0.15
fi5	-2.4	225.7	0.17
fi6	-2.6	226.6	0.17

Microthermometry	T_m(ice)	T_h(LV-L)	Volume area fraction (vap)
fi7	-3.3	243.2	0.19
fi8	-3.3	215.7	0.15
fi9	-3.4	199.3	0.14
fi10	-3	213	0.15
fi11	-3.2	215.7	0.15
fi12	-2.9	212.8	0.15
fi13	-2.8	219.7	0.16
fi14	-3	205.4	0.14
fi15	-2.8	184.6	0.12
fi16	-2.8	203.6	0.14
fi17	-2.8	206.4	0.14
fi18	-3.2	211.9	0.15
fi19	-3.4	217.9	0.16
fi20	-3	220.5	0.16
fi21	-2.6	220.5	0.16
fi22	-2.5	215	0.15
fi23	-2.8	201.5	0.14
fi24	-3	214.2	0.15
fi25	-3.2	212.9	0.15
fi26	-3	204.9	0.15
fi27	-2.9	201.5	0.14
fi28	-2.7	223.4	0.16
fi29	-2.4	214.9	0.15
fi30	-3.2	207.4	0.14
fi31	-4.6	216.5	0.15
fi32	-3	218.2	0.16
fi33	-3.2	218.7	0.16
fi34	-3.2	212.6	0.15
fi35	-3.6	218.7	0.16
fi36	-3.1	216.7	0.15
fi37	-2.6	222	0.16
fi38	-2.7	205.5	0.14
fi39	-2.8	219	0.16
fi40	-3.6	220.7	0.16
fi41	-3.2	184.7	0.12
fi42	-2.8	221.6	0.16
fi43	-2.8	223.7	0.16
fi44	-3.2	223	0.16
fi45	-2.9	222.4	0.16
fi46	-2.7	237.7	0.18
fi47	-3.1	217	0.16
fi48	-3.2	213.5	0.15
fi49	-3.1	221.1	0.16

Sample: A676-73.10
Inclusion type: II

Microthermometry	T_m(ice)	T_h(LV-L)	Volume area fraction (vap)
fi1	-1.9	207.4	0.14
fi2	-2.6	211.2	0.15
fi3	-2.7	210.1	0.15

Microthermometry	T_m(ice)	T_h(LV-L)	Volume area fraction (vap)
fi4	-2.8	197.3	0.13
fi5	-2.8	195.9	0.13
fi6	-2.8	208.2	0.14
fi7	-2.7	211	0.15
fi8	-2.4	205.5	0.14
fi9	-2.2	204.4	0.14
fi10	-1.7	207	0.14
fi11	-3.2	209.3	0.15
fi12	-2.7	158.4	0.10
fi13	-2.8	212.3	0.15
fi14	-2.6	204.1	0.14
fi15	-2.6	206.9	0.14
fi16	-2	188.3	0.12
fi17	-2.7	198.1	0.13
fi18	-2.8	189.6	0.13
fi19	-2.9	207.4	0.14
fi20	-1.8	203.6	0.14
fi21	-1.7	196.2	0.13
fi22	-1.8	191	0.12
fi23	-3	199.9	0.14
fi24	-1.7	199.5	0.13
fi25	-3.2	200.7	0.14
fi26	-1.2	199	0.13

Sample: A685-20
Inclusion type: II

Microthermometry	T_m(ice)	T_h(LV-L)	Volume area fraction (vap)
fi1	-2.8	191.4	0.13
fi2	-1.7	214.4	0.15
fi3	-1.6	200.1	0.13
fi4	-2.8	175.4	0.11
fi5	-3.1	216.6	0.15
fi6	-1.9	214.1	0.15
fi7	-3.1	230.4	0.17
fi8	-1.6	205	0.14
fi9	-0.5	215.7	0.15
fi10	-2	199.3	0.13
fi11	-2.5	205	0.14
fi12	-2.9	197.1	0.13
fi13	-3	225.2	0.16
fi14	-3.2	206.2	0.14
fi15	-3.2	207.5	0.14
fi16	-3	225	0.16
fi17	-3	257	0.21
fi18	-3.2	198.3	0.14
fi19	-2.8	199.6	0.14

BARREN VEINS

Sample: GRS08
Inclusion type: II

Microthermometry	T_m(ice)	T_h(LV-L)	Volume area fraction (vap)
fi1	-2.9	199.6	0.14
fi2	-1.6	212	0.15
fi3	-1.6	195.6	0.13
fi4	-1.7	199.8	0.13
fi5	-3.2	203.4	0.14
fi6	-2.9	200	0.14
fi7	-2.9	192	0.13
fi8	-3.1	207.7	0.14
fi9	-2.8	199.8	0.14
fi10	-2.8	208.9	0.15
fi11	-2.8	210	0.15
fi12	-3.1	214.1	0.15
fi13	-3.8	240	0.18
fi14	-3.2	212.7	0.15
fi15	-2.9	218.2	0.16
fi16	-2.6	203.5	0.14
fi17	-2.9	209.9	0.15
fi18	-2.8	210.1	0.15
fi19	-2.8	204.9	0.14
fi20	-2.8	198.1	0.13
fi21	-2.2	199.2	0.13
fi22	-3.4	206.8	0.14
fi23	-2.9	217.2	0.15
fi24	-2	206.8	0.12
fi25	-2.4	180.6	0.12
fi26	-3.1	193.5	0.13
fi27	-2.8	212.6	0.15
fi28	-2.1	211.6	0.15
fi29	-2.8	284	0.25
fi30	-2.6		
fi31	-2.6		
fi32	-2.6		
fi33	-2.9		
fi34	-3.1		
fi35	-2.7		
fi36	-0.8		
fi37		199.2	
fi38		222	

Sample: A687-235
Inclusion type: II

Microthermometry	T_m(ice)	T_h(LV-L)	Volume area fraction (vap)
fi1	-1.9	206.9	0.14
fi2	-1.4	206.9	0.14
fi3	-2	208.9	0.15
fi4	-2.4	219.1	0.16
fi5	-1.8	212.9	0.15
fi6	-1.8	318.6	0.33

Microthermometry	T_m(ice)	T_h(LV-L)	Volume area fraction (vap)
fi7	-1.9	262.6	0.22
fi8	-1.8	267.9	0.23
fi9	-1.7	293	0.27
fi10	-1.9	338.4	0.37
fi11	-1.6	344.7	0.39
fi12	-1.8	275.4	0.24
fi13	-2.3	165.6	0.10
fi14	-2.2	303.3	0.29
fi15	-1.4	182.9	0.12
fi16	-1.6	186.4	0.12
fi17	-2	193.3	0.13
fi18	-2	190.3	0.13
fi19	-2	197.2	0.13
fi20	-2	200.5	0.14
fi21	-1.6	223.9	0.16
fi22	-1.3	169.7	0.10
fi23	-2.3		
fi24	-2.4		

Sample:A687-235-dol
Inclusion type: II

Microthermometry	T_m(ice)	T_h(LV-L)	Volume area fraction (vap)
fi1	-1.6	317.4	0.32
fi2	-1.6	324.4	0.34
fi3	-1.7	331.5	0.37
fi4	-1.6	332.4	0.37
fi5	-1.6	364.5	0.44
fi6	-1.7	373.6	0.46
fi7	-1.6	350.3	0.40
fi8	-1.6	345.9	0.39
fi9	-1.7	348.9	0.40
fi10	-1.9	233.3	0.18
fi11	-1.8	248.9	0.22
fi12	-1.6	281.9	0.28
fi13	-1.6	291.6	0.30
fi14	-1.7	326.9	0.35
fi15	-2.5	332.6	0.34
fi16	-1.6	191.3	0.12
fi17	-1.9	194.9	0.15
fi18	-1.7	195.4	0.13
fi19	-1.6	227.6	0.17
fi20	-1.8	386.9	0.50

APPENDIX G

Representative crush leach analyses on quartz and carbonate

	Sample code		F^- µg/L	Cl^- µg/L	Br^- µg/L	SO_4^{2-} µg/L	I^- µg/L	Li^+ µg/L	Na^+ µg/L	K^+ µg/L	Mg^{2+} µg/L	Ca^{2+} µg/L	Na/Cl	Cl/Br	log (I/Cl)	log (Br/Cl)	$Br/Cl*10^3$ molar ratio
1	A192-55.2	*	23.9	3537.5	5.5	549.5	0.6	3.3	6651.8	13.3	8.8	309.7	2.90	1462.10	-3.79	-2.81	1.06
2	A192-56.5	*	17.3	3241.7	4.3	570.6	0.2	1.2	2101.9	305.7	28.0	415.8	1.00	1702.94	-4.25	-2.88	0.89
3	A198-109.80	*	32.1	1883.8	3.2	1240.4	0.3	2.3	3609.9	265.4	133.1	1034.5	2.96	1339.89	-3.84	-2.77	0.57
4	A198-11	*	15.0	4732.9	6.4	2192.5	0.3	4.7	3529.0	399.6	97.9	955.3	1.15	1676.34	-4.18	-2.87	1.88
5	A198-139.20	*	83.4	1958.8	3.4	510.6	0.1	1.2	4352.4	16.8	1921.1	7052.6	3.43	1299.77	-4.18	-2.76	0.20
6	A198-171.90	*	12.9	2981.8	3.2	3300.1	0.2	7.0	3260.3	280.2	3949.4	8280.5	1.69	2068.16	-4.22	-2.96	1.58
7	A198-29.6	*	76.8	2651.4	3.1	1330.3	0.3	3.9	3818.9	185.2	249.1	1335.4	2.22	1942.29	-3.89	-2.94	0.22
8	A198-44.2	*	6.0	2243.5	2.7	663.2	0.2	1.1	1223.5	178.9	581.4	3976.1	0.84	1900.00	-4.00	-2.93	1.46
9	A198-56	*	11.0	4125.7	6.9	913.4	0.5	4.9	3141.6	232.1	15.0	163.7	1.17	1342.42	-3.88	-2.77	2.27
10	A198-86.4	*	15.3	1327.1	2.3	223.8	0.2	1.7	2629.4	112.1	161.5	6332.1	3.06	1323.36	-3.85	-2.77	0.63
11	A634-28	*	16.5	7329.6	5.0	992.0	0.2	6.3	8464.4	2529.6	208.7	1097.6	1.78	3315.57	-4.48	-3.17	1.30
12	A634-28.3	*	13.4	5354.8	4.5	1911.4	b.d.l.	6.2	4180.9	815.7	63.1	616.5	1.20	2674.84		-3.07	1.26
13	A634-30.40	*	12.3	2028.1	3.2	741.7	0.5	4.8	5941.0	193.3	5440.0	9928.3	4.52	1437.45	-3.59	-2.80	1.44
14	A635-15.9	*	4.3	3753.0	5.0	1323.7	0.3	3.6	2947.1	301.5	18.3	221.0	1.21	1690.72	-4.11	-2.88	4.00
15	A635-21	*	51.8	1779.1	b.d.l.	692.6	0.3	3.6	4266.2	116.4	147.0	1387.8	3.70		-3.71		
16	A635-22	*	127.5	1030.1	b.d.l.	4085.8	0.2	8.1	7039.4	734.7	6326.8	22160.6	10.54		-3.66		
17	MP01	*	45.1	3107.3	3.9	4395.6	0.3	4.4	2547.0	1792.4	130.8	1280.5	1.26	1818.03	-4.07	-2.91	0.52
18	MP01.2	*	18.3	4022.5	6.0	2857.5	0.3	5.6	3316.2	867.8	125.4	9033.1	1.27	1514.85	-4.15	-2.83	1.65
19	MP02	*	20.8	3953.6	4.5	2092.5	0.2	5.6	2708.8	824.4	103.4	1596.8	1.06	1994.22	-4.22	-2.95	0.94
20	MP03	*	18.7	2546.0	1.1	4662.0	b.d.l.	3.4	1541.3	784.6	108.6	1029.3	0.93	5432.97		-3.38	0.26
21	ONG02	*	7.5	2055.9	2.2	297.7	0.2	1.1	1148.3	169.7	63.5	598.5	0.86	2074.51	-3.98	-2.96	0.98
22	ONG05	*	28.1	2221.0	1.7	1813.4	0.2	3.9	2518.7	287.0	322.6	1062.9	1.75	3006.71	-4.05	-3.13	0.32
23	ONG1-1	*	176.0	2061.4	2.0	14732.2	0.1	5.1	1610.5	1573.7	343.0	5403.0	1.20	2292.49	-4.22	-3.01	0.14
24	S53-103.00	*	29.6	1960.0	3.7	663.9	0.4	1.6	4455.0	189.4	15.8	120.1	3.51	1183.93	-3.75	-2.72	0.65
28	S69-25	*	15.6	1926.0	0.9	560.6	b.d.l.	0.8	1071.8	125.3	18.1	227.7	0.86	4632.69		-3.31	0.22
29	S94-27.65	*	28.6	3556.0	3.5	4470.1	1.4	7.4	4048.1	332.3	7481.3	13920.4	1.76	2297.25	-3.40	-3.01	0.92
30	S69-61.35	*	27.1	2536.6	2.9	1541.5	0.1	1.5	4229.1	153.9	117.2	1344.9	2.57	1966.99	-4.35	-2.94	0.63
31	A192-177.2	*	9.4	2903.5	2.8	3417.5	0.2	7.5	2265.3	586.4	111.7	852.7	1.20	2320.54	-4.10	-3.01	1.58
32	A192-225	*	13.0	4560.5	8.1	603.9	0.2	4.4	2876.2	632.7	35.2	547.2	0.97	1274.80	-4.41	-2.75	2.04

	Sample code		F^- µg/L	Cl^- µg/L	Br^- µg/L	SO_4^{2-} µg/L	I^- µg/L	Li^+ µg/L	Na^+ µg/L	K^+ µg/L	Mg^{2+} µg/L	Ca^{2+} µg/L	Na/Cl	Cl/Br	log (I/Cl)	log (Br/Cl)	$Br/Cl*10^3$ molar ratio
33	A198-176.6	*	84.7	1586.2	1.5	215.9	0.5	0.5	2912.4	50.9	6.8	65.4	2.83	2424.46	-3.47	-3.03	0.08
34	A634-35	*	257.2	1064.1	b.d.l.	2684.6	0.6	1.2	10440.6	12.4	796.1	8521.4	15.13		-3.26		
35	A192-137.1	**	6.9	4535.8	8.8	2980.7	1.9	6.6	5469.6	406.4	2344.3	3628.2	1.86	1157.37	-3.38	-2.71	2.21
36	A192-143.8	**	15.0	4343.6	9.1	344.9	0.4	2.7	2720.7	573.0	97.5	1149.1	0.97	1072.67	-4.02	-2.68	1.04
37	A192-172.6	**	0.5	b.d.l.	b.d.l.	14.5	0.3	4.0	3104.3	632.1	345.7	686.2					
38	A35-33.85	**	12.9	2547.0	5.3	182.2	0.5	5.9	2448.2	439.9	175.0	775.3	1.48	1088.37	-3.75	-2.68	0.46
39	A636-15.70	**	52.5	1327.8	b.d.l.	3180.8	0.6	3.7	4236.0	665.8	4641.6	13895.0	4.92		-3.37		
40	A636-25.65	**	7.9	3519.8	4.3	903.6	0.3	5.9	3557.0	415.6	34.0	418.5	1.56	1855.82	-4.12	-2.92	0.62
41	S50-109.40	**	18.0	2538.0	4.0	186.7	0.4	2.7	1878.9	643.6	116.9	1715.6	1.14	1444.14	-3.81	-2.81	0.39
42	S68-113.7	**	39.8	3072.9	2.7	1309.7	b.d.l.	4.7	3325.3	374.9	59.5	314.7	1.67	2601.46		-3.06	0.33
43	S68-26.5	**	11.8	3894.7	4.5	334.7	0.4	1.3	4137.0	422.7	34.6	543.4	1.64	1933.90	-3.98	-2.93	0.80
44	S68-34.9	**	12.0	3291.2	5.9	237.4	0.2	0.2	1391.1	263.1	228.6	1474.2	0.65	1255.12	-4.24	-2.75	1.11
45	S69-112.50	**	10.0	3528.2	b.d.l.	1536.4	1.3	8.4	2964.9	286.6	5543.1	19518.9	1.30		-3.44		
46	S69-32.6	**	b.d.l.	1452.0	2.5	241.0	0.2	b.d.l.	2855.9	14.7	12.5	253.7	3.03	1331.69	-3.79	-2.77	0.37
47	S69-32.8	**	35.2	1032.2	1.4	582.0	b.d.l.	b.d.l.	1973.5	14.9	b.d.l.	30.1	2.95	1715.15		-2.88	0.67
48	S69-64.45	**	29.2	2498.7	7.7	1994.7	0.3	8.0	2393.4	1025.0	11953.0	13433.6	1.48	734.78	-3.90	-2.51	0.75
49	S94-21.3	**	23.6	2465.1	2.9	225.2	0.3	1.3	2524.7	272.3	63.3	588.0	1.58	1900.57	-3.90	-2.93	0.28
50	A676-73.10	**	32.0	2950.6	4.4	780.2	0.4	5.9	3157.7	569.1	297.2	2668.8	1.65	1518.25	-3.88	-2.83	0.31
51	A683-46.80	**	14.8	1757.1	2.7	209.9	0.2	3.0	1559.2	458.1	46.5	472.6	1.37	1446.04	-3.93	-2.81	0.31
52	A683-47.00	**	17.1	2051.6	3.7	349.4	0.3	4.6	1889.3	540.0	76.8	1101.8	1.42	1247.43	-3.83	-2.74	0.35
53	A685-5	**	11.2	2144.2	3.1	797.7	0.2	7.1	1871.0	442.2	38.2	270.0	1.35	1541.55	-4.15	-2.84	0.34
54	A685-89	**	10.7	3246.5	5.6	5976.7	0.2	13.6	3433.2	831.1	344.1	2085.9	1.63	1305.26	-4.24	-2.76	1.24
55	A687-163	**	109.3	5049.1	11.4	218.9	0.4	5.5	3329.9	857.7	114.6	1106.4	1.02	1000.63	-4.09	-2.65	0.24
56	A687-165	**	15.9	2470.7	2.8	2378.8	0.9	2.4	2396.1	924.4	417.8	1874.7	1.50	1999.29	-3.45	-2.95	0.69
57	A687-235	**	11.6	3200.4	8.0	387.2	0.2	3.9	2620.7	502.7	146.3	1010.8	1.26	896.87	-4.25	-2.60	0.97
58	A687-50.35	**	19.1	4201.1	8.0	182.4	0.2	4.9	2714.4	560.2	65.6	639.3	1.00	1186.29	-4.41	-2.72	0.61
59	A687-67	**	16.7	3172.6	5.6	172.5	0.2	5.9	2634.2	500.8	75.1	895.2	1.28	1271.78	-4.19	-2.75	0.43
60	SB-01	**	11.7	3169.1	4.0	1131.5	0.1	b.d.l.	b.d.l.	b.d.l.	b.d.l.	b.d.l.		1799.54	-4.39	-2.90	0.63
61	T005-198	**	19.4	2616.4	5.0	3642.5	0.4	10.7	2345.8	392.5	368.4	1957.7	1.38	1177.59	-3.82	-2.72	0.70
62	T005-35.25	**	14.5	1337.0	1.0	611.1	0.3	1.3	1763.5	248.6	270.8	1652.0	2.03	2874.25	-3.63	-3.11	0.19
63	TRD5-30.40	**	20.6	2332.1	n.a	5308.3	0.6	5.1	3359.8	969.1	7901.9	20459.4	2.22		-3.58		

	Sample code		F^- µg/L	Cl^- µg/L	Br^- µg/L	SO_4^{2-} µg/L	I^- µg/L	Li^+ µg/L	Na^+ µg/L	K^+ µg/L	Mg^{2+} µg/L	Ca^{2+} µg/L	Na/Cl	Cl/Br	log (I/Cl)	log (Br/Cl)	Br/Cl*10^3 molar ratio
1	A198-27.65	#	19.4	5182.2	3.8	2727.4	0.2	2.4	3339.3	862.4	151.7	1312.6	0.99	3065.71	-4.50	-3.13	0.95
2	S53-57.40	#	38.3	1491.1	1.6	643.3	0.8	2.4	4910.7	138.7	1366.5	10968.0	5.08	2107.85	-3.27	-2.97	1.21
3	A634-42	§	23.6	3029.5	3.5	260.6	1.0	7.2	1340.5	654.8	5454.3	12691.1	0.68	1948.74	-3.50	-2.94	0.74
4	A634-5.5	§	18.1	3241.3	6.4	863.3	2.6	11.1	2464.3	390.2	1471.9	16491.7	1.17	1137.30	-3.09	-2.70	1.76
5	FOS	§	51.0	1255.0	4.5	3505.0	1.2	1.2	1161.3	1448.0	1963.3	10987.5	1.43	629.35	-3.02	-2.45	1.37
6	S54-72.90	§	43.5	2822.9	5.1	886.9	2.4	7.8	2551.3	310.7	15715.0	13816.1	1.39	1249.15	-3.07	-2.74	1.53
7	S54-78.30	§	23.8	4953.8	10.4	1131.7	2.5	17.8	4092.7	343.0	2549.3	10702.6	1.27	1076.89	-3.30	-2.68	2.97
8	S68-69	§	8.5	4699.7	6.5	600.3	4.6	1.3	7102.5	85.9	29.2	94.4	2.33	1618.04	-3.01	-2.86	2.74
9	S94-106.8	§	24.1	2139.5	2.6	629.2	0.9	1.0	1296.3	361.0	288.1	7199.4	0.93	1868.68	-3.39	-2.92	0.63
10	S94-40.55	§	23.5	5011.1	8.6	396.3	0.8	4.2	3468.1	784.5	83.7	1662.3	1.07	1318.11	-3.79	-2.77	2.22
11	S94-40.55	§	9.2	6318.1	19.0	734.5	5.4	15.4	5442.7	610.5	1231.7	12691.5	1.33	750.88	-3.07	-2.52	5.57
12	S94-44.30	§	20.3	3099.8	4.7	158.4	2.6	3.7	1723.0	345.2	1016.2	10682.8	0.86	1472.55	-3.07	-2.82	1.11
13	A636-31.1	§	38.2	2667.6	2.3	771.7	1.3	1.8	8066.1	25.8	51.8	160.8	4.66	2573.57	-3.31	-3.06	1.66

*Quartz veins; **Quartz separated from barren veins; #: Carbonate veins; §: Carbonate separated from barren veins; b.d.l.: below detection li

Geothermometry based on cations in fluid leachates

		Na-K[1] °C	Na-K[2] °C	Na-Li[1] °C	Mg-Li[1] °C	Na-K[1] °C
S54-72.90	Calcite	257.3	248.5	216.6	209.9	56.5
S54-78.30	Calcite	221.3	218.6	177.0	233.3	98.4
S94-27.65	Calcite	219.4	217.0	175.0	178.6	63.2
Minimum		219.4	217.0	175.0	178.6	56.5
Maximum		257.3	248.5	216.6	233.3	98.4
Average		232.7	228.0	189.5	207.3	72.7
S.D.		21.4	17.8	23.5	27.4	22.5
A198-56	Ank-Dol	210.1	209.2	165.0	170.0	136.6
A634-42	Ank-Dol	454.7	401.2	455.0	248.5	66.3
A634-5.5	Ank-Dol	286.0	271.9	249.0	235.4	92.9
S68-26.5	Ank-Dol	239.7	234.0	197.2	98.4	86.1
S68-34.9	Ank-Dol	307.2	288.9	273.3	77.4	29.8
S68-69	Ank-Dol	92.4	105.8	249.0	78.9	88.2
S69-112.50	Ank-Dol	234.4	229.6	191.3	204.8	69.7
S69-25	Ank-Dol	253.1	245.1	212.0	131.9	80.8
S94-21.3	Ank-Dol	245.0	238.4	203.0	116.8	77.9
S94-40.55	Ank-Dol	330.3	307.1	300.3	157.1	105.6
S94-40.55	Ank-Dol	248.9	241.6	207.3	204.8	104.4
S94-44.30	Ank-Dol	314.4	294.6	281.8	188.5	70.5
S53-57.40	Ank-Dol	139.6	148.2	91.2	116.3	57.7
Minimum		92.4	105.8	91.2	77.4	29.8
Maximum		454.7	401.2	455.0	248.5	136.6
Average		258.2	247.4	236.6	156.1	82.0
S.D.		89.1	72.9	85.6	57.7	26.0
A192-137.1	Quartz	210.7	209.7	165.6	156.7	74.0
A192-143.8	Quartz	320.8	299.7	289.2	148.0	91.9
A192-172.6	Quartz	316.5	296.2	284.2	160.5	85.5
A192-177.2	Quartz	348.9	321.7	322.5	214.3	118.2
A192-225	Quartz	326.5	304.2	295.9	169.1	119.7
A192-56.5	Quartz	276.4	264.1	238.0	123.2	87.3
A198-11	Quartz	249.9	242.4	208.4	162.3	106.8
A198-171.90	Quartz	223.5	220.5	179.5	188.4	69.5
A198-27.65	Quartz	348.6	321.4	322.1	131.9	82.7
A198-44.2	Quartz	277.0	264.6	238.7	143.1	50.1
A35-33.85	Quartz	300.9	283.9	266.1	195.1	104.9
A634-28.3	Quartz	311.1	292.0	277.9	167.2	121.0
A635-15.9	Quartz	239.9	234.1	197.3	158.0	123.9
A636-15.70	Quartz	285.1	271.2	248.0	141.2	53.5
A636-25.65	Quartz	253.1	245.0	211.9	173.7	129.5

		Na-K[1] °C	Na-K[2] °C	Na-Li[1] °C	Mg-Li[1] °C	Na-K[1] °C
A676-73.10	Quartz	301.3	284.1	266.5	179.8	97.3
A683-46.80	Quartz	367.5	336.0	344.9	182.0	104.5
A683-47.00	Quartz	363.3	332.8	339.9	195.2	109.3
A685-5	Quartz	336.2	311.8	307.4	224.1	133.7
A685-89	Quartz	339.5	314.3	311.3	226.6	119.3
A687-163	Quartz	348.2	321.1	321.7	173.6	109.0
A687-165	Quartz	411.5	369.3	399.4	146.7	70.1
A687-235	Quartz	308.9	290.3	275.4	167.1	95.6
A687-50.35	Quartz	318.2	297.6	286.2	177.8	113.4
A687-67	Quartz	307.8	289.4	274.1	190.3	117.0
MP01.2	Quartz	350.4	322.8	324.4	174.6	108.1
MP02	Quartz	372.9	340.1	351.5	185.6	110.7
ONG02	Quartz	278.1	265.5	240.0	144.0	73.6
S50-109.40	Quartz	391.5	354.3	374.5	166.6	89.5
S68-130.3	Quartz	260.3	251.0	220.0	195.6	113.0
S68-144.7	Quartz	335.2	310.9	306.1	168.3	107.4
S68-69	Quartz	251.5	243.7	210.2	137.0	88.6
S69-64.45	Quartz	430.0	383.0	423.0	215.0	59.8
S94-106.8	Quartz	359.5	329.8	335.3	134.7	54.9
T005-198	Quartz	292.4	277.0	256.3	236.2	111.1
TRD5-30.40	Quartz	364.7	333.8	341.6	168.3	54.5
T005-35.25	Quartz	272.9	261.3	234.2	132.1	61.0
S69-61.35	Quartz	156.1	162.7	108.1	103.2	74.7
S68-113.7	Quartz	249.5	242.1	207.9	165.5	114.1
S53-103.00	Quartz	166.9	172.1	119.3	102.8	101.5
ONG05	Quartz	250.5	243.0	209.1	169.3	85.3
A198-109.80	Quartz	209.7	208.9	164.6	127.6	83.8
A198-29.6	Quartz	176.5	180.5	129.3	149.1	89.1
A198-86.4	Quartz	167.1	172.3	119.5	126.4	73.1
A634-28	Quartz	370.1	338.0	348.1	133.7	104.1
A634-30.40	Quartz	148.6	156.2	100.4	137.9	57.5
Minimum		148.6	156.2	100.4	102.8	50.1
Maximum		430.0	383.0	423.0	236.2	133.7
Average		294.5	277.5	260.8	164.6	93.6
S.D.		69.1	55.9	78.6	30.9	22.9

[1]Kharaka and Mariner (1989, 2012) [2]Giggenbach (1988)